2nd Spanish Fluid Mechanics Conference

SFMC 2023

Barcelona, Spain | 2 - 5 July 2023

2nd Spanish Fluid Mechanics Conference

SFMC 2023

Barcelona, Spain
2 - 5 July 2023

A publication of:
International Center for Numerical Methods in Engineering (CIMNE)
Barcelona, Spain

ISBN: 978-84-123222-4-8

Printed by: Artes Gráficas Torres S.L., Huelva 9, 08940 Cornellà de Llobregat, Spain

TABLE OF CONTENTS

FOREWORD

Dear colleague,

It is our great pleasure to welcome you to the second edition of the Spanish Fluid Mechanics Conference (SFMC23) in Barcelona from July 2nd to July 5th, 2023. Hosted by Universitat Politècnica de Catalunya, this conference follows the success of its first edition in Cádiz last year. Our primary goal remains the same as when these conferences were originally conceived: to bring together the Spanish Fluid Mechanics community, along with collaborators all over the world, in order to foster valuable scientific discussion and favour future interaction among the attendees.

We appreciate and are delighted by the great support and response received for this second edition. Around 170 researches will be participating in the conference, delivering over 150 oral presentations. The sessions cover a wide range of topics, including Computational Fluid Dynamics, Turbulence, Flow Instabilities, Combustion, Bubbles and Drops, Thin Films or Microscale and Nanoscale flows, among others. All these subjects combined address most of the fundamental aspects of fluid mechanics, and explore them from all three perspectives: theoretical, computational, and experimental. Additionally, we have included sessions dedovted to Active Matter, Biological Fluid Dynamics, Aerodynamics, Industrial Applications, and Machine Learning, which highlights the diverse application of fluid mechanics across many fields and akcnowledges the emerging integration of new Artificial Intelligence techniques into the field of fluid dynamics.

Finally, we extend our gratitude to the conference's invited speakers Marc Ávila, Henar Herrero, José Miguel Rubí, and Javier Jiménez, for their participation and support. The organizing committee heartfully acknowledges the financial support provided by the Generalitat de Catalunya (SGR-AGAUR), Ajuntament de Barcelona and UPC.

We wish you a productive conference and a delightful time in Barcelona!

Arantxa Alonso, Jezabel Curbelo, Francisco Marqués, Fernando Mellibovsky, and Álvaro Meseguer.

ACKNOWLEDGEMENTS

The Conference organizers acknowledge the Support towards the organization of the 2nd SFMC 2023 Conference to the following organizations:

Universitat Poltècnica de Catalunya (Department of Physics)

Universitat Poltècnica de Catalunya (Department of Mathematics)

MicroVec

Ajuntament de Barcelona

B5tec

Fundación BBVA - Conference partially supported by a 2022 Leonardo Grant for Researchers and Cultural Creators, BBVA Foundation

INVITED SPEAKERS

Marc Ávila
ZARM, University of Bremen, Germany
Transition to Turbulence in Pipe Flow

Henar Herrero
Universidad de Castilla-La Mancha, Spain
Schwarz Legendre collocation methods for a Rayleigh-Bénard problem

Miguel Rubí
Universitat de Barcelona, Spain
Transport and Self-assembly of Active Particles with Optimal Fuel Consumption

SUMMARY

PLENARY LECTURES

CONFERENCE TOPICS

CONTENTS

PLENARY LECTURES

CONFERENCE TOPICS

Active Matter

Aerodynamics

Biological Fluid Dynamics

Combustion

Compressible Flows

Computational Fluid Dynamics

Convection and Buoyancy-Driven Flows

Drops, Bubbles and Suspensions

Flow Instabilities

Fluid-structure interaction

Free-Surface-Flows

Industrial Applications

Machine Learning

Microscale and Nanoscale Flows

Multiphase Flows

Thin films and Coating flows

Turbulence

Turbulence (jets)

Vortex Dynamics and Vortex Flows

PLENARY LECTURES

Title: Schwarz Legendre collocation methods for a Rayleigh-Bénard problem

Abstract: Spectral collocation methods are optimal numerical methods in the sense of using small meshes obtaining results with great precision. One of the problems with these methods is ill conditioning of the resulting algebraic systems when the mesh size is increased. They present a maximum mesh size that can be considered. This size is not enough to solve the problem when the solutions have many oscillations or different scales. A strategy to increase the size of the mesh is the use of domain decomposition. Schwarz alternating is the domain decomposition technique most used for fluid dynamics problems. In this work we consider an alternating Schwarz domain decomposition method to solve each time step of a time evolution scheme or Newton method used to solve a Rayleigh-B \'enard problem. The convergence of the alternating Schwarz domain decomposition method for the evolution and stationary problems in an infinite domain with overlap has been theoretically proved. An efficient algorithm with any number of subdomains has been performed. A benchmark with solutions obtained with different methods guarantees the reliability of the method. The computational cost is similar to other methods, it is parallelizable, and turbulence can be adressed.

Prof. Henar Herrero

Title: Transition to turbulence in pipe flow

Abstract: Flows through pipes undergo a sudden transition from laminar to turbulent motion as the fluid velocity increases. Understanding this transition has occupied engineers, physicists and mathematicians alike since Reynolds' ground-breaking experiments in the nineteenth century. In this talk, I will review the recent progress on this problem from three distinct perspectives: (i) hydrodynamic stability, (ii) phase transitions and (iii) dynamical systems. Similarities to other wall-bounded flows and outstanding open points will be discussed. Special attention will be paid to the mechanisms of turbulence relaminarization, which remain poorly understood. I will discuss how the relaminarization process can be understood in the context of extreme (rare) events by applying information-theoretical measures to massive statistical ensembles of direct numerical simulations.

Prof. Dr. Marc Avila

Title: Transport and self-assembly of active particles with optimal fuel consumption

Abstract: The study of the individual and collective behavior of self-propelled particles, which convert the chemical energy of the surrounding fluid into mechanical energy, is fundamental to understanding the out-of-equilibrium nature of active matter of which many biological and soft matter systems are composed. What is the energetic cost of structure formation, how to optimize fuel consumption and what are the mechanisms that lead to the formation of self-assembled structures and instabilities are problems of current interest.

We have analyzed the active particle self-assembly process by means of a multiscale stochastic model that considers the dynamics of the particles self-consistently coupled to the fuel concentration evolution equation, initially considered inhomogeneous. The proposed model allows to identify the different aggregation regimes and to calculate the energetic cost of structure formation. The analysis of the free energy of the particles leads us to establish a thermodynamic criterion of structure formation based on the behavior of the chemical potential as a function of the fraction of particles assembled. The study is extended to the case where hydrodynamic interactions take place. Periodic fuel injection into a cell containing active particles shows the existence of a resonant regime in which particle transport is amplified with minimum fuel consumption.

J. Miguel Rubi
Departament de Fisica de la Matèria Condensada, Universitat de Barcelona

CONFERENCE TOPICS

2nd Spanish Fluid Mechanics Conference
Barcelona (2 - 5 July 2023)

Brownian dynamics and spontaneous rotation of a Janus particle in a polymer solution

Noemi D'Auria[1], Paula Martínez-Lera[1], and Marco De Corato[1]

mdecorato@unizar.es

[1]Aragon Institute of Engineering Research (I3A), University of Zaragoza, Zaragoza, Spain

Active colloids in a polymer solution can rotate spontaneously due to an instability resulting from a fore-aft asymmetric interaction between the particle and the polymers. In this work, we investigate by means of simulations the Brownian dynamics and spontaneous rotation of a spherical Janus active particle moving through a polymer solution. We model the evolution of the polymer concentration using an advection-diffusion equation, including thermal fluctuations. The results show that driving a Janus particle out of equilibrium in a polymer solution has a profound impact on its Brownian dynamics and can drastically enhance the rotational diffusion.

1 Introduction

Experimental results of Janus particles moving in a viscoelastic fluid with a polymeric solute show an increase in the rotational diffusion with the propulsion velocity (Gomez-Solano, Blokhuis and Bechinger , 2016), and sustained rotation beyond a certain value of the velocity (Narinder, Bechinger and Gomez-Solano , 2018).

A mechanism that can induce the spontaneous rotation of active colloids is an instability resulting from a fore-aft asymmetric interaction between the particle and the polymers, leading to a torque (De Corato, Pagonabarraga and Natale , 2021). This mechanism is schematically depicted in Figure 1. A spherical particle generates a solute concentration gradient through an active mechanism. The interaction between the solute and the surface of the particle induces a force in the fluid, which, in the presence of a perturbation, can lead to a net torque being applied on the particle. Depending on the direction of the torque, and if the diffusion is slower than the advection, the initial perturbation can be reinforced as illustrated in the figure, and this feedback mechanism induces a sustained rotation in the particle.

In this work, we apply a simulation approach based on a finite-element method to investigate the effects of thermal fluctuations on the motion of an active Janus particle in a polymer solution. We model the evolution of the polymer concentration using an advection-diffusion equation, which includes thermal fluctuations. Since in the experiments one side of the Janus is hydrophobic and the other is hydrophilic, we assume that the polymers experience attractive and repulsive interactions with the two sides.

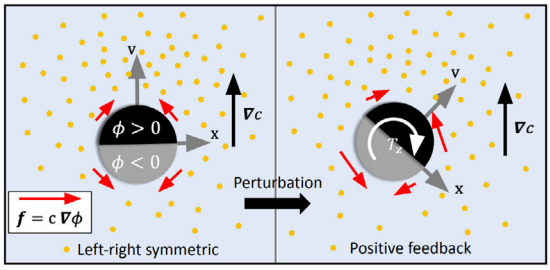

Figure 1: Schematics of the spontaneous chiralization mechanism of the active particle.

2 Governing equations

As a first step, we investigate the dynamics of the particle without thermal fluctuations. To this end, we solve an advection-diffusion equation of the polymer concentration $c = c(\mathbf{x}, t)$:

$$\frac{\partial c}{\partial t} - \nabla \cdot (D\nabla c - c\mathbf{v} + c\nabla\phi) = 0\,, \qquad (1)$$

where D is the diffusion coefficient, assumed constant, $\mathbf{v}$ is the velocity of the flow in a reference frame that moves with the particle, and ϕ is the interaction potential between the particle and the polymers, assumed to be

$$\phi = \phi_0 e^{-\lambda|r-R_p|}\cos(\theta)\,, \qquad (2)$$

where ϕ_0 is a constant, R_p is the radius of the particle, λ is a parameter that is the inverse of the characteristic interaction distance, r is the distance from the particle center, and θ is the angle respect to the polar axis of the particle.

For a given translational velocity V of the particle along the polar axis, asymmetries in the polymer concentration may lead to a torque proportional to the

force $\mathbf{f} = c\nabla\phi$ that induces an additional rotational velocity component in the total velocity vector $\mathbf{v}$.

Finally, in order to investigate the effect of thermal fluctuations on the dynamics of the particle, we consider an advection-diffusion equation with a fluctuating source term:

$$\frac{\partial c}{\partial t} - \nabla \cdot (D\nabla c - c\mathbf{v} + c\nabla\phi) = \nabla \cdot \left(\sqrt{2Dc}\zeta(\mathbf{x}, t)\right) , \tag{3}$$

where $\zeta(\mathbf{x}, t)$ is a vector of white noise in space and time following a Gaussian distribution.

3 Simulation results

We solve equations (1) and (3) in the domain with a 2D finite-element solver. The results without thermal fluctuations show that the particle presents spontaneous rotation with an angular speed that has a nonlinear dependency with the particle velocity, or, equivalently, the Péclet number $\mathrm{Pe} = VR_p/D$. This sustained rotation can be in either direction and it is observed above a certain critical velocity, above which the instability leads to a supercritical pitchfork bifurcation. Figure 2 shows the critical Péclet number $\mathrm{Pe}_{\mathrm{crit}}$ above which the particle shows spontaneous rotation as a function of the concentration, for several values of parameters ϕ_0 and λ.

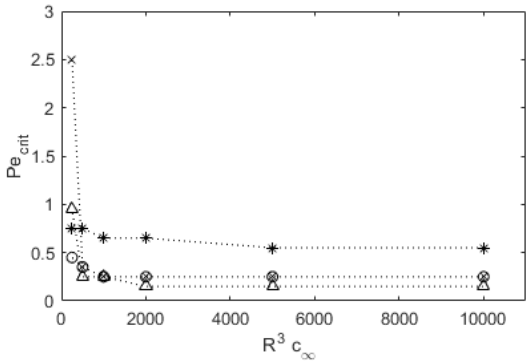

Figure 2: Critical Péclet number $\mathrm{Pe}_{\mathrm{crit}}$ above which the particle shows spontaneous rotation, as a function of the concentration, for $\phi_0 = 1$ and $\lambda = 1$ ($*$), $\phi_0 = 1$ and $\lambda = 3$ ($\times$), $\phi_0 = 0.5$ and $\lambda = 1$ ($\circ$), and $\phi_0 = 0.5$ and $\lambda = 3$ ($\triangle$)

Figure 3 shows results for the mean-square angular displacement as a function of time, obtained with the model including thermal fluctuations, for three different Péclet numbers below or equal to the critical Péclet number. The slope of each curve corresponds to the rotational diffusion coefficient D_r. It can be seen that the rotational diffusion is greatly enhanced as the Péclet number increases.

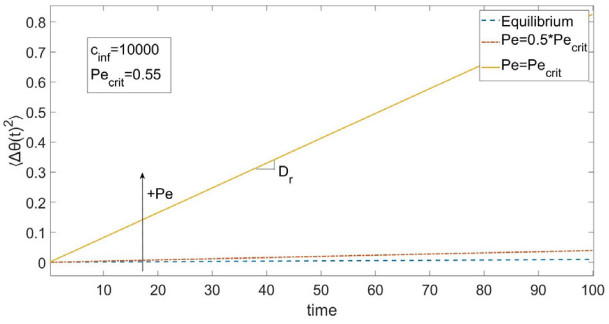

Figure 3: Mean-square angular displacement as a function of time for $\phi = 1$ and $\lambda = 1$, and three Péclet numbers: $\mathrm{Pe} = 0$ (dashed), $\mathrm{Pe} = 0.5\,\mathrm{Pe}_{\mathrm{crit}}$ (dash-dot) and $\mathrm{Pe} = \mathrm{Pe}_{\mathrm{crit}}$ (solid). The slope of the lines corresponds to the rotational diffusion coefficient D_r.

4 Conclusions

The Brownian dynamics and spontaneous rotation of a spherical Janus active particle moving through a polymer solution have been investigated through simulations based on an advection-diffusion equation, with and without thermal fluctuations. The results show sustained rotation of the particle for Péclet numbers above a critical value. When thermal fluctuations are included in the model, the results show that the rotational diffusion is drastically enhanced as the Péclet number increases below its critical value and, therefore, that driving a Janus particle out of equilibrium in a polymer solution has a profound impact on its Brownian dynamics.

References

Gomez-Solano J. R., Blokhuis A., Bechinger C. (2016) "Dynamics of Self-Propelled Janus Particles in Viscoelastic Fluids". *Physical Review Letters* **116**, 138301.

Narinder N., Bechinger C., Gomez-Solano J. R. (2018) "Memory-Induced Transition from a Persistent Random Walk to Circular Motion for Achiral Microswimmers". *Physical Review Letters* **121**, 078003.

De Corato M., Pagonabarraga I., Natale G. (2021) "Spontaneous chiralization of polar active particles". *Physical Review E* **104**, 044607.

2nd Spanish Fluid Mechanics Conference
Barcelona (2 - 5 July 2023)

Dynamic of a microsphere inside an spherical cavity with newtonian fluid subjected to periodical contractions

R. Castilla[1]

robert.castilla@upc.edu

[1]CATMech - Departament of Fluid Mechanics, Universitat Politècnica de Catalunya, Spain

The dynamics of a microsphere submerged in an spherical cavity is numerically analyzed. The cavity, filled with a newtonian fluid, is subjected to periodical contractions in its surface that create flows that affects to the microsphere dynamics. The space distributions of force and drag resistance are estimated by unsteady three-dimensional computational simulations with dynamic mesh. These distributions are functions of sphere size and position, and they are fitted to mathematical models. Dynamic simulations are performed using these mathematical models to compute the trajectory of the microsphere under the action of thousands of position-dependent pushing–pulling forces. A dynamic simulation is performed with one-dimensional finite differences. It is shown that in the long term, ball tend to migrate to the center of the cavity, especially when it is small compared with the cavity size.

1 Introduction

The dynamics of an isolated solid sphere in a Newtonian viscous fluid is given by Stokes's law [see Eq. (1)]Happel and Brenner (1983).

$$F = 6\pi\mu_{\text{eff}} RU, \tag{1}$$

However, in practical cases, the domain is not infinite and is generally bounded by walls, the presence of which modifies the dynamics of the sphere by introducing a correction factor in the viscous term, $\mu_{\text{eff}} = k_\mu \mu$, with $k_\mu > 1$. The increase in the effective viscosity experienced by a sphere falling between two parallel walls was studied theoretically by Fáxen in 1923Happel and Brenner (1983) in the case where the distance to the wall was large relative to particle diameter and later by Ganatos *et al.*Ganatos et al. (1980) for smaller distances to parallel walls. The problem of the viscosity correction for motion perpendicular to a wall was considered by BrennerBrenner (1961)

$$k_{\mu,f} = 1 + \frac{9}{8}\frac{\kappa}{1-\xi}, \tag{2}$$

where $\kappa = R/R'$ and $\xi = x/R'$. The subscript f indicates that this is valid far from the wall, i.e., $\xi \to 0$, and it is only valid for very small κ.

Cooley and O'NeillCooley and O'Neill (1969) extended it to the case of a sphere with non-negligible curvature. Considering that in this case there are two curves surfaces, the expression by Cooley and O'Neill can be written as

$$k_{\mu,n} = \frac{1}{(1-\kappa)^2}\left[\frac{2\kappa(1-\kappa)}{(1-\kappa)^2-\xi^2} + \frac{1-7\kappa+\kappa^2}{5}\log\left(\frac{\kappa^2}{(1-\kappa)^2-\xi^2}\right)\right] \tag{3}$$

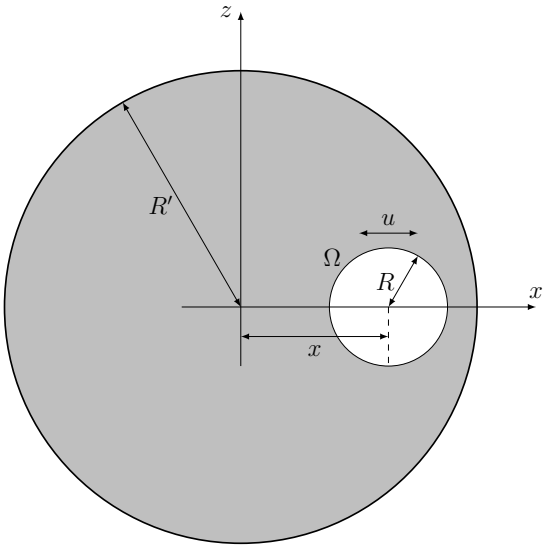

Figure 1: 2D scheme of computational domain with main geometrical parameters.

2 Numerical Simulations and main results

Two kind of simulations have been considered, both using the simpleFoam solver in the OpenFOAM toolbox. In the first simulations, the ball is moved and the effective viscosity is computed as a function of position and relative curvature. In the second case, the ball is static, and the wall are moving, in order to estimate the incident force on the microsphere. Fig 2 show an example of velocity and pressure distribution in one of this second type of cases.

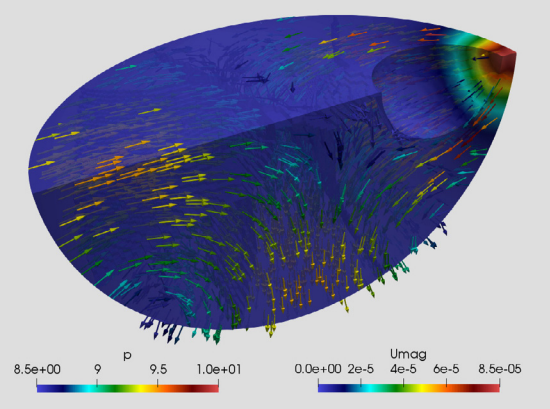

Figure 2: Contours of pressure and velocity vectors, colored by velocity magnitude in m/s, for the inward moving-wall numerical experiments for $d = 20$ µm at a distance between centers of 22.5 µm.

With this numerical experiments and using a logistic function, the effective viscosity is modelled as

$$k_\mu(\xi,\kappa) = p(\xi; C(\kappa), \xi_{0,n}(\kappa))\, k_{\mu,n}(\xi,\kappa) + [1 - p(\xi; C(\kappa), \xi_{0,f}(\kappa))] k_{\mu,f}(\xi,\kappa). \quad (4)$$

and the incident force is estimated by fitting with a power-tangent function

$$\frac{F_R}{F_{\text{ref}}} = \Lambda(\xi,\kappa) = A(\kappa)\left[\tan\left(\frac{\pi}{2}\frac{\xi}{1-\kappa}\right)\right]^{n(\kappa)}, \quad (5)$$

These models are introduced in the equation of dynamics, considering a periodical wall velocity.

$$\frac{\mathrm{d}^2\xi(t)}{\mathrm{d}t^2} + \frac{9}{2}\frac{\nu}{R^2}\left[k_\mu(\xi(t),\kappa)\frac{\mathrm{d}\xi(t)}{\mathrm{d}t} - \frac{\kappa}{R}\Lambda(\xi(t),\kappa)\, u_w(t;T)\right] = 0, \quad (6)$$

This equation is numerically solved in python with a 1-D finite difference method, introducing randomness in the wall velocity. Results are shown in figure 3.

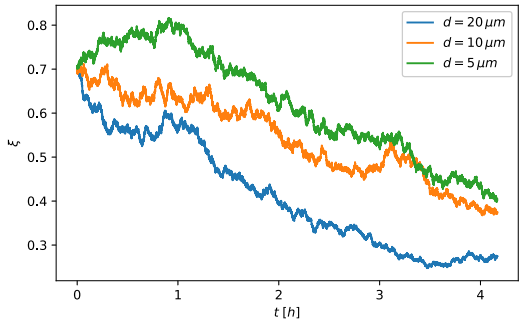

Figure 3: Migration plots of spheres of diameters $d =$ 5, 10, and 20 µm, with random wall velocity. The standard deviation of the random distribution is 1/4 of the corresponding uniform value.

3 Conclusions

It is shown that a microsphere submerged in a spherical cavity with a Newtonian fluid, subjected to periodical contractions tend to migrate to the center, due to the effective viscosity and incident forces distributions. This result can contribute to the understanding of the complex mechanism of nucleus migration is the early stages of cells development Castilla (2022)

References

Happel, J., & Brenner, H. (1983). "Low Reynolds Number Hydrodynamics: With Special Applications to Particulate Media". Springer.

Ganatos, P., Pfeffer, R., & Weinbaum, S. (1980). "A strong interaction theory for the creeping motion of a sphere between plane parallel boundaries. Part 2. Parallel motion". *Journal of Fluid Mechanics*, 99(4), 755–783.

Brenner, H. (1961). The slow motion of a sphere through a viscous fluid towards a plane surface. Chemical Engineering Science, 16(3–4), 242–251. https://doi.org/10.1016/0009-2509(61)80035-3

Cooley, M. D. A., & O'Neill, M. E. (1969). "On the slow motion generated in a viscous fluid by the approach of a sphere to a plane wall or stationary sphere." *Mathematika*, 16(01), 37.

Castilla, R. (2022). Dynamics of a microsphere inside a spherical cavity with Newtonian fluid subjected to periodic contractions. Physics of Fluids, 34(7), 071901.

Photocatalytic Janus Microswimmers as Micro-stirrers?

Maximilian R. Bailey[1*], Fabio Grillo, Federico Paratore[1], and Lucio Isa[1]

[1]*Department of Materials, ETH Zürich, SWITZERLAND*

There is a growing interest in employing synthetic microswimmers as "micro-stirrers" capable of mixing fluids without external agitation. Nevertheless, this mixing effect remain relatively unstudied to date. Here, we investigate the effect of Janus microswimmer motion on the dynamics of passive tracer particles. We find that for our system, enhancements in tracer diffusivity predominantly occur via collisions with the Janus microswimmers, similar to previous findings for living systems. In doing so, we identity several potential limitations to the "micro-stirrer" concept, as well as potential avenues to improve the overall mixing performance of synthetic active matter systems.

INTRODUCTION

Artificial microswimmers are micron-sized particles that convert energy sources - such as light or chemicals - into directed motion, and are thus intrinsically out-of-equilibrium materials [1]. They have been touted for a range of self-autonomous applications, ranging from environmental remediation to drug delivery [2]. In particular, their purported ability to induce the mixing of fluids without external agitation is promising for the "chemistry-on-the-fly" concept [3], where microswimmers enhance local mass-transfer rates while catalyzing reactions, improving overall reactor efficiency. Here, we study the enhancement in tracer diffusivity achieved in the presence of our photocatalytic Janus microswimmers [4], and by increasing their number density and making simple scaling arguments, we demonstrate that enhancements in tracer diffusivity predominantly occur via collisions with the microswimmers, similar to previous findings for living systems [5].

EQUATIONS, FIGURES AND TABLES

By simple scaling arguments, we arrive at the following expression for τ_c in equation (1), the expected time for collisions between Janus microswimmers and tracer particles for a given number density in the experiment.

$$\tau_c = \frac{2 * \sqrt{A_{system}}}{< v_0 > * \sqrt{N_{swim} * N_{trac}}}, \quad (1)$$

From the kurtosis (γ) of the distribution of tracer displacements, we observe a positive correlation between this expected collision time τ_c, and the lag-time τ_γ at which the peak in the kurtosis occurs (Figure 1, right). We also qualitatively note the outweighed contribution of large "jumps" to the distribution of tracer displacements, following the protocol provided in [5]. We thus hypothesise that collisions between our Janus microswimmers and the tracer particles lead to large displacements of the tracer particles, in turn increasing their overall diffusivity. This agrees with the "entrainment" mechanism previously proposed by Pushkin and Yeomans [6]

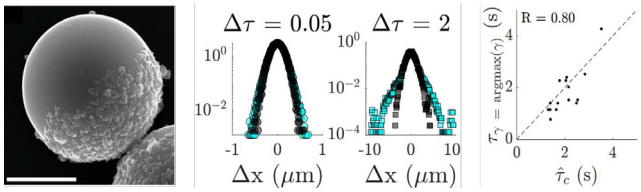

FIG 1. Influence of microswimmer motion on the dynamics of passive tracer particles. Left: HR-SEM of our synthesized, photocatalytic Janus microswimmers (scale bar 1 μm) (taken from [4]). Middle: Distribution of tracer displacements in the presence of microswimmers at different lag times (Δτ = 0.05s, 2s respectively) with (cyan) and without (black) tracer jumps extracted using the methodology provided in [5]. Right: Predicted collision time between microswimmers and passive tracers obtained from simple scaling arguments (x-axis) vs the experimentally observed lag time at which the kurtosis of the distribution of displacements (γ) is at its maximum (y-axis).

CONCLUSIONS

We have shown that our model Janus microswimmers mix predominantly via collisions in an entrainment-like mechanism. Due to constraints in achievable microswimmer density (e.g. due to out-of-equilibrium effects), this provides an upper-bound on the effective mixing enhancement achievable with the most popular synthetic microswimmer systems. To overcome such issues, design parameters such as shape or squirmer type should be optimized for synthesis.

* maximilian.bailey@mat.ethz.ch

[1] Popescu, M., *Langmuir*, **36**, 6861-6870 (2020)
[2] Yuan, K., Pacheco, M., Jurado-Sánchez, B., & Escarpa, A., *Advanced Intelligent Systems*, **3**, 2100002 (2021)
[3] Karshalev, E., Esteban-Fernández de Ávila, B., & Wang, J. *Journal of the American Chemical Society*, *140*(11), 3810-3820. (2018)
[4] Bailey, M. R., Grillo, F., Spencer, N. D., & Isa, L., *Advanced Functional Materials*, **32**, 2109175 (2022)
[5] Jeanneret, R., Pushkin, D. O., Kantsler, V., & Polin, M., *Nature Communications*, **7**, 1-7 (2016)
[6] Pushkin, D. O., & Yeomans, J. M. *Physical review letters*, *111*(18), 188101. (2013)

2nd Spanish Fluid Mechanics Conference
Barcelona (2 - 5 July 2023)

Simulating microswimmers under confinement with Dissipative Particle (hydro)Dynamics

C. Miguel Barriuso G.[1,4], José Martín-Roca[1,3,4], Valentino Bianco[3], Ignacio Pagonabarraga[2], and Chantal Valeriani[1,4]

carbarri@ucm.es

[1]Departamento de Estructura de la Materia, Física Térmica y Electrónica, Universidad Complutense de Madrid
[2]Departament de Física de la Matèria Condesada, Facultat de Física - Universitat de Barcelona
[3]Dpto. de Química Física, Facultad de Química - Universidad Complutense de Madrid
[4]GISC - Grupo Interdisciplinar de Sistemas Complejos

In this work (1) we develop a framework to study active agents with explicit DPD (2) hydrodynamics inspired by the *squirmer* model (3). We study the solvent velocity fields and the diffusion and orientation dynamics of an active colloid and the diffusion and radius of gyration of an active polymer embedded in bulk or in cylindrical confinement. This approach allows us to properly deal with thermal fluctuations and microswimmers with complex shapes. We will also present our current work in which we are studying the sedimentation of a microswimmer with mass imbalance under gravity.

The active agents achieve their propulsion via force redistribution among their neighboring solvent particles. We study the following redistribution fields (fig. 1),

$$\boldsymbol{f}(r,\theta) = (B_1 \sin\theta + B_2 \sin\theta\cos\theta)\hat{\boldsymbol{e}}_\theta \qquad \equiv \boldsymbol{f}_{\text{col}}$$

$$\boldsymbol{f}(r,\theta) = -\cos\left(\frac{\theta}{2}\right)\hat{\boldsymbol{e}} \qquad \equiv \boldsymbol{f}_{\text{pol}}$$

where θ is the polar angle w.r.t. the colloid orientation axis or w.r.t. the tangent to the polymer chain $\hat{\boldsymbol{e}}$. Then, a reaction thrust force is applied to the agent's k-th particle $\boldsymbol{f}_T^k = -\sum_{i\in\mathcal{N}_k} \boldsymbol{f}^i(r,\theta)$ where $\mathcal{N}_k$ is the set of nearest solvent particles to the k-th agent's particle. In this way we locally preserve linear and angular momentum conservation. The total force that is applied to the active agents is $\boldsymbol{F} = \boldsymbol{F}_C + \boldsymbol{F}_D + \boldsymbol{F}_R + \boldsymbol{F}_T$, where the first three terms correspond to the conservative, dissipative and random (thermal) forces of the DPD interaction, and $\boldsymbol{F}_T = \sum_k \boldsymbol{f}_T^k(r,\theta)$ is the thrust force that propels the agent.

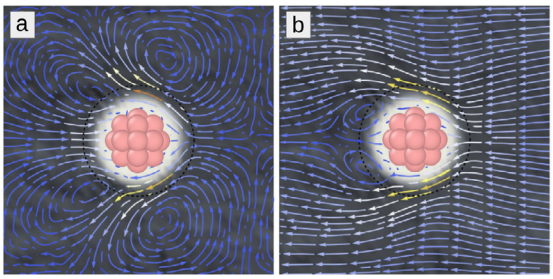

Figure 1: Fluid velocity fields for a raspberry-like puller squirmer as seen in the lab's frame (a) and in the squirmer's frame (b). The color of the arrows shows the magnitude of the velocity. The color of the background represents the fluctuations in the solvent density.

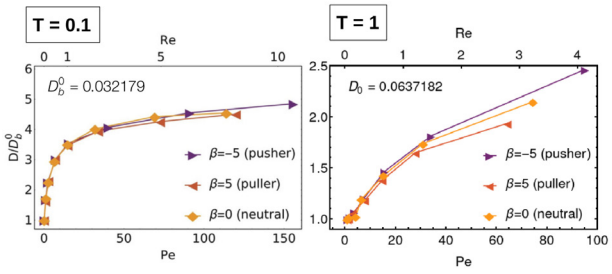

Figure 2: Effective diffusion (normalized by passive diffusion D_0) computed from the colloids MSDs as a function of the Péclet and Reynolds numbers at low and moderate temperatures for three types of squirmers.

References

[1] C.M. Barriuso G., J. Martín-Roca, V. Bianco, I. Pagonabarraga & C. Valeriani (2022) "Simulating microswimmers under confinement With Dissipative Particle (Hydro)Dynamics". *Front. Phys.*, **10**, 926609.

[2] M.B. Liu, G.R. Liu, L.W. Zhou & J.Z. Chang (2015). Dissipative Particle Dynamics (DPD): An Overview and Recent Developments, Arch. Comput. Methods Eng., **22**, 529–556.

[3] Downton, M. T., & Stark, H. (2009). Simulation of a model microswimmer. Journal of Physics: Condensed Matter, **21** (20), 204101.

2nd Spanish Fluid Mechanics Conference
Barcelona (2 - 5 July 2023)

Aerodynamic forces and wake structure on a 2D model of a vehicle in ground effect

Pedro Solís-García[1], Khaled Zerzeri[1,2], Mariem Nouailli[1,2], Luis Parras[1], and Eduardo Durán-Venegas[1]

eduran@uma.es

[1] Universidad de Málaga, Escuela de Ingenierás Industriales, Málaga, Spain
[2]University College of Aviation & Technology, Ariana, Tunisia

In this research we perform numerical simulations and wind tunnel experiments of a D-shaped bluff body. Different flow conditions and ground-body distances are considered to analyse the ground effect on aerodynamic forces and wake structure.

1 Introduction

Terrestrial transportation of goods and people grow daily and, consequently, CO_2 and other polluting gas emissions. The reduction of the transportation volume would imply a change in the logistic model unapproachable in the short term. However, technical solutions can be implemented to reduce fuel consumption and, at the same time, emissions. At high velocities, flow separation is the main responsible of drag forces in bluff bodies, as those of terrestrial vehicles. In this sense, many technical solutions proposed in the last decades have focused on wake control to improve aerodynamic performance.

In recent years there has been a growing interest in the creation of devices that allow the control of the wake of simplified ground vehicle models, either by passive methods, such as the use of rigid Lorite-Díez *et al.* (2018) or flexible flaps Lorite-Díez *et al.* (2017), or by active methods such as blowing in the rear side of the object (Lorite-Díez *et al.* , 2019). In order to determine the best choice for this type of control devices, it is necessary to have precise knowledge of the wake created behind the object.

In this research, a numerical study of the aerodynamic coefficients and wake structure for high Reynolds numbers is performed on a simplified 2D vehicle model that has been widely used in recent works. In particular, the effect of proximity to the ground on the parameters studied is analyzed.

2 Numerical setup and results

The vehicle is modeled as a bluff body of height H with a rounded front and rectangular rear (Lorite-Díez *et al.* (2017)) in an incompressible free-stream of velocity U_∞, density ρ and viscosity μ (figure 1). The front of the body is designed as an ellipsoidal nose with a major-minor axes aspect ratio of 2 to avoid flow separation. To avoid edge effects during the experiments, the body is fixed to lateral plates. Numerical simulations are performed solving incompressible Navier-Stokes equations in the computational domain of figure 1. The Reynolds number of the problem is defined as $Re = \rho U_\infty H/\mu$.

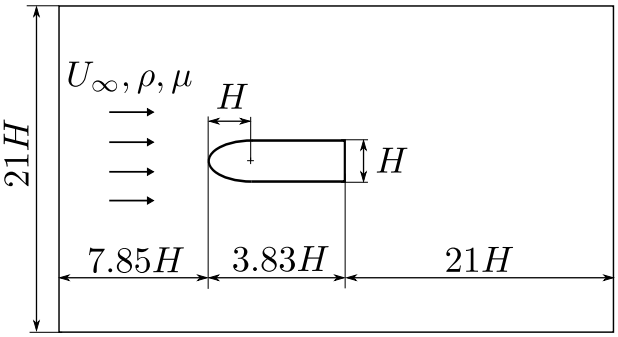

Figure 1: Scheme of the problem configuration and computational domain.

Experiments and numerical simulations are performed for different ground-body distances and Reynolds numbers. The distance d between the ground and the lower surface of the body is varied from $d = H$ to $d = 10H$. In figure 2, we show the structure of the wake from a numerical simulation for $Re = 40000$ and $d = 10H$ (figure 2a) and $d = 10H$ (figure 2b). The effect of the ground can be clearly appreciated, affecting the flow around the body, the structure of the wake, and, hence, the aerodynamic forces on the body.

3 Conclusions

We have generated a database of numerical and experimental results of aerodynamic forces and wake

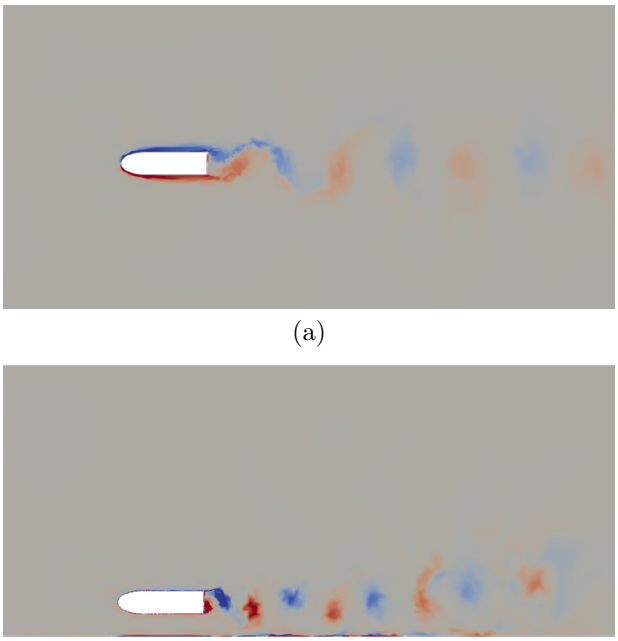

(a)

(b)

Figure 2: Wake structure for $Re = 40000$ and (a) $d = 10H$ and (b) $d = H$.

structure of a 2D model of a vehicle for different ground-body distances and flow conditions. We have analyzed these results to characterize the effect of proximity to the ground and better understanding the behaviour of the wake. These results will be used to design a control device to improve aerodynamic performance of the body.

Acknowledgements

This work has been supported by Junta de Andalucía under Project P21-00313.

References

Lorite-Díez, M., Jiménez-González, J.I., Gutiérrez-Montes, C. & Martínez-Bazán, C. (2017) "Drag reduction of slender blunt-based bodies using optimized rear cavities". *Journal of Fluids and Structures*, **74**, 158–177.

Lorite-Díez, M., Jiménez-González, J. I., Gutiérrez-Montes, C. & Martínez-Bazán, C. (2018) "Effects of rear cavities on the wake behind an accelerating D-shaped bluff bod", *Physics of Fluids* 30, 044103

García-Baena, C., Camacho-Sánchez, J.M., Lorite-Díez, M., Gutiérrez-Montes, C. & Jiménez-González, J.I. (2023) "Drag reduction on a blunt body by self-adaption of rear flexibly hinged flaps",*Journal of Fluids and Structures* 118, 103854.

Lorite-Díez, M., Jiménez-González, J., Martínez-Bazán, C., Cadot, O. and Pastur, L. (2019), Perimetric blowing at the rear of a bluff body: consequences on the wake dynamics and drag reduction. *Proc. Appl. Math. Mech.*, 19, e201900044.

2nd Spanish Fluid Mechanics Conference
Barcelona (2 - 5 July 2023)

Aerodynamic forces in deformed wings

Luis Parras[1], Paloma Gutiérrez-Castillo[1], Francisco J. Blanco-Rodríguez[2], and Carlos del Pino[1]

lparras@uma.es

[1]Universidad de Málaga, Escuela de Ingenierías Industriales, Málaga, Spain
[2]Área de Mecánica de Fluidos, Departamento de Ingeniería Aeroespacial y Mecánica de Fluidos, Universidad de Sevilla, Spain

In this work, we carry out a detailed study of the change in aerodynamic forces due to wing deformation in flight. The results presented are for a wing model of a fixed semi aspect ratio $sAR = 4$, and different chord-based Reynolds numbers in the range of application of UAVs. Our results show that numerical simulations with turbulence models are able to accurately simulate these aerodynamic forces when compared to experimental results obtained in the wind tunnel.

1 Introduction

One of the advances in aeronautics in recent years has been the reduction of aircraft consumption in flight, with a view to complying with European energy saving regulations. In particular, Civil aviation accounts for 13,4% of total CO2 emissions from EU transport. The ReFuelEU Aviation initiative is part of the "Fit for 55 in 2030 package", the EU's strategy to reduce greenhouse gas emissions by at least 55% by 2030 compared to 1990 levels, in line with the European Climate Law (ReFuelEU Aviation initiative , 2022). The solutions to this problem include the development of more efficient turbojets and the reduction of the aircraft weight. This weight reduction involves using lighter materials, increasing the wingspan, making them slimmer and lightweight. This reduction of weight means that in normal flight conditions, wings can have tip deformations of more than 10% of their wingspan. Rapid methods of predicting lift and drag, such as the panel method, do not usually include this possibility of wing deformation. For this reason, the aeronautic manufacturer is demanding an exhaustive knowledge through experiments and numerical simulations to determine the performance of these deformed wing surfaces in order to be able to compare with the fast methods used in the industry.

To obtain the results in a realistic case of deformed wings we have to solve a complex fluid-structure interaction (FSI) problem, where aerodynamic forces act on the wing, which, depending on the internal structure and its inertia, responds by deforming. To avoid the complexity of this FSI problem, we will assume an imposed deformation, obtained from literature results Farnsworth *et al.* (2015), and we will start from these results to perform the aerodynamic study.

2 Formulation of the problem and results

In this study we will use `OpenFOAM` to solve the Reynolds Averaged Navier Stokes equations (RANS) using different turbulence models ($k-\epsilon$, $k-\omega$ and $k-\omega$ SST) around a straight and deformed wing with a NACA0012 wing profile (see figure 1). We generated a mesh using the utility `snnapyHexMesh`. Once the mesh is tested against previous 2D studies for very high Reynolds numbers Frost (1970), we perform the simulations for the 3D case for different Reynolds numbers and angles of attack, α, in the pre-stall region.

Figure 1: 3D schematic of the two configurations studied for a wing model: straight wing (light color) and deformed wing (dark color) with a NACA0012 airfoil.

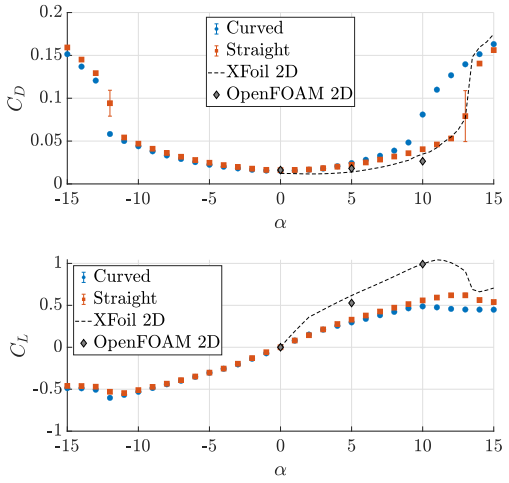

Figure 2: Experimental drag coefficient, C_D and lift coefficient, C_L for the case of $sAR = 4$ and $Re = 1.6 \times 10^5$. We have included as a reference the 2D results provided by XFoil and the 2D numerical results obtained from `OpenFOAM` for the same Reynolds number.

The main difference observed in the results is the loss of symmetry in the aerodynamic coefficients in the case of deformed wings (for positive angles of attack), along with an increase in drag force of up to 360% and a reduction in a lift of up to 30%. Likewise, the onset of stall appears at lower angles of attack.

3 Conclusions

In this research, we have performed a numerical simulation of the turbulent flow around straight and deformed wings. The aerodynamic forces are compared to experiments performed in the wind tunnel, allowing us to select the turbulence model and mesh to replicate the experimental data accurately. The effect of the curvature makes the aerodynamic coefficients lose symmetry, increasing the drag force, decreasing the lift force and advancing the stall to lower angles of attack. The simulations provide other interesting data as the pressure distribution over the wing and the detachment of the boundary layer, allowing us to physically explain the reasons for the differences between the experimental results.

Acknowledgements

This research has been supported by the project PID2021-124692OA-I00 from the Ministerio de Ciencia e Innovación, and by 'Ayuda II Plan Propio' from Universidad de Málaga.

References

Jaan Soone (2022). ReFuelEU Aviation initiative. Sustainable aviation fuels and the 'fit for 55' package.*BRIEFING, EU Legislation in Progress*, PE 698.900.

John A. Farnsworth, Stuart Corbett, Jurgen Seidel and Thomas E. McLaughlin (2015). "Aeroelastic Response of a Finite Span NACA 0018 Wing Part 1: Experimental Measurements", *AIAA 2015-0249. 53rd AIAA Aerospace Sciences Meeting.*

Hoar Frost (1970). Low-Speed Aerodynamic Characteristics of NACA 0012 Aerofoil Section, including the Effects of Upper-Surface Roughness Simulating, *Report of the Aeronautical Research Council*, 3726.

2nd Spanish Fluid Mechanics Conference
Barcelona (2 - 5 July 2023)

Automatic Parameter Selection for Model Predictive Control for Fluid Flows

Luigi Marra[1], Andrea Meilán-Vila[2], and Stefano Discetti[1]

lmarra@pa.uc3m.es

[1]Aerospace Engineering Research Group, Universidad Carlos III de Madrid, Spain
[2]Department of Statistics, Universidad Carlos III de Madrid, Spain

Model-based techniques, such as model predictive control (MPC), have recently gained remarkable interest for controlling complex dynamics. MPC has demonstrated excellent capability in constrained highly non-linear models which are difficult to handle with traditional linear control systems. MPC has taken advantage of progress in data-driven modeling techniques for system identification for the plant. Nonetheless, the performance of this control logic is highly dependent on parameters that are typically tuned by trial and error. Moreover, the tuning process is heavily influenced by the noise in the sensors and the plant parameters uncertainty. The goal of this work is to present a noise-robust self-tuning control framework for fluid flows based on MPC and characterized by minimal user interaction.

The prediction and control of fluid flows is a major research topic due to its wide-ranging practical applications in many industrial fields. The developments in this area offer numerous benefits, such as reducing energy consumption, enhancing safety, and minimizing the environmental impact of systems involving fluid flows. In this context, Model Predictive Control (MPC) has emerged as a powerful technique offering the ability to handle nonlinear dynamical systems with complex constraints. MPC is a control strategy that uses a mathematical model of the system to predict its future behavior. The optimal control actions are found by iteratively solving an optimization problem. The MPC optimization is performed in a receding horizon manner with the goal of minimizing an appropriate user-defined cost function.

Notwithstanding, a gap that needs to be filled is that of providing techniques capable of automatically tuning control parameters while optimizing controller performance. Most often the cost function which drives the optimization contains parameters weighing targets to be achieved and constraints of the process (for instance, time variability and/or intensity of the control input). Furthermore, in the case of turbulent flows the plant is often unknown, or too complex to be used for real-time analysis.

In this work, we propose an automated architecture, which self-tunes the parameters for the plant and the optimization process with minimal user input, and adapts to different noise conditions and/or limited state knowledge. We build upon three main pillars: identification of a compact model, discovered from system input-output data and a sparse identification of nonlinear dynamics (SINDy), following the MPC implementation of Kaiser (2018); a black-box optimization via Bayesian methods (Hewing, 2020) for hyperparameter tuning; reduction of noise effects using a local polynomial regression (LPR, Nottingham, 2001).

The Direct Numerical Simulation of the wake of a fluidic pinball (Deng, 2020) is used here to test the MPC-based control framework. The fluidic pinball is a configuration of three cylinders whose centres form an equilateral triangle. The objective of the control is to minimize the drag by active tuning of the rotation rate of the three cylinders. The simulation is run at a Reynolds number (Re) of 150 (based on the cylinder diameter and on the freestream velocity), which is sufficiently large to guarantee a laminar chaotic behavior. The compact model discovered by the SINDy method and used to make an online prediction is based on a state vector that includes the aerodynamic drag (C_d) and lift (C_l) coefficients, their corresponding derivatives with respect to time, and takes cylinder rotation rates b_i into account. Polynomial functions up to the second order are used. The cost function for the MPC (and its analogous one for the hyperparameter tuning with the Bayesian optimization) includes the drag coefficient reduction with respect to the unperturbed wake, the variance of the lift coefficient, and terms accounting for the power input and the variability of the input over time. Figure 1 shows the results of the MPC with and without the hyperparameter tuning, at different measurement noise levels (measured as the normalized standard deviation of C_d and C_l). For data with-

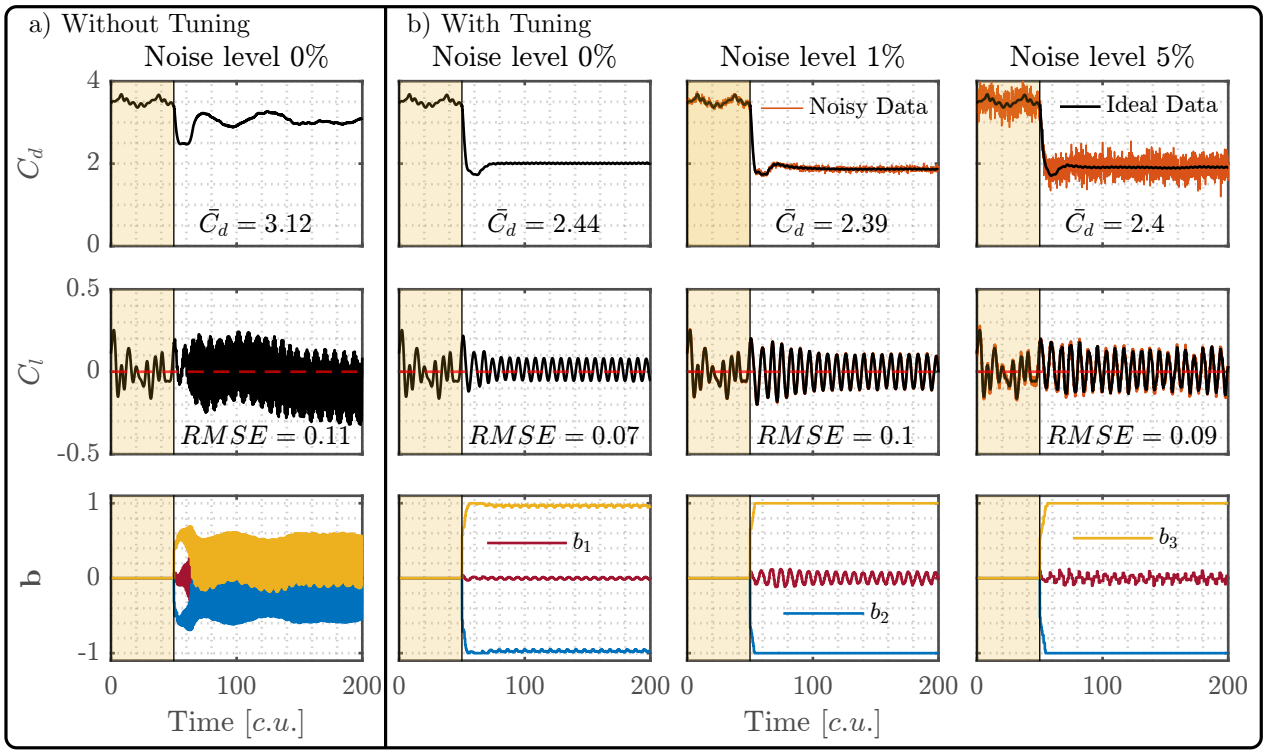

Figure 1: Time series of C_d, C_l and exogenous input b_i at free and forced stage according to the MPC-based control framework applied to the fluidic Pinball. The panels in a) show the results when the cost function parameters are hand-selected and equal to the unity. The panels in b) show the result when Bayesian Optimization is used for hyperparameter tuning. b_1, b_2, b_3 refer to the rotation rate of front, top and bottom cylinders, respectively. The mean value of C_d and the Root Mean Square Error (RMSE) of C_l in the forced stage are also provided. LPR is included in the MPC control framework in all cases where measurement noise is present.

out noise, it is clear that the hyperparameter tuning is able to reach better performances, with lower oscillations of the C_l and an overall lower C_d. LPR allows good noise robustness in the explored scenarios and the performance remarkably improves when switching from hand selection of control parameters to an optimal tuning according to Bayesian Optimization.

Acknowledgements

The authors acknowledge the support from the research project PREDATOR-CM-UC3M. This project has been funded by the call "Estímulo a la Investigación de Jóvenes Doctores/as" within the frame of the Convenio Plurianual CM-UC3M and the V PRICIT (V Regional Plan for Scientific Research and Technological Innovation). This project has received funding from the European Research Council (ERC) under the European Union's Horizon 2020 research and innovation programme (grant No 949085).

References

Deng N., Noack B.R., Morzyński M. , Pastur L.R. (2020) "Low-order model for successive bifurcations of the fluidic pinball". *Journal of Fluid Mechanics*, **884**.

Hewing L., Wabersich K.P. , Menner M., Zeilinger M.N. (2020) "Learning-based model predictive control: Toward safe learning in control". *Annual Review of Control, Robotics, and Autonomous Systems*, **3**, 269-296.

Kaiser E., Kutz J., Brunton S. (2018) "Sparse identification of nonlinear dynamics for model predictive control in the low-data limit". *Proceedings of the Royal Society A*, **474(2219)**.

Nottingham Q.J., Cook D.F. (2001) "Local linear regression for estimating time series data". *Computational Statistics & Data Analysis*, **37(2)**, 209-217.

2nd Spanish Fluid Mechanics Conference
Barcelona (2 - 5 July 2023)

Drag reduction in simplified geometries of blunt vehicles by means of different base blowing strategies

J.M. Camacho-Sánchez[1], C. García-Baena†[1], M. Lorite-Díez[2], C. Gutiérrez-Montes[1], J.I. Jiménez-González[1], and C. Martínez-Bazán[2]

† *cgbaena@ujaen.es*

[1]Departamento de Ingeniería Mecánica y Minera. Universidad de Jaén, Spain.
[2]Departamento de Mecánica de Estructuras e Ingeniería Hidráulica, Universidad de Granada, Spain.

We perform an experimental and numerical study on the turbulent flow around a square-back Ahmed body, to analyze the effect of steady base blowing on both the near wake dynamics and the model drag coefficient. Several arrangements of blowing configurations have been compared by varying the injected flow rate. The obtained experimental results suggest an interesting potential in drag reduction induced by the steady blowing, which is able to increase the base pressure by approximately 12.6% in comparison to baseline case during blowing mass regime.

1 Introduction

Heavy vehicles' major source of CO_2 emissions and energy consumption comes from their large aerodynamic loads related to their geometric bluffness (Hucho et al. , 1993). The flow around trucks or buses is massively separated at their rear edges, which creates a large recirculation bubble, associated to a low base pressure, and consequently to a large drag coefficient (Choi et al. , 2014).

Among the different drag reduction strategies proposed in the literature, base blowing has been shown to be an efficient way of increasing bluff bodies base pressure as it was shown in the seminal studies of Wood (1964) and Bearman (1967). Applied to simplified models of heavy vehicles, as the square-back Ahmed body (Ahmed et al. , 1984), this open loop control strategy is able to reduce efficiently its drag by recovering base pressure, modifying the associated near wake (Lorite-Díez et al., 2020). Such a wake is mainly characterized by two phenomena of different timescales and spatial distributions, as the periodic vortex shedding (VS) phenomena and the quasi-steady reflectional symmetry breaking (RSB) modes. In the present work, we will compare different blowing configurations in wind tunnel experiments and numerical simulations to elucidate the role of the blowing geometry on the drag reduction, base pressure recovery and near wake dynamics.

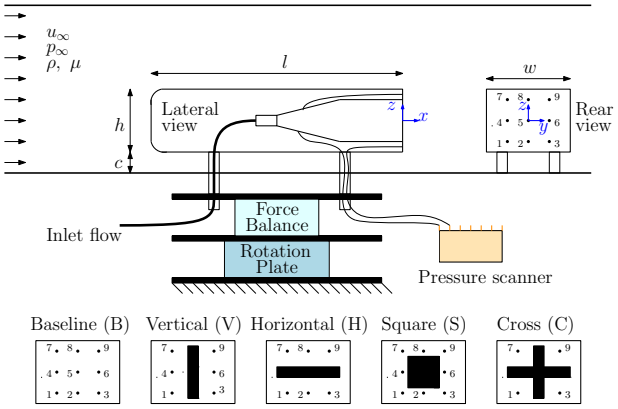

Figure 1: Sketch of the experimental set-up, including different blowing configurations.

2 Problem description and experimental details

In the experiments, we employ a square-back Ahmed body whose corresponding height is $h = 72$ mm, length is $l = 261$ mm and width is $w = 97.25$ mm. The model is precisely set and aligned inside an open wind tunnel with a 400 mm x 400 mm test section, at a ground clearance of c/h= 0.278 (see Fig.1). The incoming free-stream flow is characterized by its velocity u_∞=13.5 m/s, density ρ_f, viscosity μ_f and pressure p_∞; resulting in a Reynolds number $Re = \rho_f u_\infty h/\mu_f \simeq 65000$. The same Reynolds number is employed in the numerical simulations which replicate the aforementioned experimental conditions.

Four steady blowing configurations are tested (Vertical, Horizontal, Square, Cross) and compared to the baseline configuration (B) at the given Reynolds

number (see Fig.1). The tested configurations have the same ratio between the blowing surface,S_b, and the base area, $S_b/hw = 0.1$. In order to produce an uniform air injection, several valves, stagnation pressure chambers and a convergent nozzle are employed in the experiments. Also, the blowing flow rate is measured by precise flowmeters. That air injection is characterized by the blowing flow rate coefficient $C_q = u_b S_b / u_\infty hw$, where u_b is the blowing velocity.

In the experiments, base pressure is measured with a 64-channel pressure scanner while the aerodynamic forces acting on the model are captured by a 6-axis force balance. Base pressure values p_i $(i = 1, 2, ..., n)$ are measured at different locations $(x_i/h = \pm 0.22, y_i/h = \pm 0.22)$, which allows us to obtain base pressure coefficients as

$$C_{p,i} = \frac{p_i - p_\infty}{\rho_f u_\infty^2 / 2} \tag{1}$$

Additionally, the base drag coefficient is computed by integrating all the pressure taps, n_a, in the body base as

$$C_B = -\frac{1}{n_a} \sum_{i=1}^{n_a} c_{p,i} \tag{2}$$

3 Results

The evolution of the base drag coefficient, C_B, with the blowing coefficient, C_q, can be seen in Fig.2 for all the tested configurations. The results show a nearly identical values of C_B for non-blowing cases, which is similar to the baseline case. When a steady blowing is employed, base pressure is effectively increased, reducing the base drag coefficient and therefore, decreasing the drag. This behaviour has been previously identified as the mass regime (Lorite-Díez et al., 2020), consisting in a mass injection on the recirculation bubble due to the blowing which provokes their lengthening, increasing the base pressure. Once the greatest C_B reduction is reached, at C_q^{Opt}, the base pressure starts to be reduced due the high momentum jet induced by the blowing at high C_q values, which is known as the momentum regime (Lorite-Díez et al., 2020). Among the different configurations, the square (S) geometry is able to achieve the greatest pressure recovery, reaching a 12.6% C_B reduction with respect to baseline case. It is also interesting to see that the Cross (C) geometry combines the effect of Horizontal (H) and Vertical (V) arrangements, matching the same base drag reduction of the former ($\Delta C_B^C \simeq \Delta C_B^H \simeq 10.5\%$) and the same optimal blowing coefficient of the latter ($C_q^{Opt,V} \simeq C_q^{Opt,C} \simeq 0.0245$). Drag measurements and numerical results are also in line with the trends shown in Fig.2.

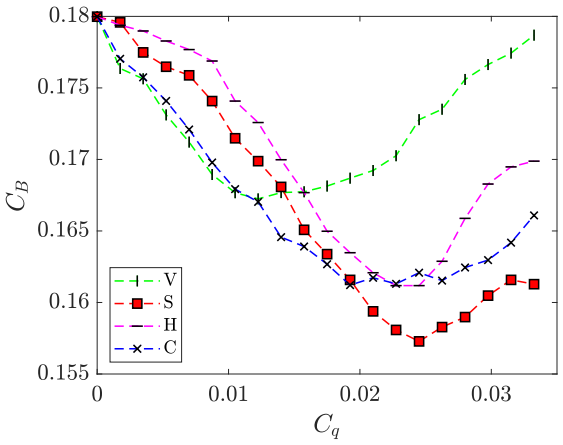

Figure 2: Base drag C_B evolution with the blowing coefficient C_q for all the tested configurations.

4 Conclusions

Wind tunnel tests and numerical simulations are carried out to characterize the effect of steady blowing in flow around a square-back Ahmed body at $Re \simeq = 65000$. The air injection is produced by different blowing arrangements whose area is constant. Results show important differences between the tested configurations in both mass and momentum blowing regimes, suggesting an important role of the blowing geometry in terms of drag reduction and near wake manipulation.

This work is funded by Project PDC2021-121288-I00, financed by the Spanish MCIN and European Union.

References

W. Hucho and G. Sovran (1993). *Annual Review of Fluid Mechanics*, **25**, 485–537.

H. Choi, J. Lee and H. Park (2014). *Annual Review of Fluid Mechanics*, **46**, 441–468.

C.J. Wood (1964) *The Aeronautical Journal*, **68** (643), 477–482.

P.W. Bearman (1967) *Aeronautical Quarterly*, **18** (3), 207–224.

S. R. Ahmed, G. Ramm and G. Faitin (1984). *SAE Transactions*, **93 (2)**, 473–503.

M. Lorite-Díez and J.I. Jiménez-González *et al.* (2020). *Journal of Fluid Mechanics*, **883**, A53.

2nd Spanish Fluid Mechanics Conference
Barcelona (2 - 5 July 2023)

DRAG REDUCTION OF A SQUAREBACK AHMED BODY USING REAR FLEXIBLE DEVICES

J.C. Muñoz-Hervás†[1], J.M. Camacho-Sánchez[1], M. Lorite-Díez[2], J.I. Jiménez-González[1], O. Cadot[3], and C. Martínez-Bazán[2]

† *jcmunoz@ujaen.es*

[1]Departamento de Ingeniería Mecánica y Minera. Universidad de Jaén, Spain.
[2]Departamento de Mecánica de Estructuras e Ingeniería Hidráulica, Universidad de Granada, Spain.
[3]Departament of Aerospace Engineering, University of Liverpool, UK.

We perform an experimental study on the turbulent wake of a squareback Ahmed body, to analyze the use of rear deformable solutions as control strategies to reduce the drag. Two rear deformable devices are compared, namely flexible foils and flexibly-hinged rigid plates. The results shows that both solutions decrease the drag over the range of Cauchy number investigated $Ca < 10^2$, by means of passive reconfiguration processes.

1 Introduction

Heavy transport represents an important source of CO_2 emissions, due to their bluff geometries and associated aerodynamics, which fosters the fuel consumption. One feasible approach to increase their energetic efficiency is to reduce their aerodynamic drag. In particular, it is estimated that approximately 25% of the aerodynamic drag of a truck is created at the base due to flow separation (Hucho et al. , 1993). As a result, many scientific works have been devoted to test devices implemented at the base of simplified models of heavy vehicles (Choi et al. , 2014), such as the Ahmed body. Among other strategies, mounting a rear cavity is one way to reduce the drag and control the long-time bi-stable dynamics characterizing the wake behind simplified 3D blunt models Evrard et al. (2016) However, the performance of rigid systems is not always optimal under changing flow conditions, e.g. transient flow or cross-flow Lorite-Diez et al. (2020). Thus, we propose to explore flexible adaptive solutions that may adapt passively to changing flow conditions and reduce drag robustly.

2 Experimental set-up

We study experimentally the wake behind an squareback Ahmed body, of height $h = 72$ mm, length $l = 4.04h$ and width $w = 1.35h$ (see Fig. 1), placed inside a wind tunnel of 400 mm x 400 mm test. Two different adaptive control solutions are tested. First, two flexible foils of brass of length $B = 0.5h$ and calibrated thickness e are embedded at the base edges, allowing their deflection as cantilevered flaps when subjected to the flow. The performance of such flexible device is compared against the use of flexibly-hinged rigid flaps, whose torsional joint is built embedding the previous flexible foils of brass. As illustrated in Camacho-Sanchez et al. (2023), the flaps dynamics can be approximated as that of a one-degree-of freedom angular oscillator. The Reynolds

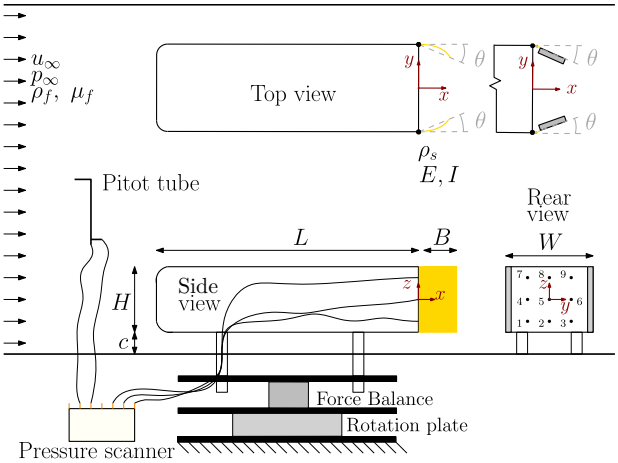

Figure 1: Sketch of the experimental set-up.

number is set between $Re = \rho U_\infty h/\mu \simeq 5 \cdot 10^4$ and 10^5, where U_∞, ρ_f and μ_f are respectively the velocity, density and viscosity of the free-stream. Besides, the coupled dynamics of the fluid-structure problem is characterized by means of the Cauchy number, defined as $Ca = \frac{\rho_f u_\infty^2 B^3}{2EI}$, where E and I are respectively the Young's Modulus and moment of inertia of the rotation axis, of the calibrated brass foil. Thus, the range of Cauchy number investigated is $Ca = [20, 100)$. Moreover, both systems feature similar values of the density ratio $m^* = \rho_s/\rho_f \simeq 8500$.

Force and base pressure measurements are performed using a 6-axis load cell and a multi-channel pressure scanner. The base drag coefficient is defined as $C_B = -\frac{1}{n}\sum_{i=1}^{n}\frac{p_i - p_\infty}{\rho U_\infty^2/2}$, with p_i denoting the pressure measured at each base tap i and p_∞ being the reference static pressure. Similarly, the drag coefficient is obtained as $C_x = \frac{F_x}{0.5\rho_f U_\infty^2 HW}$, where F_x is the measured time-averaged drag force. Finally, the angular displacement θ of plates is also obtained using high-speed visualizations (Fig. 2).

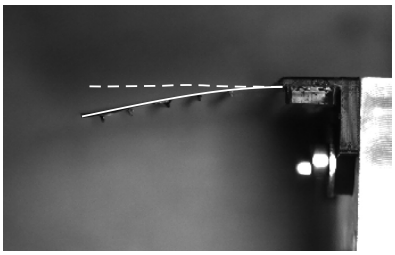

Figure 2: Illustration of average deflection of the flexible flaps for $Ca = 90$ ($Re = 9.7 \cdot 10^5$).

3 Results

Figure 3 shows relative variation of the drag and base drag coefficients with respect to reference values of the baseline Ahmed body for each Re, i.e. ΔC_x and ΔC_B. First, it is observed that the implementation of either the flexible or hinged lateral plates induces a pressure recovery at the base, as the base drag coefficient C_B decreases for both solutions. In particular, ΔC_B features an increasing reduction with Ca, reaching maximum values of $\Delta \simeq 18\%$ and 19% for the hinged and flexible plates respectively. This indicates a progressive pressure recovery as the relative stiffness reduces, which is more efficient in the case of the flexible foils. The drag reduction achieved by the flexible solutions is slightly lower, but still important, obtaining maximum values of $\Delta C_x \simeq 4.5\%$ and 6% when the hinged and flexible foils are mounted. Visualizations of the near wake region show that the plates undergo a progressive passive reconfiguration adapting to the flow detachment at the rear edge, as illustrated in figure 2, where the average chord angle is approximately $\theta = 8°$. These results could open a new perspective in the design of efficient adaptive control systems applied to heavy transport, where changing flow conditions take place. As shown by Camacho-Sanchez et al. (2023) drag reductions above 10% may be expected under cross-wind conditions, highlighting the potential of these adaptive solutions in realistic configurations.

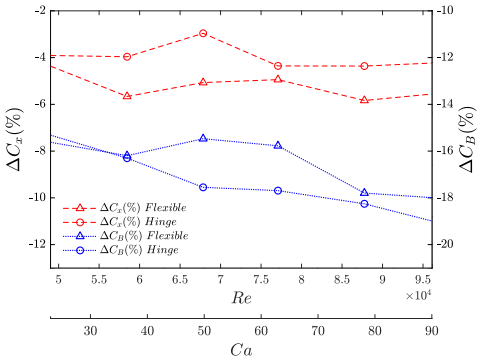

Figure 3: Evolution with Ca and Re of the relative variations of drag ΔC_x and base drag ΔC_B coefficients with respect to reference values for the baseline body, corresponding to flexible and hinged flaps.

4 Conclusions

We have investigated the use of rear adaptive solutions of flexible plates to improve the aerodynamics features of a squareback Ahmed body. The results shows that the drag coefficient decreases due to passive adaptation of flaps to the separated flow. This may open a new perspective for the design of efficient control strategies in heavy transport industry.

This work is funded by Projects PDC2021-121288-I00 and TED2021-131805B, financed by the Spanish MCIN and European Union.

References

Hucho W. & Sovran. G. (1993) "Aerodynamics of road vehicles", *Annu. Rev. Fluid Mech.* **25**(1), 485–537.

Choi H., Lee L. & Park. H. (2014) "Aerodynamics of heavy vehicles", *Annu. Rev. Fluid Mech.* **46**(1), 441–468

Evrard A., Cadot O. *et al.* (2016) "Fluid force and symmetry breaking modes of a 3D bluff body with a base cavity", *J. Fluids Struct.* **61**, 99–114.

Lorite-Díez M., Jiménez-González J.I., *et al.* (2020) "Drag reduction on a three dimensional blunt body with different rear cavities under cross-wind conditions", *J. Wind Eng. Ind. Aerod.* **200**, 104145.

Camacho-Sánchez J.M., Lorite-Díez M., *et al.* (2023) "Experimental study on the drag reduction of a 3D bluff body by rotary plates", Submitted to *Phys. Rev. Fluids.*

2nd Spanish Fluid Mechanics Conference
Barcelona (2 - 5 July 2023)

Experimental measurements of particle dispersion and concentrations in the turbulent wake of Ahmed body and effects of rear slant angle

Manish Kumar[1*], Srinivas V. Veeravalli[1], and Murali R. Cholemari[1]

[*] *manish.kumar@am.iitd.ac.in*

[1]Department of Applied Mechanics, Indian Institute of Technology, Delhi, New Delhi-110016, India

This study investigated particulate dispersion in the turbulent wake of a simplified vehicle model (Ahmed body). It focused on the effects of the Ahmed body rear slant angles ($\phi = 25^o$, 40^o) on flow structures, particle dispersion, and particle concentration fields in the turbulent wake. In wind tunnel experiments, particle dispersion and concentration fields were measured in the near wake. As a result, the near wake turbulent structures and concentration fields are found to be highly dependent on the rear slant angle (ϕ). The rear slant angle determines trailing vortices strength, recirculation region size, and dispersion characteristics in Ahmed body near wake. For the $\phi = 25^o$ model, the attached flow is observed over the rear slant. A pair of trailing vortices were observed, producing a downwash. The $\phi = 40^o$ model has a massive separation on the rear slant but no trailing vortices. Backflow over the rear slant was found responsible for increased vertical dispersion ($y/h > 1$).

1 Introduction

Due to the wake created by moving vehicles on roads, particulates are mixed due to the turbulence, which raises the ambient PM levels. The wake region is a key feature of the flow field around a vehicle. Particle dispersion characteristics are studied by analyzing the smoke particle dispersion behind a simplified vehicle model Ahmed body (after Ahmed et al. (1984)). Wind tunnel simulations are performed at $Re_l = U_\infty l/\nu = 1.72 \times 10^5$ (where 'U_∞' is free stream velocity, 'l' is Ahmed body length and 'ν' is kinematic viscosity of the air). Measurements of particle dispersion and concentration fields in the near wake of Ahmed body (at three downstream locations; $x/h = 0.25$, 1, and 5, where 'h' is Ahmed body height) with two rear slant angles, $\phi = 25^o$, 40^o were performed.

2 Methodology

A non-intrusive smoke particle concentration measurement technique, Quantitative Smoke Visualisation (QSV), similar to Planar Laser Induced Fluorescence (PLIF)[1] but adapted for scattering of light instead of laser induced fluorescence, was used to get spatially and temporally resolved concentration measurements in the turbulent wake. Experiments involved releasing smoke particles (Ethylene-Glycol, diameter $d_s \approx 1\mu m$) from a source behind the model. The smoke particles were illuminated using a laser sheet. The scattered light from smoke particles was captured by the camera, and the acquired images were post-processed to obtain the concentration field (refer to Fig. 1).

[1]More details about PLIF can be found in Crimaldi (2008)

3 Results and Conclusions

The results show that the rear slant angle (ϕ) plays a significant role in determining the turbulent structures and concentration fields in the near wake. Different flow topologies cause different dispersion patterns. For the $\phi = 25^o$ model, an attached flow over the rear slant is observed (Fig. 2). The flow rolls up toward the rear slant to form trailing vortices from the side edges of the rear slant, the influence of trailing vortices on the concentration field is predominant. The signatures of trailing vortices are evident in the instantaneous frames and concentration fields (Fig. 1). The presence of trailing vortices induced by the rear slant concentrates the scaler field on the two wake edges and lowers the concentration levels along the model midplane ($z/h = 0$); this is in agreement with the findings of Goose et al. (2006). For the $\phi = 40^o$ model, we observe a massive separation on the rear slant surface (Fig. 3 shows the backflow due to separation); the trailing vortices do not form, unlike $\phi = 25^o$ case (as also observed by Goose et al. (2006)). Backflow over the rear slant increases the

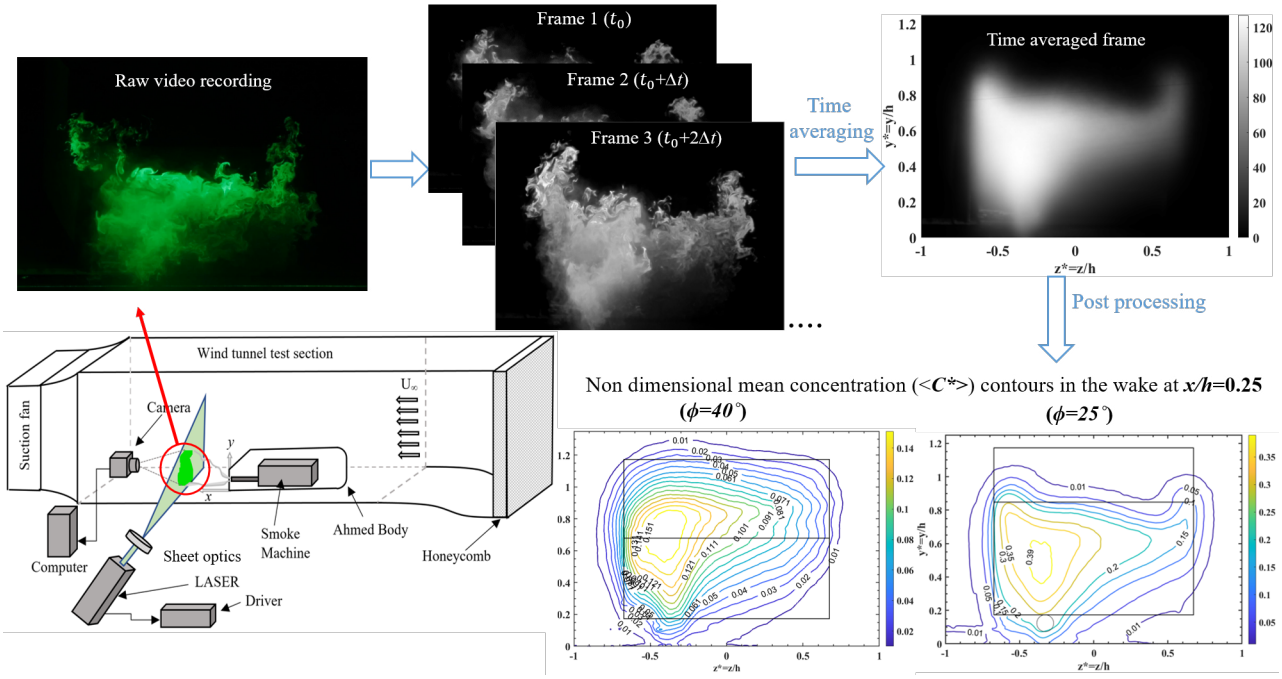

Figure 1: Experimental setup and Technique for concentration measurements. Concentration contours at $x/h = 0.25$ is shown for Ahmed body with $\phi = 25^o$ and $\phi = 40^o$.

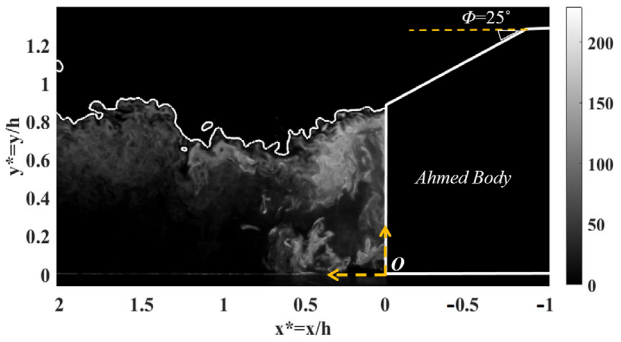

Figure 2: Visualisation of the flow (in longitudinal $x - y$ plane, $z/h = -0.31$) over the rear part of the Ahmed body ($\phi = 25^o$), (there is no backflow over the rear slant), flow is from Right to Left.

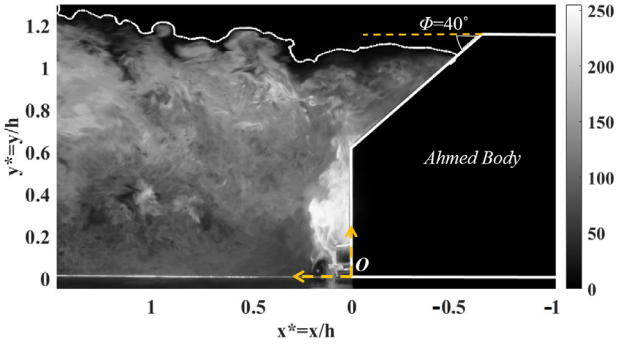

Figure 3: Visualisation of the flow (in longitudinal $x - y$ plane, $z/h = -0.31$) over the rear part of the Ahmed body ($\phi = 40^o$), (backflow of smoke over the rear slant is visible) , flow is from Right to Left.

vertical dispersion of smoke particles ($y^* > 1$). The model with, $\phi = 40^o$ has higher vertical and lateral dispersion than the model with $\phi = 25^o$. Specifically, at $x/h = 0.25$, the dispersion contours extend vertically up to $y^* = 1.31$ for the $\phi = 40^o$ model and $y^* = 1.06$ for the $\phi = 25^o$ model (see Fig. 1). Likewise, The contours reach $y^* = 1.4$ for the $\phi = 40^o$ model and $y^* = 1.17$ for the $\phi = 25^o$ model at $x/h = 1$. From the observations, it can be concluded that the rear slant angle (ϕ) is a critical parameter that decides the strength of trailing vortices, size of the recirculation region, and consequently, dispersion scales in the near wake of Ahmed body.

References

Ahmed, S. R., Ramm, G., and Faltin, G. (1984). "Some salient features of the time-averaged ground vehicle wake". *SAE transactions*, 473-503.

Crimaldi, J. P. (2008). "Planar laser induced fluorescence in aqueous flows". *Experiments in fluids*, **44**, 851-863.

Gosse, K., Paranthoën, P., Patte-Rouland, B., and Gonzalez, M. (2006). "Dispersion in the near wake of idealized car model". *International journal of heat and mass transfer*, **49**(9-10), 1747-1752.

2nd Spanish Fluid Mechanics Conference
Barcelona (2 - 5 July 2023)

Generation of free-stream perturbations in direct numerical simulation for low-Reynolds aerodynamics

Stefano Olivieri[1], Juan Manuel Catalán[1], Oscar Flores[1], and Manuel García-Villalba[2]

solivier@ing.uc3m.es

[1]Department of Aerospace Engineering, Universidad Carlos III de Madrid, Spain
[2]Institute of Fluid Mechanics and Heat Transfer, TU Wien, Austria

Unsteady aerodynamics and fluid-structure interaction at relatively low Reynolds number (i.e., $Re \sim 10^2 - 10^4$) concern problems attracting considerable scientific and technological interest, such as the design of micro-aerial vehicles or energy harvesting from environmental flows. In these applications, external flow perturbations typical of the atmospheric boundary layer (ABL) can have a dramatic effect on the aerodynamic performance. In fact, relatively high turbulence conditions can be met when comparing the low velocities involved in these problems with the characteristic intensity of the ABL turbulence (Watkins *et al.*, 2006). Moreover, the size of the energy-containing turbulent eddies can often be comparable to the wing chord, thus representing a condition remarkably different from those typically experienced by more conventional aircraft. Nevertheless, the present knowledge on this kind of problems remains essentially limited to configurations where the free stream is assumed to be laminar and unperturbed.

In this work, we aim at developing and testing suitable strategies to obtain free-stream perturbations with well defined and controllable properties (e.g., intensity, homogeneity, isotropy, and scale-by-scale energy distribution) in the framework of high-fidelity, direct numerical simulation (DNS), with the subsequent goal of using these tools for the investigation of low-Reynolds aerodynamics problems (e.g., flapping flight in ABL turbulence).

Seeking for a realistic yet general configuration (i.e., not constrained to specific geometrical features), we consider and compare two distinct approaches that can be used to generate a perturbed/turbulent free stream (fig. 1):

1. The first is using a *synthetic turbulence inflow generator* (STIG). Specifically, we consider the implementation based on digital filters as proposed by Klein *et al.* (2003); Kempf *et al.* (2012), and, in particular, the approach proposed by Schmidt & Breuer (2017) where the flow is forced by means of a source term active in a relatively narrow region of influence (here, located shortly after the inlet of the computational domain). The generated fluctuations fulfill an input intensity TI_0 and input integral lengthscale Λ_0. In the vicinity of the region of influence, the random velocity perturbations induced by the STIG have a relatively narrow banded spectral energy distribution (centered around Λ_0), a feature that can be exploited to isolate the effect of perturbations having a specific lengthscale.

2. The second is the simulation of *grid-induced turbulence* (GT), i.e., placing after the domain inlet a (passive) solid grid with a suitable geometry (e.g., made of evenly spaced rods with square cross-section). Although more demanding than other simulation strategies, such a fully resolved approach ensures a physically based generation of the flow perturbations (Olivieri *et al.*, 2021). Sufficiently far from the grid, the turbulence intensity decays along the streamwise direction

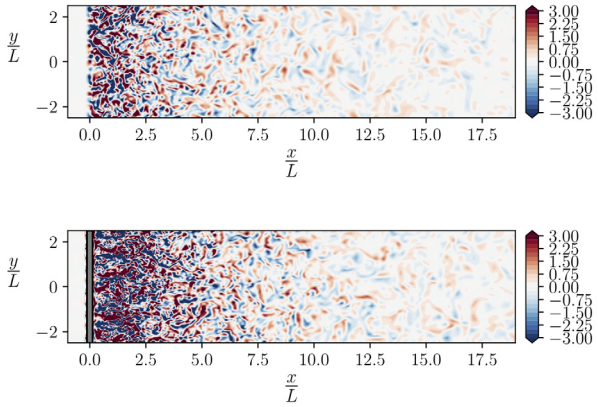

Figure 1: Snapshots from DNS performed with the STIG (top) and GT (bottom) approach in order to generate a (three-dimensional) turbulent free stream (flowing from left to right along the streamwise direction x). The colormap shows the instantaneous (out-of-plane) z-component of the vorticity field for the longitudinal plane at $z = 0$. For both cases, the reference lengthscale L is equal to the spacing between the rods of the solid grid used in the GT approach.

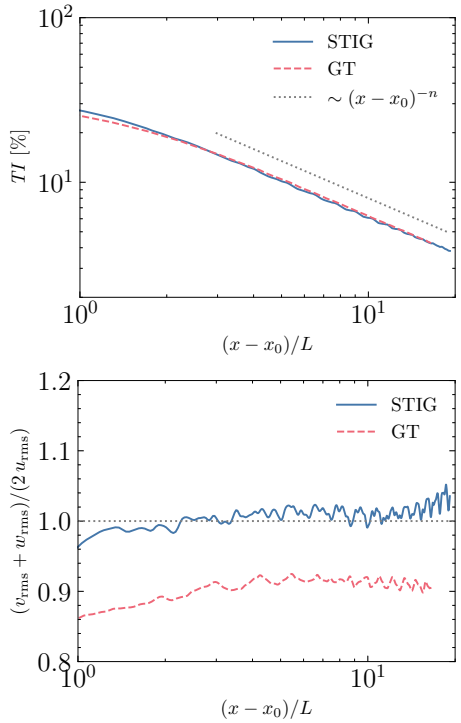

Figure 2: Evolution of turbulence properties along the streamwise direction (note that x is properly shifted by a virtual origin x_0), obtained with the STIG (solid blue) and GT (red dashed) approach. Top: decay of turbulence intensity (with the dotted line depicting a power law with decay exponent n). Bottom: large-scale anisotropy (with the dotted horizontal line indicating the isotropic case).

with a power-law behavior. The resulting energy spectrum is broad banded and manifests (for sufficiently large Re) the classical phenomenology of fully developed turbulence.

Both approaches have recently been implemented and tested in TUCAN, a massively parallel in-house code developed by the CFD Lab research group at UC3M (Moriche, 2017). The code solves the full incompressible Navier-Stokes equations with a finite difference method and fractional-step procedure on a Cartesian mesh, using an immersed boundary method to model the presence of moving bodies of arbitrary shape and motion.

We carry out a comparative study between the STIG and GT approach to highlight the key aspects in using such complementary strategies. Preliminary results are shown in fig. 2 for two main observables, i.e., the turbulence intensity (top panel) and large-scale anisotropy (bottom panel), as a function of the streamwise coordinate. For a sufficiently large Reynolds number (here we choose $Re = UL/\nu = 1000$, where U is the uniform flow velocity imposed at the inlet, L is the unitary reference lengthscale, and ν is the kinematic viscosity) and sufficiently downstream of where the perturbations are generated, the resulting phenomenology is that of decaying turbulence, as it can be noted by the power-law behavior of the turbulence intensity (fig. 2 top). Furthermore, it can be observed that the fluctuations generated by the STIG are almost perfectly isotropic, in comparison to those obtained with the GT approach (fig. 2 bottom).

In the talk, we will present the results of the on-going activity devoted to the analysis of the spectral energy distribution and characteristic spatial/temporal scales of the generated perturbations.

References

Kempf, A. M., Wysocki, S., & Pettit, M. (2012). "An efficient, parallel low-storage implementation of Klein's turbulence generator for LES and DNS". *Computers & Fluids*, 60, 58-60. DOI:10.1016/j.compfluid.2012.02.027.

Klein, M., Sadiki, A., & Janicka, J. (2003) "A digital filter based generation of inflow data for spatially developing direct numerical or large eddy simulations". *Journal of Computational Physics*, 186(2), 652-665. DOI:10.1016/S0021-9991(03)00090-1.

Moriche, M. (2017). "A numerical study on the aerodynamic forces and the wake stability of flapping flight at low Reynolds number". Ph.D. dissertation, Dept. Bioengineering and Aerospace Eng. Universidad Carlos III de Madrid. Available at https://e-archivo.uc3m.es/handle/10016/24960

Olivieri, S., Viola, F., Mazzino, A., & Rosti, M. E. (2021) "Direct numerical simulation of flapping flags in grid-induced turbulence". *Physics of Fluids* 33(8), 085116. DOI:10.1063/5.0060181.

Schmidt, S., & Breuer, M. (2017). "Source term based synthetic turbulence inflow generator for eddy-resolving predictions of an airfoil flow including a laminar separation bubble". *Computers & Fluids*, 146, 1-22. DOI:10.1016/j.compfluid.2016.12.023.

Watkins, S., Milbank, J., Loxton, B. J., & Melbourne, W. H. (2006). "Atmospheric winds and their implications for microair vehicles". *AIAA Journal* 44(11), 2591-2600. DOI:10.2514/1.22670.

2nd Spanish Fluid Mechanics Conference
Barcelona (2 - 5 July 2023)

Numerical study of the flow past a three-element high-lift airfoil at different angles of attack

Ricard Montalà[1], Oriol Lehmkuhl[2], and Ivette Rodriguez[1]

ricard.montala@upc.edu

[1]TUAREG - Turbulence and Aerodynamics Research Group, Universitat Politècnica de Catalunya, Spain
[2]Large-scale Computational Fluid Dynamics Group, Barcelona Supercomputing Center, Spain

A parametric study of the 30p30n three-element high-lift airfoil is conducted by changing the angle of attack at $\alpha = 5$, 9 and 23° at a constant Reynolds number of $Re_c = 750,000$. Computational predictions are performed employing large eddy simulations.

1 Introduction

For many years, one of the main concerns in the aeronautical industry has been the drag and noise reduction of aircrafts. Despite many studies can be found on the literature regarding single-element airfoils, multi-element airfoils still remain an open research topic. The present work focuses on the aerodynamic study of the 30p30n three-element high lift airfoil. This was used as the reference geometry for the AIAA Workshop on Benchmark Problems for Airframe Noise Computations (BANC), so many numerical studies were published on this regard. Nevertheless, those works were focused on the noise radiated from the slat cove and most of the predictions were carried out using the hybridization of Reynolds-averaged Navier-Stokes (RANS) and large eddy simulation (LES) methods, such as detached eddy simulations (DES) or delayed detached eddy simulations (DDES). This study aims to reach a more general insight of the flow around the 30p30n wing by performing high fidelity wall-resolved LES simulations, and identify which are the main sources of drag. Here, three different angles of attack are addressed $\alpha = 5$, 9 and 23°, while the Reynolds number based on the nested chord is fixed at $Re_c = 750,000$.

2 Numerical modelling

Large eddy simulations (LES) are performed employing the low-dissipative finite element (FE) code Alya. In this code, the convective operator is approximated using a scheme that preserves linear and angular momentum, and kinetic energy at discrete level. A non-incremental fractional-step method is used to stabilise the pressure, while the set of equations are time integrated using an energy conserving fourth order Runge-Kutta explicit method combined with an eigenvalue based time-step estimator (Lemhkuhl et al. , 2019). Regarding the LES turbulence modelling, the Vreman (2004) sub-grid scale (SGS) eddy-viscosity model is considered.

3 Results

Simulations are conducted in a computational domain with a radius of $10C$ in the $x-y$ plane and extruded in the z-direction a distance of $L_z = 0.1C$, C being the stowed chord. A uniform velocity profile is applied at the inflow regions, whereas zero-gradients are imposed at the outflow zones. The z-direction is considered periodic with 128 planes. The unstructured grid contains a total of 58 million points, which are distributed in an structured-like manner nearby the airfoil, allowing to achieve a non-dimensional normal near wall distance of $\Delta y^+ \approx 1$. Along the streamwise and spanwise directions, the near wall distance is $\Delta x^+ \approx 80$ and $\Delta z^+ \approx 50$, respectively.

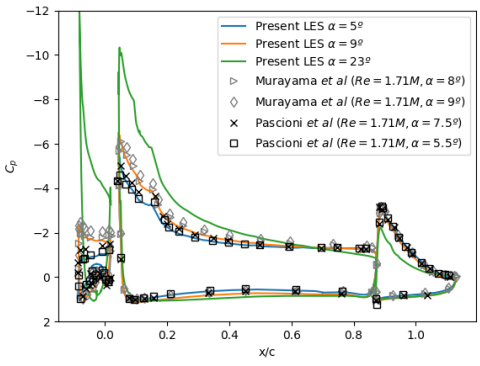

Figure 1: Pressure coefficient compared to experimental data.

Figure 1 shows the pressure coefficient at the three angles of attack considered in this study and results

are compared with the experimental data of Murayama et al. (2014) and Pascioni and Cattafesta (2016). Those experiments were performed at similar angles of attack but at a higher Reynolds number. Nonetheless, quite good agreement is observed with those of the literature. Unfortunately, no data is available for $\alpha = 23°$. In figure 2, the evolution of the drag coefficient with the angle of attack is shown, as well as the contribution of each element to the total drag. Finally, the streamlines at the slat and flap regions are depicted in figure 3 for the three angles of attack. This figure also shows the velocity magnitude contours.

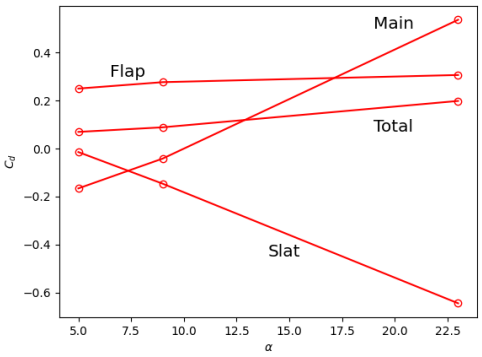

Figure 2: Contribution to the total drag coefficient of each element.

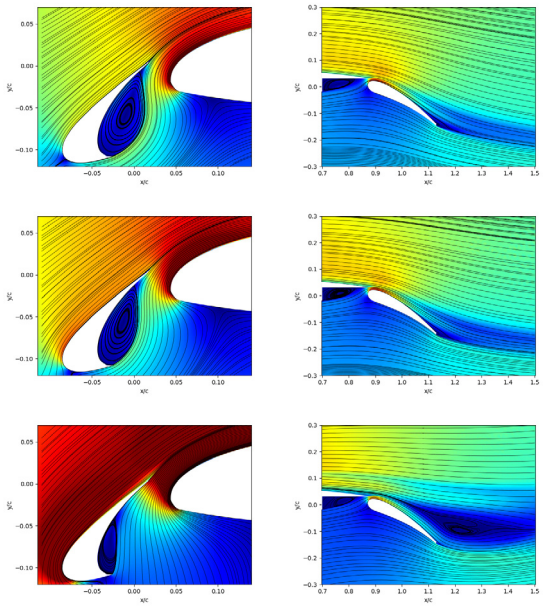

Figure 3: Velocity magnitude contours and streamlines at $\alpha = 5$, 9 and 23° from top to bottom. At the slat (left) and flap (right) regions.

4 Discussion and further work

The pressure coefficient agrees well with the literature available and the angle of attack increases the suction peak in the main element. Moreover, it is detected that the main source of drag at high angles of attack is the main element. The evolution of the streamlines is also analysed: The recirculation bubble at the slat cove gets smaller, whereas a larger wake appears downstream the flap. In the final version of the manuscript, a more extended and comprehensive comparison of the three angles of attack in terms of both the flow dynamics and topology will be done.

Acknowledgments

This work has been partially financially supported by the Ministerio de Economía y Competitividad, Secretaría de Estado de Investigación, Desarrollo e Innovación, Spain (ref. PID2020-116937RB-C21 and PID2020-116937RB-C22). We also acknowledge Red Española de Supercomputación (RES) for awarding us access to the MareNostrum IV machine based in Barcelona, Spain (Ref IM-2022-3-0005); as well as the HPC RIVR consortium (www.hpc-rivr.si) and EuroHPC JU (eurohpc-ju.europa.eu under the project ID EHPC-REG-2022R01-030) for funding this research by providing computing resources of the HPC system Vega at the Institute of Information Science (www.izum.si). R. Montalà acknowledges support of Departament de Recerca i Universitats de la Generalitat de Catalunya through a FI-SDUR graduate fellowship program.

References

Lehmkuhl, G. Houzeaux, H. Owen, G. Chrysokentis and I. Rodriguez (2019) "A low-dissipation finite element scheme for scale resolving simulations of turbulent flows". *J. Comput. Phys.*, **390**, 51–65.

Vreman A.W. (2004) "An eddy-viscosity subgrid-scale model for turbulent shear flow: Algebraic theory and applications". *Phys. Fluids*, **16**, 3670–3681.

Murayama M., Nakakita K., Yamamoto K., Ura H. and Ito Y. (2014) "Experimental study of slat noise from 30p30n three-element high-lift airfoil in JAXA hard-wall low-speed wind tunnel". *20th AIAA/CEAS Aeroacoustics Conference, Atlanta.*

Pascioni K.A. and Cattafesta L.N. (2016) "Aeroacoustics measurements of leading-edge slat noise". *22nd AIAA/CEAS Aeroacoustics Conference, Lyon.*

2nd Spanish Fluid Mechanics Conference
Barcelona (2 - 5 July 2023)

On the effect of deformation in a wing model on the correlation of the lift slope

Paloma Gutierrez-Castillo[1], Eduardo Durán-Venegas[1], Nikita Konovalov-Shishov[1], and Carlos del Pino[1]

paloma_gutierrez@uma.es

[1]Escuela de Ingenierías Industriales, Universidad de Málaga, Spain

Deformed wing models with a NACA0012 airfoil are analyzed experimentally in a wind tunnel at the University of Malaga. Measurements show the influence of the level of the deformation on the lift coefficient and, therefore, on the slope of the lift coefficient versus the angle of attack. In general, the deformation increments the value of the lift coefficient. This gain is more noticeable for higher wind models (or higher aspect ratios) and when the wing models are tested at higher Reynolds numbers. We estimated the value of the lift slope with a correlation as a function of Reynolds number and aspect ratio, showing an excellent agreement.

1 Introduction

Traditionally, aerodynamic studies have focused on a few key aerodynamic parameters such as lift, drag and lift slope (change in lift with varying angle of attack). There are multiple studies on different wing models depending on the application. Nowadays, aircraft wings are made of lighter materials, resulting in thinner wing models. These wings have a deformation associated with flight conditions, see Afonsoa *et al.* (2017) for a review of recent developments in aerospace related to high aspect ratio wings with deformations.

The influence of wind deformation on the lift coefficient and, therefore, on the lift slope has only been recently studied by (Zhong *et al.*, 2018). Our experiments further analyze this influence using rigid models with imposed deformation to isolate the effect of the deformation. Specifically, this study focuses on including the effect of deformation on a correlation to compute the lift slope.

2 Results

As mentioned above, the lift slope is a key criterion for any initial wing design. Therefore, we aim to find a correlation to obtain $C_{L\alpha}$ (the slope of the lift coefficient versus the angle of attack) as a function of the aspect ratio and the Reynolds number. We have experimentally measured different wing models using rigid wings with and without an imposed deformation. The deformation is chosen from real measurements of wing deformations from Farnsworth *et al.* (2015). The effect of the deformation on the lift coefficient is clear for big aspect ratios and Reynolds numbers (see figure 1). Note also that the deformation level and the lift coefficient change are not linearly related.

At this point, it is interesting to discuss if a first approximation for the $C_{L\alpha}$ value for the NACA0012 profile can be computed by using the correlation provided by Gutierrez-Castillo *et al.* (2021) for the flat plate with non-infinite wing aspect ratio adjusting the parameters α_1 and α_2. The equation of that reference is repeated here for clarification purposes.

$$C^*_{L\alpha} = \left(\frac{2\pi}{1+\alpha_1 * AR^{-1}}\right)\left(\frac{\alpha_2}{1+10^6/Re}\right)^{1/5} \quad (1)$$

with $\alpha_1 = 5.21$ and $\alpha_2 = 14.61$ (for flat plate).

Adjusting the same formula to our results for the NACA0012 profile. We obtain a $R^2 = 0.98$ using the parameters $\alpha_1 = 4.89$ and $\alpha_2 = 4.72$ for models without deformation. Therefore, the correlation is still useful in our ranges of aspect ratio and Reynolds number.

It is interesting how this correlation can approximate cases even with the deformation. In order to try to isolate the effect of the deformation, the same correlation was used for the deformed cases but fixing $\alpha_2 = 4.72$. Therefore, including the changes con $C_{L\alpha}$ produced by the deformation in the parameter α_1 that is equivalent to changing the wing size.

For the intermediate deformation cases, we obtained $\alpha_1 = 4.59$ and $R^2 = 0.98$, and for the big deformation cases, we obtained: $\alpha_1 = 4.63$ and $R^2 = 0.99$. To provide a better understanding, we depict in figure 2 the representation of the measured lift slope $C_{L\alpha}$ and the estimated one $C^*_{L\alpha}$. Observing the good results, we can conclude that the effect of the de-

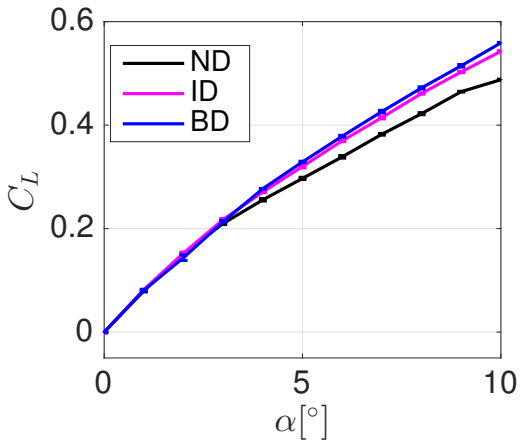

Figure 1: Lift coefficient versus angle of attack for models of $AR = 4$ at $Re = 160000$. Three wing models: non-deformed (black), intermediate deformation (pink), big deformation (blue)

formation can be absorbed in the α_1 parameter and, therefore, including a deformation in the spanwise direction is equivalent in terms of the $C_{L\alpha}$ to change the wingspan length in the wing model.

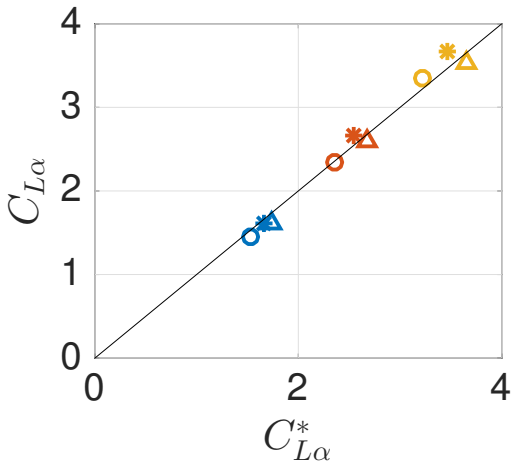

Figure 2: Lift slope $C_{L\alpha}$ versus the estimated lift slope $C^*_{L\alpha}$. Circles represent cases of Re=80000, starts Re=120000 and triangles Re=160000. Blue color corresponds to cases with $AR = 1$, red color $AR = 2$ and yellow color $AR = 4$.

3 Conclusions

We have shown that it is possible to properly include the level of the deformation of a wing model on a correlation to approximate the value of the lift slope for different cases with NACA0012 wing models. Remarkably, the effect of the deformation can be absorbed only by one geometric parameter. Therefore, the effect of deformation on the computation is equivalent to varying the wingspan length in the wing model.

Acknowledgements

This research has been supported by the project PID2021-124692OA-I00 from the Ministerio de Ciencia e Innovación and from "ayuda UMA Plan Propio".

References

Gutierrez-Castillo P, Aguilar-Cabello J, Alcalde-Morales S, Parras L & del Pino C (2021) "On the lift curve slope for rectangular flat plate wings at moderate Reynolds number". *Journal of Wind Engineering and Industrial Aerodynamics*, **208**, 104459.

Afonso F, Valea J, Oliveira D, Lau F, Suleman, A (2017) "A review on non-linear aeroelasticity of high aspect-ratio wings", Progress in Aerospace Sciences, **, 89**(3): 40–57.

Zhong M, Zheng S, Wang G, Hua J & Gebbink R (2018) "Correlation analysis of combined and separated effects of wing deformation and support system in the CAE-AVM study", Chinese Journal of Aeronautics, **, 31**(3): 429–438.

Yang Pang Z, Cesnik C E S & Atkins E M (2014) "In-Flight Wing Deformation Measurement System for Small Unmanned Aerial Vehicles", *55th Structures, Structural Dynamics, and Materials Conference*, **6**, 0330.

Farnsworth J A N, Corbett S, Seidel J & McLaughlin TE (2015) "Aeroelastic Response of a Finite Span NACA 0018 Wing Part 1: Experimental Measurements", *53rd AIAA Aerospace Sciences Meeting*, 0249.

2nd Spanish Fluid Mechanics Conference
Barcelona (2 - 5 July 2023)

Towards data driven reduced order models for the automotive industry

Benet Eiximeno[1,2], Arnau Miró[1], Ivette Rodríguez[2], and Oriol Lehmkuhl[1]

benet.eiximeno@bsc.es

[1]Barcelona Supercomputing Center, 08034 Barcelona, Spain
[2]Turbulence and Aerodynamics Research Group, Universitat Politècnica de Catalunya (UPC), 08221 Barcelona, Spain

The effects of the yaw angle in the back pressure of the Windsor body are studied by means of wall modelled LES simulations. A POD-based reduced order model for the back-pressure prediction at any yaw angle is developed.

1 Introduction

The aerodynamic performance of road vehicles is highly influenced by the wind incidence angle. Even a small perturbation on the incident velocity, breaks the symmetry of the flow field as the hairpin vortex in the leeward side of the recirculation gains intensity, increases the suction, augments the drag force and with it the fuel consumption. This effect has a major impact in square-back cars, which are models with an abrupt end that evokes a forced separation and recirculation area. The goal of the present work is to develop a reduced order model to predict the variations in the back pressure, and thus, the drag using the configuration without wheels of the Windsor body.

2 Numerical methodology

The dataset for the reduced order model analysis is based on wall-modelled large eddy simulations of the yawed Windsor body at $\delta = 2.5°$. The Reynolds number has been set to $Re = UL_{ref}/\nu = 2.9 \times 10^6$, where L_{ref} is the length of the model. The domain extension is equivalent to the wind tunnel used in the experiments of Varney et al. [2021]. The computational grid has a total amount of 41.42 million grid points with a maximum y^+ value of the mesh around the car is $y^+ = 62.5$ and a maximum ratio between the mesh size and the Kolmogorov scales in the wake of $h/\eta = 119.9$. The turbulence is treated using the Vreman model [Vreman, 2004] and the near wall region is modelled with the Reichardt wall law with an exchange location method in the fourth node [Lehmkuhl et al., 2018]. With this methodology it has been possible to obtain similar results as the ones in the experiment of Varney et al. [2021] (e.g. $C_D = 0.3400$ vs $C_D = 0.3298$ (exp)).

Proper orthogonal decomposition (POD) [Lumley, 1981] is applied to the simulation to highlight patterns in the dataset linked with the yaw angle. The database is formed by 569 snapshots which extend over a period of $t = 21.2$TU.

3 Results

Figure 1 shows an instantaneous snapshot of the back recirculation at a horizontal plane located at $z/L = 0.186$ together with its reconstruction using only the first 10 POD modes of the velocity field. The reconstruction filters the smaller scales and shows how the recirculation is dominated by the hairpin vortices. Due to the yaw angle, the hairpin vortex from the leeward side (1) is bigger than the one in the windward side (2), hence the suction in the back face is bigger than in the case of a symmetric flow.

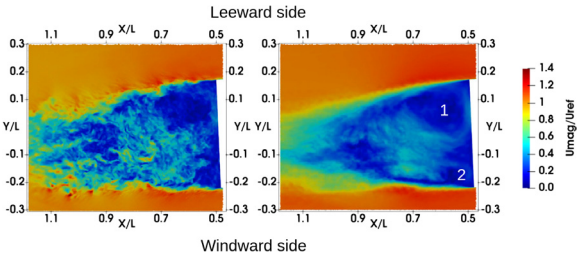

Figure 1: Velocity magnitude at an horizontal plane located at $z/L = 0.186$. Left: all scales, right: reconstructed with the first 10 POD modes

This suction increase due to the changes in the intensity of the leeward hairpin vortex is highlighted by the two most dominant POD modes (Figure 2) of the surface pressure coefficient in the car, which contain a 8.37% of the total energy. Here we propose the following model:

$$P_{mean}[\delta] = P_{mean}[2.5°] + S_1[\delta]M_1 + S_2[\delta]M_2 \quad (1)$$

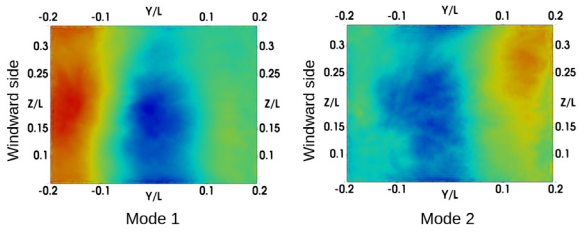

Figure 2: Two most dominant surface pressure coefficient modes

where M_1 and M_2 are the spatial distributions coming from the POD of the car rotated 2.5° in the yaw axis. S_1 and S_2 are the contributions of each mode in the studied yaw angle. First of all, S_1 and S_2 are computed at $\delta = 5°$ and $\delta = 10°$ by minimizing the mean error of the back-pressure in the location of the experimental probes used by Varney et al. [2021]. Figure 3 illustrates, for the case of $\delta = 5°$,

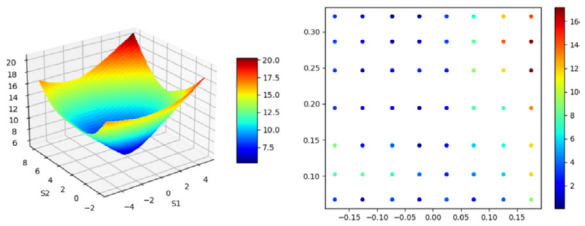

Figure 3: Mean error function (left) and error in the probes from Varney et al. [2021] (right) for $\delta = 5°$

the mean error function and the relative error of the back-pressure in the experimental probes. The results obtained with the with the optimal S_1 and S_2 values are rather good for $\delta = 5°$ with a mean error in the back pressure of $\varepsilon = 5.34\%$ (see Figure 4) although the error in the top leeward corner increases with the yaw angle (the mean error for $\delta = 10°$ is of $\varepsilon = 14.64\%$). As the coefficients are null at $\delta = 2.5°$, it is possible to do a linear regression to find an expression for S_1 and S_2 at any yaw angle between $\delta = 2.5°$ and $\delta = 10°$. This is a first and simplistic approach of the model, which will be improved in the final version of the manuscript with new wall modelled LES simulations in different yaw angles. It will also be discussed if the addition of lower rank modes can improve the accuracy of the model or if minimizing the error function with machine learning techniques can help to capture any non-linearity in the physics. Finally, the possibility to stablish a relation between the modes at different yaw angles will also be analyzed using the dynamic mode decomposition (DMD) [Schmid, 2010] and the modal assurance criterion (MAC) [Allemang, 1982].

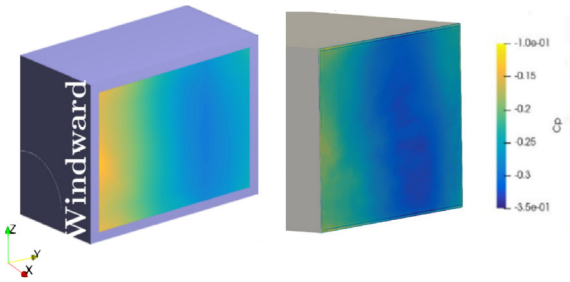

Figure 4: Experimental back-pressure Varney et al. [2021] (left) and model prediction (right) at $\delta = 5°$

Acknowledgements

This work has been partially financially supported by the Ministerio de Economía y Competitividad, Secretaría de Estado de Investigación, Desarrollo e Innovación, Spain (ref. PID2020-116937RB-C21 and PID2020-116937RB-C22).

References

Max Varney, Giancarlo Pavia, Martin Passmore, and Conor Crickmore. Windsor model experimental aerodynamic dataset, 2021. URL `https://repository.lboro.ac.uk/articles/dataset/Windsor_Body_Experimental_Aerodynamic_Dataset/13161284`.

AW Vreman. An eddy-viscosity subgrid-scale model for turbulent shear flow: Algebraic theory and applications. *Physics of fluids*, 16(10):3670–3681, 2004.

O Lehmkuhl, GI Park, ST Bose, and P Moin. Large-eddy simulation of practical aeronautical flows at stall conditions. *Proceedings of the 2018 Summer Program, Center for Turbulence Research, Stanford University*, pages 87–96, 2018.

J. L. Lumley. Rational Approach to Relations between Motions of Differing Scales in Turbulent Flows. *The Physics of Fluids*, 10(7):1405, December 1981. ISSN 0031-9171. doi: 10.1063/1.1762299. URL `https://aip.scitation.org/doi/abs/10.1063/1.1762299`. Publisher: American Institute of PhysicsAIP.

Peter J Schmid. Dynamic mode decomposition of numerical and experimental data. *Journal of fluid mechanics*, 656:5–28, 2010.

Randall J Allemang. A correlation coefficient for modal vector analysis. In *Proc. of the 1st IMAC*, pages 110–116, 1982.

2nd Spanish Fluid Mechanics Conference
Barcelona (2 - 5 July 2023)

A noninvasive method to determine intracranial pressure fluctuations from MR measurements of cerebrospinal fluid flow in the spinal canal

Wilfried Coenen[1], Stephanie Sincomb[2], Victor Haughton[3], and Antonio L. Sánchez[2]

wcoenen@ing.uc3m.es

[1]Departamento de Ingeniería Térmica y de Fluidos, Universidad Carlos III de Madrid, Spain
[2]Department of Mechanical and Aerospace Engineering, University of California San Diego, USA
[3]Department of Radiology, University of Wisconsin–Madison, USA

The periodic fluctuation of the intracranial pressure induced by the cardiac cycle is an important physiological signal that plays a role in many pathologies of the central nervous system. Currently, it can only be measured invasively with a pressure sensor inserted through a burr hole in the skull. Here, we present a noninvasive method to determine the intracranial pressure fluctuations from magnetic resonance measurements of cerebrospinal fluid flow in the spinal canal.

1 Introduction

The intracranial pressure (ICP) is known to fluctuate in a periodic fashion about its mean value (Wagshul et al. , 2011) (fig. 1b). These fluctuations are mainly driven by the cardiac cycle, in which blood is pumped through the arteries into the rigid cranial vault, and venous blood is being evacuated through the veins. Simultaneously, in response to the over- and under-pressures that occur in this process, a small volume of cerebrospinal fluid (CSF) streams out of the cranial vault into the spinal canal and back in a cyclical fashion. It is the compliance of the spinal canal—closed at its bottom end—that allows it to accommodate and return this small volume of CSF every heart beat. Because of the slender nature of the spinal canal (fig. 1a), the resulting CSF flow is principally aligned with the longitudinal (along-spine) direction, and its measurement is nowadays fairly straightforward using cardiac-gated phase contrast magnetic resonance imaging (MRI). For example, the blue lines of fig. 2 show the temporal variation of the flow rate $Q(x,t)$ (appropriately nondimensionalized) over three cardiac cycles, measured at 13 different spinal levels x, the top panel corresponding to the craniospinal junction, and the bottom panel corresponding to the closed sacral end. The blue dots in the panel on the right-hand-side show the craniocaudal decay of the corresponding stroke volume $\Delta V(x) = \int_0^{2\pi} Q(x,t)dt$. The CSF flow in the spinal canal being driven by the ICP fluctuations, its relative geometric simplicity, and the ease with which it can be measured noninvasively, opens up an avenue for a method to infer ICP fluctuations from measurements of CSF flow, this being the objective of the present work.

2 Model

To model the flow in the spinal canal, we employ the simplified, one-dimensional, description developed by Sincomb et al. (2022), in which the spatio-temporal

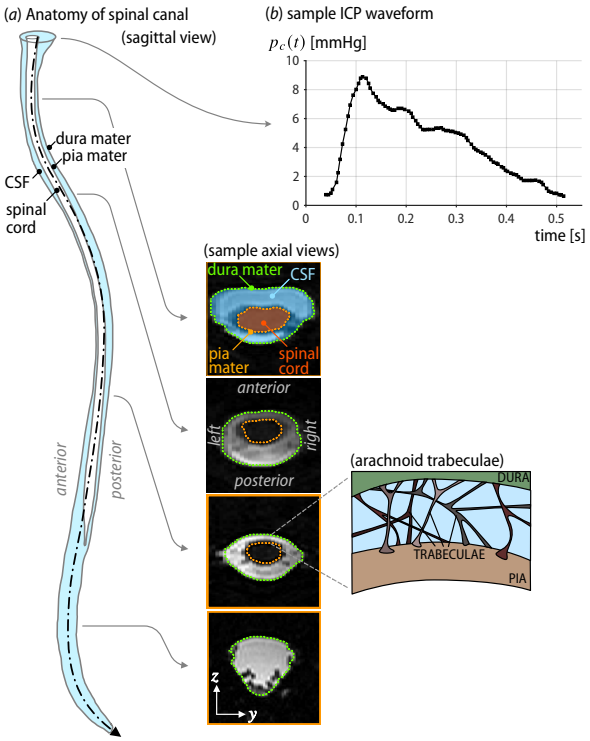

Figure 1: (a) Schematic diagram of the spinal canal, with indication of the principal anatomical features. (b) Typical intracranial pressure (ICP) waveform [from Wagshul et al. (2011)].

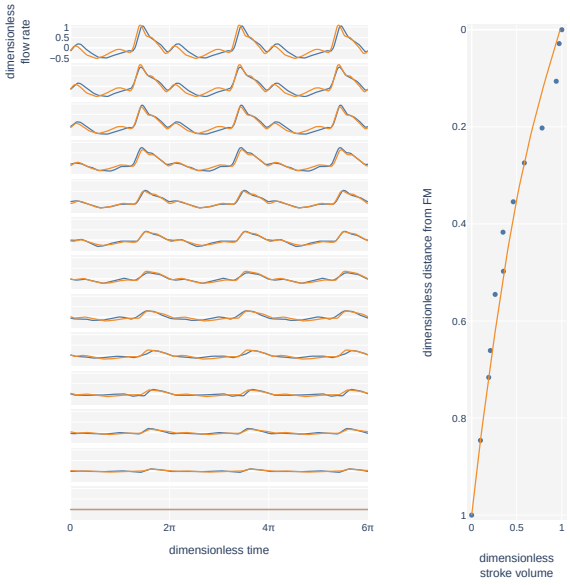

Figure 2: (left) Temporal evolution of the dimensionless flow rate $Q(x,t)$ over 3 cardiac cycles, measured using MRI (blue), compared with the model predictions (orange), at 13 locations along the spinal canal (top panel corresponds to craniospinal junction and bottom panel to sacral end of the canal). (right) Corresponding dimensionless stroke volume $\Delta V(x) = \int_0^{2\pi} Q(x,t)dt$ as a function of distance from FM. Blue dots: MRI; orange solid line: model.

variations of flow rate $Q(x,t)$ and cross-sectional area $A(x,t)$ are related to the departures $P(x,t)$ in pressure from the ICP $\Pi(t)$ by the continuity, momentum equation, and elastic equations,

$$\frac{\partial Q}{\partial x} + \frac{\partial A}{\partial t} = 0, \tag{1}$$

$$\frac{\partial Q}{\partial t} = -\bar{A}\frac{\partial P}{\partial x} - RQ, \tag{2}$$

$$\frac{\partial A}{\partial t} = \gamma\left(\frac{\partial P}{\partial t} + \frac{\partial \Pi}{\partial t}\right), \tag{3}$$

(all expressed in dimensionless terms, see (Sincomb et al. , 2022) for details). The boundary conditions that need to be satisfied are $P(x=0,t)=0$, corresponding to the pressure being equal to the ICP at the foramen magnum, together with $Q(x=1,t)=0$, i.e. zero flow rate at the closed sacral end of the canal.

Two key features of this model are the compliance γ of the spinal canal and the flow resistance R induced by microanatomical features such as trabeculae that are present in the spinal canal (fig. 1). Unlike other anatomical features such as the longitudinal variation of the time-averaged cross-sectional canal area $\bar{A}$, the parameters γ and R cannot be measured, nor is there

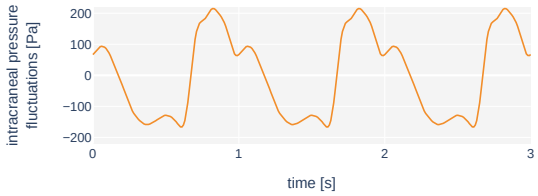

Figure 3: Computed (dimensional), intracranial pressure fluctuations, $\Pi^*(t^*)$, over 3 cardiac cycles.

reliable data on them available in the literature. Nevertheless, the linear nature of the governing equations permits to derive a modal optimization problem for R and γ, in which the optimal, subject-specific, values of R and γ can be determined by minimizing the difference between the flow rates (appropiately normalized) predicted by the model and those measured by MR, and in which the ICP fluctuations come out as a by-product of the procedure.

3 Results & Conclusions

The orange lines in fig. 2 show the model prediction of flow rate, using the optimal values of the canal compliance γ and the trabecular resistance factor R, for a particular subject. The accompanying ICP fluctuation waveform computed for this subject is given in fig. 3.

Future efforts will be focused on the quantitative validation of our method. To this aim, patients who require invasive ICP monitoring will be scanned to obtain flow rate measurements at multiple spinal levels. By contrasting the predictions of our method to the invasive pressure measurements a degree of fidelity can be established.

Acknowledgements This work was supported by the coordinated project PID2020-115961RA-C33, RB-C31, RB-C2, financed by MCIN/AEI/10.13039/501100011033.

References

M.E. Wagshul, P.K. Eide & J.R. Madsen (2011) "The pulsating brain: A review of experimental and clinical studies of intracranial pulsatility". *Fluids and Barriers of the CNS* **8**, 5.

S. Sincomb, W. Coenen, C. Gutiérrez-Montes, C. Martínez Bazán, V. Haughton & A.L. Sánchez (2022) "A one-dimensional model for the pulsating flow of cerebrospinal fluid in the spinal canal". *J. Fluid Mech.*, **939**, A26.

Fluid Mechanics of saliva transport during human respiratory events: Insights gained using DNS

Wayne Oaks[1], Hossein Seyyedzadeh[1], Mario Sanchez Sanz[2], and Ali Khosrornejad[1*]

[1]*Department of Civil Engineering, College of Engineering & Applied Sciences, The State University of New York at Stony Brook, New York, USA*
[2]*Department of Thermal and Fluids Engineering, Carlos III University of Madrid, Madrid, Spain*

The flow and saliva particulate transport dynamics during normal human breathing was studied via direct numerical simulation (DNS). The human breathing DNS was coupled with a Lagrangian approach for the transport of saliva particles. The coupled Eulerian-Lagrangian (EL) simulation results reveal new striking insights into the rich dynamics of the Lagrangian coherent structures (LCS) that arise from saliva particles during normal breathing.

INTRODUCTION

The basis for the social distancing standards on general virus transmission for the last 100 years was questioned by Bourouiba [1], commenting that the historical dichotomy of big and small droplets did not reflect the reality of the rapid progression of COVID-19.

Herein, we seek to elucidate the Lagrangian dynamics of saliva particle transport during human breathing through the mouth using a coupled Eulerian-Lagrangian (EL) approach. The Lagrangian particle tracking approach, coupled with the direct numerical simulation (DNS), was adopted to simulate the one-way coupling of saliva particle transport [2]. For the fully coupled EL simulations, we employed an Eulerian DNS for the time-periodic flow coupled with a Lagrangian approach for the transport of saliva particles. We carried out a high-resolution numerical simulation involving computational grids fine enough to resolve all relevant scales of motion for a velocity flow field. The human body is represented using the sharp interface curvilinear immersed boundary method.

GOVERNING EQUATIONS

The Eulerian equations of motion for the air-saliva mixture include the spatially-filtered continuity and Navier-Stokes equations [11]. Further, we use a Lagrangian particle tracking framework to calculate the transport of individual saliva particles in a one-way coupling manner. To obtain the trajectory of individual saliva particles in the Eulerian flow field, we considered a dilute mixture of air and saliva and solve the following equations for each saliva particle [2]:

$$\frac{d\boldsymbol{x_p}}{dt} = \boldsymbol{u_p} \qquad (1)$$

$$m_p \frac{d\boldsymbol{u_p}}{dt} = \boldsymbol{f_g} + \boldsymbol{f_D} + \boldsymbol{f_L} + \boldsymbol{f_{AM}} + \boldsymbol{f_S} + \boldsymbol{f_P} \qquad (2)$$

where $\boldsymbol{x_p}$ and $\boldsymbol{u_p}$ are the particle's position and velocity, respectively, m_p is the mass of the particle, $\boldsymbol{f_g}$ is the gravity force, $\boldsymbol{f_D}$ is the drag force, $\boldsymbol{f_L}$ is the lift force, $\boldsymbol{f_{AM}}$ is the added mass, $\boldsymbol{f_S}$ is the collision forces from solid boundaries on the particle, and $\boldsymbol{f_P}$ is the force due to fluid stresses.

FIG 1. This plot shows the simulated saliva particle

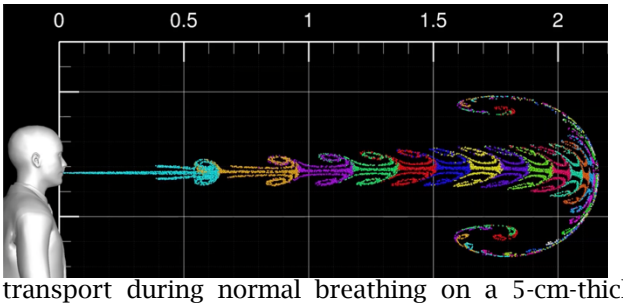

transport during normal breathing on a 5-cm-thick layer around the sagittal plane after about 2 min of breathing. Saliva particles of each breathing cycle are tagged with a distinct color to show their position. Numbers are in meters from the mouth.

CONCLUSIONS

The Lagrangian analysis of the saliva particle transport using the coupled EL method revealed that saliva particle transport leads to a fractal-like LCS that extends beyond 2.5 m away from the person. The building block of the LCS consists of the vortex ring and associated trailing structures shed during successive breathing cycles.

—

* ali.khosronejad@stonybrook.edu

[1] Bourouiba, L, (2020), Turbulent gas Clouds and respiratory pathogen emissions: Potential implications for reducing transmission of COVID-19," JAMA, 323 (18), 1837–1838 (2020).

[2] W. R. Oaks, S. Kang, X. Yang, A. Khosronejad, (2022), Lagrangian dynamics of contaminant particles released from a point source in New York City, *Physics of Fluids,* 34 (7), 073303.

2nd Spanish Fluid Mechanics Conference
Barcelona (2 - 5 July 2023)

In-vitro experimental characterization of the transmantle pressure in the cerebral aqueduct

Francisco Moral-Pulido[1], Stephanie Sincomb[2], Obed A. Campos[2], Carlos Martínez-Bazán[3], Victor Haughton[4], and Antonio L. Sánchez[2]

fmoral@ujaen.es

[1]Departamento de Ingeniería Mecánica y Minera, Universidad de Jaén, Spain
[2]Department of Mechanical and Aerospace Engineering, University of California- San Diego, CA, United States
[3]Departamento de Mecánica de Estructuras e Ingeniería Hidráulica, Universidad de Granada, Spain
[4]School of Medicine and Public Health, University of Wisconsin, WI, United States

The present work aims at characterizing the transmantle pressure $\Delta p(t)$, being the instantaneus pressure difference between the lateral ventricles and the cerebral subarachnoid space. This pressure drop reaches its largest value in the cerebral aqueduct, a narrow canal which connects the third and fourth ventricles. This dynamic phenomenon, relevant to understand ventriculomegaly in cases of normal pressure hydrocephalus (NPH), is difficult to characterize from in-vivo measurements. Therefore, in-vitro experiments, involving an MRI-informed experimental model of the cerebral aqueduct flow, are performed here to determine the transmantle pressure and its corresponding phase lag with the flow rate. The experimental results are in good agreement with those provided by the analytical model developed by Sincomb et al. (2020).

1 Introduction

The cerebrospinal fluid (CSF) fills the cerebral ventricles and the subarachnoid space (SAS), which surrounds the brain and the spinal cord. This liquid presents several mechanical and physiological properties, which make the study of its dynamics relevant in clinical research. The CSF flow has been studied deeply (see Linninger et al., 2016; Kelley and Thomas, 2023) not only because of the role it plays on the transport of substances, but also because its involvement in the development of pathologies related to abnormal flow behaviour, such as normal pressure hydrocephalus (NPH). Indeed, the largest oscillatory velocities of the CSF are located in the cerebral aqueduct, a narrow canal of length $L \sim 10 - 15$ mm and average radius $a \sim 1 - 1.5$ mm. These velocities have clinical potential value in investigating the development of NPH, and are closely related to the transmantle pressure, $\Delta p(t)$. This pressure drop, of a few pascals, reaches its maximum across the aqueduct, driving an oscillatory flow having peak values of $Q \sim 0.1$ ml/s. The cyclic forces acting over long time can explain changes in the brain viscoelastic properties in NPH patients, altering the CSF flow dynamics:

To clarify the relationship between these parameters and diseases, direct simultaneous measurements of $\Delta p(t)$ and $Q(t)$ need to be performed, resulting a very invasive technique which requires surgery. Therefore, efforts have been re-conducted in obtaining both signals by noninvasive MRI measurements. Different models have been developed for the relation between $\Delta p(t)$ and $Q(t)$ (Sincomb et al., 2020), needed to enable estimates of the former from measurements of the latter (Sincomb et al., 2021). Moreover, additional experimental investigations have been conducted (Holmlund et al., 2019), although detail information about the corresponding pressure fluctuations and the related phase lag, of clinical interest, is still lacking.

Consequently, the present in-vitro study complements the previous one by Holmlund et al. (2019) with a more complete description of the interventricular pressure difference for a range of flow conditions of healthy subjects. Here, the dimensionless time-averaged transmantle pressure $\langle \Pi \rangle = \langle \Delta p \rangle / (\rho \omega^2 L^2 L_s / L)$ is evaluated, varying the aspect ratio of the canal, a/L, the stroke length of the CSF motion, $L_s/L \sim V_s/(\pi a^2 L)$, and the Womersley number, $\alpha = (a^2 \omega / \nu)^{1/2}$, considering the simplified model of Sincomb et al. (2020) and a real geometry obtained by MRI.

2 Materials and methods

In this work, in-vitro experiments were performed to evaluate $\Delta p(t)$. To that end, an in-vitro facility was manufactured, consisting of two reservoirs (third and fourth ventricles) connected by a slender canal, which represents the cerebral aqueduct. Two different canal

geometries were tested: a) a canonical aqueduct, involving a circular cylinder of constant radius whose edges were rounded to avoid flow separation during inflow, and b) a realistic model of the cerebral aqueduct, corresponding to a subject-specific anatomy. The CSF flow was induced by a programmable piston pump, connected to one of the reservoirs. Two different waves were set: a harmonic wave and a realistic wave, obtained from MRI measurements. In addition, a differential pressure transducer was connected at both reservoirs to measure the pressure wave, $\Delta p(t)$, simultaneously with the flow rate, $Q(t)$.

3 Results and discussion

The dimensionless time-averaged pressure difference, $\langle \Pi \rangle$, and the phase lag between the pressure wave and the flow rate, φ, have been evaluated for the most common physiological ranges of α and L_s/L. Figure 1 shows the evolution of $\langle \Pi \rangle$ with L_s/L for a sinusoidal waveform, and $\alpha = 2$, 3 and 4, using the patient-specific geometry with different glycerol-water mixtures to change the liquid viscosity. It can be observed that $\langle \Pi \rangle$ increases with L_s/L for all the values of α, being each set shifted with each other. In contrast, the value of $\langle \Pi \rangle$ decreases with the value of α for a given L_s/L, being this trend not linear.

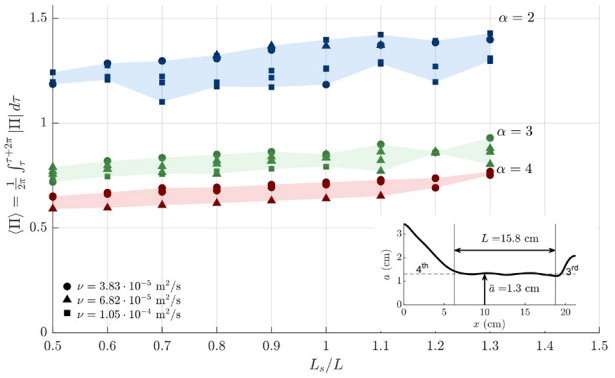

Figure 1: Dependence of the dimensionless transmantle pressure, $\langle \Pi \rangle$, with the main parameters of the problem (α and L_s/L).

For the phase lag, Fig. 2 shows that there is a decreasing trend of φ with L_s/L within the range of values of L_s/L explored in this work. Moreover, the phase lag increases with α for a given value of L_s/L. Although not show here, similar results are using a MRI waveform.

4 Conclusions

In-vitro experiments have been used to characterize the time-averaged transmantle pressure and its phase lag with the CSF flow rate along the cerebral aqueduct. The results, which are in good agreement with the model devolped by Sincomb et al. (2020), opens new approaches to tackle diseases associated to alterations in CSF flow, such as NPH.

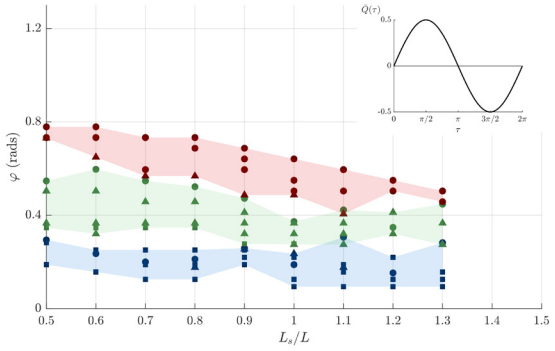

Figure 2: Effect of the phase lag between the pressure wave and the flow rate, φ, with the main parameters of the problem (α and L_s/L).

5 Acknowledgements

This work was supported by the National Institute of Neurological Disorders and Stroke through contract No. 1R01NS120343-01, by the National Science Foundation through grant No. 1853954, by the Spanish MICINN through grant PID2020-115961, and by the Junta de Andalucía and European Funds through grant No. P18-FR-4619. F Moral-Pulido wants to thank the Spanish Ministry of Universities, grant No. FPU18/05694.

References

Sincomb, S. et al. (2020) "A model for the oscillatory flow in the cerebral aqueduct". *J. Fluid Mech.*, **899**.

Linninger, A.A. et al (2016) "Cerebrospinal fluid mechanics and its coupling to cerebrovascular dynamics".*Annu. Rev. Fluid Mech.*,**48**,219-257.

Kelley, D.H. & Thomas, J.H. (2023) "Cerebrospinal fluid flow". *Annu. Rev. Fluid Mech.*,**55**.

Sincomb, S. et al. (2021) "Transmantle pressure computed from MR Imaging measurements of aqueduct flow and dimensions". *American Journal of Neuroradiology*,**42**,(10),1815-1821.

Holmlund, P. et al. (2019) "Can pulsatile CSF flow across the cerebral aqueduct cause ventriculomegaly? A prospective study of patients with communicating hydrocephalus". *Fluid Barriers CNS*,**16**,1-10.

2nd Spanish Fluid Mechanics Conference
Barcelona (2 - 5 July 2023)

Multi-Fidelity Models for Thrombosis Risk Evaluation in the Left Heart Using Patient-Specific Data

M. Guerrero-Hurtado[1], M. Garcia-Villalba[2], E. Durán[3], A. Gonzalo[4], P. Martinez-Legazpi[5], A. M. Kahn[6], J. Bermejo[7], J. C. del Álamo[4], and O. Flores[1]

[1]Universidad Carlos III de Madrid, Spain
[2]Institute of Fluid Mechanics and Heat Transfer, TU Wien, Austria
[3]Universidad de Málaga, Spain
[4]University of Washington, USA
[5]Universidad Nacional de Educación a Distancia, Spain
[6]University of California San Diego, USA
[7]Hospital General Universitario Gregorio Marañón, Spain

Coagulation is a multi-scale process that involves a cascade of enzymatic reactions resulting in thrombin production that converts fibrinogen into fibrin via polymerization, forming the main scaffold of a clot. The detailed simulation of the cascade requires solving a large system of coupled partial differential equations, each of them representing a 3D unsteady advective-reaction-diffusion equations for the concentration of the i-th chemical specie, u_i:

$$\mathrm{D}u_i/\mathrm{D}t = \partial u_i/\partial t + \mathbf{v}\cdot\nabla u_i = R_i + D_i\nabla^2 u_i. \quad (1)$$

In this system of equations $\mathbf{v}(\mathbf{x},t)$ represents the flow velocity, D_i is the diffusion coefficient of each species, and R_i is the source term of the kinetic reaction. This last term couples the spatiotemporal evolution of all species. We denote this system of N PDEs as the high-fidelity (HiFi) model. Because of the large number of species involved in the coagulation cascade process, with over 80 kinetic reactions, the HiFi model is typically computationally intractable in cases of clinical interest, like evaluating the risk of thrombosis in patients with left atrial fibrosis.

In this work, we introduce a strategy to significantly reduce the computational burden of coagulation models in complex geometries. The disparity of time-scales between the advective (t_a) and reaction (t_r) terms and the diffusive time scale (t_d) in the human circulation ($t_d/t_a \simeq 10^6$) allows us to neglect diffusion in the HiFi PDEs system. Consequently, this model simplifies to

$$\mathrm{D}g_i/\mathrm{D}t = R_i. \quad (2)$$

where g_i approximates u_i in the limit of zero molecular diffusivity. Moreover, using the definition of the blood residence time $\overline{t_R}$,

$$\mathrm{D}\overline{t_R}/\mathrm{D}t = 1, \quad (3)$$

it is possible to express equation (2) as a system of ODEs that depends only on $\overline{t_R}$. This allows the integration of the system of ODEs, to provide $u_i^{(1st} = g_i(\overline{t_R})$, and then, mapping these concentrations in space and time with the transport of $\overline{t_R}(\mathbf{x},t)$. Since this solution combines a set of ODEs and one unique PDE integration, the approximation is multi-fidelity of first order (MuFi-1).

However, this model ignores completely the internal variance of the concentrations within each fluid particle, which arises from the small diffusivity present in eq (1). As we will show in the presentation, it is possible to take into account these effects considering an extra PDE for the variance of the residence time (σ^2_{tr}). This allows us to describe u_i as a function of these two variables, $u_i^{(2nd} = f_i(\overline{t_R}, \sigma^2_{tr})$ (MuFi-2).

To validate our methodology, we performed numerical simulations of a pulsating flow in an 2D idealized aneurysm, with a simplified model of the intrinsic pathway of the coagulation cascade, as described in previous studies by Ermakova and Zarnistan [2, 3]. The flow velocity was obtained through numerical simulations using our in-house code TUCAN [4]. With this velocity field as input, we then solved equations (1) and (3) to directly compare the performance of the multi-fidelity models (MuFi-1, MuFi-2) and the high-fidely model (HiFi). Our results show that after 15 cycles, the maximum differences in $u_1^{(1st}$ and $u_1^{(2nd}$ compared to the HiFi results (u_1) were found to be below 16% and 5%, respectively. Figure 1 shows the non-dimensional concentration of thrombin (u_1) after 15 cycles, for the HiFi and MuFi-2 model.

To evaluate the risk of thrombosis in the left atrium

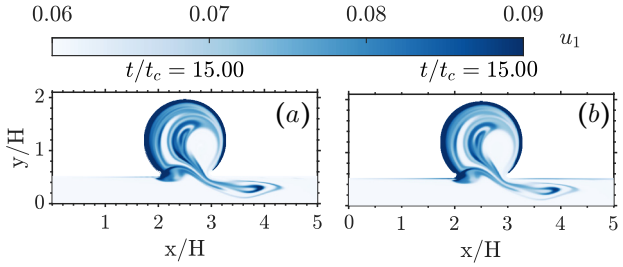

Figure 1: Non-dimensional thrombin concentration for HiFi (a) and MuFi-2 (b) after 15 cycles.

(LA), we apply the MuFi-1 and Mufi-2 models to a database of patient-specific left atrial flows [5]. The database includes three patients with impaired left atrial function (2 of them had a thrombus in the Left Atrium Appendage at the time of imaging), and 5 patients with normal atrial function. The simulations were performed using patient-specific 4D kinematic LA models acquired from CT imaging, as explained in [5]. Once we obtained a converged solution for the flow dynamics during a whole cardiac cycle, we proceed to calculate the residence time ($\overline{t_R}$) and its variance (σ^2_{tr}) for 20 consecutive cardiac cycles. Then, we applied first and second order multi-fidelity models to assess the likelihood of thrombosis in the LA.

For reference, figure 2 displays the spatial arrangement of the thrombin concentration for MuFi-2 following 20 cardiac cycles under prothrombotic inlet conditions in a healthy case (where LA function was normal) and unhealthy case (where reservoir function was impaired). The distribution map ($u_1^{(2nd}$) indicates that the highest concentrations are located in the left atrial appendage (LAA), which is a commonly observed site for thrombus formation in the LA [6][7].

The analysis of the probability density functions of thrombin concentration and residence time distribution in the LAA (shown in figure 3) suggests that the differences between the MuFi-1 and MuFi-2 models are small for cases with normal atrial function, and moderate for cases with impaired atrial function. Moreover, the results in figure 3 hint that thrombin concentration at the LAA might be a better discriminator between normal and impaired atrial functions than residence time alone.

Overall, both MuFi-1 and MuFi-2 are cost-effective solutions that can be trivially extended to more complex models of the coagulation cascade. This approach can help in the uncertainty quantification of blood coagulation models, and in the development of more accurate patient-specific metrics of thrombogenesis risk.

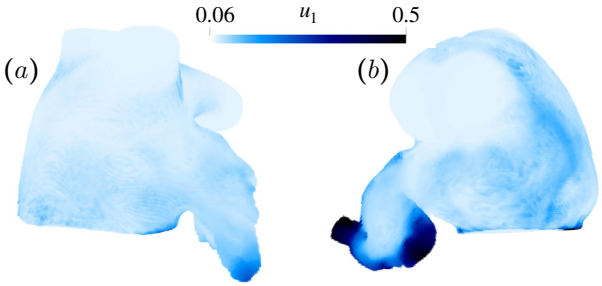

Figure 2: MuFi-2 Non-dimensional thrombin concentration ($u_1^{(2nd}$) after 20 cardiac cycles for case with normal LA function (a) and case with impaired function (b) under prothrombotic inlet conditions.

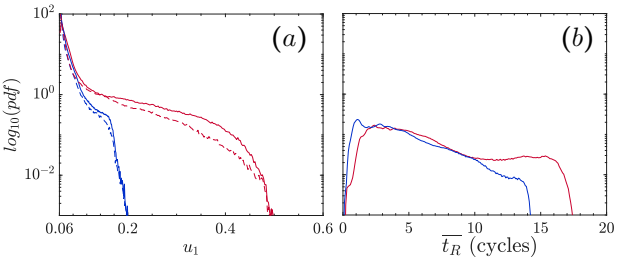

Figure 3: Probability density functions at the 20th cycle for (a) LAA Non-dimensional thrombin and (b) LAA residence time. MuFi-1 in dashed and MuFi-2 solid. (—) normal and (—) impaired LA function.

Acknowledgements

This work was supported by grants Y2018/BIO-4858 (PREFI-CM, Comunidad de Madrid) and PID2019-107279RB-I00 (AEI/FEDER, UE).

References

[1] Cito, Mazzeo & Badimon (2013) *Thromb. Res.*, **131**, 116–124.

[2] Ermakova, Panteleev & Shnol (2005) *Pathophysiol. Haemost. Thromb.*, **34**, 135–142.

[3] Zarnitsina, Ataullakhanov, Lobanov & Morozova (2001) *Chaos*, **11**, 57–70.

[4] Moriche, Flores & Garcia-Villalba (2017) *J. Fluid Mech.*, **828**, 395–423.

[5] Garcia-Villalba et al (2021) *Front. Physiol.*, **12**, 596596.

[6] Santiago et al (1994) *J. Am. Coll. Cardiol*, **24**, 159–164.

[7] Ito & Suwa (2023) *Heart Fail. Rev.*, 1–11.

2nd Spanish Fluid Mechanics Conference
Barcelona (2 - 5 July 2023)

On the effect of trabeculae on steady streaming in the subarachnoid space

G. L. Nozaleda[1], J. Alaminos-Quesada[1], W. Coenen[2], and A. L. Sánchez[1]

glpeznozaleda@ucsd.edu

[1]Department of Mechanical and Aerospace Engineering, University of California San Diego, La Jolla, CA 92093 USA
[2]Grupo de Mecánica de Fluidos, Universidad Carlos III de Madrid, Leganés, 28911 Spain

The pulsating motion of the cerebrospinal fluid in the subarachnoid space (SAS) surrounding the brain and the spinal cord is known to be affected by the presence of trabeculae. Effects of trabeculae on steady streaming are addressed in this paper using as a model problem that of oscillatory flow in a slender channel subject to a harmonic longitudinal pressure difference. The presence of trabeculae is described using a homogenized model accounting for the disparity of length scales present in the problem, resulting in a resistance term linearly proportional to the flow velocity. The asymptotic analysis for small stroke lenghts provides a closed-form solution for the steady–streaming motion. The analysis reveals significant differences between the secondary flow developed in the presence of trabeculae and that of unobstructed flow, with the former exhibiting much smaller velocities, especially for the moderately large values of the Womersley number characterizing flow in the SAS.

1 Introduction

The subarachnoid space (SAS) is filled with cerebrospinal fluid (CSF), which exhibits a pulsating motion driven by the cardiac and respiratory cycles. This motion is affected by different anatomical features that obstruct the flow. Besides nerve roots and ligaments, both the cerebral and spinal SAS are populated by a fine distribution of trabeculae, which are thin collagen-reinforced microscopic elements of varying shape that form a supporting structure extending from the pia across the SAS to attach to the arachnoid. Previous studies have found, for instance, that trabeculae increase significantly the pressure loss and enhance shear-induced diffusion.

In addition to the fast oscillatory motion, CSF exhibits a slow streaming flow associated with the nonlinear convective acceleration Sánchez et. al (2018). Effects of trabeculae on the resulting steady–streaming are evaluated here using as canonical model a two–dimensional slender channel.

2 Formulation of the problem

Consider the oscillatory flow of a viscous fluid with constant density ρ and kinematic viscosity ν in a slender channel of length L subject to a pressure difference between its ends varying harmonically in time according to $\Delta P\cos(\omega t')$, with ΔP and ω representing the pressure-fluctuation amplitude and the angular frequency. The channel width h varies with the distance to the entrance x' according to $h/h_o = H(x'/L)$, where $h_o \ll L$ is the characteristic value of h and H represents a dimensionless order-unity function. The order-of-magnitude balance between the pressure gradient and the local acceleration yields $u_c = \Delta P/(\rho\omega L)$ for the characteristic value of the longitudinal velocity, which is much larger than the characteristic transverse velocity $v_c = (h_o/L)u_c \ll u_c$, as follows from continuity. The flow will be described in terms of dimensionless cartesian coordinates $x = x'/L$ and $y = y'/h_o$, where y' is the distance from the bottom wall, assumed to be flat. Correspondingly, the longitudinal and transverse velocity components u' and v' will be scaled with its characteristic values to yield the dimensionless variables $u = u'/u_c$ and $v = v'/v_c$ and the pressure difference from the entrance p' will be scaled with ΔP to give $p = p'/\Delta P$, which takes the values $p = 0$ at $x = 0$ and $p = \cos t$ at $x = 1$, with $t = \omega t'$ representing the dimensionless time.

In the lubrication approximation, discarding small terms of order $(h_o/L)^2$ and transverse pressure variations, the problem is reduced to the integration of

$$\frac{\partial u}{\partial x} + \frac{\partial v}{\partial y} = 0, \tag{1}$$

$$\frac{\partial u}{\partial t} + \varepsilon\left(u\frac{\partial u}{\partial x} + v\frac{\partial u}{\partial y}\right) = -\frac{\partial p}{\partial x} + \frac{1}{\alpha^2}\frac{\partial^2 u}{\partial y^2} - \mathcal{R}u, \tag{2}$$

subject to the no-slip boundary conditions $u = v = 0$ at the walls $y = 0, H(x)$ and the pressure conditions $p = 0$ at $x = 0$ and $p = \cos t$ at $x = 1$.

The solution to the canonical problem defined above depends on three parameters, namely, the di-

mensionless stroke length (ε), the Womersley number (α) and the dimensionless resistance factor ($\mathcal{R}$), which are defined as follows

$$\varepsilon = \frac{u_c/\omega}{L}, \quad \alpha = \left(\frac{h_o^2\omega}{\nu}\right)^{1/2} \text{ and } \quad \mathcal{R} = A\frac{\nu}{\omega\ell^2}. \quad (3)$$

In exploring the range of values of the above parameters that are relevant for SAS applications, we may use the angular frequency of the cardiac rate $\omega = 2\pi$ s^{-1} along with the kinematic viscosity of CSF $\nu \simeq 0.7$ mm^2/s and the characteristic dimensions of the SAS width $h_o \sim 2-4$ mm and trabecular-network spacing $\ell \sim 0.5$ mm to yield $\alpha \sim 6-12$ and $\mathcal{R} \sim 2.8$. Values of the dimensionless stroke length in the SAS are much smaller. For instance, in the spinal SAS, where $L \simeq 50$ cm and $u_c \simeq 5$ cm/s, we find $\varepsilon = 0.02$. Characteristic velocities and lengths in the cranial SAS are both an order of magnitude smaller, resulting in comparable values of $\varepsilon \ll 1$. There is therefore interest in exploring the limit $\varepsilon \ll 1$ with $\mathcal{R} \sim 1$.

3 Results

The solution procedure of (1)–(2) in the asymptotic limit $\varepsilon \ll 1$ employs expansions of the form

$$u(x,y,t) = u_0 + \varepsilon u_1 + \varepsilon^2 u_2 + \cdots, \quad (4)$$
$$v(x,y,t) = v_0 + \varepsilon v_1 + \varepsilon^2 v_2 + \cdots, \quad (5)$$
$$p(x,y,t) = p_0 + \varepsilon p_1 + \varepsilon^2 p_2 + \cdots. \quad (6)$$

We are primarily interested in the quantification of the steady–streaming velocities $u^s = u_0^s + \varepsilon u_1^s + \cdots$ and $v^s = v_0^s + \varepsilon v_1^s + \cdots$ induced along the channel, where $u^s = \langle u \rangle$ and $v^s = \langle v \rangle$ with $\langle \cdot \rangle = \frac{1}{2\pi}\int_t^{t+2\pi} \cdot \, \mathrm{d}t$. While the leading-order solution is purely harmonic, so that $u_0^s = v_0^s = 0$, the first-order correction contains a steady component.

Regardless of the inclusion of the fine structures, the canal geometry results crucial in determining steady–streaming and two differentiated patterns, already predicted by Hall (1974) for unobstructed pipes, are found. If the ends of the canal are of the same dimensions, regions of recirculation arise. Otherwise, net flux is directed towards the widest end of the channel.

To illustrate the influence of the trabeculae on steady–streaming in figure 1 streamlines and vorticity contours are represented for different values of α and $\mathcal{R}$ in a channel whose ends are of the same dimensions, for which regions of recirculation arise. According to the results here represented, there is a drastic reduction of steady–streaming as trabeculae are introduced in the canal ($\mathcal{R}$ increases). Moreover, for the given canal geometry $\mathcal{R}$ has the effect of shrinking the steady motion to the boundary layers for large values of α.

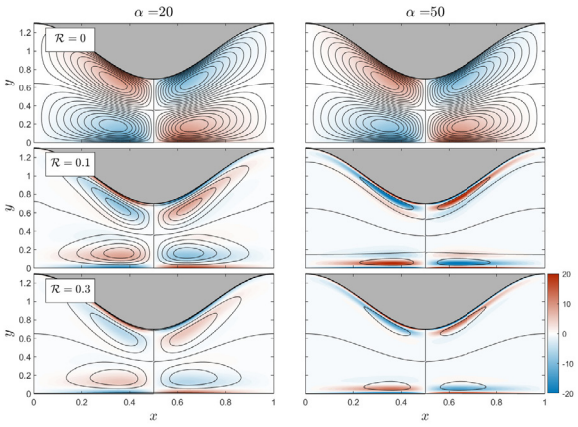

Figure 1: Streamlines with color contours of vorticity corresponding to steady-streaming motion in the geometry $H(x) = 1+0.5\cos(2\pi x)$. A fixed streamline spacing of $\delta\psi = 0.015$ has been used.

4 Conclusions

Steady–streaming has been examined in the presence of trabeculae for a prescribed harmonic pressure gradient. As in the classical case of oscillatory flow in an unobstructed pipe analyzed by Hall (1974), a net flow appears only when the two ends of the channel have different widths. A fundamental conclusion of our analysis is the important attenuation effect that trabeculae has on steady–streaming, result that is magnified for the large values of α found in CSF flow.

References

Hall, P. (1974) "Unsteady viscous flow in a pipe of slowly varying cross-section". *J. Fluid Mech.* **64** (2), 209–226.

Sanchez, A. L., C. Martinez-Bazan, C. Gutierrez-Montes, E. Criado-Hidalgo, G. Pawlak, W. Bradley, V. Haughton, and J. C. Lasheras. (2018) "On the bulk motion of the cerebrospinal fluid in the spinal canal". *J. Fluid Mech.* **841**, 203–227.

2nd Spanish Fluid Mechanics Conference
Barcelona (2 - 5 July 2023)

A hybrid predictive reduced order model for laminar flames

Adrián Corrochano[1], Rodolfo S.M. Freitas[2], Alessandro Parente[2], and Soledad Le Clainche[1]

adrian.corrochanoc@upm.es

[1]E.T.S.I. Aeronáutica y del Espacio,Universidad Politécnica de Madrid, Spain
[2]Université Libre de Bruxelles, École polytechnique de Bruxelles, Aero-Thermo-Mechanics Laboratory, Brussels, Belgium

This work proposes a new hybrid reduced order model (ROM) based on physical principles, which combines modal decomposition and neural networks. The ROM is applied to predict the temporal evolution of reactive flows. The algorithm is composed of two steps. In the first step, a dimensionality reduction is performed via Proper Orthogonal Decomposition (POD), which extracts the main patterns of the flow. In the second step, a deep learning model is introduced to predict the temporal coefficients of the POD modes. Results show that this novel algorithm is capable to predict the evolution in laminar flames with relative error smaller than 3%.

1 Introduction

Halting climate change is one of the greatest challenges facing the modern world. Development of combustion systems plays a key role for mitigating its effect. Strong efforts have been made to improve the energy efficiency, reduce the pollutants or in the creation of new synthetic fuels.

Combustion databases are highly complex and are difficult to create. On the one hand, combustion experiments are difficult to perform because the reaction happens in a small lapse of time and they are expensive in terms of monetary costs. On the other hand, the complex pattern of chemical reactions which are involved, as well as the presence of different phases and the turbulence-chemistry interaction, makes Direct Numerical Simulations (DNS), as well as Large Eddy Simulations (LES), still unfeasible for industrial applications. Because of this, reduced order models (ROMs) are increasingly appearing as they can reproduce the main dynamics of a system with small level of error and at a reduced computational time.

In this work, a new ROM is created for the prediction of reacting flow databases.

2 Hybrid ROM

This section briefly summarises the algorithm used in the work. Firstly, the data is organised as follows

$$\mathbf{V}_1^K = [\mathbf{v}_1, \mathbf{v}_2, \dots, \mathbf{v}_k, \mathbf{v}_{k+1}, \dots, \mathbf{v}_{K-1}, \mathbf{v}_K], \quad (1)$$

known as the snapshot matrix. This matrix has dimension $J \times K$, with $J = N_v \times N_x \times N_y$, where N_v is the number of variables studied; and N_x and N_y are the number of grid points considered along the streamwise and normal direction, respectively. K is the number of snapshots $\mathbf{v}_k$ (for $k = 1, \cdots, K$).

Once the data is organised, Singular Value Decomposition (SVD) (1) is applied for reducing the dimensionality of the dataset. Next, a deep learning model is used to predict the evolution of the flow in time. The architecture of the model is inspired by Abadía et al. (2021) (2) and is presented in Tab. 1. Details of the algorithms will be presented at the time of the conference.

# Layer	Layer details	Dimension
0	Input	$10 \times N$
1	LSTM	100
2	FC	$6 * 100$
3	Reshape	6×100
4	FC	6×80
5	Split(p)	80
6	$p*$ FC	N

Table 1: Architecture details in the RNN, inspired by (2).

3 Prediction of a laminar flame

Numerical simulations have been carried out to simulate an axisymmetric, time-varying, laminar co-flow flame, where the fuel is nitrogen-diluted methane (65% methane, 35% nitrogen, on a molar basis) and the oxidizer is air. Figure 1 shows a representative snapshot of the temperature of this configuration. More details of the simulation can be found at (3).

A database is extracted from the simulation, consisting of the temperature and 9 chemical species. The database has been extracted in a structured mesh of dimensions 100×75 and the number of snapshots extracted is 999. For the deep learning model, the first 68% of the snapshots compose the training set, the next 12% is the validation set and the last 20% of the snapshots has been used as the test set.

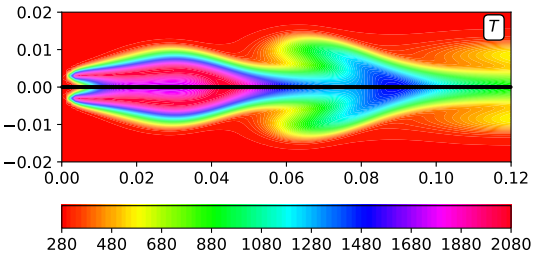

Figure 1: Representative snapshot of the temperature of the database used for the analysis. The black line represents the axi-symmetric axis.

As shown in Fig. 2, with this predictive ROM, the temporal modes are correctly predicted, with an error on the predicted modes smaller than 3%. Fig 3. compares the original solution with the predictions of the simulations carried out using the ROM, showing the good agreement between the two results.

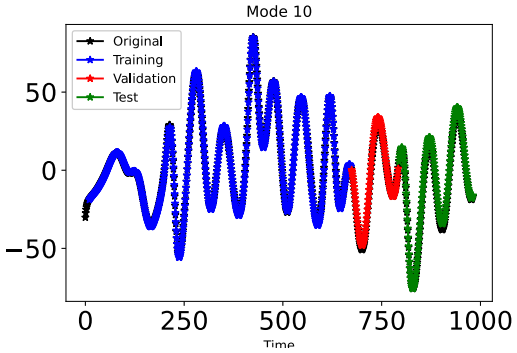

Figure 2: Prediction of the temporal mode 10 using the deep learning model. **Blue:** training set, **red:** validation set, **green:** test set and **black:** original mode.

The hybrid ROM has been tested in various databases. Transfer learning strategies allow this model to predict reactive flows with errors smaller than 3%. The robustness of the method as well as its good properties for temporal predictions of reactive flows will be presented at the time of the conference.

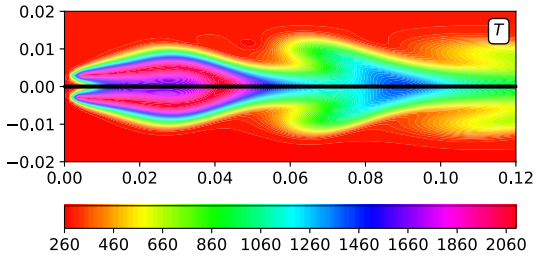

Figure 3: Contours of the prediction of a representative snapshot of the temperature. The bottom part of the contour is the original snapshot, while the top part is the prediction using the deep learning model. The black line represents the axi-symmetric axis.

References

[1] Sirovich L. (1987) "Turbulence and the dynamics of coherent structures. Parts I - III". *Quart. Appl. Math.*, **45(3)**, 561–571.

[2] Abadía-Heredia R., López-Martín M., Carro B., Arribas J.I., Pérez J.M. & Le Clainche S. (2021) "A predictive hybrid reduced order model based on proper orthogonal decomposition combined with deep learning architectures". *Exp. Syst. Appl.*

[3] D'Alessio G., Parente A., Stagni A. & Cuoci A. (2020) "Adaptive chemistry via pre-partitioning of composition space and mechanism reduction". *Combustion and Flame* **211**, 68–82.

2nd Spanish Fluid Mechanics Conference
Barcelona (2 - 5 July 2023)

Experimental evidence of the multiplicity of stationary solutions in ultra-lean hydrogen flames

Rubén Palomeque-Santiago[1], Alba Domínguez-González[2], Daniel Martínez-Ruiz[1], Mariano Rubio-Rubio[1], Eduardo Fernández-Tarrazo[1], and Mario Sánchez-Sanz[1]

rpalomeq@ing.uc3m.es

[1]Dpto. de Ing. Térmica y de Fluidos, Universidad Carlos III de Madrid, Spain
[2]Dpto. de Mecánica de Fluidos y Propulsión Aeroespacial, ETSIAE, Universidad Politécnica de Madrid, Spain

The morphology and propagation speed of premixed flames are mainly controlled by the fuel-air concentration and by the environmental conditions (temperature, pressure and geometry). Changes in these parameters induce large variations of the flame shape and speed compared to the theoretical planar construct. As shown in recent numerical simulations, very lean hydrogen flames in narrow confined geometries can form either circular or double-cell isolated flames propagating at different velocities under the same controlling parameters. In this work, we show numerical and experimental evidence of this multiplicity of flame solutions and, using the equivalence ratio ϕ as the controlling parameter, we determine the critical values of ϕ that define the flame characteristics in a bifurcation diagram.

1 Introduction

Hydrogen has been recognized as a key option to reach the net zero greenhouse gas emissions by 2050. The deployment of technology for hydrogen production three-folded in 2021 with respect to the year 2020 and the global demand reached in 2021 about 2.5% of the total energy consumption (IEA , 2022), with fuel cell electric vehicles among the new applications that are pushing the demand of hydrogen in the large scale. On the other hand, the increment in the utilization brings a growing concern about the risks and threats of widespread use of hydrogen in power and transport sectors. The minimum concentration of hydrogen in air that might ignite is about 4-5% vol at Earth's gravity, and the minimum ignition energy lay between 4 and 20 μJ, between 10 and 1000 times lower than other fuels (Ono et al. , 2007; Fernández-Tarrazo et al. , 2023). Its relative risk of ignition and explosions upon leakage into confined spaces with no ventilation is, therefore, relatively high. A representative example of this concern is the ignition and posterior propagation of hydrogen flames formed from fuel cell leakages. This work studies, both numerically and experimentally, precisely that scenario to set the limits below which ignition is not possible and to determine the consequences that a propagating flame might provoke.

2 Definition of the problem

Fuel-air mixtures are characterized as ultra-lean if the fuel concentration in the reactant mixture is near the fuel-lean flammability limit for a freely propagating flame. In this limit, to simulate an undesired fire in a stack of hydrogen fuel cells we consider flames confined in thin gaps of less than 1 cm, where extinction and quenching events are expected as a consequence of the heat losses. In this regime, Veiga-López et al. (2020) recently demonstrated the existence of flames capable of withstanding such stringent conditions even in gaps as small as 1 mm. To do so, the reactive front splits to form isolated flame fronts that propagate steadily, surrounded by unburned mixture, consuming a small fraction of the available hydrogen. For these settings, major heat losses combined with the high diffusivity of hydrogen enable an unexpected wide atlas of non-planar flame front configurations. One of the possible configurations was described recently in the numerical simulations by Domínguez-González et al. (2022). In this work, two stationary flame front morphology, circular and double-cell flames, can be expected for the same set of chemical

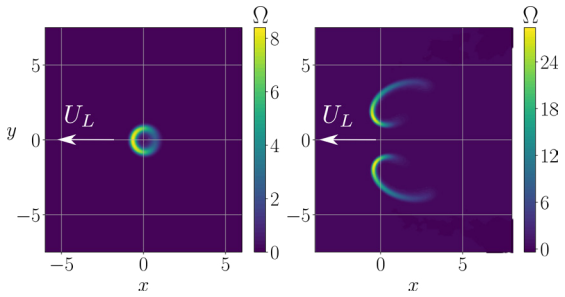

Figure 1: Reaction rate isocontours of simulated stable circular and double-headed flames.

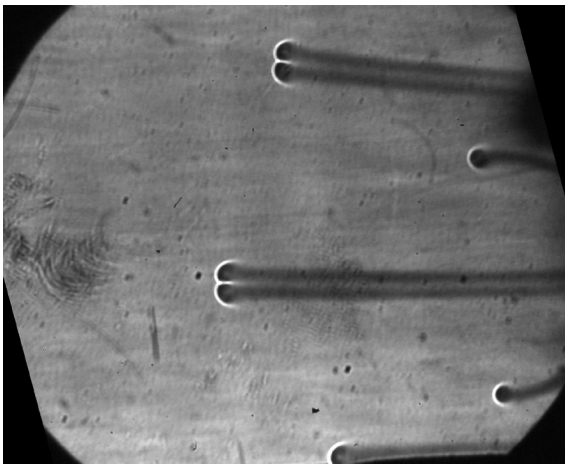

Figure 2: Stationary circular and two-headed flames propagation in a H_2-air mixture with $\phi = 0.2063$.

properties (equivalence ratio ϕ, activation energy E_a, heat release $q\ldots$) and boundary conditions (geometry and heat losses). The results of the computations are plotted in figure 1, where we show the reaction rate Ω isocontours of the two canonical flame fronts, circular (left) and double-headed (fight) flames calculated using a simple 1-step Arrhenius irreversible chemical scheme.

To answer whether or not the multiplicity of stable solutions can be found in real-life scenarios, a new experimental set-up was specifically built. Two parallel glass plates of size $W \times L$ are separated a small distance apart, $h \ll W \sim L$, to promote heat losses and to avoid the interaction of autoinduced acoustic pressure waves with the reactive front. Horizontal placement of the plates was selected to eliminate the acceleration effect of gravity on the flames in their propagation direction. Relative heat losses can be controlled by changing the gap width h, while the chemical heat release is controlled by regulation of the equivalence ratio ϕ of the mixture. Once the chamber volume is filled, the ultra-lean mixture is ignited using a spark-plug and the reaction propagates through the chamber. Owing to the low visible emissions, a Schlieren set-up is used to visualize the propagation of the flame through density/temperature changes of the gas mixture. In this configuration, both the high-speed camera and the light source are aligned perpendicularly to the glass plates.
The coexistence of two stationary solutions is illustrated in figure 2. This picture shows various circular and two-headed flames traveling in the combustion chamber parallel to each other. The traveling velocity of double-headed flames $v_L \simeq 11$ cm/s, that remains constant after a short transient period after the ignition, is roughly two times larger than the velocity of circular flames $v_L \simeq 5$ cm/s.

3 Conclusions

This work illustrates a range of hydrogen concentration, near the lean flammability limit, in which we experimentally observed several isolated flame fronts propagating simultaneously in a narrow gap. In this limit of ultra-lean H_2-air mixtures, the gas remains mostly unburned and only small isolated circular or double-headed reactive fronts consume a small portion of the available fuel. The numerical modeling of the problem shows that both flame structures are stationary solutions of the unsteady reactive conservation equations. Therefore, for a set of boundary conditions, namely equivalence ratio, geometry and heat losses, we can expect two steady flames with different shapes and propagation velocities. Such multiplicity of solutions is relatively common in non-linear problems, but is rarely observed in experiments. Nevertheless, our experiments illustrate a range of equivalence ratios in which both flame fronts emerge naturally and simultaneously, constituting one of the few examples in which multiple stable solutions are observed during experimental testing.

References

Domínguez-González, A., Martínez-Ruiz, D. & Sánchez-Sanz, M. (2023) "Stable circular and double-cell lean hydrogen-air premixed flames in quasi two-dimensional channels", *Proc. Combust. Inst.* In press.

Fernández-Tarrazo, E., Gómez-Miguel, R. & Sánchez-Sanz, M. (2023) "Minimum ignition energy of hydrogen–ammonia blends in air", *Fuel* **337**, 127128.

International Energy Agency (2022) "Global Hydrogen Review 2022", *https://www.iea.org/reports/hydrogen.*

Ono, R., Nifuku, M., Fujiwara, S., Horiguchi, S. & Oda, T. (2007) "Minimum ignition energy of hydrogen air mixture: Effects of humidity and spark duration", *Journal of Electrostatics* **65**, 87-93.

Veiga-López, F., Kuznetsov, M., Martínez-Ruiz, D., Fernández-Tarrazo, E., Grune, J. & Sánchez-Sanz, M. (2020) "Unexpected propagation of ultra-lean hydrogen flames in narrow gaps", *Phys. Rev. Lett.* **124**, 174501.

2nd Spanish Fluid Mechanics Conference
Barcelona (2 - 5 July 2023)

Influence of preferential diffusion on the dynamics of laminar bidimensional premixed hydrogen flames

Phivos Koumides[1], Eduardo J. Pérez-Sánchez*[1], Daniel Mira[1], J. García-Tíscar[2], and M. Rodríguez-Pastor[2]

[1] *Corresponding author: eduardo.perez@bsc.es*

[1]Barcelona Supercomputing Center (BSC), Plaça Eusebi Güell, 1-3, 08034, Barcelona, Spain
[2]CMT - Motores Térmicos, Universitat Politècnica de València, Camino de Vera, 46022, Valencia, Spain

The need for decarbonization of the energetic and transport sectors requires shifting to non-conventional clean technologies which provide high efficiencies, situation that has boosted the research of hydrogen combustion as a competitive option. However, many aspects related to its modelling have still to be elucidated. In particular, the need for considering preferential diffusion effects, which has been traditionally treated with constant non-unity Lewis numbers, should be addressed in order to determine in which conditions unity Lewis number is not acceptable and quantify the differences. In this work, an analysis of the steady regime as well as the dynamic response to velocity fluctuations is carried out with unity Lewis number and mixture averaged model for a laminar bidimensional premixed hydrogen flame.

1 Introduction

The need for decarbonization of the energetic and transport sectors requires shifting to non-conventional clean technologies which provide high efficiencies while being competitive. Between the different possibilities, hydrogen has received a renewed attention over the last few years due to its clean combustion (only nitrogen oxides as pollutants) and highly energetic mass-density content (around three times that for hydrocarbons). However, its high flame speed makes premixed flames extremely prone to flashback while the different diffusivities can lead to thermodiffusive instabilities (Beita (2021); Vance (2020)), phenomena that may force the burner redesign.

The path to make hydrogen combustion a reality cannot be implemented without the application of Computational Fluid Dynamics (CFD) techniques. CFD codes allow to drastically reduce costs by avoiding the manufacturing of test combustion chambers. However, the hypotheses assumed in the modelling become crucial in the quality of the results.

In the case of modelling hydrogen combustion, with a behaviour susceptible of being strongly conditioned by the differential diffusion effects, great efforts have been made to understand the structure of the flame submitted to such effects and translate this knowledge into the formulation of advanced models. Even most of the turbulent combustion modelling studies have been performed under the assumption of constant non-unity Lewis number, the incorporation of the mixture averaged approach in models like the Flamelet Generated Manifold (FGM) still poses some challenges.In this work, the authors have simulated laminar bidimensional premixed hydrogen flames for different boundary conditions in order to determine the extent of the differences between assuming unity Lewis numbers and mixture averaged models. The multi-physics code Alya (Vazquez (2016)), developed at the Barcelona Supercomputing Center, has been applied for this purpose using a finite rate model. The study focuses on the comparative analysis of the flame structure in steady regime as well as its dynamic response when submitted to velocity fluctuations through the Flame Transfer Function (FTF).

2 Analysis of the flame structure

Two equivalence ratios ϕ have been analysed, 0.5 and 0.7. The first one is a very lean mixture with differences in the unstretched laminar flame speed s_L^0 between Le=1 and mixture averaged of 2:1, while for $\phi = 0.7$ s_L^0 is almost identical.

As part of the steady regime study, figure 1 shows the comparison of the steady flames in physical space for equivalence ratios of $\phi = 0.5$ (left) and 0.7 (right) for unity Lewis number and mixture averaged. The figure clearly shows that for the leanest mixture the difference between the models becomes more accentuated while for a higher equivalence ratio such differences are attenuated. In the case of $\phi = 0.5$ the tip of

the flame does not exist for mixture averaged as the local equivalence ratio drops below the flammability limits, a phenomenon that cannot be reproduced by the Lewis unity model.

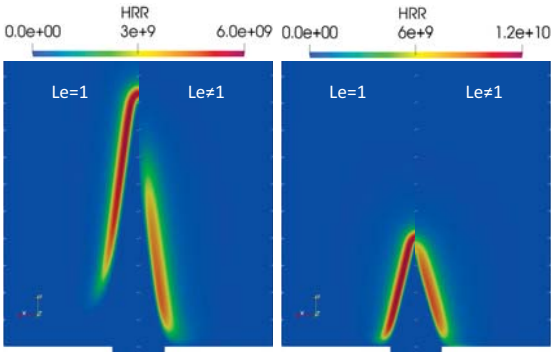

Figure 1: Comparison of hydrogen flames at ϕ=0.5 (left) and 0.7 (right) with Le=1 and mixture averaged models in steady regime.

3 Analysis of the flame dynamics

As part of the dynamic response study, figure 2 shows the Flame Transfer Functions, which describe the flame response in terms of the heat release fluctuations with regards to the velocity fluctuations in the frequency domain. Such characterization is done through a gain and a phase, which correspond to the amplitude relationship and delay for the velocity and heat release fluctuations, respectively.

It is observed that there exist differences between both models, in agreement with what was observed in steady regime for $\phi = 0.5$. Nevertheless, such differences strongly decay as the equivalence ratio is increased to $\phi = 0.7$. Another aspect is that the differences between models become larger as the frequency is increased. In conclusion, except for very lean mixtures there exists a range in equivalence ratios for which the Lewis number hypothesis can provide acceptable results.

Finally, it is worth mentioning that the frequency range where the flame is sensitive to the velocity fluctuations, is shifted towards higher frequencies, when compared to other fuels like methane at similar conditions, due to the lower flame time scale (or higher characteristic frequency) of hydrogen.

4 Conclusions

The unity Lewis number and mixture averaged models have been compared for a laminar bidimensional

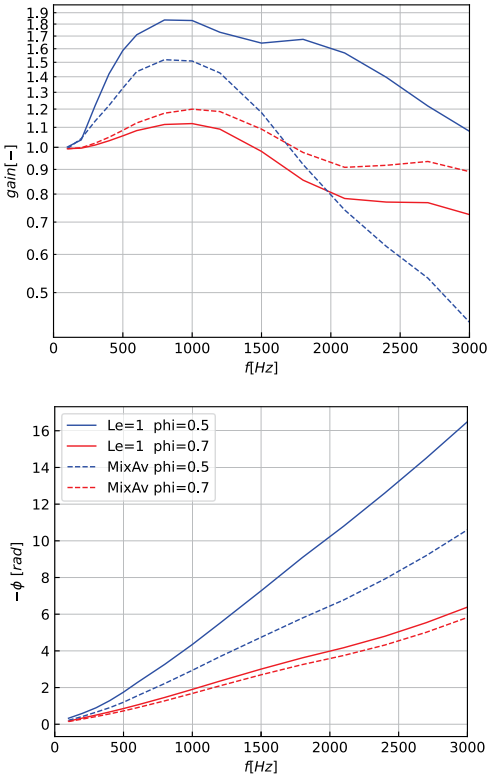

Figure 2: FTFs hydrogen flames at ϕ=0.5 and 0.7 with Le=1 and mixture averaged models.

premixed hydrogen flame. Such analysis has comprised the flame in steady regime and its dynamic response to velocity fluctuations. The comparison has shown that for very lean mixtures substantial discrepancies are found between both models. However, there exists a range of richer mixtures where the differences are strongly attenuated and the unity Lewis number hypothesis can provide acceptable results.

References

Beita et al. (2021) "Thermoacoustic Instability Considerations for High Hydrogen Combustion in Lean Premixed Gas Turbine Combustors: A Review", *Hydrogen*, **1** 33–57

Vance et al. (2020) "The effect of thermal diffusion on stabilization of premixed flames", *Combustion and Flame*, **216** 45–57

Vázquez et al. (2016) "Alya: Multiphysics engineering simulation toward exascale", *Journal of Computational Science*, **14** 15–27

2nd Spanish Fluid Mechanics Conference
Barcelona (2 - 5 July 2023)

Numerical study of propagation patterns of lean hydrogen-air flames under confinement

Anne Dejoan*, Daniel Fernández-Galisteo, and Vadim N. Kurdyumov

*anne.dejoan@ciemat.es

Department of Energy, CIEMAT, Avda. Complutense 40, 28040, Madrid, Spain

Two-dimensional (2D) and quasi-two-dimensional (quasi-2D) simulations of lean premixed hydrogen-air flames have been performed using a reduced one-step kinetics and simple transport model to analyze how the resulting losses of momentum and heat affect the characteristic flame propagation patterns under confinement.

1 Introduction

The present work is motivated by experimental observations on the structure of lean premixed hydrogen-air flames propagating in a Hele-Shaw chamber; see Shen et al. (2016); Veiga-López et al. (2020). For large enough distance, h, between the plates of the Hele-Shaw chamber, these experiments show angular sawtooth-shaped flame structures at the large scales and small flame cells at the small scales. However, as the distance h is reduced and closes the planar adiabatic flame thickness, δ_f, the experiments report the existence of isolated flame cells that can propagate steadily in the form of a one-headed or two-headed type and can develop into a fractal-like pattern. These phenomena, observed for very lean hydrogen-air mixtures, is an anomaly to the traditional quenching limit given by a Peclet number, $Pe = h/\delta_f \approx 40$ (Jarosinski (1983)).

The propagation of lean hydrogen-air flames have been studied before in 2D simulations; see for example Berger et al. (2019), where angular sawtooth shapes and cellular structures are reported. In cases of small h, 2D simulations can not capture the effects of confinement (losses of momentum and heat) inherent to the Hele-Shaw chamber when the plates are very close. In that cases, the effects of confinement must be analyzed by making use directly of three-dimensional (3D) simulations or by employing a quasi-2D approximation.

2 Formulation

The quasi-2D formulation is obtained in the limit of very small distance between the plates of the Hele-Shaw burner ($h/\delta_f \to 0$). In this limit, the 3D reactive Navier-Stokes equations, written in the low-Mach number approximation, can be reduced to a 2D set of equations with the flow quantities averaged across the gap distance h; see Fernández-Galisteo et al. (2018). This limit reduces the momentum equation to $\vec{u} = -\nabla p/12\mu Pr$ (similar to Darcy's law), where μ is the viscosity of the gas mixture, Pr is the Prandtl number, and p is the hydrodynamic pressure. Within this limit, a volumetric heat-loss parameter, $b = 2\lambda_w/hh_w$, emerges in the formulation (with λ_w and h_w the thermal conductivity and thickness of the solid wall, respectively).

The chemistry is described by the one-step reduced kinetics developed for lean hydrogen-air deflagrations in Fernández-Galisteo et al. (2009). The reduced kinetics has the advantage to tackle the relevant physics at a relatively low computational cost. In the simulations, the equivalence ratio and the fresh gas temperature is set to $\phi = 0.4$ and $T_u = 298$ K. The species diffusivities are imposed by setting spatially homogeneous Lewis numbers, and the thermal conductivity of the gas mixture is computed with the approximation $\lambda/c_p = 2.58 \times 10^{-5}(T/T_u)^{0.7}$ kg/m·s, with c_p evaluated by NASA polynomials. Soret effects are not included. For the considered conditions, the velocity and thickness of the planar adiabatic flame take the values $S_L = 32.9$ cm/s and $\delta_f = 0.06$ cm, respectively. The adiabatic flame temperature is 1438 K.

3 Some selected results

Instantaneous 2D and quasi-2D flame fronts are illustrated in Fig. 1 for the adiabatic case. Under momentum loss the corrugated flame front tends to form more elongated cells in a finger-like structure, which increases the total flame surface area. As can be seen, the maximum temperature, located at the head of the cells, is higher for the quasi-2D case (1760 K) than for the 2D case (1610 K), thus enhancing the consumption speed.

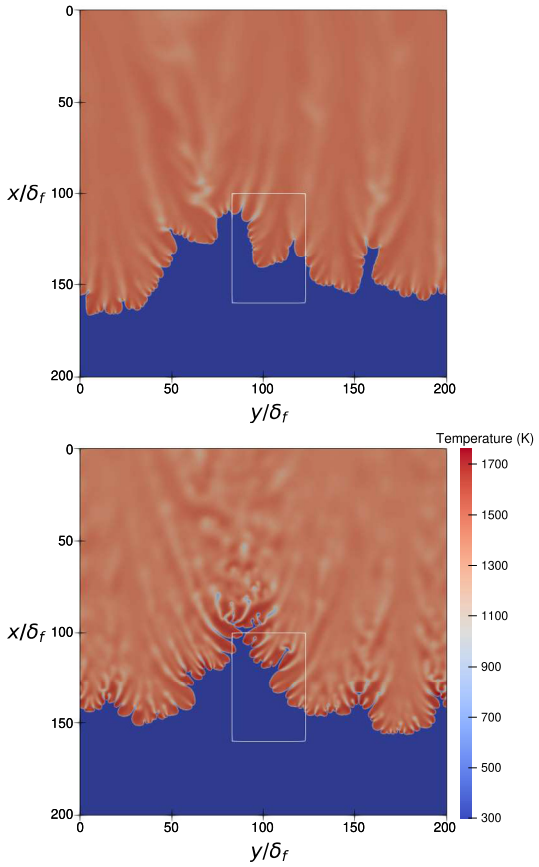

Figure 1: Visualization of the temperature field at time $t = 0.3$ s ($\sim 165\delta_f/S_L$) for the 2D simulation (upper) and the quasi-2D simulation (bottom). The white box is drawn to highlight the characteristic flame scales as done in Berger et al. (2019).

Figure 2 shows the water mass fraction field (selected as a marker for tracking the front evolution) for non-adiabatic cases. Isolated two-headed flame cells, that propagate throughout the chamber, are observed for $b = 0.136$ cal/(cm^3·s·K). The size of these cells are in agreement with the experimental values (around 2 or 3 mm) given by Veiga-López et al. (2020).

4 Conclusions

The effect of confinement in lean hydrogen-air flame propagation is simulated by employing a quasi-2D formulation with a one-step reduced kinetics and simple transport model. Loss of momentum is seen to increase flame corrugation in the form of small fingers and to increase flame temperature at the head of the cells. Loss of heat is seen to form steady propagating two-headed cells. Isolated one-headed cells where not found in the present simulations, as done in Domínguez-González et al. (2022).

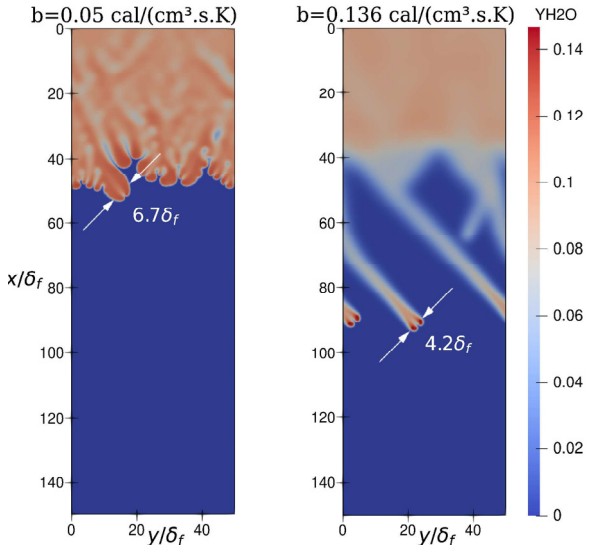

Figure 2: Visualization of the water mass fraction field for different values of the heat-loss parameter b.

References

Shen S & Wongwiwat J & Gross J & Ma X & Ronney PD (2016) "Flame propagation in narrow channels at varying Lewis numbers". *WSSCI Spring Meeting 2016: 139LF-0020.*

Veiga-López F & Kuznetsov M & Martínez-Ruiz D & Fernández-Tarrazo E & Grune J & Sánchez-Sanz M (2020) "Unexpected propagation of ultra-lean hydrogen flames in narrow gaps". *Physical Review Letters*, **124**, 174501.

Jarosinski J (1983). "Flame quenching by a cold wall". *Combustustion and Flame*, **50**, 167–175.

Berger L & Kleinheinz K & Attili A & Pitsch H (2019). "Characteristics patterns of thermodiffusively unstable premixed lean hydrogen flames". *Proceedings of the Combustion Institute*, **37**, 1879–1886.

Fernández-Galisteo D & Kurdyumov VN & Ronney PD (2018). "Analysis of premixed Flame propagation between two closely-spaced parallel plates". *Combustion and Flame*, **190**, 133–145.

Fernández-Galisteo D & Sánchez AL & Liñán A & Williams FA (2009). "One-step reduced kinetics for lean hydrogen-air deflagration". *Combustion and Flame*, **156**, 985–996.

Domínguez-González A & Martínez-Ruiz D & Sánchez-Sanz M (2022). "Stable circular and double-cell lean hydrogen-air premixed flames in quasi two-dimensional channels". *Proceedings of the Combustion Institute*. In press.

2nd Spanish Fluid Mechanics Conference
Barcelona (2 - 5 July 2023)

Premixed flames in narrow heated circular channels: steady-state solutions, and linear stability analysis

Vadim Kurdyumov, Daniel Fernández-Galisteo, and Carmen Jiménez

vadim.k@ciemat.es

Departamento de Energía, CIEMAT, Madrid, Spain

In this work we present a study of the dynamics of premixed flames in externally heated narrow circular channels. The use of a simplified model (constant-density, one-step chemistry) permits to carry out a global stability analysis in addition to time-dependent numerical simulations. We find a rich dynamics, with oscillating flames and cellular structures as well as chaotic flame dynamics.

1 Introduction

Understanding the structure and dynamics of flames in narrow channels is important in the design of small-scale combustion devices, as these small size systems can present instabilities, leading to uncontrolled flame behavior. A canonical configuration for flames in channels is a partially heated channel, with a controlled external wall temperature profile, for which numerical analysis has shown an unexpectedly rich set of possible flame behaviors (1; 2; 3).

2 Formulation

We consider a combustible mixture with initial temperature T_0 and fuel mass fraction Y_{F0} flowing in a cylindrical channel with radius R. The mass flow rate through the channel is fixed and the temperature of the outer wall surface is given by a profile $T_w(z')$.

We adopt a diffusive-thermal model, so that the mixture density ρ, and its heat capacity c_p, thermal and molecular diffusivities D_T and D are all constants and the flow field, unaffected by combustion, is given by a Poiseuille flow with mean U_0. Moreover, we assume a global irreversible reaction: $F+O \to P+Q$.

The reference scales are chosen as $\delta_T = D_T/S_L$ (S_L is the planar flame speed) and R for the lengths in axial and radial directions, z and r, δ_T^2/D_T for time, and Y_{F0} for the fuel mass fraction, $Y = Y_F/Y_{F0}$. The dimensionless temperature is $\theta = (T-T_0)/(T_e-T_0)$, where $T_e = T_0+(QY_{F0})/_p$ is the adiabatic flame temperature. The dimensionless equations in cylindrical coordinates (z, r, ϕ) in the moving reference frame become:

$$\begin{aligned}\frac{\partial\theta}{\partial t} + 2m(1-r^2)\frac{\partial\theta}{\partial z} &= \frac{\partial^2\theta}{\partial z^2} + \frac{1}{a^2}\nabla_{r\phi}\theta + \omega \\ \frac{\partial Y}{\partial t} + 2m(1-r^2)\frac{\partial Y}{\partial z} &= \frac{1}{Le}\left(\frac{\partial^2 Y}{\partial z^2} + \frac{1}{a^2}\nabla_{r\phi}Y\right) - \omega,\end{aligned}$$

where $\nabla_{r\phi} = \partial^2/\partial r^2 + r^{-1}\partial/\partial r + r^{-2}\partial^2/\partial\phi^2$, $m = U_0/S_L$, $a = R/\delta_T$, $Le = D_T/D$ and $\omega = \beta^2/(2Leu_p^2)Y\exp\beta(\theta-1)/(1+\gamma(\theta-1)]$, with $\beta = \mathcal{E}(T_e-T_0)/(\mathcal{R}T_e^2)$, $\gamma = (T_e-T_0)/T_e$, $\mathcal{E}$ the activation energy and $\mathcal{R}$ the universal gas constant. We assume that the mixture is fuel-lean, the oxidizer mass fraction is nearly constant, and ω depends only on Y.

As boundary conditions, we impose periodicity in ϕ, an impermeable wall with temperature linear in r:

$$r = 1: \quad \partial Y/\partial r = 0, \partial\theta/\partial r = -1/2a^2 b\left[\theta - \theta_w(z)\right],$$

with $b = 2\lambda_w\delta_T^2/(\lambda R h_w)$, with λ and λ_w the gas and wall thermal conductivities and h_w the wall thickness. At the inlet and outlet:

$$\begin{aligned} z \to -\infty: &\quad Y = 1, \theta = 0; \\ z \to \infty: &\quad \partial^2\theta/\partial z^2 = \partial^2 Y/\partial z^2 = 0. \end{aligned}$$

Steady and unsteady computations are carried out in a $-50 < z < 50$ domain. The spatial derivatives are discretized on a uniform grid using 2nd order, 3-point central differences with 2001 grid points for 1D calculations, 1001×101 for 2D and $501 \times 51 \times 81$ for 3D. For unsteady calculations an explicit 1st-order marching procedure with step $\tau = 10^{-4}$ to 10^{-5} was used. To find the steady (not necessarily stable) solutions, the steady version of the equations for θ and Y was solved using a Gauss-Seidel method with over-relaxation. In addition to unsteady calculations, we also performed a linear stability analysis of the steady state solutions.

3 Results

Axisymmetric flame solutions for different Le are shown in Fig. 1. It can be seen that for $Le < 1$ the peak of the reaction zone is located at a distance from the channel axis. As the Lewis number increases, the

reaction rate maximum moves towards the axis. At large Le the transverse flame profile becomes almost planar near the axis.

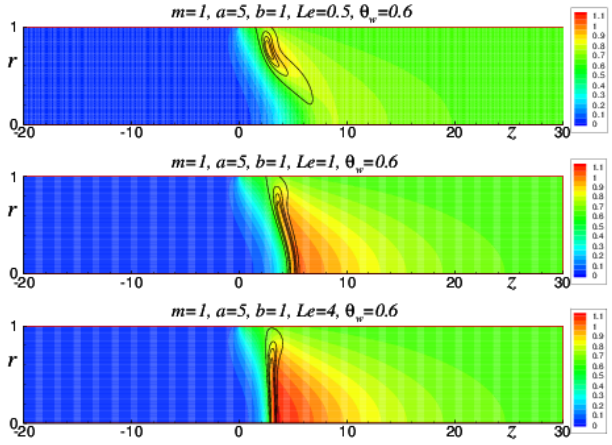

Figure 1: Temperature contours and reaction rate isolines for steady axisymmetric flames at several Le.

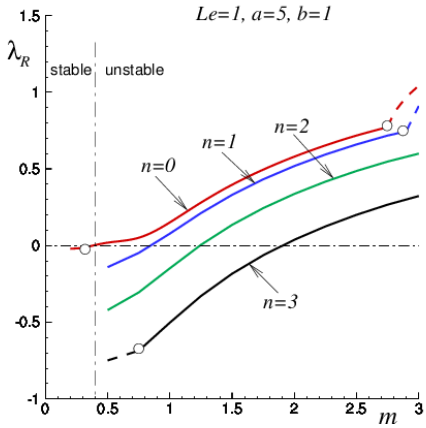

Figure 2: Real part of the main eigenvalues for $Le = 1$ for the first four azimuthal eigenmodes. The dashed lines correspond to eigenvalues with $\lambda_i = 0$

Figure 2 shows the real part of the main eigenvalue from stability analysis for $Le = 1$, $a = 5$, $b = 1$ and different modes with $n = 0, 1, 2, 3$, versus m. At low flow rates, the steady-state axisymmetric solution is stable. As m increases the eigenvalue for $n = 0$ first becomes imaginary and then its real part passes to the right half-plane of the complex λ plane, that is, a Hopf's bifurcation occurs. The value of the critical flow rate is plotted with a vertical dash-dotted line. A similar behavior is observed for modes $n > 0$: the real part of the eigenvalues becomes also positive as m increases, but modes with $n > 0$ are less unstable than the axisymmetric $n = 0$ mode. For sufficiently large m, the main eigenvalues become purely real (dashed lines in the figure).

Finally, at $Le > 1$ chaotic dynamics appear, as shown in Fig. 3, where we plot a Poincaré map built from the local maxima of the flame position evolution for $Le = 4$. The map consists of several continuous segments, which indicates the chaotic behavior of the flame.

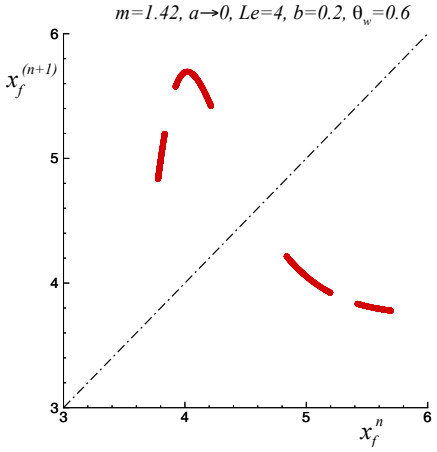

Figure 3: The Poincaré map built from the local maxima of the flame position x_f for a $Le = 4$ flame.

4 Conclusions

The analysis of a simplified model for narrow circular channels has shown that for $Le \leq 1$, a combination of oscillatory and cellular instability can take place, while for $Le > 1$ chaotic flame dynamics may appear for some values of the flow rate.

References

[1] Pizza G, Frouzakis CE, Mantzaras J, Tomboulides AG & Boulouchos K (2010) Three-dimensonal simulations of premixed hydrogen/air flames in microtubes. *J. Fluid Mech.*, **658**, 463491.

[2] Kurdyumov VN, Pizza G, Frouzakis CE & Mantzaras J (2009) Dynamics of premixed flames in a narrow channel with a step-wise wall temperature. *Combust. Flame*, **156**, 2190–2200.

[3] Kurdyumov V N, Fernández-Galisteo D & Jiménez C (2021) Premixed flames in a narrow slot with a step-wise wall temperature: linear stability analysis and dynamics. *Combust. Theor. Modell.*, **25**, 1132–1157.

2nd Spanish Fluid Mechanics Conference
Barcelona (2 - 5 July 2023)

Single-step chemistry validation in turbulent flame cases

A. Millán-Merino , S. Taileb , M. Tayyab , S. Zhao , and P. Boivin

alejandro.millan-merino@univ-amu.fr

Aix Marseille Univ, CNRS, Centrale Marseille, M2P2, Marseille, France.

Recent progress in reduced kinetic modeling has allowed the accurate reproduction of premixed hydrocarbon combustion with an efficient single-step mechanism. The presented methodology has proven to be accurate in a wide range of equivalence ratios for adiabatic temperatures, ignition delay times, and laminar premixed flame propagation velocities. Here, we will extend the application of this methodology in the frame of turbulent combustion. Large-eddy simulations of 3D turbulent flames will be presented using the reduced 1-step mechanism in a hybrid Lattice Boltzmann solver. Two configurations, a premixed CH4/air swirl burner and a partially premixed CH4 lifted flame, will be presented.

1 Introduction

In the modeling of combustion chambers, the implementation of detailed chemistry is a significant challenge because the number of species and reactions can be considerably large. Additionally, small radicals present in detailed chemistry require shorter time step integration making the problem stiffer from the numerical point of view. These constraints are more accused in complex 3-dimensional simulations where flows are typically turbulent.

In that sense, many reduced models emerge in the literature. Starting from skeletal descriptions to global reactions that bypass the intermediate species all of them agree on two main objectives: an accurate description of the heat release and a specific set of kinetic properties, e.g. Laminar flame propagation velocity or ignition delay time. Between the options found in the literature, we remark on the approach presented in our previous work, Millán-Merino et al. (2022). It consists of a single global reaction with variable stoichiometric coefficients that ensure the correct equilibrium temperature.

Although the mechanism provided good results in canonical laminar flame configurations, its performance in complex configurations is still an open question. In the present work, we will provide a more extensive validation of the mechanism in turbulence flame cases well addressed in the literature.

2 Formulation

In the present work, the reactive Navier-Stokes equations read as follows,

$$\frac{\partial \rho}{\partial t} + \frac{\partial \rho u_\beta}{\partial x_\beta} = 0 \tag{1}$$

$$\frac{\partial \rho u_\alpha}{\partial t} + \frac{\partial \rho u_\alpha u_\beta + p\delta_{\alpha\beta}}{\partial x_\beta} = \frac{\partial \tau_{\alpha\beta}}{\partial x_\beta} \tag{2}$$

$$\frac{\partial \rho E}{\partial t} + \frac{\partial \rho u_\beta (E + p/\rho)}{\partial x_\beta} = \frac{\partial \tau_{\alpha\beta} u_\alpha}{\partial x_\beta} - \frac{\partial q_\beta}{\partial x_\beta} \tag{3}$$

$$\frac{\partial \rho Y_k}{\partial t} + \frac{\partial \rho u_\beta Y_k}{\partial x_\beta} = \frac{\partial \rho V_{k,\beta} Y_k}{\partial x_\beta} + \dot{\omega}_k \tag{4}$$

where u_α is the α^{th} component of the fluid velocity, ρ is the density of the mixture, E is the total energy, and Y_k is the mass fraction of kth specie. The species diffusion velocity $V_{k,\alpha}$ is computed via a constant Lewis number definition, q_α is the thermal heat flux obtained using the generalized Fourier's Law, and $\dot{\omega}_k$ is the mass production or consumption rate using the 1-step mechanism. The viscous stress tensor $\tau_{\alpha\beta}$ is defined as

$$\tau_{\alpha\beta} = (\mu + \mu_t)\left(\frac{\partial u_\alpha}{\partial x_\beta} + \frac{\partial u_\beta}{\partial x_\alpha} - \frac{2}{3}\delta_{\alpha\beta}\frac{\partial u_\gamma}{\partial x_\gamma}\right) \tag{5}$$

where μ_t is the subgrid-scale turbulent viscosity, $\delta_{\alpha\beta}$ is the Kronecker symbol and $\mu = \mu_0 (T/T_0)^{0.7}$ is the dynamic viscosity of the mixture. Energy and species equations are complemented with constant turbulent Prandtl and Schmidt numbers and a turbulent combustion model defined on each test case. The previous set of equations is closed with the equation of state for an ideal gas and the constitutive relations for the thermodynamic properties computed using the NASA polynomials.

The previous equations are solved using a hybrid compressible Lattice-Boltzmann method. Mass and momentum equations are reconstructed from the Boltzmann equation while energy and species conservation equations are solved using a Finite Volume method. Finally, the temporal integration is made by an explicit first-order Euler scheme.

3 Results

The PRECCINSTA burner, see Moureau et al (2011), consists of an inlet premixed injection that undergoes a swirler before its entrance into the combustion chamber. For this test, the classical thickened flame model has been used for combustion modeling. To compare the performance of the present mechanism, simulations have been carried out for two additional mechanisms: a 2-step mechanism and a detailed mechanism composed of 17 species and 73 reactions.

Fig. 1 presents a volumetric rendered view of the heat release along with mean and RMS temperature profiles in the axisymmetric cut-plane. Results are characterized by an M-shape flame front which separates two Recirculation zones. Similar behavior has been obtained for the other two mechanisms simulations.

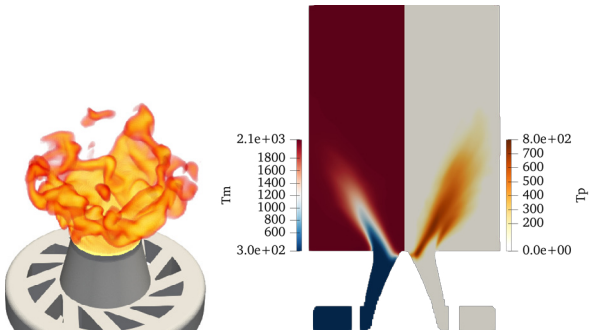

Figure 1: Volumetric rendering of the heat release rate, left plot, and mean and RMS axisymmetric cut-planes for the temperature profile, right plot.

The Cabra flame, see Cabra et al. (2005), consists of a lifted turbulent flame of a CH_4 jet vitiated in a hot coflow. In the present work, Eddy Dissipation Concept was used in turbulence modeling. The 1-step model is complemented with a passive scalar transport equation η that serves as an ignition detector. When its value $\eta \ll 1$ heat release reaction is restrained and reactivated as η approaches 1.

In fig. 2 instantaneous structure of the flow is shown with mean and RMS temperature profiles. Coherent structures are generated at the end of the tube and propagated downstream until the flow is destabilized. Then, mixing is promoted and the ignition detector is produced. When η approaches 1 the heat release reaction is enabled and thermal ignition occurs. A lift-off distance of $\approx 30D$ is predicted showing a reactive W-shape front characteristic from triple-flame structures.

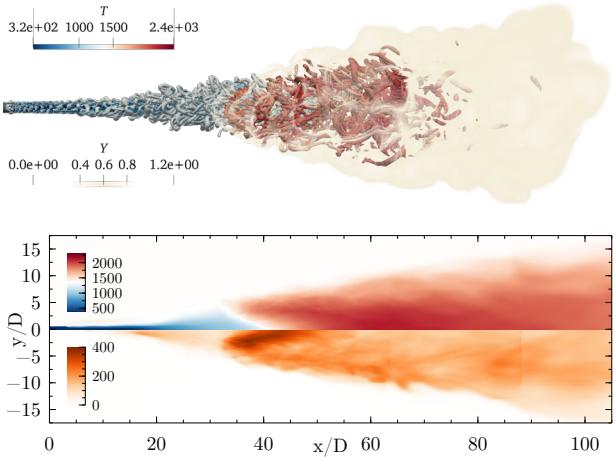

Figure 2: The top plot represents an instantaneous representation of the iso-surface of Q-criterion colored with temperature field joined with a superposition of volumetric rendering of ignition detector. The bottom plot represents the mean and RMS axisymmetric cut-planes for the temperature profile.

4 Conclusions

Two turbulent flame configurations have been chosen, a premixed swirl burner and a lifted jet flame. Different strategies for turbulent combustion modeling have been chosen for each test case, proving the flexibility of the original mechanism in complex applications. The results obtained are in good agreement with other chemical schemes (reduced and detailed) as well as the experimental results of the literature.

References

Millán-Merino A., Taileb S. and Boivin, P (2022) "A new method for systematic 1-step chemistry reduction applied to hydrocarbon combustion". *Proceedings of the Combustion Institute.*

Cabra R., Chen J.Y., Dibble R.W., Karpetis A.N. and Barlow R.S. (2005) "Lifted methane–air jet flames in a vitiated coflow " *Combustion and Flame*, **143**, 491–506.

Moureau V., Domingo P. and Vervisch L. (2011) "From large-eddy simulation to direct numerical simulation of a lean premixed swirl flame: Filtered laminar flame-pdf modeling ". *Combustion and Flame*, **158**, 1340–1357.

2nd Spanish Fluid Mechanics Conference
Barcelona (2 - 5 July 2023)

A High-Order Lagrange–Galerkin Method for Compressible Flows

Manuel Colera[1], Jaime Carpio[1], and Rodolfo Bermejo[2]

m.colera@upm.es

[1]Departamento de Ingeniería Energética, Universidad Politécnica de Madrid, Spain
[2]Departamento de Matemática Aplicada a la Ingeniería Industrial, Universidad Politécnica de Madrid, Spain

We present a novel Lagrangian–Eulerian scheme for the resolution of two-dimensional compressible and inviscid flows. The scheme considers arbitrary-order continuous space discretizations on unstructured triangular meshes, as well as arbitrary-order implicit–explicit Runge–Kutta time marching schemes. The method preserves mass, momentum and total energy as long as the integrals in the formulation are computed exactly. The recent model proposed by Brenner (2006) for viscous flows is employed to define the operators needed to stabilize the continuous Galerkin formulation. The method has been tested on several benchmark problems using a fourth-order time-marching formula and up to fifth-order elements, showing good accuracy both for smooth and discontinuous solutions.

1 Formulation

In this work, we focus on the Euler equations for compressible and inviscid flows,

$$\partial_t u_I + \partial_j \left(v_j u_I\right) = \partial_j \left(f_{Ij}\right), \tag{1}$$

with $\partial_t \equiv \partial/\partial t$, $\partial_j \equiv \partial/\partial x_j$, t the time, $\mathbf{x}$ the position vector, $\mathbf{u} = [\rho, m_1, m_2, \mathcal{E}]^T$ the vector of conservative variables, $\mathbf{f} = \mathbf{f}(\mathbf{u})$ the pressure flux matrix, $f_{1,j} = 0$, $f_{1+i,j} = -p\delta_{ij}$, $f_{4,j} = -pv_j$, ρ the density, $\mathbf{v}$ the velocity, $\mathbf{m} = \rho\mathbf{v}$ the momentum per unit of volume, $\mathcal{E} = p/(\gamma - 1) + \rho v_i v_i/2$ the total energy per unit of volume and γ the adiabatic constant of the gas. We adopt Einstein's summation convention, with uppercase and lowercase indices varying from 1 to 4 and from 1 to 2, respectively.

The so-called *weak Lagrange–Galerkin formulation* (Colera et al. (2020)) associated with Eq. (1) is

$$\frac{\mathrm{d}}{\mathrm{d}t}\int_{\Omega_f} u_I \psi \,\mathrm{d}\Omega = -\int_{\Omega_f} f_{Ij}\partial_j\psi \,\mathrm{d}\Omega + \oint_{\partial\Omega_f} f_{Ij}\psi n_j, \tag{2}$$

where $\Omega_f(t) := \left\{\mathbf{x}(t) \in \mathbb{R}^2 : \mathrm{d}\mathbf{x}/\mathrm{d}t = \mathbf{v}(\mathbf{x}(t), t)\right\}$ is a domain that moves with the fluid, $\mathbf{n}$ is the outward normal vector to the boundary $\partial\Omega_f$, and $\psi(\mathbf{x}, t)$ is a continuous test function such that remains constant along the trajectories of the fluid particles, i.e., $\mathrm{D}_t\psi := \partial_t\psi + v_j\partial_j\psi = 0$.

Following Colera et al. (2022), Eq. (2) is first discretized in space with a *multiscale* finite element method. The mesh moves with $\Omega_f(t)$ and therefore the method is Lagrangian. Then, we march in time with an implicit–explicit Runge–Kutta (RK) method. Specifically, for each stage of the RK method we perform the following steps: (i) the mesh is displaced with the explicit part, (ii) Eq. (2) is solved as is (without any stabilization terms) with the explicit part, and hence we obtain a non-stabilized solution $\mathbf{u}_*$, (iii) the latter is post-processed to detect the discontinuities and to compute an artificial-viscosity based stabilization operator, and (iv) Eq. (2) is equipped with the stabilization operator and solved with the implicit part of the method to yield a smooth solution $\mathbf{u}_h$. Periodically, $\mathbf{u}_h$ is remapped from the moving mesh to a fixed (reference) mesh to avoid mesh distortion problems.

2 Numerical experiments

To check the accuracy of the method, we have solved several benchmark problems using up to fifth-order elements and a fourth-order RK. As an example, we show the results for the shock–vortex interaction (Rault et al. (2003)) and for the triple-point (Zeng and Scovazzi (2014)) problems in figures 1-2.

The numerical experiments performed confirm that the artificial viscosity is only active at the discontinuities, and therefore does not spoil the solution at the smooth regions. The multiscale stabilization operator is also necessary to remove acoustic instabilities. For the same computational effort, high-order elements yield much smaller errors than low-order ones when the solution is smooth, and similar errors when the solution is discontinuous. Finally, the relative errors in the conservation of mass, momentum and total energy are of single-precision ($\mathcal{O}(10^{-7})$) accuracy.

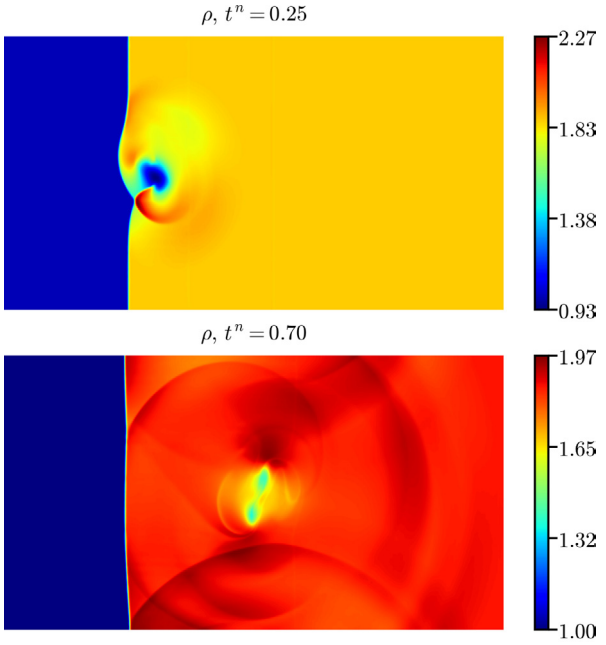

Figure 1: Density in the shock–vortex interaction problem for fifth-order elements and mesh size $h \simeq 0.010$.

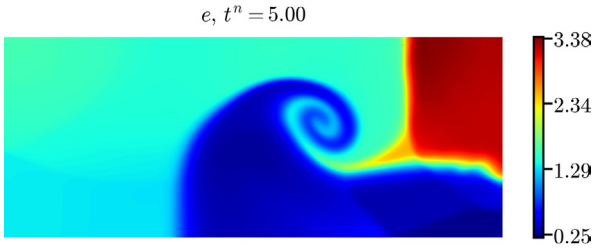

Figure 2: Internal energy in the triple-point problem for fifth-order elements and mesh size $h \simeq 0.014$.

3 Conclusions

We have developed a Lagrangian–Eulerian method for the resolution of compressible and inviscid flows. As main features, the scheme considers continuous high-order space discretizations and an implicit–explicit RK time-marching scheme, has good conservation properties and makes use of the recent model by Brenner (2006) for viscous flows.

Acknowledgements

This research has been partially funded by project PGC-2018-097565-BI00 from the "Ministerio de Ciencia, Innovación y Universidades" of Spain and the European Regional Development Fund, and by the FPU16/05509 grant to M. Colera from the "Ministerio de Ciencia, Innovación y Universidades" of Spain.

References

H. Brenner. Fluid mechanics revisited. *Physica A: Statistical Mechanics and its Applications*, 370(2): 190–224, Oct. 2006. ISSN 0378-4371. doi: 10.1016/j.physa.2006.03.066.

M. Colera, J. Carpio, and R. Bermejo. A nearly-conservative high-order Lagrange–Galerkin method for the resolution of scalar convection-dominated equations in non-divergence-free velocity fields. *Computer Methods in Applied Mechanics and Engineering*, 372:113366, Dec. 2020. ISSN 00457825. doi: 10.1016/j.cma.2020.113366.

M. Colera, J. Carpio, and R. Bermejo. A nearly-conservative, high-order, forward Lagrange–Galerkin method for the resolution of compressible flows on unstructured triangular meshes. *Journal of Computational Physics*, 467:111471, Oct. 2022. ISSN 0021-9991. doi: 10.1016/j.jcp.2022.111471.

A. Rault, G. Chiavassa, and R. Donat. Shock-Vortex Interactions at High Mach Numbers. *Journal of Scientific Computing*, 19(1):347–371, Dec. 2003. ISSN 1573-7691. doi: 10.1023/A:1025316311633.

X. Zeng and G. Scovazzi. A frame-invariant vector limiter for flux corrected nodal remap in arbitrary Lagrangian–Eulerian flow computations. *Journal of Computational Physics*, 270:753–783, Aug. 2014. ISSN 0021-9991. doi: 10.1016/j.jcp.2014.03.054.

2nd Spanish Fluid Mechanics Conference
Barcelona (2 - 5 July 2023)

Assessing the Accuracy of Immersed Boundary Methods for High-Fidelity Computational Aeroacoustics

A. Lázaro[1], S. Madriñan[2], O. Carrasco[2], J. Grau[1], R. Torres[1], L. Jofre[1], and F. Capuano[1]

aleix.lazaro.i@upc.edu

[1]Department of Fluid Mechanics, Universitat Politècnica de Catalunya · BarcelonaTech
[2]QEV Technologies S.L.

This work presents the assessment of the suitability of different IBM approaches, and underlying discretization accuracy, for high-fidelity aeroacoustics. The IBM schemes are used in conjunction with recently developed non-dissipative and non-dispersive numerics [1], an essential component for the physical realism of multi-scale simulations. The analyzed IBM strategies are compared with canonical aeroacoustic benchmarks [2]. Finally, the work critically discusses the suitability of such techniques for Direct Sound Computation (DSC) constrained by the limiting computational schemes used in highly parallel codes.

1 Introduction

Computational Aeroacoustics (CAA) is an increasingly relevant topic in multiple sectors of engineering. Its practice has historically been limited by the high-demanding resolution typically required to accurately predict sound, and the resulting adoption of lower accuracy methods. However, with the current increasing accessibility to high computational resources, DSC slowly emerges as a realistic option for high-fidelity CAA. Furthermore, to maintain this high-fidelity attribute, it is essential that the CAA simulation is performed using non-dissipative and non-dispersive computational methods [3, 4].

In the framework of engineering-applied CAA, the Immersed Boundary Methods (IBM) present themselves as a very attractive option, given that they do not require a body conformed grid (unlike traditional flow solvers), their straight-forward treatment of complex and moving geometries and their fitting to the high-fidelity sound capturing requirements.

2 Method and results

The aeroacoustics problem considered in this work is governed by the ideal-gas compressible Navier-Stokes equations, which are numerically solved according to a standard semi-discrete approach. The building block of the spatial discretization is a robust kinetic-energy-preserving formulation for compressible flows based on the KGP split formulation [1]. The resulting system of ordinary differential equations is advanced in time using a Runge-Kutta method. The overall methodology has been implemented into a flexible pseudo-spectral solver, where finite-differencing schemes of various order of accuracy can be easily mimicked using the modified wavenumber approach.

We explore two IBM: i) an Eulerian-Forcing scheme and ii) a Lagrangian-Forcing scheme. The former is implemented with a Ghost-Cell approach similarly as in [5], while the latter uses a moving-least-square reconstruction as a transfer operator [6]. They both treat the forcing term in a discrete manner, but the Ghost-Cell method does not compute it directly; rather, it defines flow conditions at precise locations (inside the body) that replicate the forcing.

Representative results are depicted in Figure 1, which refers to one of the problems of the *Second Computational Aeroacoustics (CAA) Workshop on Benchmark Problems* [2], i.e., the acoustic scattering from a circular cylinder of diameter $D = 1m$.

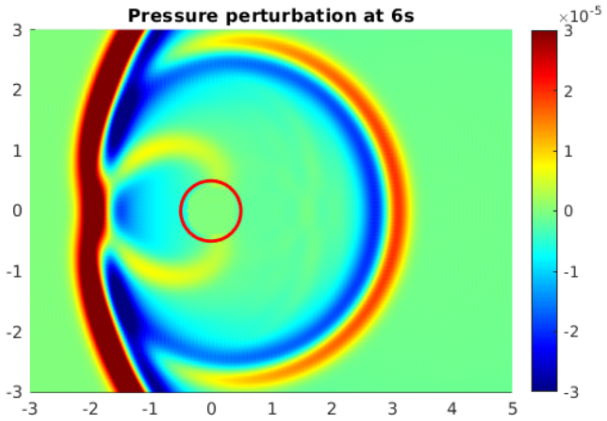

Figure 1: Pressure perturbation at $t = 6s$ of the simulation results with a Ghost-Cell IBM and a resolution of $\Delta x/D = 1/30$.

3 Conclusions

The Ghost-Cell IBM approach rapidly tends to the reference results [7] as the resolution is increased. Figure 1 shows the contour of the pressure perturbation, which visually shows no significant artifacts or dispersive behaviour with $\Delta x/D = 1/30$ and a sixth-order spatial scheme. When pressure profiles are compared to the reference solution in more detail, the errors appear to be mostly influenced by the spatial accuracy of the discretization scheme, rather than by the IBM implementation.

Quantification of errors and the extensive results comparing second-order discretizations with higher-order schemes, as well as the two IBM approaches, will be discussed at the 2^{nd} Spanish Fluid Mechanics Conference.

Acknowledgements

This work is supported by the *Industrial Doctorate* programme (2022-DI-040) of the *Generalitat de Catalunya* (Catalonia), the *Beatriz Galindo* programme (Distinguished Researcher, BGP18/00026) of the *Ministerio de Ciencia, Innovación y Universidades* (Spain), and the *Serra Húnter* programme (Catalonia).

References

[1] Gennaro Coppola, Francesco Capuano, and Luigi De Luca. Discrete energy-conservation properties in the numerical simulation of the navier-stokes equations. *Applied Mechanics Reviews*, 71(1), 2019.

[2] Christopher K.W. Tam and J.C. Hardin. Second Computational Aeroacoustics (CAA) Workshop on Benchmark Problems. *NASA Conference Publication*, (June 1997):377–380, 1997.

[3] Christopher K.W. Tam. Computational aeroacoustics: An overview of computational challenges and applications. *International Journal of Computational Fluid Dynamics*, 18(6):547–567, 2004.

[4] Tim Colonius and Sanjiva K. Lele. Computational aeroacoustics: Progress on nonlinear problems of sound generation. *Progress in Aerospace Sciences*, 40(6):345–416, 2004.

[5] Francesco De Vanna, Francesco Picano, and Ernesto Benini. A sharp-interface immersed boundary method for moving objects in compressible viscous flows. *Computers and Fluids*, 201:104415, 2020.

[6] Marcos Vanella and Elias Balaras. A moving-least-squares reconstruction for embedded-boundary formulations. *Journal of Computational Physics*, 228(18):6617–6628, 2009.

[7] Qianlong Liu and Oleg V. Vasilyev. A Brinkman penalization method for compressible flows in complex geometries. *Journal of Computational Physics*, 227(2):946–966, 2007.

2nd Spanish Fluid Mechanics Conference
Barcelona (2 - 5 July 2023)

Exploring the artificial compressibility method in high-pressure transcritical fluids

Ahmed Abdellatif[1], Jordi Ventosa-Molina[2], Joan Grau[1], Ricardo Torres[1], and Lluís Jofre[1]

ahmed.abdellatif@upc.edu

[1]Dept. Fluid Mechanics, Universitat Politècnica de Catalunya · BarcelonaTech (UPC), Barcelona 08019, Spain
[2]Dept. Heat Engines, Universitat Politècnica de Catalunya · BarcelonaTech (UPC), Terrassa 08222, Spain

This work presents the investigation of a solution to accelerate computations of high-pressure transcritical fluids at low-Mach number regimes based on the artificial compressibility method. The highly adaptable nature of this approach is particularly well suited for conducting complex, high-fidelity simulations on GPU-based computer architectures. The initial exploratory results presented provide speedups of 10× without significantly compromising the simulation accuracy in terms of flow physics.

1 Introduction

The current trend in computational fluid dynamics is to focus on the development of explicit compressible flow solvers due to their inherent capacity to scale up to very large node counts. These algorithms are very well suited for high-speed flows. However, they suffer from time step limitations for low speed flows. Thus, for applications related to high-pressure transcritical fluids, like for example gas turbines and liquid rocket engines (Jofre et al., 2021), which are characterized by small Mach numbers, the utilization of such solvers is challenging, as a result of the significantly small time steps required. This is due to the arbitrarily large speed of the acoustic waves relative to the fluid velocities. In this regard, the exploration of a solution based on the artificial compressibility method (ACM) is proposed in this work. The main idea of this method is to artificially reduce the speed of the traveling acoustic waves without appreciably impacting the flow physics of the problem. Over the past years, several variations of ACM have been developed. For example, Turkel (1987) introduced pseudo-time derivatives to accelerate solution convergence, and Malan et al. (2002) proposed a generalized preconditioner to implicitly solve the equations of fluid motion. In this context, the objective of this work is to explore ACM in high-pressure transcritical fluids. To that end, the work is organized as follows. First, in Section 2, the equations of fluid motion and real-gas thermodynamics are described. Second, the ACM is briefly presented in Section 3. Next, in Section 4, current results are discussed. Finally, the work is concluded and next steps are proposed in Section 5.

2 High-pressure transcritical fluids

The framework utilized for studying supercritical fluids in terms of (i) equations of fluid motion and (ii) real-gas thermodynamics is shortly introduced below.

2.1 Equations of fluid motion

The turbulent flow motion of supercritical fluids is described by the following set of transport equations of mass, momentum, and total energy

$$\frac{D\rho}{Dt} = -\rho(\nabla \cdot \mathbf{v})\,, \tag{1}$$

$$\rho\frac{D\mathbf{v}}{Dt} = -\nabla P + \nabla \cdot \boldsymbol{\tau}, \tag{2}$$

$$\rho\frac{DE}{Dt} = -\nabla \cdot \mathbf{q} - \nabla \cdot (P\mathbf{v}) + \nabla \cdot (\boldsymbol{\tau} \cdot \mathbf{v})\,, \tag{3}$$

where ρ is the density, $\mathbf{v}$ is the velocity vector, P is the pressure, $\boldsymbol{\tau}$ is the viscous stress tensor, E is the total energy, and $\mathbf{q}$ is the Fourier heat flux.

2.2 Real-gas thermodynamics

The relation between the thermodynamic variables is described by the Peng-Robinson equation written as (Jofre et al., 2021)

$$P = \frac{R_u T}{\bar{v} - b} - \frac{a}{\bar{v}^2 + 2b\bar{v} - b^2}, \tag{4}$$

with R_u the universal gas constant, T the temperature, $\bar{v} = W/\rho$ the molar volume, and W the molecular weight. The coefficients a and b take into account real-gas effects related to attractive forces and finite packing volume, respectively.

3 Artificial compressibility method

As previously introduced, the fundamental idea of ACM is to artificially reduce the acoustic time scales of the problem such that time stepping increases without severely affecting the flow physics. The first step is to express the flow variables as asymptotic expansions in the powers of the Mach number, which results in the decomposition of pressure in terms of a thermodynamic pressure P_0 and a hydrodynamic pressure P_1. Next, the Mach number is modified to a larger value in the form $Ma' = \alpha Ma$, where $\alpha > 1$ is a speedup factor; the underlying assumption is that the Ma of the initial flow is extremely small such that αMa is also sufficiently small. As a result, the total pressure is approximated as

$$P \approx P_0 + \alpha^2 \gamma Ma^2 P_1, \tag{5}$$

where γ is the heat capacity ratio. Consequently, the speed of sound reduces to $c' = c/\alpha$, and the time step roughly increases by a factor of order α.

4 Exploratory results

As a first step, the performance of ACM has been explored for the lid-driven cavity. The simplest configuration of the problem corresponds to a square cavity of size $L = 1\,\mathrm{m}$, delimited by three no-slip walls and a lid moving with a prescribed tangential velocity $U_{\mathrm{lid}} = 1\,\mathrm{m/s}$. The cavity contains a fluid of kinematic viscosity $\nu = 0.01\,\mathrm{m^2/s}$ with Prandtl number $Pr = 0.71$, and the Mach number of the flow is $Ma = 0.1$. Following the reference solutions provided by Ghia et al. (1982), this work focuses on the particular case of Reynolds number $Re_L = 100$. The results are depicted in Figure 1 for $\alpha = 3$, showing that they fully agree with the reference data while providing a speedup of approximately $10\times$.

5 Conclusions

This work has briefly discussed the suitability of the artificial compressibility method for high-pressure transcritical fluids at low-Mach-number flow regimes. Initial results showcase speedups of $10\times$, achieved without significantly compromising the simulation accuracy in terms of flow physics. The next step is to assess the performance of the method for 1D inviscid cases, 2D deferentially-heated cavities, and 3D turbulent channel flows at different values of the dimensionless numbers characterizing high-pressure fluids.

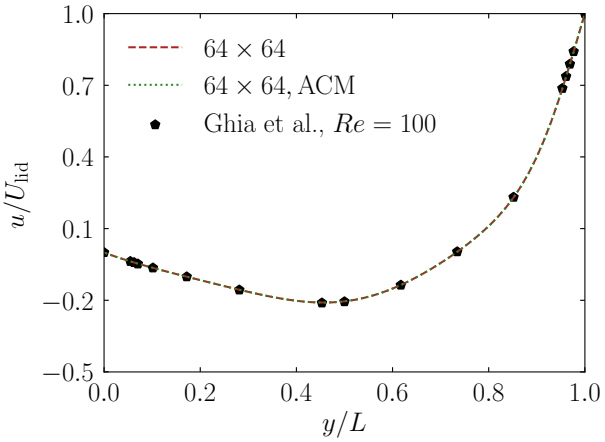

Figure 1: Normalized profile of u velocity along the y centerline with/without utilizing the ACM on a uniform mesh of size 64×64.

Acknowledgements

This work is funded by the European Union (ERC, SCRAMBLE, 101040379). Views and opinions expressed are however those of the authors only and do not necessarily reflect those of the European Union or the European Research Council. Neither the European Union nor the granting authority can be held responsible for them. Support is also acknowledged from the *Beatriz Galindo* program (BGP18/00026, Spain), the SRG program (2021-SGR-01045, Catalonia), and the computer resources at FinisTerrae III provided by CESGA (RES-IM-2023-1-0005).

References

Jofre L. and Urzay J. (2021) "Transcritical diffuse-interface hydrodynamics of propellants in high-pressure combustors of chemical propulsion systems", Prog. Energy Combust. Sci. 82 100877.

Turkel E. (1987) "Preconditioned methods for solving the incompressible and low speed compressible equations", J. Comput. Phys. 71 (2) 277–298.

Malan A. G., Lewis R. W. and Nithiarasu P. (2002) "An improved unsteady, unstructured, artificial compressibility, finite volume scheme for viscous incompressible flows: Part I. Theory and implementation", Int. J. Numer. Methods Eng. 54 (5) 695-–714.

Ghia U., Ghia K. N. and Shin C. T. (1982) "High-Re solutions for incompressible flow using the Navier-Stokes equations and a multigrid method", J. Comput. Phys. 48 (1982) 387—411.

2nd Spanish Fluid Mechanics Conference
Barcelona (2 - 5 July 2023)

On the wake dynamics of the flow past a subsonic and transonic circular cylinder

Ivette Rodriguez[1], Benet Eiximeno[1,2], Lucas Gasparino[2], Carlos Tur-Mongé[1], Jordi Muela[2], and Oriol Lehmkuhl[2]

ivette.rodriguez@upc.edu

[1]Turbulence and Aerodynamics Research Group, Universitat Politècnica de Catalunya, Spain
[2]Large-scale Computational Fluid Dynamics Group, Barcelona Supercomputing Center, Spain

Compressible large-eddy simulations of the flow past a circular cylinder at Reynolds numbers $Re = 10^4$ and Mach numbers in the range $M_0 = 0.05 - 1.2$ are performed. Changes in the wake dynamics, coherent structures and flow topology brought about compressibility effects are discussed and analysed in detail.

1 Introduction

The flow over a bluff body has received much attention due to its importance in many engineering applications. In particular, significant efforts have been devoted to the flow past a circular cylinder, which in spite of its simple geometry the flow involves many phenomena depending on the Reynolds number ($Re = \rho U_{ref} D/\mu$). The incompressible flow past cylinders has been widely study in the literature; e.g. comprehensive descriptions about the different wakes regimes can be found in (Roshko 1993, Williamson 1996). However, studies considering compressibility effects are more scarce in the literature. Compressibility dominates the flow producing a steady increase in the drag with the Mach number, with a local maximum which precedes the absolute maximum at nearly $M_0 = 1$. At supersonic Mach numbers, a decrease in the drag coefficient up to $M_0 = 1.6$ occurs, above which it stabilises to a value near that of low Mach numbers. There are several experimental works documenting the variation of the drag coefficient with the Mach number (see for instance Welch (1953), Macha (1976), Murthy & Rose (1978)). In addition to the variation in the drag forces, compressibility also produces important changes in the flow dynamics. For instance, in the transonic regime, the flow is characterised by moving shock waves which interact with the boundary layer instabilities and the vortex shedding process, shock/turbulent boundary layer interaction in the cylinder shoulders, shock/wake interaction and the appearance of local supersonic zones in the vortex formation region. In the present work, compressibility effects on the flow past a cylinder at the subcritical Reynolds number $Re = 10^4$ will be studied for the range of Mach numbers $M_0 = 0.05 - 1.2$. This encompasses both subsonic and transonic regimes. The changes in the forces, wake dynamics and topology brought about compressibility will be discussed in detail.

2 Results and discussion

Compressible large eddy simulations (LES) of the flow at $Re = 10^4$ are carried out by means of a low-dissipation high-order spectral elements in-house code (Sod). The code is based on the spectral element method (SEM) and combines a spectral-method version of Galerkin's finite-element continuous model with a modified version of Guermond's Entropy Viscosity stabilisation, tailored to work with this spectral elements approach. For the time-advancing algorithm, a fourth-order Runge-Kutta method is used. As for the LES, the ILSA sub-grid scale (SGS) model is used (Lehmkuhl et al. 2019).

Solutions are obtained in a computational domain of dimensions $x \equiv [-30D : 50D]$; $y \equiv [-30D : 30D]$; $z \equiv [0 : \pi D]$ with the cylinder located at $(0, 0, 0)$. The boundary conditions at the cylinder surface are no-slip and adiabatic, whereas non-reflecting boundary conditions are imposed in the free-stream and outlet boundary. Periodic boundary conditions are set in the spanwise direction. The computational mesh used in the simulations, generated by the extrusion in the spanwise direction of a two-dimensional grid, is a semi-structured mesh formed by 3rd-order hexahedrons (64 nodes/element) for a total of 27.3 million nodes.

Figure 1 shows the comparison of the drag coefficient obtained with results of the available literature. In general, a rather good agreement with the reference data is observed, especially for $M_0 \leq 0.8$. Larger deviations are obtained for $M_0 > 0.8$, which can be due to not only Reynolds number differences but also

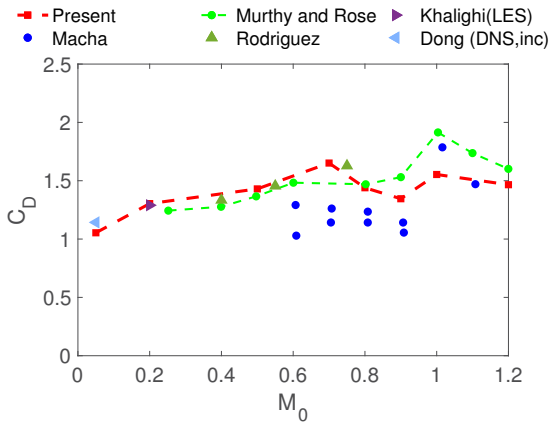

Figure 1: Variation of the drag coefficient with the Mach number. Comparison with the literature. Macha (1976) $Re = 10^5 - 10^6$,Rodriguez (1984) $Re = 10^5$, Murthy & Rose (1978) $Re = 8.3 \times 10^4$, Khalighi et al. (2010), Dong et al. (2006) $Re = 10^4$.

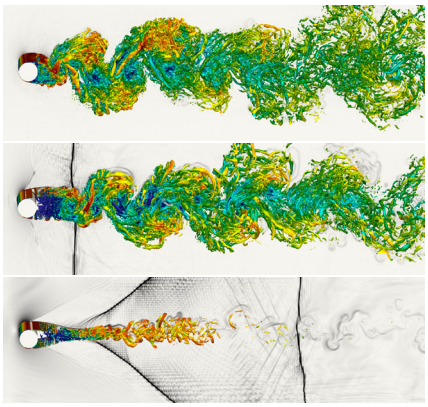

Figure 2: Instantaneous vortical structures represented by Q-isocountours $Q^* = 3$ coloured by the velocity magnitude over the density gradient field for (from top to bottom) $M_0 = 0.5$, $M_0 = 0.8$ and $M_0 = 1.2$

to differences in the conditions with the experiments, interference effects, among others. Nonetheless, numerical results follow a similar trend in the behaviour observed in the experiments. In the transonic zone, increased compressibility affects the formation and development of Kelvin-Helmholtz structures; the appearance of weak shock wakes in this zone is observed to suppress these high-frequency structures and eventually de-couple the vortex formation zone and the downstream wake for $M_0 > 1$ (see Figure 2). As a result of the increased compressibility the wake topology is changed. In the final version of the manuscript, a detailed analysis and discussion on the compressibility effects on the wake dynamics and coherent structures, as well as on the changes on the instability mechanisms of the near wake will be presented.

Acknowledgments

This work has been partially financially supported by the Ministerio de Economía y Competitividad, Secretaría de Estado de Investigación, Desarrollo e Innovación, Spain (ref. PID2020-116937RB-C21 and PID2020-116937RB-C22). We also acknowledge Red Española de Supercomputación (RES) for awarding us access to the MareNostrum IV machine based in Barcelona, Spain (Ref IM-2022-3-0005).

References

Dong, S., Karniadakis, G. E., Ekmekci, A. & Rockwell, D. (2006), 'A combined direct numerical simulation-particle image velocimetry study of the turbulent near wake', *J Fluid Mech* **569**, 185.

Khalighi, Y., Mani, A., Ham, F. & Moin, P. (2010), 'Prediction of sound generated by complex flows at low Mach numbers', *AIAA J* **48**(2), 306–316.

Lehmkuhl, O., Piomelli, U. & Houzeaux, G. (2019), 'On the extension of the integral length-scale approximation model to complex geometries', *Int J Heat Fluid Fl* **78**.

Macha, J. M. (1976), A wind tunnel investigation of circular and straked cylinders in transonic cross flow, Technical Report NASA-CR-149372, NASA.

Murthy, V. S. & Rose, W. C. (1978), 'Detailed Measurements on a Circular Cylinder in Cross Flow', *AIAA J* **16**(6), 549–550.

Rodriguez, O. (1984), 'The circular cylinder in subsonic and transonic flow', *AIAA J* **22**(12), 1713–1718.

Roshko, A. (1993), 'Perspectives on Bluff Body Wakes', *J Wind Eng Ind Aerod* **49**, 79–100.

Welch, C. (1953), The drag of finite length cylinders determined from flight tests at high Reynolds numbers for a Mach number range from 0.5 to 1.3 , Technical report TN-2941.

Williamson, C. H. K. (1996), 'Vortex dynamics in the cylinder wake', *Annu Rev Fluid Mech* **28**(1), 477–539.

2nd Spanish Fluid Mechanics Conference
Barcelona (2 - 5 July 2023)

Scramjet oblique shock waves reflection via 2D and 3D CFD analysis

Joel Gracia[1], David Zurita[1], and Josep M Bergadà[1]

joel.gracia@estudiantat.upc.edu

[1]Departamento de Mecánica de Fluidos, Universitat Politècnica de Catalunya, Spain

The paper presents several 2D and 3D CFD simulations to understand the shock wave and reflected shock waves evolution at the entrance of a scramjet engine. Pressure, temperature and Mach number fields are introduced and compared when using different turbulence models, the information obtained via CFD is employed to modify the existing two dimensional theory. Comparison between the 2D and 3D CFD results clarify which is the expected fluid evolution inside the engine and the shortcomings associated to the 2D models.

1 Introduction

Scramjet engines have gained more and more attention from scientists and engineers due to their excellent performance and potential in hypersonic flight. The development of hypersonic vehicles is of high strategic magnitude to the next generation of transportation. Scramjet performance and internal flow have been previously studied by Rincon (2012), Smart (2010), and Hong (2016). They studied analytically and via CFD scramjet flow conditions and oblique shock waves, comparing the results obtained with experimental cases. They observed the influence internal flow properties have on performance, combustion requirements, and flow separation.

This article aims to analyze via CFD the internal flow inside a scramjet engine. Initially a 2-D CFD model and considering perfect gas is considered, two further 2-D CFD simulaitions considering real gas and using two different turbulence models are investigated. The two dimensional reflected oblique shock waves theory is modified to adapt the results with the ones obtained via CFD. A 3-D CFD model of the engine entrance is also performed to properly analyze the engine geometry and its performance in order to achieve efficient combustion.

2 Analytical model

The below preseted 2-D Oblique shock waves equations have been employed to study the internal engine flow:

$$\frac{1}{\tan\delta} = \left[\frac{(\gamma+1)}{2}\left(\frac{M_1^2}{M_1^2\sin^2\epsilon - 1}\right) - 1\right]\tan\epsilon \quad (1)$$

$$\frac{\rho_2}{\rho_1} = \frac{(\gamma+1)M_1^2\sin^2\epsilon}{2+(\gamma-1)M_1^2\sin^2\epsilon} \quad (2)$$

$$\frac{V_2}{V_1} = \frac{\sin\epsilon}{\sin\beta}\left(\frac{2}{(\gamma+1)M_1^2\sin^2\epsilon} + \frac{(\gamma-1)}{(\gamma+1)}\right) \quad (3)$$

$$\frac{p_2}{p_1} = 1 + \frac{2\gamma}{\gamma+1}(M_{N1}^2 - 1) = \frac{2\gamma}{\gamma+1}M_1^2\sin^2\epsilon - \frac{\gamma-1}{\gamma+1} \quad (4)$$

$$\frac{T_2}{T_1} = \frac{P_2}{P_1}\frac{\rho_2}{\rho_1} \quad (5)$$

However, it has been proved that these equations do not correspond with the CFD results obtained, especially inside the engine where shock boundary layer interaction and, consequently, reflection of shock waves occur. Therefore, the following changes are proposed in order to obtain a representative value between shock waves.

In the first internal reflected shock wave, there is a huge rise in pressure, temperature, and density. This is due to two phenomena, two external shock waves impinge at the engine entrance upper wall causing shock boundary layer interaction, and flow deflection. Furthermore, there is a powerful Prandtl Meyer shock wave, which leads to a middle region with a strong gradient of pressure between the reflected shock wave and the Prandtl Meyer shock wave. Consequently, for the first internal oblique shock wave, it has been considered the next δ angle due to geometry:

$$\delta = 9 + 11.5 + \Delta\phi = 20.5^\circ + \Delta\phi \quad (6)$$

However, as mentioned there is a middle region with a strong gradient of pressure and an expansion wave. Therefore, in order to compute a representative value of this first zone, an angle $\Delta\phi = -17.5^\circ$ has been defined. For the following reflected shock waves, a δ angle of $\delta = 0.01^\circ$ has been chosen in order to obtain a maximum agreement with the flow properties obtained from the CFD simulations. It should be noted that these values are the optimal ones for pressure,

being the mean reltive error smaller than 4%. But they predict temperature and Mach number values along the engine with a mean relative error of 13%.

3 Results

Scramjet engines attain the necessary properties for combustion thanks to shock waves. In figure 1, the pressure field in the inlet and inside the engines is depicted, where shock waves due to flow deflection and reflection are seen.

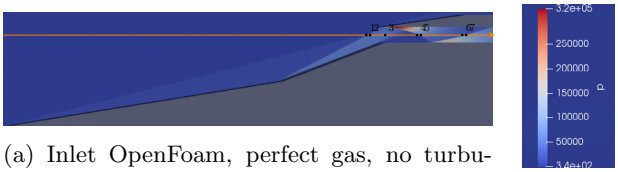

(a) Inlet OpenFoam, perfect gas, no turbulence model.

(b) OpenFoam Perfect gas No turbulence model.

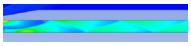

(c) Ansys Fluent KW-SST Real gas.

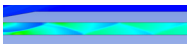

(d) Ansys Fluent KW-Standard Real gas.

Figure 1: Pressure field.

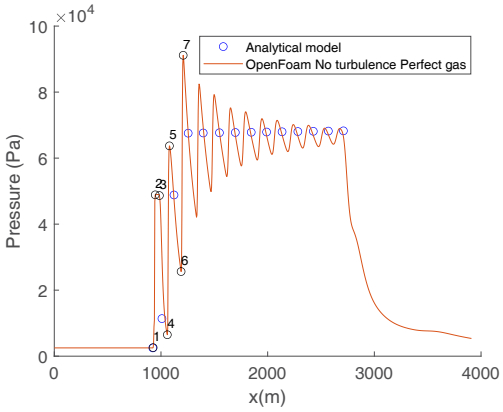

Figure 2: Pressure distribution along the engine central axis.

In figure 2, an oscillating rise in pressure along the scramjet engine is introduced. The peaks obtained represent each shock wave. As observed in figures 1 and 2, the pressure oscillations occur in different engine zones. Additionally, it is proved that the analytical model proposed rigorously predicted the changes in pressure.

The effect of considering different turbulence models is presented in figure 3, Results obtained when consider real flow and a turbulence model, clearly differ from the ideal gas and no turbulence model ones.

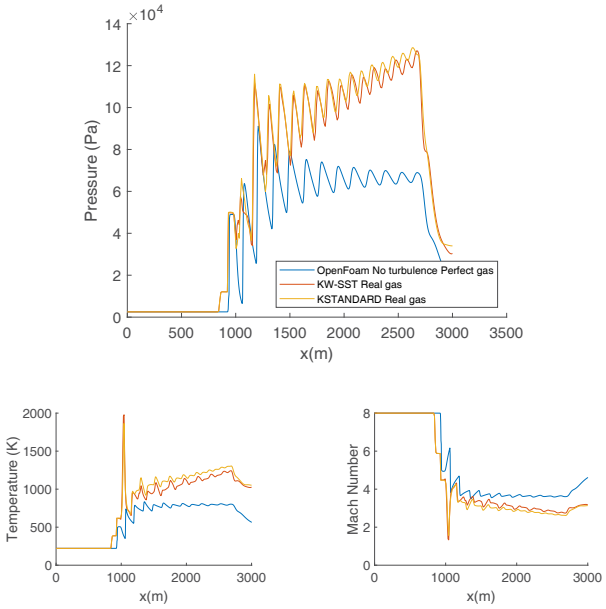

Figure 3: Comparison between different CFD models.

3-D CFD simulations with and without turbulence model are also performed, flow properties obtained via 2-D and 3-D CFD simulations are obtained and will as well be presented.

4 Conclusions

Scramjet engine internal flow evolution is studied via 2D and 3D-CFD. Different turbulence models, considering real and ideal gas are employed. The 2-D oblique shock wave theory is modified to minimize the error between the theoretical and CFD results.

References

Yao, Y. and Rincon, D. (2012) "Shock Induced Separating Flows in Scramjet Intakes". *International Journal of Modern Physics: Conference Series*, **19**, 73–82.

Smart, M. (2010)"Scramjet Inlets". *International Journal of Modern Physics: Conference Series*, Educational Notes RTO-EN-AVT-185, Paper 11. Neuilly-sur-Seine, France, 11-1–11-24.

Hong Quan, L. and Nguyen Phu, H. and Doan Quang, L. and Ngoc Long, V. (2016)"Analysis and Design of a Scramjet Engine Inlet Operating from Mach 5 to Mach 10". *International Journal of Mechanical Engineering and Applications*,**4**, 11–23.

2nd Spanish Fluid Mechanics Conference
Barcelona (2 - 5 July 2023)

Taylor-Maccoll equations modification implemented to double-cone configuration

David Zurita[1], Joel Gràcia[1], and Josep M Bergadà[1]

david.zurita@estudiantat.upc.edu

[1]Departamento de Mecánica de Fluidos, Universitat Politècnica de Catalunya, Spain

The axisymmetric-supersonic theory of Taylor and Maccoll (T-M) is studied and extended to verify its application in different cases. First, a study of the quality of the analytical approximation developed by [1] is performed by comparing the Mach field along the entire shock wave spectrum. Then, an extension to the T-M theory is performed to obtain the fluid properties along a cone with two different slopes, with a set of three-dimensional computational fluid dynamics (CFD) simulations of the double-cone systems employed to validate the extension of the theory proposed.

1 Introduction to T-M main equations

The T-M second-order differential equation is expressed as:

$$\frac{\gamma-1}{2}\left(1-\vartheta_r^2-\left(\frac{d\vartheta_r}{d\theta}\right)^2\right)\left(2\vartheta_r+\frac{d\vartheta_r}{d\theta}\cot(\theta)+\frac{d^2\vartheta_r}{d\theta^2}\right) - \frac{d\vartheta_r}{d\theta}\left[\vartheta_r\frac{d\vartheta_r}{d\theta}+\frac{d\vartheta_r}{d\theta}\frac{d^2\vartheta_r}{d\theta^2}\right]=0 \tag{1}$$

where ϑ_r is the dimensionless radial velocity, θ is the generic angle in cylindrical coordinates and γ is the specific heat ratio. The dimensionless velocity is expressed as:

$$\frac{V_{rad}}{\sqrt{2h_0}}=\vartheta_r \tag{2}$$

V_{rad} being the fluid local radial velocity and h_0 the stagnation enthalpy:

$$\mathrm{h_0}=\mathrm{h}+\frac{\mathrm{V}^2}{2}=\frac{\mathrm{V}_{max}^2}{2} \tag{3}$$

where h is the fluid static enthalpy.

Expression 1 uses the Rocco's theorem to define the relation between the radial and tangential velocities, that will end up defining the boundary condition (BC) for its solution:

$$\frac{d\vartheta_r}{d\theta}=\vartheta_{tg} \tag{4}$$

Where ϑ_{tg} is the tangential dimensionless velocity. This relation ensures the irrotationality of the fluid. Therefore, it is known that the first derivative of ϑ_r is null at $\theta=\delta$, being δ the semi angle of the cone. Two different BC can be used to solve the T-M differential equation over conical boundaries: either the freestream Mach number and the oblique shock wave semiangle β are set as BC, or the dimensionless radial velocity over the cone surface ϑ_r and the semiangle of the cone δ are employed to it (as in [2]). On the other hand, the analytical solution of the T-M equation was obtained by [1] in the form of the following two algebraic equations:

$$\frac{V_{rad}}{V_1}=\cos(\theta)+\left(1-\frac{1}{\bar{\rho}}\right)\sin^2(\beta)\cos(\beta)\cdot \left[1-\frac{\cos(\theta)}{\cos(\beta)}+\cos(\theta)\cdot\ln\frac{\tan(\frac{\theta}{2})}{(\tan\frac{\beta}{2})}\right] \tag{5}$$

$$\frac{V_{tg}}{V_1}=-\sin(\theta)+\left(1-\frac{1}{\bar{\rho}}\right)\sin^2(\beta)\cos(\beta)\cdot \left[\cot(\theta)+\frac{\sin(\theta)}{\cos(\beta)}-\sin\theta\cdot\ln\frac{\tan(\frac{\theta}{2})}{\tan(\frac{\beta}{2})}\right] \tag{6}$$

The shock wave semiangle β is now used as BC, V_1 is the freestream velocity, V_{rad} is the radial velocity and V_{tg} is the tangential velocity (normal to the radial component). Finally, $\bar{\rho}$ is the dimensionless density ratio across the shock wave, and it is defined as:

$$\bar{\rho}\equiv\frac{\rho_2}{\rho_1}=\frac{(\gamma+1)M_1^2\sin^2\beta}{(\gamma-1)M_1^2\sin^2\beta+2} \tag{7}$$

where M_1 is the freestream Mach number.

2 Results

The application of the T-M analytical approach introduces a direct way to predict the relation between the solid cone semi angle (δ) and the shock wave angle (β). Figure 1 is showing the results obtained when applying the analytical solution to a set of different free stream Mach numbers.

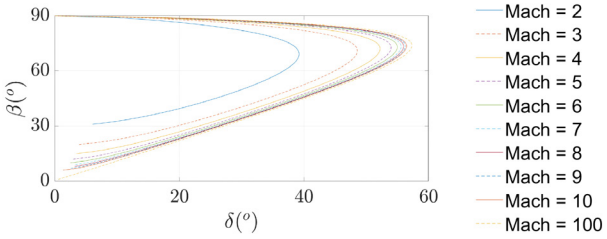

Figure 1: Relationship between solid cone semiangle (δ) and shock wave semiangle (β) extracted from the analytical approach.

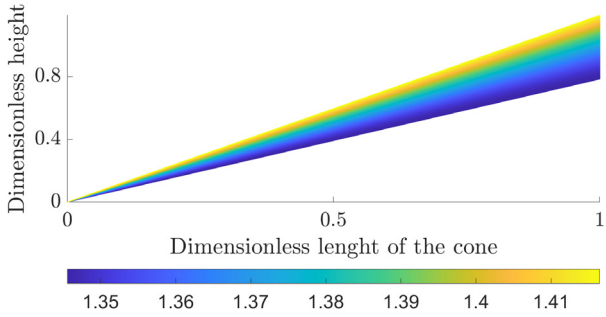

Figure 2: Mach throughout the entire 3-D shock wave using the analytical approach for $\beta = 50$ degrees and Mach 3.

Figure 2 introduces, for a given upstream Mach number of 3 and a shock wave semiangle of $\beta = 50$ degrees, the Mach number evolution between the conical surface and the shock wave, pressure and temperature fields were as well obtained. The error observed when comparing the Mach number field with the one obtained using the T-M differential equation and for the same boundary conditions, is between 4.32% and 5.06%, see figure 3. For upstream Mach numbers 4, 7 an 10, and considering the entire spectrum of possible δ angles for which the oblique shock wave β is attached, the average, maximum and minimum error between the T-M differential equation and its analytical solution are presented in figure 4. As the error is smaller than 2.5% the algebraic equations can be seen as very accurate.

In order to extend the application of the T-M differential equation to a **double-cone** configuration, it is decided to perform a set of 3D-CFD simulations to compare numerical and CFD results. Two main alternatives are considered in order to modify the T-M theory to predict the values on the second shock wave obtained by the CFD simulations.

a) From each CFD simulation β_1, β_2, δ_1 and δ_2 are known. Taking the M_{δ_1} and β_2 as initial conditions, the values of δ_2 and the Mach number spectrum between δ_2 and β_2 are obtained using the T-M equations. The process is repeated for all M_{θ_1}, $\delta_1 \leq \theta_1 \leq \beta_1$. b) The second approach is the same as the first one but the reference of β_2 and δ_2 is modified based on the M_{θ_1} associated angle ($\delta_2'(\theta_1) = \delta_2 - \theta_1$).

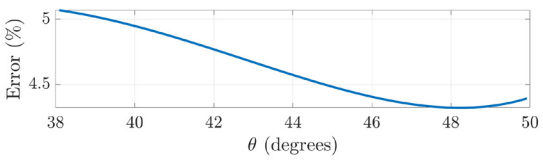

Figure 3: Error distribution in % on the entire shock wave domain. For the sake of a better understanding, θ takes its lowest value (38.09 degrees) when is equal δ. Its maximum value, 50 degrees, is achieved at β angle.

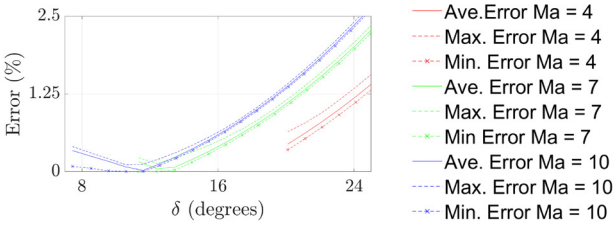

Figure 4: Average, maximum and minimum error on the flow field after the shock wave for different Mach numbers when interacting with low δ angles.

3 Conclusions

After comparing the numerical and analytical T-M equations, an extension of the T-M differential equation for a double cone configuration is introduced. A set of 3D CFD simulations are employed to validate the new approach presented.

References

[1] Takuto Ishimatsu and Etsuo Morishita. "Taylor-Maccoll Hypervelocity Analytical Solutions". In: *Transactions of The Japan Society for Aeronautical and Space Sciences - TRANS JPN SOC AERON SPACE SCI* 48 (May 2005), pp. 46–48. DOI: 10.2322/tjsass.48.46.

[2] J.W. Taylor Geoffrey Ingram Maccoll. "The air pressure on a cone moving at high speeds.-I". In: *Procedings of the Royal Society A* 139 (Feb. 1933). DOI: https://doi.org/10.1098/rspa.1933.0017.

2nd Spanish Fluid Mechanics Conference
Barcelona (2 - 5 July 2023)

GPU-Accelerated Direct Numerical Simulations with an Immersed Boundary Method

J.M. Catalán[1], M. Guerrero-Hurtado[1], M. García-Villalba[2], and O. Flores[1]

jcatalan@ing.uc3m.es

[1]Departamento de Ingeniería Aeroespacial, Universidad Carlos III de Madrid, Spain
[2]Institute of Fluid Mechanics and Heat Transfer, TU Wien, Vienna, Austria

The rapid progress of technology in recent years has paved the way for Graphical Processing Units (GPUs) to become a prominent player in the world of high-performance computing. With their highly parallel architecture and fast processing capabilities, GPUs have become a very valuable tool for researchers and engineers in the field of fluid mechanics.

In the last few years, researchers have increasingly focused on developing strategies for accelerating numerical simulations using GPUs. Special attention has been paid [1] [2] to the acceleration of Lattice-Boltzmann codes, for instance, due to the simplicity of the parallelization given its explicit character.

In this work, we exploit conveniently the architecture of these devices, presenting a novel parallelization for running direct numerical simulations massively with a significant performance boost. We have implemented the Immersed Boundary Method proposed by [3], which accounts for the fluid-body interaction by means of an additional source term in the Navier-Stokes equations, $\mathbf{f}_{\mathrm{ibm}}$. In this method, a staggered grid is used to solve the fluid in the Eulerian frame, employing centered finite differences of second order. Additionally, convective terms are treated explicitly, viscous terms implicitly, and continuity is imposed solving a Poisson problem for the pseudo-pressure ϕ, used as a correction for the pressure p and the velocity $\mathbf{u}$. Also, a Helmholtz problem needs to be solved per each velocity component.

The code has been developed in Python using Numba CUDA [4] due to its simplicity and convenience. Previous works have shown that the GPU performance of the Numba CUDA kernels is comparable to C-CUDA [5]. The structure of the code is shown in Fig. 1, where different kinds of kernel are presented:

- **Eulerian kernel**. Each GPU thread is in charge of computing the explicit quantities of one point of the Eulerian grid. The estimated velocity $\mathbf{u}_e$, the divergence of the intermediate velocity $\mathbf{u}^*$, and the pressure and velocity corrections, are computed in this type of kernel.

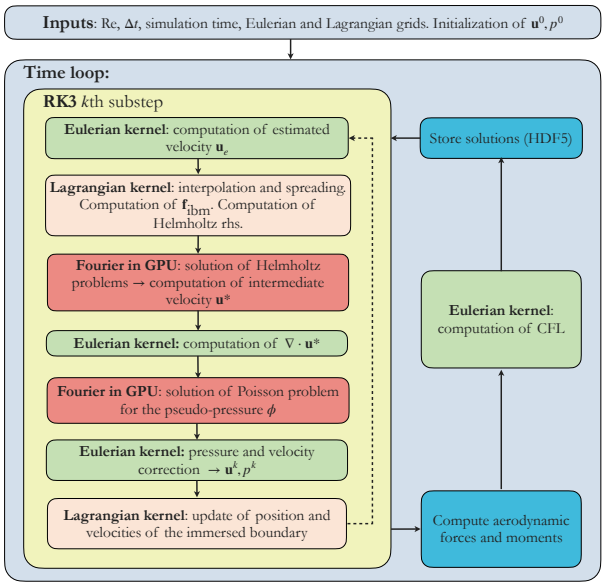

Figure 1: Block diagram showing the structure of the GPU code.

- **Lagrangian kernel**. Each GPU thread is in charge of computing the quantities of one point of the Lagrangian grid. Here, the interpolation and spreading from Eulerian to Lagrangian and vice-versa is carried out. The right-hand-sides of the Helmholtz problems are computed as well, accounting for the immersed boundary contribution.

- **Fourier**. Here, the library CuPy [6] is employed. Specifically, `cupy.fft.fftn` and `cupy.fft.ifftn` are exploited to compute the Fast Fourier Transform and its inverse, used for solving the Helmholtz and Poisson problems.

Furthermore, global memory access has been minimized to improve the simulation performance,

relying on the cache memory of the GPU block to perform as many operations as possible, which is much faster.

In order to validate the results and test the performance of the GPU code, we have run two benchmark cases consisting of a solid sphere immersed in a fully periodic flow at $\mathrm{Re}_D = 200$, with initial condition $\mathbf{u}^0 = (U_\infty, 0, 0)$: fixed in space (Fig. 2.a), and moving with sinusoidal motion along Y (Fig. 2.c).

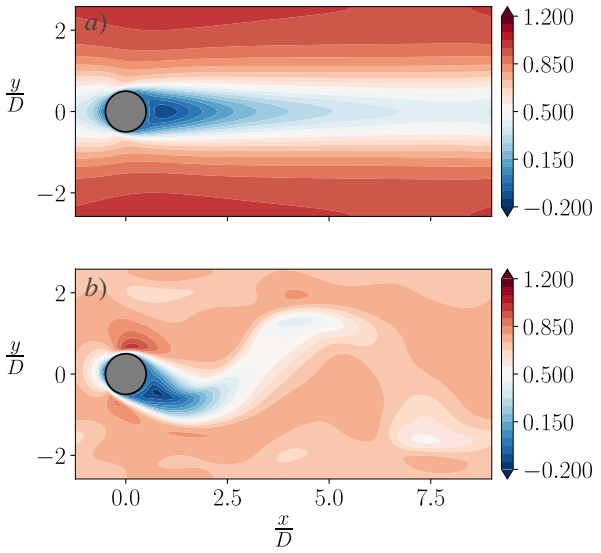

Figure 2: Simulations results at the middle plane for $tU_\infty/D = 140$. Streamwise velocity u_x/U_∞ for a fixed (a) and a moving (b) sphere.

For the sake of comparison, we have also run these cases in our in-house CPU code, TUCAN [7], an extenstively validated parallel solver for running massive direct numerical simulations with immersed boundaries, developed in our research group (CFD Lab) at Universidad Carlos III de Madrid. In TUCAN, the Poisson and Helmholtz problems are solved iteratively using HYPRE [8].

Case	$\varepsilon_{x,\max}$	$\varepsilon_{y,\max}$	$\varepsilon_{z,\max}$	$\varepsilon_{p,\max}$	
Fixed	4.44	1.64	1.64	1.75	$\times 10^{-8}$
Moving	5.19	4.33	2.26	2.82	$\times 10^{-8}$

Table 1: Maximum absolute errors for u_x, u_y, u_z, p.

Table 1 demonstrates the validity of the results, showing that maximum absolute errors in the flow field are of the order of 10^{-8}, after 140 physical time units. These errors are computed as the difference between the results from CPU and GPU codes.

The grid spacing used for the simulations is $\Delta x/D = 1/25$, and the dimensions of the domain are $10.24D \times 5.12D \times 5.12D$, resulting in a total number of points of $N_x \times N_y \times N_z = 4194304$. The GPU simulations have been carried out in a Titan V NVIDIA GPU card (12 GB of RAM and 5120 CUDA cores and 640 tensor cores), whereas the CPU simulations have been run in the mid-sized cluster of the Aerospace Department at UC3M (22 heterogeneous nodes, consisting of Intel Xeon X5650, E5-2630 and E5-2620v4 processors, interconnected with a dedicated InfiniBand QDR network, totaling 280 compute cores and about 1TB of total RAM). The number of processors used for the simulations is 96 (6 nodes of 16 cores) and 16 (1 node of 16 cores, no inter-node communication). In Table 2, we show two different performance metrics:

Hardware	WTPF	Speed-up
CPU 96 cores	5.0830 CPUh	21.38
CPU 16 cores	3.7650 CPUh	94.12
GPU	0.0025 GPUh	1

Table 2: Performance measurement table, showing the Wall-time per frame (WTPF) and the Speed-up factor.

Those quantities are calculated as:

$$\mathrm{WTPF} = \frac{\text{Simulation time [h]}}{\text{N. frames}} \times \text{N. procs} \qquad (1)$$

$$\text{Speed-up} = \frac{\text{Simulation time CPU}}{\text{Simulation time GPU}} \qquad (2)$$

References

[1] Rinaldi, P. R., Dari, E. A., Vénere, M. J., & Clausse, A. (2012). *Simul. Model. Pract. Theory*, **25**, 163–171.

[2] Valero-Lara, P., Pinelli, A., & Prieto-Matias, M. (2014). *Procedia Comp. Sci.*, **29**, 50–61.

[3] Uhlmann, M. (2005). *J. Comput. Phys*, 209(2), 448-476.

[4] Numba. https://numba.readthedocs.io

[5] Oden, L. (2020). *28th Eurom. Int. Conf. on PDP*, 216-223.

[6] CuPy. https://docs.cupy.dev/

[7] Moriche, M. (2017). PhD thesis. UC3M.

[8] HYPRE. High Performance Preconditioners. https://llnl.gov/casc/hypre.

2nd Spanish Fluid Mechanics Conference
Barcelona (2 - 5 July 2023)

Lagrangian Approach for Studying Stratospheric Flows during Sudden Stratospheric Warming Events

Albert Alcalde[1] and Jezabel Curbelo[2]

albert.alcalde.zafra@estudiantat.upc.edu

[1]Facultat de Matemàtiques i Estadística, Universitat Politècnica de Catalunya, Barcelona, Spain
[2]Departament de Matemàtiques, Universitat Politècnica de Catalunya, Barcelona, Spain

The aim of this work is to study both the dynamics and the structure of the major Sudden Stratospheric Warming (SSW) on the northern hemisphere that took place in January 2021 with the help of Lagrangian Descriptors (LD). SSWs are known to increase the likelihood of cold extremes over eastern U.S., northern Europe, and Asia, making them particularly relevant for numerical weather prediction. We use this context to study the capabilities of LD. In particular, we explore the effect of the dataset's resolution on the position of the Lagrangian Coherent Structures (LCS), which are geometric boundaries in fluid flows used to understand the organization and transport of fluid particles.

1 Introduction

Significant disruptions of the stratospheric polar vortex (SPV), also called sudden stratospheric warmings (SSWs) are rare yet important events. In these, there is a large and rapid temperature increase coupled with a complete reversal of the climatological westerly winds. According to ERA5 reanalysis, a major SSW on the northern hemisphere took place in January 2021, which caused the SPV to become significantly elongated and near-split.

2 Data and methods

We use the data from ERA5, a fifth generation ECMWF reanalysis for the global climate and weather Copernicus Climate Change Service (C3C) (Hersbach (2018)). From the wide range of variables in the dataset, we use the wind velocity, both the eastward (U) and northward (V) components, in ms^{-1}, and the temperature (T), in K. The spatial resolution of the data we analyse is 0.25° lon.× 0.25° lat. with 37 pressure levels ranging from 1000 hPa to 1 hPa. The highest temporal resolution of the data is 1 hour.

Prior to the study, the data are preprocessed in order to use the potential temperature (θ) instead of pressure (p) as the vertical coordinate. The potential temperature is defined as:

$$\theta \equiv T(p/p_s)^{\kappa}$$

where $\kappa = R/c_p \approx 2/7$ (R is the gas constant for dry air and c_p the specific heat at constant pressure) and the reference pressure is $p_s = 1000$ mb.

The reason for this change is that stratospheric flows on the timescale of SSW (around 10 days) are, to a first approximation, adiabatic and frictionless, and thus fluid particles and their trajectories are constrained to remain on surfaces of constant potential temperature, called isentropic surfaces. Once constricted to an isentropic surface, we can consider the flow as essentially 2-D, and therefore dismiss the vertical component of wind velocity.

Regarding the methods, the main tool used to carry out this study is the Lagrangian Descriptor M (Mancho et al. (2013)), defined by the expression:

$$M(\mathbf{x}, t_0, \tau) = \int_{t_0-\tau}^{t_0+\tau} ||\mathbf{v}(\mathbf{x}(t, \mathbf{x_0}), t)||\, dt$$

where $\mathbf{v}(\mathbf{x}, t)$ is the 2D velocity field on an isentropic surface and $||\cdot||$ denotes the Euclidean norm. The geometric interpretation is that M measures the arclength of the fluid-parcel trajectory located at $\mathbf{x_0}$ at time $t = t_0$.

The main power of the Lagrangian M is the geometric information it provides on LCS separating regions in which parcels have different dynamics. Applying this strategy to the SPV region, we are able to gain insight on the behavior of parcels that form the boundaries of the vortices and to examine in detail the behaviors of barriers to the flow which are represented by the singular features of M. More specifically, the curves on isentropic surfaces where $||\nabla M||$ has large magnitudes approximate manifolds that act as instantaneous flow barriers, separating regions dynamically different (Curbelo et al. (2021)).

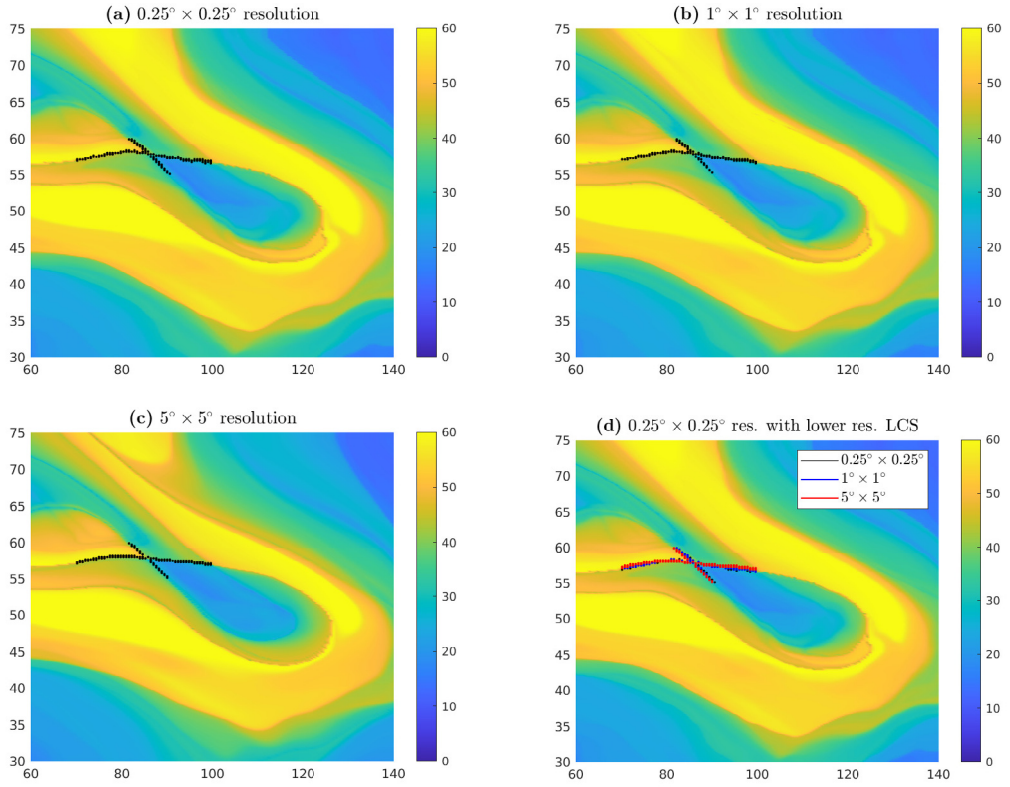

Figure 1: Maps of normalized LD M on January 5, 2021 for different spatial resolutions. The black lines in the first three subfigures outline the invariant manifolds of the HT situated approximately at 58° N and 90° E.

3 Results and conclusions

One of the objectives has been exploring the effects on the spatial resolution of the dataset. We focus on a particular day during the SSW in which the dynamics in the stratosphere are specially rich, the 5th of January 2021. We set $\theta = 530$ K and $\tau = 10$ days, the approximate timescale of the event we are trying to capture.

In Figure 1 we have isolated the invariant manifolds for the Hyperbolic Trajectory (HT) situated at 58° N and 90° E in three different spatial resolutions: $0.25° \times 0.25°$, $1° \times 1°$ and $5° \times 5°$. By simple inspection, it seems that lowering the spatial resolution of the data has little to no effect in the position of the HT for this particular case. Figure 1(d), in which both the invariant branches of the saddle are overlapped for the three resolutions considered, seems to confirm this fact.

We are trying to characterize the error produced in the position of LCS when we use different resolutions of the dataset. This is a work in progress, part of my final thesis project that I am currently doing for my Master's Degree at UPC.

Acknowledgements

We acknowledge support of the 2022 Leonardo Grant for Researchers and Cultural Creators, BBVA Foundation. The BBVA Foundation accepts no responsibility for the opinions, statements and contents included in the abstract and/or the results thereof, which are entirely the responsibility of the authors.

References

Hersbach, H. *et al.* (2018). "ERA5 hourly data on pressure levels from 1959 to present", Copernicus Climate Change Service (C3S) Climate Data Store (CDS). https://doi.org/10.24381/cds.bd0915c6

Mancho, A. M. *et al.* (2013). "Lagrangian descriptors: A method for revealing phase space structures of general time dependent dynamical systems", Commun Nonlinear Sci Numer Simul, 18, 12, 3530-3557.

Curbelo, J. *et al.* (2021). "Lagrangian analysis of the northern stratospheric polar vortex split in April 2020". Geophysical Research Letters, 48, e2021GL093874.

2nd Spanish Fluid Mechanics Conference
Barcelona (2 - 5 July 2023)

On the entropy-viscosity method for flux reconstruction

Bernat Font[1], Arnau Miró[1], and Oriol Lehmkuhl[1]

bernat.font@bsc.es

[1]Barcelona Supercomputing Center, Barcelona, Spain

1 Introduction

Recent advances in modern computer architectures for high-performance computing (HPC) are paving the path towards a wider adoption of high-order (HO) methods within the computational fluid dynamics (CFD) community (Castonguay, 2012). Compared to traditional low-order methods, HO methods promise to achieve an arbitrary level of accuracy at a reduced computational cost (Witherden, 2015), making high-fidelity scale-resolving simulations for high-speed flows a reality. Moreover, HO extensions of traditional methods are usually constructed through larger stencils – an approach tied to be memory-bounded in the new hardware architectures. In contrast, the element-local operations of HO methods helps reducing such memory overhead (Trojak, 2019) and is more aligned with the current HPC vision.

Under the high-order methods umbrella, the flux reconstruction (FR) method originally proposed by Huynh (2007) has been gaining attention due to its simple formulation and unifying framework. Similarly to other HO methods such as nodal discontinuous Galerkin (DG), the FR method considers piecewise discontinuous polynomial basis functions (usually Lagrange polynomials) defined at a set of element nodal points to spatially approximate the solution of a conservation law in a tessellated computational domain. The FR method is also linked to the spectral difference (SD) method in the sense that the differential form of the conservation law is used, differently from nodal DG which uses the integral weak form approach. It has been shown that FR can recover both nodal DG and SD schemes for linear and spatially-varying fluxes (Vincent, 2011), and non-linear fluxes (DeGrazia, 2014), hence the unifying character.

During the last decade, research on HO methods for CFD has been focused on achieving a similar level of maturity as traditional low-order methods. To do so, classical turbulence models, shock-capturing schemes, and convection schemes, among other key features, need to be revisited for the HO approach. With this purpose, we investigate the entropy-viscosity shock-capturing scheme by Guermond (2011) for the FR method. The entropy-viscosity method forces an entropy-based numerical dissipation via effective viscosity near physical discontinuities while vanishing on smooth regions. This helps stabilising the naturally arising oscillations that spectral (HO) methods trigger near discontinuities because of the Gibbs phenomenon. The main idea of this method is to capture the shocks occurring inside the element, while the discontinuities between elements are dealt by a Riemann solver. Because of the close relation of FR to nodal DG, shock-capturing schemes originally developed for DG can be translated to FR. In this context, Trojak (2021) combined a HO FR scheme with a low-order summation-by-parts scheme via convex limiting allowing to accurately capture shocks for the 1D Euler equations. The entropy-viscosity residual was used as shock sensor to lower the computational cost of the method. Asthana (2015) implemented a shock-capturing scheme based on Fourier spectral filtering which allowed to accurately capture shocks located inside an element even for high polynomial degrees.

2 Methodology and results

A 1-D flux reconstruction solver has been implemented using Julia (Bezanson, 2017): a compiled, dynamic, and composable programming language specifically designed for scientific computing. The solver features the energy-stable schemes from Vincent (2011), arbitrary polynomial degree for the Lagrange basis functions, Gauss–Legendre (GL) or Gauss–Lobatto–Legendre (GLL) collocation points, a set of different Riemann solvers for the numerical fluxes (Roe, Rusanov, HLL, HLLC), and low dissipation, low dispersion 4th order 2N Runge–Kutta temporal integration schemes (Stanescu, 1998). In contrast to other works, the implementation of the entropy-viscosity scheme is performed element-wise, *ie.* a single elemental viscosity is used taken as the maximum absolute norm of the values computed at the element solution points. This has proven to be more stable than the point-wise counterpart.

Encouraging preliminary results have been obtained for the 1D Burgers equations. This set of equations forms a shock when two or more characteristic lines intersect each other. Two initial conditions have been explored, a sine and a square wave. The solution is obtained using polynomials from third to fifth degree ($p \in \{3, 4, 5\}$) and two different quadratures (GL and GLL) with and without entropy viscosity. The numerical experiments show that the entropy

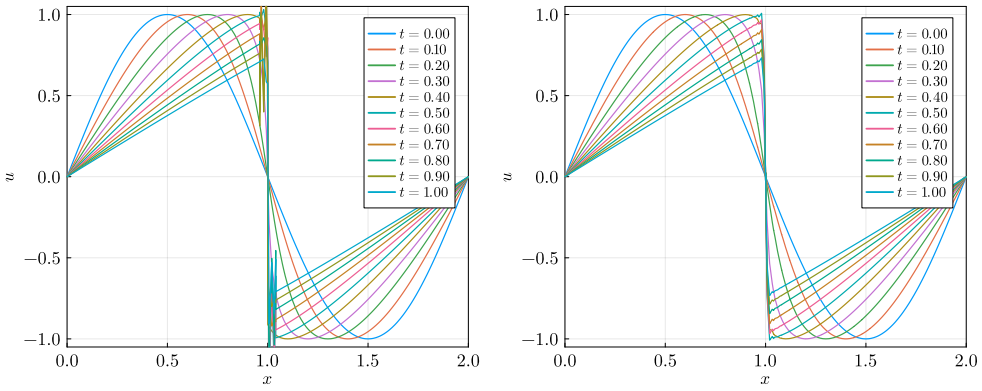

Figure 1: Comparison of the solution of the Burgers equation on a sine wave using p4 and 50 elements. Left: GLL nodes and Roe solver without entropy viscosity. Right: GLL nodes and Roe solver with entropy viscosity ($c_E = 1.0$).

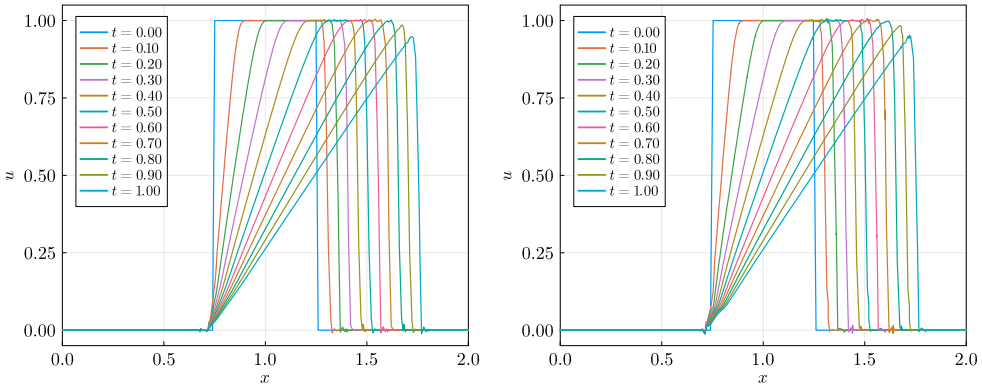

Figure 2: Comparison of the solution of the Burgers equation on a square wave using p4 and 50 elements. In both experiments the entropy viscosity is activated ($c_E = 1.0$) and a Roe solver is used at the interface. Left: GL quadrature nodes. Right: GLL quadrature nodes.

viscosity is needed to stabilize the shock when using GLL quadrature nodes and a Roe solver, as shown in fig. 1. For both quadratures points (GL results not shown here), oscillations are reduced on the shock interface without completely eliminating them, and the shock is better captured with increasing polynomial degree. For the square wave, even with a Roe solver on the element interface, the method is not able to capture the shock and the solution is very degraded or non-existent. The addition of the entropy viscosity allows to correctly capture the shock, as shown in fig. 2, although some dissipation is present since the shape of the wave is not completely recovered. With this encouraging results, the next step is to test this method in the well-known Sod shock problem for the 1D Euler equations. Moreover, split formulations of the governing equations will be explored as a de-aliasing mechanism (Abe, 2018). This will allow to further assess the validity of the entropy-viscosity shock-capturing scheme for the FR method.

References

Castonguay P. (2012) "High-order energy-stable flux reconstruction schemes for fluid flow simulations on unstructured grids". PhD Thesis.

Witherden F.D. (2015) "On the development and implementation of high-order flux reconstruction schemes for computational fluid dynamics". PhD Thesis.

Trojak W. (2019) "Numerical analysis of flux reconstruction". PhD Thesis.

Huynh H.T. (2007) "A flux reconstruction approach to high-order schemes including discontinuous Galerkin methods". 18th AIAA CFD Conference.

Vincent P.E., Castonguay P. & Jameson A. (2011) "A new class of high-order energy stable flux reconstruction". J. Sci. Comput. 47:5072.

De Grazia D., Mengaldo G., Moxey D., Vincent P.E. & Sherwin S. (2014) "Connections between the discontinuous Galerkin method and high-order flux reconstruction schemes". Int. J. Numer. Meth. Fluids, 75, pp. 840—859.

Guermond J.-L., Pasquetti R. & Popov B. (2011) "Entropy viscosity method for nonlinear conservation laws". J. Comp. Phys. 230:11, pp. 4248—4267

Trojak W., Dzanic T. & Witherden F. (2021) "Shock capturing methods in high-order flux reconstruction I: graph viscosity and convex limiting approaches". AIAA Scitech 2021 Forum.

Jeff B., Edelman A., Karpinski S. & Shah V.B. (2017) "Julia: A fresh approach to numerical computing". SIAM review, 59:1, pp. 65–98.

Stanescu D. & Habashi W.G. (1998) "2N-Storage Low Dissipation and Dispersion Runge-Kutta Schemes for Computational Acoustics". J. Comput. Phys., 143, pp. 674–681.

Abe Y., Morinaka I., Haga T., Nonomura T., Shibata H. & Miyaji K. (2018) "Stable, non-dissipative, and conservative flux-reconstruction schemes in split forms". J. Comput. Phys., 353, pp. 193–227.

Asthana K., López-Morales M. R., & Jameson A. (2015). "Non-linear stabilization of high-order flux reconstruction schemes via Fourier-spectral filtering". J. of Comput. Phys., 303, pp. 269–294.

2nd Spanish Fluid Mechanics Conference
Barcelona (2 - 5 July 2023)

Tree-based adaptive mesh refinement strategy for high-order immersed boundary methods

Hatem Kessasra[1], Marta Cordero-Gracia[1,2], Mariola Gómez López[1,2], and Eusebio Valero[1,2]

hatem.kessasra@alumnos.upm.es

[1]ETSIAE-UPM - School of Aeronautics, Universidad Politécnica de Madrid, Plaza Cardenal Cisneros 3, E-28040 Madrid, Spain

[2]Center for Computational Simulation, Universidad Politécnica de Madrid, Campus de Montegancedo, Boadilla del Monte, 28660 Madrid, Spain

We present a Fortran library for tree-based adaptive mesh refinement, coarsening and 2:1 balancing on computational domains composed of multiple connected two-dimensional quadtrees and three-dimensional octrees. The library is utilised for an AMR strategy for the immersed boundary method based on a high-order spectral discretisation, by generating adaptive balanced meshes with embedded obstacles. The treatment of the non-conforming interfaces (hanging nodes) is done using a mortar element method.

1 Introduction

In CFD and many time dependent simulations, the solution on most of the domain will be fairly smooth, with discontinuities or highly oscillatory phenomena occurring over only a small fraction of the domain. In problems such as these, a mesh refinement approach can be the most efficient, and often the only practical, solution method. Refined grids with smaller and smaller mesh spacing are placed only where they are needed. Over the past decades, many adaptive techniques have been developed and applied to a variety of fluid flow problems Marsha J et al. (1984), Sujata Prakash (1999), Carsten Burstedde et al. (2011), Johannes Holke (2018) AMR techniques present a powerful framework for achieving accurate and economical solutions.

2 AMR strategy for the immersed boundary methods

The Immersed Boundary Methods allow the mesh not to conform to obstacles, whose influence is taken into account by modifying the governing equations locally (either by a source term within the equation or by imposing the flow variables or fluxes locally, similarly to a boundary condition).
A cartesian grid method using IB technique to simulate the impact of body in fluid has become an important research topic in computational fluid dynamics because of its simplification, automation of grid generation, and accuracy of results, Kazuhiro Nakahashi (2011), Stéphanie Péron et al. (2021). Cartesian grid in conjunction with tree data structure is a natural choice for solution with adaptive grid.

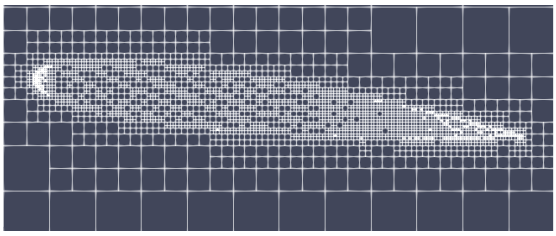

Figure 1: 2D ParaView visualisation of VTK octree, 3D Naca0012 embedded in a balanced refinement tree

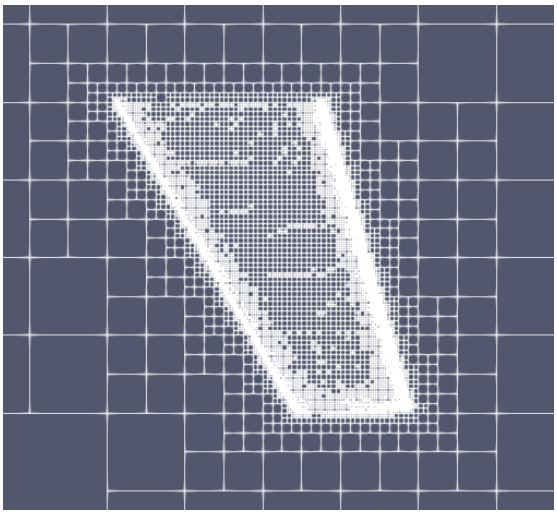

Figure 2: 2D ParaView visualisation of VTK octree, 3D Onera M6 embedded in a balanced refinement tree.

3 Treatement of non-conforming interfaces

The only difference between the conforming and the non-conforming approximations comes from how the fluxes are to be computed along the interfaces between elements. In the non-conforming cases, the edge flux points do not necessarily match along the interface, so that point by point transfer of information cannot be made from an element to its neighbour. We have chosen to implement the transfer of information between elements by a mortar method Cathy Mavriplis (1989), David A Kopriva et al. (2002). The basic idea is that the mortar (the 'cement') connects neighbouring elements (the 'bricks'). In this approach, the n-dimensional elements communicate only with an intermediate (n-1)-dimensional construct, called a mortar, not with neighbouring elements.

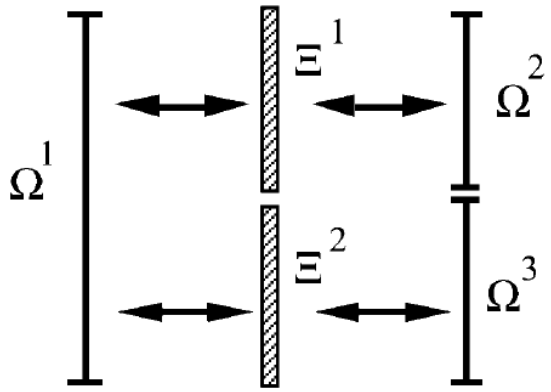

Figure 3: Mortar configuration for non conforming interfaces in 2D David A Kopriva et al. (2002).

References

Stéphanie Péron et al. (2021) "An immersed boundary method on cartesian adaptive grids for the simulation of compressible flows around arbitrary geometries". *Engineering with Computers,*, **37(3)**:2419–2437, 2021.

David A Kopriva et al. (2002) "Computation of electromagnetic scattering with a non-conforming discontinuous spectral element method". *International journal for numerical methods in engineering*, **53(1)**: 105–122, 2002

Sujata Prakash (1999) "Adaptive mesh refinement for finite element flow modeling in complex geometries.". *Unpublished PhD Thesis. University of Toronto.*

Kazuhiro Nakahashi (2011) "Immersed boundary method for compressible euler equations in the building-cube method". *In 20th aiaa computational fluid dynamics conference*page 3386, 2011.

Marsha J Berger and Joseph Oliger. (1984) "Adaptive mesh refinement for hyperbolic partial differential equations". *ournal of computational Physics,*, **53(3)**:484–512, 1984.

Cathy Mavriplis (1989) "Nonconforming discretizations and a posteriori error estimators for adaptive spectral element techniques". *PhD thesis, Massachusetts Institute of Technology.*

Carsten Burstedde et al. (2011) "p4est: Scalable algorithms for parallel adaptive mesh refinement on forests of octrees". *SIAM Journal on Scientific Computing*, **33(3)**:1103–1133, 2011.

Johannes Holke (2018) "Scalable algorithms for parallel tree-based adaptive mesh refinement with general element types". *arXiv preprint arXiv*:1803.04970,2018.

2nd Spanish Fluid Mechanics Conference
Barcelona (2 - 5 July 2023)

Bounding dissipation in Rayleigh-Benard convection

Thierry Alboussiere[1]

thierry.alboussiere@ens-lyon.fr

[1]Laboratoire de Géologie, CNRS, Univ Lyon 1, ENS de Lyon

Rayleigh-Benard convection is a configuration that has been the subject of many studies. When we have in mind the geophysical context, we are often interested in compressible effects: density in the atmosphere depends a lot on pressure (or altitude), but this is the case also in the Earth's mantle or in the Earth's core. In that case, we must consider the general equations of fluid mechanics and thermodynamics, not just the Boussinesq approximation. We also use intermediate models, anelastic equations. The amount of energy dissipation and its distribution within the fluid is an interesting quantity. If dissipation is due to Joule effects in the core, it provides a constraint on the self-generated dynamo. In the mantle, dissipation may be associated with damage and grain refinement. With the Boussinesq approximation, the total amount of dissipation is directly proportional to the convective heat flux through the layer of fluid. In compressible convection however, there is no such strong link. We have an upper bound for dissipation from the entropy balance (Backus, 1975). I will give conditions when this bound can be improved depending on the relationship between Nusselt and Rayleigh numbers.

2nd Spanish Fluid Mechanics Conference
Barcelona (2 - 5 July 2023)

Parametrically forced stably stratified flow

Juan M. Lopez[1], Bruno D. Welfert[1], and Jason Yalim[1]

jmlopez@asu.edu

[1]School of Mathematical and Statistical Sciences, Arizona State University, Tempe, Arizona, USA

The dynamics of a stably and thermally stratified fluid-filled cavity harmonically forced in the vertical direction, resulting in a periodic gravity modulation, is studied numerically. Prior simulations in a two-dimensional cavity showed a myriad of complex dynamic behaviours near the onset of instabilities, and here we address the extent to which these persist in three dimensions. Focusing on a parameter regime where the primary subharmonic mode is resonantly driven, we demonstrate comprehensive qualitative agreement between the dynamics in two and three dimensions; the quantitative difference is due to the larger forcing amplitudes needed in three dimensions to overcome the additional viscous damping from the spanwise walls. Using a small detuning of the forcing frequency, together with a relatively large forcing amplitude, leads to a wave-breaking regime where the qualitative agreement between two and three dimensions breaks down.

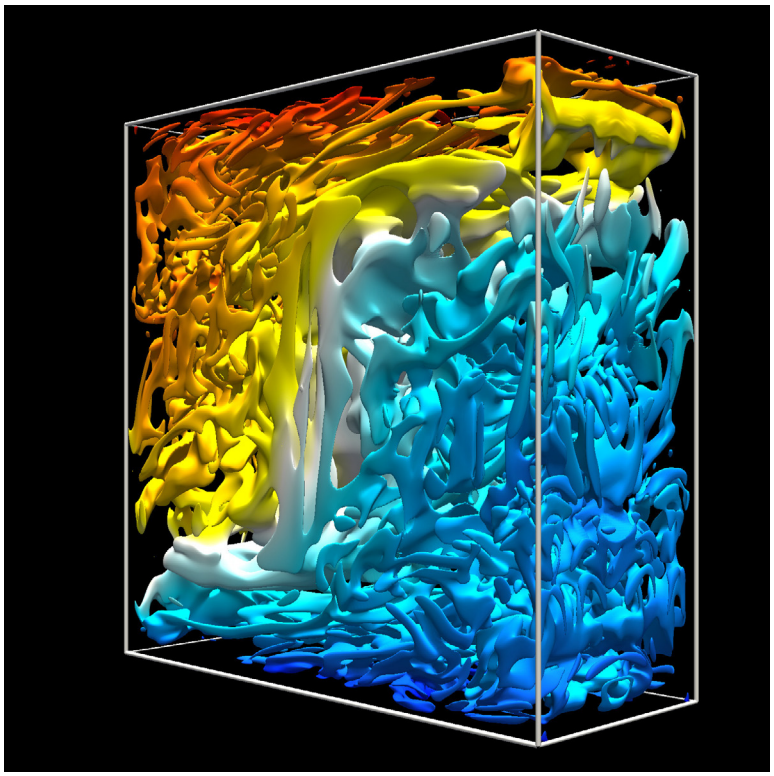

Figure 1: Snapshot of the normalize Q criterion at isolevel $Q_N = 0.04$ coloured by the temperature.

References

Yalim, J., Lopez, J.M. & Welfert, B.D. (2020) "Parametrically forced stably stratified flow in a three-dimensional rectangular container," *J. Fluid Mech.* **900**, R3.

Yalim, J., Welfert, B.D. & Lopez, J.M. (2019) "Parametrically forced stably stratified cavity flow: complicated nonlinear dynamics near the onset of instability," *J. Fluid Mech.* **871**, 1067-1096.

Yalim, J., Welfert, B.D. & Lopez, J.M. (2019) "Modal reduction of a parametrically forced confined viscous flow," *Phys. Rev. Fluids* **4**, 103903.

Yalim, J., Lopez, J.M. & Welfert, B.D. (2018) "Vertically forced stably stratified cavity flow: instabilities of the basic state," *J. Fluid Mech.* **851**, R6.

2nd Spanish Fluid Mechanics Conference
Barcelona (2 - 5 July 2023)

Temperature optimization in a gas reactor for the synthesis of carbon nanofibers: a numerical approach

María Cruz Navarro[1], José Luis Valverde[2], and Elena Castellanos[2]

mariacruz.navarro@uclm.es

[1]Departamento de Matemáticas, Universidad de Castilla- La Mancha, Spain
[2]Departamento de Ingeniería Química, Universidad de Castilla- La Mancha, Spain

In this work we address the modeling and numerical simulation of flow and temperature for a mixture of gases in a reactor to optimize the temperature inside it. The study is focused on determining appropriate temperatures at the reactor shell, to assure optimal temperatures at the catalyst support device where the reaction of formation of CNF takes place. Different locations of the support device are considered.

1 Introduction

Carbon nanotubes (CNT) and Carbon nanofibers (CNF) have become materials with a great variety of applications: Information and Communication Technologies (ICT)Ahlawat et al. (2020), construction industry Tao et al. (2019), medicine Zihui et al. (2020), among others.

The temperature at which the CNF synthesis process is carried out determines the final structure of the carbon nanofiber. At $600°C$ $(873.15K)$ the formation of the fishbone structure is favored, which is the most interesting industrially and the one with the best process performance De Lucas et al. (2006).

The combination of experiments and computer simulation in the synthesis process of carbon fibers, permit not only to verify the experimental conjecture but also to optimize the parameters determining the experiment in order to achieve production optimization. In this work, modeling and numerical simulation of the problem is addressed using COMSOL Multiphysics COMSOL (2021) focusing on the optimization of the temperature at the reactor shell and the location of the device inside the reactor, to guarantee the optimal temperature of formation of CNF.

2 Model and results

A two-dimensional model has been considered that describes the interior of the reactor taking a cross section. In figure 1 can be seen the 2D reactor for the support device located on the right. The dimensions that have been considered correspond to a pilot scale reactor of $1m$ long and $0.09m$ in diameter with N_2 inlet pipe and outlet pipe $0.15m$ long and $0.00635m$ in diameter. In the input pipe other two pipes of length $0.045m$ have been added for the entrance of H_2 and C_2H_4, respectively. The thickness of the quartz considered in the walls of the reactor is $0.00317m$. The length and height of the support device are $0.12m$ and $0.02m$, respectively. The problem involves the study of fluid flow and transfer of heat, heat transfer in solids, and mass transport of each of the species that form the mixture: ethylene (C_2H_4), hydrogen (H_2) and nitrogen (N_2).

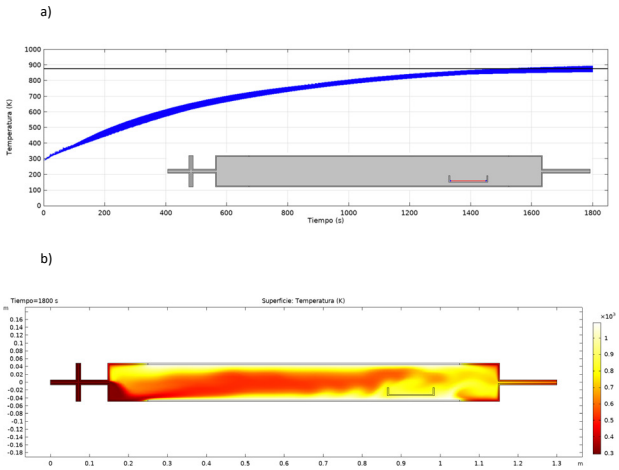

Figure 1: a) Temporal evolution of the predicted temperature of the mixture at the support device (marked in red) located at the right side of the reactor for $T_c = 1093.15K$. The black horizontal line marks the optimal temperature of CNF formation $(873.15K)$; b) Predicted temperature in the interior of the reactor for $T_c = 1093.15K$ and $t = 1800s$.

The objective is to study the appropriate temperature of the reactor shell in order to assure optimal temperatures at the support device. Differ-

ent locations of the support device are considered. We show here the case of the device located at the right side of the reactor. The optimal temperature of CNF formation ($873.15K$) is found for a temperature $T_c = 1093.15K$ at the reactor shell (figure 1). If the support device is located at the central part of the reactor, T_c needed at the reactor shell is $T_c = 1193.15K$, the maximum temperature that quartz can withstand. If the support device is located at left side of the reactor, for $T_c = 1193.15K$, maximum temperatures recorded at the base of the device are in the range $475K - 600K$, far from the required $873.15K$. This is due to the fact that the support device is localized too close to the entrance, where the gas gets inside the reactor at a temperature of $293.15K$. This suggests that the location of the device on the left is not a suitable choice since, even considering the maximum possible temperature in the reactor shell, the temperature at the base of the device does not exceed $600K$.

3 Conclusions

According to the results, for energy efficiency, it would be convenient to locate the catalyst support device displaced toward the right. Numerical results presented in this work are interesting as they provide, in silico, a full spatio-temporal description of temperature and flow velocity of the gas mixture inside the reactor depending on the thermal conditions of the reactor shell, permitting to vary these conditions to optimize the temperature inside the reactor for the synthesis of CNF.

References

Alhawat A et al. (2020) "Investigation of magneto-electric effects in (PMN-PT) @ NiFe2O4 core shell nanostructures and nanocomposites for non volatile memory applications", *Materials Letters*, **261**, 127082.

Tao S et al. (2019) "Research progress on CNTs/CNFs-modified cement-based composites ? A review", *Construction and Building Materials*, **202**, 290–307.

Zihui L et al. (2020) "The high luminescent polydopamine nanosphere-based ECL biosensor with steric effect for MUC1 detection", *Chemical Engineering Journal*, **385**, 123825.

De Lucas A et al. (2006) "Catalytic synthesis of carbon nanofibers with different graphene plane alignments using Ni deposited on iron pillared clays", *Applied Catalysis A: General*, **301**, 123–132.

COMSOL Multiphysics v. 6.0 (2021). https://www.comsol.com

2nd Spanish Fluid Mechanics Conference
Barcelona (2 - 5 July 2023)

Absence of diffusion in pilot-wave hydrodynamics

Abel J. Abraham[1], Stepan Malkov[1], Frane Sazunic[1], Matthew Durey[2], and Pedro J. Sáenz[1]

saenz@unc.edu

[1]Department of Mathematics, University of North Carolina, Chapel Hill, NC, USA
[2]School of Mathematics and Statistics, University of Glasgow, University Place, Glasgow, UK

Macroscopic particles in heterogeneous media ultimately exhibit diffusive motion when their energy is higher than the average potential barrier of the random background. In contrast, subatomic particles in a disordered medium become localized even when the disorder is weak due to their wave-particle duality, a quantum phenomenon known as Anderson localization that hinders the conductance of electrons. In this talk, we will introduce a macroscopic hydrodynamic pilot-wave system in which particles become localized like waves over random submerged topographies. The localized statistics are compared to the predictions from Schrödinger's equation, and rationalized in terms of a wave-mediated scattering mechanism.

1 Introduction

The constituents of this hydrodynamic pilot-wave system are millimetric liquid droplets that walk across the surface of a vibrating fluid bath, self-propelled through a resonant interaction with their own wave fields (1). By virtue of the coupling with their wave fields, these walking droplets, or 'walkers', extend the range of classical mechanics to include certain features previously thought to be exclusive to the subatomic, quantum realm (2). Through experiments and mathematical modeling, we investigate the motion of walkers over submerged random topographies (Figure 1,A). For sufficiently shallow liquid layers, the walker trajectory becomes chaotic due to scattering from random features at the bottom of the bath. Nevertheless, consideration of an ensemble of drop trajectories reveals that our hydrodynamic pilot-wave system displays localized statistics in the particle position histogram, an effect strongly reminiscent to the so-called Anderson localization. Particular attention is given to characterizing the influence of the submerged topography on the emergent particle dynamics and long-time probability distributions. The localized statistics are compared to the predictions from Schrödinger's equation, and rationalized in terms of a wave-mediated scattering mechanism.

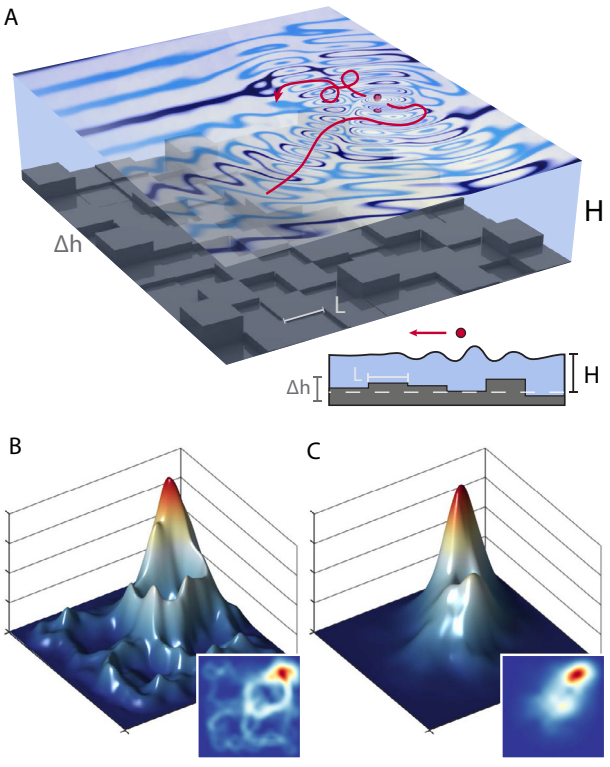

Figure 1: (A) A walking droplet moving chaotically along the free surface of a vertically vibrated fluid bath due to the influence of a random bottom topography. (B) Histogram of the droplet location. (C) First eigenmode of Schrödinger's equation for the same potential background.

2 Experiments

The drop and bath are both composed of 20 cSt silicon oil with density $\rho = 950$ kg m^{-3}, viscosity $\nu = 20.9$ cSt and surface tension $\sigma = 20.6$ mN m^{-1}. The drop, with radius $R \approx 0.4$ mm, is created using a piezoelectric drop generator. The bath is vibrated vertically with a Data Physics V55 electromagnetic

shaker and a PA300E amplifier. A spatially uniform vibration with an acceleration amplitude γ that is constant to within $\pm 0.002g$, where g is the gravitational acceleration, is achieved by using out vibrating setup. Decaying quasi-monochromatic subharmonic Faraday waves, with wavelength $\lambda_F = 2\pi/k_F$ prescribed by the standard capillary-gravity dispersion relation $\omega_F^2 = (gk_F + \sigma k_F^3/\rho)\tanh k_F h$, are excited by the impacting drop, where $\omega_F = \pi f$ and k_F are the Faraday frequency and wavenumber, respectively.

A 3D printed topography with random heights is placed below the liquid free surface. The average depth is $h \approx 1.8$ mm to ensure that the walker respond to variations in bottom topography. The resulting walker motion is characterized by the synchronous (2,1) walking mode everywhere. A total of six hours of experimental data was recorded, acquired in 30-min intervals to minimize temperature-induced drifts in γ_F, which were limited to $\pm 0.01g$. The bath is sealed with a transparent acrylic lid to shield the system from air currents. The walker motion is recorded from above with a CCD camera at 20 frames per second and tracked with an in-house particle-tracking algorithm.

3 Theory

We consider the linearized quasi-potential, weakly-viscous flow model developed by Faria (3) to account for variable bottom topography, which reduces the problem to the free surface $\eta(\boldsymbol{x}, t)$ by treating changes in topography through their influence on the local wave speed. Specifically, the wave problem becomes

$$\phi_t = -G(t)\eta + \frac{\sigma}{\rho}\nabla^2\eta + 2\nu_e\nabla^2\phi - \frac{1}{\rho}P_D(\boldsymbol{x} - \boldsymbol{x}_p)$$
$$\eta_t = -\nabla\cdot[b(\boldsymbol{x})\nabla\phi] + 2\nu_e\nabla^2\eta$$

where $\phi(\boldsymbol{x}, t)$ denotes the velocity potential $\boldsymbol{u} = \nabla\phi$ in the bath, $G(t) = g + \gamma\cos(2\pi ft - \varphi)$ the effective gravity in the bath's frame of reference, φ the drop's impact phase, ν_e the effective kinematic viscosity (chosen to match the experimental stability threshold γ_F), and $\boldsymbol{x}_p(t)$ the drop's horizontal position. The wave-drop coupling is modeled by treating the drop as an instantaneous excess point-pressure P_D in the dynamic surface condition. Changes in bottom topography are modeled by approximating the vertical gradient of the velocity potential as $\phi_z \approx -\nabla\cdot[b(\boldsymbol{x})\nabla\phi]$, where $b(\boldsymbol{x})$ is an effective depth chosen to ensure the correct the dispersion relation of Faraday waves in both the shallow and deep regions, according to

$$b(\boldsymbol{x}) = \tanh\left[k_F(\boldsymbol{x})H(\boldsymbol{x})\right]/k_F(\boldsymbol{x}),$$

where $H(\boldsymbol{x})$ denotes the submerged bottom topography, and $k_F(\boldsymbol{x})$ is the most unstable wavenumber for the given local depth.

The local gradient of the resulting wave field $\nabla\eta|_{\boldsymbol{x}=\boldsymbol{x}_p}$ determines the lateral force exerted on the drop at impact. The drop's trajectory is thus described through

$$m\frac{\mathrm{d}^2\boldsymbol{x}_p}{\mathrm{d}t^2} + D(t)\frac{\mathrm{d}\boldsymbol{x}_p}{\mathrm{d}t} = -F(t)\nabla\eta|_{\boldsymbol{x}=\boldsymbol{x}_p},$$

where $D(t) = c_4\sqrt{\frac{\rho R}{\sigma}}F(t) + 6\pi R\mu_{\text{air}}$ models the dissipation during impact and flight. The drop bounces in synchrony with the Faraday waves, the impacts thus take place at $t = nT_F$, where $T_F = 2/f$ is the Faraday period. Assuming instantaneous impacts, the force becomes $F(t) = mg\sum_{n=0}^{\infty}\delta(t/T_F - n)$, where δ is the delta function. Finally, the penetration depth of the drop is assumed to be infinitesimally small relative to the Faraday wavelength. The drop pressure thus becomes $P_D(\boldsymbol{x} - \boldsymbol{x}_p, t) = (F(t)/\lambda_F^2)\delta((\boldsymbol{x} - \boldsymbol{x}_p)/\lambda_F)$, which vanishes when the drop is not in contact with the bath (3).

4 Conclusions

Our experiments and simulations demonstrate that a macroscopic walking droplet over a weak random topography may localize instead of exhibiting diffusive motion. Our study thus reveals the first classical wave-particle analog of Anderson localization of quantum particles (Figure 1,B-C).

References

[1] Couder Y, Protière S, Fort E & Boudaoud A (2005) "Dynamical phenomena: walking and orbiting droplets", *Nature*, **437**, 208.

[2] Bush J & Oza A (2020) "Hydrodynamic quantum analogs", *Reports on Progress in Physics*, **84**, 017001: 1-41.

[3] Faria L (2017) "A model for faraday pilot waves over variable topography", *Journal of Fluid Mechanics*, **811**:51–66.

2nd Spanish Fluid Mechanics Conference
Barcelona (2 - 5 July 2023)

Analysis of evaporating droplet dynamics using computational singular perturbation

Lorenzo Angelilli[1,2], Pietro Paolo Ciottoli[2], Francisco E. Hernandez-Perez[1], Mauro Valorani[2], and Hong G. Im[1]

lorenzo.angelilli@kaust.edu.sa

[1]CCRC, King Abdullah University of Science and Technology, Thuwal 23955-6900, Saudi Arabia
[2]Sapienza University, Via Eudossiana, 18, Rome, 00184, Italy

Similarly to the existing computational singular perturbation (CSP) framework for reacting flows, the modal analysis of the an evaporating droplet provides an indication of the active modes, the relative time scales with the definition of a tangential stretching rate (TSR), and participation indices of a single process to the state variables evolution. In this work, the CSP-spray approach is introduced and applied to a set of hexane droplets to analyze the characteristics of the modes and the role of the participation indices.

1 Introduction

Computational singular perturbation (CSP) is a mathematical framework to analyze the different time scales involved in the evolution of complex systems. In computational fluid dynamics (CFD), CSP has been extensively employed to examine fast and slow dynamics of reactive systems (1). In addition, the related Tangential Stretching Rate (TSR) concept (2) allowed to characterize the explosive/contractile nature of a chemical system through a single index providing a global time scale. This mathematical tool has the advantage that can be applied whenever the evolution depends only on its state variables. Subsequently, evaporating droplets can be easily discussed in a CSP-TSR fashion. The goal of this work is to rigorously derive the evolution equation in function only of the state variables and clarify the contributions of all the processes. Additionally, the definition of the TSR is provided together with the participation indices to assess the effects of a single process in the evolution of a state variable. This framework is applied to a set of hexane evaporating droplets at different environmental temperature to assess the effects of this parameter.

2 Numerical method

In this section the spray CSP approach is derived. First, we consider the state vector $\mathbf{S} = (d \quad T)$ where d and T are the droplet diameter and temperature, respectively. Subsequently, the two-dimensional state space is described by a system of ordinary differential equations

$$\frac{D\mathbf{S}}{Dt} = \mathbf{F}(\mathbf{S}) \tag{1}$$

where the right-hand-side (RHS) is expressed explicitly in the following:

$$\begin{cases} \frac{D\,r_d}{Dt} = \dot{d}_{evap} + \dot{d}_{\dot{T}_{evap}} + \dot{d}_{\dot{T}_{ht}} \\ \frac{DT}{Dt} = \dot{T}_{evap} + \dot{T}_{ht} \end{cases} \tag{2}$$

The terms on the RHS enclose the single processes: $\dot{d}_{evap}$ is the diffusion mass transfer, $\dot{d}_{\dot{T}_{evap}}$ is the thermal dilation due to the phase change enthalpy transfer, $\dot{d}_{\dot{T}_{ht}}$ is thermal dilation due to the convective heat transfer, $\dot{T}_{evap}$ is the heat transfer due to the phase change, and $\dot{T}_{ht}$ is the convective heat transfer. In this fashion, we can define the vector of processes as

$$\mathbf{p} = (\dot{d}_{evap}\, \dot{d}_{\dot{T}_{evap}}\, \dot{d}_{\dot{T}_{ht}}\, \dot{T}_{evap}\, \dot{T}_{ht}). \tag{3}$$

Once the RHS of Eq. 1 has been derived, we can compute the Jacobian and perform the eigenvalue decomposition $\mathbf{J_S} := \frac{\partial \dot{\mathbf{S}}}{\partial \mathbf{S}} = \mathbf{A\Lambda B}$, where $\mathbf{A}$ and $\mathbf{B}$ are the matrices of right and left eigenvectors, and $\mathbf{\Lambda}$ is the diagonal matrix of eigenvalues. In this way, the linearized droplet dynamics is described by the expression $\dot{\mathbf{S}} = \sum_{i=1}^{2} \mathbf{a}_i f_i(t)$ where $f_i := \mathbf{b_i} \cdot \mathbf{S}$ are the amplitudes of the eigenmodes and $\tau_i = 1/|\lambda_i|$ are the time scales of the system. The two time scales identified with the CSP decomposition can be summarized by the Tangential Stretching Rate (TSR) concept, which expresses this index as a weighted average of the eigenvalues

$$TSR = \frac{1}{||\dot{\mathbf{S}}||^2} \dot{\mathbf{S}} \cdot \mathbf{J_S} \cdot \dot{\mathbf{S}} = \sum_{j=1}^{N} W^j \lambda^j, \tag{4}$$

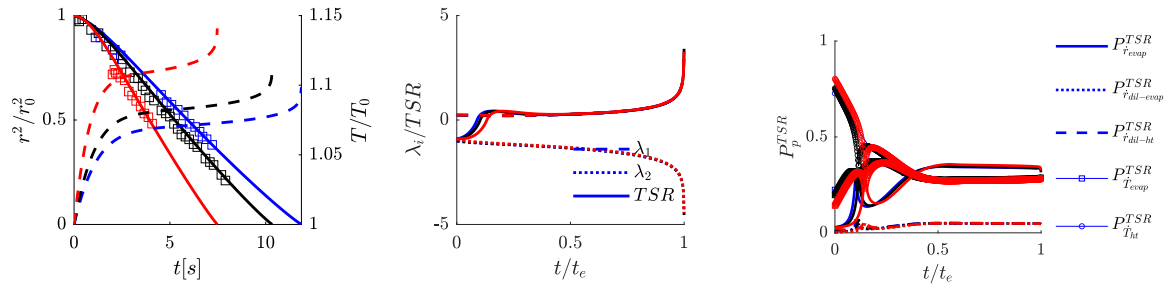

(a) (b) (c)

Figure 1: (a): evolution of droplet temperature (dashed line) and radius (continuous line and squared marker for experimental data). (b): Eigenvalues and TSR evolution. (c): participation indexes evolution. Blue: $T_a = 437$K, Black: $T_a = 464$K and Red: $T_a = 546$K.

where the weights W_i are obtained by substituting the Jacobian with its eigenvalue decomposition. The magnitude of the TSR represents the inverse of the global timescale of the system, and the positive or negative sign indicates its explosive or contractile nature. In addition, the participation indices (P_p^{TSR}) quantify the contribution of each process to the global dynamics of the system. The interested reader can find their formulation in Ref. (2).

3 Results and Discussion

The second case refers to the hexane droplets in an air stream experimentally investigated by Downing *et al.* (3) characterized by a moderate evaporation rate. A fixed hexane droplet of diameter $d = 1.76$mm at temperature of $T_d = 281$K is in an air stream with $\mathrm{Re}_d = 110$ at three different temperatures ($T_a = 437$K, 464K and 546K). Figure 1a shows the squared diameter and temperature behavior for the three subcases at different ambient temperature. By increasing the ambient temperature, the evaporation time diminishes as expected. The d^2-law trend is shown only for $t > 0.9$s because of the larger thermal relaxation time. In addition, droplet temperature grows for $t < 2$s, then becomes quasi-steady until $t \approx 0.9t_e$ where it rapidly increases. This suggests that hexane droplet experience a longer transitional regime and a steady equilibrium temperature is never achieved. Noted that dimensionless eigenvalues are normalized only by the evaporation time, fig. 1b shows that they are independent of the ambient conditions. The TSR is initially close to λ_1 and grows during the transitional regime crossing the zero line at different $(t/t_e)|_{TSR=0}$. This refers to the moment in which the evaporative system becomes explosive and physically corresponds to the quasi-linear behavior of the diameter reduction. After, we have that TSR$> \lambda_1$ for $t/t_e < 0.4$. This happens because the explosive nature of the system is still governed not only by mass transfer but also by thermal effects. Figure 1c summarized the contribution of each process. During the first transition regime, the system is governed exclusively by the heat transfer terms; and the mass transfer becomes important during the second regimes, when an "explosive" evaporation starts. During the quasi-steady regime, the effect of the thermal and mass transfer processes are similar.

4 Concluding Remarks

In this work, a CSP analysis for evaporating spray has been formulated and applied to a set of hexane droplets. The eigenvalues trend revealed the key timescales of the evaporation process and the participation indices were able to differentiate the effects of the single processes in the evaporation.

References

[1] Lam, Sau-Hai, and Dimitris A. Goussis. *Symposium (International) on Combustion*, 22, (1989), 931-941.

[2] Valorani, M., *et al. Springer, Cham*, (2020), 43-64.

[3] C. G. Downingm, AIChE Journal 12 (4) (1966) 760–766

2nd Spanish Fluid Mechanics Conference
Barcelona (2 - 5 July 2023)

Bubble velocities induced by interactions in polydisperse confined inertial swarms

Javier Ruiz-Rus[1], Véronique Roig[2], Patricia Ern[2], and Carlos Martínez-Bazán[3,4]

jrrus@ujaen.es

[1]Departamento de Ingeniería Mecánica y Minera, Universidad de Jaén. Spain
[2]Institute de Mécanique des Fluides de Toulouse, Université de Toulouse - CNRS. France
[3]Departamento de Mecánica de Estructuras e Ingeniería Hidráulica, Universidad de Granada. Spain
[4]Andalusian Institute for Earth System Research, Universidad de Granada. Spain

In this experimental work we present a study on the collective dynamics of polydisperse swarms of inertial confined bubbles. The kinematics of unequal sized bubbles, constituting a population that rises in a thin-gap cell filled with liquid at rest and which evolves due to coalescence, is deeply analyzed by means of statistically well-converged data. A Bubble Tracking Algorithm (BTA) has been developed to follow the motion of bubbles in high-speed movies registered at different downstream locations of the cell. The detailed information provided by the BTA allows an individual analysis of the time evolution of bubble velocities together with the detection of collision events, prior to which strong bubble-bubble interactions take place. To determine the effects of the local distribution of sizes and of the gas volume fraction, various gas injection conditions have been tested. The different injected fluxes of bubbles induce various coalescence rates, giving rise to different distributions of sizes throughout the cell.

1 Introduction

Several industrial, environmental and biomedical processes imply bubbly flows where bubbles rise in a quiescent fluid driven by buoyancy. Under these conditions, bubbles are free to interact giving rise to coalescence events and thus generating polydisperse populations of bubbles, like the one shown in Fig. 1. In those cases, the distribution of bubble sizes present in the population represents one of the most important characteristic of the flow since it controls the degree of agitation induced in the liquid. Many previous studies were devoted to describe the bubble-induced agitation for monodisperse bubbly flows [Risso, 2018], while less information has been reported in situations where the population is polydisperse. The present experimental work focus on the statistical analysis of the velocities of inertial confined bubbles in polydisperse swarms, where the population of bubbles evolves due to coalescence.

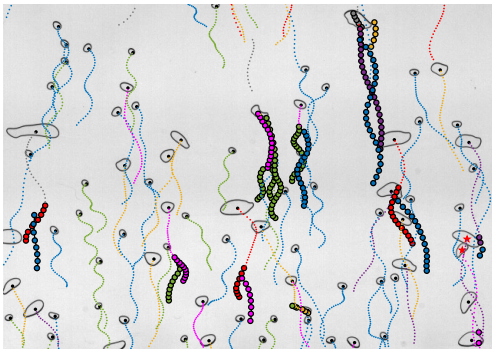

Figure 1: Snapshot of the bubble swarm along with the positions of the bubbles provided by the BTA for previous time steps. Trajectories of bubbles are plotted as dots, colored according to their sizes. Data prior to collisions is highlighted with larger symbols. A collision event is pointed out by red stars.

2 Experimental approach

Homogeneous and initially monodisperse swarms of air bubbles were generated at the bottom of a vertical cell filled with distilled water. The walls are separated with a very narrow gap, $w = 1$ mm, being the top of the cell open at atmospheric pressure. Under these conditions, if the equivalent diameter of the injected bubbles, defined from the projected area A as $D = (4/\pi A)^{1/2}$, is larger than the gap, they rise in an inertial regime [Roig *et al.*, 2012]. Four different swarms were created selecting the continuously injected air flow rate. They were characterized by the gas volume fraction at injection α_0 that was varied between 2.4 and 6.7 %, being the mean equivalent diameter almost constant at the injection, $D_0 = 3.85$ mm, for all the experiments. Depending on the injected gas volume fraction, different coalescence rates take place, inducing changes in the distribution of sizes present at different vertical positions of the cell [Ruiz-Rus *et al.*, 2022]. In order to perform

a statistical analysis of the evolution of the bubble velocity with the local distribution of sizes and the gas volume fraction α, an in-home developed Bubble Tracking Algorithm (BTA) has been used to follow the motion of all the bubbles constituting the population. Statistically well-converged data concerning the size and other geometric characteristics of the bubbles, together with the time evolution of their locations, velocities and accelerations can be extracted from the BTA results. Moreover, information related to the interaction process between the bubbles involved in collision or coalescence processes are additionally provided by the BTA, as illustrated in Fig. 1.

3 Results and discussion

The huge amount of information provided by the BTA has been spatially discretized into 15 equal measuring windows, following the idea proposed in Ruiz-Rus *et al.* [2022]. In this previous work, it was found that the evolution of the distribution of sizes can be characterized by a diameter representative of the largest bubbles, D_{V90}. Therefore, the probability density function (p.d.f.) of the bubble velocity is obtained at each measuring window and its evolution is thus discussed as a function of D_{V90} and α.

Based on the knowledge concerning the motion of isolated bubbles [Roig *et al.*, 2012, Filella *et al.*, 2015], the p.d.f. of the vertical component of the velocity of the bubbles constituting the whole swarm strongly differs from the terminal velocity corresponding to isolated bubbles of equal size. In fact, the resulting p.d.f.s are asymmetric with a strong upward fluctuation which increases with D_{V90}. This result can be attributed to the interaction of bubbles with the wakes of the neighboring ones [Bouche *et al.*, 2012] and not only to the formation of larger bubbles as the swarm evolves due to coalescence. To illustrate this, Fig. 2 allows us to discuss the joint p.d.f. of D and v_z, where the terminal velocity and the velocity fluctuations corresponding to equivalent isolated bubbles are superimposes as a function of D.

In addition, a closer inspection of the time evolution of the velocity of bubbles involved in a collision can be performed discriminating the BTA results by bubble size classes. This detailed analysis reveals that the tails of the vertical velocity p.d.f. for different populations of bubbles at different values of D_{V90} are directly related to the very close interaction with large bubbles, where some bubbles suffer a velocity increment as they interact with the wake of the larger ones in the distribution. In fact, the largest values found in the p.d.f. are associated to the latest instants of the bubble-bubble interaction process, just before the collision with a large bubble occurs.

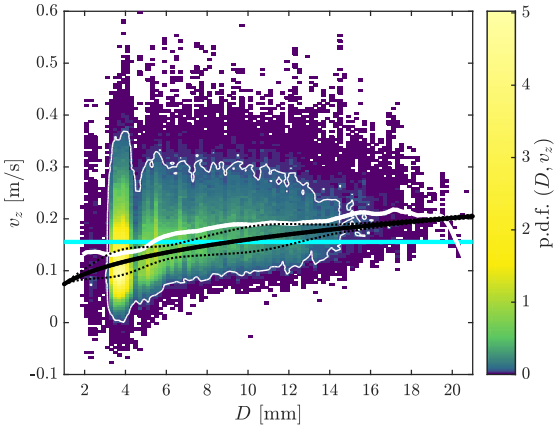

Figure 2: Joint p.d.f. of D and v_z, for a swarm of $\alpha_0 = 4.9$ % and $D_{V90} = 13.93$ mm. The thin white line delimits a region where the probability is larger than 1%. Thick white line: mean value of the distribution of v_z corresponding to each D value; cyan horizontal line: mean value of v_z for the whole distribution; thick black line: mean vertical velocity of isolated bubbles from Filella *et al.* [2015] and dotted black lines: range of fluctuation of the vertical velocity of isolated bubbles from Roig *et al.* [2012].

4 Acknowledgments

JRR acknowledges the financial support provided by the Fellowship UJAR06MS. Support from the Red Nacional para el Desarrollo de la Microfluídica, RED2018-102829-T, and from ANR-19-CE43-0002-02, is also acknowledged.

References

Risso F (2018) "Agitation, mixing, and transfers induced by bubbles". *Annu. Rev. Fluid Mech.*, 50, 25–48.

Roig V, Roudet M, Risso F & Billet A M (2012) "Dynamics of a high-Reynolds-number bubble rising within a thin gap". *J. Fluid Mech.*, 707, 444–466.

Ruiz-Rus J, Ern P, Roig V & Martínez-Bazán C (2022) "Coalescence of bubbles in a high Reynolds number confined swarm". *J. Fluid Mech.*, 944, A13.

Filella A, Ern P & Roig V (2015) "Oscillatory motion and wake of a bubble rising in a thin-gap cell". *J. Fluid Mech.*, 778, 60–88.

Bouche E, Roig V, Risso F & Billet A M (2012)"Homogeneous swarm of high-Reynolds-number bubbles rising within a thin gap. Part 1. Bubble dynamics". *J. Fluid Mech.*, 704, 211–231.

2nd Spanish Fluid Mechanics Conference
Barcelona (2 - 5 July 2023)

Capture of airborne microparticles by an ultrafine electrospray

Ignacio G. Loscertales[1], Francisco J. Higuera[2], Javier Rivero-Rodríguez[1], and Antonio J. Hijano-Reyes[1]

loscertales@uma.es

[1]Departamento de Ingeniería Mecánica, Térmica y de Fluidos, Universidad de Málaga , Spain
[2]Departamento de Mecánica de Fluidos y Propulsión Aeroespacial, Universidad Politécnica de Madrid, Spain

We present a simple model to calculate the charging of conducting inertialess airborne microparticles by an ultrafine electrospray. The kinetics of this process are coupled with the continuity equations for all the particle types and the electrospray, the Navier-Stokes equations for the gas and the Poisson equation for the electric field. The model is applied in an axisymmetric configuration to filter out and collect airborne particles in a laminar gas stream.

1 Introduction

This work is motivated by situations in which high-value airborne micro or nanoparticles, such as catalytic particles, have to be collected on substrates to form micro-layers for a given application. To do so, we use an ultrafine electrospray to charge the airborne particles and to collect them on a collector using an appropriate electric field.

2 Description of the problem

Both electrospray droplets and particles are considered inertialess. As the droplets attach to a particle, its charge state increases up to a point where the repulsive field between the charged particle and the electrospray droplets prevents any further droplet from landing on the particle. This produces charged particles with one, two, etc. up to N electrospray droplets attached.

We propose an Eulerian treatment of the charged particles and the electrospray through their corresponding continuity equations, including the rate of generation term for each type of particle, w_i, coupled with the Navier-Stokes equations for the gas, including the momentum injected by the charged entities, and the Poisson equation for the electric field, similar to Khalifehei and Higuera (2020).

The rates of generation are written in terms of *reaction constants* and particle and electrospray droplet concentrations, n_i and n_e, $w_i = K_i n_i n_e$. To determine the constants K_i we resort to the model set forth by Prem and Pilat (1978), which includes inertial impaction, brownian diffusion and electrostatic effects. In the limit where the particle diameter is much larger than the droplet diameter, $d_e/d_p \ll 1$, the collision mechanism is solely due to electrostatic interactions between the particle and the electrospray droplets. This allows computing an effective cross section for the charging process of a particle that depends on the charge state of the particle, the charge on the electrospray droplets and the local electric field. This cross section yields K_i. On the other hand, particle-particle collision are no considered based on their rather low relative velocity, which makes their collision probability very low.

3 Results

The set of non-linear partial differential equations for the droplet concentration, particle type concentration, gas velocity and pressure and electric field are completed with appropriate boundary conditions. In particular, we looked at an axisymmetric device, as sketched in figure 1. The particles, assumed monodisperse, enter along with a stream of gas through Σ_0. An electrospray of ultrafine droplets enters through Σ_2 at a given rate Φ_e (number of droplets injected per unit time). A voltage difference V_0 is applied between the electrospray injection tube, Σ_1, and the outer tube-extractor, Σ_3, which is grounded. A collector electrode, Σ_4 is set at a voltage $-V_1$ to collect all the charged entities. Finally, the gas escapes through Σ_5 along with particles that did not reach the collector. In a region downstream of the electrospray injection, the electrospray droplets attach to the particles, the later gaining charge and therefore being subjected to the drag of the local electric field, which pushes them towards the collector eventually removing a fraction of them from the gas stream.

To write the problem in dimensionless form, we scale distances with L_1, charges with the droplet

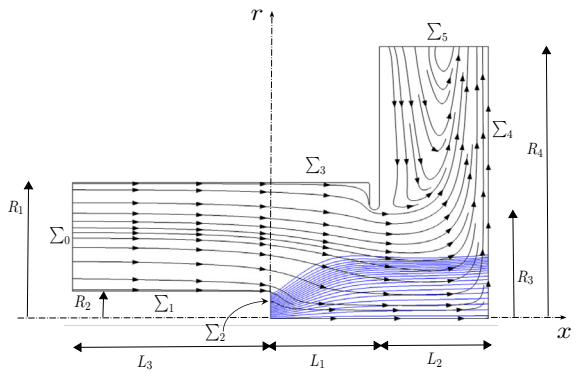

Figure 1: Sketch of the device. Black lines: gas streamlines. Blue lines: electrospray streamlines. No particles are injected.

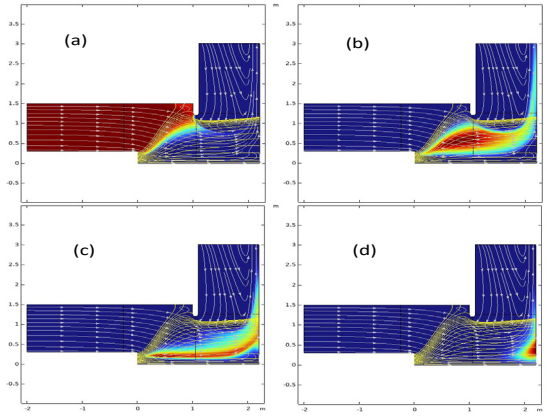

Figure 2: Particle concentration. (a) Neutrals, (b) type 1, (c) type 2 and (d) type 3. Yellow lines: electrospray streamlines. Grey arrowed lines: gas streamlines.$V_0^* = 0.28$, $V_1^* = 0.31$ and $\Phi_0^* = 0.63$.

charge q_e, and use the balances $E_c/L_1 = q_e n_c/\epsilon_0$, $\rho_g v_c^2/L_1 = q_e n_c E_c$ and $\Phi_e = n_c v_c L_1^2$ to define scales for the number densities, n_c, the electric field, E_c, and the velocities, v_c. The electric potential is then scaled with $E_c L_1$, the mobilities with v_c/E_c, and the diffusivities with $v_c L_1$. The rate constants K_i are scaled with $v_c/(n_c L_1)$. The main dimensionless parameters controlling the problem are

$$V_0^* = \frac{V_0}{E_c L_1},\ V_1^* = \frac{V_1}{E_c L_1},\ \Phi_0^* = \frac{\Phi_0}{\Phi_e}, \qquad (1)$$

where Φ_0 is the flux of neutral particles. The problem is solved using COMSOL 6.0.1. To reduce the numerical burden, the diffusivities used in the numerical computations are larger than the true physical diffusivities. It has been checked that this numerical artifact does not significantly affect the results. Figure 2 shows the dimensionless number densities of neutral particles, particles with one, two and three electrospray droplet attached (type 1, 2 and 3 respectively), for $V_0^* = 0.28$, $V_1^* = 0.31$ and $\Phi_0^* = 0.63$ for a given imposed gas flow rate. In this case, the number density of particles with four or more electrospray droplets (type 4 and above) was smaller than that of particle type 3 by more than three orders of magnitude, being irrelevant to the problem. However, the highest particle type does depend on the running conditions, and ongoing work aims to study the effect of the different dimensionless parameters.

The results show the effect of the charged particles on the structure of the gas flow. In figure 1 all the parameters are the same as those in figure 2 except for the injection of the particles; in particular, the flow rate of gas through the device is the same in both cases. In figure 2, the presence of the charged particles dragged by the electric field pushes the gas towards the collector by injecting momentum in that direction. This generates a relatively thin layer of particle-laden outwards-flowing gas close to the collector, Σ_4, and enhances recirculation in the rest of the device. If no flow rate of gas were imposed, the effect of the charged particles alone would generate a depression in Σ_0 pumping a net flow rate through the device. The collection efficiency is rather large, collecting almost 99% of the particles on the collector.

4 Conclusions

We have introduced a kinetic model to calculate the charging of neutral conducting particles by an electrospray of ultrafine droplets, coupled with the gas motion and the Poisson equation that yields the particles number distribution and particle flux on the collector.

This work has been supported by the Spanish Ministerio de Ciencia e Innovación under grants PID2020-115730GB-C21, PID2020-115730GB-C22 and RED2018-102829-T.

References

Khalifehei M. and Higuera F.J. (2020) "Neutralization of an electrospray by a corona discharge". *Journal of Aerosol Science*, **145**, 105547.

Prem A. and Pilat M.J. (1978) "Calculated particle collection efficiencies by single droplets considering inertial impaction, brownian diffusion and electrostatics", *Atmospheric Environment*, **12**, 1981-1990.

2nd Spanish Fluid Mechanics Conference
Barcelona (2 - 5 July 2023)

Challenges in Modeling Inkjet Printing: Physical and Numerical Aspects

A.R. Hashemi[2], P.B. Ryzhakov[1,2], M.R. Hashemi[1,2], R. Rossi[1,2], N. Dialami[1,2], and R. Zorrilla[1,2]

pavel.ryzhakov@upc.edu

[1]Universitat Politècnica de Catalunya (UPC), 08034 Barcelona, Spain
[2]Centre Internacional de Mètodes Numèrics en Enginyeria (CIMNE), 08034 Barcelona, Spain

In the present work, we review critical challenges faced when modeling inkjet printing and outline possible strategies for designing a robust and efficient numerical model.

1 Introduction

Whenever the application of inkjet printing is expanded to the area of cutting-edge manufacturing technologies ranging from micro-electronics and optical devices to biological applications, improving the accuracy, controllability, and efficiency of inkjet printing systems becomes essential.

In drop-on-demand, the more controllable type of inkjet printing system, the ideal is to precisely control the size and shape of the output by adjusting an input pulse. Nevertheless, during the sub-processes between input and output, numerous complex phenomena, such as the formation of satellite droplets, can occur and produce unwanted output results. Hence, optimization of the geometrical design of the system, as well as the material properties of the ink, nozzle, and substrate is a crucial task that can be achieved through numerical modeling of inkjet systems. However, simulation of these systems faces many challenges due to the complexities of the problem and the extreme sensitivity of the output to the initial conditions and control parameters.

2 Multi-scale problem

Successful optimization of inkjet printing is contingent on considering the process as a whole, while each part of the process, due to its specific length scales and effective phenomena, requires its own modeling approach (Lohse 2022). For instance, at the printhead side, the size of the ink chamber is of the order of centimeters, the entrained bubbles are of the order of micrometers and the inhomogeneities like suspended particles or floating polymers are of the order of nanometers. Therefore, the necessity of multi-scale modeling approaches is evident.

3 Multi-physics problem

The multiplicity of phenomena involved in the printing process makes the problem more complicated. For instance, for the printed droplet on the substrate, we simultaneously have partial evaporation, Marangoni surface flows, capillary forces, physical and chemical interaction with the substrate, and other droplets and solidification (Figure 1). Coupling the governing equations of these phenomena on the basis of the main numerical scheme (e.g. finite element) should be done with special considerations to avoid diverging numerical solutions.

4 Challenges at the interface

The liquid-gas or liquid-liquid interface capturing is another serious challenge. Among several approaches that are utilized for treating the discontinuity of material properties at the interface, the phase-field and level-set are the most common methods. In the phase-field method, smoothing the material properties over a few cells obliges using very fine meshes at the interface, which considerably increases the computational cost. On the other hand, the level-set approach, which provides sharp interfacial boundaries, gradually loses its regularity and requires frequent reinitialization. Moreover, the conventional level-set approach does not guarantee conservation (Olsson & Kreiss 2005).

Recently, new techniques have been introduced to cover up these inadequacies, such as enriched finite element level-set methods (Hashemi, Ryzhakov, & Rossi 2020). Additionally, an extension to this approach can overcome the inconsistencies that may arise with the discontinuity of the gradient of the velocity field over the interface.

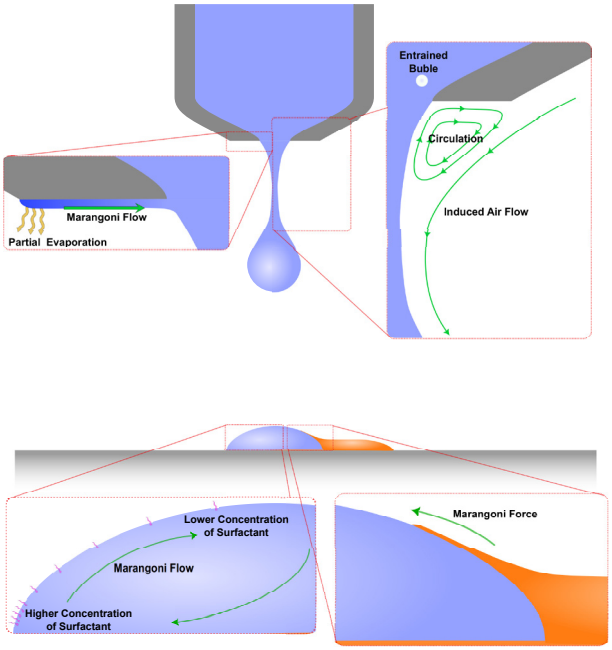

Figure 1: Different physical phenomena occur during the inkjet process. Partial evaporation at the nozzle plate produces a gradient in surface tension, which leads to Marangoni flow toward the nozzle (upper left inset). The induced air flow can entrain bubbles into the ink chamber (upper right inset). The gradient in the concentration of surfactant molecules induces Marangoni flows at the droplet's surface (lower left inset). The surface flows make the neighboring droplet creep over the other (lower right inset).

5 Conclusions

Inkjet printing modeling requires a multi-scale approach that not only considers the integrity and consistency of the system as a whole, but also realistically models the effective physical phenomena in each sub-process and implements them in numerical calculations. Moreover, numerical difficulties such as interface capturing can be overcome using recently improved techniques. Furthermore, machine learning approaches also provide effective facilities for optimizing inkjet systems (Shi, Song, Song, & Lu 2019).

References

Lohse, D. (2022). "Fundamental fluid dynamics challenges in inkjet printing". *Annual Review of Fluid Mechanics*, **54**, 349-382. https://doi.org/10.1146/annurev-fluid-022321-114001

Olsson, E., & Kreiss, G. (2005). "A conservative level set method for two phase flow". *Journal of Computational Physics*, **210(1)**, 225-246. https://doi.org/10.1016/j.jcp.2005.04.007

Hashemi, M. R., Ryzhakov, P. B., & Rossi, R. (2020). "An enriched finite element/level-set method for simulating two-phase incompressible fluid flows with surface tension". *Computer Methods in Applied Mechanics and Engineering*, **370**, 113277.

Shi, J., Song, J., Song, B., & Lu, W. F. (2019). "Multi-objective optimization design through machine learning for drop-on-demand bioprinting". *Engineering*, **5(3)**, 586-593.

2nd Spanish Fluid Mechanics Conference
Barcelona (2 - 5 July 2023)

Effect of a wall boundary on the dynamics of high-Bond bubbles rising in a still liquid at different regimes

Cecilia Estepa-Cantero[1,3], Rocío Bolaños-Jiménez[2,3], and Carlos Martínez-Bazán[1,3]

cestepa@ugr.es

[1]Departamento de Mecánica de Estructuras e Ingeniería Hidráulica, Universidad de Granada, Spain
[2]Departamento de Ingeniería Mecánica y Minera, Universidad de Jaén, Spain
[3]Instituto Interuniversitario de Investigación del Sistema Tierra en Andalucía, Granada, Spain

We present an experimental study on bubbles rising into still liquids in the vicinity of a rigid vertical wall at high Bond numbers. In particular, three different path regimes are explored, namely rectilinear, zigzag and spiral. Experiments were conducted by recording the bubble's rising motion with two synchronized high-speed cameras. The effect of the dimensionless initial distance from the surface to the bubble, L, is investigated for each regime. The results show an increasing stabilizing effect of the surface as L decreases. This effect is most evident in the spiral regime, which even becomes a zigzag regime when the wall is close enough. Moreover, an overall migration effect from the wall is observed and characterized. Finally, in the zigzagging regimes, the bubble oscillates in a plane perpendicular to the wall when it is close enough.

1 Introduction

Bubble freely rising into an unbounded liquid represents a classical an extremely rich problem in Fluid Mechanics which has received attention over decades, generating a vast literature Cano-Lozano (2016). However, in most situations in nature and industrial operations, bubbles inevitably move near a wall boundary. The solid wall introduces complex changes in the bubble dynamics whose governing mechanisms have not been fully unravelled yet. Although the effects of a solid surface in the neighbourhood of the bubble have been investigated, most of the works are theoretical and numerical. The experimental studies are mainly limited to low Bond bubbles in which their shape is almost spherical or elliptical. Thus, in this study we focus on high Bond bubbles, with important implications in nature and industrial applications.

2 Experimental methodolody and results

Experiments were performed by injecting a constant gas flow-rate in a glass tank 1.2 m high with a 15 x 15 cm^2 cross-section. A glass wall was placed inside the tank in such a way that its horizontal distance to the air injector, L^*, can be precisely controlled. In addition, different liquids (silicon oils and water-glycerol mixtures) and air injector sizes were employed.

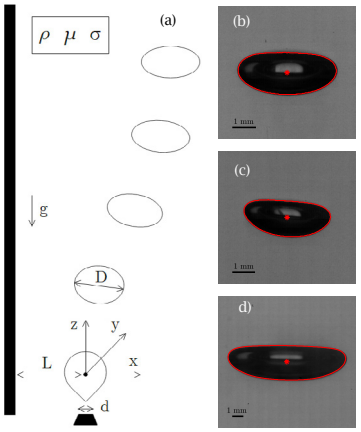

Figure 1: (a) Sketch of the problem showing the involved physical parameters. (b)-(d) Experimental images showing typical bubble shapes, together with their contour (red lines) and centroids (red symbols), for (b) rectilinear, (c) zigzag, and (d) spiral regimes.

A sketch of the problem is shown in Fig. 1(a). The problem is characterized in terms of three dimensionless numbers, namely Galilei, $Ga = \rho g^{1/2} D^{3/2}/\mu$, Bond, $Bo = \rho g D^2/\sigma$, and the initial dimensionless distance between the bubble and the wall, $L = L^*/D$, with ρ and μ the liquid density and viscosity, respectively, σ the surface tension, g the gravity and D the equivalent bubble diameter.

We focus on three specific regimes, corresponding to high Bond numbers, numerically studied without

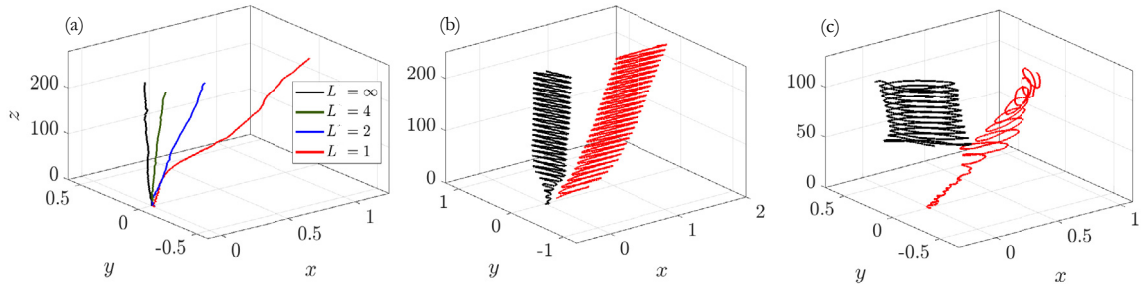

Figure 2: Experimental trajectories for bubbles in the three regimes: (a) rectilinear, (c) planar zigzag and (c) spiralling.

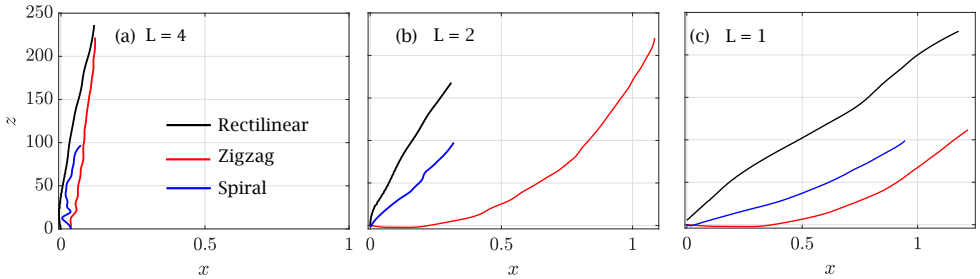

Figure 3: Time-averaged paths for the three regimes and (a) L=4, (b) L=2 and (c) L=1.

the effect of a near wall in Cano-Lozano (2016): a) rectilinear ($4.3 \leq$ Bo ≤ 5, $53.5 \leq$Ga≤ 56.1), b) planar zigzag ($3.2 \leq$ Bo ≤ 4, $86.1 \leq$Ga≤ 93.0), and c) spiral ($10 \leq$ Bo ≤ 12, $102 \leq$Ga≤ 123). Three different distances were considered in each case, namely L =1, 2 and 4, and compared with the unbounded situation, $L = \infty$. The experiments were recorded with two synchronized high-speed cameras, whose vertical positions were controlled by a linear motor, following the bubble along its entire rising movement. An in-house MATLAB code was specifically developed to process the images and obtain the main bubble characteristics (Fig. 1b).

The results show that the terminal velocity is not affected by the presence of the wall, being the Reynolds number in agreement with theoretical correlations in literature. A migration effect from the wall is induced in all the regimes, as can be noticed in Fig. 2. This perpendicular movement away from the wall increases as L reduces, being the effect almost negligible for L =4, as can be clearly seen mainly in Fig. 2(a), where all the values of L are presented for the rectilinear case. Additionally, the wall has been found to fix the zigzagging plane perpendicularly to the wall (see Fig. 2b), unlike the free rise in which the zigzag plane is established through the initial conditions. Moreover, the wall is found to has a stabilizing effect, inducing a change of the regime in the spiral case, as it is plotted in Fig. 2(c), where a transition to the zigzag regime is promoted when L is sufficiently small. Finally, if the time-averaged paths of the three regimes is compared for a given value of L (Fig. 3), the zigzag regime is the one presenting the largest displacement from the wall, while the rectilinear case exhibits the smallest migration effect.

3 Conclusions

The effect of a vertical wall on the dynamics of a rising bubble is analyzed experimentally. We focus on three particular regimes at high Bo number with different rising paths which have not been experimentally explored before. The vertical velocity is not modified by the wall presence, while the bubble is observed to migrate away from the wall, being this effect more prominent as the wall is closer to the bubble. Moreover, the wall prescribes the zigzagging plane perpendicularly and presents a stabilizing effect.

References

Cano-Lozano J.C. et al. (2016). "Paths and wakes of deformable nearly spheroidal rising bubbles close to the transition to path instability". *Phys. Rev. Fluids*, **1**, 1–30.

2nd Spanish Fluid Mechanics Conference
Barcelona (2 - 5 July 2023)

Evaluation and improvement of light transmittance for an optimal design of UV-C systems

Delia Trifi[1], Óscar Prades-Mateu[1], Sergio Chiva[1], and Raúl Martínez-Cuenca[1]

trifi@uji.es

[1]Department of Mechanical Engineering and Construction, Universitat Jaume I, Ave. Vicent Sos Baynat s/n, Castelló de la Plana, 12071, Spain.

UV disinfection is the preferred technology for treating clear waters given its low environmental impact and moderate economic cost. In the field of wastewater treatment, UV reactors are still not so efficient since the suspended solids absorb and scatter the UV light. This work has the aim to develop a novel methodology for the evaluation and improvement of these disinfection systems considering the behaviour of the optical properties in the UV-C wavelength range and the interaction of the light field with bubbly flows. The presented experiments were conducted at visible wavelengths mimicking the optical properties of UV-C by adding methylene blue at several concentrations. Results show an increased resilience of the UV-C dosage against changes in water absorption.

1 Introduction

A deeper understanding of the effects that bubbles have on light and *Escherichia coli* particles can lead to an enhancement in the design of a large number of technological processes. One of these cases is the generation of the UV dose required for the inactivation of pathogenic particles in WWTPs (Wastewater Treatment Plants), where a uniform radiation distribution is needed. In practice, this is not possible due to the huge changes in the UV absorption coefficient caused by variations in the Total Suspended Solids (TSS) of the influent water.

This effect is gradually illustrated in Fig. 1, that depicts the UV-C distribution in the vicinity of lamps inside a reactor for values of water absorbance from 2 m^{-1} to 100 m^{-1}, ($A = log_{10} \cdot (I_0/I)$) (results provided by Computational Fluid Dynamics, CFD, simulations with the Discrete Ordinates method). If a reactor is designed for waters with an absorption coefficient of $10m^-1$, when SST increases (absorption coefficient of $100m^-1$) the light field is limited to regions very close to the UV lamps so the bacteria receive a reduced dose. Conversely, when the SST decreases ($2m^-1$) the bacteria receive an overdose, i.e. we are wasting energy.

The aim of this work is to study the influence of bubbly flows on light propagation in the absorption conditions of UV reactors. The principle is simple: light propagating through air is not absorbed, so the addition of bubbles should decrease the absorption. However, bubbles also scatter light reducing the light intensity behind them. In this work we show an experimental proof of concept using a medium with similar absorption properties to that of wastewater in the UV-C range thanks to the use of methylene blue and a red-light diffuser panel.

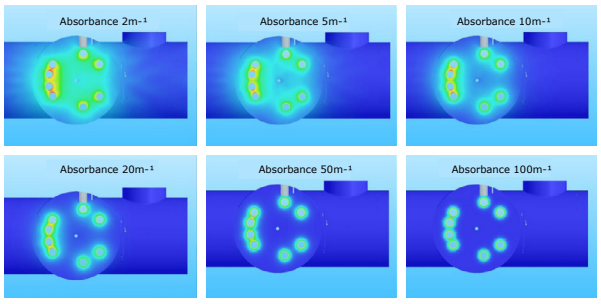

Figure 1: CFD contour of light intensity as a function of the main fluid absorbance.

2 Materials and Methods

The experimental framework is illustrated in Fig. 2, where the methylene blue media was illuminated by a red light, which corresponds to its maximum peak of absorbance ($\lambda = 668nm$), Whang (2009). This light travels though the flow region and is detected by a CMOS sensor *(UI-1220-M-BG uEye, IDS)*. Afterwards, the acquired images are processed to obtain the intensity distribution ($0 - 255$). Bubbles surfaces partially reflect and refract the incident light, generating a shadow right behind that can be interpreted as a scattering of light rays. This shadow region is illuminated by the forward scattering of other bubbles present in the medium, Fig. 2.(b).

To analyze the effect of this two-phase flow experimental setup, the void fraction (α) when the bubbly flow is enabled was evaluated to determine its influence in the intensity detected through the optical path (Fig. 3).For this optical path, 5 water-methylene blue concentrations were tested, in each concentration a scan of the air flow ranging from 0 to 20 l/min give us the variation of void fraction, determined following the procedure detailed by Kim (2000).

The light intensity at the CMOS camera sensor plane can be described in terms of the Beer-Lambert's law (Eq. 1), considering the contribution of the liquid and bubbly media through the distance traveled across liquid (L) and the bubbly flow (l):

$$I = I_0 \cdot [exp^{-(L-l)\cdot\mu_{ext_{methylene}}} \cdot exp^{-l\cdot\mu_{ext_{mixt}}}] \quad (1)$$

where:

$$\mu_{ext_{methylene}} = \mu_{abs_{methylene}} \quad (2)$$

$$\mu_{ext_{mixt}} = [1-\alpha]\cdot\mu_{ext_{methylene}} + \alpha\cdot\mu_{ext_{bubble}} \quad (3)$$

$$\mu_{ext_{bubble}} = \mu_{sct_{bubble}} \quad (4)$$

As shown in the previous equation (Eq. 3), the whole extinction coefficient ($\mu_{ext_{mixt}}$) in this case must be described as a participation of both phases. While the effect of scattering in water-methylene phase can be neglected, the bubble extinction coefficient only consideres the scattering, Eq. 4.

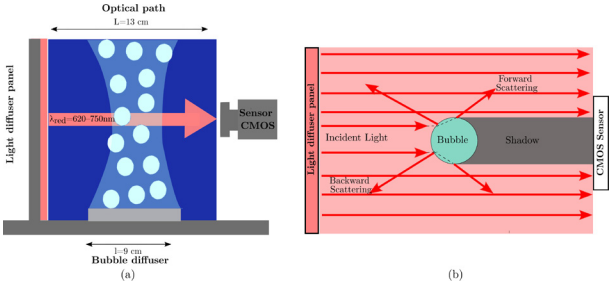

Figure 2: (a) Scheme of the experimental setup; (b) Visualization principle: interaction light-bubble.

3 Experimental Results

Fig. 3 shows the logarithmic decrease of detected intensity as a function of the increase in concentration for two scenarios: Non-bubbly and bubbly flow. The plot shows the normalized attenuation for both types of flow. Comparing both curves, it is apparent that the use of bubbles makes the system more tolerant (by almost one order of magnitude) to changes in absorption. This aeration can be applied in UV disinfection systems to reduce the huge changes in dose administration due to the variations in suspended solids.

We also note that, despite the addition of non-absorbing bubbles does not increase the light intensity at the CMOS sensor for the range of concentrations under this study. But the results indicate that this could be possible by shortening the optical path and increasing the medium absorbance.

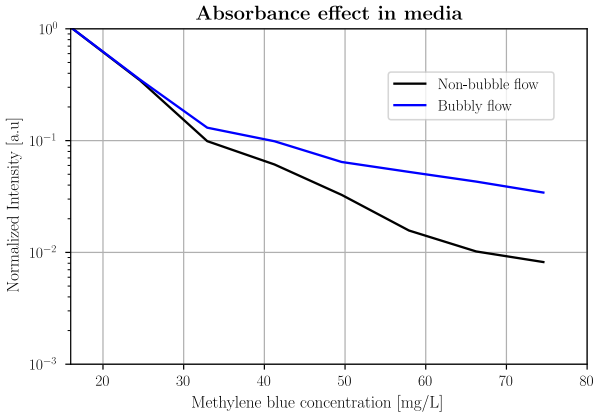

Figure 3: CMOS-detected intensity during interaction light-bubbles, compared to non-aerated conditions both in presence of methylene blue.

4 Conclusions

During the development of this work, the initial statements have been confirmed. In the experimental methylene blue media, there is a threshold concentration where the contribution of the absorption (μ_{abs}) is higher than the scattering (μ_{sca}) inside the extinction coefficient term (μ_{ext}). This is the baseline of our on going work, where we can experimentally characterize and improve UV-C facilities using non-damaging DNA light sources, preserving the optical properties (absorbance) that would be present at UV-C range, $\lambda = [200-280]nm$.

References

Whang T.J, Huang H, Hsieh M.T & Chen J. (2009) "Laser-induced silver nanoparticles on titanium oxide for photocatalytic degradation of methylene blue", *International Journal of Molecular Sciences.*, **10**, 4707-4718.

Kim S, Fu X.Y.,Wang X & Ishii M. (2000) "Development of the miniaturized four-sensor conductivity probe and the signal processing scheme". *International Journal of Heat and Mass Transfer*, **43**, 4101–4118.

Evaluation of Experimental Artifacts in the Evaporation of Droplets on Fibers

Mohamad Asrardel, Taha Poonawala, Álvaro Muelas* and Javier Ballester

Fluid Mechanics Group / LIFEn, Universidad de Zaragoza, SPAIN

In light of the potential impact of undesired experimental artifacts in the evaporation of isolated droplets suspended on fibers, a preliminary study has been carried out using a newly-developed facility and a droplet evaporation model. The conduction of heat through the suspension fiber has been found to significantly enhance the evaporation rate, leading even to the onset of internal bubbling for some cases. The absorption of thermal radiation from the environment was found to be less relevant for this specific setup, although its impact could be much larger for cases where the droplet is exposed to hot walls. Overall, it is observed that these artifacts strongly depend on the experimental conditions applied in the tests, and therefore should be carefully considered when analyzing the results obtained under this configuration.

INTRODUCTION

Experimental measurements conducted on isolated droplets are a well-known approach to extract relevant combustion behaviors for liquid fuels, such as their evaporation characteristics. However, the results obtained can significantly depend on undesired experimental artifacts, such as the absorption of heat from the fibers where the droplets are suspended [1], or the absorption of thermal radiation from the environment [2]. This work intends to quantify these effects for a recently developed suspended droplet facility, where the evaporation characteristics of a pure compound (butanol) have been extracted and characterized for high-temperature conditions.

EXPERIMENTAL AND PREDICTIVE METHODS

A scheme displaying the main elements of the Suspended Droplet Facility (SDF) used in this work is presented in Fig. 1. A single droplet of 1-butanol, with an initial diameter (d_0) ranging between 350 and 850 µm, was anchored at the intersection of fibers arranged in a cross configuration. In this work, Silicon Carbide (SiC) fibers of 15 µm in diameter, and Platinum (Pt) wires of 25 and 50 µm have been used.

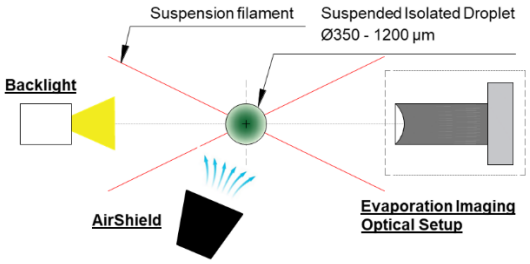

FIG. 1. Schematic of the suspended droplet facility

The droplet vaporized within an inert and high-temperature co-flow (1336 ± 50 K), consisting in the combustion products of a flat-flame burner. Due to the small slip velocities and small length-scale of this configuration, the effect of both forced and natural convection are estimated to be quite small, particularly for the smallest droplets. As for the radiative heat flux at the droplet location, it was measured with an ellipsoidal radiometer probe, providing a value of 23.5kW/m^2. The process of droplet evaporation was recorded with a high-speed camera synchronized with a LED backlight and a jet of cold air, used to shield the droplet from the hot co-flow until the start of the experiment.

A 1-D droplet evaporation model developed according to the classical theory of droplet vaporization was also used to analyze the experimental results. The absorption of radiative heat was included through the efficiency factor described in [2], whereas the heat conduction through the fiber was introduced based on the approach described in [3].

RESULTS AND DISCUSSION

The experimental droplet vaporization curves obtained with different arrangements of SiC fibers and Pt wires are compared in Fig. 2 for a fixed initial droplet size of 450 µm. It is clear that the droplet evaporation behavior strongly depends on the suspension element used in the tests. For SiC fibers, the total evaporation times are clearly reduced as the number of filaments increases. Furthermore, it can be observed that, whereas the 2x1 SiC curve shows a quite linear decrease of d^2 with the residence time (in clear agreement with the well-known d^2-law), this linearity is progressively lost when the number of fibers is increased. The higher slopes (i.e., evaporation rates) displayed at the end of the droplet evaporation curves in Fig. 2 would point to a greater effect of the fiber conduction mechanism for small-sized droplets, as it will be discussed further on. Finally, when the suspension filament was changed to Platinum, the droplets consistently displayed internal bubbling and puffing events, with the droplets expelling small fragments of liquid (also named as child droplets, see Fig. 3). This behavior can also be ascertained from the irregular

evaporation curves in Fig. 2. It is clear that the high thermal conductivity of Pt, in combination with the relatively thick filaments used, provided hot spots inside the droplet where the heterogeneous nucleation of vapor bubbles occurred. Since butanol is a pure compound, the onset of such phenomenon is a clear example of artifacts induced by the experimental conditions, not being attributable to the intrinsic characteristics of the studied fuel.

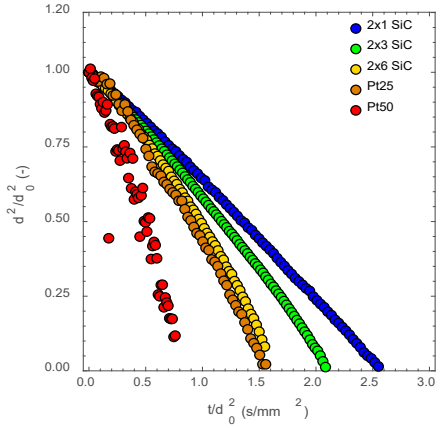

FIG. 2. Experimental evaporation curves for d_0=450 µm butanol droplets suspended at 2x1 SiC, 2x3 SiC, 2x6 SiC, Pt25 and Pt50.

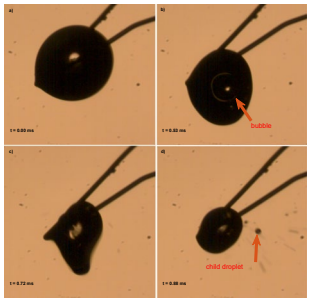

FIG. 3. Sequence of a droplet suspended on a Pt filament (50 µm) with internal bubbling and puffing.

The average evaporation rate (k) extracted for over 80 tests with SiC fibers is presented in Fig. 4 in terms of the initial droplet diameter. The predictions obtained with the model have been also included for comparison. It can be seen that this model is able to quite accurately reproduce the experimental trends, predicting evaporation rates reasonably close to the experimental values for all the cases. The validation of this model enables to use it as a most useful tool to isolate the impact of each heat transfer mechanism in the final observed behaviors. For instance, the slight increase in k with d_0 for the 2x1 case is ascribed to the enhancement of forced/natural convection and radiative heating with larger droplets. The practically flat dependency observed points to the small relevance of these mechanisms under the studied experimental conditions. Setups with higher radiative heat flux (e.g., droplet evaporating inside a furnace with hot walls) or with more convective environments would provide a steeper curve in Fig. 4.

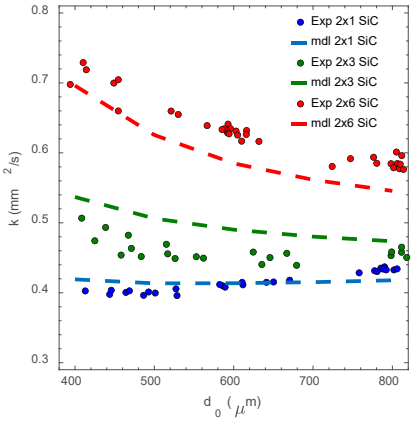

FIG. 4. Average evaporation rates for different SiC fiber arrangements in terms of d_0 (both modeling and experimental results).

On the contrary, the decrease in k with d_0 for the cases with a higher number of fibers clearly points to a dominance of fiber-induced heating, since this heat transfer mechanism is the only one that is expected to reduce its relevancy as the droplet size increases (for a fixed fiber diameter). Overall, the choice of the suspension element is found to be critical for an accurate characterization of the intrinsic evaporation behavior of any liquid fuel studied in this configuration.

CONCLUSIONS

The effect of the suspension fiber has proven to be quite relevant, significantly enhancing the droplet evaporation rate and even leading to the onset of internal bubbling for cases where Pt wires were used. This effect was more marked for small-sized droplets, being its impact reduced as the droplet-to-fiber size ratio increased. Radiative heating and forced/natural convection were found to have a much lower impact for the setup used in this work. Overall, it is concluded that these effects should be carefully considered when analyzing the results obtained under the isolated droplet configuration.

—

* amuelas@unizar.es

This work was supported by the grant PID2019-109747RB-I00 funded by MCIN/ AEI/ 10.13039/ 501100011033.

[1] Chauveau, C., et al., An analysis of the droplet support fiber effect on the evaporation process. *International Journal of Heat and Mass Transfer*, 2019. 128, 885-891.

[2] Abramzon, B. and S. Sazhin, Droplet vaporization model in the presence of thermal radiation. *International Journal of Heat and Mass Transfer*, 2005. 48(9), 1868-1873.

[3] Han, K., et al., An experimental and theoretical study of the effect of suspended thermocouple on the single droplet evaporation. *Applied Thermal Engineering*, 2016. 101, 568-575.

2nd Spanish Fluid Mechanics Conference
Barcelona (2 - 5 July 2023)

Influence of "fresh" fluid encounter on the settling of particles in the dilute regime

Manuel Moriche[1], Manuel García-Villalba[1], and Markus Uhlmann[2]

manuel.moriche@tuwien.ac.at

[1]Vienna University of Technology, Institute of Fluid Mechanics and Heat Transfer, Vienna, Austria
[2]Karlsruhe Institute of Technology, Institute for Hydromechanics, Karlsruhe, Germany

Particle laden flows are a class of dispersed multiphase flows in which the dispersed phase is composed of particles. The scientific community dedicates large efforts in understanding these flows, driven by their ubiquitous presence in nature and industrial processes. Furthermore, because of their complexity analytical solutions are seldom available and, on the other hand, experiments and numerical simulations are still challenging.

In this work we study the settling of spherical particles under the action of gravity by means of direct numerical simulations. If only one particle is considered, the problem can be solved on a body-conforming grid attached to the particle [Jenny et al., 2004]. However, when many particles are considered, this approach is not easily extendable . The method of choice of most authors to simulate many particles is the immersed boundary method [Mittal and Iaccarino, 2005], and typically in a triply periodic configuration. This configuration has shown to be very fruitful because it contains the most important ingredients of the problem, while retaining homogeneity in every direction, which simplifies the methodology itself and the interpretation of the results. There are, however, some ingredients of the problem of particle settling that a triply periodic configuration cannot represent, namely the encounter of ambient fluid by the particles as they settle [Gidaspow, 1994]. In this talk we present the settling of spherical particles in an inflow/outflow vertical configuration (see figure 1a). The main challenge of these simulations is keeping the particles inside the computational domain for large time intervals, which we are able to overcome based mostly on previous experience with free falling bodies. We assume that the fluid encountered by the particles is quiescent to reduce the complexity of the problem, therefore the problem is governed by the Galileo number, Ga, the density ratio of the particles with respect to the fluid, $\tilde{\rho}$, and the initial particle distribution. We set $Ga = 178$ and $\tilde{\rho} = 1.5$ based on the work of Uhlmann and Doychev [2014] in order evaluate the influence of particles encountering "fresh" fluid as they settle compared to a triply periodic configuration. Figure 2 shows the time evolution of the horizontally-averaged solid volume fraction for an initial distribution of particles such that $\langle \Phi \rangle_{xy} \approx 5 \cdot 10^{-3}$.

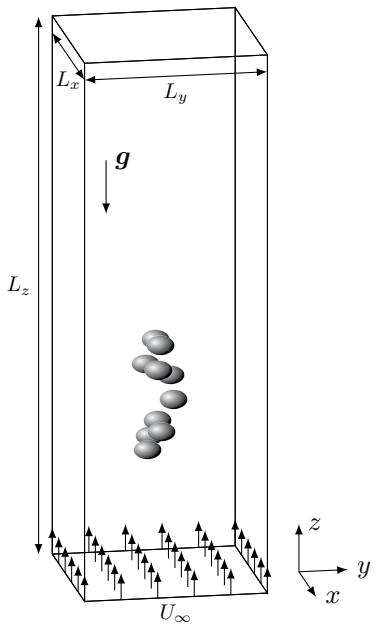

Figure 1: Sketch of the problem.

References

D. Gidaspow. *Multiphase flow and fluidization: continuum and kinetic theory descriptions*. Academic press, 1994. doi: 10.1016/C2009-0-21244-X.

M. Jenny, J. Dušek, and G. Bouchet. Instabilities and transition of a sphere falling or ascending freely in a Newtonian fluid. *J. Fluid Mech.*, 508:201–239, 2004. doi: 10.1017/S0022112004009164.

R. Mittal and G. Iaccarino. Immersed boundary methods. *Annu. Rev. Fluid Mech.*, 37(1):239–261, 2005. doi: 10.1146/annurev.fluid.37.061903.175743.

M. Uhlmann and T. Doychev. Sedimentation of a

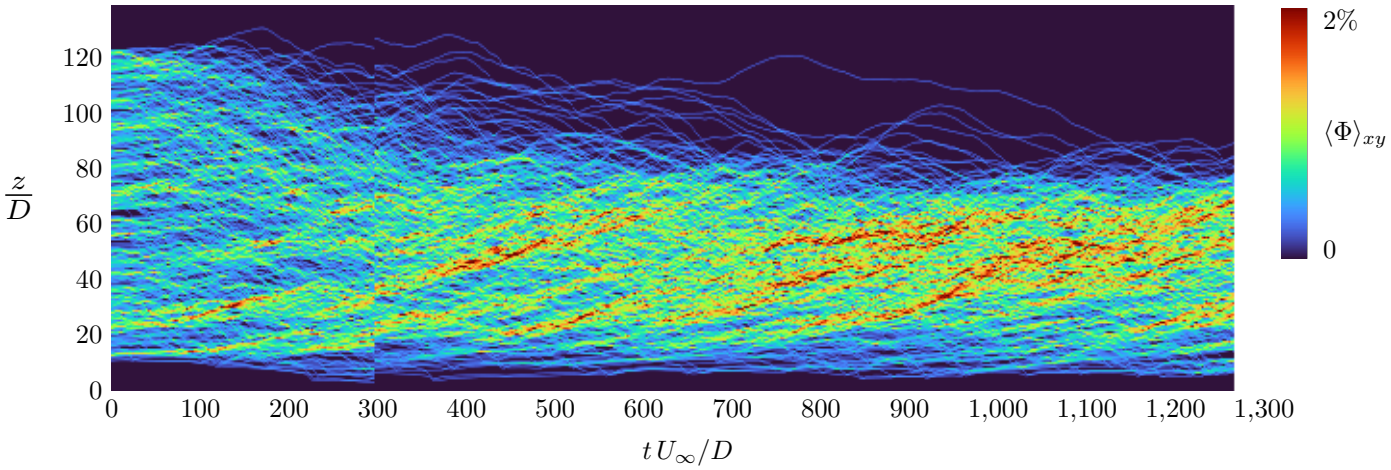

Figure 2: Contour of solid volume fraction averaged over the horizontal directions ($\langle\Phi\rangle_{xy}$) versus time.

dilute suspension of rigid spheres at intermediate Galileo numbers: the effect of clustering upon the particle motion. *J. Fluid Mech.*, 752:310–348, 2014. doi: 10.1017/jfm.2014.330.

Merging theory-based cavitation model adaptable with non-condensable gas effects

Emad Hasani Malekshah[1,*] and Włodzimierz Wróblewski[1]

[1]*Department of Power Engineering and Turbomachinery, Silesian University of Technology, Gliwice, Poland*

The phenomenon of turbulent cavitating flow, with phase change, becomes more complicated taking into account the non-condensable gas as an additional phase. The water, which is the operating fluid, contains a specified amount of dissolved air; as a result, the cavitating flow needs to be considered as a three-phase (i.e. water, vapor and air) flow. Although the existence of dissolved air is well known, most numerical models neglect it; as such, its effect is usually underestimated so far. To this end, the present work is devoted to developing a modified cavitation model based on the merging theory, taking into account the dissolved air in an Eulerian approach. The diffusion process is modeled to constitute the new bubble of the mixture; as a result, the bubble pressure is corrected based on the local air level.

INTRODUCTION

The cavitation phenomenon appears in the liquid flow where the local pressure drops below the saturation pressure. This phenomenon has transient nature and generates noise, vibration and erosion around the object. In the real condition, all liquids contain some amounts of dissolved gas which is inevitable to remove from any substantial volume of liquid. The nuclei are the initiation points for the cavitation phenomenon. Considering the dissolved gas, the partial pressure of the nuclei is composed of the partial pressure of the created vapor in the phase transition and the partial pressure of the non-condensable gas. . Figure 1 illustrates the cavitation around the hydrofoil consisting of the attached sheet cavity, detached sheet cavity and detached bulk/cloud cavity. Moreover, the focus of the present work, which is considering the non-condensable gas, is represented.

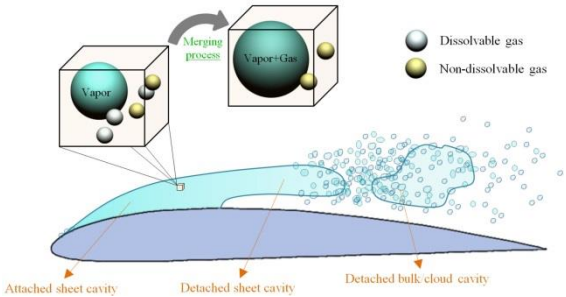

FIG 1. Schematic of cavitation around the hydrofoil and content of cavity.

MULTIPHASE FLOW MODELLING

To treat the multiphase flow, the homogenous mixture model is employed. The governing equations (Eqs.1) are mass and momentum conservation laws. Furthermore, the mass transfer between a liquid and a mixture of gaseous phases (Eqs.2) was modelled between species:

$$\frac{\partial \rho}{\partial t} + \nabla \cdot (\rho \boldsymbol{u}) = 0$$
$$\frac{\partial}{\partial t}(\rho \boldsymbol{u}) + \nabla \cdot (\rho \boldsymbol{u}\boldsymbol{u}) = -\nabla p + \nabla \cdot [\mu(\boldsymbol{\nabla u} + \nabla \boldsymbol{u}^T)] + \rho \boldsymbol{g} \quad (1)$$

$$\frac{\partial \rho_g \alpha_g}{\partial t} + \nabla \cdot (\rho_g \alpha_g \boldsymbol{u}) = 0$$
$$\frac{\partial \rho_v \alpha_v}{\partial t} + \nabla \cdot (\rho_v \alpha_v \boldsymbol{u}) = R \quad (2)$$

The standard $k-\varepsilon$ RNG turbulence model is used where the turbulent viscosity is modified based on Density-Corrected based Model (DCM).

- **Modified cavitation model**

The present cavitation model is inspired by the mass transfer equation of vapor volume fraction, which originated from the Rayleigh-Plesset (RP) equation. The modified RP equation is given as follows:

$$R_B \frac{d^2 R_B}{dt^2} + \frac{3}{2}\left(\frac{dR_B}{dt}\right)^2 + \frac{4\mu_l}{\rho_l R_B}\left(\frac{dR_B}{dt}\right) + \frac{2S}{\rho_l R_B} = \frac{p_B - p}{\rho_l}$$
$$p_B = p_V + p_{G0}\left(\frac{R_0}{R}\right)^{3\gamma}$$

To estimate the mixture bubble pressure (p_B), the merging process is employed which is illustrated as follows (Fig.2):

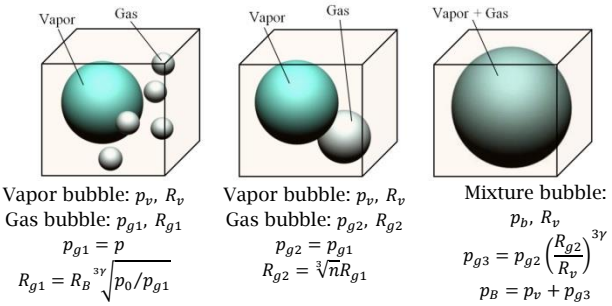

FIG 2. Merging process.

The modified source terms are as:

$$R_e = F_{vap}\frac{3\alpha_{nuc}(1-\alpha_v)\rho_v}{R_B}\sqrt{\frac{2}{3}\frac{p_B - p}{\rho_l}},\ p_B > p$$
$$R_c = -F_{cond}\frac{3\alpha_v \rho_v}{R_B}\sqrt{\frac{2}{3}\frac{p - p_B}{\rho_l}},\ p_B < p \quad (3)$$

RESULTS

To validate the developed modified RP equation, the collapse process of a single bubble predicted by Eq.46 compared with experimental data reported by Tinguely et al. [1] for the case with $p_v = 3460Pa$, $p = 80000Pa$, $\alpha_v = 1.0$ and $\alpha_{ng} = 0.0$ is shown in Fig.3.

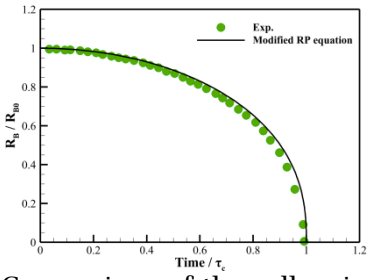

FIG 3. Comparison of the collapsing process of a single bubble predicted by RP equation and experimental measurements.

Impacts of modified cavitation model on the morphological and periodical characteristics are illustrated in this section. Fig.4 declares the changes on shedding frequency in the modified zone which is closer to experimental data.

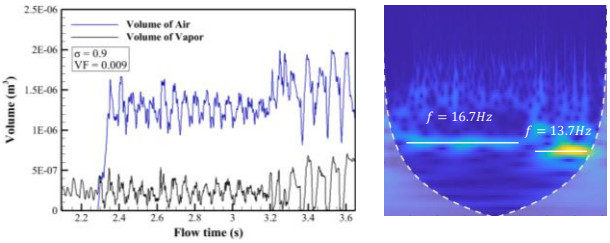

FIG 4. PSD based on vapor VF and lift coefficient distributions.

The effect of cavitation number and volume fractions of dissolved air on the shedding frequency is shown in Fig.5-6. The Temporal-spatial distribution of grey level is used and presented in Fig.6 to detect the re-entrant jet.

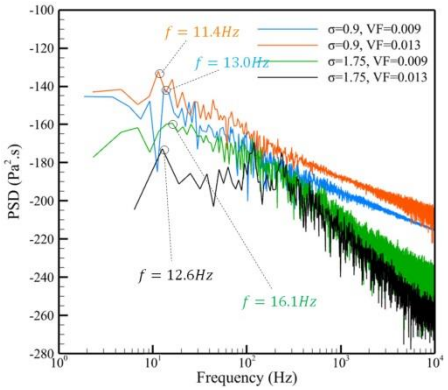

FIG 5. PSD based on vapor VF distribution.

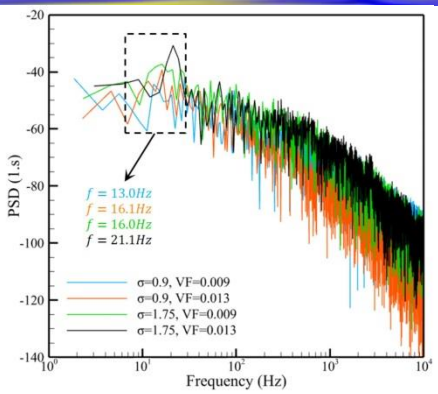

FIG 6. PSD based on vapor lift coefficient distribution.

One of the important characteristics of the cavitating flow which is highly influenced by numerical methods is the structure of the cavity during the periods. The corrected turbulence model reduces the overestimation of turbulent viscosity and damping of the flow, especially inside the cavity region. The evolutions of the cavitation based on the experimental observation, semi-modified and modified numerical approaches are illustrated in Fig.7. Based on the experimental photos, it is observed that the cavitation starts from sheet cavity-type and extends with time. In the middle of the period, the largest cavity length so-called cloud cavity appears. Then, the cloud cavity is collapsed and shed downstream.

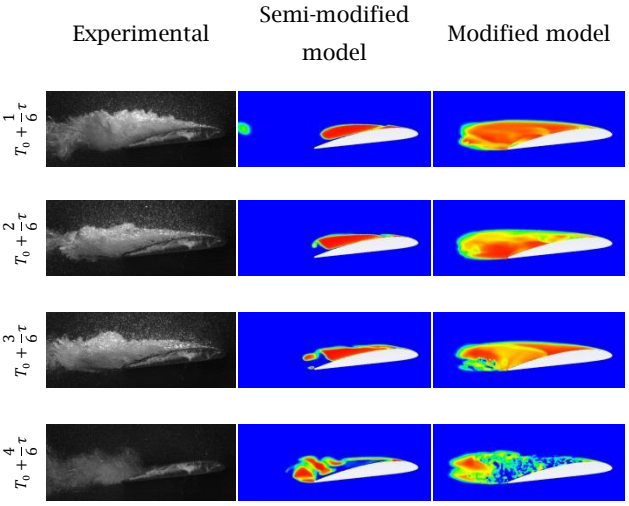

FIG 7. PSD based on vapor VF distribution.

CONCLUSIONS

The modified cavitation model leads to more realistic results comparing with Exp. observations. The shedding frequency is corrected. Also, the larger cavitation which is well-matched with the experimental observations.

* emad.hasani@polsl.pl

[1] M. Tinguely, D. Obreschkow, P. Kobel, N. Dorsaz, A. De Bosset, and M. Farhat, "Energy partition at the collapse of spherical cavitation bubbles," *Physical Review E,* vol. 86, no. 4, p. 046315, 2012.

Modeling Wildland Fire Spot Ignition by Metal Sparks: Fluid Mechanics Aspects

[a] Carlos Fernandez-Pello and [b]James Urban

[a] Department of Mechanical Engineering, University of California Berkeley,
Berkeley, CA, 94720, USA
[b] Department of Fire Protection Engineering, Worcester Polytechnic Institute (WPI),
Worcester, MA 01609, USA

Extended Abstract

Wildland, and Wildland Urban Interface (WUI), fires are a problem in many areas of the world, and may have major consequences in terms of safety, air quality, damage to the infrastructure and the ecosystem. It is expected that with climate change the wildland fire and WUI fire problem will only intensify. The spot fire ignition of a wildland fire by hot metal particles/sparks is an important fire ignition pathway by which wildfires, WUI fires, are started, and may propagate. There are numerous cases reported of wildland fires started by hot metal particles from clashing power-lines, or generated by machines. Spot ignition of a wildland fire by hot metal particles can be separated in three major processes: particle generation and ejection characteristics; coupled transport and thermochemical change during the particle flight to the ground; and potential ignition of target fuel bed. The particle characteristics at generation are normally obtained from experiments. Once the metal particles are ejected from their source, the particles experience both drag by the wind and gravitational forces during their flight. The model used to calculate the trajectory and temperature history uses conventional fluid mechanics calculations and is basically a ballistic trajectory simulation with a hot body cooling to the ambient air. The resulting particle trajectory is roughly parabolic, and the landing location depends on the particle generation location, ejection velocity (magnitude and direction), the wind velocity (magnitude and direction) and particle characteristics (diameter, temperature). During the trajectory the metal particles cool down by convection and radiation reaching the ground at a temperature that depends of the particle initial characteristics and ambient air conditions. After landing the particles may have the potential to ignite a bed of vegetation depending on their size and temperature at landing, and the characteristics of the fuel bed. The fuel bed ignition process has a strong thermo-fluids component, including: the heating of the fuel by the spark in a porous media convective environment; the fuel gasification; the mixing of the gaseous fuel and air; and finally the ignition of the flammable mixture by the metal particle. All of these processes involved several complex thermofluidic mechanisms. In this study we present a methodology to analyze the problem and an application to a specific wildland fire case that occurred in the estate of Washington, USA.

Background

Spot ignition of a wildland fire by hot metal particles can be separated in three major processes [2]: particle generation and characteristics; coupled transport & thermochemical change; and potential ignition of target fuel either as a smolder or flaming. This methodology is applied in the present study to determine if hot particles generated during the hot work at the Taylor bridge was capable of igniting the Taylor Bridge wildland fire. The particle characteristics at ejection, both from grinding and welding, are obtained from experiments conducted in the reports of Refs. [3] and [4]. The model used to calculate the trajectory and temperature history is that of Ref. [5], which is basically a ballistic trajectory simulation with a hot body cooling to the ambient air. In the model application, the ejected particles are characterized by their generation location, initial size, ejection velocity, and initial temperature. Once the particles are ejected by the saw blade or the welder, the particles experience both drag and gravitational forces during their flight. The resulting particle trajectory is roughly parabolic and the landing location depends on the particle size,

ejection velocity (magnitude and direction), and the wind velocity (magnitude and direction). During the trajectory the metal particles cool down reaching the ground at a temperature that depends of the particle initial characteristics and ambient conditions. After landing the particles may have the potential to ignite (smolder or flaming) a bed of vegetation depending on their size and temperature at landing and the characteristics of the fuel bed [2, 5]. The issue in the present study is whether some of the particles generated during the grinding or welding could fall in the alleged area of fire origin [1] and could have the thermal characteristics necessary for igniting the thin vegetation (duff, grass) at the landing location.

Analysis

Scenario 1: Rebar Cutting (grinding) on the Top of the Bridge

During the rebar cutting (grinding) a shower of hot steel particles is generated by the grinding blade of the cutting tool. The particles would have different sizes and would be ejected in the direction of rotation of the blade at velocities that depend on the blade rotation speed and characteristics. The particle temperature at ejection woud depend on the blade speed and force applied by the blade on the steel during cutting.These particles would be carried by the wind in its prevailing direction falling to the ground at distances from the rebar cutting location that depended on the wind velocity, and particle ejection velocity and size. The issue is whether some of these particles could fall in the alleged area of fire origin [1] and could have the thermal characteristics necessary for igniting the thin vegetation (duff, grass) at the landing location [6]. As mentioned above there is an established methodology to calculate the trajectories that the particle would follow [5] for a given set of conditions, that has been applied here to calculate the trajectories that particles generated by the rebar cutting would follow. The parameters used for the calculations are as follows: particle diameters for the ejecta from the abrasive cutting (grinding), between 1.0 mm and 2.5 mm, is based on data provided by [3] and [4]; the ejection height, approximately 12 m [1], and the wind speed of 11 m/s is based on information from [1]; an initial particle temperature of 1310 C is selected based on data provided in [7]; and two ejection velocities of 4.65 m/s and 11 m/s are obtained from [4]. An example of the calculated particle trajectories is given in Figure 1 for particles with different diameters and two different ejection speeds. Also indicated in the figure is the approximate region (section of radial distance from the location of rebar cutting) for the origins of the fire identified in the DNR Fire Investigation Report [1].

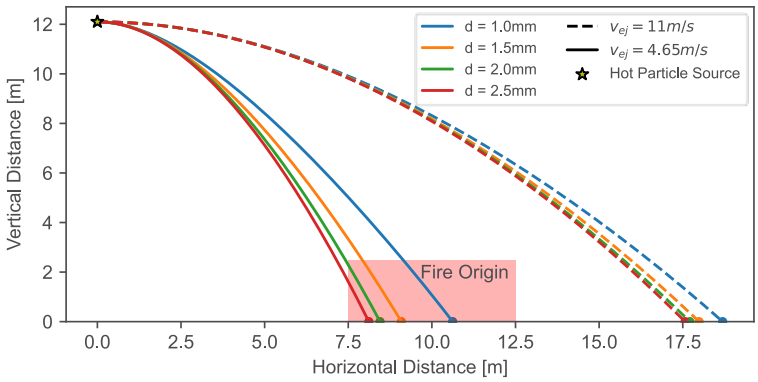

Figure 1. Trajectories of rebar cutting particles for different diameters, two ejection velocities and a wind of 11 m/s. Boundaries of approximate fire origin are also indicated.

The distribution of the landing locations of the particles in relation to the bridge and the origin of the sparks are shown in Fig. 2 for several particle diameters, ejection velocities, and wind speed. The landing locations of the sparks are colored according to the size of the generated particles. The sparks land in different

locations depending on the ejection velocity (speed and direction) and the wind velocity (speed and direction). The fire origins denoted determined by the DNR report are shown with white circles [1].

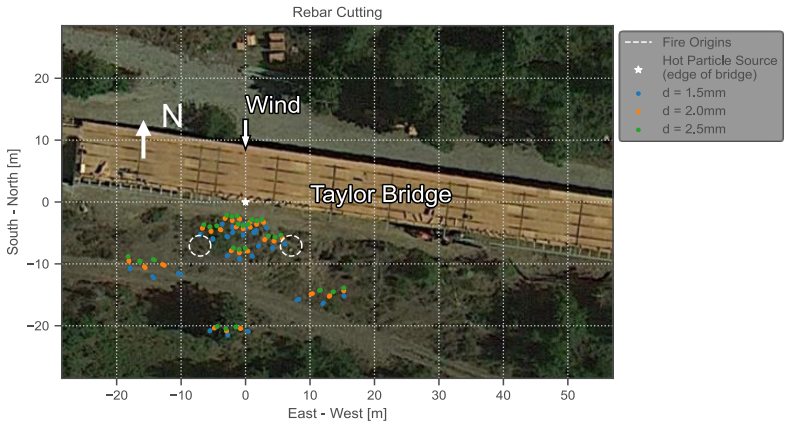

Figure 2 Landing locations of particles generated by the rebar cutting in a southern wind of 11 m/s. Map image obtained using Google Earth for July 10th, 2012

The ability of these particles to ignite a fire after landing on the ground depends on their size and temperature at landing as well as the type of fuel they land on. To evaluate the ignition capability of these particles we can compare the ignition conditions to the ignition boundaries determined through controlled experiments [6]. The calculated conditions (temperature and diameter) of the grinding sparks at the time of landing are shown in Fig. 3, together with ignition boundaries (flaming and smoldering ignition) for a powdered grass fuel bed by hot steel particles [6]. The ignition boundaries were determined through experiments dropping steel particles of known size and temperature onto a well characterized fuel be. It is seen that particles with sizes larger than 2 mm in diameter could initiate a smolder fire upon landing on fine vegetation.

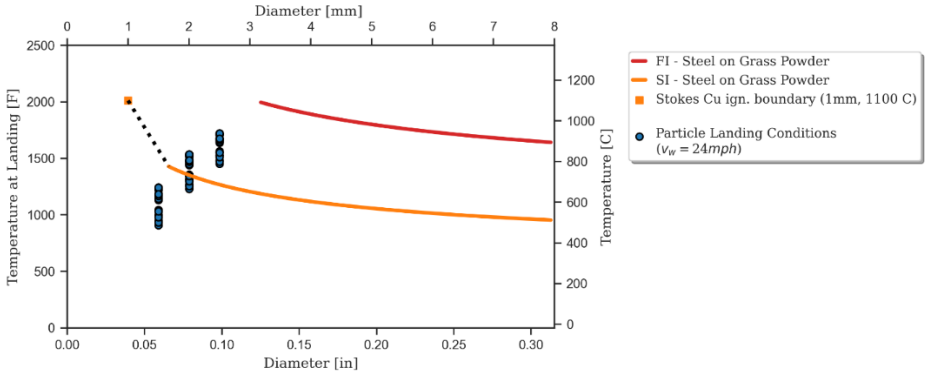

Figure 3 Landing conditions of particles generated by the rebar cutting. The particle diameters and temperature are compared to ignition boundaries for a grass blend powder by hot steel particles.

Scenario 2: Welding Beneath the Bridge

During the process of welding of the bottom structure of the bridge a shower of hot/molten steel particles would be generated by arcing of the welding rod and steel structure. These particles would have different diameters and be ejected in different directions, and would be carried by the prevailing wind falling to the ground at distances from the particle origin depending on the wind velocity and particle size. As in the case of the rebar cutting, the trajectories of these particles are calculated with the methodology of [5]. The

parameters used for the calculations are as follows: the particle diameters are based on data provided by [3] and [4]; the welding spatter is assumed to be generated at a height of 10 m above the ground at the base of the piers, corresponding the underside of the bridge [1]; the spatter initial temperature it is assumed to have a maximum value of 2862 C, the boiling point of steel; the wind speed is 11 m/s; and ejection velocities of 2, 3, 4, 5 m/s are selected from [5].

An example of the calculated particle trajectories is given in Fig. 4 for particles with 2 mm diameter and various ejection velocities. Also indicated in the figure are the approximate boundaries (distance for the bridge) identified in [1] for the origin of the fire.

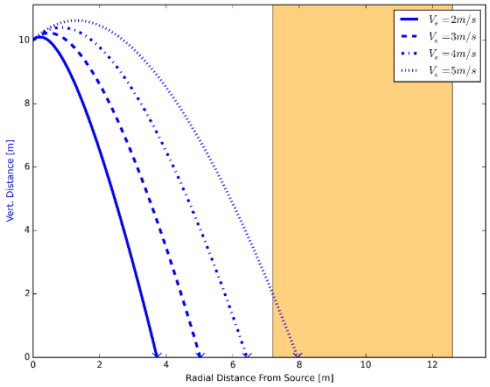

Figure 4. Trajectories of welding particles 2 mm in diameter and several ejection velocities. Boundaries of approximate fire origin are also indicated.

The possible landing locations of particles generated by the welding beneath the bridge superimposed over image obtained using Google Earth are presented in Fig. 5 for different particle diameters. It should be noted that the particles would have landed under the bridge, not on it. The figure shows that particles of sizes up to 1.5 mm could have landed on the norther region in the fire origin area.

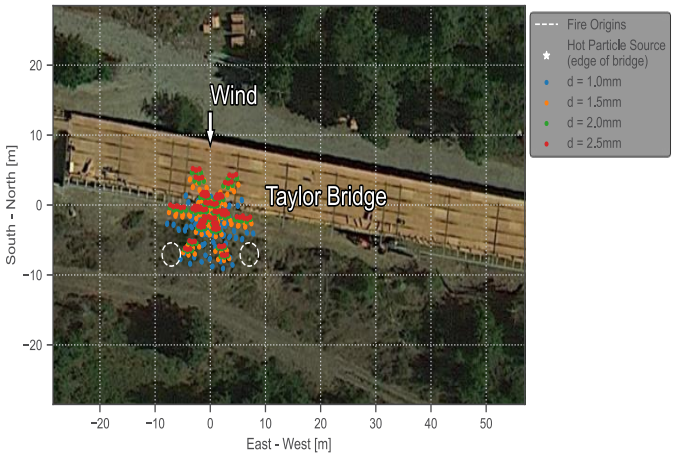

Figure 5. Landing locations of particles generated by the rebar cutting for a southern wind. Map image obtained using Google Earth for July 10th, 2012

The calculated conditions (temperature and diameter) of the welding particles at the time of landing are shown in Fig. 6. plotted with ignition boundaries (flaming and smoldering ignition) for a powdered grass fuel bed by hot steel particles [6]. It is seen that particles with sizes smaller than 1.5 mm in diameter could barely initiate a smolder fire upon landing on fine vegetation. Larger particles would have a higher probability of igniting a fire but would land short of the identified location of fire initiation.

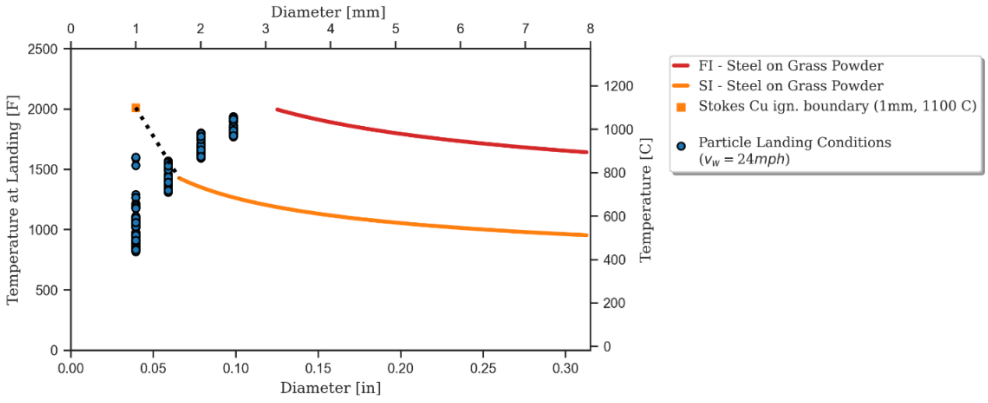

Figure 6 Landing conditions of particles generated by welding. The particle diameters and temperature are compared to ignition boundaries for a grass blend powder by hot steel particles.

Conclusion

The present analysis indicates that although both the hot particles generated by rebar cutting, or welding of the bridge structures, had the potential to ignite a wildland fire, there are differences in their landing location and ignition characteristics that show different probabilities of ignition. The grinding steel particles would have landed at longer distances from the bridge, at and beyond the area of fire origin, than the welding particles, thus with more potential for igniting the fire. However, the grinding particles would land with smaller sizes and temperatures, and consequently less potential for igniting the fire. Although the welding generated particles were hotter and bigger at landing, and consequently with more potential for ignition, their landing locations were somewhat shorter than the alleged location of fire origin, although that location of the ignition area is only approximate.

It should be noted, however, that the results presented above are for single particles. In the case of rebar cutting with a grinding disc a shower of particles would have been generated. This may cause the accumulation of multiple particles at the landing location with the result of having an equivalent larger particle with a higher capability of igniting the vegetation. At the same time, the determination of the area of fire origin is somewhat empirical and it is possible that the fire origin was closer to the bridge than alleged. However, although there is not a clear conclusion of what hot-work caused the fire, it is more likely that it was the rebar cutting than the welding, because the grinding sparks would have reach a wider area with a higher probability of landing on a finer and easier to ignite fuel

References

[1] D. E. Heryford, "Incident Number: 12-E-CBX County : Kittitas State of Washington, Department of Natural Resources, Wildland Fire Investigation Report. 2012.
[2] A. C. Fernandez-Pello C. Fernandez-Pello “Wildland Fire Spot Ignition by Sparks and Firebrands” Fire Safety Journal, 91, p. 2-110 (2017)
[3] M. Suryan, “Flight characteristics and thermal behavior of hot work particles near the Taylor Bridge fire" Case report 2014.
[4] J. Zicherman, “Rebar Cutting and the Taylor Bridge Fire,” Case report 2014.
[5] S. D. Tse and A. C. Fernandez-Pello, “On the flight paths of metal particles and embers generated by power lines in high winds - a potential source of wildland fires,” *Fire Saf. J.*, vol. 30, pp. 333–356, 1998,
[6] J. L. Urban, C. D. Zak, J. Song, and C. Fernandez-Pello, “Smoldering spot ignition of natural fuels by a hot metal particle,” *Proc. Combust. Inst.*, vol. 36, no. 2, pp. 3211--3218, 2017,
[7] V. Babrauskas, *Ignition Handbook*. Fire Science Publishers, 2003.

2nd Spanish Fluid Mechanics Conference
Barcelona (2 - 5 July 2023)

On the purely inertial collapse of gas cavities: Bubble bursting jets

José M. Gordillo[1] and Francisco J. Blanco-Rodríguez[1]

jgordill@us.es

[1]Área de Mecánica de Fluidos, Departamento de Ingeniería Aeroespacial y Mecánica de Fluidos, Universidad de Sevilla, Avenida de los Descubrimientos s/n 41092, Sevilla, Spain

Our numerical simulations reveal that the jets originated from the bursting of bubbles are driven by the condition that the dimensionless liquid flow rate per unit length directed towards the axis of symmetry, q_∞, remains nearly constant in time. This is so because liquid inertia prevents appreciable changes in q_∞ during the short time scale characterizing the jet ejection process, which justify the purely inertial scalings for the jet width and velocity found here, $r_{jet} \propto \sqrt{q_\infty \tau}$ and $v_{jet} \propto \sqrt{q_\infty/\tau}$, with τ indicating the dimensionless time after the jet is ejected, a result which notably differs from the common belief that the jet width and velocity follow the inertio-capillary scaling $r_{jet} \propto \tau^{2/3}$ and $v_{jet} \propto \tau^{-1/3}$. Our physical description, which neglects capillary forces, is in close agreement with numerical simulations from the instant of jet inception until the jet width is comparable to that of the initial bubble.

1 Introduction

In a recent contribution, Lai, Eggers and Deike (2018) studied the spatio-temporal evolution of the shapes of the jets ejected after a bubble bursts at an interface, like the ones depicted in Fig. 1, finding that their results are compatible with the inertio-capillary scaling $r_{jet}(\tau) \propto \tau^{2/3}$; in contrast, we find here that this scaling is not valid to quantify the instants *after* the jet is ejected. Indeed, the inertio-capillary scaling is characterized by the fact that the capillary and the dynamic pressure terms in the governing equations balance each other and, if the conclusions in Lai, Eggers and Deike (2018) were correct, the value of the dimensionless number expressing the ratio between the dynamic and capillary pressures namely, the local Weber number defined as $We_l = v_{jet}^2 r_{jet}$, see the rightmost panel in Fig. 1a, should remain constant in time along the whole jet ejection process. However, the results depicted in Fig. 2 reveal that: i) $We_l \gg 1$ for all values of $\tau > 0$, a fact already suggesting that the jet dynamics cannot be driven by capillary forces and ii) We_l is far from being a constant since $We_l \propto \tau^{-1/2}$ for $\tau \gtrsim 10^{-3}$.

The reason why $We_l \propto \tau^{-1/2}$ for $\tau \gtrsim 10^{-3}$ is explained in the inset of Fig. 2, where we find that the value of the dimensionless flow rate per unit length $q = -r\, v_r$ remains approximately constant in time for different values of $r/r_{jet}(\tau)$ and $z/z_{jet}(\tau)$, with v_r denoting the radial velocity. Indeed, if $r_{jet} \propto z_{jet} \propto \tau^\alpha$, velocities are proportional to $v_{jet} \propto \tau^{\alpha-1}$ and, since the results shown in the inset of Fig. 2 indicate that $r_{jet} v_{jet} \propto \tau^{2\alpha-1} \approx const$, we conclude that $\alpha = 1/2$, which explains the result $We_l \propto \tau^{-1/2}$ for $\tau \gtrsim 10^{-3}$ depicted in Fig. 2. The physical mechanism driving the ejection of bubble bursting jets can be summarized as follows: during the capillary collapse of the cavity, the liquid is accelerated inwards, inducing a radial inflow per unit length towards the axis of symmetry which, in dimensionless terms, is $q_\infty \approx 1$. Then, along the very short transient $\tau \ll 1$ during which the conical cavity collapses –see Figs. 1-2–, the flow rate q_∞ acts as the far field boundary condition driving the jet ejection process. Hence, liquid inertia ensures the constancy of the flow rate per unit length, which forces the inward motion of the conical cavity walls –see Fig. 1– and, therefore, the jet is issued as a mere consequence of mass conservation.

The reason why the local Weber number deviates from $We_l \propto \tau^{-1/2}$ for $\tau \ll 1$, see Fig. 2, relies on the fact that, in analogy with the case of the purely inertial pinch-off of bubbles, the flow rate per unit length of liquid directed towards the axis of symmetry is no longer a constant for $r_{jet} \ll 1$, but $q_\infty(r_{jet})$ decreases with r_{jet} logarithmically, see Gordillo and Blanco-Rodríguez (2023)a for details.

2 Conclusions

To conclude, here we have shown that high speed jets result from an imposed far field value of the flow rate per unit length and, consequently, the smaller is the radius of the bottom of the cavity from which the jet is issued and the larger is the value of the forcing flow rate per unit length q_∞, the larger is the jet velocity.

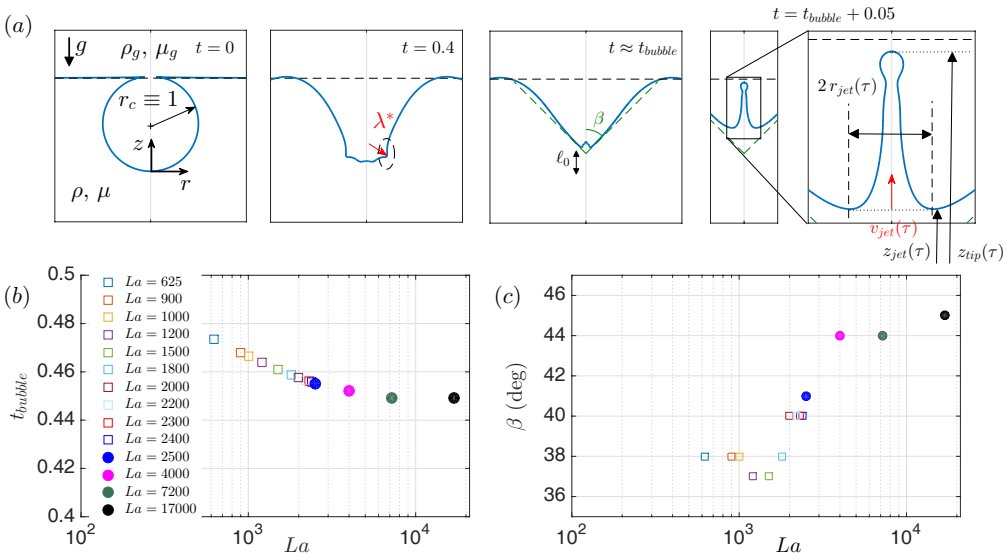

Figure 1: (a) Bursting of a bubble of radius R_b in a liquid of density ρ, viscosity μ and interfacial tension coefficient σ for a negligible value of the Bond number and $La = Oh^{-2} = \rho R_b \sigma/\mu^2 = 7200$. The rightmost panel shows the definitions of the jet width, $r_{jet}(\tau)$ and of the jet velocity, $v_{jet}(\tau)$. (b) Time taken by the capillary waves to reach the bottom of the cavity as a function of La. (c) Semiangle of the truncated cone from which jets are ejected as a function of La.

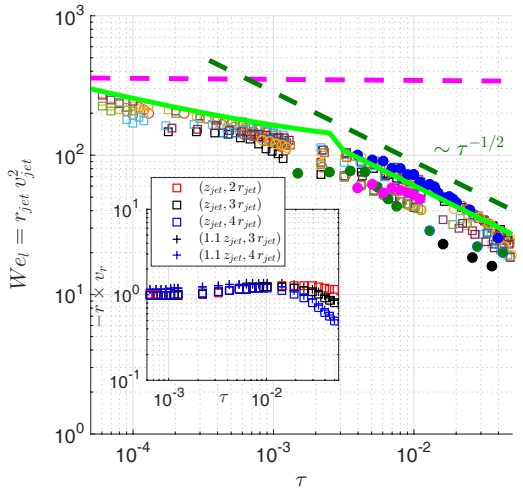

Figure 2: The value of the local Weber number is such that $We_l = r_{jet} v_{jet}^2 \gg 1$, with $We_l \propto \tau^{-1/2}$ for $\tau \gtrsim 10^{-3}$, a result indicating that $r_{jet} \propto \sqrt{q_\infty \tau}$ and $v_{jet} \propto \sqrt{q_\infty/\tau}$, as it is explained in the text using the results in the inset, where it is shown that the values of the flow rate per unit length calculated using `GERRIS` as $q = -r\, v_r$ for $La = 2400$ and different values of $r/r_{jet}(\tau)$ and $z/z_{jet}(\tau)$, remain nearly constant along two decades in time. The green line indicates the predicted values of $We_l(r_{jet}(\tau)) = v_{jet}^2\, r_{jet} = [3.4\, q_\infty(r_{jet}(\tau))]^2 / r_{jet}(\tau)$, with r_{jet} and v_{jet} calculated using the results in Gordillo and Blanco-Rodríguez (2023)(a,b).

Our results are further supported by the theory in Gordillo and Blanco-Rodríguez (2023)b, where we analyze the 'impact' of an axisymmetric irrotational flow over $r = 0$ using Wagner's framework, originally envisaged to study the impact of two dimensional solids with a small deadrise angle over a free interface. Notice that the results in Gordillo and Blanco-Rodríguez (2023)(a,b) might well be applied to describe the very fast jets, with velocities up to 1000 ms^{-1} emerging from the tip of the imploding bubbles produced when a liquid cavitates in very close proximity to a wall.

References

C.Y. Lai, J.G. Eggers and L. Deike (2018) "Bubble bursting: Universal cavity and jet profiles". *Phys. Rev. Lett.*, **121**, 144501.

J.M. Gordillo and F.J. Blanco-Rodríguez (2023) "Bubble bursting jets are driven by the purely inertial collapse of gas cavities". *Phys. Rev. Lett.* (Submitted), **arXiv:2303.03847**.

J.M. Gordillo and F.J. Blanco-Rodríguez (2023) "On the jets ejected after the inertial collapse of cavities". *Phys. Rev. Fluids* (Submitted), **arXiv:2303.03815**.

2nd Spanish Fluid Mechanics Conference
Barcelona (2 - 5 July 2023)

Response of a Drop of Eutectic Indium-Gallium to an Electric Current

Javier Otero Martínez[1], Ana García Armada[1], and Javier Rodríguez Rodríguez[2]

jotero@pa.uc3m.es

[1]Department of Signal Theory and Communications, Universidad Carlos III de Madrid, Spain
[2]Department of Thermal and Fluid Engineering, Universidad Carlos III de Madrid, Spain

This work describes the response of a drop of eutectic Indium-Gallium alloy (eGaIn) when excited with alternating electric currents of different amplitudes and frequencies. We report the measured velocities of the drop as a function of the distance to the electrodes, peak-to-peak voltage, and frequency. The outcome would enable the development of new antenna-related applications.

1 Introduction and Motivation

Eutectic Indium-Gallium (commonly known as eGaIn) is liquid at room temperature. In consequence, it has become a trendy, non-toxic replacement for mercury. Consequently, it is necessary to focus on its fundamental properties to develop new applications in relation to next-generation communication devices. As it is going to be described, electrowetting may play a vital role in achieving real-time reconfiguration in such antennas. However, it is needed to further characterize this technique and its application to eGaIn to be able to incorporate the technology into the antenna framework. This work studies the motion of an eGaIn drop when different voltage inputs are applied.

1.1 Electrowetting

Electrowetting is the name of the phenomenon that occurs when the drop changes its wettability towards a given direction, being defined by the application of an electric tension [2]. For this to happen, our eGaIn drop must be submerged in an electrolyte able to conduct such electric impulses. When a voltage is applied to the drop-electrolyte system, a potential gradient appears, changing the charge distribution along the interface of the drop and hence creating a gradient in the surface tension of the eGaIn. This results in a pressure modification along the system, producing motion toward the positive electrode thanks to Marangoni forces.

Therefore, the buffer solution plays a double role in this setup. Firstly, it serves as an electrolyte capable of guiding electricity to the liquid metal. Secondly, it forms a barrier that prevents the formation of oxide, which steadily happens when eGaIn is exposed to air. This layer of oxide is totally undesirable for this application. It prevents the drop from flowing through the capillary, limiting the usability of this technique.

1.2 Antenna Applications

The idea behind liquid antennas is to use the physical shape of such devices as an additional degree of freedom, which may reduce the hardware complexity and scalability of some systems. Antennas that are able to change their radiation parameters to match different specifications are called reconfigurable antennas. It is particularly interesting to do it in a real-time approach. There are already ways to achieve reconfiguration in antenna theory, but they require costly, space-consuming electronic devices. Being able to achieve this spatial reconfigurability could be very useful for a variety of applications that nowadays impose the use of many communication protocols, which require different specifications. Undoubtedly, a pumping method is required to shape the antenna. In comparison to mechanical pumping devices, electrowetting allows to minimize the use of mobile parts, which are more likely to malfunction after long usage. However, the application of this technique to radio-frequency (RF) devices must overcome several challenges. The accuracy of the position of the drop is crucial for RF applications, as a minimum misplacement may severely degrade the performance of the system. Moreover, the high density of eGaIn has a direct effect on the inertial forces of the drop, which needs not only to move but also to 'brake' in a controlled manner. Note that the challenges mentioned also apply to mechanical pumps; here the motivation is to exploit the possibilities of electrowetting.

2 Methodology

A channel is created by drilling a slender slot in a nylon plate. Such a plate is glued to another glass plate

that has no drilling. Since the slot would contain the buffer solution, it is guaranteed that there are no leaks between the plates. When a PTFE capillary of 1/16" inner diameter is inserted into the slot, it is possible to fill it with the buffer solution. An eGaIn drop is then placed inside the tube using a syringe, and two platinum electrodes are introduced to provide the current, as shown in Figure 1. The use of a PTFE capillary is almost a must due to its low friction coefficient, with allows eGaIn to move with ease. As mentioned, eGaIn must not be in contact with air to prevent oxidation. According to many authors [3], a suitable solution would be using a 1 Molar NaOH buffer solution, as it was mentioned above.

With this setup, it is possible to use different currents with variations in peak-to-peak voltage, frequency, and pulse shape i.e. sinusoidal, squared, etc.). It is also possible to change the length of the eGaIn drop in different repetitions. Both electrodes are connected to a screw that allows their placement to be precise.

3 Experimental Results

In this first series of experiments, a drop with fixed length - throughout the repetitions - is placed and different values of amplitude and frequency are tested. After the processing stage, Figure 2 shows the position, length, and speed of the drop when exciting the system with a sinusoidal current.

Generally, it is observed that the shape of the drop position does not perfectly match a sinusoidal shape hence, some kind of distortion is occurring. For higher voltages and frequencies, it has been seen that the uniformity of the drop is not maintained. Due to inertial forces, the drop can no longer be considered cylindrical as its edges get thicker or thinner, depending on the sign of the excitation. For large values and long drops, splitting is also observed. Rigorous characterization of these phenomena can be extracted from the experiments, which are currently in progress.

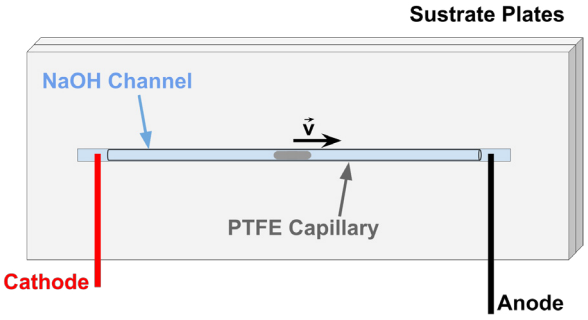

Figure 1: Experimental setup sketch (upper view).

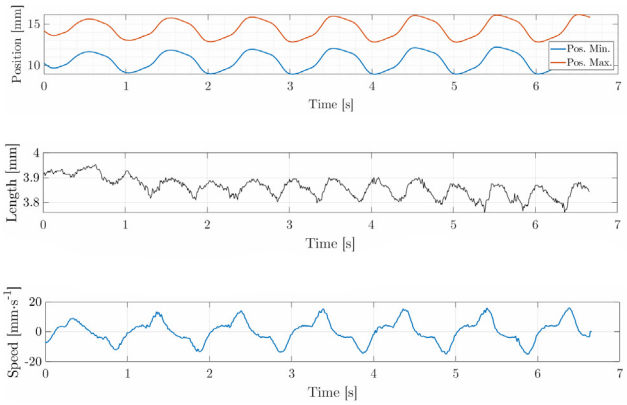

Figure 2: Experimental result example for 1Hz and 1.5Vpp. Drop edges position (above), drop length (middle) and drop velocity (beneath).

4 Conclusions

We have observed and documented the effect of exposing a drop of eGaIn to different excitations. These experiments are still taking place. However, we expect to provide a transfer function that allows us to characterize the time response of the drop to different currents, which will be fundamental in order to design and manufacture new generation devices based on liquid antennas.

References

[1] J. Otero Martınez, J. R. Rodrıguez, Y. Shen, K.-F. Tong, K.-K. Wong, and A. G. Armada , *IEEE Comms. Mag.*, **60** (2022)

[2] R. C. Gough, A. M. Morishita, J. H. Dang, W. Hu, W. A. Shiroma, and A. T. Ohta, *IEEE Access*, **2** (2014)

[3] M. D. Dickey, R. C. Chiechi, R. J. Larsen, E. A. Weiss, D. A. Weitz, and G. M. Whitesides, *Advanced functional materials*, **18** (2008)

Acknowledgments

Part of this work has been financed by IRENE-EARTH Project (PID2020-115323RB-C33 / AEI / 10.13039/501100011033) and by Spanish MCIN/AEI/10.13039/501100011033 through Grant No. PID2020-114945RB-C21.

2nd Spanish Fluid Mechanics Conference
Barcelona (2 - 5 July 2023)

Short and long term dispersion of airborne pathogen-laden aerosols expelled in a violent expiratory event

Jordi Pallares[1], Akim Lavrinenko[1], Salvatore Cito[1], Anton Vernet[1], and Alexandre Fabregat[1]

jordi.pallares@urv.cat

[1]Departament d'Enginyeria Mecànica. Universitat Rovira i Virgili, Tarragona, Spain

In this paper, we summarize the efforts of our research group to analyze the physics behind the short-term and long-term indoor dispersion of pathogen-laden aerosols generated in a violent expiratory event. The Coronavirus Disease 2019 (COVID-19) pandemic has revealed the need for a better understanding of the flow physics that govern the airborne transmission of infectious diseases via pathogen-laden aerosols expelled during coughs, sneezes or while talking or singing. Numerical and experimental analyses of the short-term and long-term flow and particle dispersion produced by expiratory events have unveiled important underlying physical mechanisms and allowed prediction of the short-range risk of infection one to two seconds after expiration and during the long-term aerosol cloud indoor dispersion produced by the background ventilation currents.

1 Short-term dispersion

To analyze the short-term flow and particle dispersion we performed a reference Direct Numerical Simulation (DNS) of an idealized mild cough (Fabregat et al. 2021a) (Fabregat et al. 2021b), Large-Eddy Simulations (LES) considering the complex geometry of the upper respiratory tract and a typical head movement during coughing (Pallares et al. 2022) and developed a theoretical model for a fast prediction of the shape and range of the thermal cloud generated in a violent expiratory event (Pallares and Fabregat 2022). In addition, and to determine the capabilities of the current available Computational Fluid Dynamics (CFD) techniques, we have organized the "2022 International CFD Challenge on violent expiratory events" aimed at assessing the ability of different computational codes and turbulence models to reproduce the flow generated by a rapid prototypical exhalation and the dispersion of the aerosol cloud it produces. Given a common flow configuration, a total of seven research teams from different countries have performed a total of twelve numerical simulations of the flow and particle dispersion by solving the Unsteady Reynolds Averaged Navier-Stokes (URANS) or using LES techniques. The results of each team have been compared with each other and assessed against a DNS of the exact same flow.

2 Long-term dispersion

Long-term aerosol dispersion has been studied numerically by analyzing the mixing of particle clouds produced by a turbulent natural convection flow in a room-size ($L \approx 3m$) enclosed cavity. In this case, the flow is generated by differentially heating two opposite consecutive horizontal and vertical walls of the cavity. Direct Numerical Simulations of the flow at $Ra = 3.6 \cdot 10^9$ ($Pr = 0.71$) have been conducted. We tracked clouds of particles, initially located at different positions inside the cavity to determine the rate of mixing and dilution of the cloud. It has been found that particle clouds released near the thermally active walls disperse at a larger rate than clouds initially located near the center of the cavity.

References

Fabregat et al. (2021). Physics of Fluids, 33(3), 035122.

Fabregat et al. (2021). Physics of Fluids, 33(3), 033329.

Pallares et al. (2022). Journal of Aerosol Science, 166, 106052.

Pallares, J. and Fabregat, A. (2022). Indoor and Built Environment, 31.5: 1393-1404.

2nd Spanish Fluid Mechanics Conference
Barcelona (2 - 5 July 2023)

Stable production of liquid jets with vanishing diameters via tip streaming

J. M. Montanero[1], M. Rubio[2], J. Eggers[3], and M. A. Herrada[4]

jmm@unex.es

[1]Departamento de Ingeniería Mecánica, Energética y de los Materiales, Universidad de Extremadura, Spain
[2]Departamento de Ingeniería Energética y Fluidomecánica, Universidad de Vallalodid, Spain
[3]School of Mathematics, University of Bristol, Fry Building, Bristol BS8 1UG, UK
[4]Departamento de Ingeniería Aeroespacial y Mecánica de Fluidos,, Universidad de Sevilla, Sevilla, Spain

We analyze the linear stability of the tip streaming produced by a linear extensional flow. Our numerical results show that jets with vanishingly small diameters can be formed for sufficiently large inner and outer viscosities, independently of the jet density and the outer flow intensity. These results may guide the production of monodisperse collections of drops and capsules with arbitrarily small diameters.

1 Introduction

The stable production of arbitrarily thin fluid jets from much bigger tubes has become the Holy Grail for many microfluidic applications that demand monodisperse collections of tiny droplets, bubbles, capsules, and emulsions. To this end, the microjetting mode of tip streaming has been the preferred method in most cases [1]. In principle, the jet diameter can be indefinitely reduced by lowering the injected flow rate Q. However, all the experiments and numerical simulations have shown that the flow inevitably becomes unstable at a critical value of Q, which sets a minimum value of the jet diameter.

This work examines the microjetting mode obtained when a fluid is injected through a tube submerged in a uniaxial extensional flow [2]. We analyze the flow stability as the injected flow rate decreases. Our results show that infinitely thin jets can be produced for a sufficiently large outer viscosity, regardless of the jet's viscosity and density and the outer flow intensity.

2 Results

We consider the linear uniaxial extensional flow sketched in Fig. 1. A fluid of density ρ_i and viscosity μ_i is injected through a tube of radius a at a constant flow rate Q_i. The density and viscosity of the outer fluid are ρ_o and μ_o, respectively, and the surface tension of the interface is σ. The tube is placed in linear uniaxial extensional flow given by the equations $u^{(o)} = -Gr/2$ and $w^{(o)} = G\,z$, where $u^{(o)}$ and $w^{(o)}$ are the radial and axial components of the outer velocity field, and G is the intensity of the extensional

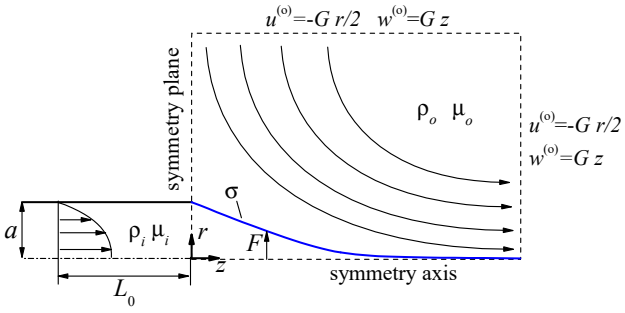

Figure 1: Sketch of the fluid domain. The dashed line indicates the computational domain.

flow. The viscosity-dominated flow is characterized by the viscosity ratio $\lambda = \mu_i/\mu_o$, the capillary number $C = \mu_o a/\sigma$, and the dimensionless injected flow rate $Q = Q_i/(a^2\sigma/\mu_0)$. Inertia is quantified by the inner and outer Reynolds numbers $\mathrm{Re}_i = \rho_i\sigma a/\mu_i^2$ and $\mathrm{Re}_o = \rho_o\sigma a/\mu_o^2$.

The steady base flow is calculated by solving the Navier-Stokes equations and the corresponding boundary conditions with a boundary-fitted method [3] (Fig. 2). Increasing the inner viscosity ($\lambda = 0.1$) enhances the diffusion of axial momentum from the interface toward the tapering meniscus. The inner fluid spatial acceleration increases, making the meniscus shrink, and the recirculation cells enter the feeding tube. For $\lambda = 0.0125$, the inner fluid spatial acceleration decreases due to the reduction of the inner viscosity. The tapering meniscus stretches, and the recirculation cell does not penetrate the feeding tube (Fig. 2).

The linear eigenmodes, $U = U_0 + \delta U\, e^{-i\omega t}$, are

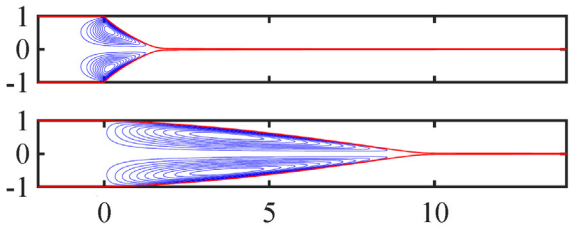

Figure 2: Streamlines of the viscosity-dominated marginally stable flow for ($\lambda = 0.1$,$C = 0.425$,$Q = 0.00126$) (upper graph) and ($\lambda = 0.0125$,$C = 0.130$,$Q = 0.00126$) (lower graph).

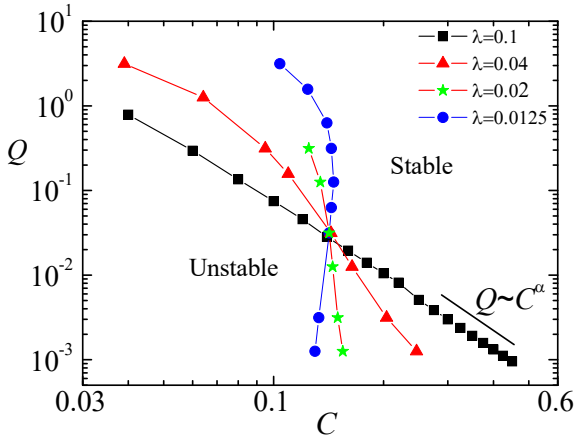

Figure 3: Stability map for viscosity-dominated flow.

calculated to determine the flow stability. Here, U represents any unknowns of the problem. If the dominant mode's growth rate ω_i is positive, then the base flow is unstable. Figure 3 shows the stability map in the parameter plane (C,Q) for several values of the viscosity ratio λ in the Stokes regime. The stability limit $Q(C)$ behaves as $Q \sim C^{\alpha}$ as $Q \to 0$. Two types of asymptotic behavior can be observed. For sufficiently large values of λ, we obtain $\alpha < 0$, which implies that there is a finite value of Q below which the steady flow becomes unstable. In contrast, $\alpha > 0$ for small enough values of λ. This means that the flow remains stable for infinitely small values of Q provided that the outer viscosity is sufficiently large. The dependence of the exponent α on the viscosity ratio λ indicates that the critical viscosity ratio is $\lambda_c \simeq 0.016$. The jet diameter scales as $Q^{-1/2}$ at a fixed distance from the feeding capillary. Therefore, jets with vanishing diameters can be produced with the uniaxial extensional flow for a sufficiently large outer viscosity, independently of the jet viscosity and the outer flow intensity.

Figure 4 shows the role of the inner inertia. The asymptotic behavior with $\alpha < 0$ is recovered for a sufficiently large value of the inner Reynolds number.

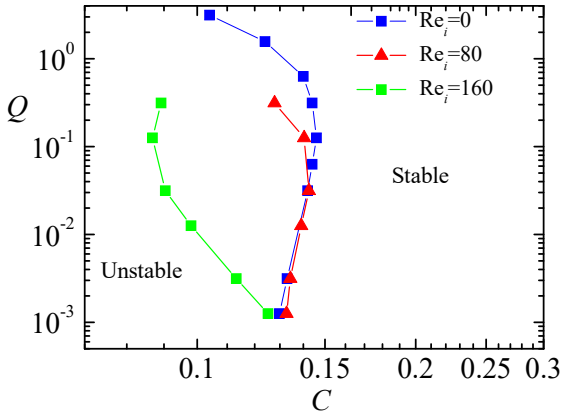

Figure 4: Stability map for $\lambda = 0.0125$ and $\mathrm{Re}_o = 0$.

This implies that infinitely thin jets can be produced only for large enough values of the inner liquid viscosity.

3 Conclusions

We numerically show that infinitely thin jets can be produced from much bigger tubes by the hydrodynamic focusing effect caused by the uniaxial extensional flow, provided that the inner and outer viscosities take sufficiently high values. We hope our results constitute a guide to producing monodisperse collections of drops and capsules with vanishingly small diameters.

Acknowledgement. This research has been supported by the Spanish Ministry of Economy, Industry and Competitiveness under Grant PID2019-108278RB.

References

[1] J. M. Montanero and A. M. Gañán-Calvo, Rep. Prog. Phys. **83**, 097001 (2020)
[2] W. Zhang, Phys. Rev. Lett. **93**, 184502 (2004)
[3] M. A. Herrada and J. M. Montanero, J. Comput. Phys. **306**, 137 (2016)

The Fluid Mechanics of Splat Painting

Diego Ávila García[1], Lucía Lacambra Asensio[1], Javier Rodríguez Rodríguez[1,2], Roberto Zenit[3], and Lorène Champougny[1,2 *]

[1] *Fluid Mechanics Group, Department of Thermal and Fluid Engineering, Universidad Carlos III de Madrid, 28911 Leganés (Madrid), Spain*
[2] *Gregorio Millán Institute for Fluid Dynamics, Nanoscience and Industrial Mathematics, Universidad Carlos III de Madrid, 28911 Leganés (Madrid), Spain*
[3] *Center for Fluid Mechanics, Brown University, Providence, RI 02912, USA*

This work aims at unravelling the physical phenomena at play in an artistic technique known as "splat painting", which consists in projecting a spray of liquid droplets on a substrate by the means of a controlled impact on a paint-loaded brush. We perform a series of experiments where the liquid viscosity and brush acceleration upon impact are varied systematically. The resulting spotted patterns projected on the substrate are then characterized as a function of these control parameters.

INTRODUCTION

In art, splat painting consists in subjecting a paint-loaded brush to an acceleration (for example by "flicking" the brush or tapping its handle) to detach paint droplets or filaments. These are projected onto the canvas, leaving stringy or spotty patterns [1] such as those shown in Fig. 1. In this technique, perhaps most emblematically used by American painters Jackson Pollock (1912-1956) [2] and Sam Francis (1923-1994) [3], the brush never touches the canvas, and tuning the final deposited pattern is a challenge for the artist.

Acceleration-driven ejection of liquid can be encountered in a variety of contexts. In nature, wet mammals shake [4] and insects flutter their wings [5] at given frequencies to get rid of undesired moisture or droplets. In industrial processes, the rotary atomization of liquids submitted to centrifugal acceleration is commonly used to produce droplets or sprays (see [6] and references therein).

While in the abovementioned cases liquid ejection can be adjusted by changing the shaking frequency (or angular velocity), the splat painting artist must rely on other control parameters to fine-tune the final pattern. To unravel the physical mechanisms at play in splat painting, we propose to explore the effects of paint viscosity and brush acceleration on liquid ejection and on the resulting spotted pattern.

METHODOLOGY

We developed an experimental setup to produce repeatable tapping on a paint-loaded brush. The brush is held horizontally and fixed in the reference frame of the laboratory. A small brass weight guided by a vertical rod is dropped from a given height onto the wooden handle of the brush. The impact generates a transverse wave that propagates in the handle all the way to the tip of the brush, where it is transmitted to the paint-loaded bristles.

FIG 1. Artwork based on splat painting by Caroline Champougny. "Sunday Afternoon" (acrylic paint on paper, 15 x 20.5 cm), 2022, used with permission.

The vertical displacements of the extremity of the handle and of the bristles, as well as the resulting liquid atomization, are visualized from the side and recorded by a high-speed camera at a framerate of 30,000 fps. A typical image sequence is presented in Fig. 2 in the case of a brush loaded with white acrylic paint. The total mass of liquid ejected Δm is measured by weighting the brush before and after impact with a high-precision scale.

To simplify the problem, we started working with Newtonian fluids, namely silicone oils of viscosities ranging from 2 to 350 cSt. However, it is important to note that most paints are non-Newtonian fluids [7]. The ejected droplets resulting from the tapping are collected on a white paper sheet laid down horizontally at a fixed distance below the brush. The final droplet pattern is then photographed with backlighting, to be subsequently analyzed.

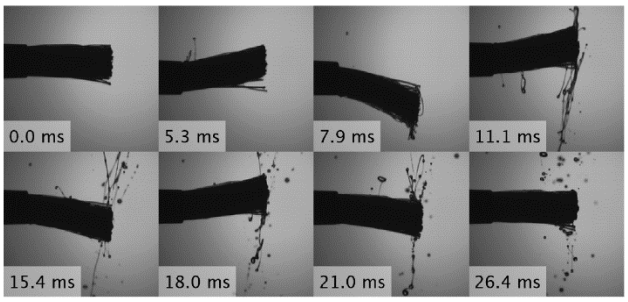

FIG 2. High-speed snapshots showing ejection of 40 cSt silicone oil from a round brush of base diameter 4.7 mm subjected to an impact on its wooden handle.

RESULTS

We show that repeatable forcing of brush (*i.e.* vertical displacement versus time at the foot of the bristles) is achieved with our impact setup. The instantaneous acceleration is then computed by digital image processing, and it is also found to be reasonably reproducible from experiment to experiment. This allows us to use the forcing acceleration as a control parameter, that we vary by changing the height from which the weight is dropped on the brush handle.

High-speed imaging of the motion of the bristles shows that liquid ejection occurs mostly when the instantaneous acceleration is maximum at the tip of the bristles. This behavior can be qualitatively recovered with a simple mechanical model, based on Timoshenko's beam equations, to compute the longitudinal acceleration projected along the bristles' mean line. Experimentally, the mass of liquid ejected due to the impact, Δm, is obtained as a function of the liquid viscosity and brush acceleration. Modelling the bundle of bristles as an anisotropic porous medium, the flow rate leaving the brush upon impact can then be predicted and compared to the experimental data.

Once the fluid is expelled from the brush, the elongation of fluid filaments leads to fragmentation and droplet formation. The analysis of the final spotted patterns on the paper allows to evaluate how the amount of liquid that detached from the brush is fragmented (size distribution of spots) and where these fragments land on the substrate (spatial distribution of spots).

CONCLUSIONS

In summary, we investigated the artistic technique of splat painting from a fluid mechanical perspective. Inspired by the empirical know-how developed by artists, we explored the influence of two key parameters – liquid viscosity and brush acceleration – on the quantity of liquid ejected from the brush and on the final spotted pattern landing on the substrate. Next steps may include investigating how the brush-to-substrate distance and liquid viscoelasticity affect the abovementioned observables.

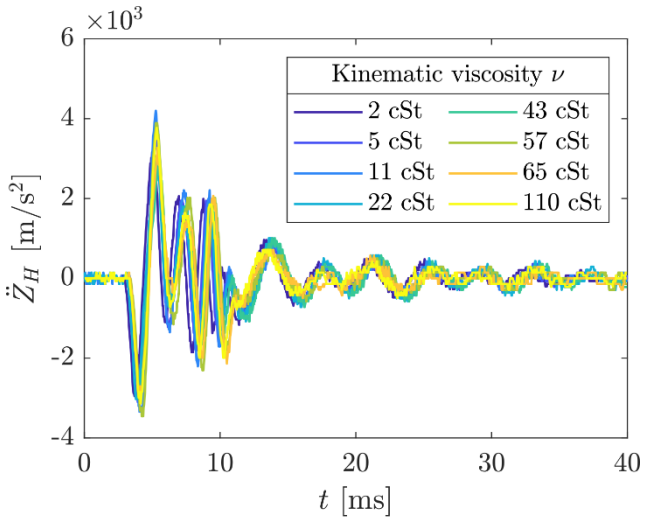

FIG 3. Instantaneous acceleration of brush handle, for a fixed drop height $\Delta H = 3$ cm and various oil viscosities, showing the repeatability of our impact system.

ACKOWLEDGMENTS

J.R.R. acknowledges funding from the Spanish MCIN/AEI/10.13039/501100011033 through Grant No. PID2020-114945RB-C21.

L.C acknowledges funding from the European Union's Horizon 2020 research and innovation programme under the Marie Sklodowska-Curie grant agreement No 882429.

—

* lchampou@ing.uc3m.es

[1] Herczynski, A., Cernuschi, C., & Mahadevan, L. (2011). Painting with drops, jets, and sheets. *Physics Today.*
[2] Zenit, R. (2019). Some fluid mechanical aspects of artistic painting. *Physical Review Fluids*, **4** (11), 110507.
[3] Burchett-Lere, D., & Zebala, A. (2019). Sam Francis: The Artist's Materials. Getty Publications.
[4] Dickerson, A. K., Mills, Z. G., & Hu, D. L. (2012). Wet mammals shake at tuned frequencies to dry. *Journal of the Royal Society Interface*, **9** (77), 3208-3218.
[5] Alam, M. E., Kauffman, J. L., & Dickerson, A. K. (2020). Drop ejection from vibrating damped, dampened wings. *Soft Matter*, **16** (7), 1931-1940.
[6] Keshavarz, B., Houze, E. C., Moore, J. R., Koerner, M. R., & McKinley, G. H. (2020). Rotary atomization of Newtonian and viscoelastic liquids. *Physical Review Fluids*, **5** (3), 033601.
[7] Blair, G. S. (1969). Rheology and painting. *Leonardo*, 51-53.

2nd Spanish Fluid Mechanics Conference
Barcelona (2 - 5 July 2023)

The skating of impacting drops over gas or vapor layers

Paula García-Geijo†, Guillaume Riboux†, and José Manuel Gordillo†

†*Área de Mecánica de Fluidos, Departamento de Ingeniería Aeroespacial y Mecánica de Fluidos, Universidad de Sevilla, Spain*

Here we present numerical simulations performed using `Basilisk` aimed at elucidating the precise physical mechanism by which a drop of a low viscosity liquid impacting over a smooth solid substrate skates over a thin gas or vapor layer. The analysis of the results obtained along the spatio-temporal region where the thickness of the gas film is minimum reveals that the predictions in Gordillo and Riboux (2022) agree well with the time evolution of the minimum gas vapor thickness from the very early instants of time considered in Mandre and Brenner (2012) to later instants of time for which the drop deformation is comparable to the initial radius of the drop. The results of our numerical study confirm that the reason why the drop skates over a gas film resorts on the classical hydrodynamic lubrication mechanism, once the relative velocity between the liquid and the solid and the pressure gradient are calculated using the results provided by potential flow theory at the spatio-temporal region where the minimum film thickness is attained.

The impact of a drop over a substrate has been the subject of intense research efforts during the past decades as a consequence of its relevance in a myriad of natural and technological processes. One of the many open questions that remains to be solved and has received attention in the recent years refers to the description and quantification of the conditions under which a drop impacting a superheated substrate skates over a vapor film, a phenomenon referred as dynamic Leidenfrost effect. The reason for this renewed interest lies on the fact that, as a consequence of the small thermal conductivity of the vapor, the heat flux between the solid and the liquid is reduced, thus limiting the cooling capacity of liquid drops impacting a heated solid substrate.

There exist several theoretical, numerical and experimental works in the recent literature aimed at expressing the minimum distance between the wall and the solid in terms of the control parameters (Duchemin and Josserand, 2011; Mandre and Brenner, 2012; de Ruiter *et al.*, 2012; Chantelot and Lohse , 2021; Gordillo and Riboux, 2022; Chantelot and Lohse, 2022). Since there remains some controversy about the relevant physical mechanism preventing the liquid-solid contact, here we have made use of `Basilisk` and have simulated the impact of a drop of radius R, density ρ, viscosity μ and interfacial tension coefficient σ, falling with a velocity U over an impermeable substrate. Using R, R/U and ρU^2 as the characteristic values of length, time and pressure, the physical situation at hand (see Fig. 1) can be described in terms of the following dimensionless parameters:

$$St = \frac{\rho U R}{\eta_a}, \quad We = \frac{\rho U^2 R}{\sigma}, \quad \frac{\mu_a}{\mu} \quad \frac{\rho_a}{\rho}, \qquad (1)$$

where ρ_a and μ_a indicate, respectively, the gas density and viscosity. Our numerical simulations spans along the range of values $3.9 \leq We \leq 64$, $1.50\times10^4 \leq St \leq 3.03\times10^4$, $\mu_a/\mu = 1.8\times10^{-5}$, $\rho_a/\rho = 1.0\times10^{-3}$. Figure 1 shows the results of the numerical simulations corresponding to $We = 3.9$, $St = 3.03 \times 10^4$.

As the drop approaches the solid, the gas pressure increases and a dimple is formed. The periphery of the dimple, located at $a = \sqrt{3\tau}$, is the part of the drop closest to the wall and slides radially outwards over the air layer with a velocity $da/d\tau = 1/2\sqrt{3/\tau}$, with $\tau = TU/R$ indicating here the dimensionless time with origin at the instant when the drop would contact the solid if air was not present. The maximum liquid pressure is attained in this spatio temporal region, where $\Delta p = 1/2\rho U^2 \left(da/d\tau\right)^2$ and the length scale characterizing pressure variations is given by

$$\frac{\ell_c}{R} \propto \left(\tau St^{2/3}\right)^{5/6} We^{-2/3}\, St^{-8/9}. \qquad (2)$$

for the range of values of We considered in this study (Gordillo and Riboux, 2022). The results in Fig. 1c show the comparison between the superposition of the Couette and Poiseuille flows calculated using the velocity $Uda/d\tau$ and the pressure gradient given by $K\Delta p/\ell_c$ with K a time-independent We-independent and St-independent constant as our numerical simulations show, finding a fair agreement between the simulations and the predictions. Hence, the reason

why the drop can levitate over the wall is that the Couette flow rate induced by the difference of velocities between the interface and the wall is balanced by the gas flow rate caused by the pressure gradient (Poiseuille flow) at the neck ensuring that mass conservation is preserved.

Making use of the framework in Gordillo and Riboux (2022), now supported by the numerical results of the type shown in Fig. 1, we also deduce here an algebraic equation expressing the minimum distance between the liquid and the wall in terms of the control parameters which is equally valid to describe the cases of isothermal and superheated substrates and compares favourably with the experimental measurements reported in de Ruiter *et al.* (2012); Chantelot and Lohse (2021); Chantelot and Lohse (2022).

References

Gordillo J. M. & Riboux G. (2022) "The initial impact of drops cushioned by an air or vapour layer with applications to the dynamic Leidenfrost regime", *J. Fluid Mech.*, **941**, A10.

Mandre S. & Brenner M. P. (2012) "The mechanism of a splash on a dry solid surface", *J. Fluid Mech.*, **690**, 148.

Duchemin L. & Josserand C. (2011) "Curvature singularity and film-skating during drop impact.", *Physics of Fluids*, **23** (9), 091701.

de Ruiter J., Oh J.M., van den Ende D. & Mugele F. (2012) "Dynamics of collapse of air films in drop impact.", *Phys. Rev. Lett.*, **108**, 074505.

Chantelot P. & Lohse D. (2021) "Drop impact on superheated surfaces: short-time dynamics and transition to contact", *J. Fluid Mech.*, **928**, A36.

Chantelot P. & Lohse D. (2022) "Drop impact on superheated surfaces: from capillary dominance to non-linear advection dominance", *arXiv preprint arXiv:2211.12772*.

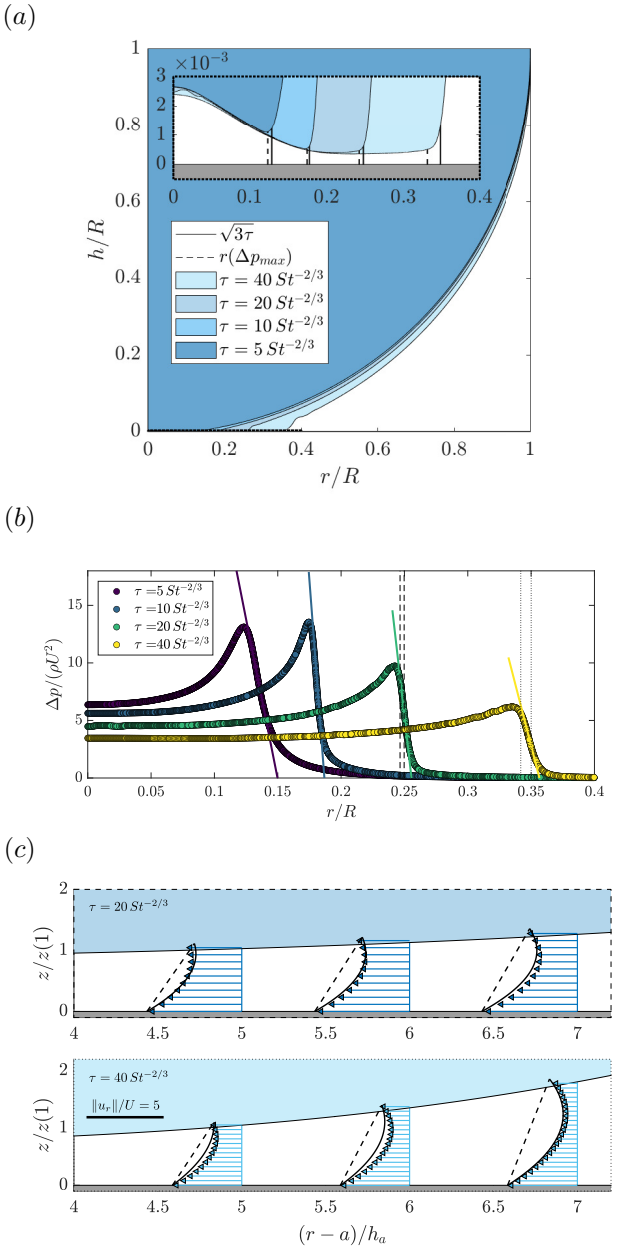

Figure 1: (*a*) The drop entraps an air pocket in the near axis region and the minimum distance between the liquid and the solid is attained at the periphery of the dimple, located at $a = \sqrt{3\tau}$, with $\tau = TU/R$ the dimensionless time with origin at the instant when the drop would contact the solid if air was not present. (*b*) Air pressure along radial direction for different instants of time. Dotted and dashed lines indicate region plotted in (*c*), where the velocity field in the lubrication layer is plotted in the frame of reference moving with the wetting velocity $da/d\tau = 1/2\sqrt{3/\tau}$. The solid line corresponds to the theoretical solution reported by Gordillo and Riboux (2022) (Poiseuille + Couette flow). Here $h_a = 2\,a^3/(9\pi)$.

2nd Spanish Fluid Mechanics Conference
Barcelona (2 - 5 July 2023)

When slower is faster: understanding the striking clogging of suspensions through constrictions

Alvaro Marin[1], Mathieu Souzy[2], Edgar Ortega-Roano[1], Stefan Luding[3], Thomas Weinhart[3], and Devaraj van der Meer[1]

a.marin@utwente.nl

[1]Physics of Fluids, University of Twente, The Netherlands
[2]INRAE, Aix-Marseille Univ, UMR RECOVER, 13182 Aix-en-Provence, France
[3]Multi Scale Mechanisms, University of Twente, The Netherlands

When objects are forced to flow through constrictions their transport can be frustrated temporarily or permanently due to the formation of arches in the region of the bottleneck. While such systems have been intensively studied in the case of solid particles in a gas phase being forced by gravitational forces, the case of solid particles suspended in a liquid phase, being forced by the liquid itself, has been so far barely explored. Therefore, the influence of the liquid flow on the transport efficiency is not well understood yet, leading to several apparently trivial, but yet unanswered questions, e.g., would an increase of the liquid flow improve the transport of particles or worsen it? In this work, we will attempt to answer this question both experimentally and numerically.

Many-body systems flowing through narrow channels and/or constrictions show different flowing regimes, but they might also block (Zuriguel and Garcimartín, 2020). As long as the flowing elements remain as individuals, such flows present several analogies among each other, for example grains in a silo, pedestrians or animals passing through a door (Zuriguel *et al.*, 2014). Interestingly, whenever entities flow within a fluid phase, there are a surprising number of features that remain identical as in the absence of fluid.

While the flow of grains by gravity in silos is a well-studied problem (Zuriguel and Garcimartín, 2020), the flow of particles driven by liquid flow is a much more unexplored and complex problem, since two phases need to pass through the constriction. Unlike gravitational forces, driving these systems using a liquid flow it is a great advantage since it conveys a higher level of control. However, the interaction of the liquid flow with the particles in suspension is a very complex problem and leads to complex particle-fluid and particle-particle interactions (Marin *et al.*, 2018; Souzy *et al.*, 2020).

The typical system we are considering is shown in Figure 1. A dense suspension, with particles of average diameter d, is being forced by the liquid flow through the narrow constriction of size D. On the one hand this can be done by forcing a constant volume of fluid per unit time, for example using a piston or a syringe pump. On the other hand, the system can be driven by a hydrodynamic pressure difference, for example by imposing a high pressure upstream and opening the exit to atmospheric pressure.

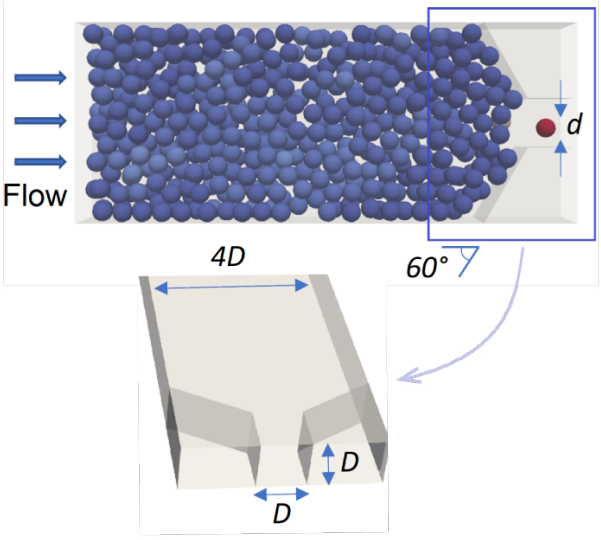

Figure 1: The system used for both numerical simulations and experiments consists of a constricted channel of width $4D$, with a constriction size of $D = 100$ μm. A monodisperse suspension of particles with diameter d is forced through the constriction through a liquid flow driven either by a controlled pressure or flow rate.

In this work, we will show experimentally that the flow driving (either volume-controlled or pressure-controlled) plays an important role in the particle transport performance (Souzy and Marin, 2022) and

we will analyze the issue using a discrete element code (Weinhart *et al.*, 2020) and a drag closure approach to model the effect of the drag on the particles.

Our final aim is to find optimal strategies for the transport of suspensions through constrictions. Several strategies have already been investigated based on different parameters. For example, Arévalo *et al.* (2014) showed using simulations that gravity decreases both the probability of clogging and of unclogging for granular inert particles passing through a bottleneck. Janda *et al.* (2009) and Mankoc *et al.* (2009) both showed experimentally that for dry granular silos, applying strong vibrations decreases the clogging probability, and that the remaining clogs break also more easily. Hidalgo *et al.* (2018) showed using simulations that increasing the thermal fluctuations in Brownian suspensions leads to an increase of both the clogging and the unclogging probabilities.

Our results will provide new efficient strategies for controlling the transport of non-cohesive particle suspensions driven through constrictions by making a smart design of the liquid flow.

References

I. Zuriguel and A. Garcimartín, Statistical mechanics of clogging, in *Encyclopedia of Complexity and Systems Science*, edited by R. A. Meyers (Springer Berlin Heidelberg, Berlin, Heidelberg, 2020) pp. 1–32.

I. Zuriguel, D. R. Parisi, R. C. Hidalgo, C. Lozano, A. Janda, P. A. Gago, J. P. Peralta, L. M. Ferrer, L. A. Pugnaloni, E. Clément, *et al.*, Scientific Reports **4**, 1 (2014).

A. Marin, H. Lhuissier, M. Rossi, and C. J. Kähler, Physical Review E **97**, 021102 (2018).

M. Souzy, I. Zuriguel, and A. Marin, Physical Review E **101**, 060901 (2020).

M. Souzy and A. Marin, Journal of Fluid Mechanics **953**, A40 (2022).

T. Weinhart, L. Orefice, M. Post, M. P. van Schrojenstein Lantman, I. F. Denissen, D. R. Tunuguntla, J. Tsang, H. Cheng, M. Y. Shaheen, H. Shi, P. Rapino, E. Grannonio, N. Losacco, J. Barbosa, L. Jing, J. E. Alvarez Naranjo, S. Roy, W. K. den Otter, and A. R. Thornton, Computer Physics Communications **249**, 107129 (2020).

R. Arévalo, I. Zuriguel, D. Maza, and A. Garcimartín, Physical Review E **89**, 042205 (2014).

A. Janda, D. Maza, A. Garcimartín, E. Kolb, J. Lanuza, and E. Clément, Europhysics Letters **87**, 24002 (2009).

C. Mankoc, A. Garcimartín, I. Zuriguel, D. Maza, and L. A. Pugnaloni, Physical Review E **80**, 011309 (2009).

R. Hidalgo, A. Goñi-Arana, A. Hernández-Puerta, and I. Pagonabarraga, Physical Review E **97**, 012611 (2018).

2nd Spanish Fluid Mechanics Conference
Barcelona (2 - 5 July 2023)

Edge states alternation and period doubling cascades in subcritical Taylor-Couette flow

Roger Ayats[1], Baoying Wang[2], Kengo Deguchi[3], Fernando Mellibovsky[2], and Alvaro Meseguer[2]

roger.ayatslopez@ist.ac.at

[1]Institute of Science and Technology Austria (ISTA), Klosterneuburg 3400 (Austria)
[2]Departament de Física, Universitat Politècnica de Catalunya, 08034 Barcelona (Spain)
[3]School of Mathematics, Monash University, Clayton, Victoria 3800 (Autralia)

Coexistence of both laminar and non-trivial stable attractors is one of the main features in subcritical transition to turbulence in shear flows. By studying the Taylor-Couette flow, the fluid flow between independently rotating coaxial cylinders, we study the process by which the boundary between the two attractors acquires sensitivity to the initial conditions. In addition, when studying the non-trivial stable chaotic attractor, we analyse a period-doubling cascade using a one-dimensional discrete map reduction that confirms Feigenbaum's universal theory accurately.

1 Edge state alternation

Subcritical transitional scenarios are strongly dominated by exact coherent structures (ECS), usually in the form of travelling waves and periodic orbits, emanating from saddle-node bifurcations. While ECS upper branches participate in the formation of chaotic attractors, lower branches typically act as a separatrix between the basins of attraction of laminar and non-trivial solutions, dictating the amplitude of the disturbances triggering transition (Mellibovsky & Eckhardt (2012); Kreilos & Eckhardt (2012)). Near to the saddle-node, we start by confirming the typical scenario described in the literature, where the separation role of the ECS lower branch persists up to a global bifurcation involving a boundary crisis (Ritter *et. al* (2016)). At this point, the global bifurcation causes the lower branch to move off the edge of the basin of attraction of the non-trivial state, so that when increasing the Reynolds number, the role of the edge state is then played by a chaotic saddle that appears independently of the travelling waves. Therefore, we analyse how the subsequent equilibria acting as edge states alternate, and demonstrate the importance of unstable solutions within chaotic saddles for understanding the dynamics.

2 One dimensional map

Finally, we also analyse the stable chaotic attractor for the same parameter range and show that the dynamics can be very well approximated by a reduction in a one-dimensional discrete map on the Poincare section. We report two different period-doubling cascades at the onset of the chaos, being one of them much cleaner than those previously seen in fluid systems, and allowing us to confirm Feigenbaum's universal theory accurately (Feigenbaum (1978)). Moreover, the probability distribution produced by the chaos and the periodic points embedded in it can be reproduced surprisingly well by the one-dimensional map obtained by interpolation. Remarkably, this provides direct evidence for the existence of infinitely many periodic solutions in fluid chaos via Sharkovsky's theorem (Sharkovskii (1995)).

References

Mellibovsky, F. and Eckhardt, B. (2012). "From travelling waves to mild chaos: a supercritical bifurcation cascade in pipe flow", *J. Fluid Mech.*, **709** 149–190.

Kreilos, T. and Eckhardt, B. (2012). "Periodic orbits near onset of chaos in plane Couette flow", *Chaos*, **22** 047505.

Ritter, P. Mellibovsky, F. and Avila, M. (2016). "Emergence of spatiotemporal dynamics from exact coherent solutions in pipe flow", *New J. Phys.*, **18** 083031.

Feigenbaum M. J. (1978). "Quantitative universality for a class of nonlinear transformations", *J. Stat. Phys.*, **19** 25–52.

Sharkovskii A. N. (1995). "Coexistence of cycles of a continuous map of the line into itself", *Int. J. Bifurc. Chaos Appl. Sci. Eng.*, **5** 1263–1273.

2nd Spanish Fluid Mechanics Conference
Barcelona (2 - 5 July 2023)

Ferrofluidic wavy Taylor vortices under alternating magnetic field

Sebastian A. Altmeyer[1]

sebastian.andreas.altmeyer@upc.edu

[1]Departamento de Física, Universitat Politècnica de Catalunya, Spain

Many natural and industrial flows are subject to time-dependent boundary conditions and temporal modulations (e.g. driving frequency), which significantly modify the dynamics compared with their static ounterparts. The present problem addresses ferrofluids (Rosensweig (1985)) in particular wavy vortex flow in Taylor-Couette system (TCS) (Taylor (1923)), with the outer cylinder at rest in a spatially homogeneous magnetic field subject to an alternating modulation. Using a modified Niklas approximation (Niklas (1987),Altmeyer (2021)), the effect of frequency modulation on non-linear flow dynamics and appearing resonance phenomena are investigated in the context of either period doubling or inverse period doubling. Flow structures of particular interest in the present work are wavy Taylor vortex flows (wTVFs) (Wereley and Lueptow (1998)) (which already have a natural frequency) with main focus on resonance phenomena when the modulation frequency reaches multiples or ratios of the natural, that is characteristic, frequency of the studied flow states.

1 System and Methods

1.1 Geometry and system parameters

In the TCS (Fig. 1(a)) the flow strength is represented in terms of the Reynolds number $Re = \omega r_i d/\nu$ (the ratio between inertia and viscous forces), which is a very well suited parameter to describe the driving of the system. Here r_i is the non-dimensionalized radius and ω the angular velocity of the inner cylinder. No-slip boundary conditions are used on the cylinder surfaces. The system can be characterized in the cylindrical coordinate system (r, θ, z) by the velocity field $\mathbf{u} = (u, v, w)$ and the corresponding vorticity field $\nabla \times \mathbf{u} = (\zeta, \eta, \xi)$. The radius ratio of the cylinders, is kept fixed at 0.5. The time, and length scales are made dimensionless by diffusion time d^2/ν and gap width d. The pressure in the fluid is normalized by $\rho\nu^2/d^2$.

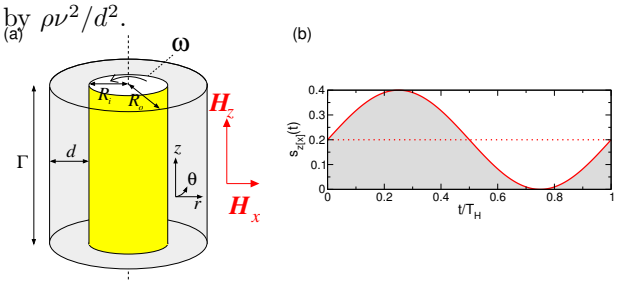

Figure 1: Schematic diagram for the Taylor-Couette system (TCS) with an external applied homogeneous transverse [axial] magnetic field $H_{ext} = H_x\mathbf{e}_x[H_z\mathbf{e}_z]$.

To realise a periodically modulated TCS, we apply a sinusoidal modulation signal (Fig. 1(b)) to the external magnetic field, which is oriented either parallel (z) or transverse (perpendicular) (x) to the system symmetry axis. The fields are further assumed to be uniform in space and harmonic in time, that is, $H_{z[x]} = \{H_{S,z[x]} + H_{M,z[x]}\sin(\Omega_{H_{z[x]}}t)\}\mathbf{e}_z[\mathbf{e}_x]$. It is important to mention that a pure axially oriented magnetic field does not change the system symmetry, while a pure transversally oriented magnetic field does and renders all flow states to become inherently three-dimensional Altmeyer *et. al* (2010).

By using a modified Niklas approach (Niklas (1987),Altmeyer (2021)) the effect of the magnetic field and the magnetic properties of the ferrofluid on the velocity field can be characterised by a single (time-dependent) function,

$$s_{z[x]}(t) = s_{S,z[x]} + s_{M,z[x]}\sin(\Omega_{H_{z[x]}}t),$$

with $s_{S,z[x]}$ being the static contribution of the driving, $s_{M,z[x]}$ the modulation amplitude, and $\Omega_{H_{z,[x]}}$ the modulation frequency, respectively.

1.2 Ferrohydrodynamical equations

The non-dimensionalised hydrodynamical equations are derived from

$$\begin{aligned}(\partial_t + \mathbf{u}\cdot\nabla)\mathbf{u} - \nabla^2\mathbf{u} + \nabla p &= (\mathbf{M}\cdot\nabla)\mathbf{H} + \frac{1}{2}\nabla\times(\mathbf{M}\times\mathbf{H}),\\ \nabla\cdot\mathbf{u} &= 0.\end{aligned} \tag{1}$$

Equation (1) is solved with an equation describing the magnetisation of the ferrofluid. Here, we consider an equilibrium magnetisation of an unperturbed state with homogeneously magnetised ferrofluid at rest. Thereby the mean magnetic moment

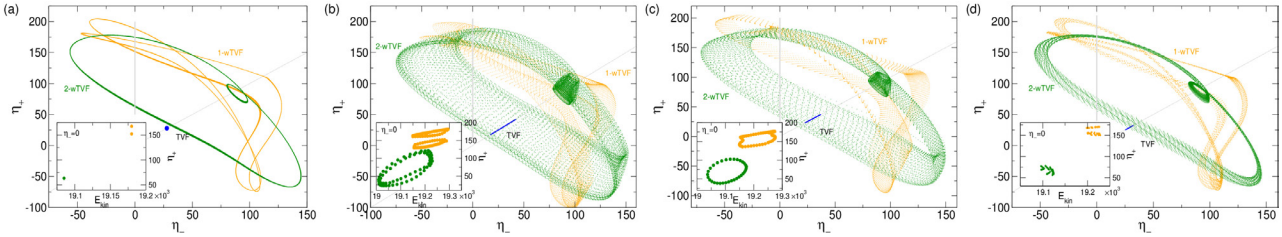

Figure 2: Phase portrait of 1-wTVF and 2-wTVF under axial magnetic field and different driving frequencies: (a) $\Omega_H = 0$, (b) $\Omega_H = 15$, (c) $\Omega_H = 30$, and (d) $\Omega_H = 100$.

is oriented (aligned) in the direction of the magnetic field: $\mathbf{M}^{\mathrm{eq}} = \chi\mathbf{H}$. Here, we consider the ferrofluid APG933. The near-equilibrium approximation by Niklas (1987) assumes small derivations $||\mathbf{M} - \mathbf{M}^{\mathrm{eq}}||$ and small magnetic relaxation time τ: $|\nabla \times \mathbf{u}|\tau \ll 1$. Using these approximations, the following magnetisation equation can be obtained:

$$\mathbf{M} - \mathbf{M}^{\mathrm{eq}} = c_N^2 \left(\frac{1}{2} \nabla \times \mathbf{u} \times \mathbf{H} + \lambda_2 \mathbb{S}\mathbf{H} \right), \qquad (2)$$

where $c_N^2 = \tau / \left(1/\chi + \tau\mu_0 H^2/6\mu\Phi\right)$.
Using (2), the magnetisation in (1) can be eliminated and with further simplification one obtains the following ferro-hydrodynamical equation of motion:

$$(\partial_t + \mathbf{u}\cdot\nabla)\mathbf{u} - \nabla^2\mathbf{u} + \nabla p_M = s_N^2 \left\{ \nabla^2\mathbf{u} - \frac{4}{5}\left[\nabla \cdot (\mathbb{S}\mathbf{H})\right] - \mathbf{H} \times \left[\frac{1}{2}\nabla \times (\nabla \times \mathbf{u} \times \mathbf{H}) - \mathbf{H} \times (\nabla^2\mathbf{u}) + \frac{4}{5}\nabla \times (\mathbb{S}\mathbf{H}) \right] \right\} .$$

2 Resonances

In the case that an alternating magnetic field is present, the flow dynamics become more complex (Fig. 2). To be precise, the complexity increases by one order. Due to the added time dependence, Taylor vortex flow (TVF) change from fixed point (fp) to limit-cycle (lc(, while 1-wTVF and 2-wTVF change from lc to quasi-periodic (qp) solutions living on a 2-torus (T2). The latter is visible in the observation of closed cycles within the Poincaré sections (E_{kin}, η_+) for $\eta_- = 0$ (insets in Fig. 2). With variation in the forcing frequency Ω_H of the alternating magnetic field the system undergoes different resonances, when Ω_H reaching integer multiples or ratios of the natural frequency of the wavy vortex flows. For $\Omega_H = 15$, about half the natural frequency for 2-wTVF ($\Omega_H = 30$), period doubling is found (Poincaré section (E_{kin}, η_+) in Fig. 2(b)). For larger Ω_H, after the resonance, the Poincaré sections again illustrate a single circle)(Fig. 2(c). An alternating field with the driving frequency $\Omega_H = 30$ forces the natural frequency of 2-wTVF. Meanwhile, $\Omega_H = 30$ is just double of the natural frequency (half of the period) of 1-wTVF, and one see a resonance with modified dynamics in half the natural period. In some way, this is like an inverse-period doubling described by Hana *et al.* (2016), although here it only appears at discrete frequency Ω_H and afterward disappear again.

3 Conclusions

The flow dynamics for 1-wTVF and 2-wTVF are observed to undergo different resonances when forcing frequency Ω_H of the alternating magnetic fields are integer multiples or ratios of the natural frequency of the wavy vortex flows. In particular, detected resonance cases are *period doubling* and *inverse period doubling*, when stimulation of the wavy states with half or double (multiples) of their natural frequency. It is worth mentioning that these are *discrete* phenomena appearing only in the resonance case and disappearing for other frequencies.

References

Rosensweig, R. E. "Ferrohydrodynamics". *Cambridge University Press, Cambridge.*

Taylor, G.I."Stability of a Viscous Liquid contained between Two Rotating Cylinders", *Phil. Trans. Roy. Soc. A*, **223** 289–343.

Niklas, M. "Influence of magnetic fields on Taylor vortex formation in magnetic fluids". *Z. Phys. B* **68**, 493.

Altmeyer, S. "On the ridge of instability in ferrofluidic Couette flow via alternating magnetic field". *Scientific Reports* **11**, 4705.

Wereley, S. T. and Lueptow, R. M. "Spatio-temporal character of non-wavy and wavy Taylor-Couette flow", *J. Fluid Mech.* **364**, 59.

Altmeyer, S. Hoffmann, C. Leschhorn, A. and Lücke, M. "Influence of homogeneous magnetic fields on the flow of a ferrofluid in the Taylor-Couette system". *Phys. Rev. E* **82**, 016321.

Hana, X. Chen, Z. and Bi, Q. "Inverse period-doubling bifurcations determine complex structure of bursting in a one-dimensional non-autonomous map" *Chaos* **26**, 023117.

2nd Spanish Fluid Mechanics Conference
Barcelona (2 - 5 July 2023)

Floquet stability analysis of a two-layer oscillatory flow near a flexible wall.

Antonio José Bárcenas-Luque[1], Carlos Martínez-Bazán[1], Cándido Gutiérrez-Montes[2], and Wilfried Coenen[3]

ajbarcenas@ugr.es

[1]Department of Structural Mechanics and Hydraulic Engineering, University of Granada, Granada, Spain
[2]Department of Mechanical and Mining Engineering, University of Jaen, Jaen, Spain
[3]Department of Thermal and Fluids Engineering, University Carlos III of Madrid, Leganés, Spain

Floquet stability analysis of a two-layer oscillatory flow near a flexible wall has been carried out. Two layers of the same fluid are separated by a flexible wall whose deformation is taken to be linearly proportional to the pressure difference across it. An oscillatory linear pressure gradient per unit of length drives an oscillatory motion parallel to the walls. The critical Reynolds number at which the problem becomes unstable and the corresponding wave number are characterized as a function of the control parameters, namely the membrane stiffness, and the dimensionless widths, H_1 and H_2.

1 Introduction

The hydrodynamic stability of flows near flexible walls has been mainly focused on steady configurations. Canonical examples include the Couette and Poiseuille flows past a flexible membrane as in Kumaran (2021) and Davies (1997). However, the stability of the oscillatory flow with solid flexible boundaries has been barely considered.

It is therefore of interest to understand whether instability occurs and how it does, in addition to understanding the role played by each of the fundamental parameters that govern the problem.

Applications of this analysis could be seen as a first step towards a better understanding of complex fluid-structure interaction problem such that occuring in the development of syringomyelia, that is a condition in which fluid accumulates in the spinal cord in or near the central canal, forming macroscopic fluid-filled cavities, called syrinxes. This study would be a simplified model problem, involving the Floquet stability analysis of the oscillatory flow of two layers of fluid (representing the Cerebrospinal fluid in the subarachnoid space and the intrasyringal fluid), separated by an initially undeformed flexible solid (the spinal cord).

2 Mathematical Model

The basic flow configuration is sketched in figure 1. Two layers of the same fluid, of widths are $\mathcal{H}_1$ and $\mathcal{H}_2$ respectively, with velocity fields $(u_j, v_j, 0)$ and pressure fields p_j, are separated by a flexible wall, whose deformation $h(x,t)$ is considered to be linearly proportional to the pressure difference across it, i.e. $Kh = [\![p]\!]_{0^-}^{0^+}$, where K is the stiffness of the wall. An oscillatory linear pressure gradient per unit of length, i.e. $-\partial p_j/\partial x = \Pi\cos(t)$, drives an oscillatory motion parallel to the wall. We are concerned with the stability of the basic oscillatory state in which the wall remains undeformed.

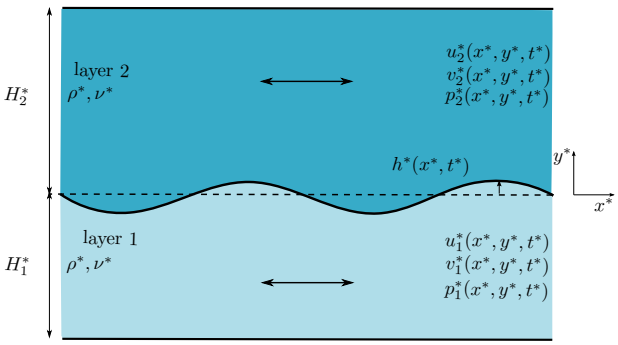

Figure 1: Schematic diagram of the flow configuration.

To that aim, Floquet modes $\phi_j'(x,y,t) = \tilde{\phi}_j(y,t)\mathrm{e}^{\mathrm{i}kx}\mathrm{e}^{\sigma t}$ are introduced in the perturbed and linearized governing equations (the Navier-Stokes equations supplemented with the linear equation for the wall deformation), where $\sigma \in \mathbb{C}$ is the Floquet exponent, and $k \in \mathbb{R}$ is the perturbation wavenumber. After expanding the amplitude functions $\tilde{\phi}_j(y,t)$, which are 2π-periodic in time, as Fourier series, $\tilde{\phi}(y,t) = \sum_{n=-\infty}^{\infty} \tilde{\phi}_{j,n}(y)\mathrm{e}^{\mathrm{i}nt}$, we obtain a set of cou-

pled stability equations. For $n = -\infty, \ldots, \infty$:

$$ik\tilde{u}_{j,n} + \mathcal{D}\tilde{v}_{j,n} + ik\partial_y \bar{u}_j^{\oplus}\tilde{h}_{j,n-1} + ik\partial_y \bar{u}_j^{\ominus}\tilde{h}_{j,n+1} = 0, \tag{1}$$

$$\begin{aligned}
&[\sigma + in - Re^{-1}(\mathcal{D}^2 - k^2)]\tilde{u}_{j,n} + \bar{u}_j^{\oplus} ik\tilde{u}_{j,n-1} + \bar{u}_j^{\ominus} ik\tilde{u}_{j,n+1} \\
&\partial_y \tilde{u}_j^{\oplus}\tilde{v}_{j,n-1} + \partial_y \tilde{u}_j^{\ominus}\tilde{v}_{j,n+1} - \partial_y \tilde{u}_j^{\oplus}\left[\sigma + i(n-1)\right]\tilde{h}_{n-1} - \\
&\partial_y \tilde{u}_j^{\ominus}\left[\sigma + i(n+1)\right]\tilde{h}_{n+1} - \bar{u}_j^{\oplus}\partial_y \bar{u}^{\oplus} ik\tilde{h}_{n-2} - \bar{u}_j^{\ominus}\partial_y \bar{u}^{\ominus} ik\tilde{h}_n \\
&-(\bar{u}^{\oplus}\partial_y \tilde{u}^{\ominus} + \bar{u}^{\ominus}\partial_y \tilde{u}^{\oplus}) - Re^{-1}k^2(\partial_y \bar{u}^{\oplus}\tilde{h}_{n-1} + \partial_y \bar{u}^{\ominus}\tilde{h}_{n+1}) \\
&ik\tilde{P}_{j,n} = 0,
\end{aligned} \tag{2}$$

$$\begin{aligned}
&[\sigma + in - Re^{-1}(\mathcal{D}^2 - k^2)]\tilde{v}_{j,n} + \bar{u}_j^{\oplus} ik\tilde{v}_{j,n-1} + \bar{u}_j^{\ominus} ik\tilde{v}_{j,n+1} \\
&+\mathcal{D}\tilde{P}_{j,n} = 0,
\end{aligned} \tag{3}$$

$$\mathcal{K}\tilde{h}_{j,n} - (\tilde{P}_{1,n}(y=0) - \tilde{P}_{2,n}(y=0)) = 0, \tag{4}$$

subject to $\tilde{u}_{j,n} = \tilde{v}_{j,n} = 0$ as $y \to \pm\infty$, and $\tilde{u}_{j,n} = 0$, $\tilde{v}_{j,n} = (\sigma + \mathrm{i}n)\tilde{h}$ at $y = 0$.

The above set of equations is an eigenvalue problem for σ that is discretized with a Chebyshev spectral collocation method, and solved numerically using a finite number of Fourier modes. The stability of the flow is determined by the absolute value of the Floquet multiplier $\mu = \mathrm{e}^{2\pi\sigma}$. For $|\mu| < 1$ the flow is stable, whereas for $|\mu| > 1$ the flow is unstable.

3 Conclusions

The flow becomes unstable to perturbations in a range of wavenumbers, k, for a critical value of the Reynolds number, Re_{cr}, that depends on the stiffness of the membrane $\mathcal{K}$ and on the channel dimensionless widths H_1 and H_2.

A curve of marginal stability can be traced in the $(Re - k)$-plane by obtaining, for each value of k, the value of Re for which the most unstable mode has $|\mu| = 1$ (figure 2). We can then define a critical Reynolds number, Re_{cr} as the minimum Re-value of the marginal curve.

The occurrence of the instability strongly depends on the value of the dimensionless stiffness $\mathcal{K}$. Figure 3 shows, in blue, how the most unstable wave number k_{uns} decays with increasing stiffness $\mathcal{K}$.

4 Acknowledgments

This work was supported by the coordinated project, PID2020-115961RB-C31,-RBC2,-RAC33, financed by MCIN/AEI/10.13039/501100011033. WC and AJBL acknowledge the support of the CAM through the contract CSFFLOW-CM-UC3M. CMB, CGM and AJBL also acknowledge the support provided by JdA and EF through grant P18-FR-4619.

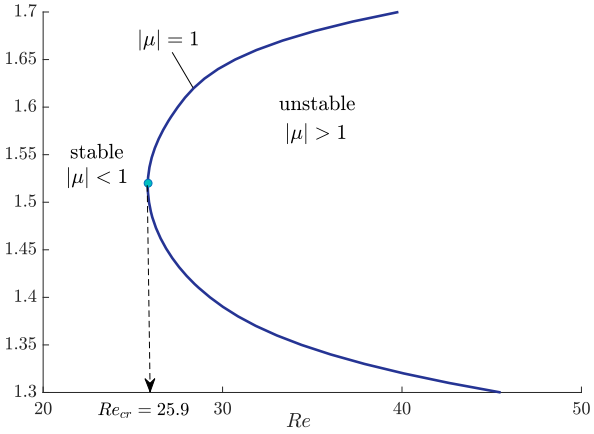

Figure 2: The curve of marginal stability corresponding to $|\mu| = 1$ in the (Re, k)-plane, for $= 1$ and $H_2 = H_1 = \infty$. The critical Reynolds number Re_{cr}, indicated with a dot, is defined as the minimum Re-value of the marginal curve.

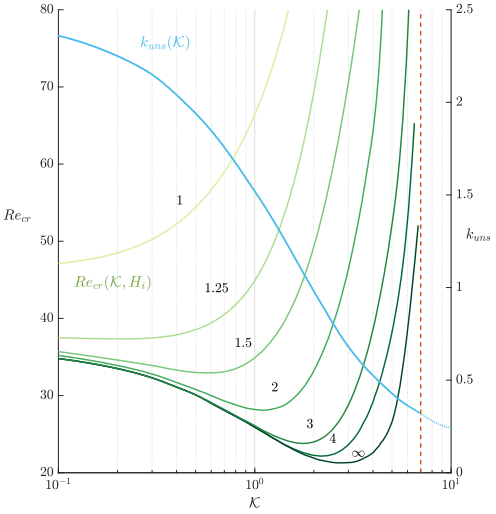

Figure 3: Critical Reynolds number Re_{cr} and corresponding wave number k_{uns} as a function of the wall stiffness for symmetric channel configurations with $H_1 = H_2$.

References

V. Kumaran (2021). *J. Fluid Mech.*, **924**, P1-2–80.

C. Davies and P. W. Carpenter (1997). *J. Fluid Mech.*, **352**, 205–243

Linear Rayleigh-Taylor instability of rotating viscous fluids

Ángel de Andrea González[1], José María Gandarias Villanueva[2], Leo Miguel González Gutiérrez[2]

[1]*Universidad Carlos III de Madrid, SPAIN*
[2]*Universidad Politécnica de Madrid, SPAIN*

The Rayleigh-Taylor instability is studied for the viscous and non-viscous case of two fluids of finite thickness, subjected to rotation around an axis perpendicular to the direction of acceleration. The effect of surface tension is also considered for both cases. In contrast of the non-viscous case where the combined effect of finite thickness and rotation modify the cut-off wave number due to surface tension, for the viscous case, the cut-off wave number remains unchanged. Likewise, it is verified that the wavelength of the mode of maximum instability reaches a limit value due to the action of surface tension. These computations are performed as a 1D problem assuming the other two directions as periodic, but the results are confirmed in 2D when a rectangular domain is used.

INTRODUCTION

Baldwin *et al.* [1] show experimentally that rotation about an axis normal to the interface between two uniform viscous fluids acts to retard the growth rate of the Rayleigh-Taylor instability (RTI) and stabilise long wavelength modes. The results agree qualitatively with Hide's [2]. Moreover, these authors suggest that rotation acts to stabilise long wavelength instabilities, while viscosity stabilises short wavelength instabilities. Tao *et al.* [3] obtained an analytical expression of the RTI linear growth rate in a rotating system with the axis of rotation normal to the acceleration of the interface between two uniforms inviscid fluids. They found that the Coriolis force always diminished the aforementioned growth rate and that this retardation effect becomes stronger when the Atwood number is increased. These authors also speculated on the use of rotation to suppress RTI in the spherical pellets used in inertial confinement fusion. However, to the best of our knowledge no study of rotating RTI including viscosity, surface tension and finite thickness effect has been performed.

We will extend Tao's model [3] in two stages: first, we will incorporate the effects of finite thickness and surface tension; Secondly, we will take into account the effect of the viscosity of the fluid. In this last case we will consider that the kinematic viscosity is constant in the two fluid phases.

In this paper we perform this survey in the case of one-dimensional (1D) and two dimensional (2D) geometries.

Similarly to [4], a hyperbolic tangent distribution for the density and viscosity profiles are imposed, which allows skipping the compatibility conditions when sharp interfaces are simulated.

$$\bar{\rho} = 1 + A_\rho tanh(y/L_s), \qquad \bar{\mu} = 1 + A_\mu tanh(y/L_s) \quad (1)$$

where L_s is the gradient scale length of the density and viscosity A_ρ , A_μ the Atwood numbers associated to density and viscosity.

THEORETICAL BACKGROUND AND RESULTS

First, the inviscid case is analyzed. Looking for the cut-off wave number, *i.e.* the wave number where the growth rate vanishes, figure [1] shows the dependence of the dimensionless cut-off k_c wave number as a function of the dimensionless angular velocity Ω_z for different dimensionless thicknesses H of the fluids, being the dimensionless surface tension and the Atwood number $S = 0.2$ and $A_\rho = 0.2$, respectively.

In general it is observed, for a given angular velocity, the existence of two cut-off wave numbers. The upper cutoff wave number k_c^+ is the result of the joint action of surface tension and the Coriolis force. This last force reinforces the action of the first one, since that cut-off wave number decreases with respect to the case in which there is no rotation ($k_c = 1$) . On the other hand, the lower cut-off wave number k_c^- is due to the exclusive action of the Coriolis force.

For the case of $H \to \infty$ and $\Omega_z = 1.135$, the upper wave is $k_c^+ = 0.828394$ and $k_c^- = 0.140303$. Therefore, it can be deduced that the cut-off wave number, due to the exclusive action of surface tension in the absence of rotation ($k_c = 1$) , has decreased by about 17% due to the action of rotation. In order to analyze the effect of finite thickness, we consider the particular case of $H = 3$ and $\Omega_z = 1.135$. We can verify that the upper cut-off wave number is $k_c^+ = 0.833726$, *i.e.* it increases with respect to that corresponding to the case $H \to \infty$. Furthermore, it is observed that for a given thickness H there is a critical angular velocity Ω_z^* above which the

modes are stable. For the case $H = 3$, we obtain $\Omega_z^* = 1.43957$. Likewise, as H decreases, Ω_z^* increases.

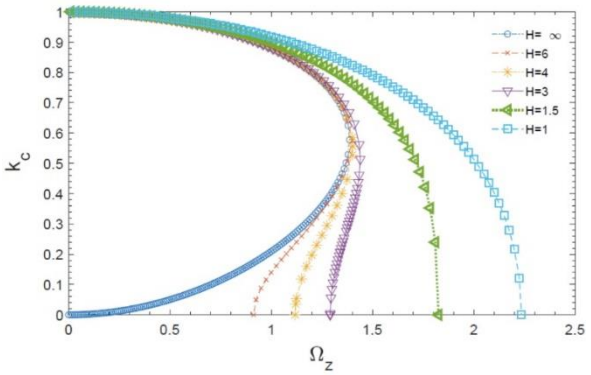

FIG 1. Dimensionless cut-off wave k_c number versus dimensionless angular velocity Ω_z different values of fluid dimensionles thickness H.

Secondly, the viscous case is considered. The results obtained show that the cut-off wave number of the surface tension remains unchanged with respect to the case of absence of rotation. However, the growth rate of instability is reduced, as found in previous works [1], [2]. On the other hand, it is found that the dimensionless wavelength of the maximum instability mode λ_m decreases with an increase in angular velocity Ω_z until it reaches an asymptotic value that is not reached when the effect of surface tension is neglected. The graph shows that for the case $H = 1$, $A_\rho = A_\mu = 0.2$, $S = 3 \cdot 10^{-4}$ this asymptotic value is $\lambda_m \approx 0.997331$.

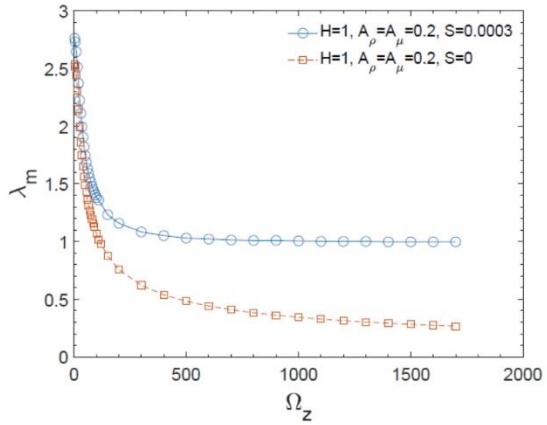

FIG 2. Plot of the wavelenght λ_m of the fastest growing mode against angular velocity Ω_z

CONCLUSIONS

The most important conclusions obtained in this work are the following:

Neglecting viscosity, the cut-off wave numbers due to rotation and surface tension depend on the thickness of the fluids and the angular velocity. Therefore, this shows that the cut-off wavenumber due to surface tension is not always independent of the thickness of the fluids as previously believed. Furthermore, when the thickness of the fluids decreases, the number of excited RTI modes increases. Actually, this is because a decrease in such a thickness leads to an increase in the angular velocity above which the system is stable.

For the viscous case, the cut-off wave number due to surface tension is independent of the rotation, as well as the thickness of the fluids. Also, it is found that, due to surface tension, the wavelength of the mode of maximum instability saturates for very large angular velocities.

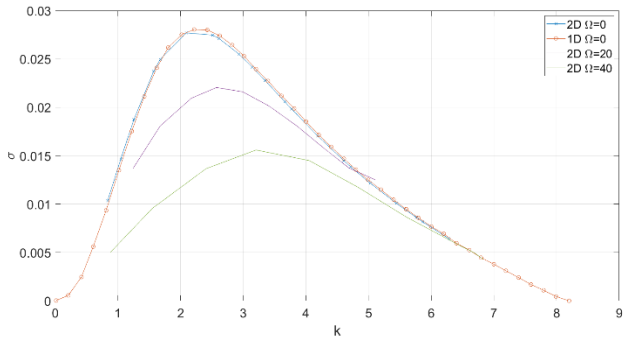

FIG 3. Growth rate of the Rayleigh-Taylor instability versus dimensionless wavenumber for different values of the angular velocity Ω_z.

* leo.gonzalez@upm

[1] Baldwin K. A., Scase M. M., and Hill R.J. A. (2015) "The Inhibition of the Rayleigh-Taylor Instability by rotation". *Sci. Rep.* **5**, 11706.
[2] Hide R. (1956) "The character of the equilibrium of a heavy, viscous, incompressible, rotating fluid of variable density II: two special cases". *Q. J. Mech. Appl. Math.* **9**, 35–50.
[3] Tao J. J., He X. T., Ye W. H., and Busse F. H. (2013) "Nonlinear Rayleigh-Taylor instability of rotating inviscid fluids". *Phys. Rev. E* **87,** 013001.
[4] Martínez-Carrascal J, Calderón-Sánchez, González-Gutiérrez L. M. , and De Andrea González A. (2021) "Extended computation of the viscous rayleigh-taylor instability in a horizontally confined flow," *Phys. Rev. E* **103**, 053114.

2nd Spanish Fluid Mechanics Conference
Barcelona (2 - 5 July 2023)

Linear stability analysis of a two-layer channel flow with a train of solid particles flowing parallel to the interface

Désirée Ruiz-Martín [1], Javier Rivero-Rodríguez[2], and Mario Sánchez-Sanz[1]

deruizm@ing.uc3m.es

[1]Departamento de Ingeniería Térmica y de Fluidos, Universidad Carlos III de Madrid, Spain
[2]Departamento de Ingeniería Mecánica, Térmica y de Fluidos, Universidad de Málaga, 29071, Spain

The present study analyses the global linear stability of a two-layer channel flow when a train of solid particles is flowing near the deformable liquid-liquid interface. Three different mechanisms of instability are identified: shear, interfacial and migration modes. We demonstrate that the interfacial instability, associated to the viscosity jump at the interface, is coupled to the migration of the particle. The stability of the flow configuration is assessed for different values of the governing parameters - fluids viscosity and flow rate ratios, particle position, interparticle distance and Reynolds and capillary numbers. Our numerical results are compared with those corresponding to the particle-free flow configuration to show that, if the particle is immersed in the more-viscous fluid, its effect is always destabilizing. Remarkably, for certain flow parameters the presence of the particle stabilizes the interface when it is flowing in the less-viscous liquid. The effect of the particles becomes more significant as the Ohnesorge number $Oh = \sqrt{Re/Ca}$ increases.

1 Introduction

Despite the potential instability problems, many engineering applications use immiscible fluids to transport solid particles along channels, see e.g. Lee *et al.* (2010). As described in the literature (Yiantsios and Higgins, 1988), two parallel immiscible fluids might become unstable either as a consequence of shear or viscosity-induced instabilities. The presence of a train of particles flowing in the two-layer flow introduces a new instability mechanism, via the migration of the particle, that might or not interact with other instability mechanisms to stabilize or destabilize the interface. In a previous study, we extensively described the migration of the train of particles (Ruiz-Martín *et al.*, 2022). This work aims precisely to study the effect that particles migrating in one of the fluids might have on the stability of the interface separating both liquids.

2 Formulation of the problem

2.1 Unperturbed base-state flow

The flow configuration consists of two immiscible liquids co-flowing in a channel with heigth h (see figure 1). The liquids have equal density $\rho_1 = \rho_2$ but different viscosity $\mu_1 \neq \mu_2$. The total volumetric flow rate of the two liquids is $Q = Q_1 + Q_2$ and the interface is located at $y = \Gamma$. A train of particles of diameter d travels at its terminal velocity V in the upper fluid forming a periodic flow structure, with each particle separated by a distance L from the closest neighbour. The transverse location of the particle depends on the intensity of a uniform body force $\boldsymbol{f} = f\boldsymbol{e_y}$ acting on both fluids. To write the problem in non-dimensional form, we choose the channel height h, the average velocity $\bar{u} = Q/h$ and $p_c = \mu_2\bar{u}/h$ as the characteristics length, velocity and pressure to define the non-dimensional variables. The average velocity $\bar{u}$ and the properties of fluid 2 define the Reynolds number of the flow $Re = \rho Q/\mu_2$ and the capillary number $Ca = \mu_2 Q/\gamma$. The non-dimensional continuity and momentum equations are

$$\nabla \cdot \boldsymbol{v}_i = 0\,, Re\left(\frac{\partial \boldsymbol{v}_i}{\partial t} + \boldsymbol{v}_i \cdot \nabla \boldsymbol{v}_i\right) = \nabla \cdot \hat{\boldsymbol{T}}_i\,. \qquad (1)$$

with $\hat{\boldsymbol{T}}_i = -\hat{p}_i\boldsymbol{\mathcal{I}} + \mu(\nabla \boldsymbol{v}_i + \nabla \boldsymbol{v}_i^T)$ and being $\hat{p}_i = p_i - \boldsymbol{f}\cdot(\boldsymbol{x} - \boldsymbol{x}_p)$, the reduced pressure. The viscosity ratio is defined as $\mu = \mu_1/\mu_2$ if $y < \Gamma$ and $\mu = 1$ if $y > \Gamma$. Non-slip boundary condition is imposed at the channels walls $y = 0$ and $y = 1$, $\boldsymbol{v} = -V\boldsymbol{e}_x$ whereas at the extremes of the computational domain $x = \pm L/2$ we assume periodic boundary conditions, $\boldsymbol{v}|_{L/2} = \boldsymbol{v}|_{-L/2}$, $\partial_x \boldsymbol{v}|_{L/2} = \partial_x \boldsymbol{v}|_{-L/2}$, $p|_{L/2} = p|_{-L/2} - \Delta p$. The interface position and Δp are obtained by imposing the flow rates as total flow rate and flow ratios $\int_0^\Gamma (u_1 + V)\,\mathrm{d}y + \int_\Gamma^1 (u_2 + V)\,\mathrm{d}y = 1$, $\int_0^\Gamma (u_1 + V)\,\mathrm{d}y = Q_1/Q_2 \int_\Gamma^1 (u_2 + V)\,\mathrm{d}y$. To determine the motion of the rigid particles, we impose equilibrium of forces, zero net torque and non-slip conditions.

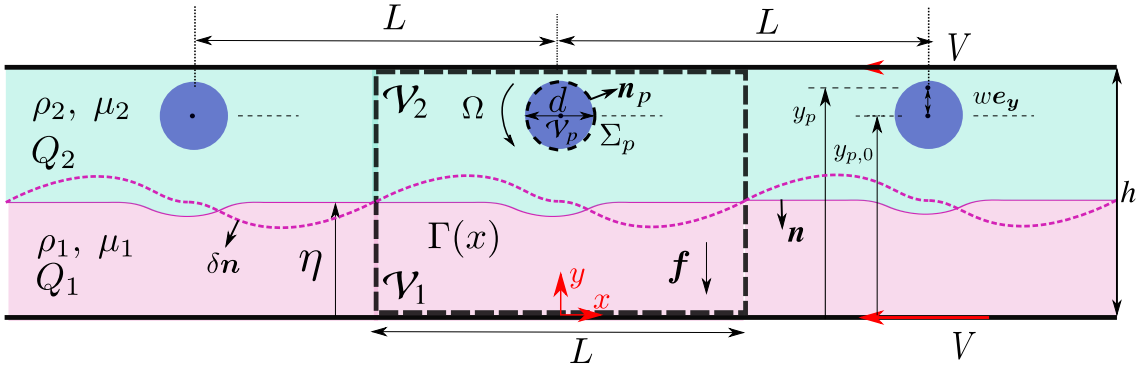

Figure 1: Schematics of the flow configuration, including the geometrical and fluid-dynamical relevant parameters.

2.2 Linear stability problem

The configuration considered in 2.1 provides the solution upon which we will perform a global stability analysis. To initiate the study, we introduce a small periodic normal perturbation to the interface $\boldsymbol{\delta} = \epsilon e^{\lambda t}\delta(\boldsymbol{x})\boldsymbol{n}$, so that $\boldsymbol{x}' = \boldsymbol{x} + \delta\boldsymbol{n}$ with $\epsilon e^{\lambda t} \ll 1$ and $\boldsymbol{x}' \in \Gamma'$, $\boldsymbol{x} \in \Gamma_0$. The base flow is then unstable when the real part of the eigenvalues is positive $\lambda_r > 0$. Periodic perturbations in the value of the volumetric force are not considered. The rest of variables $\psi = (\hat{p}_i, \boldsymbol{v}_i, V, \Omega, \Delta p)$ are also perturbed periodically with the same frequency λ, yielding

$$\psi(t) = \psi_0 + \epsilon e^{\lambda t}\psi_1\,. \tag{2}$$

Similarly, the position of the centre of mass of the particle is perturbed periodically in the transverse direction $\boldsymbol{w} = w\boldsymbol{e}_y$, such that $\boldsymbol{x}_p(t) = \boldsymbol{x}_{p,0} + w\ \epsilon e^{\lambda t}\boldsymbol{e}_y$. Substituting (2) in the dimensionless Navier-Stokes equations, and neglecting terms of order $O(\epsilon^2)$, we obtain the following system for the linearized problem,

$$\nabla\cdot\boldsymbol{v}_{i,1} = 0\,, \tag{3}$$

$$Re\left(\lambda\boldsymbol{v}_{i,1} + \boldsymbol{v}_{i,0}\cdot\nabla\boldsymbol{v}_{i,1} + \boldsymbol{v}_{i,1}\cdot\nabla\boldsymbol{v}_{i,0}\right) = \nabla\cdot\hat{\boldsymbol{T}}_{i,1}\,, \tag{4}$$

with $\hat{\boldsymbol{T}}_{i,1} = -p_{i,1}\boldsymbol{I} + f_0 w + \mu\left(\nabla\boldsymbol{v}_{i,1} + \nabla\boldsymbol{v}_{i,1}^T\right)$ the perturbed reduced stress tensor at first order. The local displacement of a point on the surface of the particle in the normal direction is defined as $\tilde{\boldsymbol{\delta}} = \tilde{\delta}(\boldsymbol{x})\boldsymbol{n}$, i.e. $\boldsymbol{x} = \boldsymbol{x}_0 + \epsilon e^{\lambda t}\tilde{\boldsymbol{\delta}}$ at Σ_p. The condition of rigid particle renders $\tilde{\delta} = w\boldsymbol{e}_y\cdot\boldsymbol{n}$. At the perturbed particle surface, non-slip, equilibrium of forces and zero net torque conditions are enforced. To do so, the non-slip condition is linearized and we impose the momentum and angular momentum equations to the control volume that encompasses the fluid volume generated by the particle displacement.

3 Conclusions

This study considers the effect of a train of particles on the stability of the interface formed by two immiscible liquids. Three different instability mechanisms have been identified: shear, migration and interfacial modes. The migration mode is uncoupled from the other instability modes and can be studied separately. The interfacial mode, however, is clearly affected by the migration of the particle. Our numerical results show that the presence of a migrating particle always promotes the unstable character of the interface when the particle is in the more viscous fluid $\mu_1/\mu_2 < 1$. Yet, when the particle is in the less viscous fluid $\mu_1/\mu_2 > 1$, we find a range of parameters for which the particle stabilizes the interface, regardless of the inter-particle distance. The influence of the particle position becomes more significant as the Ohnesorge number ($Oh^2 = Ca/Re$) increases.

References

Lee, W., Amini, H., Stone, H. A., & Di Carlo, D. (2010). "Dynamic self-assembly and control of microfluidic particle crystals". *Proceedings of the National Academy of Sciences*, **107(52)**, 22413-22418.

Yiantsios, S. G., & Higgins, B. G. (1988). "Linear stability of plane Poiseuille flow of two superposed fluids". *The Physics of fluids*, **31(11)**, 3225-3238.

Ruiz-Martín, D., Rivero-Rodriguez, J., & Sánchez-Sanz, M. (2022). "Solid particles moving parallel to a deformable liquid–liquid interface in a microchannel: migration forces". *Journal of Fluid Mechanics*, **948**, A44.

2nd Spanish Fluid Mechanics Conference
Barcelona (2 - 5 July 2023)

Regularized four-sided cavity flows: A spectral bifurcation benchmark implemented in Julia

Moritz Waldleben[1], Álvaro Meseguer[2], Oriol Batiste[2], and Arantxa Alonso[2]

moritz.waldleben@epfl.ch

[1]Section de Mathématiques, École Polytechnique Fédérale de Lausanne, EPFL (Switzerland)
[2]Departamento de Física, Universitat Politècnica de Catalunya, Barcelona, UPC (Spain)

This work presents a regularized version of the four-sided lid-driven cavity for incompressible fluids. The four-sided driven cavity is an extension of the simple lid-driven case where all lids move with the same velocity profile and parallel lids move in opposite directions. Lid-driven cavity flows are used to validate Navier-Stokes solvers. This study focuses on the regularized version to overcome corner singularities. The proposed method recovers near exponential convergence in spectral discretization schemes. The flow presents a variety of bifurcation scenarios and can make up for an amenable Navier-Stokes bifurcation benchmark. The algorithms are implemented in Julia, a high-performance language for scientific computing. A developed Julia module provides a reproducible example of spectral discretization for the proposed benchmark.

1 Introduction

Driven cavity flows are commonly used as benchmarks to validate Navier-Stokes solvers. These problems can test spatial discretization methodologies such as finite elements, finite differences, and spectral methods. They also assess a variety of boundary condition implementations and time-stepping schemes. The simple lid-driven cavity flow has received considerable attention. This flow is steady for high Reynolds numbers, with the first instability due to a supercritical Hopf bifurcation occurring within a large uncertainty interval (7500, 8100) [Kuhlmann (2018)].

More recent variants, such as the four-sided version of the cavity flow, have been proposed [Wahba (2009)]. Here the four lids are moving at the same speed (top-bottom and right-left lids moving rightwards-leftwards and upwards-downwards, respectively). Later works tested different numerical techniques and studied the bifurcations with linear stability analysis, arc-length continuation, and time-stepping [Perumal (2011), Cadou (2012), Chen (2013)]. This cavity has the computational advantage of exhibiting a variety of bifurcations at low or moderate Reynolds numbers.

Still, the problem suffers from corner singularities due to the discontinuous boundary conditions and affects the exponential convergence of spectral methods. This work presents a regularized version of the four-sided cavity flow to address the issue. A spectral Chebyshev discretization of the flow problem is implemented in Julia, a high-performance language for scientific computing. Julia is free, open-source, and provides good performance comparable to compiled C/Fortran codes, making it an attractive platform for scientific computing. A developed Julia module provides a reproducible example of the proposed cavity.

The regularized four-sided lid-driven cavity shows most of the primary bifurcation scenarios. The flow undergoes instabilities, such as pitchfork, saddle-node (fold), and Hopf. Predicting the precise location of the bifurcations could present an amenable benchmark when testing and comparing different schemes and implementations.

2 Mathematical formulation

We consider the two-dimensional and time-dependent Navier-Stokes equations in streamfunction formulation $\Psi(x,y,t)$ for incompressible fluids,

$$\partial_t \Delta\Psi = \frac{1}{\mathrm{Re}}\Delta^2\Psi + (\partial_x\Psi)\partial_y(\Delta\Psi) - (\partial_y\Psi)\partial_x(\Delta\Psi), \quad (1)$$

within the square domain $(x,y) \in [-1,1]\times[-1,1]$.

To discretize (1) using a spectral method, we define regularized boundary conditions in terms of exponential functions

$$u(\pm 1,y,t) = 0, \quad (2)$$
$$v(x,\pm 1,t) = 0, \quad (3)$$
$$u(x,\pm 1,t) = \pm(\mathrm{e}^{k_0(x-1)} - 1)(\mathrm{e}^{-k_0(x+1)} - 1)^2, \quad (4)$$
$$v(\pm 1,y,t) = \pm(\mathrm{e}^{k_0(y-1)} - 1)(\mathrm{e}^{-k_0(y+1)} - 1)^2. \quad (5)$$

The regularized boundary conditions impose a zero velocity at all four corners of the cavity. Figure 1 shows such a profile for the regularization parameter $k_0 = 10$.

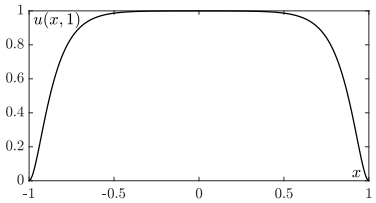

Figure 1: Regularized horizontal velocity profile (4) at the top wall $y = 1$ for $k_0 = 10$.

3 Computational methods and Results

The cavity is discretized using a two-dimensional Chebyshev grid $[\cos(\frac{i\pi}{m}), \cos(\frac{j\pi}{n})]$ where $i = 0,1,...,m$ and $j = 0,1,...,n$.

To incorporate the boundary condition, the streamfunction is set to be zero at the lids. The first inner grid points are defined through the derivative of the streamfunction (2-5).

For the steady-state flows, the zeros of equation (1) have to be computed. As the outer grid points are explicitly known through the boundary conditions, a reduced system of equations $F(\psi, \mathrm{Re}) = 0$ can be formulated. $\psi \in \mathbb{R}^{(m-1)\times(n-1)}$ corresponds now to the inner grid points.

We apply a Newton-Raphson algorithm to solve this system of non-linear equations, and discretize the associated Jacobian using finite differences. This Newton method can then be used in a pseudo-arclength continuation algorithm to track the solutions as a function of the Reynolds number.

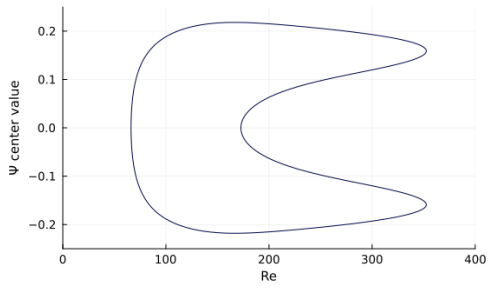

Figure 2: Branch of asymmetric solutions on a 32×32 grid obtained with pseudo-arclength continuation

Figure 2 shows the asymmetric branches obtained by the continuation algorithm and figure 3 illustrates one of these solutions. The pitchfork bifurcations seem to agree with the ones found in [Wahba (2009), Chen (2013)] whereas the locations of the saddle nodes are different as a result of the regularization process. Furthermore, it has been vindicated that there is a Hopf bifurcation occurring at a Reynolds number of around 350.

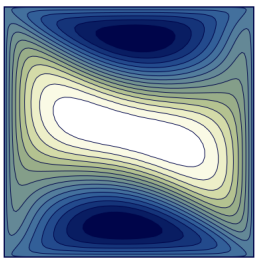

Figure 3: Asymmetric solution for 64×64 at Reynolds 100

4 Conclusions

We have shown some primary results of the regularized four-sided cavity flow. The problem has been discretized with a Chebyshev spectral method and provides a way to accurately determine a rich number of bifurcation scenarios. The computed pitchfork bifurcations seem to coincide with the un-regularized version. Additionally, it could be used as a benchmark to test other discretization schemes.

Acknowledgement

This research was supported by the Spanish Ministerio de Ciencia e Innovación, under grant No. PID2020-114043GB-I00.

References

Wahba E. M. (2009) "Multiplicity of states for two-sided and four-sided lid driven cavity flows", *Comput. Fluids*, **38**, 247–253

Arumuga Perumal D., Dass A. K. (2011) "Multiplicity of steady solutions in two-dimensional lid-driven cavity flows by Lattice Boltzmann Method", *Comput. Math. with Appl.*, **61**, 3711–3721

Cadou J. M., Guevel Y. and Girault G. (2012) "Numerical tools for the stability analysis of 2D flows: application to the two- and four-sided lid- driven cavity", *Fluid Dyn. Res.*, **44** (3), 031403

Chen, K. T., Tsai C. C. and Luo W. J. (2013) "Multiplicity Flow Solutions in A Four-sided Lid-driven Cavity", *Appl. Mech. Mater.*, **368-370**, 838–843

Kuhlmann H., Romanò F. (2018) "The Lid-Driven Cavity", *Comput. Methods Appl. Sci.*

2nd Spanish Fluid Mechanics Conference
Barcelona (2 - 5 July 2023)

Self-sustainment, Period Doubling and Boundary Crisis of Subcritical Rotating Waves in Taylor-Couette Flow

Baoying Wang[1], Roger Ayats[2], Kengo Deguchi[3], Fernando Mellibovsky[1], and Alvaro Meseguer[1]

baoying.wang@upc.edu

[1]Departament of Physics, Universitat Politècnica de Catalunya, Barcelona, Spain
[2]Institute of Science and Technology Austria (ISTA), 3400 Klosterneuburg, Austria
[3]School of Mathematics, Monash University, VIC 3800, Australia

1 Introduction

Self-sustaining process (SSP) (Waleffe, 1997) is normally studied in parallel shear flows or in the subcritical regime of Taylor-Couette flow (TCF). Compared with shear-driven flows, the self-sustainment of exact coherent structures in TCF is more involved because of the coexistence of shear and centrifugal instabilities. We study a series of self-sustained drifting-rotating waves (DRW) underlying spiral turbulence (SPT) with rich dynamical behaviors.

2 Methods and Main Results

The control equations are the incompressible Navier-Stokes equations of the perturbation field:

$$\begin{aligned}\partial_t \mathbf{u} = &-\nabla q + \nabla^2 \mathbf{u} - (\mathbf{v}_\mathrm{b}\cdot\nabla)\mathbf{u} - (\mathbf{u}\cdot\nabla)\mathbf{v}_\mathrm{b} \\ &- (\mathbf{u}\cdot\nabla)\mathbf{v}_\mathrm{b} - (\mathbf{u}\cdot\nabla)\mathbf{u},\end{aligned} \tag{1}$$

$$\nabla\cdot\mathbf{u} = 0, \tag{2}$$

in which $\mathbf{u}$ is the velocity of perturbation expressed in cylindrical coordinates (r,θ,z) and $\mathbf{v_b}$ is the base flow velocity. Solenoidal Petrov-Galerkin scheme formerly formulated by Meseguer et al. (2007) is adapted to annular-parallelogram domains for discretization:

$$\mathbf{u}_\mathrm{s} = \sum_{\ell=-L}^{L}\sum_{n=-N}^{N}\sum_{m=0}^{M} a_{\ell nm}(t)\mathbf{\Phi}_{\ell nm}(r,\xi,\zeta). \tag{3}$$

And the solenoidal velocity perturbation is approximated through a Fourier-Chebyshev spectral expansion. Forth order linearly implicit time scheme is chosen for DNS computations. Newton-Krylov (Kelley , 2003) pseudo-arclength continuation, along with Arnoldi eigenvalue methods are used to track and monitor the exact coherent structures and their linear stability, respectively.

The DRW is captured in minimal computational box with two of whose sides aligned with the cylindrical helix described by the spiral pattern. In a narrow region of parameter space close to the saddle-node bifurcation where they are created, the DRW are linearly stable. These stable solutions undergo a Hopf bifurcation, generating periodic solutions that eventually lead to a chaotic attractor via period doubling cascade. As the Reynolds number increases, the chaotic attractor undergoes a boundary crisis and finally becomes a chaotic saddle.

The SSP is proved to be at work in the subcritical regime, as roll and streak constituents of the DRW trigger the azimuthally-dependent wave component and are, at the same time, regenerated by it. The rapid and monotonic decay of energy in the time evolution starting from merely roll-streak components shown in figure 1 (black dashed line) indicates the indispensable role of the wave components in sustaining DRW in the subcritical regime. We also find that the unstable eigenmode of the roll-streak system resembles that of DRW, as shown in figure 2, indicating the wave components are triggered by the instability of the roll-streak components.

These DRW solutions can be tracked up to supercritical regime. We have explored their dynamical relevance with supercritical SPT by replicating the solution in the azimuthal direction to fulfill the whole perimeter. The results show the self-sustained vortices eventually concentrate into a localized pattern which satisfactorily reproduces the topology and properties of the SPT calculated in classical orthogonal computational box.

3 Conclusions

We have reported a family of high subcritical three-dimensional nonlinear wave solutions that spread over both subcritical and supercritical regimes of

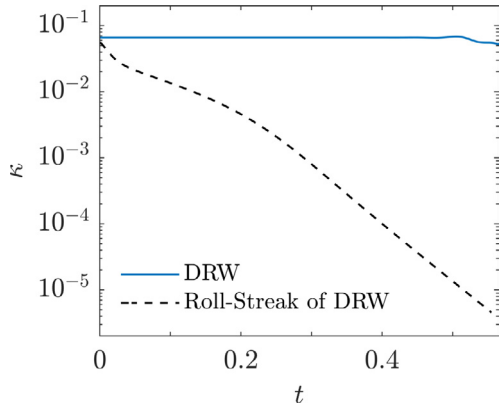

Figure 1: Time evolution of normalized kinetic energy κ starting from either the DRW (solid blue line) for $(R_o, R_i) = (-1200, 450)$ or only its roll–streak components (dashed black), showing the role of the wave component in sustaining DRW in subcritical regime. (Wang et al., 2022)

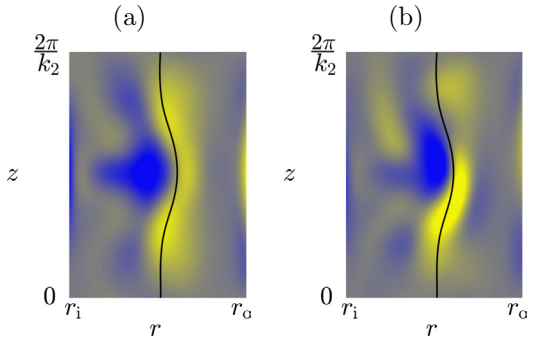

Figure 2: Azimuthal vorticity colormaps at $\theta = 0$ of (a) the only unstable eigenmode of the roll-streak system and (b) the wave field. Colormaps are $\omega_r \in [-90, 90]$ and $\omega_r \in [-700, 700]$ for caption a and b, respectively. (Wang et al., 2022)

counter-rotating Taylor-Couette flow. In the subcritical regime, the SSP is proved to be the reason for the self-sustainment of DRW. In the supercritical regime, where SPT exists, the dynamical relevance of the DRW within SPT dynamics is shown by replicating the wave in the azimuthal direction so that it fills in a narrow parallelogram domain revolving around the apparatus perimeter. Results show that the self-sustained vortices eventually concentrate into a localized pattern which satisfactorily reproduces the topology and properties of the SPT calculated in a large periodic domain of sufficient aspect ratio that is representative of the real system.

References

Waleffe, F. (1997). "On a self-sustaining process in shear flows",*Phys. Fluids*, **9**(4), 883–900, 1997.

Meseguer, A., Avila, M., Mellibovsky, F., & Marques, F. (2007). "Solenoidal spectral formulations for the computation of secondary flows in cylindrical and annular geometries: Solenoidal spectral formulations.",*Eur. Phys. J. Special Topics*,**146**, 249.

Kelley, C. (2003). "Solving nonlinear equations with Newton's method.",*Society for Industrial and Applied Mathematics*.

Wang, B., Ayats, R., Deguchi, K., Mellibovsky, F., and Meseguer, A. (2022). "Self-sustainment of coherent structures in counter-rotating Taylor–Couette flow.",*J. Fluid Mech.*, **951**, A21.

2nd Spanish Fluid Mechanics Conference
Barcelona (2 - 5 July 2023)

Stability of magnetohydrodynamic shock waves

Andrés Calvo-Rivera[1], César Huete[1], Fernando García Rubio[2], and Alexander L. Velikovich[3]

andcalvo@ing.uc3m.es

[1]Departamento de Ingeniería Térmica y de Fluidos, Universidad Carlos III de Madrid, Leganés 28911, Spain
[2]Laboratory for Laser Energetics, University of Rochester, Rochester, New York 14623-1299, USA
[3]Plasma Physics Division, U.S. Naval Research Laboratory, Washington, DC 20375, USA

The approach of magnetized target fusion (MTF) to inertial confinement fusion (ICF) entails the creation of strong shock waves that propagate through a magnetized plasma. These shocks, which assume a pivotal role in the process of thermalizing the kinetic energy generated in the implosion stage, are often subject to perturbations and may deform in response to disturbances upstream or downstream. Prior experiments involving Z-pinch have demonstrated that pre-embedded axial magnetic fields can effectively mitigate plasma instability. In the present work, we aim to examine the effect of perpendicular magnetic field on planar shock stability.

1 Introduction

Within the extensive parameter space of magnetized target fusion (MTF), the region investigated in magnetized liner inertial fusion (MagLIF) has emerged as a prominent area of fusion research over the past decade. In brief, MagLIF schemes involve a cylindrical liner-on-target implosion and comprise three primary stages: fuel magnetization with an axial magnetic field, fuel preheating using a laser beam, and liner compression via a pulsed-power machine, although laser-driven versions have also been examined. (Slutz, 2012). Akin to MagLIF, a new approach known as Staged Z-pinch (SZP) (Rahman, 1995; Wessel, 2015) predicts high fusion yields with driver parameters typical of the Sandia Z machine. The efficacy of SZP relies on the implementation of a liner with a high atomic number to achieve substantial fuel magnetization through B-field diffusion and provide fuel preheating via fast magnetohydrodynamic (MHD) shock waves. Generally, MTF designs involve the formation of shock waves within a magnetized medium, the thermodynamic properties of which may not be accurately described by an ideal gas equation of state.

To further understand the effect of magnetic fields on the shock dynamics, we carry out an analytical model to solve the initial-value problem (IVP) in isolated-shock conditions. Besides, a numerical analysis is performed on perpendicular fast magnetosonic shocks. In particular, a theoretical study of the stability of planar MHD shocks is developed to explore the boundaries associated with neutral stability, also known as spontaneous acoustic emission (SAE), and those associated with exponentially growing disturbances. In this work we extend the analysis of (Gardner, 1964; Trakhinin, 2003) to provide information, not only on the stability boundaries, but also on the transient evolution of the shock and the post-shock variables. For this particular configuration, where the magnetic field is perpendicular to the shock direction and also perpendicular to the perturbation wavenumber vector, the governing equations can be reduced to a sound-wave-like equation whose characteristic information propagation speed is the fast magnetosonic speed rather than the acoustic (thermal) sound speed.

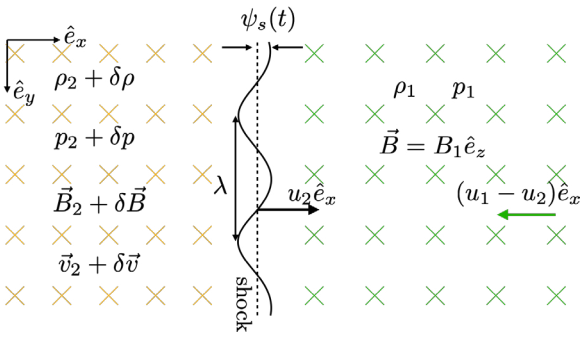

Figure 1: Sketch of the corrugated shock moving through the magnetized medium. Velocities are measured in the compressed gas reference frame $\vec{v}_2 = 0$.

2 Problem Description

Let a planar shock front move with velocity $\vec{u}_1 = u_1\hat{e}_x$ in a uniform medium with known pressure p_1, density ρ_1 and internal energy E_1. Let's consider a magnetic field ahead of the shock $\vec{B}_1 = B_1\hat{e}_z$ that is perpendicular to the shock propagation direction.

In a reference frame attached to the shock front, the conservation equations across read as

$$
\begin{aligned}
[\rho u] &= 0, && \text{(1a)}\\
\left[p + \rho u^2 + \frac{B_t^2}{8\pi}\right] &= 0, && \text{(1b)}\\
[B_t u] &= 0, && \text{(1c)}\\
\left[\rho u\left(e + \frac{p}{\rho} + \frac{u^2}{2}\right) + u\frac{B_t^2}{4\pi}\right] &= 0, && \text{(1d)}
\end{aligned}
$$

provided that the normal component of the magnetic field must be continuous across the shock: $B_{x1} = B_{x2} = 0$. In writing (1) we have identified the post-shock flow variables with the subscript 2. In our case, the initial small shock corrugation amplitude $\epsilon\lambda = \psi_s(t=0) = \psi_{s0}$ provides the small parameter of our linear formulation, see the sketch depicted in Fig. 1.

The problem formulation continues with the formulation of the linearized ideal MHD equations that govern the unsteady post-shock flow, namely

$$
\begin{aligned}
\frac{\partial \delta\rho}{\partial t} + \rho_2 \nabla\cdot\delta\vec{v} &= 0, && \text{(2a)}\\
\rho_2\frac{\partial \delta\vec{v}}{\partial t} + \nabla\delta p & \\
-\frac{1}{4\pi}\left(\nabla\times\delta\vec{B}\right)\times\vec{B}_2 &= 0, && \text{(2b)}\\
\frac{\partial \delta p}{\partial t} - c_{T2}^2\frac{\partial \delta\rho}{\partial t} &= 0, && \text{(2c)}\\
\frac{\partial \delta\vec{B}}{\partial t} - \nabla\times\left(\delta\vec{v}\times\vec{B}_2\right) &= 0, && \text{(2d)}
\end{aligned}
$$

written in a reference frame co-moving with the fluid particles. They correspond to the continuity equation, the conservation of linear momentum, the conservation of energy for an isentropic and adiabatic flow, and the magnetic induction equation. The parameter c_{T2} corresponds to the speed of sound in the shocked gas. The formulation assumes that the base-flow is uniform, that the medium is a perfect conductor, and that all perturbations are of the same order. Dimensionless equations can be combined as a parameter-free transverse-periodic sound wave equation, which requires two initial conditions and two boundary conditions in the streamwise direction. One boundary condition is given by the shock driving mechanism, while the other is given by the linearized Rankine-Hugonoit conservation equations.

3 Results

The evolution of the shock ripple amplitude is shown in Fig. 2 (a) for a fast MHD shock in an ideal gas, with adiabatic index $\gamma = 4$, mass-compression ratio $\rho_2/\rho_1 = 1.56$ and two distinguished cases: non-magnetized and highly magnetized pre-shocked matter. The former, plotted in blue, is associated with a regular decaying solution; while the latter, in orange, corresponds to a long-time non-decaying condition. The dimensionless time is scaled with perturbation wavenumber $2\pi/\lambda$ and the fast magnetosonic speed, namely $c_{F2}^2 = B_2^2/(4\pi\rho_2) + \gamma p_2/\rho_2$.

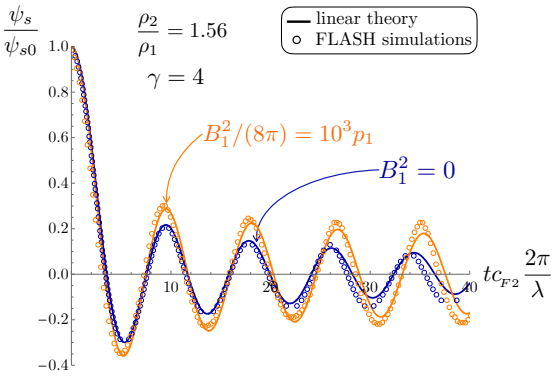

Figure 2: Evolution of the shock ripple amplitude for the non-magnetic and magnetic cases.

We have found that for an ideal gas EoS, when $\gamma < 2$, the effect of the magnetic field is to decrease the amplitude of the shock oscillations, while the opposite is observed for $\gamma > 2$. When the adiabatic index $\gamma > 1 + \sqrt{2}$, the shock can enter the neutrally stable regime, or SAE, if the magnetic field intensity is sufficiently large and the shock is sufficiently strong. Weak shocks are always found to be stable regardless of the adiabatic index and the magnetic intensity.

References

Gardner C.S. & Kruskal M.D. (1964) "Stability of plane magnetohydrodynamic shocks". *Phys. Fluids*, **7(5)**, 700–706.

Trakhinin Y. (2003) "A complete 2D stability analysis of fast MHD shocks in an ideal gas". *Commun. Math. Phys.*, **236(1)**, 65–92.

Slutz S. & Vesey R.A. (2012) "High-gain magnetized inertial fusion". *Phys. Rev. Lett.*, **108(2)**: 025003.

Rahman H., Wessel F. and Rostoker N. (1995) "Staged z pinch". *Phys. Rev. Lett.*, **74(5)**:714.

Wessel F.J., Ney P., Presura R., et al. (2015) "Fusion in a staged z pinch". *IEEE Trans. on Plasma Sci.*, **43(8)**:2463–2468.

2nd Spanish Fluid Mechanics Conference
Barcelona (2 - 5 July 2023)

Aerodynamic enhancement of spanwise-flexible flapping wings via fluid-structure resonance

C. Martínez-Muriel[1], M. García-Villalba[2], and O. Flores[1]

caymarti@ing.uc3m.es

[1]Departamento de Ingeniería Aeroespacial, Universidad Carlos III de Madrid, Spain
[2]Institute of Fluid Mechanics and Heat Transfer, TU Wien, Vienna, Austria

Micro-air vehicles (MAVs) are becoming increasingly important in society, being demanded for security services, protection, surveillance, etc. One of the most promising configurations for these vehicles consists of producing aerodynamic forces and thrust using flapping wings, with the potential to mimic the maneuverability and versatility of nature's fliers [1]. Besides the complex unsteady mechanisms associated to flapping wings, these configurations are also expected to take advantage of the wing flexibility, to enhance their aerodynamic performance. Two non-exclusive mechanisms have been proposed in the literature to explain the effect of flexibility on the aerodynamic performance of flapping wings, namely fluid-structure resonance [2] and aerodynamic tailoring [3]. These two mechanisms have been analyzed with some detail in chordwise-flexible airfoils, but they have not been properly characterized in spanwise-flexible wings.

In this talk, we will present direct numerical simulations of the flow around a spanwise-flexible flapping wing in forward flight, with the aim of clarifying the role of the aforementioned mechanisms (and the non-linearities of the system) in the propulsive performance of the wing [4]. The simulations are performed at $Re = 1000$ for a wing undergoing a heaving and pitching motion at a Strouhal number $St_c \approx 0.5$ based on the chord of the wing, c. Two different aspect ratios are considered, $\mathit{AR} = 2$ and 4, varying the material properties of the wing to cover a wide range of effective stiffness $\Pi_1 \in [0.1 - 100, \infty]$, with an effective inertia $\Pi_0 = 0.1$. The structural model of the wing consists of a series of rigid segments joined by torsional springs, as shown in figure 1.

It has been found that there exists an ideal aerodynamic performance for a wing, which is linked to a fluid-structural resonance. This phenomenon occurs when the oscillation frequency approaches the first natural frequency of the wing in fluid, $\omega_{n,f}/\omega \approx 1$. In such a scenario, the average thrust generated by the wing reaches its maximum, increasing by a factor of two compared to a rigid wing, as seen in figure 2. If the flexibility of the wing exceeds the optimal range, $\omega_{n,f}/\omega < 1$, both the thrust production and propulsive efficiency decrease considerably.

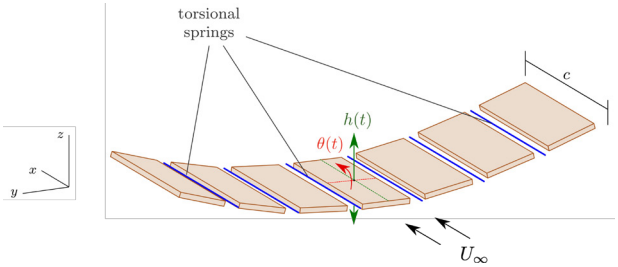

Figure 1: Sketch of the multi-body model.

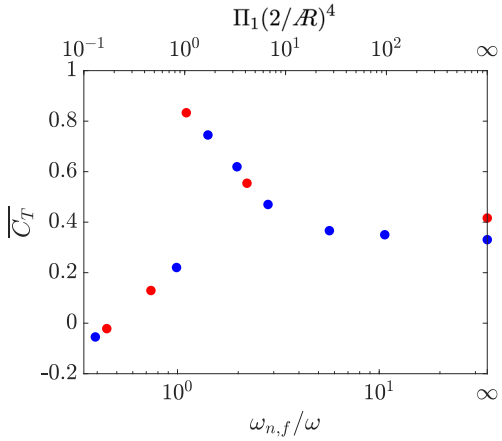

Figure 2: Mean thrust coefficient $\overline{C_T}$ for $\mathit{AR} = 2$ (blue) and $\mathit{AR} = 4$ (red) wings.

The impact of the aspect ratio AR on the aerodynamic performance of flexible wings appears to be primarily related to its influence on the first natural frequency of the wing. Evidence shows that flexible wings with the same value of $\omega_{n,f}/\omega$ but different values of AR exhibit almost identical aerodynamic performance in terms of average thrust coefficients and propulsive efficiencies. This suggests that the benefits of aerodynamic resonance are more important than the effects associated with larger aspect ratios. However, there may still be some weak AR effects on the amplitude and phase lag of the structural response.

Our analysis of the structural response of the wing revealed that, for all cases considered, the mid-chord

line of the wing exhibited a bending pattern corresponding to the first bending mode of an Euler-Bernoulli beam. This result was not unexpected, given that there was a substantial difference of about 10 in the natural frequencies between the first and second modes of the wings studied. Consequently, the frequency ratios examined in this work were still relatively far from the second mode. Therefore, the decline in aerodynamic performance could not be attributed to the excitation of a second bending mode. Instead, our investigation of the wing tip motion relative to the root motion indicated a pattern consistent with the response to periodic forcing of a nonlinearly-damped harmonic oscillator .

When the flexibility of the wing is increased from $\omega_{n,f}/\omega > 1$ to $\omega_{n,f}/\omega < 1$, there is a noticeable rise in the deflections between the tip and root of the wing. The amplitude of these deflections undergoes a sharp transition at around $\omega_{n,f}/\omega$ equal to 1, while the phase lag between the tip and root motions undergoes a gradual transition from 0 to 180°. The observed amplitude of the tip displacement h_{tip}/c suggests that fluid damping plays a significant role, as the value of h_{tip}/c is only approximately 1.5 times larger than the amplitude of the heaving motion. The phase lag at resonance is $\phi_{\text{tip}} \approx 45°$, which is considerably different from the expected value of linear oscillators (i.e. $\phi_{\text{tip}} \approx 90°$).

The enhanced aerodynamic performance resulting from structural resonance can be attributed to two factors. Firstly, the increased amplitude of motion of the outboard wing sections leads to larger effective angles of attack. Secondly, the motion of the outboard wing sections is delayed compared to the motion of the mid-span section of the wing. As a result, the development of the leading edge vortex is also delayed, see figure 3. This, together with the larger effective angles of attack, explains the higher aerodynamic load in the outboard sections of the optimal wing. However, this fluid-structure interaction is only beneficial when the bending deformation and pitching motion of the wing are synchronised. In contrast, the outboard wing sections of sub-optimal cases are out-of-phase, resulting in drag generation during the first half of each stroke.

Overall, the coupling among deformation, force generation, and wing orientation (i.e., pitching angle) in our study resembles the streamlining arguments of [3] for chordwise-flexible wings. Despite fundamental differences between both configurations, the results suggest that streamlining can also play a crucial role in the aerodynamic performance of flexible wings.

Compared to the existing studies on spanwise-flexible wings [5]-[7], our results suggest that the discrepancies between their results can be attributed to the linear versus non-linear nature of the structural models used.

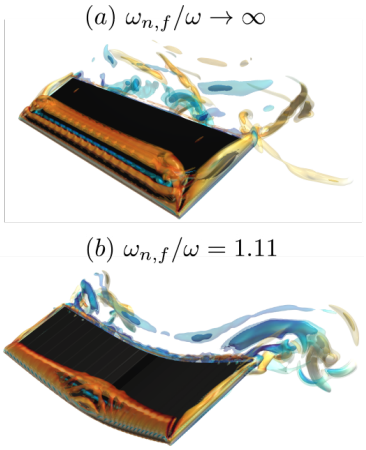

Figure 3: Flow visualization using iso-Q contours representing vortical structures for rigid and optimal wings at $t/T \approx 1/4$.

Acknowledgements

This work was supported by grant DPI2016-76151-C2-2-R (AEI/FEDER, UE). The computations were partially performed using RES resources under the activities RES-IM-2020-2-0006 and RES-IM-2020-3-0024.

References

[1] Haider, N., Shahzad, A., Mumtaz Qadri, M. N. and Ali Shah, S. I. (2021). *Proc. Inst. Mech. Eng. C J. Mech. Eng. Sci.*, 235(2), 245–264.

[2] Goza, A. and Floryan, D. and Rowley, C. (2020). *J. Fluid Mech.*, 888.

[3] Ramananarivo, S., Godoy-Diana, R. and Thiria, B. (2011). *Proc. Natl Acad. Sci.*, 108(15), 5964–5969.

[4] Martínez-Muriel, Arranz, García-Villalba and Flores, *Submitted*, (2023).

[5] Kodali, D. and Medina, C. and Kang, C.-K. and Aono, H. (2017). *J. Royal Soc. Interface*, 14(136), 20170725.

[6] Zhu, Q. (2007). *J. Royal Soc. Interface*, 45(10), 2448–2457.

[7] Qi, D. and Liu, Y. and Shyy, W. and Aono, H. (2010). *Phys. Fluids*, 22(9), 091901.

2nd Spanish Fluid Mechanics Conference
Barcelona (2 - 5 July 2023)

An asymptotic analysis of cavity flow induced by a flexible membrane in an oscillatory channel flow: case study of syringomyelia

G. L. Nozaleda[1], J. Alaminos-Quesada[1], and A. L. Sánchez[1]

glpeznozaleda@ucsd.edu

[1]Department of Mechanical and Aerospace Engineering, University of California San Diego, La Jolla, CA 92093 USA

In an effort to shed light into the role of pulsatile motion in the development of syringomyelia, asymptotic methods are employed to analyze departures from harmonic Womersley flow in a two dimensional channel separated by an elastic membrane from a slender fluid-filled cavity. Closed-form expressions are derived for the mean Lagrangian motion induced in the channel and in the cavity, given by the sum of steady-streaming and Stokes drift velocities, as well as for the induced pressure difference.

1 Introduction

Syringomyelia is a condition characterized by the appearance of a cavity filled with CSF, known as syrinx, within the spinal cord. Although frequently associated with Chiari malformation, syringomyelia can also develop as a result of meningitis, certain tumors of the spinal cord, and trauma (Greitz, 2006). The asymptotic analysis developed below, complementing the experimental and numerical work presented in an accompanying paper by Durán-Venegas et al. (2023), aims at providing additional understanding concerning the role of fluid flow in the pathophysiology of syringomyelia.

2 Formulation of the problem

Consider a two–dimensional channel of width h_o separated from a slender cavity of width h_c and length $L \gg h_o$ by an elastic membrane, as sketched in Figure 1. Both regions are filled with the same viscous fluid of constant density ρ and kinematic viscosity ν. The fluid is forced to move along the channel (i.e. by the use of a peristaltic pump) with a harmonic flow rate $Q = Q_0 \cos(\omega t)$. The deformations of the membrane induce an oscillatory motion in the cavity, intrinsically coupled with the accompanying departures from Womersley flow emerging in the channel, both oscillatory motions involving a steady-streaming component.

The response of the elastic membrane to the forcing frequency ω depends on its longitudinal tension T. The resulting deformations have a characteristic wave length $\lambda_e = [(Th_o)/(\rho\omega^2)]$, which is assumed to be comparable to the cavity length, so that

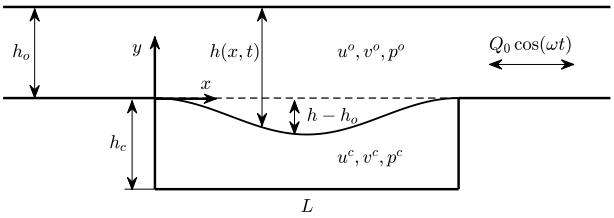

Figure 1: Schematic representation of the problem.

$\ell = L/\lambda_e \sim 1$. The associated wave velocity $c_e = \lambda_e\omega$ is assumed to be much larger than the characteristic flow speed $u_c = Q_0/h_o$, their ratio defining an asymptotically small parameter $\varepsilon = u_c/(\lambda_e\omega) \ll 1$. The problem will be described with use of Cartesian coordinates with longitudinal and transverse components (x, y) scaled with λ_e and h_o, respectively, and accompanying velocity components (u, v) scaled with u_c and $u_c h_o/\lambda_e$. In the slender-flow approximation, which applies with small relative errors of order $(h_o/L)^2$, the problem reduces to the integration of

$$\frac{\partial u}{\partial x} + \frac{\partial v}{\partial y} = 0, \tag{1}$$

$$\frac{\partial u}{\partial t} + \varepsilon\left(u\frac{\partial u}{\partial x} + v\frac{\partial u}{\partial y}\right) = -\frac{\partial p}{\partial x} + \frac{1}{\alpha^2}\frac{\partial^2 u}{\partial y^2}, \tag{2}$$

together with the elastic equation

$$\frac{\partial^2 \xi}{\partial x^2} = p^o - p^c, \tag{3}$$

where $\alpha = \left(h_o^2\omega/\nu\right)^{1/2}$ is the Womersley number and $\xi = \varepsilon^{-1}\left(h_o - h\right)/h_o$ characterizes the membrane deformation. The superscripts o and c denote properties in the channel and in the cavity, respectively.

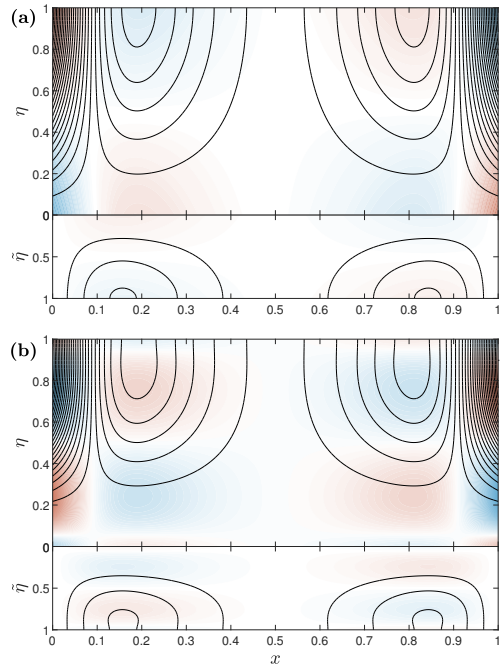

Figure 2: Streamlines with color contours of vorticity corresponding to steady-streaming **(a)** and Stokes drift **(b)** for $\alpha = 0.7$, $H = 0.6$ and $\ell = 1$. A fixed streamline spacing of $\delta\psi = 0.04$ has been used and the colormap of vorticity is the same as in figure 3.

3 Results

The solution procedure employs regular asymptotic expansions in powers of ε for all variables of the problem (i.e. $\boldsymbol{u}^o, \boldsymbol{u}^c, p^o, p^c$, and ξ) along with normalized coordinates $\eta = (y - \varepsilon\xi)/(1 - \varepsilon\xi)$ and $\tilde{\eta} = -(y - \varepsilon\xi)/(H + \varepsilon\xi)$, which are introduced to account for the membrane deformation in computing higher-order terms. While the leading-order solution is purely harmonic, first-order corrections contains a non–zero steady component. For example, for the canal streamwise velocity $u^o = u_0^o + \varepsilon u_1^o + \ldots$ we find $\langle u_0^o \rangle = 0$ but $u_{\text{SS}}^o = \langle u_1^o \rangle \neq 0$, where $\langle \cdot \rangle = \frac{1}{2\pi} \int_t^{t+2\pi} \cdot \, \mathrm{d}t$ denotes the time-average operator, with the time scaled with ω. The mean Lagrangian velocity is given by the sum of the steady-streaming velocity and the Stokes drift velocity, the latter exhibiting a contribution stemming from the membrane deformation. An interesting finding of the analysis is that the steady-streaming and Stokes-drift motions have a non-zero flow rate, of equal magnitude and opposite sign, so that the mean Lagrangian motion recovers its expected zero flow rate.

In figure 2 streamlines and vorticity contours are represented separately for the steady–streaming $(\boldsymbol{u}_{\text{SS}}^c, \boldsymbol{u}_{\text{SS}}^s)$ and Stokes drift $(\boldsymbol{u}_{\text{SD}}^c, \boldsymbol{u}_{\text{SD}}^s)$ velocities. The Lagrangian drift, obtained as the sum of both contributions (i.e. $\boldsymbol{u}_{\text{L}} = \boldsymbol{u}_{\text{SS}} + \boldsymbol{u}_{\text{SD}}$), is represented in figure 3 along with the steady deformation of the membrane $\langle \xi_1 \rangle$.

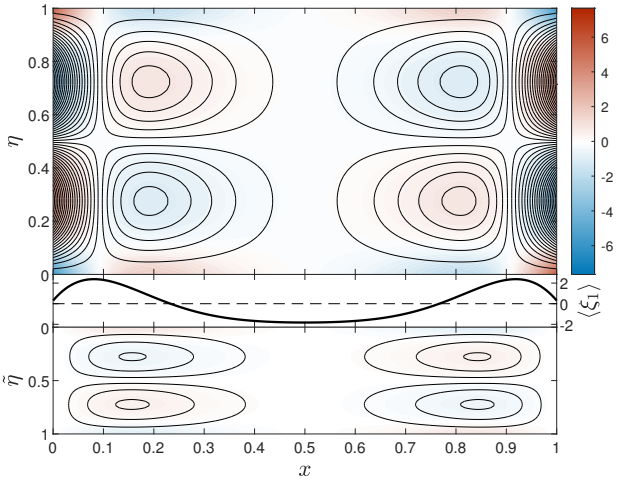

Figure 3: Steady deformation of the membrane $\langle \xi_1 \rangle$ and streamlines with color contours of vorticity corresponding to the Lagrangian drift motion for $\alpha = 0.7$, $H = 0.6$ and $\ell = 1$. A fixed streamline spacing of $\delta\psi = 0.004$ has been used in plotting the streamlines.

4 Conclusions

The analysis suggests that CSF pulsatile flow in the spinal canal is responsible for the observed fluid motion within the syrinx. The resulting time-averaged pressures could play an important role in the development of syringomyelia by driving a slow inflow of cerebrospinal fluid from the subarachnoid space to the central canal of the spinal cord.

References

Greitz, D. (2006) "Unraveling the riddle of syringomyelia". *Neurosurgical review* **29**, 251–264.

Durán-Venegas, E., Gutiérrez-Montes, C., Coenen, W., Martínez-Bazán, C. (2023) "Cavity flow induced by a flexible membrane in an oscillatory channel flow: case study of syringomyelia". *2nd Spanish Fluid Mechanics Conference.*

Calibration of a porous surface model for fishing nets

Sergio Roget[1], Marcos Lema[2,*], Anne Gosset[1]
Alonso de Entrerríos[1] and Laurencio de los Montes[2,*]

[1]*Universidade da Coruña, Campus Industrial de Ferrol, CITENI, Ferrol, SPAIN*
[2]*Universidade da Coruña, CITIC, A Coruña, SPAIN*

The design of fishing nets can be improved in terms of energy efficiency and selectivity using Computational Fluid Dynamics simulations. Because they are highly flexible and complex structures, geometric simplifications need to be made to reduce the computational cost. This work uses a methodology based on a porous surface model to account for the net. The calibration of the porous coefficients is carried out using experimental measurements on a net sample in a wind tunnel, and the results are validated with CFD computations in OpenFOAM.

INTRODUCTION

Industrial fishing relies on bag-shaped nets, that are towed by one or several boats, capturing the species found in their path. Nowadays, the industry demands fishing gears that are energy efficient with improved selectivity, which makes the design process more complex and requires expensive test campaigns in open sea or in towing tanks. Computational Fluid Dynamics (CFD) tools can be used to reduce the number of tests to be carried out, providing enough data for a better understanding of all the phenomena involved. Furthermore, different design alternatives can be simulated without the cost and the time needed when done experimentally.

Unfortunately, fishing nets are complex structures that deform easily under hydrodynamic forces, making the CFD simulations a real challenge. For that reason, geometric simplifications need to be adopted to reduce the total number of cells in the final mesh. In this study, the simplification is done by replacing the net with a porous surface (PS) that generates an equivalent pressure loss, using a novel surface porous model [1].

POROUS SURFACE DEFINITION

The porous coefficients need to be obtained experimentally by measuring the drag force in the net, which is done traditionally in towing tanks. These facilities incur in high operating costs, and without the flexibility that a wind tunnel can provide [2,3]. For that reason, in the present study the forces are measured in an open return wind tunnel, with a net segment mounted on a frame that allows to change the angle of attack. Two strain gauges in both sides of the frame measured the force in the flow direction, as shown in figure 1.

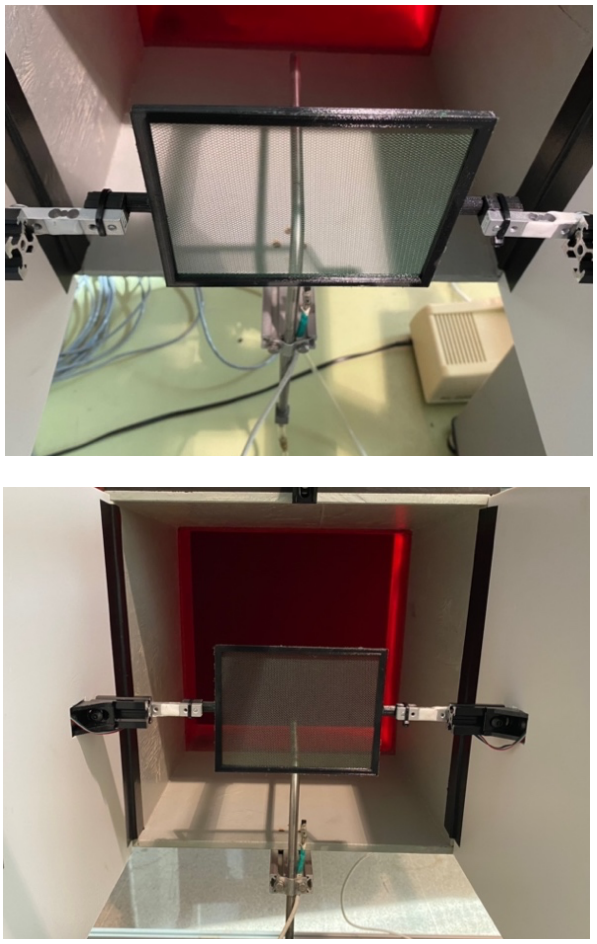

FIG 1. Experimental setup in the wind tunnel test section

Once the drag force is known for a given flow velocity and angle of attack, to obtain the porous surface coefficients we need to optimize the least squared error between the drag force experimentally measured and the calculated value as follows:

$$LSE = \frac{1}{N} \cdot \sum_{1}^{N} (F_D - F_{D\,exp.})^2$$

The theoretical drag force value can be computed with the following equation:

$$F_D = S_x' t A$$

Where t and A are the thickness and area of the porous surface, and S_i' is the source term or pressure loss. Once this value is known, the equivalent porous surface can be defined by using the Darcy- Forchheimer equation [4]:

$$\frac{\partial p}{\partial x_i'} = S_i' = -D_{ij}' \mu u_j' - \frac{1}{2} C_{ij}' \rho u_{mag} u_j'$$

Where D_{ij}' and C_{ij}' are the porous coefficients matrices, μ and ρ the fluid viscosity and density, and u_j' and u_{mag} are the fluid velocity and velocity magnitude, which are equal to the incoming flow velocity in the present configuration. Following an iterative method, the porous coefficients are computed for each flow velocity and net angle, and they all need to be transformed into an absolute frame-of-reference by applying the rotation matrix, R:

$$R = \begin{bmatrix} sin\alpha & cos\alpha & 0 \\ -cos\alpha & sin\alpha & 0 \\ 0 & 0 & 1 \end{bmatrix}$$

VALIDATION AND DISCUSSION

The drag force computed with the porous surface are compared with the values measured experimentally in figure 2, to verify the validity of the method. One can observed that the drag force is correctly computed with the porous media when compared to the experimental value measured for each velocity. The comparison can also be done in terms of the drag coefficient, as in figure 3, where the value computed with the porous surface correctly follows the experimental drag coefficients. The main differences are observed with the lowest angles and the lowest velocity used in the experiments but still showing a good agreement. In this way, the fishing net will be replaced in the CFD simulations by the porous surface defined by the porous coefficients D_{ij}' and C_{ij}'. The forces obtained numerically with the CFD simulations will be confronted with the experimental measurements.

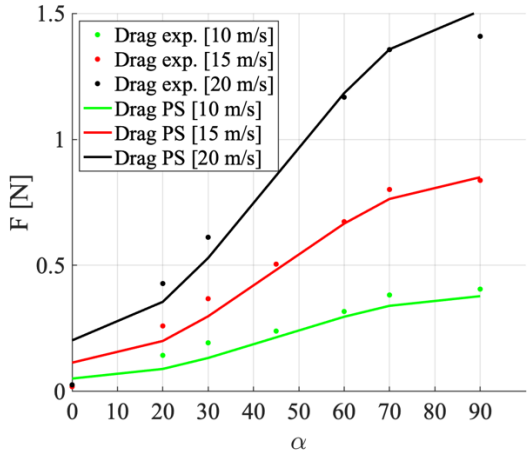

FIG 2. Measured drag forces compared with the values computed with the porous surface.

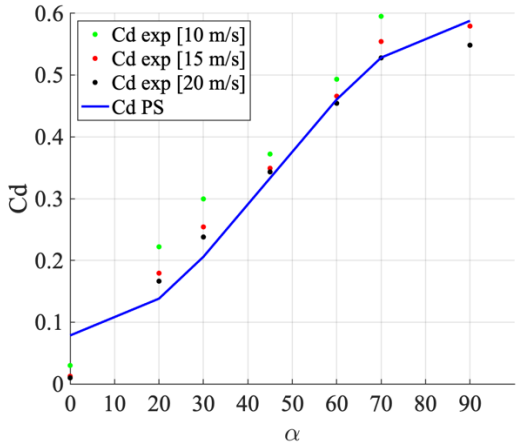

FIG 3. Measured drag coefficients compared with the values computed with the porous surface.

[1] S. K. Karumathil, 'Numerical simulation of the interaction between flow and flexible nets using a porous surface model', PhD thesis, 2022.
[2] U. Lichtenstein, K. Breddermann, S. Kosleck, "Experiments on thin-twine net panels", In Proceedings of DEMaT 2022, Rostock, Germany.
[3] F. Mellibovsky, J. Prat, E. Notti, A. Sala, "Testing otter board hydrodynamic performances in wind tunnel facilities", Ocean Engineering, vol. 04, 2015, 52-62

2nd Spanish Fluid Mechanics Conference
Barcelona (2 - 5 July 2023)

Cavity flow induced by a flexible membrane in an oscillatory channel flow: case study of syringomyelia

Eduardo Durán-Venegas[1,2], Cándido Gutiérrez-Montes[3], Wilfried Coenen[4], Antonio L. Sánchez[5], and Carlos Martínez-Bazán[1]

eduran@uma.es

[1]Departamento de Mecánica de Estructuras e Ingeniería Hidráulica, Universidad de Granada, Spain
[2]Escuela de Ingenierías Industriales, Universidad de Málaga, Spain
[3]Departamento de Ingeniería Mecánica y Minera, Universidad de Jaén, Spain
[4]Departamento de Ingeniería Térmica y de Fluidos, Universidad Carlos III de Madrid, Spain
[5]Department of Mechanical and Aerospace Engineering, UC San Diego, USA

In this work, we study the flow inside a Syringomyelia, modelled by a cavity separated from a channel with an elastic membrane. The oscillatory flow of the channel is transmitted to the cavity through the deformation of the membrane. We study the structure of the time-dependent and stationary flow induced inside the cavity and the deformation of the membrane under different problem conditions.

1 Introduction

Syringomyelia is a condition in which fluid accumulates in the spinal cord in or near the central canal, forming macroscopic fluid-filled cavities called syrinxes (Elliott et al., 2013). Enlarging syrinxes often cause progressive neurological damage through a combination of direct pressure on neural tissue and ischemia. Although the exact mechanisms behind the generation of syringomyelia are still unknown, changes in hydrodynamics inside syrinxes alter the distribution of forces acting on the spinal cord and hence the stresses that can favor syrinxes enlarging.

Since the spinal cord is an elastic material, it undergoes fluid-structure interactions between the oscillatory motion of the cerebrospinal fluid and the fluid inside the developing syrinx (Linninger et al., 2016). However, the two very disparate time scales hinder the search for how these interactions can cause the development of syringomyelia in the problem: the physical processes associated with the oscillatory flow, with a period on the order of seconds, generate small changes that accumulate over thousands or millions of cycles, to cause macroscopic changes in the development of a syrinx.

In this work we study the hydrodynamics inside the syrinx and the stresses acting on its walls through a simplified model of a cavity separated from an oscillating channel flow by a flexible membrane.

2 Framework

In particular, we study the flow inside a rectangular cavity of length L, separated from a channel by an elastic membrane of thickness h_m (see Fig. 1). We consider the same height H for both the channel and the cavity. The flow inside the channel is oscillatory, with imposed Womersley velocity profiles following a sinusoidal oscillation of amplitude U and angular frequency ω at the inlet and outlet surfaces. The properties of the fluid are defined through the density ρ_f and the cinematic viscosity ν, while those of the membrane are defined by its density ρ_m, Young's modulus E, and Poisson ratio ν_m.

The problem is controlled by the following dimensionless parameters: the aspect ratio of the cavity $AR = L/H$, the Womersley number $\alpha = H\sqrt{\omega/\nu}$, the dimensionless stroke length $\varepsilon = U/\omega L$, the dimensionless membrane thickness $h^* = h_m/H$, the density ratio $\rho^* = \rho_m/\rho_f$, the Poisson ratio ν_m and the reduced velocity $U^* = U/(h_m f_n)$, where f_n is the natural frequency of the membrane.

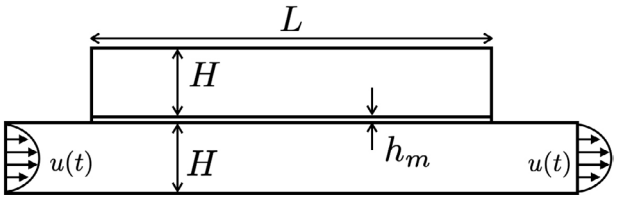

Figure 1: Scheme of the problem. Inlet and outlet velocities $u(t)$ are imposed as a Womersley profile oscillating with an angular frequency ω.

A Finite Element Method is used to solve incompressible Navier-Stokes equations for the fluid and Navier equations for the membrane. For both domains, second-order triangular elements are used in a moving mesh that adapts to the deformation of the membrane. Simulations are started from static fluid and membrane and are run until a periodic state is

reached after 10-20 cycles.

3 Results

The flow inside the cavity and the deformation of the membrane have been studied for different channel flow conditions. The geometry has been fixed at $AR = 14$ and $h^* = 0.1$ and the membrane parameters at $U^* = 35$ and $\rho^* = 1$.

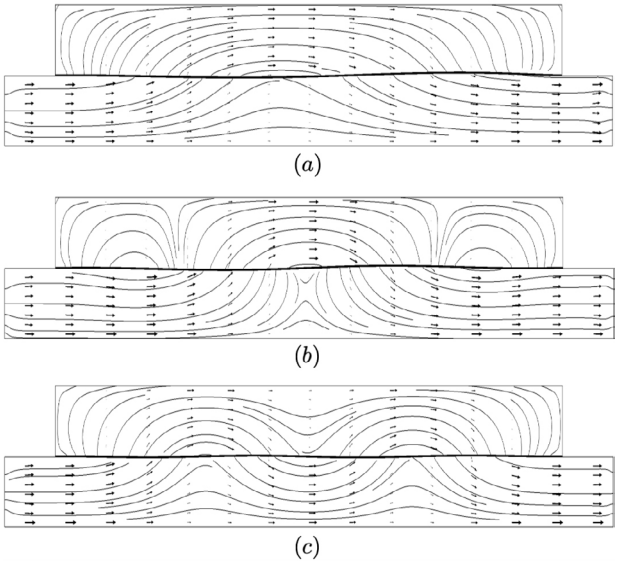

Figure 2: Flow vectors and streamlines inside the channel and the cavity at the instant of maximum deformation of the membrane for different flow conditions. (a) $\alpha = 7$, $\varepsilon = 0.028$ (b) $\alpha = 10$, $\varepsilon = 0.014$ (c) $\alpha = 14$, $\varepsilon = 0.007$. The plots are scaled for showing purposes by reducing the length by two in the horizontal axis.

When the periodic state is reached, an oscillatory flow is induced by the outter channel flow inside the cavity through the deformation of the membrane. The waves generated on the membrane move the fluid inside the cavity, coupling it with the channel flow and generating global flow patterns between the cavity and the channel (see Fig. 2). At this periodic state, the membrane and the flow in both regions oscillate at the same frequency in the range of parameters considered herein.

Depending on the channel flow conditions, different deformation modes appear at the membrane. In turn, this deformation affects the flow, generating different circulation patterns. In Fig. 2, we show the flow field and the membrane for three different sets of parameters. When the Womersley number and the stroke length are modified, the number of waves at the membrane changes and different flow cells appear.

Additionally to this main periodic flow, a secondary flow appears inside the cavity. To visualize it, we have studied the trajectories of Lagrangian particles during a large number of cycles. Along a single cycle, each particle describes a loop following the flow; however, they also experiment a net displacement $\delta << L$. The accumulation of this net displacement generates recirculation cells inside the cavity with a temporal scale several orders of magnitude bigger than the main flow oscillating period. In Fig. 3, we show the path described by Lagrangian particles inside the cavity along 250 cycles.

In addition to the numerical simulations, experiments are also performed under the same conditions. Results of the flow field established inside the cavity and the membrane deformation are also presented and compared with the numerics.

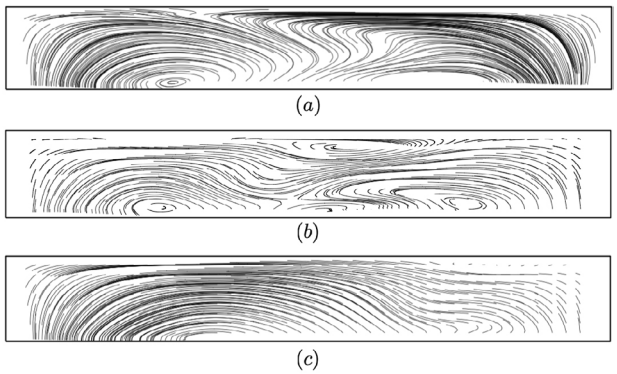

Figure 3: Structure of the secondary flow inside the cavity for the cases of Fig. 2. The lines represent the paths of the net displacement Lagrangian particles.

4 Conclusions

The flow in the channel moves the fluid inside the cavity through the deformation of the membrane. Both the main and the secondary flows inside the cavity are highly influenced by the channel flow conditions, such as the stroke length and the flow frequency. From this, we can deduce that the fluid inside the syrinx may be affected by the conditions of the cerebrospinal flow, generating flow patterns and stress conditions that can contribute to the enlarging of the cavity.

References

Linninger A, Tangen K, Hsu C & Frim D. (2016) "Cerebrospinal Fluid Mechanics and Its Coupling to Cerebrovascular Dynamics". *Annu.Rev.Fluid Mech.*, **48**, 219–257.

Elliott NSJ, Bertram CD, Martin BA & Brodbelt AR. (2013) "Syringomyelia: A review of the biomechanics". *J. Fluids Struct.*, **40**, 1–24.

2nd Spanish Fluid Mechanics Conference
Barcelona (2 - 5 July 2023)

CFD simulations of various heave plates using a lagrangian approach

Javier Armañanzas[1*], Juan Pablo Fuertes[1], Alexia Torres[1], Javier León[1] and Miguel Gil[1]

[1]Department of Engineering, Public University of Navarre, SPAIN

javier.armananzas@unavarra.es

In the present document, different models of heave plates coupled to a cylinder are simulated using the Lattice-Bolztmann method (which allows for the use of the Large Eddy Simulation turbulence model [1]), rather than the usual finite volume method used in other software in the field. In order to validate the results, the models used will be some of the proposed in Rao et al. [2], allowing for a comparison with experimental data and other CFD results obtained in the cited article using the finite volume method with Unsteady Reynolds Averaged Navier Stokes approach.

1 Introduction

Heave plates are damping elements used in order to reduce the response of floating structures, such as offshore wind platforms, wave energy converters and spar platforms for oil and gas production.

Nowadays, many researchers apply CFD numerical simulation tools to carry out different investigations on heave plates, such as the work of Philip et al. [3], where different heave plates are attached to a spar and experimented and simulated in presence of waves, obtaining good correlation between results. Moreover, in Bezunartea et al. [4] simulations of a simplified model of a leg from the floating platform developed for the Hiprwind project are carried out; and in Mello et al. [5] and Wang et al. [6] complete floating wind turbine platforms are simulated, the latter also comparing different CFD codes.

In Rao et al. [2], different damping configurations using heave plates for a spar are simulated with ANSYS FLUENT and experimented, in order to assess the applicability of linear and quadratic heave damping models. To achieve that, different initial displacements are applied to the models, after which the heave response of the system is studied. This article will be the base for the simulations developed for this work.

Among CFD software, a finite volume approach is usually used, like in ANSYS FLUENT and OpenFOAM. However, SIMULIA XFlow 2022x uses the particle-based Lattice-Boltzmann method, which tackles some of the disadvantages presented by the finite volume method.

2 Simulated models

The selected models for simulation correspond to Cases 1, 6, 11 and 13 from Rao et al. [2], which also include experimental data. FIG 1 shows their different configurations: cylindrical body, single heave plate and double heave plate.

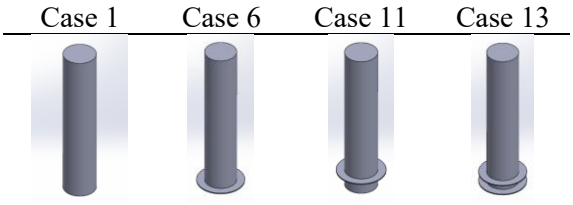

FIG 1. Simulated models according to Rao et al. [2].

3 Simulation setup

Simulations were carried out using the CFD software SIMULIA XFlow 2022x. Domain parameters and simulation time (12 s) are established in Rao et al. [2] and have been kept the same in order to achieve comparability.

A 3D approach was applied, with standard water properties. The main difference was the meshing process: a general lattice cell size of 0,1 m was established, with 4 different re-meshing regions, one for the free surface with a cell size of 0.0125 m, and three around the model with cell sizes of 0.0015625 m, 0.00625 and 0.0125 m. The total number of elements was 6673108, and a time step of 0.008 s was fixed. Moreover, a minimum of 3 refinement transition length levels were established. FIG 2 showcases the simulation domain. The average simulation time was of 4.5 days with a 12 core, 2.4 GHz processor, whereas in Rao et al. it an 8 core, 2.6 GHz was used, with a simulation taking up to 25 days.

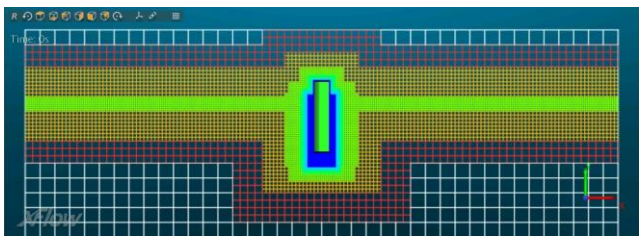

FIG 2. Domain lattice structure with coloured different levels.

4 Results

After applying the same displacements as in the base article to the different models, their response was studied. The obtained graphs can be seen in FIG 2, along with the ones from Rao et al. [2]. Moreover, their linear damping ratio corresponding to the first five cycles (ξ_{lin}) was calculated and compared to the results obtained in Rao et al. [2]. To calculate it, equations (1) and (2) were used and the mean between the first 5 upper and lower cycles (starting after the first half cycle) was considered. Results are shown in TABLE 1, along with the ones obtained in Rao et al. [2] and their respective errors in comparison with the experimentation carried out in the article.

$$Logaritmic\ decrement: \delta_k = ln(z_k / z_{k+1}) \quad (1)$$

$$Damping\ ratio: \zeta_{t,k} = \frac{\delta_k}{\sqrt{4\pi^2 + \delta_k^2}} \quad (2)$$

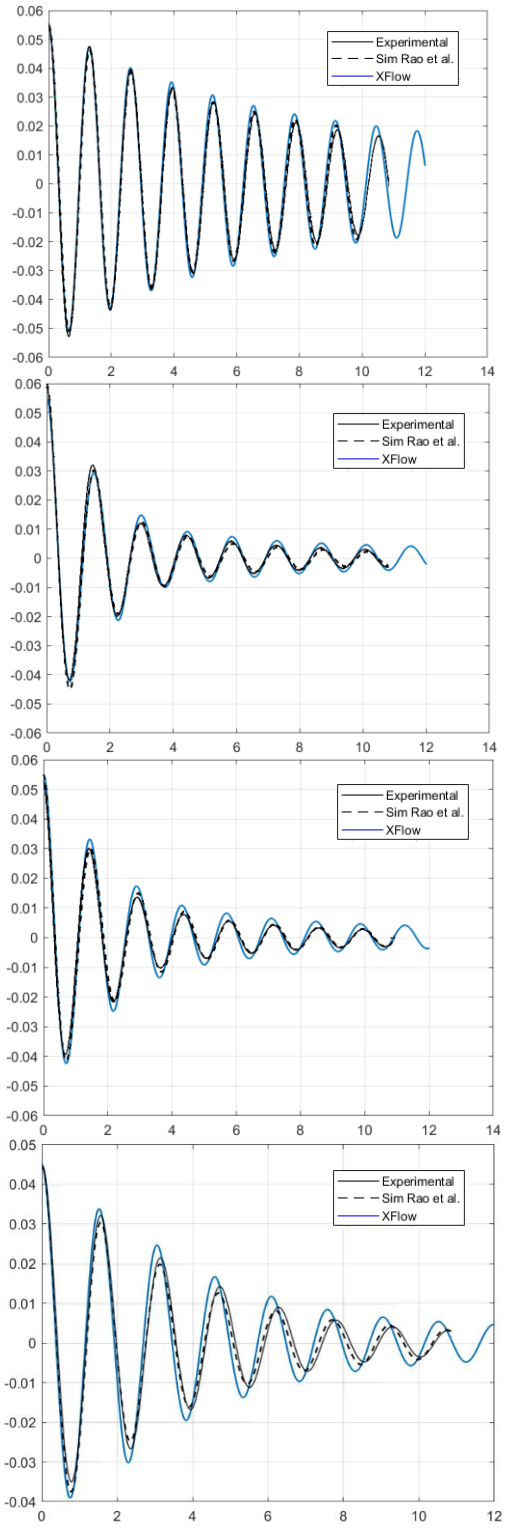

FIG 3. Comparison between XFlow simulations and article data for Cases 1, 6, 11 and 13.

Results show that the mesh developed was adequate for Case 1 (cylindrical body), but the behaviour starts to differ once the heave plate is introduced, with the maximum difference being noticeable for Case 13, which includes 2 heave plates. These errors are translated to the calculation of the linear damping ratios, which are shown in TABLE 1.

Case	ξ_{XFlow}	ξ_{FLUENT}	XFlow error (%)	FLUENT error (%)
1	0.0228	0.0245	7.02	-7.54
6	0.0703	0.073	11.83	8.41
11	0.0680	0.0739	7.03	1.14
13	0.0553	0.0654	15.37	2.68

TABLE 1. Linear damping ratio and errors.

5 Conclusions

As seen in the results, the error in the simulations increases with the presence of the damping element, being the biggest when two plates are attached to the cylindrical body.

However, simulations with one heave plate and just the cylinder show good correlation in behaviour, especially considering that the simulation time is reduced to a fifth of the one required in Rao et al. [2].

Considering that, an improvement could be proposed in which the mesh size around the plates was decreased and the transition length between mesh sizes was increased, including buffer zones for more stable calculations. This would result in larger simulation times, but that could be assumable.

Acknowledgements

The authors acknowledge the support given by the Government of Navarre (Research project: PC042-043 COSTA).

References

[1] Dassault Systêmes. (2021). “SIMULIA XFlow 2022x: Theory Guide.”

[2] Rao, M. J., Nallayarasu, S., & Bhattacharyya, S. K. (2021). “CFD approach to heave damping of spar with heave plates with experimental validation”. *Applied Ocean Research,* **108**.

[3] Thankom Philip, N., Nallayarasu, S., & Bhattacharyya, S. K. (2019). “Experimental investigation and CFD simulation of heave damping effects due to circular plates attached to spar hull”. *Ships and Offshore Structures,* **14** (4), 396-411.

[4] Bezunartea Barrio, A., Fernández Ruano, S., Maron Loureiro, A., Molinelli Fernández, E., Moreno Buron, F., Oria Escudero, J., Souto Iglesias, A. (2019). “Scale effects on heave plates for semi-submersible flolating offshore wind turbines: case study with a solid plain plate”. *Offshore Mechanics and Arctic Engineering.*

[5] Mello, P. C., Malta, E. B., da Silva, R. O., Candido, M. C., do Carmo, L. H., Alberto, I. F., Gonsalves, R. T. (2021). “Influence of heave plates on the dynamics of floating offshore wind turbines in waves.” *Journal of Marine Science and Technology,* **26**, 190-200.

[6] Wang, L., Robertson, A., Jonkman, J., Kim, J., Shen, Z.-R., Koop, A., Sarlak, H. (2022). “OC6 Phase Ia: CFD Simulations of the Free-Decay Motion of the DeepCwind Semisubmersible.” *Energies,* **15**(1).

Experimental Evidence of the Effect of Permeability on Falling Porous Plates

Jesús Sánchez-Rodríguez[1,2] and François Gallaire[2]

[1]*Departamento de Física Fundamental, Universidad Nacional de Educación a Distancia, 60141, 28080 Madrid, Spain*
[2]*Laboratory of Fluid Mechanics and Instabilities, École Polytechnique Fédérale de Lausanne, Lausanne CH-1015, Switzerland*

In this work, we study experimentally the dynamical regimes of falling permeable plates. Permeability and porosity are systematically varied by drilling several hole patterns, characterized by the spatial arrangement, number of holes and diameter of holes. We track the plates trajectories and classify the falling trajectories according to tumbling, fluttering, steady descent or change of orientation. We conclude the stabilizing effect of permeability observing that, even for low permeable plates, the tumbling behavior is totally suppressed.

The fuid-structure interaction between a falling object and the surrounding fluid is an exciting and challenging problem both because of the everyday nature of this subject and the number of biological and industrial applications it encompasses [1]. The different dynamical regimes observed in impervious objects have been extensively studied and treated both theoretically and experimentally. There is, however, a knowledge gap when adding the effect of porosity and permeability, both features that are indeed very present in nature. This problem is of great interest because of its wide range of applications, both in biology and engineering: Seed dispersal and transport is an important ecological process for the maintenance of ecosystem biodiversity and for the regeneration of plant communities [2]. The aerodynamics of many animals is also influenced by the porosity of their wings. Several insects, such as thrips and wasps, present bristled wings, offering a considerable aerodynamic benefit when compared with impervious wings in terms of propulsion efficiency [3].

Our objective is to investigate experimentally the role of permeability and porosity in the stability of trajectories, as already pointed out by a recent study [4], where the effect of a central hole in falling disks is analyzed. We have constructed an experimental setup to perform the experiments. It is composed of a 50x50x60 cm aquarium filled with water and from which we release the perforated plates. We use steel and aluminum plates with thicknesses of 1, 1.5 and 2mm to explore a wide range in the space of parameters. Plates are released from rest at zero initial conditions obtaining the same falling trajectory. The videos are recorded with a Sony RX10 IV and the images analysis performed with ImageJ.

The experimental results are shown in Fig. 1, where the classical dimensionless inertia-Reynolds number phase diagram is superposed [5]. Squares and triangles correspond to steel and aluminum plates and border colors identify different porosities: 0% for black symbols, 23% for purple, 30% for green, 40% for red and 60% for blue. In our study we have found four falling behaviors shown in the figure: tumbling, fluttering, steady descent and change of orientation. Tumbling plates are identified by opaque figures with the same fill color as the boundary, while fluttering plates correspond to empty symbols. Filling with yellow denotes steady descent while orange is identified with a change of orientation: the plate is released at 0 angle but experiences a 90° turn and flutters around that mean value. This last falling mode has not been observed in the classical phase diagram of impervious falling plates.

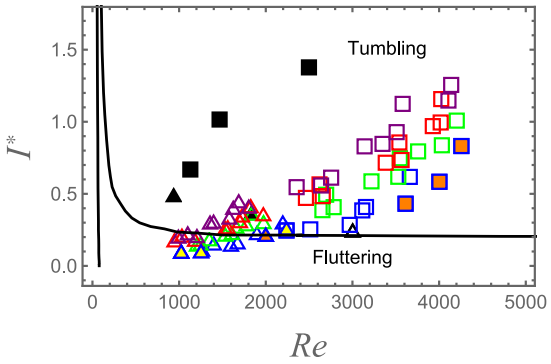

FIG 1. Phase diagram of the falling permeable plates. See main text for symbols description.

We conclude the stabilizing effect of permeability on these plates. Even for heavy plates falling at high velocities which should tumble according to the phase diagram, they oscillate around an equilibrium value and fall with no deviation with respect to the release point.

—

[1] Ern P., Risso F., Fabre D. & Magnaudet J. (2012) "Wake-induced oscillatory paths of bodies freely rising or falling in fluids". *Annual Review of Fluid Mechanics*, **44**, 97-121.
[2] Burrows F. M. (1975) "Wind-borne seed and fruit movement." *New phytologist,* **75**, 405-418.
[3] Ellington, C. P. (1980) "Wing mechanics and take-off preparation of thrips (Thysanoptera)." *Journal of Experimental Biology,* **85**, 129-136.

[4] Vincent L., Shambaugh W. S. & Kanso E. (2016) "Holes stabilize freely falling coins." *Journal of Fluid Mechanics,* **801**, 250-259.
[5] Smith E. H. (1971) "Autorotating wings: an experimental investigation." *Journal of Fluid Mechanics,* **50**, 513-534.

2nd Spanish Fluid Mechanics Conference
Barcelona (2 - 5 July 2023)

Numerical simulation of flow around spanwise-flexible tandem flapping wings

C. Martínez-Muriel[1], M. García-Villalba[2], and O. Flores[1]

cayetano.martinez@uc3m.es

[1]Departamento de Ingeniería Aeroespacial, Universidad Carlos III de Madrid, Spain
[2]Institute of Fluid Mechanics and Heat Transfer, TU Wien, Vienna, Austria

In recent years, it has become possible to design bioinspired robotic devices such as flapping-wing micro-air vehicles, resembling the flight of insects and small birds. However, the performance of these devices is still far from that of their natural counterparts [1]. Of particular interest for the present investigation are dragonflies which are able to fly efficiently exceeding the average capabilities of other insects [2]. Dragonflies have two pairs of flexible wings that may be actuated differently. Around their wings and due to their motion, vortical structures are developed, leading to complex vortex-structure interactions. The development of the vortical structures, their interaction with the wings, and the deformation and force generated by the latter are all coupled, resulting in a highly complex fluid-structure interaction (FSI) problem where the mechanisms driving the efficient flight are not well understood.

Our aim in the present work is to contribute to the knowledge on the topic by studying a simplified configuration which is loosely inspired by a dragonfly. We simulate numerically the forward flight of a pair of rectangular, spanwise-flexible flapping wings in horizontal tandem configuration. We vary the flexibility of the wings and this allows to study the aeroelastic response and the aerodynamic performance of the wings both near and far away from resonance. This study builds upon our previous work on the aerodynamic performance of rigid wings in horizontal tandem configuration [3, 4] and isolated spanwise-flexible wings [5].

Two finite spanwise-flexible wings are immersed in a free stream of constant speed, U_∞. Wings are modelled as rectangular flat plates of chord c, thickness $h_s/c = 0.02$ and aspect ratio $\mathcal{AR} = 4$. The Reynolds number based on the free-stream velocity and the chord of the wing is $Re = U_\infty c/\nu = 1000$. A heaving and pitching motion is prescribed at the mid section of the wings, following the laws

$$h_i(t) = h_0 \cos(\omega t + \phi_{fh,i}), \quad (1)$$

$$\theta_i(t) = \theta_0 \cos(\omega t + \phi_{hp} + \phi_{fh,i}), \quad (2)$$

where the subscript i refers to the forewing ($i = f$) or the hindwing ($i = h$). Both wings have the same heaving amplitude (h_0), pitching amplitude (θ_0), angular frequency (ω), and phase lag between heaving and pitching (ϕ_{hp}). The phase lag between the forewing and hindwing is controlled by $\phi_{fh,i}$. The frequency of the motion is given in terms of the Strouhal number based on the chord of the wing, $St_c = \omega c/(2\pi U_\infty)$. The values defining the kinematics are presented in table 1, and are based on a 2D optimal kinematics that maximizes the propulsive efficiency of a pair of airfoils. The wings are arranged

i	h_0	θ_0	St_c	ϕ_{hp}	$\phi_{fh,i}$
f	0.388	26.19°	0.496	90°	0
h					347.1°

Table 1: Kinematic parameters of the midsection of the forewing ($i = f$) and the hindwing ($i = h$)

in horizontal tandem with a separation $s = 0.5c$.

The wings are modeled using a multi-body system (MBS) of connected rigid segments interacting with the surrounding fluid using the same parameters as was done for isolated wings in a previous work [5]. The flexibility of the wings is measured in terms of the ratio of natural frequency of the wing immersed in fluid over the angular frequency of the imposed motion, $\omega_{n,f}/\omega$ (See [5] for details). A density ratio of $\rho_s/\rho_f = 20$ is chosen, yielding values of the effective inertia typical of dragonfly wings.

Direct numerical simulations of the flow are performed using the in-house code TUCAN, a constant-density fluid solver that models the presence of the bodies using a direct forcing immersed boundary method [6]. More details on the flow solver and its validation can be found elsewhere [7]. The time step is selected such that the CFL number is maintained under 0.3. Simulations are performed in a domain of $14c \times 11c \times 7c$ in the streamwise, spanwise and vertical directions, respectively. A refined zone is defined roughly at the middle of the domain with a uniform grid size of $\Delta r = c/96$.

Figure 1 shows the time-averaged thrust coefficient of each wing, $\overline{C_T}$, as a function of $\omega_{n,f}/\omega$. The base-

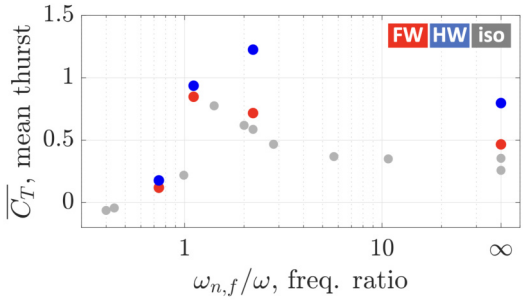

Figure 1: Averaged thrust coefficient $\overline{C_T}$ as a function of flexibility. $\omega_{n,f}/\omega \to \infty$ means rigid. Grey, red and blue dots refer to isolated wings, forewings and hindwings respectively.

line is provided by the flexible isolated wings (grey bullets), which show that decreasing $\omega_{n,f}/\omega$ (i.e. increasing the flexibility) leads to increased thrust generation. An optimal aerodynamic performance is achieved when $\omega_{n,f}/\omega \approx 1$. This suggests that the optimal performance of isolated flexible wings may be linked to a resonance phenomenon.

When comparing the isolated wing with the tandem wings, two main results can be highlighted. First, the forewing behaves as the isolated wing, with an optimal performance at $\omega_{n,f}/\omega \approx 1$. Second, Figure 1 shows that the optimal frequency ratio for the hindwing is $\omega_{n,f}/\omega \approx 2$, roughly twice larger than the optimal values for forewing and isolated wings. As will be discussed in the presentation, this is due to two additional mechanisms that influence the hindwing performance, namely, i) the hydrodynamic interaction with the vortices shed from the forewing [8](for illustration snapshots are shown in Fig. 2) and ii) the aerodynamic tailoring [9]: a synchronization of the aerodynamic forces with the pitching angle of the wing, maximizing thrust generation during the cycle.

Acknowledgements

This work was supported by grant DPI2016-76151-C2-2-R (AEI/FEDER, UE). The computations were partially performed using RES resources under the activities RES-IM-2020-2-0006 and RES-IM-2020-3-0024.

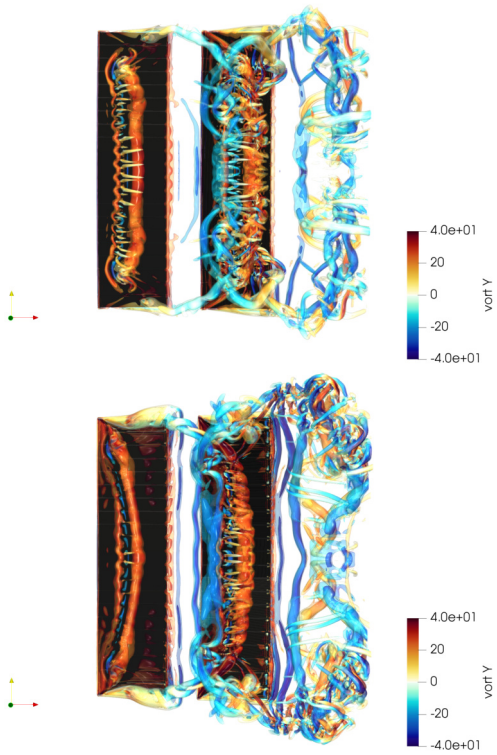

Figure 2: Top view of the iso-Q contours representing vortical structures for cases with (top) $\omega_{n,f}/\omega \approx 2$ and (bottom) $\omega_{n,f}/\omega \approx 1^+$. Free stream comes from the left. Iso-Q contours are coloured with the spanwise vorticity.

References

[1] Haider, Shahzad, Mumtaz Qadri and Ali Shah, *Proc. Inst. Mech. Eng. C J. Mech. Eng. Sci.*, **235**(2), 245–264 (2021).

[2] Salami, Ward, Montazer, and Ghazali , *Proc IMechE Part C J. Mech. Eng. Sci.*, **233**(18), 6519–6537 (2019).

[3] Arranz, Flores and García-Villalba, *J. Fluids Struct.*, **94**, 102893 (2020).

[4] Jurado, Arranz, Flores and García-Villalba, *Phys. Fluids*, **34**(1), 017114 (2022).

[5] Martínez-Muriel, Arranz, García-Villalba and Flores, *Submitted*, (2023).

[6] Uhlmann, *J. Comput. Phys.*, **209**(2), 448–476 (2005).

[7] Arranz, Martínez-Muriel, Flores and García-Villalba, *J. Fluids Struct.*, **110**, 103519 (2022).

[8] Broering and Lian, *Acta Mech. Sinica*, **28**, 1557–1571 (2012).

[9] Ramananarivo, Godoy-Diana and Thiria, *Proc. Natl Acad. Sci.*, **108**, 5964–5969 (2011).

2nd Spanish Fluid Mechanics Conference
Barcelona (2 - 5 July 2023)

Suspended mooring line static analysis using internal XFlow capabilities

Miguel Gil[1], Alexia Torres[1], Juan Pablo Fuertes[1], Javier Armañanzas[1], Javier León[1]

[1]Department of Engineering, Public University of Navarre, SPAIN

miguel.gil@unavarra.es

In the present study, different configurations of a mooring line under static case are analysed using CFD software SIMULIA XFLOW 2022X. The location of different points of the suspended chain in the resting catenary shape are compared to the Quasi-Static model implemented by Masciola et al. [1]. Additionally, fairlead tensions are compared to experimental data obtained by Azcona et al. [2] and to computational model using OPASS.

1 Introduction

Currently, the use of several CFD software is being employed in the simulation of dynamics of mooring lines and the integration on simulations with floating platforms for Floating Offshore Wind Turbines (FOWT).

Chen et al. [3] integrate OpenFOAM and MoorDyn as open-source libraries for the calculation of tensions of mooring lines, coupled to a body motion solver to update the floating body dynamics.

Coupling DualSPHysics with MoorDyn has also been implemented by Dominguez et al. [4] for the simulation of the movement of floating structures moored to the sea bottom under action of different incoming regular waves.

Azcona et al. [2] carry out an experimental analysis of hanging suspended chains under static case for two different chain configurations. An OPASS code [5] coupled to FAST V6.02 was also implemented and validated under the same case scenario. In the present paper SIMULIA XFlow 2022x is employed and the static tensions of the chain in the fairlead are compared to the experimental and computational ones extracted by Azcona et al. [2].

Also, the hanging position of the chain in catenary shape under equilibrium is compared to a multisegmented Quasi-Static theory (MSQS), MAP++ [1].

This way, a single software is in charge of the calculation of both the dynamics and the mooring line tensions, avoiding the co-simulations with external software and leading to reduce computational cost.

2 Simulate models

The simulated models correspond to Case ID 1 and 2 from Azcona et al. [2]. The selected chain has 21 m length, a density of 7850 kg/m^3, an axial stiffness of 3.4e5 N and a damping ratio of 0.8.

The distance between anchor and fairlead X coordinates varies from 19.364 m to 19.872 m depending on the chain configuration, and the fairlead is located 5 m above the anchor, as can be seen in FIG 1.

The chain is discretized in 42 segments united by 6 DOF joints, whose initial positions are introduced into the calculation program according to MSQS model [1].

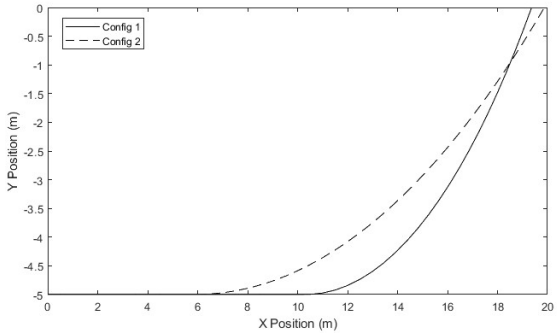

FIG 1. Simulated models according to Azcona et al. [2]

3 Simulation setup

Simulations were carried out using the CFD software SIMULIA XFlow 2022x. Domain is 30 m long, 6 m wide and 6 m high. In XFlow, no interaction between cables and fluid is implemented. For that reason, a general lattice cell of 0.1 m is established. Inertia forces are also not taken into account, so static equilibrium is reached rapidly from initial position. The simulation time is set then to 7 s, although equilibrium is reached in 2 or 4 s, depending on the chain configuration.

The total number of elements is 1080000, and the simulation time step is set fixed to 0.00111 s. FIG 2 shows the simulation setup, displaying in blue each of the joints that connects the segments that make up the chain.

The average simulation time was 3.5 hours with a 12 core, 2.4 GHz processor.

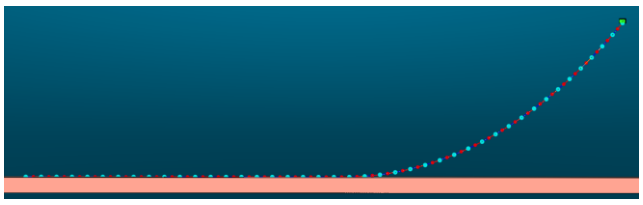

FIG 2. XFlow Simulation setup.

In order to avoid collisions between each segment ends, a clearance is set in the joints. The initial position of the catenary is placed according to equations (1) ad (2) [1].

$$x(s) = \begin{cases} 0 & for\ 0 \le s \le \gamma \\ s + \frac{C_B W}{2EA}[s^2 - 2s\gamma + \gamma\lambda] & for\ \gamma \le sz \le L_B \\ L_B + \frac{H}{W}\sinh^{-1}\left[\frac{W(s-L_B)}{H}\right] + \frac{Hs}{EA} + \frac{C_B W}{2EA}[\lambda\gamma - L_B^2] & for\ L_B \le s \le L \end{cases} \quad (1)$$

$$z(s) = \begin{cases} 0 & for\ 0 \le s \le L_B \\ \frac{H}{W}\left[\sqrt{1 + \left(\frac{W(s-L_B)}{H}\right)^2} - 1\right] + \frac{W(s-L_B)^2}{2EA} & for\ 0 \le s \le L \end{cases} \quad (2)$$

4 Results

The coordinates of each of the joints that conforms the cable are extracted and shown in FIG 3 for each of the configurations. These are compared to the MSQS. The bottom of the image shows the experimental and OPASS computational results obtained by Azcona et al. [2].

This shows the agreement of the computational static shape in comparison to MSQS and to experimental data.

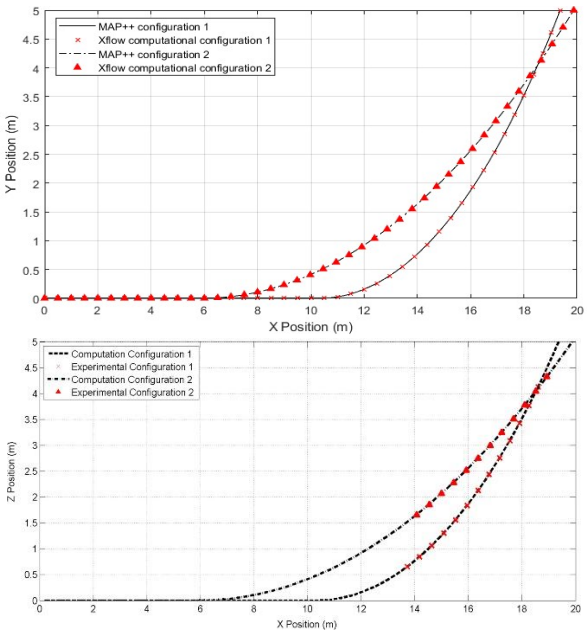

FIG 3. Catenary coordinates. XFlow (above) and experimental (below).

Fairlead tension is also evaluated once the chain is in equilibrium and the results are shown in TABLE 1, in comparison with experimental and OPASS results. The difference in percentage between experimental and computational models are also shown.

	CONFIGURATION 1	CONFIGURATION 2
Experimental	8.13	14.48
OPASS	8.10	14.70
Difference	0.37%	1.52%
XFLOW	8.14	14.79
Difference	0.15%	2.12%

TABLE I. Fairlead tension in Newtons.

5 Conclusions

Two different configurations of a chain in static case have been simulated. Coordinates of the joints that conform the chain and fairlead tension have been calculated by CFD simulations with XFlow software.

According to the results shown for both configurations, SIMULIA XFlow 2022x recreates chains in quasi-static equilibrium with high accuracy. Further, the results of the first configuration are more accurate than in the reference article. Although in the case of the second configuration the error is greater, this does not mean more than a 1% increase.

6 Acknowledgements

The authors acknowledge the support given by the Government of Navarre (Research project: PC042-043 COSTA).

References

[1] Masciola, M., Jonkman, J., Robertson, A., (2013). “Implementation of a multisegmented, quasi-static cable model”. The Twenty-third International Offshore and Polar Engineering Conference. International Society of Offshore and Polar Engineers.

[2] Azcona, J., Munduate, X., Gonzalez, L., Nygaard, T., (2017). “Experimental validation of a dynamic mooring lines code with tension and motion measurements of a submerged chain”. Ocean Engineering, 129, 415-427.

[3] Chen, H., Hall, M., (2022). “CFD simulation of floating body motion with mooring dynamics: Coupling MoorDyn with OpenFOAM”. Applied Ocean Research, 124. 103210.

[4] Domínguez, J.M., Crespo, A.J., Hall, M., Altomare, C., Wu, M., Stratigaki, V., Gómez- Gesteira, M., (2019). “SPH simulation of floating structures with moorings”. Coastal Engineering. 153, 103560.

[5] Azcona, J., Munduate, X., Nygaard, T., Merino, D., 2011. “Development of opass code for dynamic simulation of mooring lines in contact with seabed”. EWEA Offshore.

Two-way fluid-structure interaction for the study of advanced turbine control systems

Christian Santoni[1], Xiaolei Yang[2], Peter Seiler[3], Fotis Sotiropoulos[4], Ali Khosronejad[1*]

[1]*Department of Civil Engineering, Stony Brook University, USA*
[2]*Insititute of Mechanics, Chinese Academy of Science, China*
[3]*Department of Electrical engineering and Computer Science, University of Michigan, USA*
[4]*Department of Mechanical and Nuclear Engineering, Virginia Commonwealth University, USA*

A large-eddy simulations (LES) framework that enables control co-design of wind turbines has been developed. The framework couples our in-house Navier-Stokes equation solver with the actuator surface model, advanced turbine control system, and a blade aeroelasticity model for the high-fidelity simulations of wind turbines. The baseline collective (CPC) and individual pitch control (IPC) algorithms are incorporated into the simulation framework. Simulations are carried out to investigate the impact of collective and individual pitch control strategies on the deflection of turbine blades. The results show that the IPC reduces the blade tip deflection fluctuations in the out-of-plane direction, while the fluctuations of the blade tip deflection along the in-plane direction are barely affected by the IPC.

INTRODUCTION

A proposed approach for decreasing the levelized cost of energy (LCOE) is to increase the size of wind turbines. However, for the feasibility of larger rotors, it is necessary to reduce the mass of the blade. Moreover, fatigue loads are of special consideration for larger-scale wind turbines as they are subjected to unbalanced loads due to the considerable variation of wind-shear-induced aerodynamic forces across the rotor diameter.

Feedback control to reduce the load fluctuations due to wind shear and tower shadowing has been proposed in the past [1] [2]. However, advanced control strategies have been studied using simplified turbine models. For this reason, the VFS-Wind fluid flow solver has been coupled with the actuator surface model and advanced individual pitch control (IPC) to study the controller performance in realistic atmospheric conditions. Moreover, the blade deflection has been considered using a second-order Euler-Bernoulli beam theory model [1].

Fatigue Loads

Fatigue loads due to the heterogeneity of the velocity at the rotor have been quantified by means of the damage equivalent loads (DEL). The DELs are given by [2]:

$$DEL = \left(\frac{\sum_i n_i L_i^m}{n^{ST_{eq}}} \right)^{1/m},$$

where n_i is the damage count for cycle i, L_i is the Goodman-corrected load range, $n^{ST_{eq}}$ is the time series equivalent counts, and m is the Whöler exponent. A comparison of the DELs of the turbines with the baseline collective and IPC (Figure 1), shows that the DEL can be reduced by up to 40% by the individually pitching the blades.

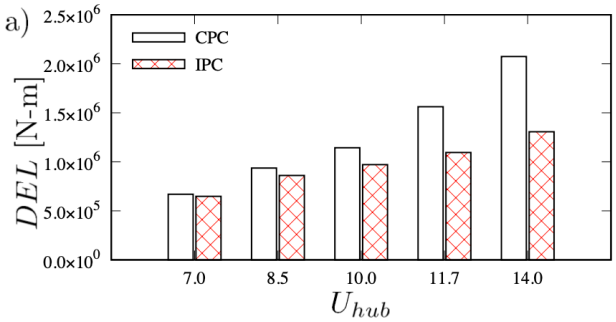

FIG 1. Damage equivalent loads (DEL) on the turbine with the baseline collective pitch control (——) and individual pitch control (——).

CONCLUSIONS

Results show that the IPC reduces the damage equivalent loads and the blade tip deflection fluctuations in the out-of-plane direction, while the fluctuations of the blade tip deflection along the in-plane direction are barely affected by the IPC. It was also shown that, despite its minor impact on the turbulence kinetic energy of the wake, the IPC controller did not influence the recovery of the turbine wake. The findings of this study reveal the importance of advanced control systems in reducing the dynamic loads on wind turbine blades and underscore the potential of control co-design to reduce the levelized cost of wind energy.

—

* ali.khosronejad@stonybrook.edu

[1] Santoni, C., Khosronejad, A., Yang, X., Seiler, P. Sotiropolous, F., (2023), "Coupling turbulent flow with blade aeroelastics and control modules in large-eddy simulation of utility-scale wind turbines," *Physics of Fluids*, 35, 0151409.

[2] Santoni, C., Khosronejad, A., Seiler, P. Sotiropolous, F., (2023), "Toward control co-design of utility-scale wind turbines: Collective vs. individual blade pitch control," *Energy Reports*, 9, 793-806.

Wall shear stress on an elastic boundary or structure

Siew-Wan Ohl[1,2*], Hendrik Reese[1] and Claus-Dieter Ohl[1]

[1]*Institute of Physics, Otto-von-Guericke University Magdeburg, Universitätsplatz 2, 39106 Magdeburg, Germany*
[2]*Research Campus STIMULATE, University of Magdeburg, Otto-Hahn-Straße 2, 39106 Magdeburg, Germany.*

The stresses induced by a cavitation bubble on an elastic boundary is studied experimentally and numerically. Experimentally we tracked the displacement of embedded particles on an elastic layer and the deformation of an elastic ring strucutre. The corresponding simulations are done with Volume-of-Fluid solver in OpenFOAM. Good agreement between the experiments and simulation is found in terms of bubble dynamics and particle displacement or structural deformation. This lends credibility to the stresses calculated. We found a highest wall shear stress of 250 kPa at a bubble stand-off distance of 1.1*R_{max} (maximum bubble radius). The largest overall shear stress of 1.9 MPa is found, however, whithin the elastic layer. Thus fracture may start whin the elastic material rather than on its surface which is nearer to the collapsing bubble.

INTRODUCTION

Impact of the jet from a collapsing bubble is known to be responsible for the damages on fast-rotating ship propellers [1]. However near an elastic boundary, the bubble may collapse differently, for example splitting into two bubbles and then jetting away from one another [2]. When the elastic layer is very thin and is attached to a rigid boundary, the bubble jets towards the elsatic boundary creating high stresses on the elastic surface and causing damages and erosions [3].

Experimental and simulation results

The cavitation bubble is generated in water in a glass cuvette with a focused pulsed laser. The bubble interacts with an 60 µm thick elastic PDMS layer spin-coated on a custom-made acrylic cuvette cap. The interaction is filmed with two high speed cameras: one with a 10x lens to track the particles and the other to film the bubble dynamics.

The simulation is done by coupling a finite-volume solver for two compressble viscous fluids with a solver for a linearly elastic solid (density = 1000 kg/m^3, Possion ratio = 0.4). Refinement on the boundary layer is carefully done to ensure sufficient resolution to resolve the wall shear stress.

Fig. 1 shows the experimental and numerical results for bubble dynamics, and lateral displacements of particle 1 (at position 1) and particle 2 (at position 2). It is seen that particle 1 which is further away from the bubble center is displaced more than particle 2. This is because the axis of symmetric perclude a stagnation point at bubble center (x = 0). A maximum wall shear stress of 159.5 kPa is calculated at x = 25 µm at bubble collapse (t = 103 µs).

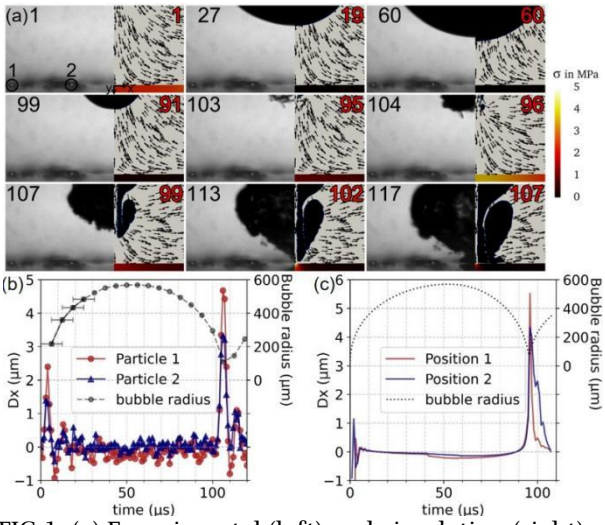

FIG 1. (a) Experimental (left) and simulation (right) of a cavitation bubble near an elastic layer where R_{max} = 569 µm, standoff γ = 1.5R_{max}, sheet thickness = 60 µm amd elastic modulus, E = 1.4 MPa. (b) Tracked movement of particle 1 and 2 as shown in (a). (c) Simulated movement of layer at position 1 and 2 of the particles.

CONCLUSIONS

We summarize the maximum lateral displacements of particles with bubbles at different stand-off distances, γ, non-dimensionalized by R_{max}. From the corresponding calculation, a maximum wall shear stress of 250 kPa is found for γ = 1.1. Recently, Zeng et al. [4] reported a wall shear stress of 100 kPa for a collapsing bubble at γ = 1.We also studied the interaction of a bubble with an elastic ring structure and found good agreement between experimental and simulation results.

[1] Rayleigh,Philosophical magazine series 6, 34, 94–98 (1917).
[2] Turangan, G. Ong, E. Klaseboer, and B. C. Khoo, Journal of applied physics 100, 054910 (2006).
[3] Gong, S. Ohl, E. Klaseboer, and B. Khoo, Journal of Fluids and Structures 76, 336 (2018).
[4] . Zeng, H. An, and C.-D. Ohl, Journal of Fluid Mechanics 932 (2022).

2nd Spanish Fluid Mechanics Conference
Barcelona (2 - 5 July 2023)

On the limitations of the level set method in the simulation of interfacial flows involving contact lines

Pablo Gómez[1], Adolfo Esteban[1,2], Félix Berlanga[1], Claudio Zanzi[1], Joaquín López[2], and Julio Hernández[1]

pgomez@ind.uned.es

[1]Dept. de Mecánica, E.T.S. de Ingenieros Industriales, Universidad Nacional de Educación a Distancia (UNED), Spain
[2]Dept. de Ingeniería Mecánica, Materiales y Fabricación, ETSII, Universidad Politécnica de Cartagena, Spain

The level set method presents particular difficulties related to the reinitialization procedure when used in the simulation of 3D interfacial flows in which the interface intersects a solid wall. Due to the appearance of a blind zone that the characteristic lines of the Hamilton-Jacobi equation cannot reach, the reinitialization procedure requires a specific boundary condition for the level set function to avoid inconsistent results. Although several approaches have been recently proposed in the literature, further improvement is necessary. In this work, a revision of the most recent advances is made, and some preliminary results obtained with a new proposed model are presented.

1 Introduction

The contact line appears in interfacial flows when the interface intersects a solid surface, which happens in many situations in nature and engineering applications (Sui et al., 2014). The simulation of the contact line dynamics requires to address two issues: to reproduce the intermolecular forces between the fluid and the solid wall, and to solve the "stress singularity" at the contact line, which arises in the resolution of the Navier-Stokes equations subject to a no-slip boundary condition at the solid surface. The level set formulation is an approach widely used to reproduce the interface evolution in the simulation of unsteady interfacial flows due to its several advantages, particularly its simplicity to calculate geometric parameters such as curvature and the fact that it does not require special procedures to handle topological changes of the interface (Osher and Fedkiw, 2001). However, this method presents an added difficulty, associated with the reinitialization procedure used to maintain the level set function as a signed distance to the interface when this intersects a solid surface, which has limited its use in interfacial problems involving moving contact lines. Different alternatives have been proposed to remedy this issue (Abu-Al-Saud et al., 2017; Xu & Weiqing, 2016; Bogdanov et al., 2022), but the problem has not been completely solved yet.

2 Numerical procedure

In the level set formulation, the reinitialization procedure is typically based on solving a Hamilton-Jacobi equation, $\phi_\tau = S_\varepsilon(\phi_0)(1-|\nabla\phi|)$, where $\phi_0(\vec{x},t)$ is the level set function, τ is an artificial time, $\phi(\vec{x},\tau=0) = \phi_0(\vec{x},t)$ is the initial condition, and S_ε is a smoothed sign function (see, e.g., Gómez et al. (2019)). Since the characteristic lines are perpendicular to the interface, a blind zone that the characteristics cannot reach appears when the interface intersects a solid surface. Figure 1 shows a schematic representation of a typical blind zone not reached by the characteristic lines of the Hamilton-Jacobi equation, represented by black arrows, in the vicinity of the intersection between the interface and a solid wall. In this zone, the reinitialization does not work correctly, and it is necessary to introduce a boundary condition at the wall

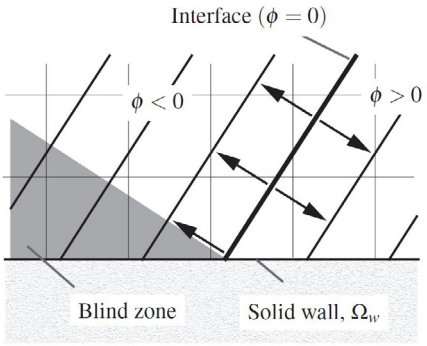

Figure 1: Schematic representation of the level set function, ϕ, in the vicinity of the intersection of the interface with a solid surface, Ω_w. Positive contours correspond to the liquid. The black arrows represent the direction of the characteristic lines of the Hamilton-Jacobi equation.

nodes of the blind zone, which is not an easy task, particularly in 3D problems.

In 2D problems the task is simpler since the contact line is reduced to a single point and the contact angle has a unique value (see, e.g., Rocca & Blanquart (2014)) that can be imposed at the wall nodes of the blind zone to determine the component of the ϕ gradient normal to the wall, $(\nabla\phi)_n|_w$. The application of the boundary condition in 3D problems is a complex task since, in general, particularly when the deformation of the interface is severe, the contact angle may vary from point to point along the contact line. Different alternative approaches have been proposed recently in the literature. Xu & Weiqing (2016) proposed a method based on a normal extension along the blind zone of the apparent contact angle at the interface to determine $(\nabla\phi)_n|_w$. Abu-Al-Saud et al. (2017) determine the level set function in the nodes of the blind zone by calculating the minimum distance to an extended interface reconstructed using a PLIC (Piecewise Linear Interface Calculation) method. Bogdanov et al. (2022) calculate the ϕ values at the ghost nodes inside the wall in a narrow band around the contact line using and extension of ϕ in a direction determined by an analytic contact angle. In this work, we present a method similar to that proposed by Xu & Weiqing (2016) with different improvements. An example of the results obtained with the proposed method are shown in figure 2. Although the results are reasonably good when the interface shape at the contact line is not complex and the contact line moves slowly enough, further research is needed for more complicated problems, such as drop impacts at high speeds.

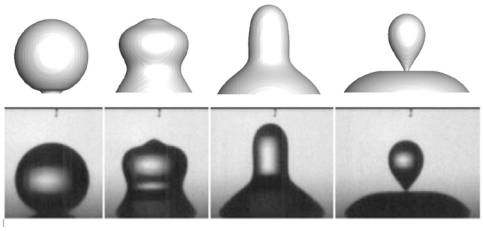

Figure 2: Example of comparison between numerical and experimental results for the first-stage pinch-off in a water drop of 0.486 mm in diameter (Oh = 0.0069) deposited on a hydrophilic glass substrate (Ding et al., 2012).

3 Conclusions

A review of the most recent avances in the use of the level set method to simulate interfacial flows with moving contact lines is presented. Preliminary results of a new proposed model that will be presented in this work show good agreement with experimental results, although further research is needed.

4 Acknowledgments

The authors gratefully acknowledge the support of the Spanish Ministerio de Ciencia e Innovación - Agencia Estatal de Investigación (MCIN/ AEI / 10.13039/501100011033) through projects PID2020-120100GB-C21 and PID2020-120100GB-C22. A.E. acknowledges the support of the Spanish Ministerio de Universidades through a Margarita Salas grant.

References

Abu-Al-Saud M.O., Soulaine C., Riaz A., Tchelepi H.A. (2016) "Level-set method for accurate modeling of two-phase immiscible flow with moving contact lines". *arXiv e-prints*, https://doi.org/10.48550/arXiv.1708.04771.

Bogdanov V., Schranner F.S., Winter J.M., Adami S., Adams N.A. (2022) "A level-set-based sharp-interface method for moving contact lines". *Journal of Computational Physics*, **467**, 111445.

Ding H., Li E.Q., Zhang F.H., Sui Y., Spelt P.D.M., Thoroddsen S.T. (2016) "Propagation of capillary waves and ejection of small droplets in rapid droplet spreading". *Journal of Fluid Mechanics*, **697**, 92–114.

Gómez P., Zanzi C., López J., Hernández J. (2019) "Simulation of high density ratio interfacial flows on cell vertex/edge-based staggered octree grids with second-order discretization at irregular nodes". *Journal of Computational Physics*, **376**, 478–507.

Rocca G.D., Blanquart G. (2014) "Level set reinitialization at a contact line". *Journal of Computational Physics*, **265**, 34–49.

Osher S., Fedkiw R.P. (2001) "Level Set Methods: An Overview and Some Recent Results". *Journal of Computational Physics*, **169**, 463–502.

Sui Y., Ding H., Spelt P. (2014) "Numerical simulations of flows with moving contact lines". *Annual Review of Fluid Mechanics*, **46**, 97119.

Xu S., Weiqing R. (2016) "Reinitialization of the level-set function in 3D simulation of moving contact lines". *Journal of Computational Physics*, **376**, 1163–1182.

2nd Spanish Fluid Mechanics Conference
Barcelona (2 - 5 July 2023)

On the numerical simulation of interfacial rheology

Adolfo Esteban[1,3], Javier Tajuelo[2], Pablo Sánchez-Puga[2,4], Miguel Ángel Rubio[2], and Julio Hernández[1]

aesteban@ind.uned.es

[1]Dept. de Mecánica, E.T.S de Ingenieros Industriales, Universidad Nacional de Educación a Distancia (UNED), Spain
[2]Dept. de Física Fundamental, Facultad de Ciencias, Universidad Nacional de Educación a Distancia (UNED), Spain
[3]Dept. de Ingeniería Mecánica, Materiales y Fabricación, ETSII, Universidad Politécnica de Cartagena, Spain
[4]Large Scale Structures Group, Institut Laue-Langevin, Grenoble, France

We present preliminary results of a numerical model developed to describe the complex interplay between Marangoni effects, compressibility, shear, dilational and extensional surface stresses, and subphase effects at an interface carrying a surfactant material.

1 Introduction

Computer simulation can be of great help in the study of the mechanical behavior of viscous fluid-fluid interfaces (Jaensson et al., 2021) and in the development of experimental techniques to measure their rheological properties (Tajuelo et al., 2016). In this work we will present a numerical model implemented in the OpenFOAM framework that allows to investigate the complex interfacial dynamics and the possibility to break down the different contributions to the drag force on needles and particles moving at the interface due to the subphase, Marangoni and extra surface stresses.

2 Mathematical model

For the sake of brevity, we will present here a simplified model, in which extensional and other contributions are not separated (Verwijlen et al., 2012). Consider a solid object of characteristic length L moving with velocity $\mathbf{U}(\mathbf{x},t)$ at an air-liquid planar interface carrying a surfactant forming a viscous monolayer. The liquid is considered Newtonian with constant and uniform properties and the air is assumed inviscid. The steady incompressible viscous flow of the subphase is assumed to be described by the Stokes equations (in the following, all quantities are dimensionless),

$$\nabla \cdot \mathbf{u} = 0, \tag{1}$$

$$-\nabla p + \nabla^2 \mathbf{u} = 0. \tag{2}$$

Assuming that the monolayer is insoluble, the evolution of surfactant concentration, Γ, is governed by

$$\frac{\partial \Gamma}{\partial t} + \nabla_s \left(\Gamma \mathbf{u}_s\right) = \frac{1}{\mathrm{Pe}_s} {\nabla_s}^2 \Gamma, \tag{3}$$

where $\mathrm{Pe}_s = UL/D_s$ is the surface Pèclet number (D_s being the surface diffusivity), $\nabla_s = \mathbf{I}_s \cdot \nabla$ the surface gradient operator, $\mathbf{I}_s = \mathbf{I} - \mathbf{nn}$ the surface projection tensor, $\mathbf{n}$ the interface unit normal vector, and $\mathbf{u}_s = \mathbf{I}_s \cdot \mathbf{u}$.

The extra surface stress tensor, $\boldsymbol{\tau}_s$, is assumed to be described by the Boussinesq-Scriven constitutive law for a Newtonian interface:

$$\boldsymbol{\tau}_s = \left(\mathrm{Bq}_2 - \mathrm{Bq}_1\right)\left(\mathbf{I}_s : \mathbf{D}_s\right)\mathbf{I}_s + 2\mathrm{Bq}_1 \mathbf{D}_s, \tag{4}$$

where $\mathrm{Bq}_1 = \eta_s/(L\eta)$ and $\mathrm{Bq}_2 = \kappa_s/(L\eta)$ are the Boussinesq numbers (κ_s and η_s being the dilational and shear viscosities of the interface, respectively, and η the subphase viscosity), and $\mathbf{D}_s$ the surface rate of deformation tensor, defined as

$$\mathbf{D}_s = \frac{1}{2}\left[\left(\nabla_s \mathbf{u}_s\right)\cdot \mathbf{I}_s + \mathbf{I}_s \cdot \left(\nabla_s \mathbf{u}_s\right)^T\right]. \tag{5}$$

The interfacial stress balance is given by

$$\mathbf{n}\cdot\left(-\boldsymbol{\tau}\right) = -\nabla_s \cdot \boldsymbol{\tau}_s + \mathrm{Ma}\,\Gamma \nabla_s \ln \Gamma, \tag{6}$$

where $\mathrm{Ma} = \Gamma_0 E_\Pi/(\eta U)$ is the Marangoni number ($E_\Pi = \partial\gamma/\partial\Gamma$ is a constant value resulting from the linearization of the surface tension $\gamma = \gamma(\Gamma)$ near Γ_0), $\Gamma_0 = \Gamma(\mathbf{x}, t=0)$, and $\boldsymbol{\tau} = \left[\nabla\mathbf{u} + \left(\nabla\mathbf{u}\right)^T\right]$ the viscous stress tensor in the subphase.

The boundary conditions for the velocity are the no-slip condition at the solid surface, and vanishing velocity at infinity. For the pressure, a zero gradient at the solid surface and vanishing pressure at infinity boundary conditions are applied. For the surfactant concentration, the initial condition $\Gamma = 1$ at the interface is applied, and a zero gradient is imposed at the contact line between the solid and the interface.

3 Numerical method

The Stokes flow in the subphase and the evolution of the surfactant concentration at the interface are solved in a coupled way. The mathematical model has been implemented into the OpenFOAM framework as a library `rheoFoam`. The equations are discretized using the FVM and second-order schemes on a statically-refined moving (if necessary) grid. The two sub-problems are solved together using a three-step implicit method: 1) solve Eqs. (1)-(2), 2) solve Eqs. (6)-(3), and 3) go back to 1) and repeat again until the normalized variation of $\mathbf{u}_s$ and Γ reaches a prescribed tolerance.

The implementation of the model has been validated by performing several numerical simulations of two different problems described by Pourali et al. (2021) and Verwijlen et al. (2012). As an example, Fig. 1 shows results obtained for the interfacial flow field and surfactant distribution for the Cambridge Interfacial Tensiometer (CIT), also simulated by Verwijlen et al. (2012) (Fig. 12(a),(e)).

4 Conclusions

Preliminary numerical results show good agreement with the numerical and experimental results of other authors. As expected, the stability and robustness of the numerical model and the computational effort required are strongly dependent on the combination of relevant dimensionless numbers, especially for high values of the Marangoni number. The model can incorporate effects such as surfactant solubility and viscoelastic constitutive models.

5 Acknowledgments

The authors gratefully acknowledge the support of the Spanish Ministerio de Ciencia e Innovación - Agencia Estatal de Investigación through projects PID2020-120100GB-C21 and PID2020-117080RB-C54. A.E. acknowledges the support of the Spanish Ministerio de Universidades through a Margarita Salas grant. P.S.P. acknowledges the support of the MCIN-ILL project "Simultaneous interfacial rheology and neutron scattering studies of biomolecules in interfacial films".

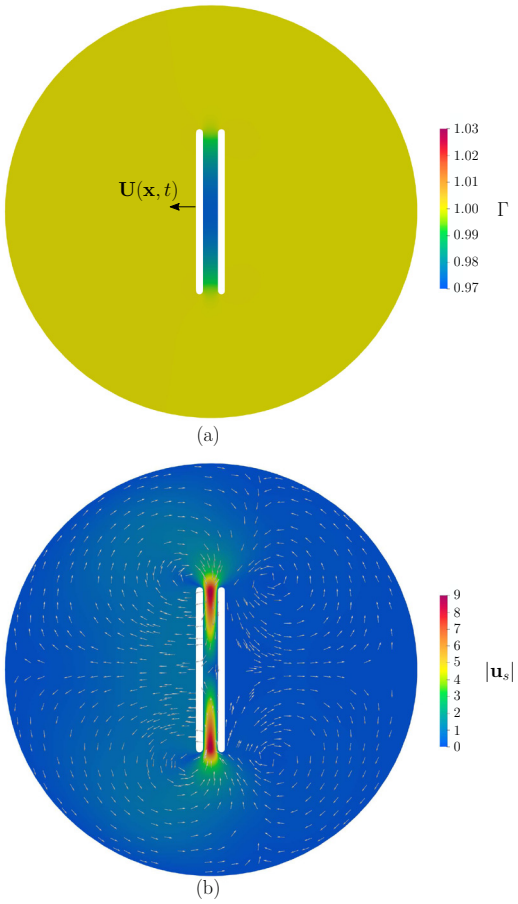

Figure 1: Numerical results for (a) the surfactant concentration distribution and (b) interfacial flow field at $t = 1$ (time made dimensionless with U and the initial separation between bars, L) obtained for the CIT device with Ma = 8000, $\mathrm{Bq}_1 = 100$, $\mathrm{Bq}_2 = 5000$, and Trouton ratio (ratio between the interfacial extensional and shear viscosities) Tr = 4.

References

Tajuelo J., Pastor J.M., Rubio M.A. (2016) "A magnetic rod interfacial shear rheometer driven by a mobile magnetic trap". *Journal of Rheology*", **60**, 1095–1113.

Jaensson N.O., Anderson P.D., Vermant J. (2021) "Computational interfacial rheology". *Journal of Non-Newtonian Fluid Mechanics*", **290**, 104507.

Pourali M., Kröger M., Vermant J., Anderson P.D. & Jaensson N.O. (2021) "Drag on a spherical particle at the air–liquid interface: Interplay between compressibility, Marangoni flow, and surface viscosities". *Physics of Fluids*, **33**, 062103.

Verwijlen T., Leiske D.L., Moldenaers P., Vermant J. & Fuller G.G. (2012) "Extensional rheometry at interfaces: Analysis of the Cambridge Interfacial Tensiometer". *Journal of Rheology*, **56**, 5, 1225–1247.

2nd Spanish Fluid Mechanics Conference
Barcelona (2 - 5 July 2023)

Pattern selection during thermocapillary-driven melting in microgravity

P. Salgado Sánchez[1], J. Porter[1], I. Tinao[1], and A. Laverón-Simavilla[1]

pablo.salgado@upm.es

[1]E-USOC, Center for Computational Simulation, Universidad Politécnica de Madrid, Spain

We analyze pattern selection for thermocapillary flow in rectangular containers in microgravity. The bifurcation picture is characterized by a transition from steady flow to either standing (pulsating) or traveling type waves. These transitions are sometimes subcritical and accompanied by a saddle-node bifurcation, which delimits a region of bistability. We apply this bifurcation analysis to explain the dynamics observed during thermocapillary-driven melting of PCMs in microgravity.

1 Introduction

Despite the well-known importance of thermocapillary flows in many technological processes, few studies have considered the coupling between these flows and the dynamic boundary conditions associated with the moving solid/liquid (S/L) front during the phase change. To the best of our knowledge, the first systematic attempt was the recent work of Salgado Sánchez et *al.* (2021), where the nature of the flow in the liquid phase was investigated throughout the melting process. Here, we analyze pattern selection in rectangular containers of liquid n-octadecane in microgravity. The identified bifurcations are then used to explain the dynamics observed during melting via an appropriately-defined path through an effective parameter space; see Salgado Sánchez et *al.* (2022) for details.

2 Stability and bifurcations

The stability map of Fig. 1 summarizes the three main flow regimes in terms of the container aspect ratio, Γ, and the applied Marangoni number, Ma. The critical boundaries separate steady flows from the two types of oscillatory convection: standing (S) wave modes (marked in blue) and traveling (T) wave modes (marked in red). Both S and T waves appear via a primary Hopf (H) bifurcation that can be either supercritical or subcritical. In the latter case, this H bifurcation is accompanied by a secondary saddle-node (SN) bifurcation; SN bifurcations are indicated by dashed curves.

The S wave mode is analogous to that reported by Peltier & Biringen (1993) while the T wave mode is analogous to that described by Smith & Davis (1983). The T waves are characterized by the cyclic creation of vortices near the cold boundary that detach and move toward the hot wall.

These bifurcation results, obtained for containers of pure liquid, can be used to understand the melting process in microgravity.

3 Melting dynamics in microgravity

During melting, the S/L front constitutes a dynamic boundary condition for the liquid phase. The varying shape of this front generally reflects two qualitatively distinct regions: one dominated by conduction and one by the thermocapillary effect near the free surface. In this latter region, the S/L front changes both its characteristic length and its depth as time passes. We define time-dependent effective values of Γ and Ma and use these to characterize the region of the flow where thermocapillary modes appear.

Figure 2 shows two examples of melting paths in the space of effective parameters (Γ_{eff}, Ma_{eff}) for a container with $\Gamma = 12$. The nature of the observed flow is indicated by the color of the curve: steady in grey and T waves in red. The temperature deviation δT of the T wave case is included in panel (b), with vertical lines marking the appearance of oscillatory flow and the completion of melting (labeled as τ and t_{melt}, respectively). Note that the instability to T waves is in good agreement with the crossing of the (pure liquid) critical boundary.

4 Conclusions

Pattern selection for thermocapillary flow in rectangular containers of liquid n-octadecane in microgravity is organized by bifurcation sets that may be expressed in terms of Γ and Ma, with corresponding regions of steady and oscillatory flow. In the case

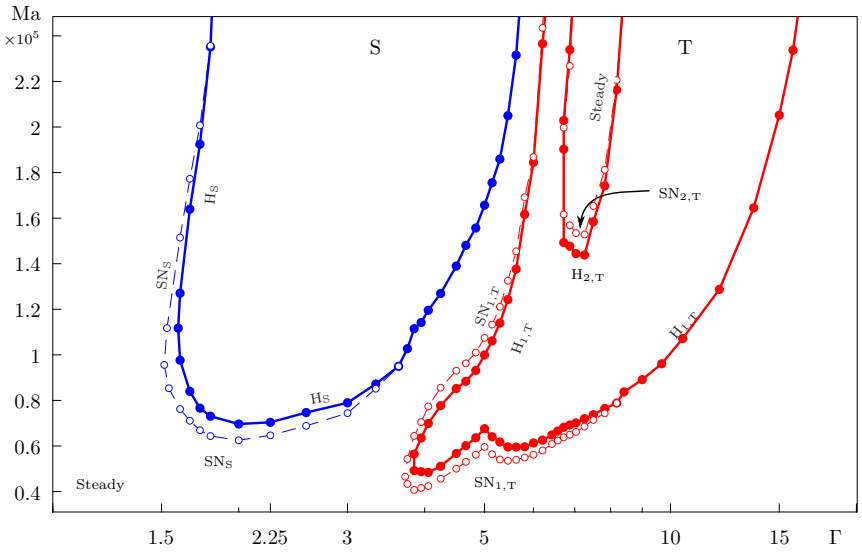

Figure 1: Stability map in terms of Γ and Ma showing the critical boundaries for oscillatory flow.

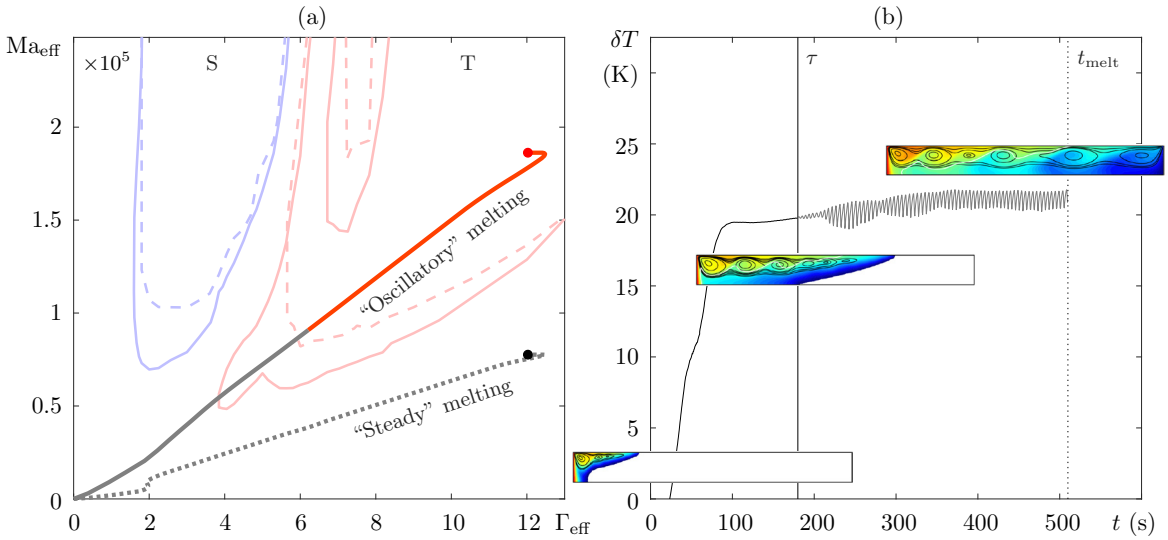

Figure 2: (a) Melting paths (steady flow in grey, T waves in red) in effective parameters (Γ_{eff}, Ma_{eff}) with $\Gamma = 12$. Solid, dotted, and dashed boundaries show the Hopf bifurcation for different (increasing) heating rates. (b) Temperature δT; vertical lines mark the appearance of oscillatory flow and full melting.

of melting, appropriate effective parameters, Γ_{eff} and Ma_{eff}, can be defined to explain the observed dynamics as a time-dependent path through distinct flow regimes.

References

Salgado Sánchez P et al. (2021) "Thermocapillary effects during the melting of phase change materials in microgravity: steady and oscillatory flow regimes". *Journal of Fluid Mechanics*, **908**, A28.

Salgado Sánchez P et al. (2022) "Pattern selection for thermocapillary flow in rectangular containers in microgravity". *Physical Review Fluids*, **7**, 053502.

Peltier L J & Biringen S. (1993) "Time-dependent thermocapillary convection in a rectangular cavity: numerical results for a moderate Prandtl number fluid". *Journal of Fluid Mechanics*, **257**, 339.

Smith M K & Davis S H. (1883) "Instabilities of dynamic thermocapillary liquid layers. Part 1. Convection Instabiloties". *Journal of Fluid Mechanics*, **132**, 19.

The impact of convection on the melting process for different g-levels

D.Dubert[1], B. Seta[2], M.J. Simon[3], J. Massons[1], Jna Gavaldà[1], X. Ruiz[1]

[1]Dept. Química Física I Inorgànica, Universitat Rovira I Virgili, Tarragona, Spain
[2]Dept. of Mechanical Engineering, Technical University of Denmark. Kogens Lynaby, Denmark.
[3]Dept. Enginyeria Mecànica, Universitat Rovira I Virgili, Tarragona, Spain

Corresponding author: Diana Dubert: dianacristina.dubert@urv.cat

This work analyzes the melting flow thermodynamics of two feasible organic PCM candidates: n-octadecane and succinonitrile and for heat management in different g-environments. The different Prandtl numbers strongly conditions the answer of the system not only concerning the bulk thermo-hydrodynamics but as well the interface shape and melting rate.

INTRODUCTION

Under the MarPCM-ESA project, and in order to analyze the heat transfer management in both terrestrial and space environments, the convective characterization of solid-liquid phase change based systems (PCM) has become of great technological and fundamental interests. On the space stations, for instance, as the natural convection is minimal, the Marangoni convection plays a fundamental role by enhancing the heat transport near the free surfaces. Moreover, the actual NASA's project, Artemis, which plans to start building a Moon village in 2030, and in longer term perspective, on Mars, make it necessary to consider the impact of different convective intensities. In other words, the relevance of the different g-environments, in the study and characterization of the different PCM based systems.

Under the above-mentioned project, Dubert et al. [1] has already reported some results concerning PCM materials, with different Prandtl values, that can fit the International Space Station scenario: sodium nitrate (NaNO3, Pr=8), succinonitrile (SCN, Pr=23) and gallium (Ga, Pr=0.02). However metals and inorganic salts, even though they can present a high heat storage capacity, are very corrosive and cannot be used in the Station for strict safety reasons. Organic paraffin-based PCM such as n-octadecane, n-C18, or n-eicosane, n-C20, can easily remedy this problem. They have a high latent heat, low densities and high chemical stability. But their low thermal conductivity makes mandatory a convective strong support to increase their efficiency in term of heat transfer rate. From this perspective, Porter et al. [2] investigates the effectiveness of Marangoni convection to improve the heat transfer rate of passive PCM devices based on n-octadecane.

The present paper, trying to complete these findings, uses a two-dimensional model of a PCM based parallelepipedic heat manager, aiming to present details of the flow and interface dynamics of two feasible organic candidates, the n-octadecane n-C18 and the succinonitrile, C4H4N2 during the melting sub-cycle of the complete solid-liquid-solid phase change process. In addition, the investigation has been extended to different g-environments such as the Moon and Mars.

METHODOLOGY, RESULTS AND DISCUSSIONS

The computational domain used for calculations has 0.8 cm of height and 8 cm in length (aspect ratio of 10). All simulations were carried out by using an "in house" OpenFOAM solver based on the entalphy method and described by Dubert et al. (see more details in Seta et al. 2021 [3]). Left wall was considered no-slip with a temperature of 20K above the solidus one. Right wall was also considered no-slip and at the solidus temperature. Bottom wall was no-slip and adiabatic while the top one was a free surface where Marangoni convection occurs. In all cases the materials were initially in the solid state, one degree below the solidus temperature. The system melts until the 100% of the global liquid fraction was attained. The dynamics of the melting for both PCM materials was first checked by studying the evolution of the global liquid fraction all along the melting process under different gravity environments, microgravity (g=0 m/s^2), gravity of the Moon (g=-1.61 m/s^2), Mars (g=-3.72 m/s^2)

and Earth (g=-9.81 m/s^2), respectively. Remark that, under the Earth's gravity influence two extra cases: with and without Marangoni convection, have been studied.

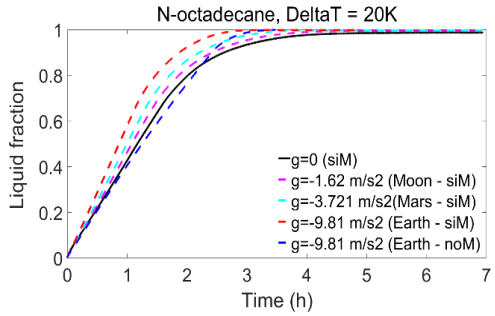

FIG 1. Global liquid fraction evolution during the n-octadecane melting process.

Fig. 1 plots the evolution of the global liquid fraction during the melting process for n-octadecane (high Pr) and all g environments considered. It can be observed that the natural convection has little influence on the melting time rushing it slightly as we increase the gravity level. Nevertheless, analyzing the evolution of the global liquid fraction for a lower Pr number (case of SCN), the above behavior changes (see Fig. 2). A reduction in the melting time exists if the experiments run under both Earth and micro-gravity conditions due to a greatest influence of the Marangoni convection on the melting process.

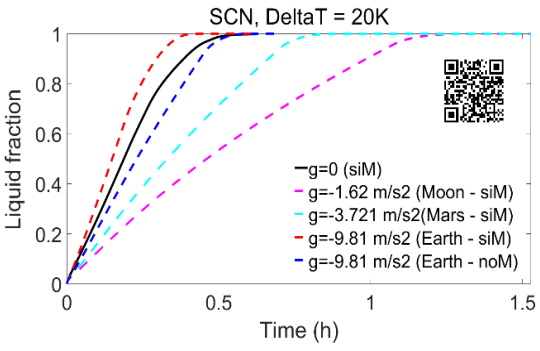

FIG 2. Global liquid fraction evolution during SCN melting process. Inset, video of the flow at g=0 for both n-ocatdecane and SCN.

Figure 3 shows a comparison of the time needed for the selected PCM materials to melt up to 95% in all cases analyzed. It is evident that the succinonitrile needs much less time to reach 95% of liquid compared to n-octadecane in all cases. This suggest this material as an alternative PCM material to n-octadecane if fast heat extraction rates are needed (as long as the melting temperature is adequate).

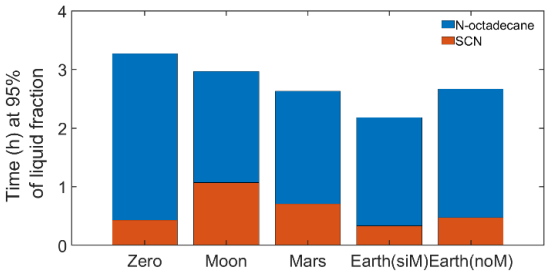

FIG 3. Melting time at 95% liquid fraction for SCN and n-octadecane in all gravity cases studied.

Finally, the complex flow behavior specially in case of thermocapillary flows alone can be observed via the QR code inside Fig. 2. It is interesting to note the presence of standing waves during the melting process damped by the join action of Marangoni and the different levels of natural convection.

CONCLUSIONS

The melting process strongly depend on the Prandtl number and gravity level conditions. In particular, the melting process of the n-octadecane is less sensitive to the natural convection, fact that makes it the perfect candidate, as phase change material, for heat extraction under any gravity environment if the heat extraction rate be slow.

Acknowledgments

This work is supported by the Ministerio de Ciencia e Innovación under Project PID2020-115086GB-C32.

REFERENCES

[1] D. Dubert, B. Seta, M.J. Simón, Jna. Gavalda, J. Massons, A. Perez-Poch, X. Ruiz, The melting-solidification cycle for materials with different Prandtl numbers, 15th International Meeting on Thermodiffusion (IMT15), Tarragona 2023, Book of abstracts (ISBN)

[2] J. Porter et al., The effect of Marangoni convection on heat transfer in phase changematerials experiment, Proceedings ELGRA symposium, 77-78 (2022). https://www.elgra.org/?page_id=908

[3] B. Seta, P. S. Sanchez, J. Massons, J. Gavalda, J. Porter, M. Bou-Ali, X. Ruiz, V. Shevtsova, Three-dimensional effects during the melting of phase-change materials with thermocapillary flow in microgravity, 27th European Low Gravity Research Association Biennial Symposium, Lisbon, 2022.

2nd Spanish Fluid Mechanics Conference
Barcelona (2 – 5 July 2023)

A Joule-Thomson process of a vapor with condensation and evaporation through anodic alumina membranes

Thomas Loimer[1], Javad Sodagar-Abardeh[1], Dmitrii I. Petukhov[2], and Stepan K. Podgolin[3]

thomas.loimer@tuwien.ac.at

[1]Institut für Strömungsmechanik und Wärmeübertragung, TU Wien, Austria
[2]Department of Chemistry, Lomonosov Moscow State University, Russia
[3]Department of Materials Science, Lomonosov Moscow State University, Russia

In a Joule-Thomson process, a vapor becomes colder. If the vapor is sufficiently close to saturation, it condenses, liquid flows through part of the porous anodic alumina membrane, and the liquid evaporates within the membrane. Vapor having a smaller pressure and smaller temperature than the vapor at the upstream side leaves the membrane. The Joule-Thomson effect needs to be considered if the temperature difference is appreciable, i.e., the pressure difference and hence the flow resistance of the membrane is large, and the membrane pore size is small. Experimental data for the flow of isobutane and of freon 142b (1-chloro-1,1-difluoro-ethane) through anodic alumina membranes with pore sizes between 18 nm and 60 nm is presented. The data is compared to a theoretical description. The heat transfer to the downstream side of the membrane can have a significant influence on the mass flow rate through the membrane.

1 Introduction

A vapor that flows through a membrane with small pores may condense due to two reasons: One is the Joule-Thomson effect, the other is capillary condensation, or a combination of the two.

Condensation due to the Joule-Thomson effect was investigated by Schneider (1983). It was found that a characteristic permeability depending on the fluid properties and on the thermal conductivity of the liquid-filled membrane exists: Vapor that flows through a membrane with a permeability smaller than the characteristic permeability would condense completely, otherwise the vapor would condense partially. For complete condensation capillary forces play an important role and strongly influence the mass flow rate, but for partial condensation, they do not. A peculiar application for the effect of full condensation was a small pocket lighter: The flame was fed through a porous, stretched polyethylene membrane, and the length of the flame remained the same, regardless whether saturated vapor or saturated liquid contacted the membrane.

Capillary condensation was studied mainly in the field of membrane processes and separation. Account was taken of the large capillary forces and the reduced vapor pressure at curved menisci, but the flow was assumed to be isothermal. The large capillary pressure at curved menisci caused a several-fold increase of the mass flow rate with respect to its value for purely gaseous flow (Lee & Hwang, 1986).

Anodic alumina membranes are produced by electrolytic oxidation of aluminum foils. The end result is a porous membrane containing straight, parallel, uniformly spaced and homogeneously sized, round pores. Hence, a one-dimensional description of the flow through a bundle of parallel capillaries is applied. Account is taken of the real gas properties of the fluid, viz. the Joule-Thomson effect, Kelvin's and Young-Laplace equations at curved interfaces and of heat transfer and the release and consumption of energy due to condensation and evaporation (Loimer et al., 2023).

2 Theoretical description

The flow is governed by the balances of mass, momentum and energy,

$$j = constant$$
$$j = -\frac{\kappa}{\nu}\frac{\mathrm{d}p}{\mathrm{d}x}$$
$$jh + \dot{q} = constant$$

where j is the mass flux, κ, ν, p and x refer to the permeability of the membrane, the kinematic viscosity, the pressure and the spatial coordinate, respectively, the specific enthalpy is given by h and $\dot{q}$ is the heat flux. The governing equations are supplemented by the thermal and caloric equations of state, by Fourier's law of heat conduction and by the Young-Laplace and Kelvin's equations at interfaces. At the upstream side of the membrane, the state is given by

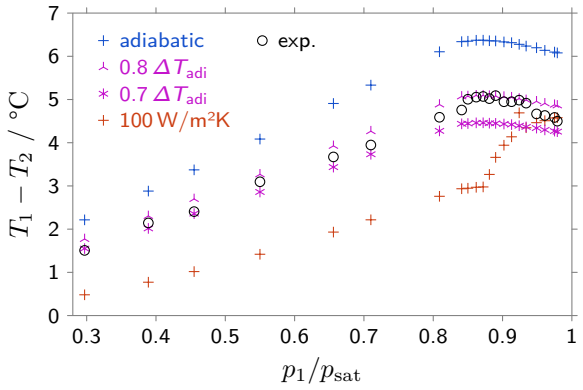

Figure 1: Measured and computed temperature differences for different downstream boundary conditions, pore size 40 nm.

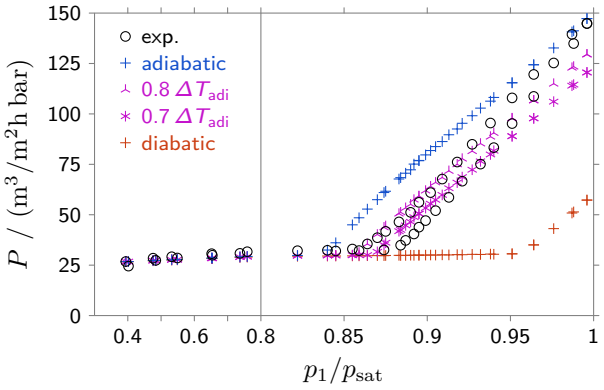

Figure 2: Mass flow data of isobutane through a membrane with pore size 40 nm.

T_1 and p_1 and there is no heat flux towards the membrane. At the downstream front the pressure is given to be equal to p_2. At the downstream front different boundary conditions were applied to the temperature or heat flux: adiabatic, diabatic, a heat transfer coefficient or a peculiar partially adiabatic condition with a factor ϕ that gave best agreement with data,

$$\begin{aligned} &\text{adiabatic:} && \dot{q}_2 = 0, \\ &\text{diabatic:} && T_2 = T_1, \\ &\text{heat transfer coeff.:} && \dot{q}_2 = -h_T(T_1 - T_2), \\ &\text{partially adi.:} && T_1 - T_2 = \phi(T_1 - T_{2,\text{adiabatic}}). \end{aligned} \quad (1)$$

3 Experimental

Porous anodic alumina membranes with an average pore diameter from 18 nm to 60 nm were obtained by anodization of electropolished aluminum. After anodization, the remaining aluminum was selectively dissolved, followed by removing the barrier layer and electrochemical detection of the opening of the pores. A thickness of 0.1 mm was obtained. The average pore diameter and porosity was characterized using scanning electron microscopy. The mass fluxes were determined with mass flow controllers while measuring the pressures at the feed and the permeate side of the membrane and also the saturation pressure on the feed gas vessel. An experiment was typically started with 1 bar at the feed and the permeate side of the membrane and stepwise increasing the feed side pressure until the saturation pressure was reached. A duration of up to 60 min was allowed after changes to reach steady state. The experimental cell was placed into a thermostat. For one experimental run, the temperature of the permeate side of the membrane was monitored with an infrared sensor.

4 Results and Conclusions

Figure 1 shows the downstream temperature of a membrane, and a comparison with computed results. For diabatic downstream boundary condition, the temperature difference is zero. The measured temperature differences probably do not follow any heat flux or heat transfer boundary condition, but are best described by a fraction of the adiabatic temperature difference, eq. (1). The mass flow data presented in Fig. 2 also seems to confirm the use of eq. (1) as boundary condition. Moreover, Fig. 2 shows that the choice of the downstream boundary condition has a significant influence on the mass flow rate under conditions where condensation occurs.

References

Schneider W (1983). "Vapor flow through a porous membrane — a throttling process with condensation and evaporation." *Acta Mech.*, **47**(1):15–25.

Lee K-H & Hwang S-T (1986). "The transport of condensible vapors through a microporous Vycor glass membrane." *J. Colloid Interf. Sci.*, **110**(2): 544–555.

Loimer T, Podgolin S K, Sodagar-Abardeh J, Petukhov D, Eliseev A A (2023). "Influence of heat transfer and wetting angle on condensable fluid flow through nanoporous anodic alumina membranes." *Phys. Chem. Chem. Phys.*, **25**:3240–3250.

2nd Spanish Fluid Mechanics Conference
Barcelona (2 - 5 July 2023)

Design and experimentation of a hydrokinetic turbine for electricity generation in closed pipes

Javier Armañanzas[1], Marina Alcalá[1], Juan Pablo Fuertes[1], Javier León[1] and Alexia Torres[1]

[1]Department of Engineering, Public University of Navarre, SPAIN

javier.armananzas@unavarra.es

In the present research work, a device for electrical energy generation from water pipeline has been designed, simulated and tested. To achieve this, a study of the most influential parameters involved in the experiment has been carried out and both, the turbine model and the geometry of the experimental test pipe, have been selected through CFD simulations. Next, Design Of Experiments (DOE) has been used in order to obtain the configuration with a higher energy extraction to running water. Finally, the turbine and the test pipe section have been manufactured by 3D printing and the experimental tests have been carried out with the optimal configuration so as to validate the results obtained in the CFD simulations. To simulate the exchange of energy between the water and the turbine, the CFD XFlow software has been used.

1 Introduction

Generating electricity and conserving water have become an increasingly important topic of research and a major concern for humanity over the years. As a result, global investment in micro-pico-electric generation has increased due to the availability of zero-emission, sustainable, and eco-friendly hydro energy sources [1]. From this premise, in this work, the capacity to generate electrical energy of an in-pipe hydrokinetic turbine has been studied. For this, CFD simulations have been carried out and complemented with experimental tests to validate them. It should be noted that research to obtain electrical energy using in-pipe hydrokinetic turbines is quite recent and more and more articles are being published demonstrating the feasibility and sustainability of this device for power generation [2].

Some examples of the application of this technology where CFD simulations are implemented are shown in [3, 4]. On the one hand, in [3] a 76 mm diameter propeller-type turbine is numerically investigated using a parametric study and computational fluid dynamics, while in [4], an in-pipe cross-flow turbine is modelled.

2 CAD process

To carry out the present study, different system configurations were designed and the one shown in FIG 1 was selected, since it proved to be the most efficient in preliminary simulations. This configuration took advantage of the Venturi effect, that allowed for an acceleration of the turbine. It was designed as a 3-piece assembly that allowed the use of only one pipe with interchangeable pieces. The system was also designed so it could be manufactured and coupled into a sensorized test rig.

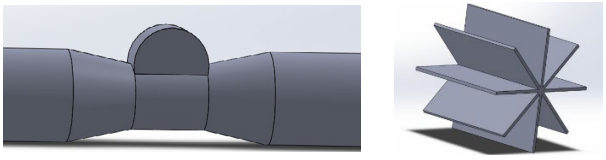

FIG 1. Pipe and hydrokinetic turbine CAD design.

In order to avoid calculation errors due to high pressures in small cavities resulting from CAD assembly, all gaps were eliminated in the final assembly. Moreover, friction between parts was not considered.

3 Simulation setup

CFD study was carried out by using the XFlow software, which uses the Lattice-Boltzmann methodology. The simulations were designed in 3D, with a single fluid that was water.

The selected boundary conditions were the following: a constant rotational speed of 1500 rpm, a flow rate of 28.83 m^3/h and a convective outlet. The size of the lattice was 0.5 mm and no remesh was used. FIG 2 shows the velocity distribution and the vorticity generated as it passes through the device, respectively.

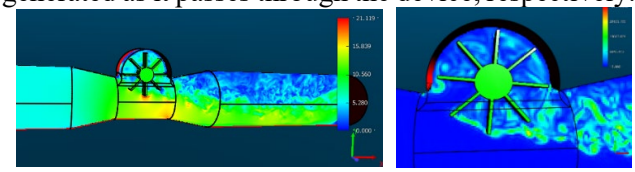

FIG 2. Velocity distribution and vorticity generated.

4 Experimental study

This device consists of two differentiated parts: a coupling with a geometry that tries to take advantage of the Venturi effect to accelerate the water in the place of contact with the turbine and a turbine-generator set.

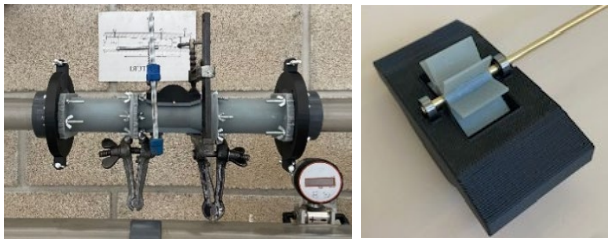

FIG 3. Installation configuration.

Due to the physical limitation of the test panel, the experiments were conducted varying the flow rate and without brake torque to avoid breakage of the turbine prototype. Thus, a turbine model of 10, 8 and 6 blades was used.

5 Results

First of all, a validation process was developed, in which the turbine was simulated and experimented achieving its runaway its speed in different cases. Validation for the 8-blade and 10-blade turbine is shown in FIG 4.

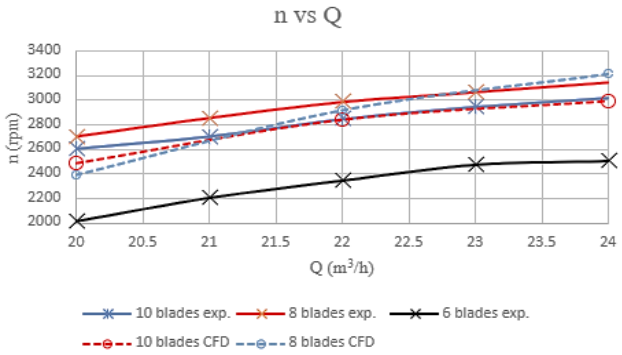

FIG 4. RPM vs. Flow rate in experimentation and CFD

It can be observed that the error between the experimental data and CFD is less than 10% at higher flow rates.

Once the CFD models were validated, a study to observe their behaviour under different braking moments was developed. For that, the defining parameters obtained in the validation process were kept the same, so the models were still valid.

For the CFD simulations design, statistical techniques based on the Design Of Experiments (DOE) were employed. The selected design was a 2^2 second-order model with one central point and four additional star points. Moreover, the design factors were the number of blades and the braking torque, while the two response variables were the angular velocity and the power. TABLE 1 and FIG 5. show the results obtained.

Nº blades	Torque (Nm)	Ang. velocity (rad/s)	Power (W)
10	0.027	244.42	6.60
10	0.0185	265.46	4.91
10	0.01	342.76	3.43
8	0.027	228.10	6.16
8	0.0185	249.69	4.62
8	0.01	317.42	3.17
6	0.027	218.91	5.91
6	0.0185	231.10	4.28
6	0.01	336.68	3.37

TABLE I. DOE results

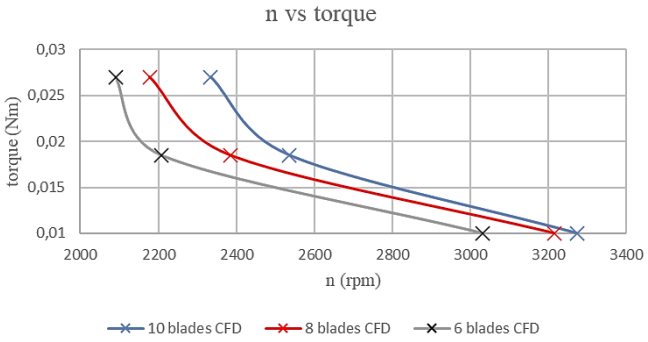

FIG 5. RPM vs. torque in CFD

6 Conclusions

In the present study, different CAD designs of the device and CFD simulations with XFlow software have been carried out. With that base, a geometry with a narrowing in the central area was chosen to take advantage of the Venturi effect and generate electrical energy. Likewise, various turbine models were generated in order to get the maximum efficiency and finally a straight 8-bladed geometry was chosen.

With the objective of finding the optimal configuration that allows for a greater generation of electricity, a design of experiments with CFD simulations was carried out under certain conditions of torque and number of blades. After testing a prototype made of carbon fibre, it was decided to discard it due to the excessive porosity of the material and all the components were manufactured by 3D printing. Although the same experiments could not be replicated in the simulations, it was possible to verify that the prototype generates energy.

References

[1] Paish, O. (2002) "Small hydro power: technology and current status", *Renewable and Sustainable Energy Reviews*, 6, 537 - 556.

[2] Hasanzadeh N., Payambarpour S.A., Najafi A.F., Magagnato F. (2021) "Investigation of in-pipe drag-based turbine for distributed hydropower harvesting: Modeling and optimization", *Journal of Cleaner Production*, 298.

[3] Monsalve O.D., Graciano J., Zuluaga D.A.H. (2021) "Numerical Simulation of a Propeller-Type Turbine for In-Pipe Installation", *Journal of Advanced Research in Fluid Mechanics and Thermal Sciences,* 83 (1), 1 – 16.

[4] Muratoglu, A., Demir, M.S. (2022) "Modeling spherical turbines for in-pipe energy conversion", *Ocean Engineering*, 246, 110497.

Design and optimization of an InFlow Radial (IFR) turbine for Oscillating Water Column (OWC) devices

Aitor Vega-Valladares[1] and Bruno Pereiras[1]

[1]*Department of Energy, University of Oviedo, SPAIN*

Oscillating Water Column (OWC) devices are one of the most studied among the different technologies which allow us to harness the large amount of wave energy available in our coasts. The Double Decker Turbine (DDT) concept has been recently introduced in order to overcome the drawbacks of the most commonly adopted solutions in these devices. In this work, a CFD analysis and performance optimization in Direct Mode (DM) of an InFlow Radial (IFR) turbine are presented for its later application in the radial version of a DDT.

INTRODUCTION

Oscillating Water Column (OWC) devices are composed of three parts: the chamber, the Power Take Off (PTO) and a generator.

The most convenient topology of the PTO has been discussed over the years, self-rectifying air turbines being adopted as the most common solution. However, these bidirectional turbines usually reach lower efficiencies than the unidirectional ones, hence the Twin Turbine Configuration (TTC), based on the use of two unidirectional turbines, each one exploiting one of the flow directions, was introduced some years ago. Obviously, the main drawback of the TTC is the duplicity of equipment.

To overcome these problems, the Double Decker Turbine (DDT) concept has been recently introduced [1]. Figure 1 shows a scheme of this concept, which consists of a single turbomachine composed of two unidirectional turbines working in parallel, the External Turbine (ExT) and the Internal Turbine (InT).

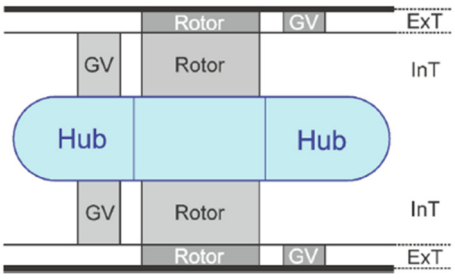

FIG 1. DDT longitudinal scheme [1].

Figure 1 shows the scheme of the DDT concept in its axial version. While one of the turbines is working in Direct Mode (DM), extracting energy, the other one is working in Reverse Mode (RM), acting as a backflow preventer.

In the DDT concept, as it happens with the TTC, part of the flow passes through the turbine that is not really exploiting the flow. More promising results have been already obtained working with TTCs which incorporate OutFlow Radial (OFR) turbines instead of axial ones [2].

In this work, a CFD analysis of a preliminary geometry and an optimized one of an InFlow Radial (IFR) turbine working in DM is presented as a first step for the development of the radial version of the DDT concept.

DATA POSTPROCESSING

The analysis of the steady results is made in terms of the classical coefficients for OWCs: flow coefficient (ϕ) and total-to-static efficiency (η).

$$\phi = \frac{v_R}{u_R}, \quad (1) \qquad \eta = \frac{T_0\,\omega}{\Delta P\,Q}, \quad (2)$$

Being the v_R the mean radial velocity at the mean radius (r_R), u_R the circumferential velocity at r_R, T_0 the torque, ω the rotation speed, ΔP the total-to-static pressure drop and Q the flow rate.

GEOMETRY

The IFR turbine presented in this work is composed of 48 rotor blades and 72 upstream Inlet Guide Vanes (IGV). Figure 2 shows the main view and geometric parameters of the rotor blades.

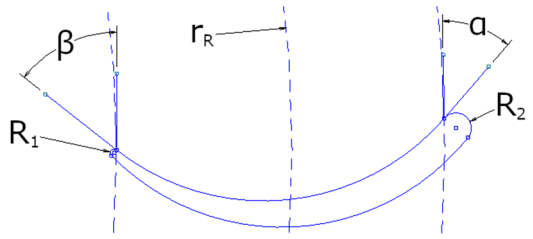

FIG 2. Main view and geometric parameters for the rotor blades of the preliminary geometry.

Having the same number of blades and vanes and the same size, the unique difference between the preliminary geometry and the optimized one is the value of the beta angle (β). This and other geometric data can be seen in table 1.

IFR Geometry	r_R [mm]	β/α [°]	R_1/R_2 [mm]
Preliminary	87.5	51.9/42.1	0.25/1
Optimized	87.5	40/42.1	0.25/1

TABLE I. Geometric data.

NUMERICAL MODEL

The boundary conditions of the model can be found in figure 3. Using periodic surfaces, the model has been built over an angular sector comprising 1/24 of the full annulus.

Two set of interfaces have been introduced in the computational domain. These interfaces separate the whole domain in three parts: diffuser+IGV, rotor and elbow. Sliding mesh technique was used to simulate the rotor movement, set to 500 rpm.

The simulations were carried out in steady flow rate, setting the velocity inlet within the range of [0.6, 7.4] m/s depending on the flow coefficient, whereas the pressure outlet was set as atmospheric. The rest of the surfaces of the model were set as non-slip walls.

The simulations were made using ANSYS Fluent v16.2. Two-equation k-ε Realizable model was selected for the simulations, using the enhanced wall treatment function. SIMPLE scheme was used for the pressure-velocity coupling, a second order discretization for pressure and third order for momentum and the transient formulation, turbulent kinetic energy and turbulent dissipation rate. Residuals were set to 10^{-5} and the time step size was fixed to $5{\cdot}10^{-5}$ s.

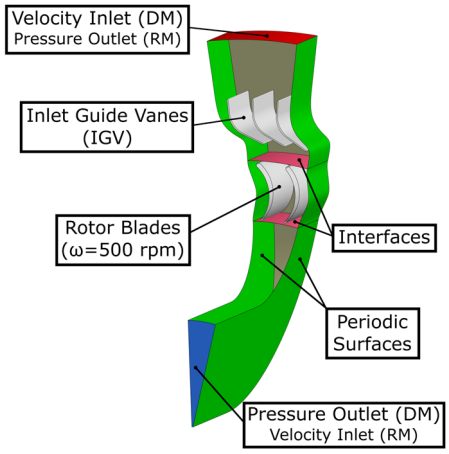

FIG 3. Periodic domain and boundary conditions.

RESULTS

A performance comparison between both proposed geometries for the IFR turbine is shown in figure 4 in terms of total-to-static efficiency. Results are also compared with those previously obtained for an OFR turbine [2], all of them being numerical results.

Both preliminary geometries reach a similar peak efficiency of around 40%. Nevertheless, the one that corresponds to the OFR turbine reaches this efficiency at a lower flow coefficient ($\phi = 0.75$), as well as the optimized geometry of that same turbine.

The peak efficiency of the IFR has been improved by around 9 %. Note that, this peak has also shifted towards lower flow coefficients similar to those of the OFR turbines, which is more interesting since these are the most frequent under real operating conditions.

However, although its peak efficiency has clearly improved, the efficiency reached by the optimized IFR turbine at high flow coefficients is penalized and takes lower values than in the case of the OFR turbine.

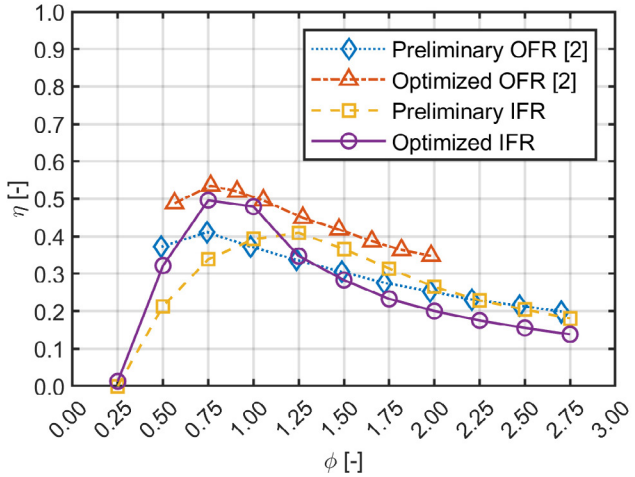

FIG 4. Total-to-static efficiency of the analyzed IFR turbines geometries vs OFR turbines geometries [2].

CONCLUSIONS

A preliminary geometry for an IFR turbine has been analyzed and optimized using CFD techniques.

Promising results have been obtained in terms of peak efficiency when the turbine is working in DM in comparison with the results obtained in previous studies for an OFR turbine.

The behavior of the IFR turbine must be analyzed when it is working in RM to prove its capacity for acting as a backflow preventer and then assess the possibility of integrating it in the radial version of the DDT.

ACKNOWLEDGEMENTS

Aitor Vega Valladares is supported by the “Administración del Principado de Asturias” within the “Severo Ochoa” Program (grant number PA-22-BP21-160).

—

* vegaaitor@uniovi.es

[1] M. García-Díaz, B. Pereiras, C. Miguel-González, L. Rodríguez, and J. Fernández-Oro, “Design of a new turbine for OWC wave energy converters: The DDT concept,” *Renew. Energy*, vol. 169, pp. 404–413, May 2021, doi: 10.1016/j.renene.2020.12.125.

[2] L. Rodríguez, B. Pereiras, M. García-Diaz, J. Fernández-Oro, and F. Castro, “Flow pattern analysis of an outflow radial turbine for twin-turbines-OWC wave energy converters,” *Energy*, vol. 211, Nov. 2020, doi: 10.1016/j.energy.2020.118584.

Design of a Non-invasive Cardiovascular Assist Device based on Asymmetric Valveless Pump Technology

J. Anatol, M. García-Díaz, C. Barrios-Collado, J. A. Moneo-Fernández, F. Castro-Ruiz, J. Sierra-Pallares

Departamento de Ingeniería Energética y Fluidomecánica & ITAP
Universidad de Valladolid, Paseo del Cauce 59, 47011 Valladolid, SPAIN.

The aim of this study is to design an asymmetrical valveless pump based on soft robotics technology. Asymmetric pumping is achieved by periodically compressing a flexible tube in its plane of symmetry by means of an actuator, as long as the rigid pipes connected at its ends are hydraulic asymmetrical. One of the most interesting applications is the use of valveless pumping to improve blood circulation in patients with hypoplastic left heart syndrome who have undergone the Fontan surgery.

INTRODUCTION

In many applications in biomedical engineering, it is necessary to pump fluids without coming into contact with them. One option is to use the so-called valveless pumping, the most well-known types of which are peristalsis and the Liebau phenomenon [1].

Valveless pumping based on the Liebau effect [2] works by the periodic pinching of a flexible element (a compliant tube) asymmetrically in terms of either the pincher position, or the circuit, or a combination of both [3].

This simple pumping mechanism allows, for example, blood circulation in the embryonic phase due to the absence of valves in the heart [4] .It has also been studied in other physiological fields as a pumping system in the human aorta [5].

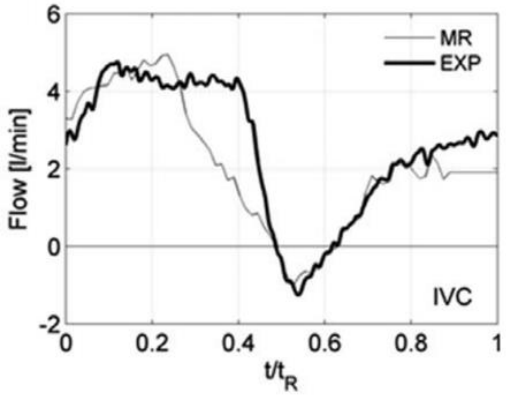

FIG 1. Temporal evolution of the flow in the inferior vena cava (IVC). t_R: respiratory cycle period [6].

Establishment of the so-called Fontan circulation is a palliative surgical treatment for patients with an univentricular heart condition. These patients undergo a series of surgical procedures in which the left ventricle is reconstructed from the right ventricle and a graft is placed connecting the inferior and superior venae cavae to the pulmonary arteries. Blood flow through the inferior vena cava (IVC) is intimately related to the respiratory cycle because of the proximity of the blood vessel to the lungs., the variation in lung volume modifies the IVC environment and thus the flow rate. On the other hand, diaphragm movement also influences IVC flow during the respiratory cycle as the shape of the mediastinum varies, where the IVC is located. Blood flow through the IVC increases during inspiration and decreases during expiration [6], figure 1. The objective of this work is to increase this flow and minimize the reverse flow phase. To this end, it is proposed to include a graft assist device based on asymmetric valveless pump technology.

DESIGN

The core of a Liebau pump is a flexible compliant tube and the pinching mechanism. The pinching mechanism consists of an actuator, based on soft robotics technology, that compresses the compliant tube, referred to as the pincher. The performance of this type of pump has been described in depth in [3]. Figure 2 shows the evolution of the instantaneous flow

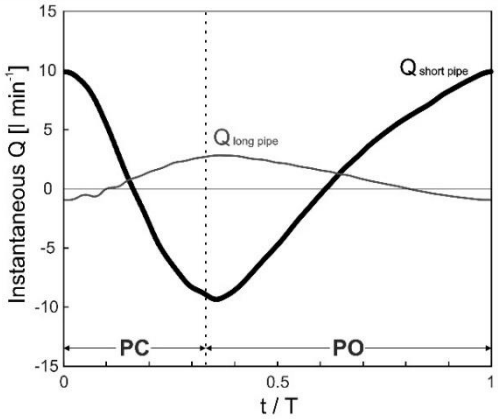

FIG 2. Temporal evolution of instantaneous flows in the rigid pipes. PC: Pincher closed (33% of T), PO (Pincher open). T: compression cycle period.

rate in the pipes connected to the compliant tube where one of them was several times longer than the other. This asymmetry results in the appearance of a net flow towards the longer side. Figure 3 shows the flowrate-head curve provided by the pump in stationary tests.

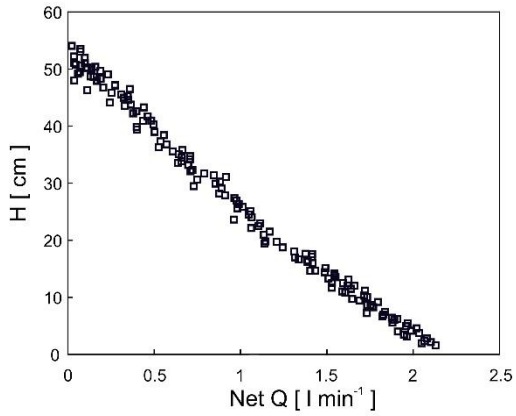

FIG 3. Flowrate-head curve provided by the pump in stationary tests.

A mock circulation loop, figure 4 was used to mimic a Fontan circulation and to study the performances of our pump under physiological-like conditions. This installation consists of two constant level reservoirs, silicone pipes and a transparent Fontan graft model. The reservoirs can vary their vertical position by means of two displacers. The fluid flows from the N reservoir to the grafting model and from there to the S reservoir and from there to the discharge reservoir. The working fluid has been a mixture of water and glycerin with blood-like properties.

To achieve a flow rate evolution similar to that shown in figure 1, two servomotors have been used as valves. These modify the head loss in the model's inlet piping. This system allows to achieve a negative flow for short periods of time, simulating reverse flow.

The instrumentation consists of four pressure sensors and two unidirectional ultrasonic flowmeters. The pressure sensors were located at each of the inlets and outlets of the model. The uncertainties in the pressure sensors and flow meters were 4% and 2%, respectively.

The prototype assist device consists of a compliant tube with a pneumatic pincher and two compliant chambers, to dampen flow peaks, figure 2. The prototype is mounted at the entrance of the model corresponding to the inferior vena cava.

CONCLUSIONS

The use of valveless pumping could be a good option to improve blood circulation in patients with Fontan surgery. Nevertheless, the pump design achieved would have to be transformed into a biologically compatible design. Finally, this design would be necessary to tested in vitro before its possible implantation in patients.

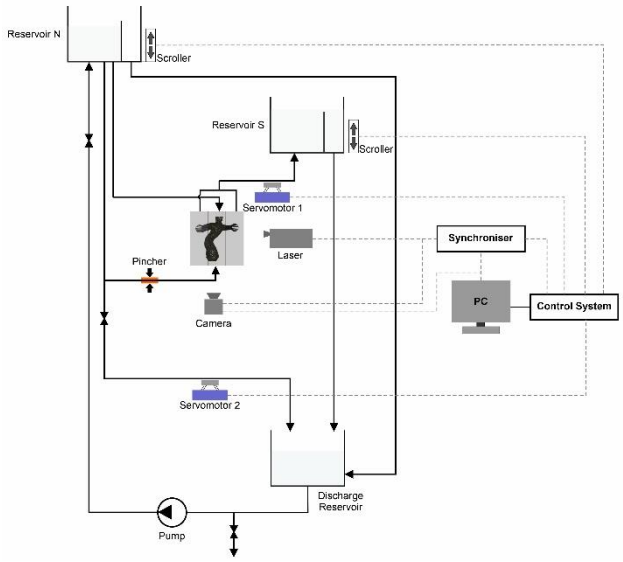

FIG 4. A mock of a Fontan circulation loop.

ACKNOWLEDGEMENTS

The authors would like to thank the Junta de Castilla y León for funding this work as part of the program “Subvenciones del programa de apoyo a proyectos de investigación financiados por fondos FEDER”, project number VA182P20.

REFERENCES

[1] T. Kenner, M. Moser, I. Tanev y K. Ono, «The Liebau-effect or on the optimal use of energy for the circulation of blood,» *Scripta Medica Facultatis Medicae Universitatis Brunensis Masarykianae,* vol. 73, nº 1, p. 9–14, 2000.

[2] G. Liebau, «On a valveless pump principle (Ger),» *Naturwissenschaften,* vol. 327, p. 1, 1954.

[3] J. Anatol, M. García-Díaz, C. Barrios-Collado, J. A. Moneo-Fernández, M. Horvath, T. Parra, F. Castro-Ruiz, E. T. Roche y J. Sierra-Pallares, «Experimental study of an asymmetric valveless pump to elucidate insights into strategies for pediatric extravascular flow augmentation,» *Scientific Reports,* vol. 12, nº 1, p. 22165, 2022.

[4] F. Hiermeier y J. Männer, «Kinking and Torsion Can Significantly Improve the Efficiency of Valveless Pumping in Periodically Compressed Tubular Conduits. Implications for Understanding of the Form-Function Relationship of Embryonic Heart Tubes,» *Journal of Cardiovascular Development and Disease,* vol. 4, nº 4, 2017.

[5] N. M. Pahlevan y M. Gharib, «In-vitro investigation of a potential wave pumping effect in human aorta,» *Journal of Biomechanics,* vol. 46, nº 13, p. 2122–2129, 2013.

[6] M. Vukicevic, T. Conover, M. Jaeggli, J. Zhou, G. Pennati, T.-Y. Hsia y R. S. Figliola, «Control of respiration-driven retrograde flow in the subdiaphragmatic venous return of the Fontan circulation,» *ASAIO Journal,* vol. 60, nº 4, p. 391–399, 2014.

2nd Spanish Fluid Mechanics Conference
Barcelona (2 - 5 July 2023)

Development of local capacitance sensor for two-phase measurements

Óscar Prades-Mateu[1], Guillem Monrós-Andreu[1], Raúl Martínez-Cuenca[1], Salvador Torró[1], and Sergio Chiva[1]

oprades@uji.es

[1]Departamento de Ingeniería Mecánica, Universitat Jaume I, Spain

The objective of the present study is to develop a miniaturized impedance sensor probe, applicable to a wide range of two-phase flows, to obtain the time-averaged local two-phase flow parameters. This work describes a novel needle probe measuring system based on impedance measurements for two-phase flows composed by one sensing needle. This miniaturized needle probe can be employed for the investigation of dynamic processes in two-phase flow mixtures, virtually providing the most important time-averaged local parameters. Benchmark experiments employing the high speed image analysis method have been performed. The results from the benchmark experiment assess both the measurement principle and signal processing scheme of the newly developed probe method.

1 Introduction

For two-phase flow systems assessments is necessary to accurately recover the most relevant local-flow parameters, such as, void fraction, interfacial velocity and interfacial area concentration which are the key geometric parameters in view of mass and heat transfer phenomena.

The conductivity and optical probes have been the most widely used intrusive measurement technique in obtaining local two-phase flow parameters (Kim (2000); Cartellier (2001)). Accounting for the fundamental media differences (conductivity or refractive index), these probes can provide the local-flow parameters throughout the characteristic rise/fall of measured signals as bubbles pass through the sensor(s), i.e. acting as a local phase identifier. With the acquired signals from the sensor, the local time-averaged void fraction can be easily obtained from the raw signals. Furthermore, its capability of measuring the local interfacial velocity of bubbles with multiple sensors, based on the different time delays between probes, makes the conductivity/optical probes the most popular measurement technique in recent experimental studies. However, one of its major drawbacks is that these parameters are strongly related to local interface detection, thus, highly influenced by bubble local deformation and curvature among others.

Sensor and methodology presented in this work attempts to overcome this cited limitations by measuring in a small area (volume) continuous bubble information during the whole bubble passing time along the sensor. Benchmark experiments in bubbly regime have been performed, where the processed output sensor signals have been compared to image processed data from high-speed camera.

2 Methodology and experimental setup

As shown in figure 1-A, the sensor consists of two electrodes (0.2 mm diameter stainless steel needles), emitter (E) and receptor (R) placed in a double coaxial geometry. Electrodes are isolated from the sensor body ground (GND) using 0.1 mm thick PTFE as insulating layer.

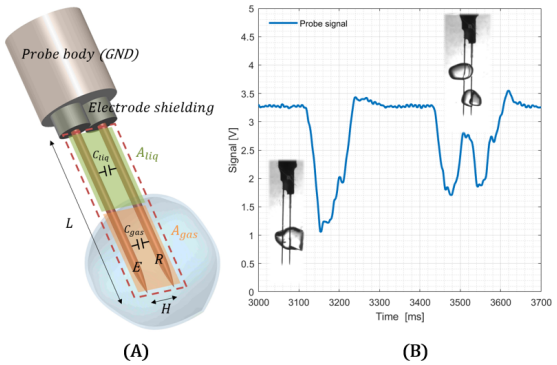

Figure 1: Sensor probe schematic (A) and probe signal voltage output: example of single and multiple bubble detection (B).

The measurement principle is as follows: a sinusoidal voltage is injected by means of a signal generator through the excitation electrode (E), controlling its frequency and amplitude. The measured signal

at receiving electrode (R) is DC converted through a trans-impedance amplifier (TIA) and a rectifier. The output voltage is proportional to the inter-electrode capacitance (C_{liq} and C_{gas}), and it provides direct information of time-evolution of the gas phase (figure 1-B): output voltage is proportional to inter-electrode area void fraction, bubble size is directly related to local signal peaks and bubble velocity proportional voltage change rate.

Experiments have been conducted in a narrow channel (300 × 150 × 15 mm) filled with water. The excitation signal frequency has been set to 1MHz in order to work in the capacitance dominant region (Silva (2007)). The channel has an air injector (capillary tube) located at the bottom to generate controlled size bubbles using a pulse-controlled opening air micro-valve.

Acquired images (figure 2-A) have been processed to obtain representative data. Firstly, binary signals from three sample control points to evaluate the interface velocity (point to point delays) and bubble size (binary signal pulse duration). Secondly, bubble mask points are spatially averaged along the sensor length line to obtain the void fraction measured to the inter-electrode sensing area.

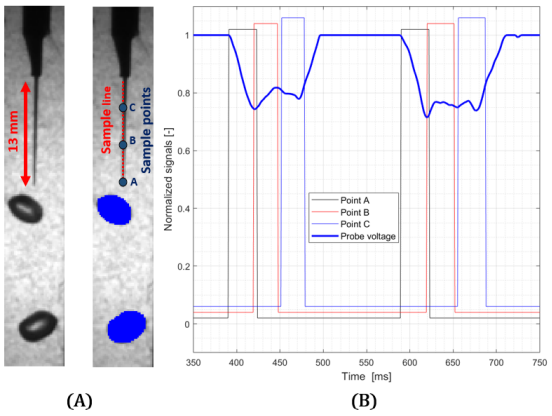

Figure 2: Image binarization and sample regions of interest, line and control points (A). Sensor output signal and corresponding image binary signals at control sampling points A, B and C.

According to the sample measurement example depicted in figure 2-B, a good agreement has been found between the processed image data and the sensor output. It shows a consistent bubble size determination from both methods, as the voltage signal falling time matches to the binary signal at the bottom control point (equal interface detection time and maximum size located at voltage signal peak). Also, good agreement has been found in the instantaneous void fraction, as depicted in figure 3, where sensor signal output has been normalized attending to the limit measurement conditions, i.e., inter-electrodes filled with water or air.

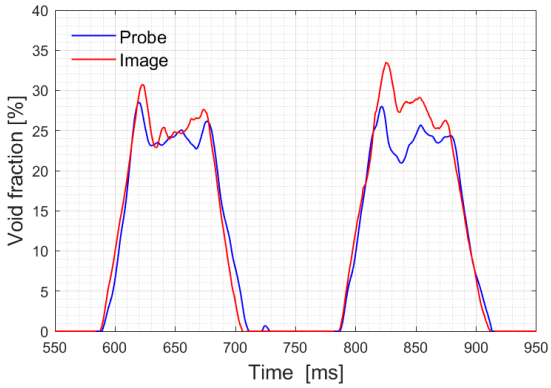

Figure 3: Comparison between measured void fraction from probes (normalizaed output) and images.

3 Conclusions

New probe sensor design and methodology has been presented. Preliminary results show good agreement between obtained sensor and processed image data. This sensor can provide continuous measurement of local-flow parameters during the bubble transit time along the sensor, not only reliant on the interface detection. Thus, it can be used to complement or extend the application of existing intrusive sensors. Moreover, due its principle of measurement, it can be adapted for measuring in conductive or non-conductive two-phase flow mixtures by means of the excitation signal frequency.

References

Silva, M. J., Schleicher, E. & Hampel, U. (2007). "A Novel Needle Probe Based on High-Speed Complex Permittivity Measurements for Investigation of Dynamic Fluid Flows". *IEEE Transactions on Instrumentation and Measurement*, 56(4), 1249–1256.

Kim, S., Fu, X.Y., Wang, X. & Ishii, M (2000). "Development of the miniaturized four-sensor conductivity probe and the signal processing scheme". *International Journal of Heat and Mass Transfer*, 43(22), 4101–4118.

Cartellier, A. (2001). "Optical Probes for Multiphase Flow Characterization: Some Recent Improvements". *Chemical Engineering and Technology*, 24(5), 09307516.

2nd Spanish Fluid Mechanics Conference
Barcelona (2 - 5 July 2023)

Experimental investigation of turbulent swirling jets

Antonio Cuéllar Martín[1], Luca Franceschelli[1], Carmen Márquez García[1], Stefano Discetti[1], and Andrea Ianiro[1]

acuellar@ing.uc3m.es

[1]Department of Aerospace Engineering, Universidad Carlos III de Madrid, Spain

The objective of this work is to reconstruct the flow field of swirling jets using pointwise probes. For the training, a dataset of synchronized flow field measurements with Tomographic Particle Image Velocimetry and measurements with microphones is acquired. We investigate potential and limitations of the reconstruction process, assessing the results for different swirl numbers and probe configurations.

Swirling jets are of special interest for different applications in the aerospace industry, especially when dealing with combustion to both enhance mixing and improve flame stabilization. The flow produced by swirling jets is characterized by unsteady dynamics, mostly related to the phenomena of vortex shedding, vortex breakdown, and the presence of the precessing vortex core Liang H. & Maxworthy T. (2005). Thus practical applications require to have a description of the characteristics of the instantaneous flow field.

For the present study, we design a swirling jet facility consisting of a swirling nozzle connected with a pressurized air supply. The nozzle contains an internal insert with blades to provide a tangential velocity component to the flow. We defined several swirling devices, with different blade arrangements as shown in figure 1, to provide a flow with a different swirl number (S), defined as the ratio of azimuthal momentum flux to axial momentum flux times the radius:

$$S = \frac{2\int_0^\infty \bar{u}\bar{u}_\theta r^2 dr}{D\int_0^\infty \left(\bar{u}^2 - \frac{\bar{u}_\theta^2}{2}\right) r dr} \,. \qquad (1)$$

where D is the nozzle diameter, $\bar{u}$ and $\bar{u}_\theta$ are respectively the mean streamwise and azimuthal velocity, and r is the radial coordinate. The swirlers are attached to a piece with a conical shape at the centre of the nozzle, ensuring that the cross-section of the flow decreases and making sure that separation is avoided. Different values of S are expected to trigger different flow phenomena as discussed by Liang H. & Maxworthy T. (2005). Oberleithner K. H. *et al.* (2011) investigated the phenomenon of vortex breakdown and instabilities are controlled with a set of actuators. The breakdown and precession of vortices is a strongly periodic phenomenon and the authors employed a set of loudspeakers to produce a periodic forcing able to trigger and synchronize the precessing motion of the vortex core. This control was instrumental to reconstruct the three-dimensional flow organization with a phase-averaging process.

Figure 1: Components inserted within the nozzle to provide tangential velocity to the flow with different swirl number S.

In the present work, we plan to study the vortical motions within swirling jets without forcing. Nevertheless, we plan to exploit the strong coherence of the unsteady jet features to reconstruct the instantaneous flow organization with a limited set of sensors, i.e. we assume that most of the flow information resides on a low-dimensional space.

The flow at the exhaust of the nozzle is measured with Tomographic Particle Image Velocimetry (Tomo-PIV). A 6mm thick laser sheet illuminates the exhaust (Figure2). The flow is seeded with $1\mu m$ DEHS droplets acting as seeding particles.

Moreover, the region of the jet is surrounded by a

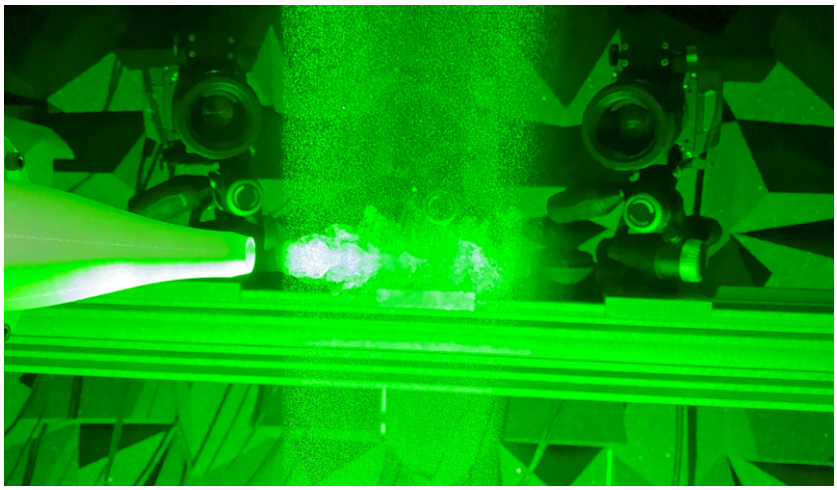

Figure 2: Setup of the experiment, showing the cameras for the Tomo-PIV acquisition, focusing at the illuminated region at the exit of the nozzle, with the jet ejecting PIV particles.

set of microphones. Tomo-PIV and data from microphones are captured simultaneously. The final goal of this implementation would be to establish a correlation between the flow characterization from PIV and the microphone sensing, allowing to reconstruct the flow field from sensor data. This is potentially convenient for control applications, where the microphones can be *trained* to identify flow field features that can be targeted to enhance mixing, with lower latency time than if using Tomo-PIV on the fly. In order to establish the mapping from sensors to flow field information, a dimensionality-reduction based on modal analysis can be used, as reported by Zeng X. *et al.* (2023), where different data reduction methodologies based on proper orthogonal decomposition (POD) are employed to swirling jets. POD has also been used in different setups in the field of fluid dynamics, showing the utility of this technique to reduce information while most of the fluid can be accurately reconstructed, preserving the largest and most-energetic scales Güemes A. *et al.* (2019); Guastoni L. *et al.* (2021). Non-linear methods can also be explored to establish mapping from sensor to fields, owing to the nonlinear relation between pressure and velocity.

For the conference contribution, we expect to include results from the reconstruction of the swirling jet flow for the full range of swirl numbers and explore different methods to perform the task based on linear and nonlinear methods.

Acknowledgements

This contribution has received funding from the Spanish Ministry of Universities under the *Formación de Profesorado Universitario (FPU) 2020* programme, and from the European Research Council (ERC) under the European Union's Horizon 2020 research and innovation programme (grant agreement No 949085).

References

Guastoni L., Güemes A., Ianiro A., Discetti S., Schlatter P., Azizpour H. & Vinuesa R. (2021) "Convolutional-network models to predict wall-bounded turbulence from wall quantities". *J. Fluid Mech.* **928**, p.A27.

Güemes A., Discetti S. & Ianiro A. (2019) "Sensing the turbulent large-scale motions with their wall signature". *Phys. Fluids*, **31** (12), 125112.

Liang H. & Maxworthy T. (2005) "An experimental investigation of swirling jets". *J. Fluid Mech.*, **525**, pp.115-159.

Oberleithner K., Sieber M., Nayeri C. N., Paschereit C. O., Petz C., Hege H. C., Noack B. R. & Wygnanski I. (2011) "Three-dimensional coherent structures in a swirling jet undergoing vortex breakdown: stability analysis and empirical mode construction". *J. Fluid Mech.*, **679**, pp.383-414.

Zeng X. , Zhang Y., He C. & Liu Y. (2023) "Time- and frequency-domain spectral proper orthogonal decomposition of a swirling jet by tomographic particle image velocimetry". *Exp. Fluids (2023)*, **64(1)**, p.5.

Flow effects of the radial gap on a centrifugal pump using deterministic analysis and cavitation measurements

Jesús M. Fernández Oro[1], Mónica Galdo Vega[1], Raúl Barrio Perotti[1], Aitor Vega Valladares[1,*], Álvaro Pardo Vigil[1] and José González[1]

*UO258022@uniovi.es

[1]Fluid Mechanics Area, Department of Energy, University of Oviedo, C/Wifredo Ricart s/n, Gijon, Asturias, 33204, Spain

The results of a previously existing numerical model compared with experimental measurements are shown regarding the volute tongue radial gap variation effect on the main flow behaviors in a centrifugal pump. Relevant experiments on the cavitation effects are also shown in the present article.

1 Introduction

The study of the flow in turbomachines has become one of the most relevant industrial problems in the last decades and historically is one of the most important Fluid Mechanics applications. The geometry-flow interaction problem becomes of particular interest when dealing with a turbomachine. Particularly, when considering a centrifugal pump, the effects have been widely mentioned in the classic bibliography for steady state interactions [1]. In the last decades, the focus has been set on the dynamic kind of interaction and several approaches are also available [2].

2 Experimental data and validation

An experimental set-up is available at the Área de Mecánica de Fluidos (Universidad de Oviedo, Campus de Gijón) for the testing of water pumps. Figure 1 shows the correspond to a centrifugal pump with specific diameter, $D_s = 5.41$ and specific speed, $n_S = 0.52$, equipped with a set of pressure taps for unsteady measurements in the volute.

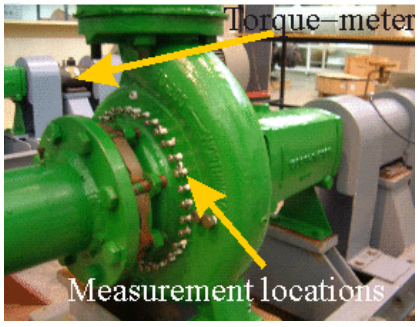

Figure 1: Centrifugal pump set-up.

On the other hand, the developed numerical model uses the commercial code ANSYS-Fluent ® with a 3D mesh of around 800 k cells. Special care was taken in the near-tongue region discretization. A sliding mesh method was introduced to account for the relative impeller motion. For such, a $t = 1.65 \cdot 10^{-4}$ s was chosen. The boundary conditions chosen were a total pressure equal to 0 at the inlet and a valve closure at the outlet, simulating the "as close to real" as possible conditions. The SIMPLEC algorithm was used for the pressure-velocity coupling, when solving the incompressible N-S Equations. As turbulence model, the Standard κ–ε was chosen.

Model validation has been widely performed along the last years and comparison with the existing experiments have shown the model strength to achieve the flow definition in the pump on a steady and unsteady basis, [3]. An example for the unsteady pressure fluctuation force (non-dimensional values) along the volute is shown in Figure 2 for off-design conditions.

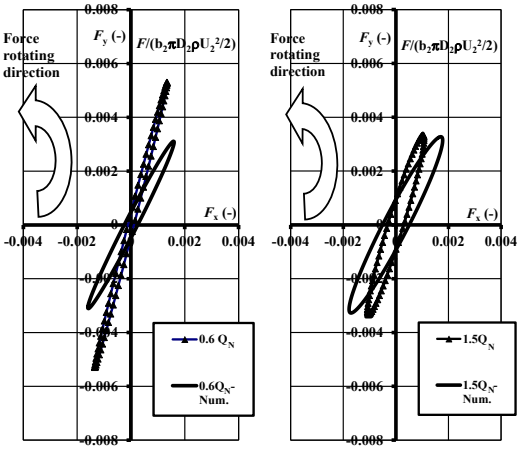

Figure 2: Pressure fluctuations force on the volute of a centrifugal pump, $Q = 0.6Q_N$ and $Q = 1.5Q_N$.

The deterministic analysis is then applied to the existing numerical results and for a set of radial gaps, as explained in [4] and, additionally, experimental cavitation measurements are performed.

3 Results on the radial gap

The influence of the radial gap on the flow discharge in the impeller is illustrated in Figure 3. The map shows the non-dimensional distribution of the radial velocity at the impeller exit. All the flow rates analyzed are represented for the case with the largest radial gap. For a better representation, the circumferential coordinate has been extended and drawn in the x-axis. Note that the position of the volute tongue has been identified with a red vertical line at 11.8 deg in all the maps. The white dashed lines indicate the impeller width. All the distributions correspond to one instantaneous capture of the 32 time-steps evolution for the blade passing period.

Several radial gaps were analyzed and results are available. Those results reveal how the flow discharge at the impeller is blocked at different flow rates when the radial gap to the volute tongue is significantly reduced. At lower flow rates, it is a common feature the existence of flow recirculation in the upper clearance of the impeller (close to the shroud). At 60% and especially at 20%, there are recirculation cells with small and even negative values of radial velocity in that zone, while in the inner part (close to the hub) positive values of velocity are observed, especially for positive angles where the volute is narrower. The distribution of radial velocity on the blade surfaces is not symmetrical but displaced downwards, towards the hub zone. This is especially evident in the central zone of the maps at 20% and 60% for the two gaps, where the tongue block becomes more significant.

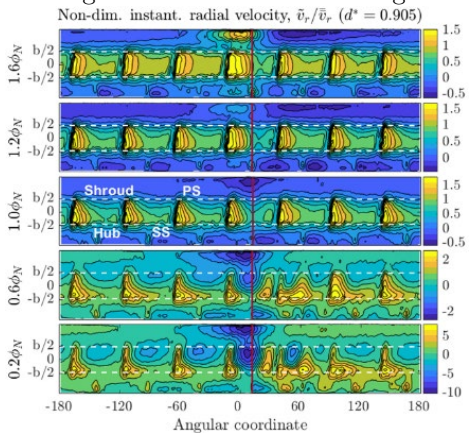

Figure 3: Unsteady radial velocity at the impeller exit, for different flow rates and one radial gap.

4 Cavitation measurements

Finally, some cavitation measurements have been carried out for the pump. The effects of cavitation, despite being a non-stationary phenomenon, are usually grouped into a design parameter that allows to be on the side of safety and thus to avoid the appearance of it. The so-called NPSH, or Net Positive Suction Head, is usually defined for pumps, that is, positive net height in the suction constitutes a measure of the energy (or height, because it is an incompressible flow) available at the suction of the pump above the energy (height) that would result in the appearance of cavitation. Cavitation number is preferred here and calculation shown in [5] is considered.

The obtained results, plotted in Figure 4, follow the trends expected found in classic references.

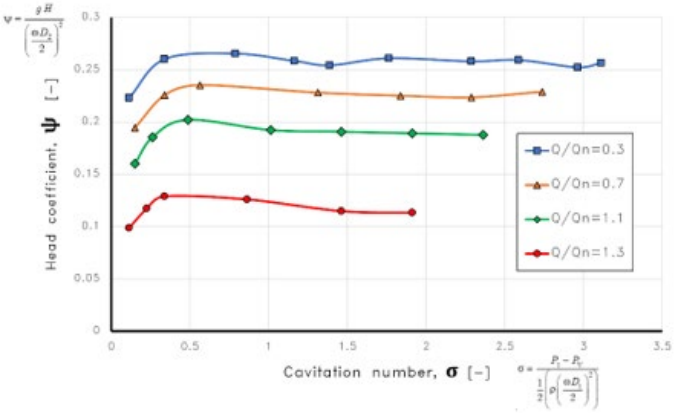

Figure 4: Cavitation breakdown curves for different flow rates at 1800 rpm.

5 Conclusions

An experimental and numerical study on the unsteady flow in a centrifugal pump is developed here.

Two specific issues have been shown and analyzed: the deterministic study of the radial gap effect on the flow unsteadiness and a first experimental campaign on the cavitation of the unit.

An extensive zone of negative radial velocity is produced by the blockage of the predominantly tangential flow recirculating from the diffuser area towards the tongue, promoting the outflow to concentrate in a narrow and downward outlet section.

[1] Neumann, B., "The interaction between geometry and performance of a centrifugal pump" MEP, London, 1991.
[2] Tsukamoto, H., Uno, M., Hamafuku, N., Okamura, T., "Pressure fluctuation downstream of a diffuser pump impeller", ASME FED, 216, pp.133-138, 1995.
[3] Fernández, J., González, J., Barrio, R., Galdo, M., "Numerical Analysis of the Deterministic Stresses associated to Impeller-Tongue Interactions in a Single Volute Centrifugal Pump". Trans. of the ASME J. of Fluids Eng. Vol. 141, article 091104, pp. 1-12, 2019.
[4] Fernández, J.M., Barrio, R., Galdo, M., Pereiras, B., Miguel, C., González, J., "Centrifugal pump design guidelines using deterministic flow analysis". 1st Spanish Fluid Mechanics Conference, Cádiz 19-22 June, Congress Proceedings, pp. 1-2, 2022.
[5] Brennen, C.E., "Cavitation and bubble dynamics", Oxford University Press, 1995.

2nd Spanish Fluid Mechanics Conference
Barcelona (2 - 5 July 2023)

Implementing Multi-Factor Design for Vacuum Ejector Improvement through Comprehensive Analysis of Construction Parameters

Llorenç Macià[1], Robert Castilla[1], Pedro Javier Gamez-Montero[1], and Gustavo Raush[1]

llorenc.macia@upc.edu

[1]Fluid Mechanics department, Universitat Politècnica de Catalunya, Spain

A vacuum supersonic ejector is characterized by its maximum entrained flowrate and its minimum secondary pressure. Numerical simulations were carried out by means of the CFD toolbox OpenFOAM. A single-factor analysis of the eight inner geometry parameters was performed and a total enhancement of 10% was found. A multi-factor analysis, based on a fractional factorial design, is carried out with the four relevant parameters. Results indicate that the multi-factor analysis enhances the performance of the ejector by 10.4%. The improved performance of this device leads to a reduction in operating time and, as a consequence, results in significant energy savings.

1 Introduction

A common approach for handling products in a production line is to use a vacuum ejector with suction cups, as explained in L Macia et al (2019). Vacuum ejectors use compressed air and rely on the Venturi effect to operate.

The efficiency of a vacuum ejector depends on its maximum entrained flowrate and maximum vacuum (minimum secondary pressure). Higher values for these characteristics (lower secondary pressure value) result in more efficient handling of the product. This study aimed to improve the performance of these devices by an in-depth analysis using CFD, as described in L Macia (2022).

2 Methodology

Since a vacuum ejector has no moving components, its performance depends exclusively on its internal geometry, with the most relevant design parameters depicted in Fig. 1, and operating diagram.

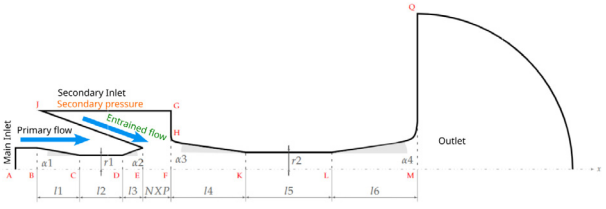

Figure 1: Operating diagram and geometrical parameters in a vacuum ejector design.

This study uses OpenFOAM with the High-Speed Aerodynamic solver (HiSA), as shown in JA Heyns (2014), which models compressible transonic and supersonic flows and allows for the resolution of numerical discontinuities including shock waves. HiSA is an implicit density-based solver that enables high CFL number simulations with more stability.

Two types of simulations were conducted to improve the characteristics of a vacuum ejector, one fixing the secondary pressure to 1 bar(a) and computing the maximum entrained flowrate, and the other fixing the secondary pressure gradient to zero and computing the min pressure value. The simulations performances were compared with the Reference Value (RV) geometric parameter and determined if there were any improvement. After conducting two simulations, enhancements in max flowrate and min pressure achieved were analyzed. Additionally, the overall enhancement, the sum of both, was also evaluated.

The flowchart shown in Fig.2 illustrates a single-factor analysis that was performed to evaluate the ejector's performance, where only one parameter was varied while keeping the others constant.

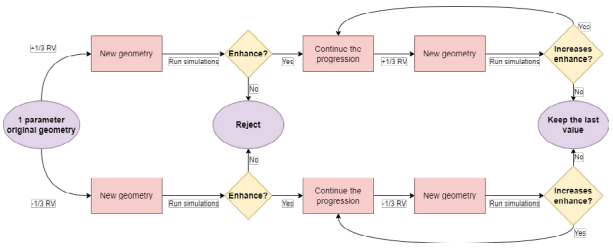

Figure 2: Flowchart to analyse the geometry.

The flowchart proposes to reject some parameters

and test only those that significantly improve performance. Then, a multi-factor analysis was conducted on selected parameters using a factorial combination design. To avoid excessive redundancy in combinations, a fractional factorial design was utilized instead of a full factorial. The combinations were decided by the n° of selected parameters with two levels each: the RV (level A) and the new improved (level B).

3 Results

Fig. 3 shows single-factor analysis results. The selected parameters were α_3, NXP, l_4 ad l_5. The mixing chamber length (l4) is the key parameter, that shows an overall 10% improvement.

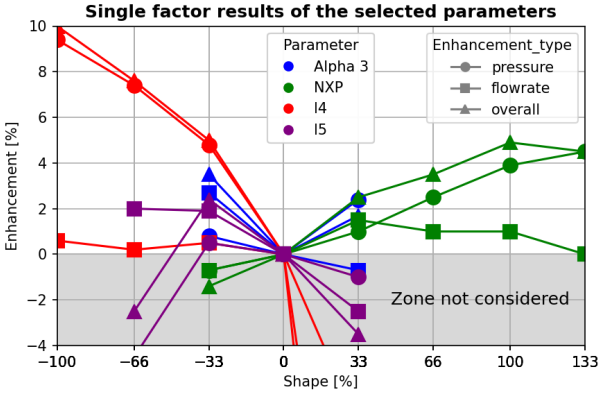

Figure 3: Single-factor improvement results in the selected parameters.

Multi-factor analysis, which the results are shown in Fig 4, utilized eight combinations as there were four selected parameters with two levels each.

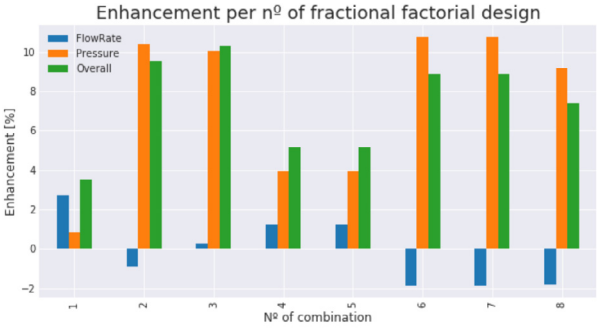

Figure 4: Multi-factor improvement results per combination number in the fractional factorial design.

Combination number three shows the best overall enhancement. It is made of α_3 at level A and the other three at level B. Thus, combination three is the new geometry.

The Mach number and pressure distribution with the RV geometry and the new geometry are shown in Fig 5 and Fig 6, respectively.

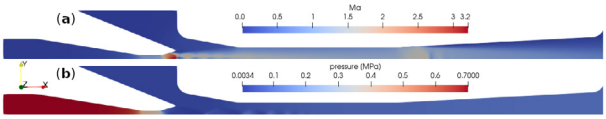

Figure 5: RV geometry. Simulation results for: (**a**) max entrained flowrate, (**b**) min secondary pressure.

The new geometry, depicted in Fig 6, outperforms the RV geometry with lower secondary pressure (higher vacuum) and fewer shock-waves, leading to better ejector performance.

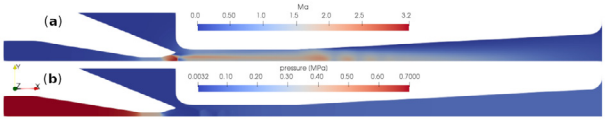

Figure 6: New geometry. Simulation results for: (**a**) max entrained flowrate, (**b**) min secondary pressure.

4 Conclusions

A single-factor analysis identified the mixing chamber length (l4) as the key parameter that led to a 10% improvement in performance . A multi-factor analysis identified combination number three as the best overall improvement, resulting in a 10.4% enhancement. Although no significant relevance was found in the multi-factor improvement over the single-factor, the former involves more geometries, resulting in a more accurate enhancement process. Even small improvements in this widely used device can lead to significant energy savings.

References

Ll Macia, R. Castilla, P. J. Gamez-Montero, (2019); "Numerical Simulation of a Supersonic Ejector for Vacuum Generation with Explicit and Implicit Solver in Openfoam". *Energies*, **12**, 3553

Ll Macia, R. Castilla, P. J. Gamez-Montero, G. Raush (2022); "Multi-Factor Design for a Vacuum Ejector Improvement by In-Depth Analysis of Construction Parameters". *Sustainability*, **14**, 10195

JA Heyns, OF Oxtoby and A Steenkamp (2014); Modelling high-speed viscous flow in OpenFOAM, *9th South African Conference on Computational and Applied Mechanics*, SACAM

Modelling the catalytic layer of a PEM Fuel Cell with adsorption-desorption kinetics

S. Martín[1], L. González-Rodríguez[2], J.L. Castillo[1] and P.L. García-Ybarra[1,*]

[1]*Department of Mathematical Physics and Fluids, UNED, 28232 Las Rozas, SPAIN*
[2]*National Hydrogen and Fuel Cell Technology Testing Centre (CNH2), 13500 Puertollano, SPAIN*

The cathodic catalytic layer of a PEM fuel cell has been described by a reaction-diffusion model with first-order kinetics. The reactant consumption through the whole layer, as well as the current intensity delivered by the fuel cell, is shown to depend simply on the hyperbolic tangent of the corresponding Damköhler number. By using the effective diffusion coefficient of the reactant as the fitting parameter, a suitable fit of the experimental results to a tanh-law in terms of the square root of the Damköler number has been achieved. The model has been extended to account for the absorption-desorption kinetics of the reactant on the catalytic sites.

INTRODUCTION

Electrospraying deposition of catalytic inks generates nano-structured catalytic layers by random aggregation of Pt/C nanoparticles [1, 2]. Catalytic inks can be prepared from Pt/C nanopowders with different mass percentage of platinum. By electrospraying these inks on the carbon microporous layer of commercial carbon paper, electrodes for PEM fuel cells are obtained with Pt-loadings in an ample range of values [3].

When compared the power density delivered by several electrode Pt-loadings, a linear increase in power is observed when increasing loading from the lowest values, whereas at high Pt-loadings the power saturates to an almost common value independently of the catalyst type [4].

MODELLING AND FITTING

A rough reaction-diffusion model with first-order kinetics was implemented to describe the cathodic catalytic layer of PEM fuel cells. Reactant consumption through the whole catalytic layer shows to depend simply on the hyperbolic tangent of the corresponding Damköhler number and the same is true for the current intensity delivered by the fuel cell, which reaches a maximum value in the limit of very large Damköhler numbers. The experimental results have been fitted to a tanh-law in terms of the square root of the Damköhler number, as shown in FIG. 1. The effective diffusion coefficient of the reactant has been used as fitting parameter.

The model has been extended to account for the absorption-desorption steps related to the oxidizer reactant on to the catalytic sites, in addition to the proper reaction step.

Under these assumptions, the reduced concentration of reactant n is shown to follow the Langmuir-Hinshelwood (Michaelis-Menten) kinetics which is well defined in terms of the involved rates of the elementary steps and leads to the expression of the effective Damköhler number Da. In addition, the governing equation for the reactant concentration depends also on an additional independent parameter related to the rates of the elementary steps κ:

$$\frac{d^2n}{d\xi^2} - Da\frac{n}{1+\kappa n} = 0. \qquad (1)$$

Here ξ is the dimensionless spatial coordinate through the thickness of the layer.

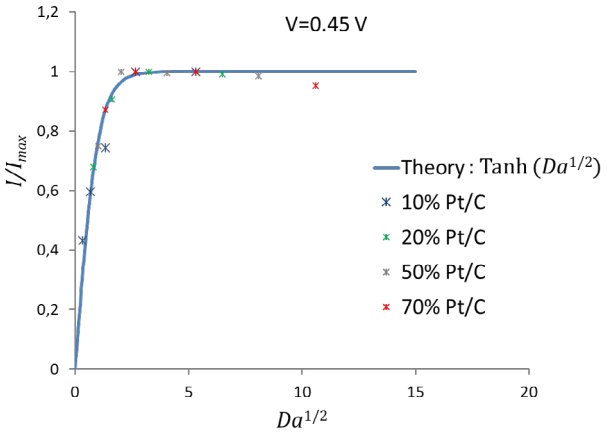

FIG 1. Experimental current intensities obtained with different catalysts at 0.45 V *versus* the square root of the Damköhler number. The line is the hyperbolic tangent.

CONCLUSIONS

For all catalysts (10, 20, 50, 70 % Pt/C), at low electrode Pt-loadings (≅ 0.04 mg_{Pt}/cm^2) the specific power grows almost linearly with the Pt-loading whereas, at relatively high Pt-loadings, the specific power saturates to a value that depends slightly on the catalysts (≅ 1 W/cm^2).

This behavior can be described by a simple reaction-diffusion model with absorption-desorption processes and a first order kinetics in terms of the Damköhler number and the occupation-evacuation rates ratio κ of the catalytic sites.

According to this model, the current intensity at a given overpotential follows approximately a tanh-law in terms of the square root of the Damköler number with decreasing values for increasing κ.

The fitting of the experimental results leads to conclude that the void regions of the catalytic layer are almost filled with liquid water but still allowing an efficient transport of oxygen through the small fraction of gas phase.

This work was supported by project PID2019-108592RB-C44 granted by:
AEI / 10.13039/501100011033.

—

* pgybarra@ccia.uned.es

[1] P.L. Garcia-Ybarra, J.L. Castillo, S. Martin, “Procedimiento de depósito nano-estructurado uniforme de partículas catalíticas por electrospray”, OEPM (2014) Patent no. ES2427647.

[2] Castillo J.L., Martin S., Rodriguez-Perez D., Higuera F.J., Garcia-Ybarra P.L. (2018) “Nanostructured porous coatings via electrospray atomization and deposition of nanoparticle suspensions”. *J. Aerosol Science*, **125**, 148—163.

[3] Martin S., Garcia-Ybarra P.L., Castillo J.L. (2010) “Electrospray deposition of catalyst layers with ultra-low Pt loadings for PEM fuel cells cathodes”. *J. Power Sources*, **195**, 2443—2449.

[4] Martin S., Martinez-Vazquez B., Garcia-Ybarra P.L., Castillo J.L. (2013) “Peak utilization of catalyst with ultra-low Pt loaded PEM fuel cell electrodes prepared by the electrospray method”. *J. Power Sources*, **229**, 179—184.

2nd Spanish Fluid Mechanics Conference
Barcelona (2 - 5 July 2023)

Numerical and experimental evaluation of the transmittance of an AHU

Paula Torres[1], Robert Castilla[1], Gustavo Raush[1], Mónica Morte[2], and Daniel Moreno[2]

[1]*paula.torres.perez@estudiantat.upc.edu*
[1]CATMech-Departament de Mecànica de Fluids, Universitat Politècnica de Catalunya, Spain
[2]Servoclima, Spain

This study is based on evaluation of the transmittance of an air handling unit. Conduction, convection and radiation will be taken into account. OpenFoam 9 will be used to perform the necessary computational simulations. In addition, in order to test the numerical results, experiments will be carried out to validate them.

1 Introduction

An air treatment unit is a box in which air handling for air-conditioning is carried out. In general, ventilation, quality, temperature and humidity are controlled. In this study, numerical simulations and experimental validation of the transmittance of the AHU will be undertaken. Transmittance is a dimensionless parameter that relates the power consumed to the heat transferred through the surfaces and is defined as

$$U = \frac{P_{el}}{A\Delta T_{air}} \tag{1}$$

where P_{el} is the consumed electric power, A is the total area and ΔT_{air} is the difference between average inside and outside temperatures.

Thermal bridge is an area which has higher thermal conductivity that creates a path of least resistance for heat transfer and its coefficient is defined as

$$k_b = \frac{\Delta T_{min}}{\Delta T_{air}} \tag{2}$$

where ΔT_{min} is minimum temperature difference between inside and outside surface.

Mainly, the project is based on heat transfer, energy exchange by temperature difference. The heat transfer coefficient is determined by 3 different and independent phenomenons: conduction, convection and radiation.

The main objective of the project is to estimate the transmittance of an air handling unit by computational simulations. Furthermore, laboratory experiments will be carried out in order to validate the computational simulations.

2 Theoretical estimation

In general, heat transfer is determined by Newton's equation,

$$Q = \alpha A \Delta T \tag{3}$$

where α is the heat transfer coefficient, A the transfer area and ΔT the temperature difference. Cengel (2020)

In **conduction**, heat is conducted through a material with a specific conductivity k for a certain length d. The transfer coefficient in this case is

$$\alpha_{cond} = \frac{k}{d} \tag{4}$$

Convection involves fluid dynamics and can be either forced (by fans) or natural (by the bouyancy of less dense air). The **forced convection** coefficient is

$$\alpha_{conv,f} = \frac{\mathrm{Nu}k}{d_h} \tag{5}$$

If the flow is laminar (Re<10e5), the Nusselt number (Nu) will be

$$\mathrm{Nu} = 0,66\mathrm{Re}^{0,8}\mathrm{Pr}^{1/3} \tag{6}$$

and if it is turbulent (Re>10e5) it will be

$$\mathrm{Nu} = 0,037\mathrm{Re}^{0,8}\mathrm{Pr}^{1/3} \tag{7}$$

where Re is the Reynold number and Pr the Prandtl number. In **natural convection** case, the Nusselt number will be

$$\mathrm{Nu} = 0,069\mathrm{Ra}^{1/3}\mathrm{Pr}^{0,074} \tag{8}$$

adequate for horizontal rectangular boxes, where Ra is the Rayleigh number. Inside the box, there is both forced and natural convection, although natural convection dominates. Cengel (2020)

Finally, in **radiation**, a black body is considered to be radiating when it is at a certain temperature. Its heat flux is

$$q = \sigma T^4 \tag{9}$$

where σ is the Stefan-Boltzmann constant. As the bodies are not completely black and have emissivity, the heat flux is as follows

$$q = \epsilon \sigma T^4 \tag{10}$$

where ϵ is the emissivity.

3 Simulations

OpenFoam version 9 will be used to execute all the simulations with **chtMultiRegionFoam**, a conjugate heat transfer solver. Simulations will be 2 dimensional in order to reduce the computational and time resources. Also, the incorporation of radiation models in the numerical simulations will be considered. 3 models will be applied, each of them with a different insulation.

4 Experiments

In order to validate the simulation results, some experiments will be undertaken. Lopes (2021)

The experimental transmittance measurement will be carried out on a AHU which contains 4 fans, 2 heaters, 1 temperature controller and 20 thermocouples.

This project will be undertaken by the standard UNE-EN 1886:2008 named "Ventilation of buildings - Air handling units - Mechanical performance".

5 Conclusions

This study will allow us to obtain the transmittance value of the AHU. Moreover, it will be possible to validate the simulations through the experiments done while improving the energetic efficiency.

References

Çengel Y.A., Ghajar A.J., Muñoz Díaz E., Cordero Pedraza C.R., Robledo Rella V.F., Ochoa López A. y Ghajar A.J. (2020) "Transferencia de calor y masa : fundamentos y aplicaciones". *McGraw-Hill*

Lopes J, Silva J, Teixeira S, Teixeira J. (2021) "Numerical Modeling and Optimization of an Air Handling Unit". *Energies*

Numerical Modeling and Experimental Validation of a Liebau Effect-based Valveless Pump

C. Barrios-Collado, J. Anatol, M. García-Díaz, J. A. Moneo-Fernández, F. Castro-Ruiz, J. Sierra-Pallares

Departamento de Ingeniería Energética y Fluidomecánica & ITAP
Universidad de Valladolid, Paseo del Cauce 59, 47011 Valladolid, SPAIN.

The Liebau effect is a well-known valveless pumping mechanism ubiquitous in biological systems, which is of great interest in technological applications where the fluid cannot come into contact with mechanical elements. In this work, we propose and validate a new one-dimensional computational model to simulate the dynamics of a device based in such phenomenon.

INTRODUCTION

Liebau effect [1] devices feature a flexible segment (compliant tube) embedded within a hydraulic circuit, which is rhythmically compressed (pinched). If there is an asymmetry in any circuit parameter, different pressure waves traveling towards both directions generate a net pressure gradient, which results in a flow rate. Regarding the asymmetry in the circuit, it can be applied on the pinching location on the flexible element (impedance pumping); on the rigid pipe layout (asymmetric pumping); or both (Liebau effect) [2]. As the Liebau mechanism naturally works in biological systems, such as embryos (which still have not developed heart valves) or Amphioxi (lancelets), its potential application in cardiovascular applications is increasingly studied.

Efforts to understand this phenomenon and its dependence on the pinching frequency and geometric boundaries have led to the development of several numerical approaches, from simple one-dimensional models to fluid-structure simulations [3, 4, 5]. However, most of them are computationally too expensive for practical uses (such as parametric studies) or lack experimental validation.

METHODS

In our one-dimensional model, the computation domain recreates the experimental setup shown in [2], figure 1, where an asymmetric pump is used to create a hydraulic head between two reservoirs, initially leveled. Most of the hydraulic circuit is made of rigid pipe (PVC), except for the compliant tube (latex).

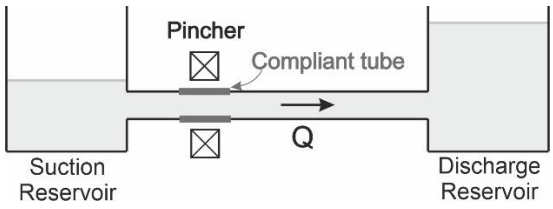

FIG 1. Diagram of the simulated asymmetric pump, based on the experimental setup described in [2].

The governing equations are the following:

- Mass conservation at both reservoirs (1),

$$\frac{dH}{dt} = \pm u \frac{\pi D^2}{4A_d}, \quad (1)$$

- The classic water hammer equations at the hydraulic circuit rigid pipes (2),

$$\frac{du}{dt} = -\frac{fu|u|}{2D} - \frac{\nabla P}{\rho}, \quad \frac{dP}{dt} = -\rho c^2 \nabla u \quad (2)$$

- The viscoelastic water hammer equations at the compliant tube, according to the Kelvin-Voigt model (3),

$$\frac{du}{dt} = -\frac{\nabla P}{\rho}, \quad \frac{dP}{dt} = -\rho {c_l}^2 \nabla u - 2\rho {c_l}^2 \frac{d\epsilon_r}{dt}, \quad \frac{d\epsilon_r}{dt} = \sum_{k=1}^{N} \left[\frac{\alpha D}{2s} \frac{J_k}{\tau_k} (P - P_0) - \frac{\epsilon_{rk}}{\tau_k} \right] \quad (3)$$

The numerical scheme features central differences to model gradients and an Ordinary Differential Equation solver for stiff problems.

RESULTS

We validated our model with experimental data from an asymmetric pump [2]. Figure 2 compares the experimental instantaneous flowrate measured in [3] with the numerical one. Both curves follow the same trend and are in good agreement.

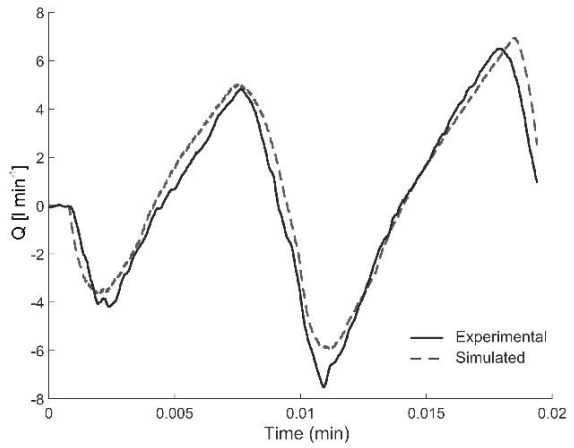

FIG 2. Simulated vs experimental instantaneous flowrate for the first two pinching cycles of the experiment described in [2].

CONCLUSIONS

Our one-dimensional numerical model, which solves the mass conservation equation, the wave equation and the viscoelastic constitutive equation has proven itself to predict correctly experimental data. Our simulations show the same trend and good agreement with experiments. This model let envisage further optimization of Liebau devices, as well as produce insight about the involved phenomena.

ACKNOWLEDGEMENTS

The authors would like to thank the Junta de Castilla y León for funding this work as part of the program “Subvenciones del programa de apoyo a proyectos de investigación financiados por fondos FEDER”, project number VA182P20.

REFERENCES

[1] G. Liebau, «On a valveless pump principle (Ger),» *Naturwissenschaften,* vol. 327, p. 1, 1954.

[2] J. Anatol, M. García-Díaz, C. Barrios-Collado, J. A. Moneo-Fernández, M. Horvath, T. Parra, F. Castro-Ruiz, E. T. Roche y J. Sierra-Pallares, «Experimental study of an asymmetric valveless pump to elucidate insights into strategies for pediatric extravascular flow augmentation,» *Scientific Reports,* vol. 12, nº 1, p. 22165, 2022.

[3] I. Avrahami y M. Gharib, «Computational studies of resonance wave pumping in compliant tubes,» *Journal of Fluid Mechanics,* vol. 608, p. 139–160, 2008.

[4] E.-O. Jung y D.-W. Kim, «Valveless pumping in open tank system using energy conserving compartment model,» *Bulletin of the Korean Mathematical Society,* vol. 49, nº 5, p. 961–987, 2012.

[5] S. J. Shin y H. J. Sung, «Three-dimensional simulation of a valveless pump,» *International Journal of Heat and Fluid Flow,* vol. 31, nº 5, p. 942–951, 2010.

2nd Spanish Fluid Mechanics Conference
Barcelona (2 - 5 July 2023)

On the role of electrolyte mixing in vanadium redox flow battery tanks: CFD and experimental approaches

Pablo Ángel Prieto-Díaz, Andrea Trovò, and Marcos Vera

paprieto@ing.uc3m.es

Departamento de Ingeniería Térmica y de Fluidos, Universidad Carlos III de Madrid,
Avda. de la Universidad 30, 28911, Leganés, Spain

Redox Flow Batteries are electrochemical energy storage systems that reversibly transform electrical energy into chemical energy using two redox pairs dissolved in separated electrolytes. After flowing through the electrochemical reactor cell, the electrolytes are stored in separate tanks where they discharge as submerged jets with slightly different density and viscosity than the fluid already in the tanks. The resulting mixing process, determined by the competition between jet momentum and buoyancy effects, is essential for battery performance since imperfect mixing causes significant losses in energy storage capacity. Preliminary results based on numerical simulations of industrial-scale tanks and experimental validation tests are presented and discussed.

1 Introduction

Redox flow batteries (RFBs) constitute a promising technology for large-scale energy storage [1]. Using a reactor cell, the electrical energy is converted into chemical energy by means of two redox pairs that are stored in independent tanks, reversing the process when power is needed. Figure 1 shows an schematic representation of the all-vanadium system considered in this work.

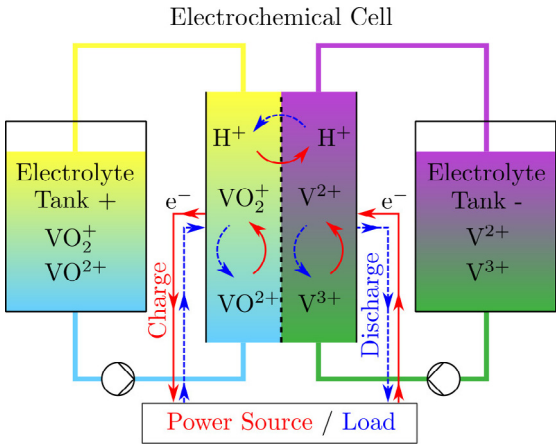

Figure 1: Schematic of a vanadium RFB.

The fluid dynamics of the electrolyte within tanks has been largely overlooked to date, with most previous works using the continuous stirred tank model. In a recent work, the authors [2] simulated the mixed convection flow in small lab-scale two-dimensional tanks, obtaining different flow regimes depending on the operating conditions. These regimes included quasi-steady jets, drops, stratified flows, or transient (i.e., secular) buoyancy effects. Zatta et al. [3] confirmed the importance of buoyancy using experiments that showed that the cell response was delayed by the fluid dynamics inside tanks. However, these first attempts relied on strong simplifications (e.g., laminar flow in two-dimensional geometries) [2] or poor data of the flow inside the tanks (focusing mainly on the cell response) [3]. In this work, we investigate the effect of tanks on battery performance using numerical simulations to study industrial-scale tanks, where turbulence appears, and also a new experimental campaign to deepen our understanding of the problem.

2 Modeling of industrial scale Vanadium RFB tanks

RFBs have a prominent advantage in separating the power rating (related to the reactor cell and flow rate) and the energy storage capacity (related to the tank size). As this technology is typically focused on large-scale plants, the energy storage capacity must be designed for industrial-scale applications. The tank geometries are different in each implementation but most of them share certain characteristics, such as the cylindrical shape, the characteristic length in the scale of meters, and the turbulent flow regime.

Considering an initial tank design that fulfills these conditions, this work uses CFD to determine how the geometry, operation conditions, and modifica-

tions thereof affect the battery's response in a typical charge-discharge cycle. The mathematical model is based on that of our previous work [2] but including more realistic boundary conditions and implementing a low Re $k - \epsilon$ turbulent model. Results show how design variations of a simple empty tank (which is the usual choice in the industry) can significantly increase the battery capacity without needing complex geometries or baffles that raise the fabrication costs.

3 Experimental validation

The mathematical model and simulation results must be confirmed using experimental tests. This works exploits the experimental work carried by Zatta et al. [3] but using a medium size battery. Measuring the open circuit voltage and varying the tank geometries, the tank responses are estimated and so the fluid dynamics. Experimentally obtained battery results are presented and discussed and compared to the CFD results.

4 Conclusions

This work confirms that the fluid dynamics of the electrolyte in the tanks is relevant in designing high-efficiency redox flow batteries. Turbulence improves mixing within the tanks, but geometry modifications may enhance electrolyte homogeneization, and thus energy capacity, even further. The experimental tests confirm that including the effect of buoyancy is highly relevant in obtaining accurate results from CFD. These results call for additional experimental data from large-scale batteries and for improved CFD models that provide industrial-scale results in a less computationally costly way.

References

[1] M. Skyllas-Kazacos, L. Cao, M. Kazacos, N. Kausar, and A. Mousa, "Vanadium electrolyte studies for the vanadium redox battery—a review," *ChemSusChem*, vol. 9, no. 13, pp. 1521–1543, 2016.

[2] P. A. Prieto-Diaz, A. A. Maurice, and M. Vera, "Modelling the electrolyte flow in the tanks of vanadium redox flow batteries: A CFD perspective," *ECS Meeting Abstracts*, vol. MA2022-01, p. 2009, jul 2022.

[3] N. Zatta, A. Trovo, F. Picano, and M. Guarnieri, "A fluid dynamic analysis of mixing phenomena inside electrolyte tanks to enhance performance of industrial-scale vanadium redox flow batteries," *ECS Meeting Abstracts*, vol. MA2022-01, p. 478, jul 2022.

Shear stress measurements by Preston tubes

Aitor Vega Valladares[1], Celia Miguel González[2], Alejandro Rodríguez de Castro[2] and Bruno Pereiras

[1]*Department of Energy, University of Oviedo, SPAIN*
[2]*R&D, ArcelorMittal, SPAIN*

This work deals with some problems found by the authors when using Preston tubes for measuring shear stress in planar jets. In spite of the well-known underestimation of the maximum shear stress made by the Preston tubes, they have revealed as a reliable way to make the measurements, predicting the location of the maximum shear stress and being accurate out of this location. However, many problems were reported before reaching successful test campaigns. Those are related in this work.

INTRODUCTION

Removing liquids in the steel industry is a problem directly related to the productivity of continuous production lines such as cold rolling mills or tin plate. Several techniques are used but using air jets to wipe out these liquids is the most extended one, mainly applied by "air-knives" which are basically planar jets impinging on the steel strip while it is moving. Nevertheless, new arrangements based on combination of round jets are coming to the forefront.

Analyzing the characteristics of any systems implies that, apart from measuring the pressure impingement on the surface, measurements of the shear stress caused by the wall jet should be made. Then, the issue of how to measure the shear stress pops up. Specially if the solution must be accurate, cheap, reliable and harsh conditions are expected.

During the development of the measuring rig some issues about using Preston tubes were found. Those are the core of this work.

MATERIALS AND METHODS

A test bench has been built at the Fluid Mechanics Laboratory of the University of Oviedo in order to measure impinging pressure profiles and shear stress of drying/wiping systems, including impinging planar jets. It is equipped with a three axes (XYZ) movement system. It also incorporates the instrumentation for impact pressures, flowrate, velocity, and shear stress values acquisition. Measurements of pressure impingement and shear stress were made using a pressure scanner of 16 ports (NetScanner 9116, range of ±9 kPa and error of ±0.05% FS)

A methacrylate, acting as impact surface, is housed in the main rig. In this methacrylate, a row of 16 holes of 0.9 mm of diameter, separated 2 mm from each other, are drilled along OX direction and centred in the impact line (see FIG *1*). They have been used as pressure taps to measure the impinging pressure profiles. Besides, another row of 16 holes of 0.4mm diameter every 5mm along OZ direction, was drilled downstream the impact line to house 16 27G-gauge needles, bended 90 degrees, which were used as Preston tubes for shear stress measurements.

For this work, an air knife bilaterally fed, with a gap length of 160 mm and a gap nozzle (D) of 2 mm, has been used. In all the tests, the planar jet was perpendicular to the impact surface.

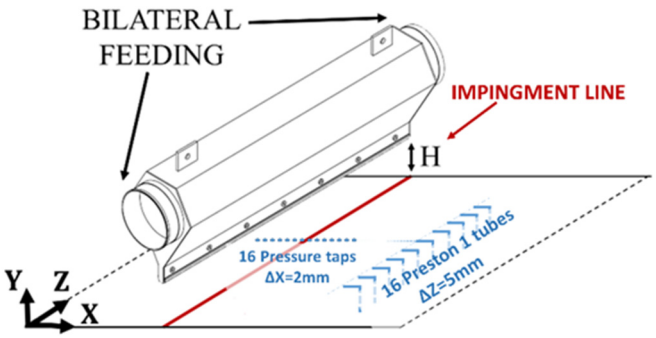

FIG 1. Sketch of the Preston tubes and taps location.

NOTES ON PRESTON TUBES

First of all, why using preston tubes instead other techniques such as Stanton probes or fences [1]. The main reason because a researcher decide to use preston tubes are three: 1) they are cheap, 2) they are "easy" to mount and, 3) they allow a spatial resolution very small in the transversal direction. Some comments about the first two will be made in the following paragraphs, but the real reason to use preston tubes in this study was the third one.

The main characteristics of the preston tubes used in this work are shown in TABLE 1. It is clearly seen that using hypodermic needles has many advantages except the size. Note that the smallest diameters of hypodermic needles are manufactured in too short lengths.

According to [2], despite playing an important role, the importance of the tube diameter fades below certain values (0.5mm). The results of this work agree partially with that statemen, but certain differences were found between the diameters tested in this work, FIG 2. On the other hand, it is clear that larger diameters only show weakness when the gradients are stronger, but this is inherent in Preston tubes.

Preston	1	2
Dout/in[mm]	0.4/0.2	0.2/0.1
Length [mm]	40	[20, 30, 40]
Material	Cr-Ni SS	SS - AISI 304
Finishing	Fine	Rough (very)
Cost	≈6€/100ud	≈280-320 €/m
Ductility	High	Low

TABLE 1. Preston tubes characteristics

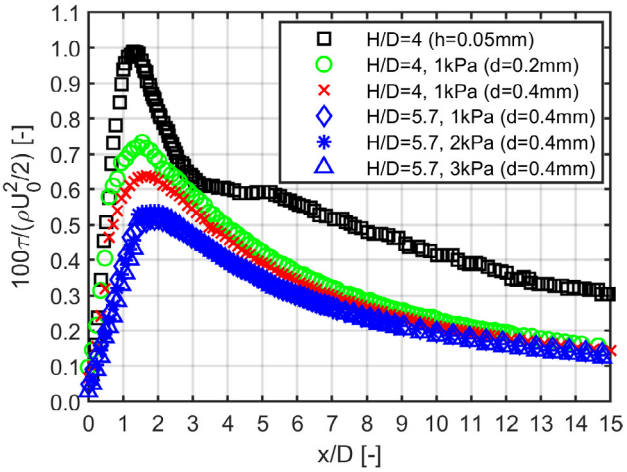

FIG 2. Diameter influence on the measurements of Preston tubes.

On the other side, the influence of the length was unexpectedly high. In FIG 3, the response time of the preston tube reading is shown and the differences turned to be of great importance. Mainly in negative pressure gradients. Using lengths below 1cm is possible, but complicated because the preston tube is not manageable. The recommendation is using lengths around 5cm (l/d=180).

Apart from the diameter and length, the finished of the tubing revealed as critical. In case of Preston 2 type the cutting process made by the manufacturer is clearly improvable, FIG 4. In case of the original, the losses at the entrance of the tube affect the measurement, making it unreliable. This problem was not found in the G-27 needles used as Preston 1 type, because they are obviously subjected to a more specific quality control.

Another "trick" the authors want to report here is not directly related to the Preston tubes but to the boundary conditions of the measurement itself: The flatness of the impact surface was found critical. In our case, the machining of some of the holes used as the pressure taps had slightly deformed the methacrylate surface, creating small bulges with the hole in the middle. Thus, out of the pure stagnation zone, a venturi effect was created driving the static pressure measurement to be false. After having the surface treated, the results improved quite a lot.

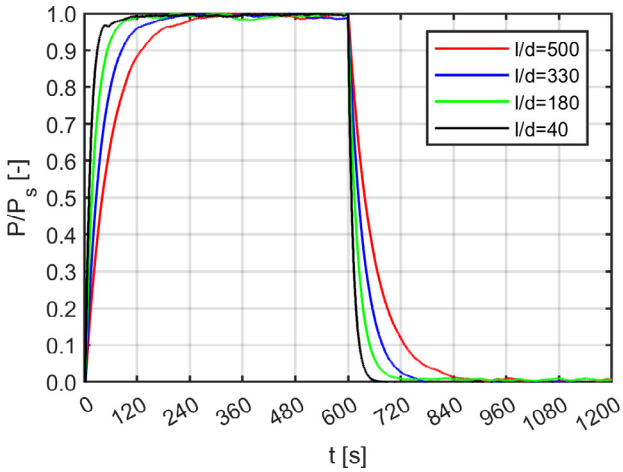

FIG 3. Response time of the Preston tubes against their length for both positive and negative pressure gradients. Tests made exposing all the Preston tubes inlet to a certain static pressure, returning later to P_{atm}.

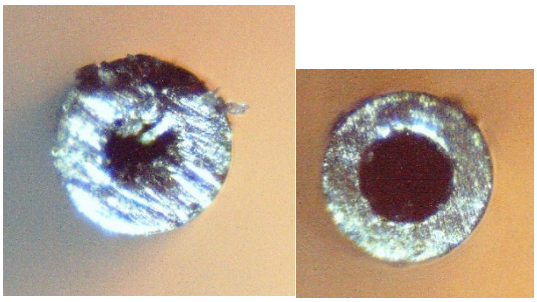

FIG 4. Left: original Preston2 type. Right: sanded using grit 1000.

Finally, the shear stress results are very sensitive to the spatial correlation between the preston location with respect to the air knife and the location of the air knife during the static pressure tests. This dependence is extremely critical. Therefore, having a completely reliable movement system is mandatory in order to assess precisely the shear stress.

CONCLUSIONS

It was found that using Preston tubes to measure shear stress in wall jets is a reliable technique. However, it, presents some issues to be resolved before obtaining reliable data. This work, dealing with these problems, cold serve to any researcher as guidance to make accurate measurements.

—

* pereirasbruno@uniovi.es

[1] K. G. Winter, "An outline of the techniques available for the measurement of skin friction in turbulent boundary layers," *Prog. Aerosp. Sci.*, vol. 18, no. C, pp. 1–57, 1979, doi: 10.1016/0376-0421(77)90002-1.

[2] C. V. Tu and D. H. Wood, "Wall pressure and shear stress measurements beneath an impinging jet," *Exp. Therm. Fluid Sci.*, vol. 13, no. 4, pp. 364–373, Nov. 1996, doi: 10.1016/S0894-1777(96)00093-3..

2nd Spanish Fluid Mechanics Conference
Barcelona (2 - 5 July 2023)

Using CFD simulation to evaluate the passive odour emission from open-roof tanks

Aina Macias[1], Francesca Tagliaferri[2], Marzio Invernizzi[2], Selena Sironi[2], and Sergio Chiva[1]

amacias@uji.es

[1]Departamento de Ingeniería Mecánica y construcción, Universitat Jaume I, Spain
[2]Dipartimento di Chimica, Materiali e Ingegneria Chimica "Giulio Natta", Politecnico di Milano, Italy

This work describes a quantitative evaluation through CFD simulations of air flow and passive odour emission from open-roof tanks, as for example wastewater treatment tanks, to find out a numerical correlation to evaluate the specific emission rate (SER) of the source emission. This approach allows it to be implemented as a pollutant emission source in large-scale simulations obtaining a reduction in the necessary computational resources.

1 Introduction

Complex odours emissions arise from several points of Waste Water Treatment Plants (WWTPs), causing impacts to the quality of life of the surrounding community, by generating nuisance and discomfort.

In WWTPs there are tanks that present area sources without a predetermined outward flow (high variability due to changes in wind velocity and ambient conditions such as temperature or relative humidity). Therefore it is difficult to estimate an emission rate(Capelli et al., (2009)), as it is not easy to measure a representative odour concentration and there is no well-defined airflow.

Computational Fluid Dynamics (CFD) has been widely used for studying pollutant dispersion around buildings(Blocken (2014)). Such models are used for extremely time and spatially detailed simulations, considering the presence of obstacles explicitly in the model, and are currently applied also to odour dispersion modeling (Capelli et al., (2013)). Moreover, the consideration of detailed simulation of small-area odour sources inside a large-scale domain increases dramatically the computational cost of CFD simulations.

For that reason, the aim of this study is to accurately model and simulate using CFD techniques the air flow and tracer dispersion from the cavity surface using different configurations to obtain a huge dataset in order to enable the evaluation of the specific emission rate and be able to implement an expression instead of an specific cavity in large-scale simulations.

2 CFD modelling setup

Figure 1 depicts a vertical section of the computational domain under study, being $Z = 2m$ the height of the domain, and $L1 = 2m$ and $L2 = 5m$ the distances upstream and downstream the cavity, that is treated as two dimensional (2D) case.

The CFD simulations are performed for uncompresible and isothermal conditions using OpenFOAM, an open source, freely available CFD toolbox. Flow equations are modeled using the Reynolds-averaged Navier-Stokes (RANS) equations in combination with the standard k-epsilon model (Launder et al., (1972)) for closure for incompressible turbulent flow. Particularly, the simpleFOAM solver was used for their numerical resolution, providing an accurate description of the flow evolution and PimpleFoam solver was used for the numerical resolution of the tracer equation transport (Figure 1).

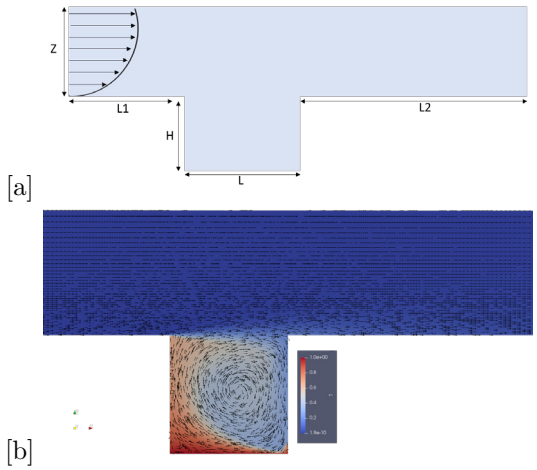

Figure 1: Schematic of the cavity geometry: (a) Parametrized dimensions; (b) Velocity vectors and tracer concentration contour.

As reported in Table 1, a total of 64 simulations were launched varying the deep of the cavity (H) from 0.5 to $5m$, the length (L) from 1 to $10m$, and the

frictional velocity (u^*) from 0.1 to 0.98m/s.

Case	H [m]	L [m]	u* [m/s]	H/L
01	0.5	1	0.10	0.05
.	.	.	.	.
64	5	10	0.98	5

Table 1: Cavity geometries and parameters used in CFD simulations.

3 Model evaluation

Similar to Oke et al., (2017), we can split data in three regions: $H/L > 3$ (negligible velocity influence), $0.5 < H/L < 3$ (small velocity influence) and $H/L < 0.5$ (where SER behaves exponentially with H/L and strongly affected by velocity). The observation of three different patterns or regions (Figure 2) difficults the two variable fitting optimization problem, i.e. according to Equation 1:

$$SER = a(u^*)^b \left(\frac{H}{L}\right)^c \quad (1)$$

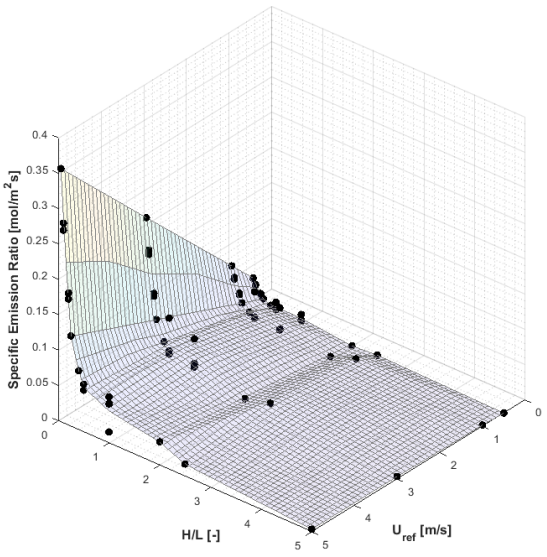

Figure 2: Simulated data cases and fitting surface according to Equation 1.

We considered linear, exponential and power law regression, but only the power law regression appears pretty satisfying (Figure 3). We tried to split the domains considering the three possible situations of "canyons" mentioned by Oke et al., (2017): $H/L < 0.35$ (isolated roughness flow), $0.35 < H/L > 0.65$ (wake interference flow)and $H/L > 0.65$ (skimming flow).

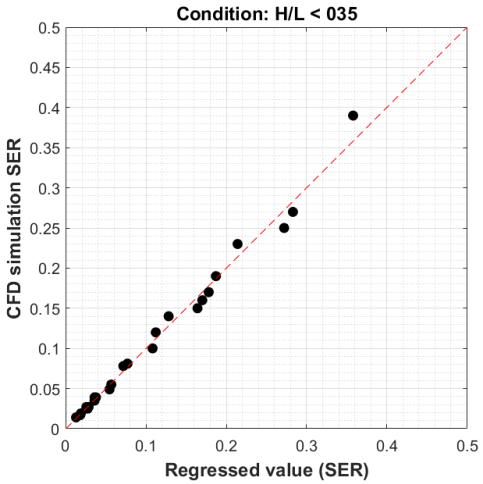

Figure 3: Example of model fitting for isolated roughness flow condition.

4 Conclusions

Considering the results obtained, simplified numerical correlation can be obtained for tracer dispersions (i.e. odour dispersion) modelling a high variety of complex scenarios. The implementation of simplified expressions for odour transport, instead of a complete and detailed open-roof tank simulation, helps to greatly reduce the overall computational costs if large-scale simulations are considered.

References

Capelli L, Sironi S, Del Rosso R, Céntola (2009) "Design and validation of a wind tunnel system for odour sampling on liquid area sources". Water Sci Technol, 59(8):1611-20.

Blocken, B. (2014) "50 years of Computational wind engineering: past, present and future". J. Wind Eng. Indus. Aerodynamics 129, 69e102.

Capelli, L., Sironi, S., Rosso, R., Guillot, J. (2013) "Measuring odours in the environment vs. dispersion modelling: A review". Atmospheric Environment, 79, pp. 731-743.

Oke, T., Mills, G., Christen, A., Voogt, J. (2017) "Urban Climates". Cambridge: Cambridge University Press.

Launder, B.E., Spalding, D.B. (1972) "Mathematical Models of Turbulence". Academic Press, New York.

2nd Spanish Fluid Mechanics Conference
Barcelona (2 - 5 July 2023)

A Data-driven non-equilibrium wall model for LES of transitional flows

Sarath Radhakrishnan[1] and Oriol Lehmkuhl[2]

sarath.radhakrishnan@bsc.es

[1]Large-scale Computational Fluid Dynamics Group, Barcelona Supercomputing Center, Spain
[2]Large-scale Computational Fluid Dynamics Group, Barcelona Supercomputing Center, Spain

A data-driven non-equilibrium wall model for Large Eddy Simulation (LES) is developed from high-fidelity data from the Direct Numerical Simulation (DNS) of the flow through a diffuser. The model is trained with non-dimensional and reference frame invariant input features to predict the wall-shear stress. The wall shear stress obtained from the model is used as an approximate boundary condition in wall modeled LES(WMLES). The trained model is tested a posteriori on the NASA hump experiment. It has been shown to perform remarkably better than a state of the art wall model, especially at the turbulent to laminar transition region.

1 Introduction

Over the last decade, Large Eddy Simulation has received an increased attention as a predictive tool for industrial fluid dynamics. However, it is still very expensive when it comes to wall-bounded turbulent flows. As most of this expense is attributed to resolving the region of the boundary layer close to the wall, a feasible way to use LES would be by resolving the outer boundary layer alone. Since the grid size to resolve the outer layer is coarser, the velocity gradient and in turn, the wall-shear stress are underpredicted. This has to be balanced by an appropriate Wall Model(WM). Different types of wall models are reviewed by Bose (Sanjeeb T. and Park). One of the key limitations of the State of the Art(SoA) WM's is their inability to perform under non-equilibrium conditions, especially when there is a strong and favorable or adverse pressure gradient. When there is a strong and favorable pressure gradient, the flow may change from turbulent to laminar which no model has ever been able to detect yet. The purpose of this study is to address this problem by augmenting the wall model using information obtained from high-fidelity data. Data-driven approaches in WMing is still at a budding stage in the research community. A review of all the data-driven wall models is given by Vadrot (Aurélien and Yang). The methodology of data-driven model development is briefly described in the section that follows.

2 Methodology and Results

The high-fidelity data used for training the model is derived from the Direct Numerical Simulation of the flow through a 3D diffuser. It is an excellent choice for training as the simulation carries information regarding various non-equilibrium phenomena such as flow around corners, three-dimensional separation, transition, etc. The generated data is used to build the wall model using the machine learning technique of gradient boosting by Friedman (Jerome H.). The gradient boosting system used to train the model is XGBoost by Chen (Tianqi and Guestrin). Gradient boosting uses decision trees as "weak learners" for making predictions. The model is an additive function in the form of tree structures that maps the input space to the output space. The inputs are the features processed from the flow that carry the necessary information to build a model that can be generalizable to all types of flows. Two non-dimensional, reference-frame invariant features that have been shown to have this property are used to train this model. The first one is called the "Local Reynold's Number" given by,

$$u_d = \frac{u\delta_n}{\nu} \tag{1}$$

where, u is the magnitude of the instantaneous velocity parallel to the walls and δ_n is the normal distance from the wall. The second one, which is also a velocity scaling, is based on the magnitude of the pressure gradient. It is computed as,

$$u_p = \frac{u}{\sqrt[3]{\nu\partial_t p}} \tag{2}$$

where, ρ is the fluid density, $\partial_t p$ is the magnitude of the stream-wise pressure gradient at a normal distance δ_n. The model output is u^+ given by,

$$u^+ = \frac{u}{\sqrt{\tau_\omega}} \tag{3}$$

where τ_ω is the magnitude of the wall shear stress.

Like any other machine learning system, XGBoost also provides hyper-parameters to tune the model. The size of each 'tree' in the model is controlled by the hyper-parameter '*max_depth*'. It is set to 7 such that each tree will have 2^7 leaves. The leaves contain the image of the tree functions. The rate at which the learning takes place is controlled by the '*learning_rate*' parameter. This hyper-parameter is responsible for the extent to which the model is altered in response to the loss after each iteration. This is set to a value of 0.1 for this study. The rest of the parameters are set to default values.

The trained model is coupled with the in-house multi-physics solver Alya. The results shown here are from the WMLES simulation of the flow over the NASA hump. This is an interesting numerical experiment particularly to test non-equilibrium wall models as it involves relaminarization, flow separation, and re-attachment. The computational domain for this case is $4.64c$, $0.909c$, and $0.3c$ in the stream-wise, normal, and span-wise directions, respectively, where c is the chord length of the hump(cf. Fig. 1). The inlet and outlet planes of the domain are at $x/c = -2.14$ and $x/c = 2.5$, respectively, so that the leading edge of the hump can be placed at $x/c = 0$.

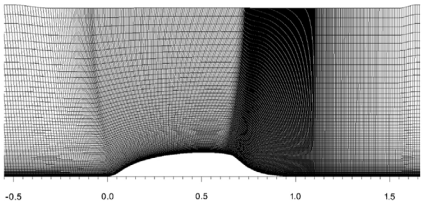

Figure 1: Computational mesh around the hump.

The mesh used for this test is a coarse mesh of $742 \times 70 \times 80$ elements in the stream-wise, wall-normal, and span-wise directions, respectively. The Coefficient of Drag(C_d) predicted by the Machine learning based wall model(MLWM) is compared with the predictions of an algebraic wall shear stress model(EQWM) in Fig. 2. The MLWM outperforms the EQWM in all the key areas. Near the re-circulation region, the MLWM has better performance and the recovery is much better. However, the most remarkable feature is the ability of the model to capture the turbulent to laminar transition over the hump. This has always been a herculean task for all of the SoA wall models. However, the MLWM has learned to capture this phenomenon during the training process.

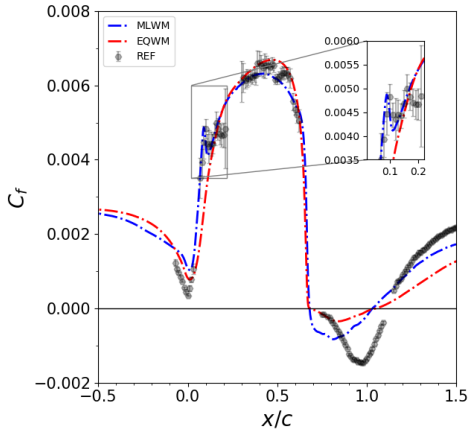

Figure 2: Comparison of the C_d predicted by the MLWM and the EQWM. The black circles are experimental results. The inset shows a zoom of the relaminarization region

3 Conclusions

A data-driven non-equilibrium wall modeling method for LES is breifly described here. The high-fidelity data is generated from the DNS of the flow through a diffuser. The model is trained with non-dimensional and reference frame invariant input features to predict the wall-shear stress which in turn is used as an approximate boundary condition in WMLES. The trained model is tested a posteriori on the WMLES simulation of the flow over the NASA hump. It has been shown to perform remarkably better than a SoA wall shear stress model, especially at the turbulent to laminar transition region over the hump.

References

Sanjeeb T Bose & George Ilhwan Park(2018) "Wall-Modeled Large-Eddy Simulation for Complex Turbulent Flows", *Annual Review of Fluid Mechanics*, **1**, 531–565.

Aurélien Vadrot, Xiang IA Yang & Mahdi Abkar(2022) "A survey of machine learning wall models for large eddy simulation" *arXiv preprint arXiv:2211.03614*

Jerome H Friedman(2000) "Greedy Function Approximation: A Gradient Boosting Machine", *Annals of Statistics*, **29**, 1189–1232

Tianqi Chen and Carlos Guestrin(2016) "XGBoost", *Proceedings of the 22nd ACM SIGKDD International Conference on Knowledge Discovery and Data Mining*

2nd Spanish Fluid Mechanics Conference
Barcelona (2 - 5 July 2023)

Analytical solutions for vanadium membraneless micro redox flow batteries operating under different current regimes

Miguel de las Heras[1], Santiago E. Ibánez[2], Marcos Vera[3], and Alberto E. Quintero[1]

miguel.delasheras@b5tec.com

[1]R&D Department, Micro Electrochemical Technologies S.L., Avenida de Juan Caramuel, 28919, Leganés, Spain
[2]Repsol Technology Lab, Agustín de Betancourt S/N, 28935, Móstoles, Madrid, Spain
[3]Departamento de Ingeniería Térmica y de Fluidos, Universidad Carlos III de Madrid, Av. de la Universidad 30, Leganés, 28911, Spain

Redox flow batteries are a promising storage technology to tackle the intermittency of renewable sources. Vanadium micro redox flow batteries could potentially save costs by removing expensive membranes through the use of laminar flows at the micro scale to prevent turbulent mixing and mitigate diffusive mixing which is ultimately responsible for self discharge and inefficiency. A simple model for this system is obtained under symmetric conditions and analytical solutions are derived for different models of the electric current in terms of relevant non-dimensional groups that provide great insight into the best possible performance values and overall system characteristics.

1 Introduction

Redox flow batteries (RFBs) are a promising technology to meet the intermittency requirements of renewable energy. These endure much longer life cycles than lithium batteries and offer significant cost reductions in capacity storage, while allowing to diminish dependence on raw materials thanks to electrolyte recyclability. In the most common configuration, anolyte and catholyte are circulated back and forth between large tanks and a reactor through separated circuits. In the reactor, a selective membrane separates the negative and positive electrolytes while allowing the passage of electric current (1).

Selective membranes are not ideal and do allow a small amount of electrolyte crossover. They are also costly and increase ohmic battery resistance, decreasing its performance. In membraneless micro flow batteries this element is omitted and instead, two parallel streams of anolyte and catholyte are flowed in contact at low Reynolds numbers which prevent mixing among them while preserving good conductivity properties. All-Vanadium electrolytes are often used in these RFBs because any electrolyte mixing does not degrade the electrolytes. When charged electrolytes enter in contact, the chemical energy accumulated within them is released through self discharge reactions which reduce the efficiency of the battery but do not degrade the electrolytes.

Key metrics in vanadium flow batteries are the state of charge for the negative and positive electrolytes, namely:

$$\mathrm{SoC}_{23}^t = \frac{c_2^t}{c_2^t + c_3^t} \tag{1}$$

$$\mathrm{SoC}_{45}^t = \frac{c_5^t}{c_5^t + c_4^t} \tag{2}$$

where c_2^t, c_3^t, c_4^t and c_5^t are concentrations of V(II), V(III), V(IV) and V(V) in the electrolyte tanks. The quantities (1)-(2) can be obtained through simplified models without CFD simulations, saving much time and computational resources. When symmetric states of charge are assumed (i.e. $\mathrm{SoC}_{23}^t = \mathrm{SoC}_{45}^t$) a simple ODE linear system is derived by writing mass conservation equations for every vanadium ion, accounting for the main phenomena occurring in membraneless vanadium redox flow batteries:

$$\frac{\mathrm{d}c_{25}^t}{\mathrm{d}t} = \frac{Q(c_2 - c_2^t) - (\alpha_{34} + 2\alpha_{25}) + I/F}{V_t} \tag{3}$$

$$\frac{\mathrm{d}c_{34}^t}{\mathrm{d}t} = \frac{Q(c_3 - c_3^t) + (2\alpha_{34} + 3\alpha_{25}) - I/F}{V_t} \tag{4}$$

$$\frac{\mathrm{d}c_{25}}{\mathrm{d}t} = \frac{Q_(c_2^t - c_2) - \alpha_{25}}{V_c/2} \tag{5}$$

$$\frac{\mathrm{d}c_{34}}{\mathrm{d}t} = \frac{Q(c_3^t - c_3) - \alpha_{34}}{V_c/2} \tag{6}$$

where (3), (4) are mass balance equations for ions V(II) (and V(V)) and V(III) (and V(IV)) in the tanks

and (5), (6) are the corresponding equations in the reactor. The model is completed with reactor and tank volumes V_c and V_t as well as the flow rate Q. Terms α_{25} and α_{34} are the diffusive vanadium fluxes of vanadium V(II)/V(V) and V(III)/V(IV) respectively for a bidimensional planar electrode cell (2), which can be calculated from the relevant ionic transport equations as (3):

$$\alpha_i = c_i DWL\sqrt{\frac{\mathrm{Pe}}{\pi}\beta},\ i = \{2,3,4,5\} \tag{7}$$

where c_i is the corresponding reactor concentration, D is the mean diffusion coefficient of all vanadium species, $\mathrm{Pe} = (Uh)/D = Q/(WD)$ is the Peclet number expressing the ratio of electrolyte advection to transversal ion diffusion in the channel, $\beta = L/h$ is the ratio of channel length to width and W is reactor height. Diffusive fluxes in (5), (6) account for diffusive mixing in the reactor, whereas in (3),(4) they account for self discharge reactions occurring in tanks. The equivalent molar flux of charged species produced by an applied electric current is I/F. We analyze two electric current models, each one leading to a linear ODE system with different eigenvalues and eigenvectors

$$I = A(\text{const.}) \quad \text{(galvanostatic)} \tag{8}$$

$$I = Ac_{34}FDW\,(\mathrm{Pe})^{\varphi}\,(\beta)^{1-\varphi} \quad \text{(generic)} \tag{9}$$

the electric current law in (9) can represent a typical scenario such as limiting current in a planar electrode reactor ($A = 1.47$, $\varphi = 1/3$ (4)) or a stoichiometric reactor that transforms all entering ions into current ($A = 1$, $\varphi = 1$). This general expression can also be used to explore the limiting current behaviour of a porous electrode, which is expected to be an intermediate case between the previous two. In (8),(9) it is assumed that the battery is under charging operation, but corresponding expressions for discharge operation can be obtained by changing sign and substituting $c_{34} \mapsto c_{25}$.

The aforementioned ODE system (3)-(6) is dependent on the following non-dimensional groups after suitable normalization:

$$\nu = \sqrt{\frac{\beta}{\pi\mathrm{Pe}}},\ \mathrm{V} = \frac{V_t}{V_c/2},\ A,\ \varphi,\ \bar{c}_i(\tau=0) = \frac{c_i(\tau=0)}{c_0}$$

where $\tau = t(Q/V_t)$ is the non-dimensional time variable and c_0 is total vanadium concentration.

This model provides estimates for characteristic charging and discharging times, coulombic efficiencies and maximum attainable states of charge in membraneless vanadium micro flow batteries for the first time in analytical form. For example, the stationary behaviour in charge for an ideal reactor charging the maximum amount of vanadium possible is:

$$\mathrm{SoC}_\infty = \frac{1-\nu}{1+2\nu} \tag{10}$$

such that $\mathrm{SoC}_\infty \to 100\%$ when $\nu \to 0$ (i.e. there is no upper limit on the state of charge). By contrast, a planar electrode at limiting current yields:

$$\mathrm{SoC}_\infty = \frac{1.47\pi^{2/3}\nu^{1/3} - 1}{2 + 1.47\pi^{2/3}\nu^{1/3}} \tag{11}$$

which yields a maximum value of $\mathrm{SoC}_\infty \to 18\%$ when $\nu \to \nu_{\max} \approx 0.122$, this value can be derived by a scaling argument restraining the width of the mixing layer in the reactor of the channel to keep the negative and positive electrolytes well separated (3). Abandonment of the planar electrode concept is recommended for vanadium micro flow batteries, and instead implementing architectures with porous electrodes is suggested to increase stored capacity. Further improvements will consider more realistic scenarios where the electric current is controlled by voltage and limited by kinetic and electric conductivity considerations.

References

[1] Perry M. and Weber A. (2015) "Advanced Redox-Flow Batteries: A Perspective". *Journal of The Electrochemical Society*, **1**, A5064–A5067.

[2] Ferrigno R. et al. (2002) "Membraneless Vanadium Redox Fuel Cell Using Laminar Flow". *Journal of the American Chemical Society*, **124**, 12930-1.

[3] Ibáñez S.E and Quintero A.E. and García-Salaberri P. and Vera M. (2021) "Effects of the diffusive mixing and self-discharge reactions in Microfluidic Membraneless Vanadium Redox Flow Batteries". *International Journal of Heat and Mass Transfer*, **170**.

[4] Braff W.A. (2014) "Membraneless Hydrogem Bromine Laminar Flow Battery for Large-Scale Energy Storage", PhD Thesis, Massachusetts Institute of Technology.

2nd Spanish Fluid Mechanics Conference
Barcelona (2 - 5 July 2023)

Comparison of predictive models for influent parameters in the inflow of Water Resource Recovery Facilities

Alejandro González Barberá[1], Sergio Iserte Agut[1,3], Luís García García[2], Federico Piñuela García[2], and Sergio Chiva Vicent[1]

gonzalal@uji.es

[1]Department of Mechanical Engineering and Construction, Jaume I University, Spain
[2]IT Department, FACSA, Spain
[3]Barcelona Supercomputing Center, Spain

This study delves into the use of data exploration and predictive models, including machine learning algorithms such as XGBoost and deep learning neural networks named Long Short-Term Memory (LSTM), to predict the water inflow for Water Resource Recovery Facilities (WRRF). Specifically, it focuses on two influent parameters - inflow water and rain gathered - and utilizes a historical dataset spanning five years to build the predictive model. The model's validation is done with more recent cases and data from other WRRFs, and it shows promise in helping technicians properly configure WRRF in areas with infrequent but potentially damaging rain events.

1 Introduction

In Water Resource Recovery Facilities (WRRF) wasted water is treated by physical, chemical and, biotechnological methods so as to reduce contamination. In these facilities, several sensors can be found to monitor a wide range of parameters. In this reserach, two influent parameters are leveraged to model the inflow. The chosen parameters are the inflow water and the rain gathered, specifically we have at our disposal a historical of five years. Initially, the hypothesis was that with this saved data, a predictive model can be built to predict the future inflow water.

The WWRFs studied in this work are situated along the Mediterranean coast of Spain. In this area the annual rain is gathered only in one percent of the days, but these intervals can even produce floods. For the mentioned reason, predicting this water inflow in rainy intervals can give valuable insights to the technicians.

2 Experiments

In this section, we introduce both, methods which includes different predictive models approaches and the results achieved with these models.

2.1 Methods

We configured and trained three different models: recurrent neural network based on LSTM layers Nguyen et al. (2021), a statiscal tool called Prophet Taylor and Letham (2018) and the gradient boosting tree named XGBoost Chen and Guestrin (2016). All three models have been optimized with the best hyperparameters for our dataset using Optuna framework.

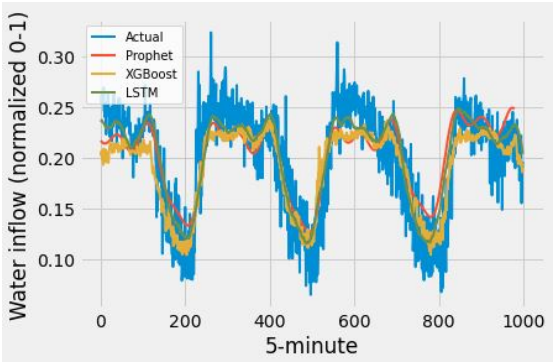

Figure 1: Model predictions comparison for non-raining conditions.

2.2 Experimental results

The experiments have been performed feeding the models with both, non-raining and raining conditions. Figure 1 shows a three days predictions with the absence of rain, where all three models were able to make accurate predictions. Nevertheless, Figure 2 shows a two day rainy interval and, while LSTM and Prophet were not effective, XGBoost demonstrated promising results. Notice that both, rainfall and inflow water were normalized with values one to

cero to reach better performance in the model and to anonymize data.

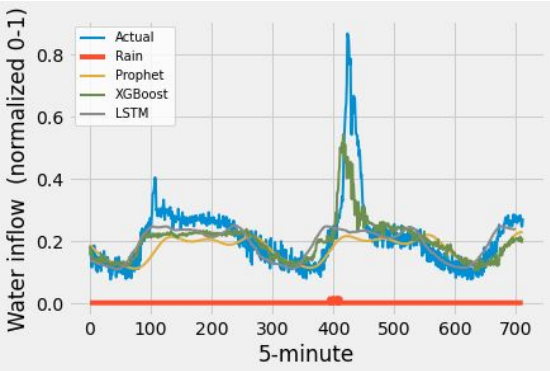

Figure 2: Model predictions comparison for raining conditions.

In addition, to evaluate the performance of these models, we used two error metrics. On the one hand, R^2 which shows the proportion of inflow water variation from rainfall. On the other hand, Mean Absolute Percentage Error (MAPE) which shows the percentage of deviation between the actual value and the prediction. With R^2, higher values are known as the best but with MAPE, lower values indicate better performance. Table 1 contains the errors from the different models in the two cases. As noted in the first figure, all models worked with the same performance as can be seen in the right columns. Notwithstanding, where the difference between models stepped up was when the rain appears. Indeed, it can be seen that XGBoost has the highest result in R^2 and the lowest in MAPE.

	Raining		Non-raining	
	R^2	MAPE	R^2	MAPE
Prophet	0.286	0.324	0.764	0.116
LSTM	0.288	0.405	0.771	0.137
XGBoost	0.668	0.228	0.752	0.128

Table 1: Models performance under rainy and non-raining conditions.

On top of that, we have leveraged XGBoost model to evaluate other WRRFs. In Figure 3 results are shown for a 6 days prediction with rainy conditions. For this case, we got such similar results with 0.645 and 0.258 values of R^2 and MAPE respectively.

3 Conclusions and future work

All things considered, the initial hypothesis was correct, which means that with a historical data of inflow water and rain, a model can be trained in order to predict future inflow water. Moreover, XGBoost has demonstrated to be suitable for this endeavour.

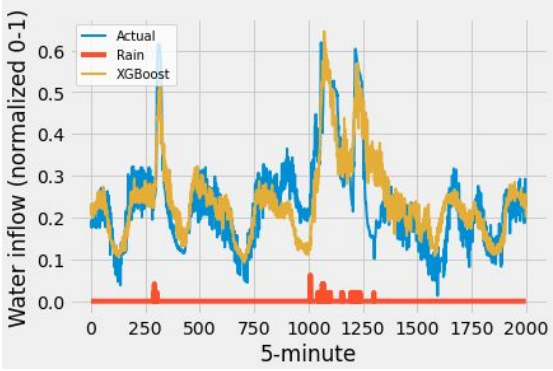

Figure 3: Model predictions validation with another WRRF.

Having only data from only one weather station cannot represent the watershed. So, our aim is to gather more information from several devices and try to improve the overall accuracy of our best model. Furthermore, it could be interesting to give a chance to some new state-of-the-art models such as Transformers Li et al. (2022) or try to create synthetic data so as to fix the imbalance problem Herrera et al. (2018).

References

Chen T, Guestrin C. (2016) "XGBoost: A Scalable Tree Boosting System". In: Proceedings of the 22nd ACM SIGKDD International Conference on Knowledge Discovery and Data Mining. San Francisco, CA, USA, 13–17 August 2016.

Taylor SJ, Letham B. (2018) "Forecasting at Scale". *The American Statistician*, **72(1)**, 37–45.

Nguyen T, Duong Q, Tran Q, et al. (2021) "LSTM-based prediction model for electricity consumption in Vietnam". *Sustainable Energy, Grids and Networks*, **28**, 100496.

Alvarez-Miranda E, Cano-Izquierdo J, Nogales-Gómez A, et al. (2022) "LSTM-based time series forecasting of environmental variables in precision agriculture". *arXiv preprint* arXiv:2205.13504.

Li K, Lu Z, Yang Y, et al. (2022) "Are Transformers Effective for Time Series Forecasting?". *arXiv preprint* arXiv:2204.04831.

Herrera F, Ventura S, Chawla NV, et al. (2018) "Resampling strategies for imbalanced time series forecasting". *Applied Soft Computing*, **69**, 743–754.

2nd Spanish Fluid Mechanics Conference
Barcelona (2 - 5 July 2023)

Control of facility´s humidity using a digital twin based on Deep Learning and CFD simulations

Jaume Luis-Gómez[1], Raúl Martínez-Cuenca[1], Francisco Martínez[2], Javier Mascarós[2], Óscar Prades-Mateu[1], Elisa Borràs[2], and Sergio Chiva[1]

jaluis@uji.es

[1]Departamento de Ingeniería Mecánica y Construcción, Universitat Jaume I, Spain
[2]Departamento de Mantenimiento, Oceanogràfic de Valencia, Spain

This study has the aim of developing a functional digital twin based on CFD simulations of a maintenance room in order to control the air circulation system to prevent vapour condensation. The digital twin will use Deep Learning to predict the state of the room from real time sensor data.

1 Introduction

The *Oceanogràfic de València* is a scientific, educational and recreational complex of aquariums reproducing ecosystems from all over the world. It is located inside the avant-garde *la Ciutat de les Arts i les Ciències* and constitutes one of the biggest touristic attractions of the city and the biggest aquarium in Europe.

Behind the scenes, there is a huge infrastructure to maintain the complex´s activity, which constitutes a series of underground galleries and rooms of thousands of cubic meters with filters, recirculating pumps, electrical instalations and so on.

From the presence of large free surfaces of water from the aquariums to the maintenance rooms arises a serious problem with the generation of water vapour and its condensation, thus affecting the electrical and mechanical equipments present.

The air circulation system must avoid this condensation by ensuring the correct renovation of air, but also controlling the levels of CO_2 at a minimum operational cost.

The present work belongs to the project *AQUAVENT*, funded by the *Agencia Valenciana de la Investigación*. And it aims to develop a real-time control algorithm for the air circulation system based on a digital twin of a room created from Deep Learning and Computational Fluid Dynamics (CFD) simulations which will use real time data from on-field sensors.

The studied room is shown in Fig. 1. From conventional models and control algorithms, it is not possible to monitor the state of the hole room. A Deep Learning-based digital-twin will be created with in-situ data from sensors and CFD simulations to recreate the velocity, temperature and humidity of the room, thus being able to better control the air circulation flow of the domain and gain energetic efficiency.

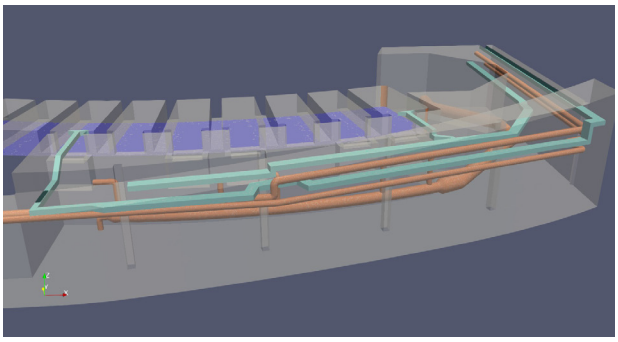

Figure 1: 3D representation of the studied room, in blue, the free surface of water; in orange, the main tubes present and in ligth blue, the air circulation ducts.

2 Field measurements and sensor network

For the characterization of the room, it was first needed to run a series of field measurements. In first place, geometrical data of the facility was taken in order to create the 3D CAD model from scratch. The domain consists of a 5 meter tall clear space with an annexed tunnel whose ceiling grows from 2.5 to 6.5 meters gradually. This constitutes the main room, which is connected to the free surface of the aquarium by seven windows opened into the concrete wall.

Only the bigger elements were reproduced in the CAD: the main tubes, the air circulation ducts from the system, columns and other structural elements. There is a walkway suspended at 4 m, but due to the complexity of the modeling and the negligible effect in

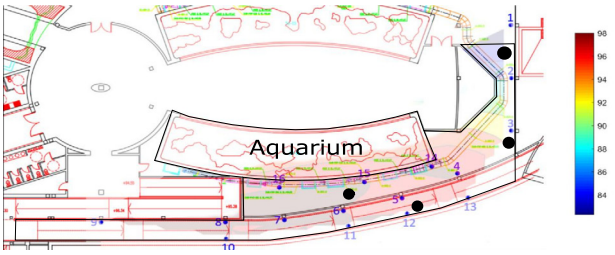

Figure 2: Colour map of the relative humidity measured in the room, in black dots, the positions of the field installed sensors for temperature, humidity and CO_2.

the air circulation, it was eliminated from the CAD.

Also, field temperature and humidity measurements were conducted to identify the humidity sources and study its effect in the domain of study. Fig. 2 shows the colour map of relative humidity in the room, showing a gradient flowing from the near region of the windows to the exit of the room. This measurements were used to conduct and validate preliminary simulations and to quantify the humidity sources.

Finally, a permanent acquisition network has been installed in the domain. The network is composed by 4 sensors for air temperature, relative humidity and CO_2 concentration and 5 velocity sensors. These sensors are constantly sending wireless signals to a radio receiver that sends these signals to a data logger. Once the digital twin is running in a PC, the program will connect to the data logger, read the sensor data and generate predictions for the state of the whole room to generate an instruction for the air circulation system.

3 CFD Simulations

The CFD simulations are executed using the open source OpenFOAM code. The room is assumed to be in a steady state if the air circulation system conditions are static, but there is a heat exchange between the inflow air, the walls and the room´s air. Thus, the buoyantBoussinesqSimpleFoam solver will be used, which treats the fluid as incompressible although the change in density via the Boussinesq assumption:

$$\rho_k = 1 - \beta * (T - T_ref) \quad (1)$$

Being ρ_k the effective density, β the thermal expansion coefficient and T_ref the reference temperature.

The specific vapour $[kg_w/m^3_{air}]$ will be modeled as a transported scalar, with a source placed in the free surface of water. From the temperature and the specific vapour, the relative humidity will be calculated, and also can be checked if there is any condensation from the walls´ temperature.

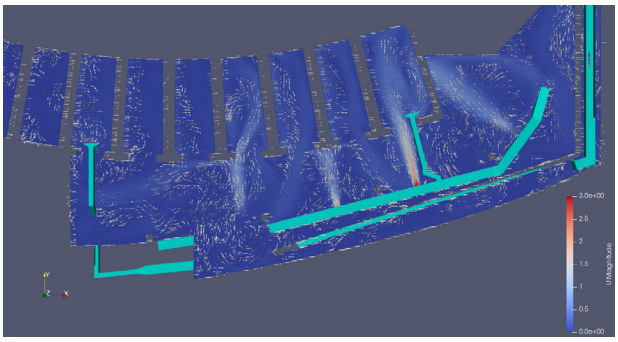

Figure 3: Section plane at 4.6 meters from ground, showing the velocity field with vectors.

Fig. 3 shows the result of a preliminary simulation only with air using the simpleFoam solver. The water´s surface was modeled as a free-slip surface. A fixed flow condition was specified for the inflow and outflow of the air circulation system, from field measurements conducted with an anemometer. Finally, the patch that connects the room with the gallery has been modelled as an opening, thus allowing free flow from or out of the domain. The preliminary simulation was validated using the field velocity sensors installed.

The next step is to conduct a series of simulations combining different flow, temperatures and specific vapour points to train the Neural Network that will act as a digital twin of the system.

4 Future work

Currently, efforts are being made to generate a wide range of simulations with different combinations of air flows, temperature and specific humidity. Once this simulations are finished, following the same approach as in Iserte (2022), one neural network will be trained to infer the velocity and temperature fields from the working state of the air circulation system and the sensor data. The relative humidity will be transported using CFD code over a coarser mesh.

References

Iserte. S (2022) “Accelerating urban scale simulations leveraging local spatial 3D structure”. *Journal of Computational Science*, **62**.

2nd Spanish Fluid Mechanics Conference
Barcelona (2 - 5 July 2023)

Fast urban flow predictions through Convolutional Neural Networks.

Joan Calafell[1], Jaime Bustillo[2], Samuel Gómez[1], Francisco Ramírez[2], Sarath Radhakrishnan[1], and Oriol Lehmkuhl[1]

joan.calafell@bsc.es

[1]Large-Scale Computational Fluid Dynamics Group, Barcelona Supercomputing Center, Spain
[2]Bettair Cities S.L., Spain

Having real-time and accurate numerical predictions of urban wind flow can be extremely useful for developing tools intended to improve citizens' life quality and health. However, traditional methods such as Computational Fluid Dynamics (CFD) are unsuitable for fast prediction. This work proposes using Convolutional Neural Network (CNN) trained with a newly-created vast dataset to enable fast and accurate flow predictions for any urban geometry. The dataset has been generated through high-fidelity CFD simulations of 30 different European Urban areas and 90 meteorological conditions. The geometries were selected to have a wide variety of urban flow patterns and geometrical features allowing the Neural Network (NN) to learn a representative range of urban flow conditions. Then, a CNN was trained to reproduce the urban wind flow for any urban geometry and meteorological condition. The strategy allows for predicting accurate mean wind flow in urban areas that have not been seen in training time, showing good generalization properties.

1 Introduction

Real-time urban wind flow predictions may help improve citizens' life quality and health since they would allow taking instantaneous countermeasures to mitigate urban pollution, for instance. CFD has been traditionally used to have a detailed insight into urban flow behavior. However, CFD is not suitable for fast prediction due to its complexity and computational cost, even using low-fidelity models such Reynolds-Averaged Navier-Stokes. Thus, alternative methods are needed.

In recent years, advances in machine learning (ML) allowed leveraging the enormous volume of data generated through CFD simulations to develop data-driven reduced models to obtain numerical predictions at a reasonable time, cost, and effort (1). Urban flows have not been an exception.

In particular, generative models have been used to produce CFD-approximated solutions. Mokhtar et al. used cGANS to predict the wind flow on urban area patches (2). However, the authors highlighted the necessity of more extensive datasets and point out the unavailability of public urban flow databases(2).

The present work is intended to create a model capable to generate accurate two-dimensional (2D) CFD-like predictions for any urban geometry without needing to perform preliminary CFD studies on it. To do so, a vast dataset with more than 20×10^3 samples has been generated to train a CNN that takes urban geometrical and meteorological parameters as input and produces the corresponding wind flow map for the specified conditions.

2 Dataset Generation

Good Generalization capabilities are one of the main goals of the proposed model. To achieve this target, a careful selection of urban geometries has been carried out. The purpose is to obtain a rich dataset containing a wide range of flow conditions and geometrical features typical of urban areas.

2.1 Geometry selection criteria

Thirty actual European urban areas of 1 km2 have been selected. Statistical analysis has been carried out to select the geometries, ensuring their representativity of the typical urban configurations that can be found in European cities. Specifically, k-means clustering has been performed from geometrical and land use parameters. The geometries showing less uniform distributions and the less cross-correlated ones (which ensures geometrical variety) have been selected.

2.2 High-fidelity wind flow simulations

Then, high-fidelity simulations were performed on the 30 selected geometries with three different wind directions, resulting in 90 micrometeorological conditions. Wall-Modeled Large Eddy Simulation has been performed to ensure accurate mean flow data. The Vreman model has been used as a subgrid model, while an equilibrium wall function with roughness has

been used to deal with the near-wall areas. On the other hand, periodic conditions have been prescribed in the wall-parallel directions while the flow motion has been enforced through a constant pressure gradient. This strategy has been successfully tested to simulate Atmospheric Boundary Layers (3).

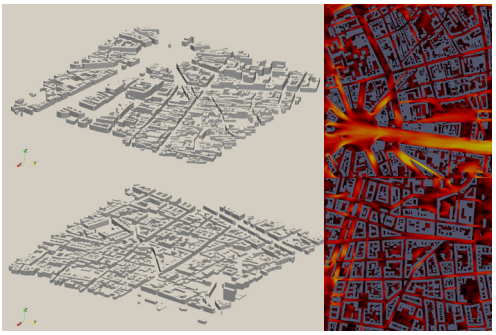

Figure 1: Urban geometry and horizontal-section mean flow dataset samples.

3 Neural Network Architecture

The proposed strategy relies on an image-to-image translation problem. For this purpose, a fully convolutional U-net has been chosen. The NN takes 2D graphical data of the urban geometry at a given height and translates it into a 2D wind flow map.

4 Data Encoding

The target is relating geometrical and meteorological conditions with their corresponding wind flow. For the NN efficiently establish this relation, it is crucial selecting the variables which enclose the most relevant problem information, and encode it into a format that can be used as input for the NN. In the present case, the urban geometrical structure has been represented as a mask distinguishing between fluid/solid areas, and the building height to give the 3D context of the original geometry on which the CFD simulation was performed, and the distance to the solid walls, a flow-relevant quantity. Regarding the meteorological data, the wind direction is assumed to be horizontal. Thus, for different wind directions, the input geometry has to be rotated accordingly. For the wind speed, Re-independence is assumed, and thus, the solution is scaled to match actual conditions.

5 Preliminary results

Preliminary results show that the NN achieves a good generalization degree. In Figure 2, a comparison between the NN-predicted wind field and its corresponding ground truth for a validation dataset sample is shown. However, statistical analysis shows that the model tends to overpredict mid-range wind speed areas and underpredicts extreme wind speed regions (Figure 3).

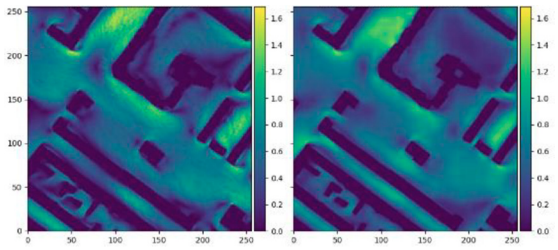

Figure 2: Comparison between the NN wind field output and the corresponding ground truth of a validation dataset sample.

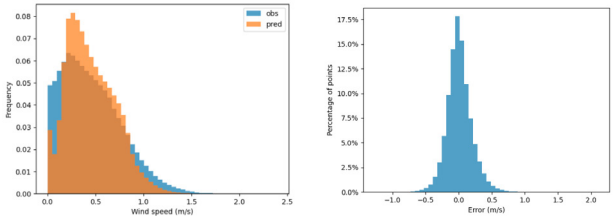

Figure 3: Averaged error frequency distribution as a function of wind speed for all the predicted points in the validation dataset (left) and absolute error frequency across the predicted domain (right)

6 Conclusions

A general predictive wind flow model for urban areas is presented. A vast dataset has been created to obtain good generalization properties for geometries not seen in training time. Reasonable generalization capabilities have been obtained with a large portion of the predicted points in a low error range. However, the NN tends to overpredict mid-range velocities and to underpredict extreme values, especially, low wind speeds. Further improvements will be conducted to enhance the current accuracy.

References

[1] S.L. Brunton et al. Machine Learning for Fluid Mechanics. *Ann Rev Fluid Mech*, Vol. 52(1) (2020) pp. 477-508

[2] S. Mokhtar et al. Pedestrian Wind Factor Estimation in Complex Urban Environments. *13th Asian Conference on ML.* (2021) Vol. 157 pp. 486-501.

[3] H. Owen et al. Wall-modeled large-eddy simulation in a finite element framework. *Int J Numer Meth Fl* Vol. 92 pp 20-37 (2019)

2nd Spanish Fluid Mechanics Conference
Barcelona (2 - 5 July 2023)

Fluid Dynamic Tool for Cardiac Diseases Analysis

Nourelhouda Groun[1], Maria Villalba-Orero[2,3], Enrique Lara-Pezzi[2], Eusebio Valero[4], Jesús Garicano-Mena[4], and Soledad Le Clainche[4]

gr.nourelhouda@alumnos.upm.es

[1]ETSI Aeronáutica y del Espacio and ETSI Telecomunicación - Universidad Politécnica de Madrid, 28040 Madrid, Spain

[2]Centro Nacional de Investigaciones Cardiovasculares (CNIC), C. de Melchor Fernández Almagro, 3, 28029 Madrid, Spain

[3]Departamento de Medicina y Cirugía Animal, Facultad de Veterinaria, Universidad Complutense de Madrid, 28040 Madrid, Spain

[4]ETSI Aeronáutica y del Espacio and Center for Computational Simulation (CCS), 28660 Boadilla del Monte, Spain

Higher Order Dynamic Mode Decomposition (HODMD) is a fully data-driven method widely used in fluid dynamics applications. In this work HODMD is applied for the first time, to the best of our knowledge, for the analysis of cardiac images. This algorithm, which is employed as feature extraction technique, is used to analyze different echocardiography datasets, taken from mice in healthy conditions and mice diagnosed with different cardiac diseases (Diabetic Cardiomyopathy, Obesity, TAC Hypertrophy and Myocardial Infarction). The main purpose of this approach is to identify and extract dominant features related to the various cardiac diseases. which will be used to classify the different cardiac diseases using convolutional neural networks (CNNs).

1 Introduction

Higher Order Dynamic Mode Decomposition (1) is an extension of the well-known fluid dynamic tool dynamic mode decomposition (2). HODMD, which was developed in the field of fluid mechanics, has shown efficiency, accuracy and robustness in numerous applications (4) (turbulent flows, aeroelasticity, bio-inspired marine propulsion...). In this work, and for the first time, the HODMD algorithm is investigated in the medical field, in particular, for the analysis of medical cardiac images. Echocardiography datasets, taken from mice in both healthy conditions and afflicted by different cardiac diseases, were analyzed separately. The HODMD algorithm works on identifying and extracting dominant features related to the different cardiac disease. These extracted features, which will be represented in what is called DMD *modes*, will be used as an input of a convolutional neural network (CNN) for cardiac diseases classification.

2 Methodology

The HODMD technique is a fully data driven method, hence, the data is arranged in matrix form as follows:

$$\boldsymbol{V}_1^K = [\boldsymbol{v}_1, \boldsymbol{v}_2, \ldots, \boldsymbol{v}_k] \quad (1)$$

where v_k is a snapshot collected at time t_k, with $k = 1, \ldots K$. Similarly to DMD, HODMD decomposes the signal into an expansion of M modes $\boldsymbol{u}_m$, each mode has its own amplitude a_m , frequency ω_m and growth rate δ_m as follows :

$$\boldsymbol{v}(t) \simeq \sum_{m=1}^{M} a_m \boldsymbol{u}_m e^{(\delta_m + i\omega_m)(t-t_1)} \text{ for } t_1 \leq t \leq t_1 + T. \quad (2)$$

The HODMD technique considers two main steps:

1. Dimension reduction using the Singular Value Decomposition (SVD) .
2. DMD-d algorithm: Standard Dynamic Mode Decomposition (DMD) + d-time lagged snapshots (Takens' delayed embedding theorem).

A detailed explanation of the methodology can be found in (1).

3 Data and Results

Regarding the data used in this work, it is described as follow: echocardiography datasets consist of video loops taken with respect to: a long axis view (LAX) and a short axis view (SAX), containing up to 300 frames (snapshots). All the frames of each dataset were extracted, cropped, converted to gray scale and arranged in an individual tensor.

The analysis of the echocardiography datasets, have resulted the following:

1. HODMD succeeded in segregating the heart rate components from the respiratory rate components. As can be seen in Fig. (1) there are two separate lines of frequencies, the upper branch representing the heart rate, and the lower branch representing the respiratory rate.

2. The HODMD algorithm was able to identify and extract the main patterns and features associated to each cardiac disease. As can be seen in Fig. (2), the DMD modes are clearly presenting more details and characteristics related to the different pathologies, when compared to the original echocardiography images.

The results included in this document are for LAX data of each healthy, myocardial infarction and obesity. Results of the rest datasets, alongside detailed explanation of the analysis can be found in (3).

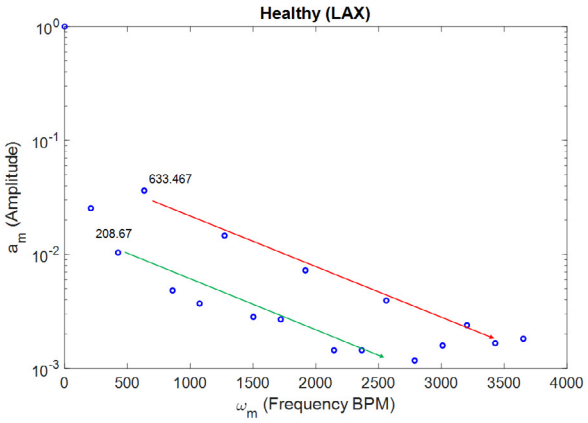

Figure 1: Frequency obtained from the LAX view of the healthy heart dataset.

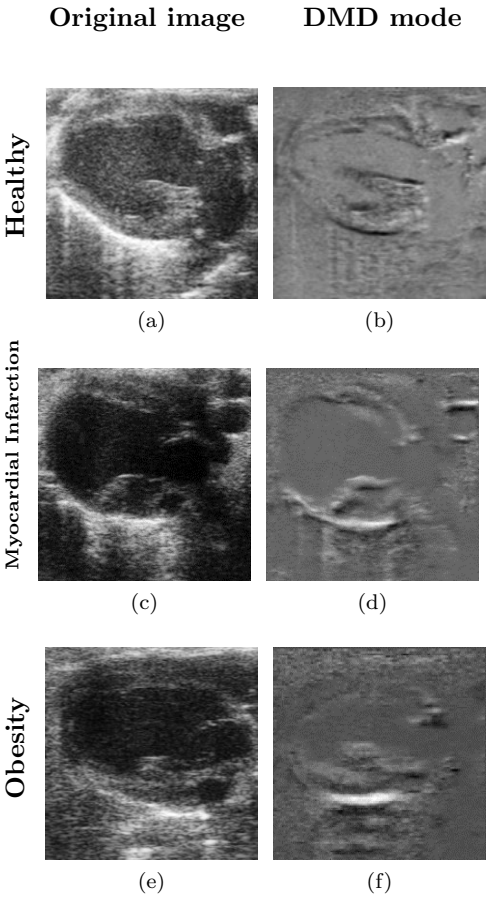

Figure 2: A comparison between the original images (first column) and the DMD modes (second column) provided by the HODMD algorithm, representing the main patterns of hearts in different health conditions: (a),(b): healthy; (c),(d): myocardial infarction, (e),(f): obesity.

References

[1] Le Clainche, S., Vega, J. M. (2017). Higher order dynamic mode decomposition. SIAM Journal on Applied Dynamical Systems, 16(2), 882-925.

[2] Schmid, P. J. (2010). Dynamic mode decomposition of numerical and experimental data. Journal of fluid mechanics, 656, 5-28.

[3] Groun, N.*et al.* (2022). Higher order dynamic mode decomposition: From fluid dynamics to heart disease analysis. Computers in Biology and Medicine, 144, 105384.

[4] Vega, J. M., Le Clainche, S. (2020). Higher order dynamic mode decomposition and its applications. Academic Press.

2nd Spanish Fluid Mechanics Conference
Barcelona (2 - 5 July 2023)

Inclusion of a biochemical model for leveraging data-driven real-time CFD simulations in reactors

Paloma Barreda[1], Sergio Iserte[1,2], Raúl Martínez-Cuenca[1], and Sergio Chiva[1]

pbarreda@uji.es

[1]Department of Mechanical Construction and Engineering, Universitat Jaume I, Spain
[2]Barcelona Supercomputing Center, Spain

In this work, an ASM1 Activated Sludge Model for a bioreactor has been implemented based on the hydrodynamic results previously obtained using a Deep Neural Network (DNN). Through this, it is aimed to continue with the methodology presented in the 1st Spanish Fluid Mechanics Conference based on the use of artificial intelligence to allow the leveraging of data-driven real-time CFD simulations for the control of a bioreactor in a Wastewater Resource Recovery Facility (WRRF).

1 Introduction

CFD simulations have become essential to analyze and reproduce the behavior of models in many fields of study. Among them, is the field of WRRFs, being able to obtain detailed solutions with high temporal and spatial resolution. However, for years it has not been possible to use CFD models for real-time control of the WRRF process units due to the high computational cost and resources of these simulations.

Recent studies such as Guo, Li & Iorio (2016), Kutz, J. N. (2017) & Brunton, Noack & Koumoutsakos (2020), have proven out that by using artificial intelligence techniques, said computing times and resources can be significantly reduced while maintaining the precision of the results.

Through these studies and with the aim of providing real-time snapshots of the hydrodynamic behavior within real Modified Ludzack-Ettinger (MLE) bioreactors, a DNN was implemented to interfer quasi-steady states from a series of input parameters (inlet and recycling flows, and the operating power of submersible mixers inside the reactor). The comparison between the hydrodynamic results obtained through conventional CFD and DNN predictions was presented last year at the 1st Spanish Fluid Mechanics Conference, Barreda P. (2022). As it was shown the implemented DNN was able to reproduce the behavior of the hydrodynamic CFD results.

Hence, to complete the modeling of the MLE bioreactor, it is necessary to include the analysis of the biochemical variables present in the bioreactors. The aim of this work is to reproduce the biochemical behavior of the biorreactor through the implementation of the transport equations of the ASM1 Activated Sludge Model.

2 Materials and methods

The configuration of the selected predicted case is defined by a velocity of 0.216 m/s in the inlet, 0.361 m/s in the recycling and both mixers operating at their usual operative condition. Once the DNN has calculated both the velocity and the turbulence viscosity results of the hydrodynamic model, the transport equation of the ASM1 model is solved.

To solve the 13 differential equations of the ASM1 biochemical model presented in Henze, Gujer, Mino, van Loosdrecht (2000), a new solver has been developed and implemented in OpenFOAM. For the model's stoichiometric and kinetic parameters, the bibliography values at 20 ^{o}C are introduced. For the values of the biochemical variables, those defined in Climent et al. (2018) have been taken into account since they were obtained through experimental measurements in the same bioreactor. The only variables which value was sightly modified were Ammonia (Snh) and Nitrate and nitrite nitrogen (Sno) since it was desired to obtain a visible change in the evolution through time. The new values are shown in table 1.

Parameter	Internal Field	Inlet	Recir
Snh [g N/m^3]	7.6	30	variable
Sno [g N/m^3]	4	0	variable

Table 1: Values of the biochemical variables Snh and Sno for the ASM1 model of the study case.

Figure 1 shows the distribution of the variables Snh and Sno throughout the anoxic tanks after 1 hour.

As it can be observed, as it progresses throughout the bioreactor, the nitrogen nitrate and nitrite (Sno) is degraded due to the lack of oxygen inside the tank. On the other hand, unlike nitrogen nitrate and nitrite (Sno), the variable ammonia (Snh) increases.

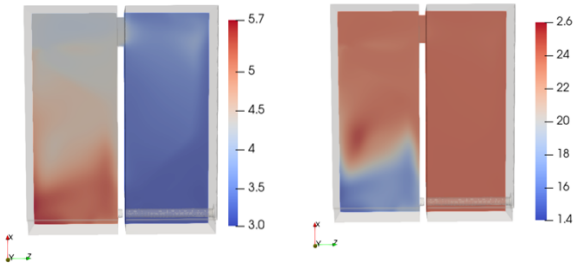

Figure 1: Distribution of the concentration of Sno (left), and Snh (right) throughout the biorreactor at a plane Y=0,97m .

The computational time of the ASM1 simulations is much shorter than the time it takes to solve the hydrodynamic model. In order to know how much the resolution of the ASM1 model can be sped up without compromising the accuracy of the results, different deltaTs are tested: 10 s, 20 s and 40 s. For a deltaT=10 s it takes around 143 s to solve the biochemical model whereas deltaT=40 s takes only 81 s. Since the accuracy of results is not compromised, for conducting the rest of the study it is selected the intermediate value of deltaT=20 s.

Furthermore, to better analyze the optimum behavior inside the bioreactor, a study of the influence of recirculation flow is carried out. Three different cases of recirculation flow are defined: min=0.333 m^3/s, usual=0.361 m^3/s and max=0.4443 m^3/s.

Figure 2 shows the temporary degradation of Sno at a point near the outlet of the biorreactor for the three recirculation flow cases defined.

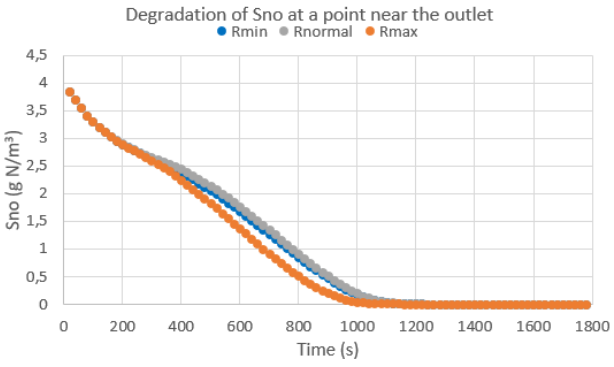

Figure 2: Evolution of Sno at a point near the outlet of the biorreactor.

The three cases present a similar behavior, reaching a total degradation of Sno in about 20 minutes. The case with the maximum flow shows the fastest degradation of Sno, while the normal and minimum flow rates show an almost identical tendency.

3 Conclusions

In the previous work, it was shown how the usage of DNN was more than capable of replicating the behavior of conventional CFD simulations. With the hydrodynamic predictions of the implemented DNN a reduction of almost five orders of magnitude was observed between both simulations. Throughout this work, the inclusion of the biochemical model on those predicted results has been analyzed to finish modeling the reactions that take place inside of biorreactor.

To sum up, a new methodology has been obtained that, with only a couple of minutes, can allow to access real-time information of hydrodynamic and biochemical parameters inside a biorreactor. As future work, a real-time SCADA control can be developed for an actual WRRF so that technicians could have immediate information on the optimal state of operation of the reactor while modifying parameters like the inflow rate, mixers operation, etc.

References

Barreda P., Iserte S., Martínez-Cuenca R., Climent J. & Chiva S. (2022) "Leveraging data-driven real-time CFD simulations in reactors". In SFMC22 Program. ABSTRACT99.

Brunton S. L., Noack B. R. & Koumoutsakos P. "Machine Learning for Fluid Mechanics". *Annual Review of Fluid Mechanics* **52**, arXiv:1905.11075.

Climent J., Basiero L., Martínez-Cuenca R., Berlanga J. G., Julián-López B., & Chiva S. (2018) "Biological reactor retrofitting using CFD-ASM modelling". Chemical Engineering Journal 348.

Guo X., Li X. & Iorio F. (2016) "Convolutional Neural Networks for Steady Flow Approximation". In Proceedings of the 22nd ACM SIGKDD International Conference on Knowledge Discovery and Data Mining (KDD '16). Association for Computing Machinery. 481—490.

Henze M., Gujer W., Mino T. & van Loosdrecht M. (2000) "Activated Sludge Models ASM1, ASM2, ASM2D, ASM3". IWA Publishing.

Iserte S., Carratalà P., Arnau R., Martínez-Cuenca R., Barreda P., Basiero L., Climent J. & Chiva S. (2021) "Modeling of Wastewater Treatment Processes with HydroSludge". Water Environment Research. Wiley Online Library.

Kutz J. N. (2017) "Deep learning in fluid dynamics". *Journal of Fluid Mechanics*, **814**, 1—4.

2nd Spanish Fluid Mechanics Conference
Barcelona (2 - 5 July 2023)

Learning extrapolation in the reconstruction and forecasting of a turbulent velocity flow field using Autoencoders and Singular Value Decomposition

Rodrigo Abadía-Heredia[1,*], Marco Crialesi-Esposito[2,†], Manuel Lopez-Martin[3], Luca Brandt[4,††] and Soledad Le Clainche[5]

[1,3,5]*ETSI Aeronáutica y del Espacio, Universidad Politécnica de Madrid, Plaza Cardenal Cisneros, 3, 28040 Madrid, SPAIN*

[2,4]*FLOW Centre and SeRC, Department of Engineering Mechanics, KTH Royal Institute of Technology, Stockholm, SWEDEN*

[†]*Istituto Nazionale di Fisica Nucleare, Sezione di Torino, Via Pietro Giuria 1, 10125 Torino, ITALY*

[††]*Department of Energy and Process Engineering, NTNU, Trondheim, NORWAY*

Singular Value Decomposition (SVD) [1] is a well-known mode-decomposition method aimed at decomposing a spatio-temporal data set in its dominant flow features, i.e., modes. In this paper we explore the learning extrapolation capability of a Deep Learning (DL) architecture, known as Autoencoder, which is similar to SVD in the sense that it is also capable of compressing and reconstructing a dataset. The main differences between these two models are that, on the one hand, the autoencoders are stochastic, use linear or non-linear functions and need to be trained, and on the other hand, the SVD is deterministic and uses linear functions. This work is focused on comparing the performance of both models either for reconstruction and forecasting tasks. In this meaning, we explore two different architectures of Autoencoders: conv-Autoencoder and dense-Autoencoder. Where the first one is composed by Convolutional layers [2] and the second one by Dense layers. The database we use in this work, to test and compare the performance of both autoencoders and SVD, corresponds to the streamwise velocity of a turbulent flow [3]. We finally show that both Autoencoders (dense and convolutional) can reconstruct the entire data set by training it only with half of the data, in contrast to SVD that requires the whole data set. Also, we show the strength of using convolutional layers to capture some spatial patterns inside the turbulent flow and use them to perform a future prediction, in contrast to both SVD and the dense Autoencoder.

INTRODUCTION

Singular Value Decomposition (SVD) [1] is a well-known mode-decomposition method aimed at decomposing a spatio-temporal data set in its dominant flow features, i.e., modes. However, to decompose and reconstruct a data set, SVD needs the entire data set available. What we propose is to use the learning extrapolation capability of Deep Learning (DL) models to see how well this decomposition and reconstruction, of the entire data set, is performed when these models are trained with both the whole and half the data set.

In this meaning, we use a specific DL architecture known as Autoencoder, which also compresses and reconstructs the dataset. In this work we use two kinds of autoencoders, one that is composed by Dense layers (dense-Autoencoder) and another one that is composed by Convolutional layers [2] (conv-Autoencoder). We show that there exists a trade-off between these two Autoencoders. On the one hand, in the dense-Autoencoder the number of modes in which to compress the data can be directly selected, like SVD. However, this architecture forces the data to be flattened before entering the Autoencoder, which worsens the reconstruction because we lose the spatial information. On the other hand, the conv-Autoencoder does not allow direct selection of the number of modes, but this architecture allows preserving the spatial information, which improves the reconstruction.

On one hand, we show that when the entire data set is used to train both autoencoders, the DL models offers a very similar reconstruction compared to SVD. Furthermore, under certain conditions both autoencoders improve reconstruction compared to SVD, as shown in figure 1 and middle row of table I. On the other hand, when half of the data set is used to train the autoencoders, the reconstruction worsens but they keep a reconstruction error similar to SVD, as shown in figure 2 and top row of Table I. The latter shows how learning extrapolation in DL models can be used to compress and reconstruct the entire data set, when these models are trained on only half of the data.

We also perform another study where we ask both autoencoders and SVD [4] to forecast the velocity flow field at time t_{i+1}, when the past five samples $(t_i, t_{i-1}, t_{i-2}, t_{i-3}, t_{i-4})$ are available. In this work we show how only the conv-Autoencoder + ConvLSTM layer can perform the forecasting. This is due to the combination of the Convolutional layers, which are capable to find the spatial patterns inside the velocity flow field,

and the ConvLSTM layer, which is capable to find the temporal correlation of these spatial patterns.

The database that we use in this work, to test and compare the performance of both autoencoders and SVD, corresponds to the streamwise velocity of a turbulent flow [3].

EQUATIONS, FIGURES AND TABLES

To measure the reconstruction and forecasting errors we use the Relative Root Mean Square Error metric,

$$RRMSE = \frac{\|T_{GT} - \hat{T}\|_n}{\|T_{GT}\|_n}, \quad (1)$$

Where T_{GT} is the ground truth data and $\hat{T}$ is the reconstructed or forecasted data obtained from Autoencoders or SVD. The operator $\|\cdot\|_n$ can be the Euclidean or Frobenius norm. The following Figures and Table shows the RRMSE obtained to measure the reconstruction error of both the Autoencoders and SVD.

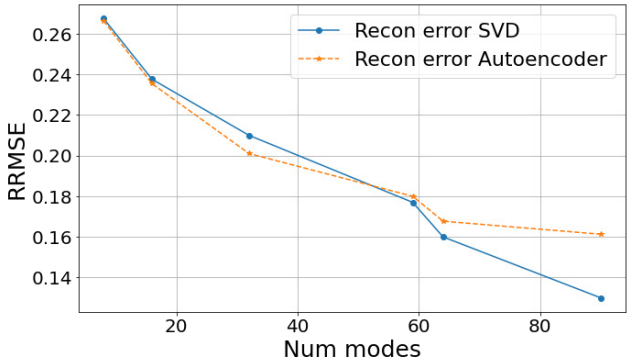

FIG 1. Comparison of the reconstruction error (1) obtained with different selections of the number of modes for the SVD (blue line) and the dense-Autoencoder (orange dotted line) trained on the entire data set.

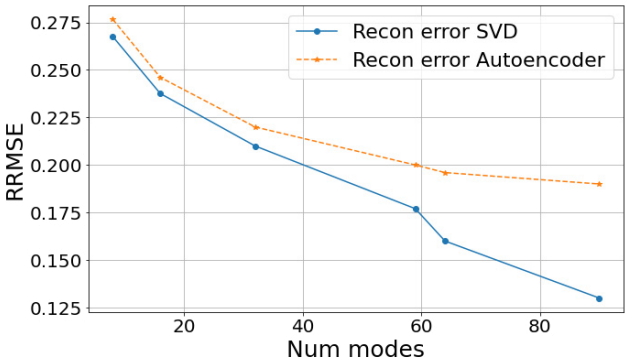

FIG 2. Comparison of the reconstruction error (1) obtained with different selections of the number of modes for the SVD (blue line) and the dense-Autoencoder (orange dotted line) trained on half of the data set.

Model	RRMSE
conv-Autoencoder (Half data set)	0.12917
conv-Autoencoder (Entire data set)	0.09597
SVD (130 modes)	0.09369

TABLE I. Reconstruction error (1) obtained for the conv-Autoencoder trained with half the data set (top), same DL model trained with the entire data set (middle) and SVD with 130 selected modes for compressing data (bottom).

CONCLUSIONS

In this work we show how the combination of the learning extrapolation capability of DL models plus the encoder-decoder architecture of Autoencoders allows to compress and reconstruct a complete dataset, using only half of the data as training, in contrast to SVD. Moreover, by adding the ConvLSTM layer to the conv-Autoencoder. It can make predictions of a future sample given the 5 previous ones, training it with only half of the data set or even less.

—

* sr.abadia@upm.es

[1] Sirovich L. (1987) “Turbulence and the dynamics of coherent structures. Parts I-III”. Quarterly of Applied Mathematics, vol. 45, no. 3, pp. 561–71. JSTOR, http://www.jstor.org/stable/43637457.

[2] Lecun Y., Bottou L., Bengio Y. & Haffner P. (1998) “Gradient-based learning applied to document recognition”. In Proceedings of the IEEE, vol. 86, no. 11, pp. 2278-2324, doi: 10.1109/5.726791.

[3] Crialesi-Esposito M., Pal S., Zaleski S., Brandt L. (2021) “Statistical dispersion of flapping events in air-assisted atomization”. ICLASS, UK, vol. 1, no. 1, paper 425, doi: 10.2218/iclass.2021.6155.

[4] Abadía-Heredia R., López-Martín M., Carro B., Arribas J.I., Pérez J.M., Le Clainche S. (2022) “A predictive hybrid reduced order model based on proper orthogonal decomposition combined with deep learning architectures”, Expert Systems with Applications, vol. 187, 115910, ISSN 0957-4174, doi: 10.1016/j.eswa.2021.115910

2nd Spanish Fluid Mechanics Conference
Barcelona (2 - 5 July 2023)

Machine learning adaptation for laminar and turbulent flows: applications to high order discontinuous Galerkin solvers

Kenza Tlales[1], Kheir-eddine Otmani[1], Gerasimos Ntoukas[1], Gonzalo Rubio[1,2], and Esteban Ferrer[1,2]

kenza.tlales@alumnos.upm.es

[1] ETSIAE-UPM - Escuela Técnica Superior de Ingeniería Aeronáutica y del Espacio, Universidad Politécnica de Madrid, Spain

[2]Center for Computational Simulation, Universidad Politécnica de Madrid, Campus de Montegancedo, Boadilla del Monte, 28660 Madrid, Spain

This study proposes a machine learning-based method for mesh refinement in steady and unsteady flows. The regions to be refined are marked by using a clustering technique presented in [5] to identify viscous and inviscid regions in a flow past a cylinder at different Reynolds numbers. After the regions have been marked, we apply p-refinement within these clustered regions to achieve a similar level of accuracy compared to uniform mesh while reducing computational cost. The data used in this work have been generated using the high-order spectral element CFD solver HORSES3D [3].

1 Introduction

CFD researchers use local refinement to improve accuracy and reduce simulation cost by enhancing mesh quality or polynomial order. To apply local refinement in CFD, criteria are needed to determine refinement location and level. These include feature-based, local error-based, and goal-oriented indicators. Feature-based indicators use physical properties, while local error-based indicators use quantified error. The latter requires multiple mesh solutions and can be costly before achieving a suitable numerical setup.

In this study, we investigate the potential of a clustering technique developed in a previous publication [5] to function as a sensor for mesh adaptation. The clustering method distinguishes between viscous and inviscid regions of flow and is effective in laminar and turbulent scenarios. The Gaussian Mixture Model and feature space used, require no threshold value tuning and are parameter-free. In order to achieve precise and efficient predictions of flow features, we propose the adoption of a dual-polynomial approach, wherein a high-order polynomial approximation is employed for the region that is dominated by viscous effects, while a low-order polynomial approximation is utilized for the inviscid region. As a result of this methodology, we were able to obtain solutions that are equivalent in accuracy to those attained through the use of a uniformly high-order polynomial approximation. The methodology, which is detailed in [6], demonstrates a broad applicability and can be implemented for both laminar-steady and turbulent-unsteady flows.

2 Results and Discussion

In this abstract, we include results for Re=40. See [6] for results at Reynolds 3900. We have applied a mesh refinement strategy to a steady laminar flow around a cylinder at Reynolds number 40. The initial mesh consists of 684 elements with 85500 degrees of freedom, and a uniform polynomial order of $P = 4$ is used to generate steady flow data. The clustered region and the resulting adapted mesh can be visualized in Figure 1, where the high polynomial order is retained in selected elements based on the mean probability of belonging to the viscous rotational region. We have employed $P_{cluster} = 4$ for the viscous regions and $P_{inviscid} \in [1, 2, 3]$ for the inviscid regions in this numerical experiment.

Table 1 presents the computational savings and the corresponding degrees of freedom for each simulation. The adapted solutions with $P_{inviscid} \in [1, 2, 3]$ exhibit a reduction in computational time by 32%, 29% and 19%, respectively, compared to the homogeneous ($P = 4$) solution. Moreover, these solutions require 67%, 55% and 35% fewer degrees of freedom.

Finally, Table 2 presents the drag values obtained from the literature. By comparing the drag coefficients from Tables 1 and 2, it can be observed that both the baseline homogeneous solution with $P = 4$

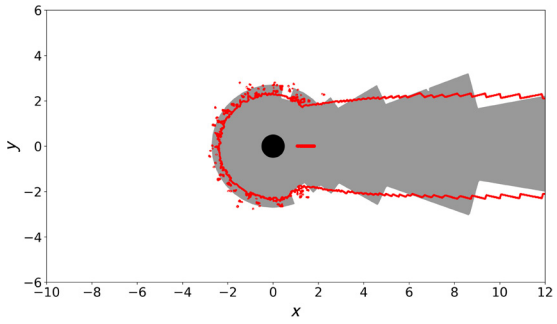

Figure 1: Polynomial order distribution of the adapted mesh for the flow past a cylinder at Re=40. **Grey**: $P_{cluster} = 4$, **White**: $P_{inviscid} \in [1, 2, 3]$, **Red line**: Boundary of the viscous dominated, rotational region detected with GMM.

P_{cluster}	P_{inviscid}	computational time(s)	C_d	DoF
2	2	8.39×10^3	1.5062	18 468r
3	3	1.23×10^4	1.5264	43 776
4	4	2.21×10^4	1.5221	85 500
4	1	1.50×10^4	1.5214	27 936
4	2	1.58×10^4	1.5225	38 460

Table 1: Comparison of the results for the drag coefficient (C_d) for flow past a cylinder at Re=40

and all clustered adapted solutions with $P_{cluster} = 4$ and $P_{inviscid} \in [1, 2, 3]$ accurately predict the drag coefficient.

Case	C_d
Dennis and Chang [2]	1.52
Fornberg [4]	1.50
Choi et al. [1]	1.49

Table 2: Comparison of the results for the drag coefficient (C_d) for flow past a cylinder at Re=40

The results of the first laminar steady case demonstrate the effectiveness of the GMM clustering technique in distinguishing the viscous region (comprising the boundary layer and wake) from the inviscid outer region. The adaptation of the viscous and inviscid regions shows that refining the clustered region improves the accuracy of the simulations by reducing errors in drag. Moreover, the use of clustering adaptation is an efficient technique for mesh adaptation in steady flows, as it accelerates convergence and reduces the computational cost.

3 Conclusions

The presented methodology accelerated fluid flow simulation around a circular cylinder using a local adaptation strategy. The p-adapted solution with polynomial orders of ($P_{cluster} = 4, P_{inviscid} \in [1, 2, 3]$) has similar accuracy as the homogeneous solution with a uniform polynomial order ($P = 4$) while reducing the number of degrees of freedom and computational time (for the Re=40 test case) by up to 67% and 32%, respectively.

This clustering-based adaptation approach is advantageous and does not require a threshold or iterative adaptation process to determine regions for refinement.

References

[1] Jung-Il Choi, Roshan C. Oberoi, Jack R. Edwards, and Jacky A. Rosati. An immersed boundary method for complex incompressible flows. *Journal of Computational Physics*, 224(2):757–784, 2007.

[2] SCR Dennis and Gau-Zu Chang. Numerical solutions for steady flow past a circular cylinder at reynolds numbers up to 100. *Journal of Fluid Mechanics*, 42(3):471–489, 1970.

[3] E. Ferrer, G. Rubio, G. Ntoukas, W. Laskowski, O. A. Mariño, S. Colombo, A. Mateo-Gabín, F. Manrique de Lara, D. Huergo, J. Manzanero, A. M. Rueda-Ramírez, D. A. Kopriva, and E. Valero. Horses3d: a high-order discontinuous galerkin solver for flow simulations and multi-physics applications, 2022.

[4] Bengt Fornberg. A numerical study of steady viscous flow past a circular cylinder. *Journal of Fluid Mechanics*, 98(4):819–855, 1980.

[5] Kheir-Eddine Otmani, Gerasimos Ntoukas, and Esteban Ferrer. Towards a robust detection of viscous and turbulent flow regions using unsupervised machine learning. *arXiv preprint arXiv:2207.02929*, 2022.

[6] Kenza Tlales, Kheir-Eddine Otmani, Gerasimos Ntoukas, Gonzalo Rubio, and Esteban Ferrer. Machine learning adaptation for laminar and turbulent flows: applications to high order discontinuous galerkin solvers. *arXiv preprint arXiv:2209.02401*, 2022.

2nd Spanish Fluid Mechanics Conference
Barcelona (2 - 5 July 2023)

Machine learning based Viscous-Inviscid coupling for high order solvers

Kheir-eddine Otmani[1], Gerasimos Ntoukas[1], and Esteban Ferrer[1,2]

otmani.kheir-eddine@alumnos.upm.es

[1]ETSIAE-UPM - School of Aeronautics, Universidad Politécnica de Madrid, Plaza Cardenal Cisneros 3, E-28040 Madrid, Spain

[2]Center for Computational Simulation, Universidad Politécnica de Madrid, Campus de Montegancedo, Boadilla del Monte, 28660 Madrid, Spain

An unsupevised learning clustering technique has been used to decompose the computational domain into a viscous, rotational region and an inviscid, irrotational region, different sets of equations have been solved in each region namely: the Navier-Stokes in the viscous dominated region and the Euler equation in the outer inviscid region. The methodology has been validated with a LES test case for a flow past a cylinder at $Re = 3900$ showing that the methodology could reduce the computational time up to 12% while maintaining the same level of accuracy.

1 Introduction

Fluid flow simulations are essential for understanding and predicting many phenomena in physical science and engineering. However, the computational cost of high fidelity simulations, such as direct numerical simulations (DNS), is prohibitive for many applications, particularly for turbulent flow simulations. To address this challenge, researchers in computational fluid dynamics (CFD) are exploring the use of data-driven tools, such as machine learning (ML) algorithms, to reduce the computational cost Maulik et al. [2019], Greve et al. [2012], Otmani et al. [2023], Tlales et al. [2022].

One promising approach is to partition the computational domain into different regions where different physical processes occur. This approach allows researchers to reduce the computational time significantly by solving the governing equations only in the relevant regions. Recent work has employed unsupervised learning clustering to identify viscous rotational regions and used them for P-adaptation of high-order methods or coupling Navier-Stokes (NS) and Euler equations to reduce the cost while maintaining accuracy.

In this work, the authors investigate the use of regions identified by clustering techniques to solve the Euler equation in the outer region and the NS equation in the viscous rotational region. The authors aim to achieve the same level of accuracy while reducing the computational cost using a high-order discontinuous Galerkin numerical solver Ferrer et al. [2022]. This approach demonstrates the potential of ML techniques to accelerate CFD simulations and provides a basis for future research in this area.

2 Methodology

To identify different flow regions, we propose in Otmani et al. [2023] to use the principal invariants of the strain and rotational rate tensors as inputs to the gaussian mixture unsupervised model to detect two different regions, a viscous, rotational region on one hand and an inviscid outer region on the other hand. The principal invariants of the strain and rotational rate tensor are defined as follows for incompressible flows:

$$Q_S = \frac{1}{2}(tr((\mathbf{S}))^2 - tr(\mathbf{S}^2)) \;\; ; \;\; R_S = -\frac{1}{3}det(\mathbf{S}),$$

where $\mathbf{S}$ is the strain rate tensor defined as: $\mathbf{S} = \frac{1}{2}(\mathbf{J} + \mathbf{J}^T)$ and $\mathbf{J} = \nabla\mathbf{U}$ is the gradient tensor of the velocity field $\mathbf{U}$. The rotational tensor Ω where $\mathbf{\Omega} = \frac{1}{2}(\mathbf{J} - \mathbf{J}^T)$ has one invariant defined as:

$$Q_\Omega = -\frac{1}{2}tr(\mathbf{\Omega}^2),$$

We train the Gaussian Mixture Model (GMM) with the aforementioned inputs to detect the viscous-dominated regions. The simulations are conducted using a high-order discontinuous Galerkin solver Ferrer et al. [2022], once the clustering with GMM is finished, each data point will be provided with two probability memberships of belonging to the regions of interest. To decide whether a control volume in the computational domain belongs to the inviscid or the viscous region, the mean of membership probabilities $p_{cj}\big|_{j=1}^{N}$, $p_{ij}\big|_{j=1}^{N}$ for each region is computed as follows,

$$\bar{p}_v = \frac{1}{N}\sum_{j=1}^{N} p_{cj}, \qquad p_{cj} \in [0,1], \tag{1}$$

$$\bar{p}_i = \frac{1}{N}\sum_{j=1}^{N} p_{ij}, \qquad p_{ij} \in [0,1], \tag{2}$$

where $N = (P+1)^3$ is the number of points of each element of the mesh, and P denotes the polynomial order associated to the high-order discretization. A control volume will be assigned to the region with the highest mean of membership probabilities $\bar{p} = \max(\bar{p}_i, \bar{p}_v)$. The full NS equation will be only solved in the elements marked as viscous while the Euler equation will be solved in the rest of the domain. In the next section, we apply this methodology to a LES test case of flow past a circular cylinder at $Re = 3900$.

3 Flow past a cylinder at $Re = 3900$

For this test case, The simulation is conducted using high order discontinuous galerkin method with a polynomial order $P = 4$ and a smagorinsky LES model. We perform the clustering methodology described in section 2 for a single snapshot once the flow has been fully developed, the clustering results are shown in figure 1. The full NS is only solved in

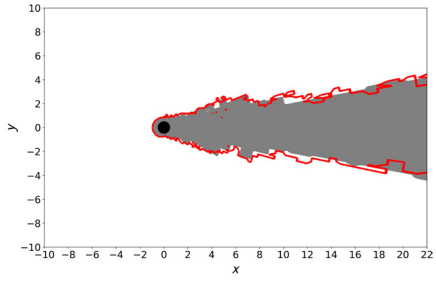

Figure 1: Partitioning of the computational domain for flow past a cylinder at $Re = 3900$. **Grey**: Viscous elements, **White**: Inviscid elements, **Red line**: Boundary of the viscous dominated, rotational/turbulent region detected with GMM

the viscous elements (grey color in figure 1) while in the inviscid elements(white color in figure 1, the Euler equation is solved, the LES model is also deactivated in the inviscid elements, and it is only activated in the viscous elements, for this test case the computational cost is reduced by 12% while maintaining the same level of accuracy. In figure 2, the Q visualizations of both the standard $P = 4$ solution (where the NS equation is solved in the hole computational domain) and the hybrid $P = 4$ solution (where the NS is solved in the viscous control volumes and the Euler equation in the rest of the mesh) are presented.

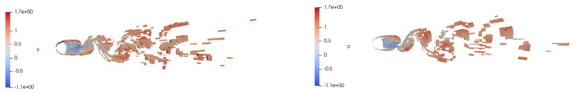

a: Standard uniform $P = 4$ b: Hybrid uniform $P = 4$

Figure 2: an isosurface of the $Qcrit = 0.1$ coloured with the axial velocity u for the standard $P = 4$ solution 2a and the hybrid $P = 4$ solution 2b

4 Conclusions

We have shown that fluid flow simulations can be accelerated using the clustering technique presented in Otmani et al. [2023], the presented methodology solves the full NS equations in the viscous region while in the outer region, the Euler equation is solved, the methodology has been validated with a flow past a cylinder at $Re = 3900$, showing that the simulation has been accelerated by 12% while maintaining the same level of accuracy.

References

Romit Maulik, Himanshu Sharma, Saumil Patel, Bethany Lusch, and Elise Jennings. Accelerating rans turbulence modeling using potential flow and machine learning. *arXiv: Fluid Dynamics*, 2019.

Martin Greve, Katja Wöckner-Kluwe, Moustafa Abdel-Maksoud, and Thomas Rung. Viscous-Inviscid Coupling Methods for Advanced Marine Propeller Applications. *International Journal of Rotating Machinery*, 2012:e743060, July 2012. ISSN 1023-621X. doi: 10.1155/2012/743060. URL `https://www.hindawi.com/journals/ijrm/2012/743060/`. Publisher: Hindawi.

Kheir-Eddine Otmani, Gerasimos Ntoukas, Oscar A. Mariño, and Esteban Ferrer. Toward a robust detection of viscous and turbulent flow regions using unsupervised machine learning. *Physics of Fluids*, 35(2): 027112, 2023. doi: 10.1063/5.0138626. URL `https://doi.org/10.1063/5.0138626`.

Kenza Tlales, Kheir-Eddine Otmani, Gerasimos Ntoukas, Gonzalo Rubio, and Esteban Ferrer. Machine learning adaptation for laminar and turbulent flows: applications to high order discontinuous galerkin solvers, 2022. URL `https://arxiv.org/abs/2209.02401`.

E. Ferrer, G. Rubio, G. Ntoukas, W. Laskowski, O. A. Mariño, S. Colombo, A. Mateo-Gabín, F. Manrique de Lara, D. Huergo, J. Manzanero, A. M. Rueda-Ramírez, D. A. Kopriva, and E. Valero. Horses3d: a high-order discontinuous galerkin solver for flow simulations and multi-physics applications, 2022. URL `https://arxiv.org/abs/2206.09733`.

2nd Spanish Fluid Mechanics Conference
Barcelona (2 - 5 July 2023)

Optimisation of open-loop control of convective heat transfer with genetic algorithms

Rodrigo Castellanos[1,2], Juan Alfaro[1], Isaac Robledo[1], Andrea Ianiro[1], and Stefano Discetti[1]

rcastell@ing.uc3m.es — rcasgar@inta.es

[1]Department of Aerospace Engineering, Universidad Carlos III de Madrid, Leganés 28911, Spain
[2]Theoretical and Computational Aerodynamics Branch, Flight Physics Department, Spanish National Institute for Aerospace Technology (INTA), Torrejón de Ardoz, Spain

An artificial intelligence approach based on linear genetic algorithm control is utilised to enhance the convective heat transfer in a turbulent boundary layer on a flat plate. The actuator consists of six fully-modulated slot jets in crossflow, which are aligned with the freestream. The cost function includes wall convective heat transfer rate and energy consumption of the actuation. Performance evaluation is conducted using infrared thermography and the interpretation of the control effects is carried out with particle image velocimetry measurements. The algorithm converges to the same frequency and duty cycle for all actuators, with the phase difference between multiple jet actuation driving flow asymmetry. The study highlights the potential of machine learning control and advanced measurement techniques in experimental investigations.

The control of turbulent flows based on artificial intelligence has gained interest due to its versatility and superlative capabilities to deal with the complexity imposed by the non-linearity, time-dependence, and high dimensionality inherent to the Navier-Stokes equations (1). In this work, we enhance the convective heat transfer in a turbulent boundary layer (TBL) using a model-free self-learning method based on linear genetic algorithm control (LGAC).

The experiments are carried out in the Universidad Carlos III de Madrid wind tunnel. The TBL develops on a smooth flat plate spanning the entire width of the test section. The unperturbed boundary layer has a friction Reynolds number $Re_\tau \approx 876$ and a thickness of 26.3mm, setting the freestream velocity at $U_\infty = 12.1$m/s. The plate is equipped with a 3D-printed flush-mounted module containing a spanwise array of 6 streamwise-aligned slots and a wall heat-flux sensor, as shown in figure 1. The slot jets feature a rectangular cross-section of 25mm in length and 1mm in width. The slots are aligned in the streamwise direction with a centre-to-centre spacing between adjacent slots of 7.5mm. The actual spacing corresponds to approximately one-third of the boundary layer thickness, which is a trade-off between large spacing to allow full development of the jet-induced flow downstream, and short spacing to ensure the interaction between adjacent jets. A flow regulator monitors the flow properties such as absolute pressure, mass or volumetric flow rate, and temperature of the flow feeding the slot jets. The convective heat transfer distribution is measured using a heated-thin-foil (HTF) heat-flux sensor (2) located downstream of the slots. Surface temperature measurements of the sensor are performed with an IR camera. Through an energy balance of the HTF, it is possible to extract the convective heat transfer coefficient distribution downstream of the actuators.

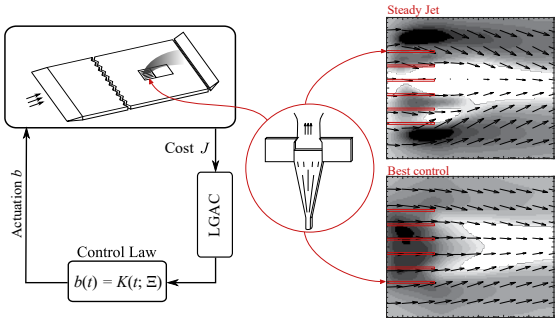

Figure 1: Schematic of the convective heat transfer control using an array of six slot-jets in crossflow controlled by a linear genetic algorithm control (LGAC) algorithm. On the right, a miniature of the velocity field for the steady jet and the best control is included.

The jets are divided into two groups, assigning independent control laws, b_1 and b_2 for odd and even jets, respectively. The actuation is achieved by the full modulation of the jet in crossflow by means of an open-loop optimal periodic forcing defined by the carrier frequency f, the duty cycle DC and the phase difference ϕ between actuators as control parameters

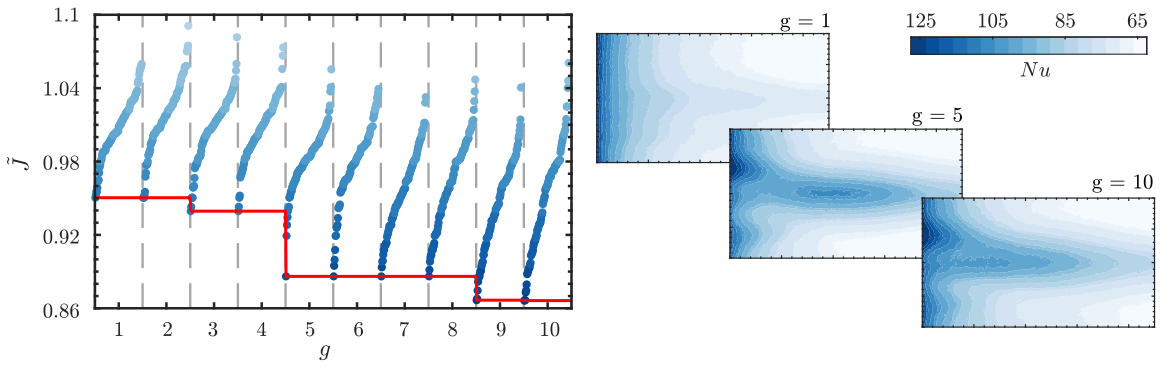

Figure 2: Optimisation process of the LGAC algorithm. (Left) progress of the cost function J along the generation. (Right) evolution of the Nusselt number distribution downstream the actuators for three selected generations.

($\Xi = [f_1, f_2, DC_1, DC_2, \phi]$). The control laws are optimised with respect to the unperturbed TBL and actuation with a steady jet. The optimisation process is driven by the cost function J, defined as a multi-purpose function that includes the wall convective heat transfer rate and the cost of the actuation. The performance of the controller is quantified by infrared thermography, providing the value of the convective heat transfer coefficient in its dimensionless form, the Nusselt number Nu. The perturbed flow field is characterised by particle image velocimetry measurements to assess the flow topology upon the action of the jets.

The action of the jets considerably alters the flow topology compared to the steady-jet actuation, as illustrated in figure 1. The LGAC controller progressively learns the best set of control parameters for the convective heat transfer enhancement problem (see figure 2, which illustrates the normalised cost $\tilde{J} = J/J_0$ with respect to the steady jet). Each point represents an individual within a given generation g, being sorted by its cost value. After a few generations, the controller converges to a characteristic actuation frequency and duty cycle, while the rest of the learning process is used to tune the phase between odd and even jets. It is worth noting that it is a common practice to fix the phase among actuators to reduce the complexity of the control optimisation problem. Our results indicate that the optimal frequency and duty cycle are identified relatively early in the optimisation process, and that relevant performance improvement can be obtained by fine phase tuning. Interestingly, the preferred frequency found by the machine-learning algorithm coincides with that identified in our previous experimental investigation employing a single jet (3). It is noted that such frequency is strikingly equal to the inverse of the characteristic travel time of large-scale turbulent structures advected within the near-wall region. The results pinpoint the potential of machine learning control in unravelling unexplored controllers within the actuation space.

The proposed study is subjected to several technical and fundamental assumptions associated with the formulation of the optimisation problem, the implementation of LGAC to an experimental plant or even the interpretations of results. Yet, our study demonstrates the viability of employing sophisticated measurement techniques together with advanced algorithms in an experimental investigation of a complex flow control problem. The results encourage exploring the full potential of the machine-learning-based control for heat transfer applications by extending the search space, e.g. by including feedback from sensor signals or multi-frequency forcing.

Acknowledgments: The work has been supported by the project ARTURO, ref. PID2019-109717RB-I00/AEI/10.13039/501100011033, funded by the Spanish State Research Agency.

References

[1] Brunton, S. L., Noack, B. R. & Koumoutsakos, P. (2020): Machine Learning for Fluid Mechanics *Annu. Rev. Fluid Mech.*, 52, 477-508.

[2] Astarita, T.& Carlomagno, G. M. (2012): *Infrared thermography for thermo-fluid-dynamics*, Springer Science & Business Media.

[3] Castellanos R., Salih G., Raiola M., Ianiro A. & Discetti S. (2023): Heat transfer enhancement in turbulent boundary layers with a pulsed slot jet in crossflow. *Appl. Therm. Eng.*, 219, 119595.

2nd Spanish Fluid Mechanics Conference
Barcelona (2 - 5 July 2023)

Study of the dispersion of pollutant over fence a using DALES and High Order Dynamic Mode Descomposition (HODMD) analysis

Juan Sánchez Martínez[1], Pedro Costa[2], Jasper Tomas[3], Soledad Le Clainche[1], and Mathieu Pourquie[2]

juan.sanchez.martinez@alumnos.upm.es

[1]Departamento de Matematica Aplicada, Universidad Politécnica de Madrid, Spain
[2]Process Energy Dept. TU Delf, Netherlands
[3]National Institute for Public Health and the Environment (RIVM)

15-03-2023

The concentration of pollutants in urban environments has become a growing concern due to their potential health risks to the population. Understanding the impact of weather conditions and obstacles on pollutant dispersion is crucial to developing effective mitigation strategies. This study aims to build on previous research by Tomas, who investigated pollutant dispersion over a fence Tomas (2015). We will replicate Tomas' work using both the modified DALES 2014 code and the current open-source DALES. Next, we will perform data analysis on the results using higher order dynamic mode decomposition (HODMD), a proven technique (Le Clainche (2020)) that allows for the identification of patterns and locations of instability in the system. By replicating and analyzing Tomas' results, this study will provide valuable insights into the physics of pollutant dispersion and inform the development of more effective mitigation strategies.

1 Introduction

The dispersion of pollutants in urban environments is a significant problem affecting the health and well-being of inhabitants. In recent years, researchers have focused on understanding the impact of obstacles and atmospheric stratification on the dispersion of pollutants. The presence of obstacles can affect the fluid's mixability and enhance pollutant dispersion, while stratification can decrease it.

The present study aims to analyze the dispersion of pollutants in an urban environment using DALES and HODMD techniques. The study is based on the research conducted by Tomas Tomas (2015), which investigated the impact of stratification and obstacles on pollutant dispersion.

2 Metodology

Tomas conducted various studies to understand the impact of stratification on pollutant dispersion. In this study, we focus on the case where a fence was present. The results of the study were analyzed using DALES and Tomas' version of DALES. HODMD was used to obtain patterns of pollutant dispersion behavior.

The results of the present study showed that the level of stratification had a significant impact on pollutant dispersion. The concentration of pollutants in the stratified case was 2.5 times higher than that in the neutral case. The DALES and Tomas' version of DALES showed similar results, as it can be seen in table 1

Richardson	0.049	0.098	0.147
$C_1/C_{neutral}$	1.3	1.62	2.27
$C_2/C_{neutral}$	1.32	1.69	2.81

Table 1: Concentration of pollutant for diferent levels of estratification

3 Conclusions

The present study analyzed the dispersion of pollutants in an urban environment with the presence of a fence using DALES and HODMD techniques. The study showed that the presence of obstacles and atmospheric stratification had a significant impact on pollutant dispersion. The findings of the study can be used to develop effective strategies for controlling pollutant dispersion in urban environments.

HODMD is a relatively new technique in the field of data analysis, and its application to the study of pollutant dispersion in urban environments is an exciting development. HODMD can analyze complex, high-dimensional data and extract patterns of behavior in a system. This technique can provide valuable insights into the behavior of pollutants, their interactions with obstacles, and their dispersion in urban environments. Additionally, HODMD can aid in the development of effective strategies for controlling pollutant dispersion in urban environments.

Future research could focus on the impact of various obstacles and atmospheric conditions on pollutant dispersion using advanced techniques.

References

Tomas J. & M.J.B.M. Pourquie & H.J.J. Jonker(2015) "The influence of an obstacle on flow and pollutant dispersion in neutral and stable boundary layers".

Le Clainche, Soledad & Vega De Prada, Jose Manuel(2017) "Higher order dynamic mode decomposition to identify and extrapolate flow patterns' "Physics of Fluids", v. 29 (n. 8); pp.. ISSN 1070-6631. https://doi.org/10.1063/1.4997206.

2nd Spanish Fluid Mechanics Conference
Barcelona (2 - 5 July 2023)

Turbulent Closure for Sediment Transport Using Symbolic Regression Based on DNS Data

Yvonne Stöcker[1,2], Christian Golla[1], Ramandeep Jain[1], Jochen Fröhlich[1], and Paola Cinnella[3]

yvonne.stoecker@tuwien.ac.at

[1]Institute of Fluid Mechanics, Technische Universität Dresden, Germany
[2]Institute of Fluid Mechanics and Heat Transfer, Technische Universität Wien, Austria
[3]Institut Jean le Rond d'Alembert, Sorbonne Université, Paris, France

This work aims to improve the turbulence modelling in RANS simulations for particle-laden flows. Using DNS data as reference, the error of the model assumptions for the turbulence transport equation is extracted and serves as target data for a machine learning process called SpaRTA. The resulting corrective algebraic expressions are implemented in the RANS solver SedFoam-2.0 for cross-validation.

1 Introduction

Transport of heavy particles of a sediment by a shear flow above represents a phenomenon which is still not fully understood. Jain et al. (2021) conducted four DNS studies of sediment transport with different particle shapes to analyse their effect on the flow. However, in real-life applications, RANS simulations are commonly used instead, where the particles are described as continuous phase. For closure of the RANS equations, modelling has to be performed for the solid phase and the turbulence of the liquid.

In the two-phase CFD solver SedFoam-2.0, developed for sediment transport applications by Chauchat et al. (2017), turbulence is accounted for by extending some classical turbulence models. However, some uncertainties in the models can be observed, especially in the effect of fluid-particle interaction on the turbulent kinetic energy.

The present work aims to improve the model by applying a machine learning (ML) process called SpaRTA, presented by Schmelzer et al. (2020). Using the data of Jain et al. (2021), the error of the model assumptions for turbulent transport was determined and used as target data for the ML algorithm. It infers corrective algebraic expressions, which were implemented in the SedFoam-2.0 solver to evaluate their predictive quality via cross-validation.

2 RANS model

A generic flow value ψ can be decomposed into a phase-weighted average $\widetilde{\psi}^{\mathrm{p}}$ and a fluctuation $\psi^{\mathrm{p}\prime} = \psi - \widetilde{\psi}^{\mathrm{p}}$, in which p refers to the phase, f (fluid) or s (sediment). The governing equations of RANS simulations for turbulent two-phase flows are based on the phase-averaged Navier-Stokes equations. In this work, the Reynolds stress tensor in these RANS equations is modelled using the Boussinesq assumption. For this, the eddy viscosity is obtained from a k-ε-turbulence model employing $\nu_{\mathrm{t}} = C_\mu k^2/\varepsilon$, with $C_\mu = 0.09$, and the turbulent kinetic energy of the fluid k is computed from the transport equation

$$D_t k = P - \varepsilon + T + I \quad . \tag{1}$$

The turbulent production P, transport T and dissipation ε are obtained in a similar manner as in pure fluid flows. The interfacial term I is supposed to capture sediment-fluid interaction and is modelled to act as a dissipative contribution (Chauchat et al. (2017)).

3 Setup and DNS data

The data which serves as high-fidelity reference is obtained from the DNS of the particle-laden turbulent open-channel flow with spherical particles by Jain et al. (2021). In the domain of size $(108 \times 23 \times 36)d$ in the stream-wise (x), wall-normal (y) and span-wise (z) direction, the mobile particles with diameter d form a rough sediment bed.

Both the exact and modelled version of Eq. (1) can be evaluated given the DNS data. Averaging in the periodic (horizontal) directions and in time yields $D_t k = 0$ in Eq. (1). The wall-normal profiles of the right-hand side (RHS) terms are shown in Fig. 1. Compared to the results of the exact formulation, the model assumptions largely overestimate the production P and the interfacial term I is of the wrong sign. As a result, the model terms do not satisfy Eq. (1). The obtained residual Δ is also depicted in Fig. 1.

4 SpaRTA approach

The SpaRTA approach was developed for correcting standard RANS models, with focus on separat-

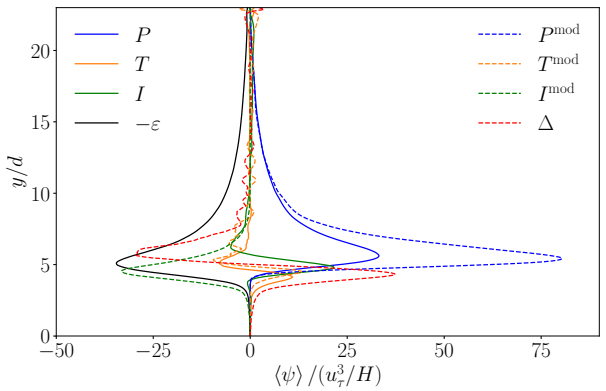

Figure 1: Wall-normal profiles for the exact RHS of Eq. (1) along with the corresponding modelled terms of the RANS model, evaluated using the DNS data by Jain et al. (2021).

ing single-phase flows. The idea is to introduce an additive term b_{ij}^{Δ} to the Reynolds stress anisotropy, and another one $\mathcal{R}$ in the RHS of the modelled k-transport equation. Hereafter, only the $\mathcal{R}$-correction is considered, since the main errors are due to the kinetic energy equation. Ideally, $\mathcal{R}$ is equal to Δ in any situation and, hence, compensates the error of the model assumptions. As this is not possible, a data-driven model for $\mathcal{R}$ that best fits Δ is generated by the ML process.

In this work, two different modelling ansatzes for $\mathcal{R}$ were considered: The turbulent production analogy, which is a tensorial approach $\mathcal{R} = 2k\left(b_{ij}^{\mathcal{R}} - 1/3\ \delta_{ij}\right)\partial_j \tilde{u}_i^{\mathrm{f}}$, and the dissipation analogy, using a scalar c as $\mathcal{R} = c\,\varepsilon$. Algebraic expressions have to be found for $b_{ij}^{\mathcal{R}}$ or c, respectively. Both are assumed to depend on the mean strain-rate tensor $\widetilde{S}_{ij}$ and the mean rotation-rate tensor $\widetilde{\Omega}_{ij}$ of the fluid.

The SpaRTA algorithm then assembles a set of polynomial expressions based on the scalar invariants of the minimal integrity basis of $\widetilde{S}_{ij}$ and $\widetilde{\Omega}_{ij}$. To provide sediment-phase related information, the sediment volume fraction α was also included. The model for the scalar c was directly built from the resulting terms, and for $b_{ij}^{\mathcal{R}}$, they were additionally multiplied with the base tensors of the minimal integrity basis.

Selection of appropriate models and inference of suitable model coefficients were conducted following Schmelzer et al. (2020), using elastic net regularisation and ridge regression. This aims to balance error and complexity of the models and avoid overfitting. In the end, numerous symbolic model expressions for $b_{ij}^{\mathcal{R}}$ and c were obtained that regress the target data.

5 Cross-validation

To assess the quality of these models, they were implemented in the SedFoam-2.0 solver and CFD simulations of a flow similar to the DNS studies were run. Although this work aims to improve the model of the k-transport equation, other flow values must not be deteriorated. Hence, the cross-validation was performed on k, the stream-wise velocities $\tilde{u}^{\mathrm{f}}$ and $\tilde{u}^{\mathrm{s}}$, the total shear stress τ_{tot} (as defined in Jain et al. (2021)) and the fluid volume fraction ϕ.

Although no model was capable of improving all quantities at the same time, especially the turbulent fluctuations were better captured. The mean-squared error on k and τ_{tot}, evaluated with respected to the DNS data, was reduced by up to 65 % compared to the results of the unmodified solver. The models of the dissipation analogy showed higher improvements than the production analogy. Models containing α yielded an additional enhancement and improved all five quantities on average by up to 35 %.

6 Conclusions

This study demonstrated the applicability of SpaRTA to multi-phase flows. The newly developed dissipation analogy yields considerably better results than the production analogy, achieving higher improvements on the assessed flow quantities. Although the improvements are not as good as in the separating single-phase flows evaluated in Schmelzer et al. (2020), the dissipation analogy provides an easy way to consider new quantities in the corrective models, e.g. the gradient of the sediment volume fraction or the sediment velocity. In further studies, the algorithm will be applied to the other test cases of Jain et al. (2021), since the sediment bed behaves substantially different when using non-spherical particles.

References

Chauchat J., Cheng Z., Nagel T., Bonamy C. & Hsu, T.-J. (2017) "SedFoam-2.0: a 3-D two-phase flow numerical model for sediment transport". *Geosci. Model Dev.*, **10**, 4367–4392.

Jain R., Tschisgale S. & Fröhlich J. (2021) "Impact of shape: DNS of sediment transport with non-spherical particles". *J. Fluid Mech.*, **916**, A38.

Schmelzer M., Dwight R. P. & Cinnella P. (2020) "Discovery of Algebraic Reynolds-Stress Models Using Sparse Symbolic Regression". *Flow Turbul. Combust.*, **104**, 579–603.

Turbulent wake flow prediction of marine hydrokinetic turbine arrays in large-scale meandering river using physics-informed convolutional neural network

Zexia Zhang[1] and Ali Khosronejad[2,*]

[1]*Civil Engineering Department, Stony Brook University, USA*

This work presents a physics-informed convolutional neural network (PICNN) algorithm for reconstructing the mean flow and turbulence statistics in the wake of marine hydrokinetic (MHK) turbine arrays installed in large-scale meandering rivers, underscoring the potential of PICNN to develop reduced order models for control co-design and optimization of MHK turbine arrays in natural riverine environments.

INTRODUCTION

Marine hydrokinetic (MHK) turbines are designed to harvest energy from tides, ocean currents, and river currents without the need for water impoundment. To maximize the power production of MHK sites and tidal farms, the positioning and layout of turbine arrays need to consider the wake-wake interactions. However, obtaining the turbulence statistics of the high-fidelity flow field data of the turbine arrays using numerical simulations is computationally expensive due to the large computational domain size and long sampling time. Therefore, in this study, we developed a convolutional neural network (CNN) algorithm based on [1-2] to efficiently predict turbine wake flow field in large-scale settings.

Methodology

We considered three layouts of MHK turbines embedded in large-scale waterways as study cases to produce training and validation data of the CNN. The training case is one single row of three turbines distributed evenly along the spanwise direction. The two validation cases are two rows of turbines with overlapping and staggered wakes, respectively. We employed our in-house open-source model, the Virtual Flow Simulator (VFS-Geophysics) code, to conduct LES of three MHK turbine layouts, to produce the training and validation datasets.

We then developed physics-informed CNN autoencoder machine-learning algorithms for generating 3D realizations of time-averaged turbulent flow. The autoencoder CNN model is composed of eight convolutional layers. The inputs include five snapshots of the velocity components in the instantaneous fully developed turbulent flow field generated by LES. The outputs are the turbulence statistics including time-averaged velocity and turbulent kinetic energy. Physics constraints such as mass and momentum conservation equations are embedded into the loss function of the CNN.

The CNN is trained using the training case and validated using the two validation cases.

Results and discussion

We compared the relative mean absolute error (RMAE) of the time-averaged streamwise velocity U and the turbulent kinetic energy (TKE) predicted by the trained CNN model with physics constraints (PICNN) and without physics constraints (CNN-AE) against the LES results in table 1. The results show that the developed CNN autoencoder algorithms hold great potential for predicting the time-averaged wake flow, and the prediction results of the physics-informed CNN further improve the accuracy of the baseline unconstrained CNN. In addition, the overall computational cost of the proposed CNN is roughly 2.8% of the LES.

Case		PICNN	CNN-AE
Training	$\overline{U} / U_b$	0.57%	0.61%
	TKE / U_b^2	3.92%	4.76%
Validation I	$\overline{U} / U_b$	0.73%	0.74%
	TKE / U_b^2	5.16%	5.56%
Validation II	$\overline{U} / U_b$	0.70%	0.72%
	TKE / U_b^2	5.03%	5.65%

TABLE I. RMAE of the turbulence statistics predicted by PICNN and CNN-AE. $\overline{U}$ is the time-averaged velocity magnitude. U_b is the bulk velocity of the river

CONCLUSIONS

We proposed and examined a novel physics-informed CNN algorithm to predict turbulence statistics of turbine wake flow field in large-scale waterways. The results show that physics-informed machine learning algorithms enable efficient high-fidelity predictions of MHK array wakes in real-life riverine environments, thus, providing a powerful computational approach for control co-design and layout optimization of tidal farms in large-scale waterways.

—

* ali.khosronejad@stonybrook.edu

[1] Zhang, Z., Santoni, C., Herges, T., Sotiropoulos, F., & Khosronejad, A. (2022). "Time-averaged wind turbine wake flow field prediction using autoencoder convolutional neural networks". Energies, **15(1)**, 41.

[2] Zhang, Z., Flora, K., Kang, S., Limaye, A. B., & Khosronejad, A. (2022). "Data-Driven Prediction of Turbulent Flow Statistics Past Bridge Piers in Large-Scale Rivers Using Convolutional Neural Networks". Water Resources Research, **58(1)**, e2021WR030163.

2nd Spanish Fluid Mechanics Conference
Barcelona (2 - 5 July 2023)

Beads, bubbles and drops in microchannels: stability of centred position and equilibrium velocity

Javier Rivero-Rodríguez[1,2], Jean Cappello[1], Youen Vitry[1,3], Adrien Dewandre[1,3], Benjamin Sobac[1,4], and Benoit Scheid[1]

jrivrod@uma.us.es

[1]Transfers, Interfaces and Processes (TIPs), Université Libre de Bruxelles, Brussels, Belgium
[2]Escuela de Ingenierías Industriales, Universidad de Málaga, Campus de Teatinos, Málaga, Spain
[3]Secoya Technologies, 1348 Louvain-la-Neuve, Belgium
[4]Laboratoire des Fluides Complexes et leurs Réservoirs (LFCR), UMR 5150 CNRS, Université de Pau et des Pays de l'Adour, Anglet, France

Understanding and predicting the dynamics of dispersed micro-objects in microfluidics is crucial in numerous natural, industrial and technological situations. We experimentally characterized the equilibrium velocity V and lateral position ε of various dispersed micro-objects such as beads, bubbles and drops, in a cylindrical microchannel over an unprecedent wide range of parameters. The experiments are compared and well-agrees with a steady 3D Navier-Stokes model for incompressible two-phase fluids including both the effects of inertia and possible interfacial deformations. This model enables to rationalize the experiments and to provide an exhaustive parametric analysis on the influence of the main parameters of the problem, mainly on two aspects: the stability of the centered position and the velocity of the dispersed object.

1 Introduction

Mastering the dynamics of dispersed micro-objects, such as beads, drops or bubbles transported by an external flow, is crucial in many situations, including biomedical and biological applications where these objects represent model systems for cell sorting. Nowadays, the emergence of microfluidics that eases manipulation of small objects with the use of a continuous phase, raises new challenges such as object focusing and separation Pamme (2007). Different strategies have been developed for continuous flow separation, most of them relying on the same fundamental principles: the hydrodynamic forces leading to a migration of the objects are modulated by the geometry, mechanical properties and external forces.

On the strategies relies on the inertial migration, which has been first observed by Segre & Silberberg (1962) for small neutrally buoyant rigid spheres transported in an axisymmetric Poiseuille flow. They noticed that the beads migrate radially to equilibrium positions located at a distance of approximately $0.3d_h$ from the cylindrical channel centreline when their diameter d is small compared that of the channel d_h.

In this work, we fully characterise the onset of lateral migration of beads, drops or bubbles in circular microchannels (Capello (2023)) and provide the stability maps varying all the parameters.

2 Description of the problem

A train of drops flowing in a microchannel with circular cross-section is under study. Beads and bubbles can be considered as limit cases of drops. We study the stability of the centred position, which reveals if the drop is travelling at the centred position or at an off-centred one, the exact position of the latter coming from a delicate lateral forces equilibrium. We characterise when it takes place and the travelling velocity at that given position.

The dynamics of the system in figure 1 is well described by Navier-Stokes equations in both, continuous and disperse phases, together with continuity of velocity and stresses accounting for surface tension at the interphase. Periodicity of the train is considered in a steady framework travelling with the drop.

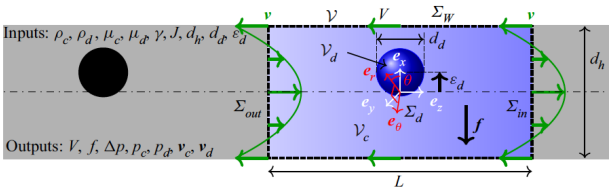

Figure 1: Sketch of the modelled train of drops flowing in a microchannel.

The main dimensionless numbers governing the problem are the Reynolds and capillary numbers,

the viscosity and density ratio, and drop diameter to channel diameter ratio:

$$\mathrm{Re} = \frac{\rho_c J d_h}{\mu_c}, \mathrm{Ca} = \frac{\mu_c J}{\gamma}, \lambda = \frac{\mu_d}{\mu_c}, \hat{\rho} = \frac{\rho_d}{\rho_c}, \hat{d} = \frac{d}{d_h}, \tag{1}$$

where subscripts c and d refer to continuous and disperse phases, respectively.

This system loses stability via Pitchfork bifurcation, which means that the stable character is determined by the sign of the derivative of the lateral force with the eccentricity or lateral position in a steady equilibrium situations. To determine it, the equations are linearly expanded in terms of the eccentricity ε

$$f = f_0 + \varepsilon f_1 + \mathcal{O}(\varepsilon^2), \tag{2}$$

being the neutral stability curved determined by f_1=0.

3 Results

The governing equations have been solved using Comsol Multiphysics and the linearised migration force f_1 around the centred position $\varepsilon = 0$ has been obtained exhaustively covering the values in (1). The velocity of the drop has been obtained at any position ε with special emphasis on the dependence on ε.

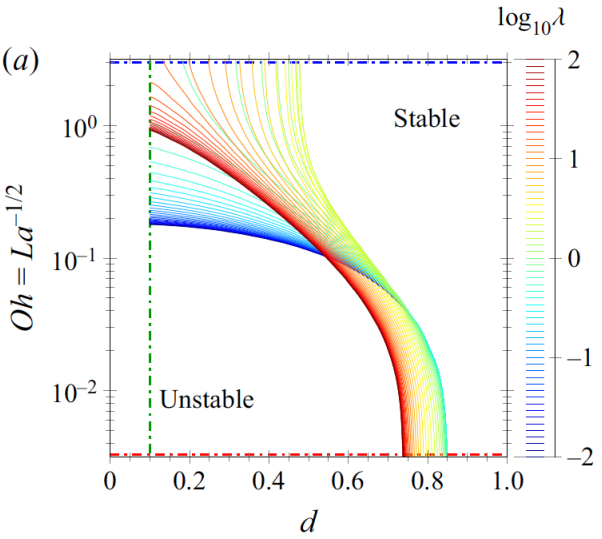

Figure 2: Stability for small We=Re Ca number.

In figure 2, it is depicted the influence of the viscosity ratio and Laplace number La=Re/Ca, which compares the ratio between inertial migration and deformation-induced migration. On the one hand, we can observe that in the absence of deformation-induced migration, there is a critical diameter, that depends on the viscosity ratio, above which lateral migration takes place. On the other hand, in the absence of inertial migration, there is a range of viscosity ratio for which lateral migrations of sufficiently small drops takes place.

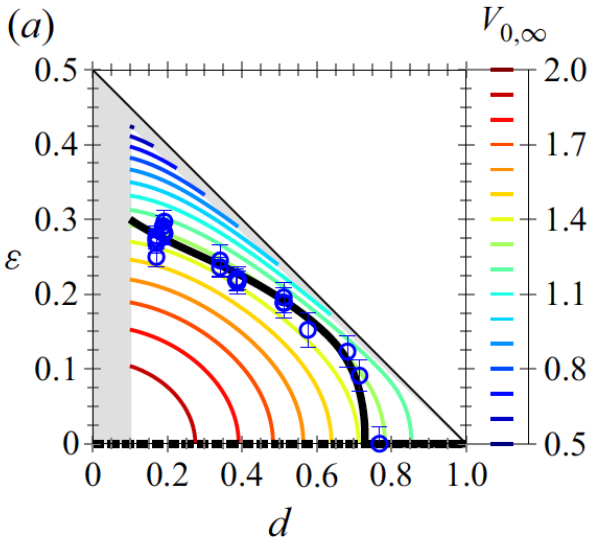

Figure 3: Velocity and equilibrium position of neutrally buoyant beads.

In figure 3, we can observe that once migration takes place, the particle reaches an off-centred equilibrium position. The velocity of the particles is larger for smaller particles and for equilibrium positions closer to the centerline.

4 Conclusions

We have shown that Navier-Stokes equations predicts the dynamics of drops in microchannels. We have also provided the stability maps that predicts for which conditions migration of drops takes place.

References

J. Cappello, J. Rivero-Rodriguez, Y. Vitry, A. Dewandre, B. Sobac, B. Scheid. (2023) "Beads, bubbles and drops in microchannels: stability of centred position and equilibrium velocity". *Journal of Fluid Mechanics*, **956**.

Pamme. (2007) "Continuous flow separations in microfluidic devices". *Lab on a Chip*, **7 (12)**, 1644?1659.

2nd Spanish Fluid Mechanics Conference
Barcelona (2 - 5 July 2023)

Drainage–imbibition cycles in a model open fracture: capillary jumps, hysteresis, memory, and dissipation

Jordi Ortín[1], Ran Holtzman[2], Marco Dentz[3], and Ramon Planet[1]

jordi.ortin@ub.edu

[1]Departament de Física de la Matèria Condensada, Universitat de Barcelona, and UBICS (University of Barcelona Institute of Complex Systems), Barcelona, Spain
[2]Centre for Fluid and Complex Systems, Coventry University, Coventry, United Kingdom
[3]Institute of Environmental Assessment and Water Research (IDAEA), Spanish National Research Council (CSIC), Barcelona, Spain

This work deals with two-phase displacements of simple fluids in disordered environments. This is a challenging multiscale problem, in which capillary processes at small disorder scales behave cooperatively to govern the interfacial dynamics at continuum and large scales. Combining theory, numerical simulations, and experiments of quasistatic pressure-driven displacements in an imperfect Hele-Shaw cell (with randomly distributed gap-thickness constrictions and expansions) we explain the origin of hysteresis in the pressure–saturation diagram, the memory properties of cyclic trajectories, and the capillary sources of energy dissipation in this problem.

1 Introduction

Displacements of one fluid by another in fractured and porous media often occur in cycles, alternating between the displacement of a less wetting by a more wetting fluid (imbibition) and vice versa (drainage). It is well known that displacement cycles exhibit hysteresis, multivaluedness, and memory. At the same applied pressure, interface configurations and fluid saturations are different in imbibition and drainage. Such behaviors are found in a wide variety of processes in nature and engineering, ranging from rainfall and evaporation in soils to flow reversals in enhanced oil recovery and CO_2 geosequestration. Yet, quantitative understanding of the complex pore-scale mechanisms that are at the root of these behaviors and their extrapolation across scales are still challenging (1).

The capillary action of a simple heterogeneity, a constriction in the fluid passage in an otherwise homogeneous Hele-Shaw cell, contains the key features of capillary hysteresis (2). This insight forms the building block for an ab initio model based on the linearized pressure balance equation at an oil-air interface, $h(x)$ (for small deformations, $|dh/dx| \ll 1$):

$$\gamma \frac{d^2h(x)}{dx^2} - \rho g \sin\alpha\, h(x) + \rho g H + p_c[x, h(x)] = 0, \quad (1)$$

This equation accounts for the competing effects of interfacial tension (first term), hydrostatic pressure (second term, with α the cell tilt), and capillary pressure fluctuations due to gap thickness variations (last term). Based solely on measurable medium and fluid characteristics, it defines the metastable two-phase configurations in mechanical equilibrium at each value of an external pressure $P = \rho g H$ applied on the side of the wetting phase (3).

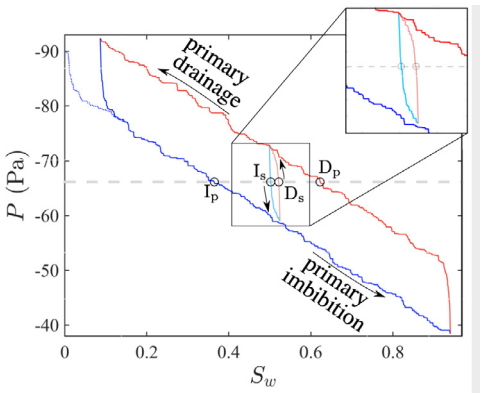

Figure 1: Primary imbibition and drainage pressure-saturation trajectories. For any given P, the saturation S_w is history-dependent (open circles). Return-point memory is apparent in the internal cycle.

2 Hysteresis and memory

Under quasistatic pressure driving, the sequence of metastable two-phase configurations resulting from Eq. (1) form the hysteresis cycle shown in Fig. 1. Partial internal cycles exhibit return-point memory (RPM), a striking property that results from (i) a partial ordering of the two-phase configurations, (ii)

the fact that they obey Middleton's no-passing rule, and (iii) the deterministic nature of the dynamics for quenched (time-independent) heterogeneities.

3 Energy dissipation

The interfacial tension in Eq. (1) (first term) introduces correlations of the interfacial height $h(x)$. In the presence of quenched heterogeneities, $p_c[x, h(x)]$, interfacial correlations trigger capillary avalanches (Haines jumps). This is the main source of energy dissipation in pressure-driven quasistatic displacements. The return-point memory property of cyclic trajectories enables to sorting out and quantifying these capillary energy losses, and their dependence on microstructure and gravity. The relative importance of viscous dissipation during Haines jumps may be deduced from comparison with experiments (4).

References

[1] Singh, K., Jung, M., Brinkmann, M., Seemann, R. (2019). Capillary-Dominated Fluid Displacement in Porous Media. Annual Review of Fluid Mechanics **51**, 429-449. https://doi.org/10.1146/annurev-fluid-010518-040342

[2] Planet, R., Diaz-Piola, L., Ortin, J. (2020). Capillary jumps of fluid-fluid fronts across an elementary constriction in a model open fracture. Physical Review Fluids **5**, 044002, 1-10. https://doi.org/10.1103/PhysRevFluids.5.044002

[3] Holtzman, R., Dentz, M., Planet, R., Ortin, J. (2020). The origin of hysteresis and memory of two-phase flow in disordered media. Communications Physics **3**, 222, 1-7. https://doi.org/10.1038/s42005-020-00492-1

[4] Holtzman, R., Dentz, M., Planet, R., Ortin, J. (2023). The relation between dissipation and memory in two-fluid displacements in disordered media (submitted).

2nd Spanish Fluid Mechanics Conference
Barcelona (2 - 5 July 2023)

Production of long micrometer jets of weakly viscoelastic liquids.

M.G. Cabezas[1], A. Rubio[1], E. J. Vega[1], F. J. Galindo-Rosales[2], A. M. Gañán-Calvo[3], and J. M. Montanero[1]

mguadama@unex.es

[1]Departamento de Ingeniería Mecánica, Energética y de los Materiales, Universidad de Extremadura, Spain
[2]CEFT, Departamento de Engenharia Química,, Faculdade de Engenharia da Universidade do Porto, Portugal
[3]Departamento de Ingeniería Aeroespacial y Mecánica de Fluidos,, Universidad de Sevilla, Sevilla, Spain

We experimentally study the effect of weak viscoelasticity on the performance of transonic flow focusing. We found that for solutions of low molecular weight polymers, there is a concentration range for which transonic flow focusing triggers the coil-stretch transition of the polymeric molecules. The resulting elastic stresses stabilize the meniscus allowing to reduce flow rate and to produce jets much thinner and longer than the Newtonian counterparts.

1 Introduction

In Gaseous Flow Focusing [1], a liquid is injected at a constant flow rate through a feeding needle located inside a converging nozzle [2]. A coflowing gas stream sharpens the meniscus and pulls a thin jet from the meniscus tip. Straight and very thing jets can be produced when the outer gas stream is accelerated up to the sound speed and discharged into a low-pressure chamber. Among other applications, transonic flow focusing has become one of the most common methods for sample supply in serial femtosecond crystallography (SFX). In this case, it is necessary to produce long jets of sufficiently low diameter to fulfill the requirements of the high pulse rates used in SFX.

Many dilute polymer solutions exhibit an almost constant viscosity over a wide range of shear rates. So, the effect of the polymer addition is an increase in the solution viscosity and elasticity. The extensional relaxation time λ_r measured in filament thinning rheometers is usually used to quantify the elastic response of viscoelastic fluid to a straining flow. This parameter is related to the polymer relaxation time and increases with the molecular polymer weight and with the polymer concentration of a dilute solution due to the hydrodynamic (flow-mediated) interaction among polymers. It has been recognized for a long time that high-velocity gradients can cause the transition from a coil to a nearly completely stretched conformation of polymer chains [3]. In this work, we analyze whether the extremely high-velocity gradients in transonic flow focusing trigger the coil-stretch transition and alter the flow stability and the performance of the technique.

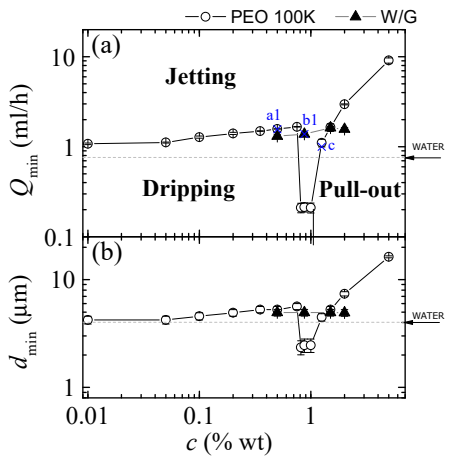

Figure 1: Minimum flow rates (a) leading to the jetting regime, and the corresponding jet diameters (b).

2 Results

We used dilute weakly viscoelastic solutions of polymers of low molecular weight (PEO 100K, 200K, and 600K). To isolate the role of the elasticity, we compared the results with those for water-glycerol mixtures with the same Ohnesorge number as the corresponding solution. All experimental results shown in this abstract correspond to PEO100K and stagnation pressure $p_0 = 2.5$ bar upstream.

Figure 1 shows the ejection modes adopted by our configuration for different concentrations of PEO100K. The smallness of the error bars shows the high degree of experimental reproducibility. For low polymer concentrations, the behavior is very similar to that of the Newtonian mixtures. The flow rate increases with the concentration, probably due to the

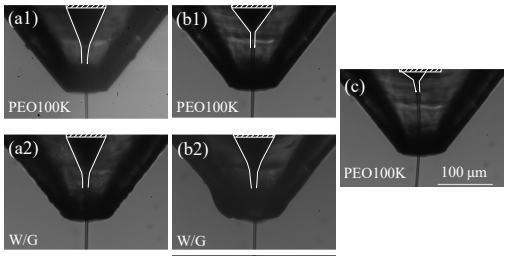

Figure 2: Newtonian-type (a1) viscoelastic (b1) and pulled-out (c) menisci formed in the experiments with PEO100K (blue symbols in Fig. 1.(a)). Images (a2) and (b2) show the menisci of the water-glycerol mixture for the same Ohnesorge number and flow rate as those of the corresponding polymer solution.

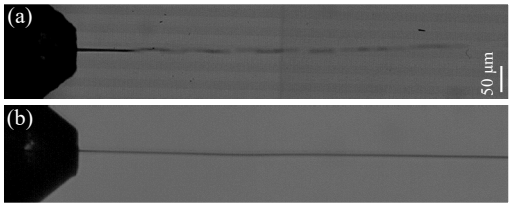

Figure 3: Comparison of the jets emitted at the corresponding minimum flow rate: (a) water at $Q = 0.75$ ml/h and (b) PEO100K at $c = 0.8125\%$ and $Q = 0.2$ ml/h.

increase in the solution viscosity, and the meniscus shape (Fig. 2.a1) is newtonian-type (Fig. 2.a2). As it is already known, for large polymer concentrations the pull-out effect occurs [4]. The large tensile stress causes the meniscus to detach from the needle end and to climb over the inner needle wall (Fig. 2.c). Interestingly, we found that there is a small range of concentrations for which the elasticity significantly enhances the meniscus stability. Viscoelasticity alters the shape of the meniscus (Fig. 2.b1), which decomes significantly shorter than the corresponding Newtonian counterpart (Fig. 2.b2). The intense extensional flow dragged by the outer gas stream, which commensurates with the inverse of the extensional relaxation time, produces the coil-stretch transition of the polymers. At the appropriate concentration, the flow rate can be reduced in around one order of magnitude while keeping the steady jetting regime running. This reduction allows one to produce much thinner jets than their Newtonian counterparts (Fig. 1.b).

Figure 3 shows a comparison of jet produced at the minimum flow rate with water (a), and a PEO100K solution at the concentration $c = 0.8125\%$ wt. The polymer addition not only allows to produce a thinner jet, but results in a significant increase in its length. Figure 4 shows the jet lengths and the onset of the

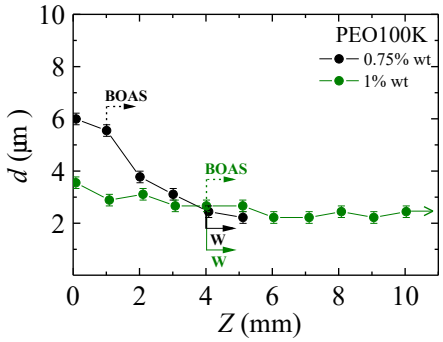

Figure 4: Jet diameter d versus the distance from the ejector exit, Z ($c = 0.75\%$ wt, $Q = 1.6$ ml/h) and supercritical ($c = 1\%$ wt, $Q = 0.4$ ml/h) PEO100K jets. The vertical solid and dashed lines indicate the beginning of whipping (W) and BOAS instability, respectively. The chevron-right green arrow indicates that the supercritical jet broke up at distances from the ejector larger than 10 mm.

beads on a string (BOAS) and whipping (W) inestability for a Newtonian type behavior, and within the viscoelastic stability enhancement region. We did not observe the breakage of the latter withing the 10 mm observation window, so the jet length was over one thousand times its diameter.

3 Conclusions

We experimentally studied the effect of weak viscoelasticity on the stability limit of gaseous flow focusing. We found that there is a parametric region in which the built elastic stress contributes to stabilize the meniscus, allowing to produce thinner and much longer jets. This may consitute a technologica advantage for some applications.

Acknowledgement. This research has been supported by the Spanish Ministry of Economy, Industry and Competitiveness under Grant No. PID2019-108278RB-C32/AEI/10.13039/501100011033.

References

[1] A. M. Gañán-Calvo, Phys. Rev. Lett. **80**, 285 (1998).
[2] D. P. DePonte, *et al*, J. Phys. D: Appl. Phys. **41**, 195505 (2008).
[3] A. Peterlin, Pure Appl. Chem. **12**, 563 (1966).
[4] T. Sridhar and R. K. Gupta, J. Non-Newtonian FluidMech. **30**, 285 (1988).

Use of nanofluids in energy applications

Rosa Mondragón Cazorla[1] and Leonor Hernández López*[1]

[1]*Department of Mechanical Engineering and Construction, University Jaume I, SPAIN*

Since 1990s, nanofluids (mixtures of liquids and solid nanoparticles with at least one dimension below 100 nm) have received growing attention due to their enhanced thermal and optical properties. In this abstract we briefly discuss some of studies we have developed in the field of nanofluids applied to different energy systems.

INTRODUCTION

The need for energy and more efficient energy systems has grown with the increasing global population and with modern society.

One possible way to improve the performance of energy systems is to harness the enhanced thermal and optical properties of nanofluids. These nanofluids are normal working fluids including small (<100 nm) solid particles. Initially nanofluids were investigated for their potential to improve thermal conductivity. After that, nanofluids were also investigated for their potential to boost other thermal properties such as sensible (specific heat capacity) and latent thermal energy storage or convective heat transfer. The optical properties of base fluids were also found to enhance due to the addition of small quantities of nanoparticles.

The Multiphase Fluids Group (MFG) in Jaume I University have been working since 2009 in the synthesis, characterization and evaluation of the nanofluids performances within different energy applications. Some of the most relevant results are presented hereafter.

THERMAL NANOFLUIDS: HEAT TRANSFER

Improving the thermal properties of the heat transfer fluids (HTF) is a key issue for many applications based in heat transfer. Several nanofluids have been synthesised (via the two-step method) or readjusted from commercially available nanofluids, covering different base fluids (water or thermal oils as Therminol 66, VP1) and nanoparticles (SiO_2, Al_2O_3, CNT, halloysite, Sn). Important variables such as nanoparticle size or concentrations were varied and different relevant properties were evaluated: stability, thermal conductivity, specific heat, viscosity, etc.) [1-6]. Heat transfer coefficients were calculated from the measured experimental values and/or also directly measured in experimental thermal hydraulic loops [2,5-6]. As an example, enhancements up to 20 % in thermal conductivity were measured for an alumina nanofluid (5 v.% concentration) with respect to water [1]. Also, the experimental heat transfer coefficient increased with respect to that of the base fluid (water) on a constant Reynolds number basis, being the enhancements up to 84 % for SiO_2 nanoparticles (5 v.%) at Re = 30000 [2]. For higher temperatures, enhancements up to 9 % at 140 ˚C in the convective heat transfer coefficient was achieved using a Sn nanofluid (1 wt.%) versus the performance of the pure base fluid (Therminol 66) [6]. These increases can play an important role to improve efficiencies and to cut the costs of many industrial applications that involve heat transfer. However, the increase in viscosity due to the addition of solid nanoparticles was found to play an important role as it significantly increases the pressure drop. Additionally, the colloidal stability of the nanofluids (with time, for high temperatures, for thermal cycling, etc.) is a key issue, so that the nanofluid maintains its properties during its life cycle. In this regard, usually surfactants are required to ensure the good stability of the nanofluids.

THERMAL NANOFLUIDS: THERMAL ENERGY STORAGE (TES)

Molten salts are used in CSP plants as a TES material because of their high operational temperature and stability of up to 500 ˚C. However, they present relative poor thermal properties and energy storage densities, which can be improved doping the molten salts with nanoparticles (nanosalts). Different nanosalts have been tested varying the base salt (solar salt, Hitec, binay carbonate) and nanoparticles (mainly SiO_2 and Al_2O_3) trying to maximise the sensible heat [7,8]. Increasements in specific heat of 25 % was measured for solar salt with SiO_2 (1 wt.%) [7]. Also the influence of the synthesis method has been analysed [8], suggesting that the method has a great influence to find a good commitment between viscosity and stability.

In order to increase the total thermal storage energy density of molten salts, nanoencapsulated phase change particles (nanoPCM with a core-shell structure) with a latent heat contribution of the nanoparticle core, has also been tested. Self-encapsulated nanoPCM ($Sn@SnO_x$, $Al\text{-}Cu@Al_2O_3$) or with coatings generated by Atomic Layer Deposition ($Sn@Al_2O_3$, $Sn@SiO_2$) have been evaluated [9-12]. Enhancements up to 18% in the total thermal energy storage (sensible + latent) for solar salt with $Al\text{-}Cu@Al_2O_3$ (10 wt.%) [11] were achieved.

The colloidal stability of nanosalts is also a key issue. To be able to evaluate it, a new

experimental set-up to measure the particle size distribution of molten salt-based nanofluids at high temperatures by means of Dynamic Light Scattering was developed [9].

SOLAR NANOFLUIDS: DIRECT ABSOPTION SOLAR COLLECTORS (DASC)

In conventional solar collectors, the absorption material is a dark surface that heats up and transfers heat to the HTF. In 1970 the idea of directly exposing the HTF to incident radiation was proposed as an alternative to avoid the thermal losses in conventional collectors. This concept, in which heat is absorbed volumetrically by the working fluid instead of the surface, is known as direct absorption solar collectors (DASC). As commonly used HTFs (water, oils, molten salts, etc.) are transparent in most of the solar spectrum and possess low solar radiation absorption capacity, the use of solar nanofluids (with enhanced optical properties) offers high solar-to-thermal conversion efficiencies. Different solar nanofluids have been evaluated in our labs, using water as base fluid and different nanoparticles (gold and carbon black) in very low concentrations [13-14]. Increments up to 200 % in photothermal efficiencies have been obtained for a water-based carbon nanofluid (33 mg/l) [13].

The combination of nanoparticles that absorb solar radiation and PCM materials that can store energy due to the latent heat, result in materials with a triple function in DASC systems: solar absorption material, HTF and TES. In this regard, hybrid carbon-paraffin/water nanoemulsions have been synthesized to evaluate the enhancement in thermal energy storage density and optical properties with good results [15].

CONCLUSIONS

Different results from nanofluids used as materials for energy systems have been presented, including heat transfer, thermal energy storage and solar energy harvesting. Although promising results have been obtained, several barriers to scale-up remain: stability, pumping power, cost, environmental issues, etc.

* lhernand@uji.es

[1] Mondragón R, Segarra, C., Martínez-Cuenca R, Juliá J.E., Jarque JC (2013) "Experimental characterization and modeling of thermophysical properties of nanofluids at high temperature conditions for heat transfer applications" *Powder Technology*, 249, 516-529

[2] Martínez-Cuenca R, Mondragón R., Hernández L., Segarra C., Jarque J.C., Hibiki T., J.E. Juliá J.E. (2016) "Forced-convective heat-transfer coefficient and pressure drop of water-based nanofluids in a horizontal pipe", *Applied Thermal Engineering*, 98, 841-849

[3] Alberola J.A., Mondragón R., Juliá J.E., Hernández L., Cabedo L. (2014) "Characterization of halloysite-water nanofluid for heat transfer applications" *Applied Clay Science*, 99, 54-61

[4] Gimeno-Furio A., Navarrete N., Mondragon R., Hernandez L., Martinez-Cuenca R., Cabedo L., Enrique Julia J.E. (2017) "Stabilization and characterization of a nanofluid based on a eutectic mixture of diphenyl and diphenyl oxide and carbon nanoparticles under high temperature conditions*" Int. Journal of Heat and Mass Transfer*, 113, 908-913

[5] Gil-Font J., Hatte M.A., Bailey M., Navarrete N., Ventura-Espinosa J., Goulas A., La Zara D., van Ommen J.R., Mondragón R, Hernández L. (2020) "Improving heat transfer of stabilised thermal oil-based tin nanofluids using biosurfactant and molecular layer deposition"*Applied Thermal Engineering*, 178, 115559

[6] Gil-Font J., Navarrete N., Cervantes E., Mondragón R., Torró S.F., Martínez-Cuenca R., Hernández L.(2022) "Convective heat transfer performance of thermal oil-based nanofluids in a high-temperature thermohydraulic loop". *Int. Journal of Thermal Sciences*, 171,107243

[7] Andreu-Cabedo, P., Mondragon, R., Hernandez, L. et al. (2014) "Increment of specific heat capacity of solar salt with SiO2 nanoparticles" *Nanoscale Res Lett* 9, 582

[8] Navarrete N., Hernández L, Vela A., Mondragón R. (2020) "Influence of the production method on the thermophysical properties of high temperature molten salt-based nanofluids" *Journal of Molecular Liquids*, 302, 112570

[9] Navarrete N., Gimeno-Furió A., Joep Forner-Escrig J., Juliá J.E., Mondragón R. (2019) "Colloidal stability of molten salt –based nanofluids: Dynamic Light Scattering tests at high temperature conditions" *Powder Technology*, 352, 1-10

[10] Navarrete N., La Zara D., Goulas A., Valdesueiro D., Hernández L., van Ommen J.R., Mondragón R. (2020) "Improved thermal energy storage of nanoencapsulated phase change materials by atomic layer deposition" *Solar Energy Materials and Solar Cells*, 206,10322

[11] Navarrete N., Mondragón R., Wen D., Navarro M.E., Ding Y, Juliá J.E. (2019) "Thermal energy storage of molten salt –based nanofluid containing nano-encapsulated metal alloy phase change materials", *Energy*, 167, 912-920

[12] Navarrete, N., Gimeno-Furio, A., Mondragon, R. et al. (2017) "Nanofluid based on self-nanoencapsulated metal/metal alloys phase change materials with tuneable crystallisation temperature". Sci Rep 7, 17580

[13] Gimeno-Furió A., Martínez-Cuenca R., Mondragón R., Vela Gasulla A.F., Doñate-Buendía C., Mínguez-Vega G., Hernández L. (2020) "Optical characterisation and photothermal conversion efficiency of a water-based carbon nanofluid for direct solar absorption applications" *Energy*, 212,118763

[14] Burgos J., Mondragón R., Begum Elcioglu E., Fabregat-Santiago F., Hernández L. (2022) "Experimental Characterization and Statistical Analysis of Water-Based Gold Nanofluids for Solar Applications: Optical Properties and Photothermal Conversion Efficiency" *RRL Solar*, 6,7, 2200104

[15] Burgos J., Ayora-Fernández M., Mondragón R., Nithiyanantham U., Fabregat-Santiago F., Hernández L., (2022) "Characterization of hybrid carbon - paraffin/water nanoemulsions for DASC: stability, thermal energy storage and optical properties" IMPRES. Barcelona, pp. 115–116

2nd Spanish Fluid Mechanics Conference
Barcelona (2 - 5 July 2023)

Multicomponent transport in OpenFoam (laminarSMOKE)

Bertrand Naud[1], Alberto Cuoci[2], and Manuel Arias-Zugasti[3]

bertrand.naud@ciemat.es

[1]Departamento de Energía, Ciemat, Madrid, Spain
[2]Department of Chemistry, Materials, and Chemical Engineering "G. Natta", Politecnico di Milano, Italy
[3]Departamento de Física Matemática y de Fluidos, UNED, Madrid, Spain

We present the implementation of an efficient multicomponent transport formulation in a CFD solver for laminar reacting flows with detailed kinetic mechanisms (laminarSMOKE). This allows to compare results obtained with the widely used mixture-averaged approximation to the complete multicomponent transport formulation, in different axisymmetric laminar diffusion jet flames.

1 Introduction

Molecular transport is important in combustion since, besides convection, it is the process that ultimately brings together reactants, products and heat, and allows or inhibits chemical reactions. Together with chemical kinetics, molecular transport is one of the key processes governing flame dynamics at the molecular level, and a correct evaluation of multicomponent transport is essential in order to obtain numerical simulations that can be considered as numerical experiments.

When a detailed description of chemistry is used, the different species involved can have very different diffusive properties since fuel species and radicals like H_2 and H coexist with larger molecules like O_2, N_2, H_2O or hydrocarbon species and the corresponding combustion products. Due to the large number of species involved, the mixture-averaged approximation is widely used for the evaluation of multicomponent diffusion fluxes at a reasonable cost.

Few comparisons have been made in calculations of realistic flames between the mixture-averaged approximation and the complete multicomponent transport formulation. The recent accurate and efficient "extended $1+M$ model" by Naud *et al.* (2023) offers a way to evaluate the multicomponent diffusion fluxes in correspondence with the complete formulation at a similar cost as mixture-averaged.

We present here the implementation of the $1+M$ formulation in the CFD code OpenFOAM, allowing to compare to mixture-averaged results in different axisymmetric laminar diffusion jet flames.

2 Multicomponent transport

Mixture-averaged In the mixture-averaged approximation, the diffusion fluxes are written as:

$$\rho \mathbf{V}_i Y_i = -\rho \frac{W_i}{\overline{W}} D_i \nabla X_i - \rho \underbrace{\frac{W_i}{\overline{W}} D_i \theta_{\mathrm{mix},i}}_{D_{\mathrm{Soret},i}} \nabla \ln T \quad (1)$$

where Y_i is the mass fraction, X_i the mole fraction, W_i the molar weight of species i, and where ρ is the density, T the temperature and $\overline{W}$ the molar weight of the mixture. A correction velocity $\mathbf{V}_c$ is added to species diffusive velocity $\mathbf{V}_i$ in order to ensure that the net species diffusion flux is zero: $\mathbf{V}_c = \sum Y_j \mathbf{V}_j$ (sum over the N species considered).

The effective diffusion coefficient D_i of the i-th species into the mixture is approximated as:

$$D_i = \frac{1 - Y_i}{\sum_{k \neq i} X_k / \mathcal{D}_{ki}} = \frac{\overline{W} - W_i X_i}{\overline{W} \sum_{k \neq i} X_k / \mathcal{D}_{ki}} \quad (2)$$

The thermal diffusion coefficients are considered to be non-zero for "light" species only (typically H, He and H_2). They are obtained as $D_{\mathrm{Soret},i} = \frac{W_i}{\overline{W}} D_i \theta_{\mathrm{mix},i}$ with:

$$\theta_{\mathrm{mix},i} = \sum_k \theta_{ik} X_i X_k \quad (3)$$

where θ_{ik} are the mixture-averaged thermal diffusion ratios obtained as temperature polynomial fits: $\theta_{ik} = \sum_{n=1}^{4} \alpha_{n,ik} T^{n-1}$.

The thermal conductivity λ of the mixture is evaluated as:

$$\lambda = \frac{1}{2} \left[\sum_k X_k \lambda_k + \frac{1}{\sum_k X_k / \lambda_k} \right] \quad (4)$$

where λ_k are the mixture-averaged pure thermal conductivities obtained as temperature polynomial fits: $\ln \lambda k = \sum_{n=1}^{4} \beta_{n,ik} \ln T^{n-1}$.

1+M formulation The 1+M formulation, based on rigorous kinetic theory of gases formulation of multicomponent transport properties, relies on efficient matrix inversions based on Neumann series approximation, and problem size reduction based on local identification of "main species". We define locally $1 + M$ "main" species, where K is the species with largest molar fraction X_K, and where the other M "main" species verify:

$$X_i \geq \gamma X_K \quad \text{with} \quad \gamma = 10^{-5}. \tag{5}$$

In the complete multicomponent formulation, the diffusion fluxes read:

$$\rho \mathbf{V}_i Y_i = -\rho \frac{W_i}{W} \sum D^*_{ij} \nabla X_j - \rho D^*_{\text{Soret,i}} \nabla \ln T \tag{6}$$

with $D^*_{\text{Soret,i}} = \frac{W_i}{W} \sum D^*_{ij} \theta^*_j$.

In the $1 + M$ formulation, (6) is used for main species, and reduces to $\rho \mathbf{V}_i Y_i = -\rho \frac{W_i}{W} D^*_{ii} \nabla X_i$ for dilute species. The diffusion coefficients D^*_{ij}, the thermal diffusion ratios θ^*_j and the thermal conductivity λ^* are obtained following Naud *et al.* (2023):

$$D^*_{ij} = \mathcal{D}_{iK} c_{ij} \tag{7}$$

$$\theta^*_j = 2.5 X_j \sum_{k \in \text{main}} M^{10,00}_{kj} \widetilde{a}_{10,k} \tag{8}$$

$$\lambda^* = -\frac{25p}{4T} \sum_{k \in \text{main}} X_k \widetilde{a}_{10,k} + \frac{X_k}{M^{01,01}_k} \left(1 - \sum_{j \in \text{main}} M^{10,01}_{jk} \widetilde{a}_{10,j} \right) \tag{9}$$

where $\mathcal{D}_{ij}$ are the binary diffusion coefficients, where $X_j M^{mn,pq}_{ij} = L^{mn,pq}_{ij}$ (with $L^{mn,pq}_{ij}$ the Dixon-Lewis multicomponent transport matrix given in Naud *et al.* (2023)) and where c_{ij} is the solution of the Fick problem and $\widetilde{a}_{10,k}$ the solution of the thermodiffusion problem according to the $1 + M$ formulation given in Naud *et al.* (2023).

Molecular viscosity In both mixture-averaged and $1 + M$ formulations, the molecular viscosity μ is obtained from Wilke semi-empirical formula. However, the $1 + M$ formulation allows to significantly reduce the cost by considering main species only.

3 laminarSMOKE validation

We implement the $1 + M$ formulation in the CFD solver for laminar reacting flows with detailed kinetic mechanisms "laminarSMOKE", based on OpenFOAM and OpenSMOKE++ framework, see Cuoci *et al.* (2013).

Since the mixture-averaged approximation is already implemented by default in the solver, we can compare results in different test cases (hydrogen and methane laminar jet flames), and using different chemical mechanisms (skeletal or detailed mechanisms). In this way, we can evaluate the quality of the mixture-averaged approximation in these cases compared to full multicomponent formulation. On the other hand, we can assess the efficiency of the $1 + M$ formulation by comparing its cost to the mixture-averaged calculations, depending on the number of species considered.

References

Arias-Zugasti M., Garcia-Ybarra P.L., Castillo J.L. (2016) "Efficient calculation of multicomponent diffusion fluxes based on kinetic theory". *Combustion and Flame*, **163**, 540–556.

Naud B. and Arias-Zugasti M. (2020) "Accurate multicomponent Fick diffusion at a lower cost than mixture-averaged approximation: validation in steady and unsteady counterflow flamelets". *Combustion and Flame*, **219**, 120–128.

Córdoba O. and Arias-Zugasti M. (2022) "Accurate and efficient calculation of multicomponent thermal diffusion coefficients and partial thermal conductivity based on kinetic theory". *Combustion and Flame*, **244**, 112202.

Naud B., Córdoba O., Arias-Zugasti M. (2023) "Accurate heat (Fourier) and mass (Fick and thermodiffusion) multicomponent transport at similar cost as mixture-averaged approximation". *Combustion and Flame*, **249**, 112599.

Cuoci A., Frassoldati A., Faravelli T., Ranzi E. (2013) "Numerical modeling of laminar flames with detailed kinetics based on the operator-splitting method" *Energy and Fuels*, **27**, 7730–7753.

Cuoci A., Frassoldati A., Faravelli T., Ranzi E. (2013) "A computational tool for the detailed kinetic modeling of laminar flames: Application to C2H4/CH4 coflow flames" *Combustion and Flame*, **160**, 870–886.

Cuoci A., Frassoldati A., Faravelli T., Ranzi E. (2015) "OpenSMOKE++: An object-oriented framework for the numerical modeling of reactive systems with detailed kinetic mechanisms" *Computer Physics Communications*, **192**, 237–264.

2nd Spanish Fluid Mechanics Conference
Barcelona (2 - 5 July 2023)

Shear-induced phase separation of chemically-responsive polymer solutions

Marco De Corato[1] and Marino Arroyo[2,3]

mdecorato@unizar.es

[1]Aragon Institute of Engineering Research (I3A), University of Zaragoza, Zaragoza, Spain
[2]Universitat Politècnica de Catalunya-BarcelonaTech, 08034 Barcelona, Spain
[3]Institute for Bioengineering of Catalonia (IBEC), The Barcelona Institute of Science and Technology (BIST), Baldiri Reixac 10-12, 08028 Barcelona, Spain

Chemically-responsive polymers are macromolecules that respond to local variations of the chemical composition of the solution by changing their conformation, with notable examples including polyelectrolytes, proteins and DNA. The polymer conformation changes can occur in response to changes to the pH, the ionic strength or to the concentration of a generic solute that interacts with the polymer. In many situations, the spatial distribution of the chemical stimuli can be highly inhomogeneous, which can lead to large spatial variations of polymer conformation and of the rheological properties of the mixture. Here, we develop a theory for the flow of a mixture of a solute and chemically-responsive polymers. To model the polymer conformation changes introduced by the interactions with the solute, we consider the polymers as linear elastic dumbbells whose spring stiffness depends on the solute concentration. We use the Onsager's variational formalism to derive the equations governing the evolution of the variables, which unveils novel couplings between the distribution of dumbbells and that of the solute. By using a linear stability analysis, we find a shear-induced phase separation whereby a homogeneous distribution of solute and dumbbells spontaneously demix. Similar phase transitions have been observed in previous experiments and may play an important role in living systems.

1 Introduction

Chemically-responsive polymers constitute a class of macromolecules that can change their conformation in response to chemical stimuli such as changing the chemical composition of a suspension. These types of polymers is commonly encountered in several biomedical and industrial applications. For instance, polyelectrolytes can change their conformation in response to changes of the pH or of the ionic strength of the solution. Change of local salt concentration screens the charges along the backbone of the polyelectrolytes thus making the polymer chain more flexible and promoting a transition from an extended semiflexible chain configuration to a flexible and coiled one.

A relevant question arises in the simulation of inhomogeneous flows of chemically-responsive polymers where the solute concentration changes in space leading to inhomogeneous rheological properties. How should one modify the viscoelastic constitutive equations [1] to include the solute-dependent rheological properties? A naive answer would be to simply use spatially-variable viscosity and relaxation time. However, this procedure might ignore important couplings between the gradients of solute and polymer density. Furthermore, since the polymer conformation depends on the local chemical composition, it is interesting to investigate if unexpected couplings between solute and polymer conformation could occur.

Here, we address these points by proposing a thermodynamically self-consistent model for the isothermal flow of a dilute mixture of solvent, solute and chemically-responsive polymers [4]. By using the Onsager's variational formalism, we derive systematically the set of equations that govern the flow of a mixture of solute and chemically-responsive polymers. These equations reveal couplings between the gradients of solute, the gradients of polymer density and the gradients of polymer conformation, which are not present in previous viscoelastic models. We show that the solute-polymer coupling leads to a shear-induced demixing of the polymer solution.

2 Theoretical model

To describe chemically-responsive polymer solutions in general flow conditions and heterogeneous concentrations, we make the simple choice of modeling polymers as dumbbells, i.e. two beads connected by a spring.We assume that the dumbbells and the solute are suspended in a solvent of viscosity η and that the solution is incompressible and isothermal. We charac-

terize the distribution of dumbbells inside a volume, Ω, through the function $\psi(\boldsymbol{x}, \boldsymbol{r}, t)$, where $\boldsymbol{x}$ denotes the position of the center of a dumbbell in space, $\boldsymbol{r}$ denotes its end-to-end vector and t is the time. The local number density of dumbbells at a given point in space is given by the integral over the end-to-end distance space:

$$n_{\mathrm{d}}(\boldsymbol{x}, t) = \int_{\boldsymbol{r}} \psi(\boldsymbol{x}, \boldsymbol{r}, t)\, d\boldsymbol{r} \ . \tag{1}$$

The distribution of solute is simply characterized by its number density $c(\boldsymbol{x}, t)$. We assume that the elastic energy stored by each dumbbell molecule is given by a linear spring:

$$U = \frac{1}{2}\, k(c)\, |\boldsymbol{r}|^2 \ . \tag{2}$$

The elastic energy, given by Eq. (2), has an entropic origin that reflects the resistance of the polymer chains to be stretched away from their equilibrium conformation. In the equation above, $k(c)$ represents a solute-dependent stiffness, which models the effects of the solute on the conformation of a polymer molecule.

2.1 Onsager's variational principle

To derive the balance of momentum and the expressions for the fluxes of momentum, dumbbell and solute, we neglect inertial effects and we employ the Onsager's variational formalism [2, 3]. This framework allows us to identify the relevant couplings between the fluxes of solute, of dumbbells and of momentum directly from the principle of least dissipation.

To constrain the Rayleighian to fulfill the incompressibility condition $\frac{\partial}{\partial \boldsymbol{x}} \cdot \boldsymbol{v} = 0$, we include the pressure p as Lagrange multiplier and we define the Lagrangian functional as

$$\mathcal{L} = \dot{\mathcal{F}} + \mathcal{D} - \int_{\Omega} p\, \frac{\partial}{\partial \boldsymbol{x}} \cdot \boldsymbol{v}\, d\Omega \ , \tag{3}$$

In Eq. (3), $\dot{\mathcal{F}}$ and $\mathcal{D}$ are the rate of change of the free energy and the energy dissipation of the system, respectively. We derive the governing equations directly from Eq. (3) by taking the variational derivatives with respect to the relevant variables. To do so, we need to specify the free energy and the dissipation of the system.

2.2 Free energy of the system

We define the free energy functional of the system, $\mathcal{F}$, as the sum of the contribution of the dumbbells and the solute

$$\mathcal{F} = k_{\mathrm{B}}T \int_{\Omega} c \log c\, d\Omega + k_{\mathrm{B}}T \int_{\Omega}\int_{\boldsymbol{r}} \psi \log \psi\, d\Omega\, d\boldsymbol{r} + \int_{\Omega}\int_{\boldsymbol{r}} \psi U\, d\Omega\, d\boldsymbol{r} \ , \tag{4}$$

where k_{B} is the Boltzmann's constant, T is the absolute temperature and U is the elastic energy, defined in Eq. (2). The first two terms represent the solute and dumbbell free energy of mixing and the third term represents the elastic energy stored by the springs.

2.3 Dissipation of the system

We assume that the energy dissipation functional is comprised of three different contributions: (i) the friction due to the viscosity of the solvent, which is proportional to the solvent shear viscosity η and to the rate of deformation tensor $\boldsymbol{D}$; (ii) the friction due to the relative motion of the solute molecules and the solvent, which is proportional to the friction coefficient of the solute ξ; and (iii) the friction between the dumbbells and the solvent, which is proportional to the friction coefficient of the dumbbell beads, ξ_{d}.

$$\mathcal{D} = \eta \int_{\Omega} \boldsymbol{D} : \boldsymbol{D}\, d\Omega + \frac{1}{2}\xi \int_{\Omega} c\, (\boldsymbol{w} - \boldsymbol{v})^2\, d\Omega + \xi_{\mathrm{d}} \int_{\Omega}\int_{\boldsymbol{r}} \psi\, (\boldsymbol{w}_{\mathrm{d}} - \boldsymbol{v})^2\, d\Omega\, d\boldsymbol{r} + \frac{1}{4}\xi_{\mathrm{d}} \int_{\Omega}\int_{\boldsymbol{r}} \psi \left(\dot{\boldsymbol{r}} - \boldsymbol{r} \cdot \frac{\partial \boldsymbol{v}}{\partial \boldsymbol{x}}\right)^2 d\Omega\, d\boldsymbol{r} \ . \tag{5}$$

3 Results and conclusions

We investigate the stability of a mixture of solute and dumbbells that is sheared between two parallel walls. We find that the homogeneous state undergoes spontaneous demixing in the case of sufficiently large shear rates. Using a linear stability analysis, we derive an approximated expression of the critical Deborah number above which the suspension of solute and dumbbell phase separates, which agrees with the numerical solution of the full eigenvalue problem. Our results show that the newly-identified couplings between the solute and the dumbbell distribution drive the phase separation. This mechanism is radically different from that driving the shear banding of micelles and of entangled polymer solutions and could act in parallel with the other two mechanisms. A suggestive application of the theory presented here concerns living systems whereby active processes, chemical reactions and inhomogeneous

straining flows could be used to control the conformation and the spatial arrangements of macromolecules and proteins.

References

[1] Larson, R. G. (2013) "Constitutive equations for polymer melts and solutions".

[2] De Corato, M., Arroyo, M. (2022). "A theory for the flow of chemically responsive polymer solutions: Equilibrium and shear-induced phase separation". *J. Rheol.*, **66**, 813-835.

[3] Doi, M. (2011) "Onsager's variational principle in soft matter". *J. Phys. Cond. Matt.*, **23**, 284118.

[4] Arroyo, M. and Walani, N. and Torres-Sánchez, A. and Kaurin, D. (2018) "Onsager's variational principle in soft matter: introduction and application to the dynamics of adsorption of proteins onto fluid membranes".

Capillary and non-linear damping mechanisms on 3D wavy thin liquid films

David Barreiro-Villaverde[1], Anne Gosset[2,*], Marcos Lema[1] and Miguel A. Méndez[3]

[1]*CITIC Research, Universidade da Coruña, SPAIN*
[2]*CITENI, Campus Industrial de Ferrol. Universidade da Coruña, SPAIN*
[3]*von Karman Institute for Fluid Dynamics, BELGIUM*

When they are deposited on solid substrates, coating flows are often subjected to disturbances while they are still in liquid phase. If those disturbances persist until solidification, they produce a wavy surface that affects the product quality. In this work, we investigate the evolution of three-dimensional non-uniformities on a thin liquid film dragged by a vertical substrate moving against gravity, a flow configuration typically encountered in coating processes. The receptivity of the liquid film to 3D disturbances is discussed with Direct Numerical Simulations, an in-house non-linear thin liquid film model, and linear stability analysis. The combination of these numerical tools allows for describing the mechanisms of non-linear and capillary damping, as well as for identifying the instability threshold of the system for the scales involved in coating processes.

INTRODUCTION

Many industrial processes and natural phenomena involve the deposition and flow of a liquid film on a solid substrate, the best example being the coating and painting processes. The presence of defects on the coating layer affects not only the aesthetics of the final products, but also their quality and performance [1]. This is why the damping phenomena ("levelling") of non-uniformities that may arise after the coating has been deposited are fundamental in the process. In this article, we explore the downstream evolution of a coating film dragged against gravity by a moving substrate (Fig.1) and exposed to 3D perturbations using three different tools: 1) BLEW, an in-house non-linear integral film model developed at the von Karman Institute, 2) its linear stability analysis (LSA), and 3) Direct Numerical Simulations (DNS) in OpenFOAM. Their range of applicability is discussed for various coating techniques, ranging from slot-die [2] to air-knife coating [3].

INTEGRAL BOUNDARY LAYER MODEL FOR THE FILM AND ITS LINEAR STABILITY

The mathematical formulation of BLEW (Boundary LayEr Wiping), the in-house thin film solver developed by Mendez et al. [4] is based on 1) the long-wave approximation (streamwise scale x much larger than cross-stream scale $y{\sim}h$), and 2) the integration of the momentum equation across the film thickness. These are the two basic ingredients of the Integral Boundary Layer models for liquid films which, combined with appropriate scaling laws and boundary conditions at the wall and at the interface, allow reformulating the Navier-Stokes equations in terms of film thickness $h(x,z,t)$ and flow rates q_x and $q_z(x,z,t)$. In this paper, we extend the 3D implementation of Ivanova et. al [5] with a specific treatment of the surface tension term that combines the benefits of spectral approaches with the flexibility of finite volume schemes.

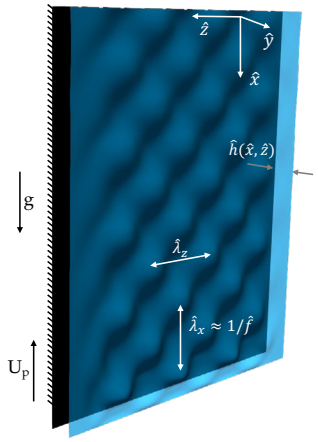

FIG 1. Flow configuration under study.

In addition, we extend the linear stability analysis in [5] to 3D perturbations. For that, we linearize the integral equations around the equilibrium state and we re-define the flow quantities as $\phi = \phi_0 + \tilde{\phi}$ where ϕ_0 denotes the steady state solution and $\tilde{\phi} = \phi_\varepsilon e^{(k_x x + k_z z - \omega t)}$ is an infinitesimal perturbation, with k_x and k_z the wave numbers in the stream-wise and spanwise directions. $\omega = \omega_r + i\omega_i$ is the angular frequency. For the adimensionalization of variables, the reader is referred to [4]. The system admits multiple solutions for ω, imposing the steady-state solution for each set of variables (δ, k_x, k_z) where δ is the film reduced Reynolds number.

TWO-PHASE DNS SIMULATIONS

For the DNS simulations, we use an algebraic formulation of the Volume Of Fluid (VOF) method in which the tracking of the interface is based on the liquid volume fraction α. This equation is solved using the Multidimensional Universal Limiter for Explicit Solution (MULES) algorithm, implemented in the finite volume libraries OpenFOAM®. The computational domain is

identical to the one in BLEW for the stream and span-wise coordinates, featuring 22M cells (40 cells across the base thickness h_0). The flow rate is synthetically perturbed in time and space with a relative amplitude $A = 0.05$.

RESULTS

The linear stability map in Fig.2 illustrates the largest amplification factors $\hat{\omega}_i$ for $\hat{h}_0 = 0.2$ and $\delta = 150$, in the range of $\hat{k}_x$ and $\hat{k}_z$ lower than 5. This value is equivalent in x to a dimensional frequency of $800\,Hz$ ($1.8\,mm$ wavelength) in the case of a $77\,\mu m$ thick water film transported by a flat strip at $U_p = 1.45\,m/s$. Higher wave numbers are not investigated because they are shown to be irrelevant in most coating processes [1-3].

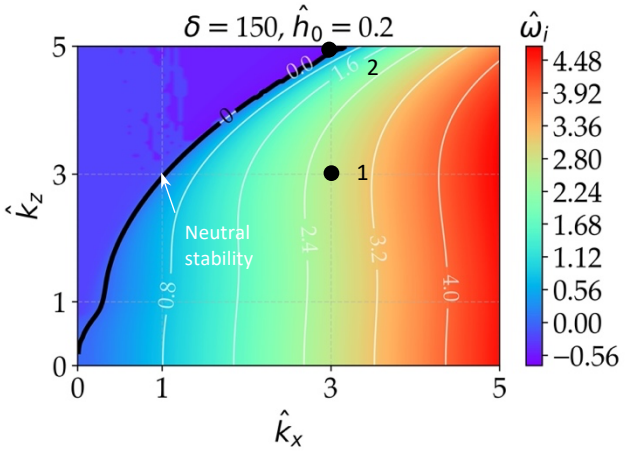

FIG 2. Color map of the amplification factor $\hat{\omega}_i$ for $\delta = 150$ and a base film thickness $\hat{h}_0 = 0.2$.

Compared to the linear stability of 2D perturbations [5], the system appears to be globally more unstable to 3D disturbances. In the LSA, the stabilization of the system is solely due to the capillarity terms proportional to $\hat{k}^3$; these compensate the inertial destabilization generated by the terms proportional to $\hat{k}$. The interplay between these forces is clear in Fig.2: inertia dominates over capillarity along the $\hat{k}_x$ axis, since the amplification factor $\hat{\omega}_i$ is a growing function of $\hat{k}_x$ (the stability region at a given $\hat{k}_z$ is reduced at larger $\hat{k}_x$), while the reverse is true along the $\hat{k}_z$ axis. The different behavior in each direction is due to the substrate motion, which destabilizes the flow in the stream-wise coordinate. On the other hand, increasing the $\hat{k}_z$ at constant $\hat{k}_x$ stabilizes the system because the capillary terms grow faster than the inertial terms even at very small wave numbers.

For sake of validating the non-linear film model, the conditions corresponding to points 1 and 2 in Fig.2 are simulated with BLEW and DNS. The results are reported in Fig.3, with the thickness maps corresponding to a similar wavenumber in x and z, $\hat{k}_x = \hat{k}_z = 3$ (point 1), and a larger $\hat{k}_z = 5$ with the same $\hat{k}_x$ (point 2). The 3D plots show a good qualitative agreement between the film solver and DNS, since both models capture the initial growth of the waves, followed by capillary damping. As in LSA, an increase in $\hat{k}_z$ induces a stronger damping. It is found in fact that the 3D components of the capillary terms stimulate the production of a spanwise flow rate q_z (inexistent in the base flow and in absence of surface tension) which contributes to damp the waves. It is remarkable that the film model succeeds to capture such a complex interaction between the stream and span-wise terms, despite a certain amount of numerical diffusion.

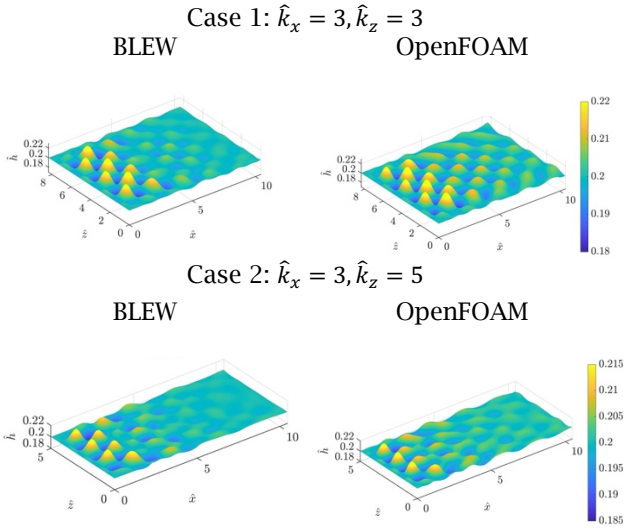

FIG 3. Dimensionless thickness mappings obtained with BLEW (left) and OpenFOAM (right) for the two points highlighted in Fig.2.

CONCLUSIONS

Three different numerical tools (linear stability analysis, non-linear integral film model, and DNS) are used to analyse the damping of perturbations on a liquid film dragged by an upwards moving substrate. The span-wise disturbances are found to have a stabilizing effect on the film, which is qualitatively well predicted by LSA.

—

* anne.gosset@udc.es

[1] Weinstein J. & Ruschak K.J. (2004) "Coating flows," *Ann. Rev. of Fluid Mech.* **36**.
[2] Perez E. B. & Carvalho M. S. (2011) "Optimization of slot-coating processes: Minimizing the amplitude of film-thickness oscillation," *J. Eng. Math.* **71**.
[3] Gosset A., Mendez M. A., & Buchlin J. M. (2019) "An experimental analysis of the stability of the jet wiping process: Part I – Characterization of the coating uniformity," *Exp. Th. and Fluid Sci.* **103**, 51–65 (2019).
[4] Mendez M. A., Gosset A., Scheid, B., Balabane M., & Buchlin J.M. (2021) "Dynamics of the jet wiping process via integral models," *J. Fluid Mech.* **911**, A47.
[5] Ivanova T., Pino F., Scheid B., & Mendez M. A. (2023) "Evolution of waves in liquid films on moving substrates,", *Phys. of Fluids* **35**, 10.1063/5.0132222.
[6] Orchard S. E. (1963) "On surface levelling in viscous liquids and gels," *Appl. Scientific Res.* **A11**, 451–464.

2nd Spanish Fluid Mechanics Conference
Barcelona (2 - 5 July 2023)

Dynamics of dewetting fronts: to pinch or not to pinch

Miguel Zürcher-Guinea[1], Daniel Moreno-Boza[1], and Alejandro Sevilla[1]

mzurcher@ing.uc3m.es

[1]Dpto. de Ingeniería Térmica y Fluidos, University Carlos III, Madrid, Spain

Thin films on hydrophobic surfaces undergo spinodal dewetting and form dry holes with moving contact lines at the solid-liquid interface. The opening of the dry holes takes place through an advancing front which accumulates liquid in a growing ridge, leaving behind a very thin precursor film. Here we report a numerical study of the dynamics of this advancing ridge, and the resulting morphology of the dewetted film. The effect of wall slip on the monotonic, oscillatory, or pinching ridge evolution are investigated.

1 Introduction

Thin films ($\sim$ 100 nm) on planar hydrophobic substrates can undergo a spinodal dewetting process where dry spots are formed in the film. This from of dewetting is initiated by infinitesimal perturbations under conditions in which the long range van der Waals forces overcome the stabilizing surface tension force. Dry spots form a contact line with the solid surface, which advances into the unperturbed film, leaving behind a precursor film of a minimum thickness dictated by the short range repulsion forces [1]. The material removed from the film is accumulated in a growing crest whose dynamics and morphology are studied herein.

The asymptotic velocity of the advancing front, $\dot{s}$, has been shown to be affected by the wall slip between the substrate and the solid surface, transitioning from a linear law, $\dot{s} \propto t$ [4] in the no-slip case, to a $\dot{s} \propto t^{2/3}$ power-law for increasing slip lengths [6]. Closely related to the dynamics of the moving front, one finds different profile shapes of the ridge in the wetted region. Experiments have revealed the existence of ridge profiles with a monotonic or an oscillatory decay into the unperturbed film [9], as well as secondary pinch-off events leading to satellite holes ahead of the ridge when the depression of the first undulation is comparable to the initial film thickness [7, 8]. These morphological differences have been attributed to the viscoelastic properties of the liquid. In particular, in [5] they developed a phase diagram classifying each possible outcome as a function of the elasticity of the liquid and a capillary number based on the ridge velocity.

Other authors studied the effect of wall slip and capillary number on the transition from monotonic to oscillatory decay. It was shown that for greater wall slips the ridge joined the unperturbed film monotonically, whereas the oscillatory behaviour was shown to take place for smaller wall slip. A linearised analysis has been employed to find the critical speed of the contact line $\dot{s}_{crit}$ separating both types of film profiles [6, 2], finding reasonably good agreement with experiments. As the ridge advances the crest height increases, and thus the relative slip length becomes smaller, inducing a transition from the oscillatory to the monotonic decaying profile that has also been observed [3].

To the best of our knowledge, the appearance of secondary pinch-offs and the subsequent formation of satellite holes during the two-dimensional retraction of the ridge has not been studied before, and hence constitutes the main objective of this investigation.

2 Weak Slip Lubrication

In our numerical simulations we take advantage of the large disparity between the horizontal and vertical length scales by making use of the non-dimensional weak-slip lubrication equation. Using the initial film thickness h_0, $U_0 = A/(6\pi\mu h_0^2)$, $t_0 = 6\pi\mu h_0^3/A$, and $\phi_0 = A/(6\pi h_0^3)$ as the characteristic scales for height, velocity, time, and pressure, the leading-order weak lubrication model reads

$$\partial_t h = \partial_x \left[\frac{h^2(h+3\lambda)}{3} \partial_x \left(\frac{\mathcal{C}}{Ca} + \frac{1}{h^3} - \frac{h_{\mathrm{prec}}^6}{h^9} \right) \right], \tag{1}$$

where $\mathcal{C} = -\partial_x^2 h[1+(\partial_x h)^2]^{-3/2}$ represents the mean curvature of the film, h_{prec} represents the precursor film thickness, $Ca = \mu U_0/\sigma$ is the capillary number, λ the dimensionless slip length, and A is the Hamaker constant associated with the disjoining pressure.

Equation (1) was simulated in a large domain $0 \leq x \leq L$, where L is several times larger than the wavelength of the fastest growing perturbation, which is used as initial condition, together with suitable boundary conditions at the lateral boundaries

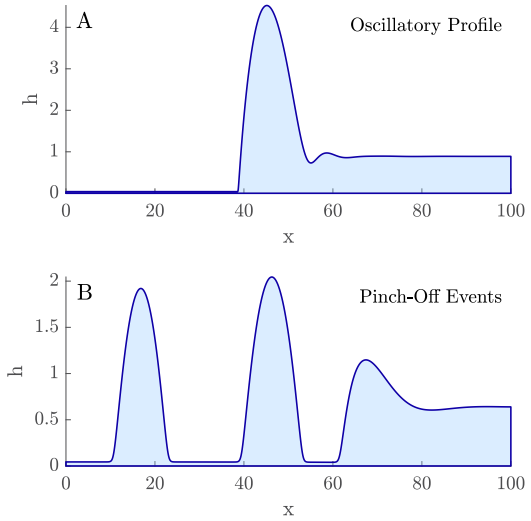

Figure 1: Profile of a dewetting front with a dampening oscillatory ridge (A), and one which has undergone secondary pinch-off events (B).

of the domain. A systematic parametric sweep is devised to assess the combined influence of the capillary number and wall slip for fixed values of the precursor film thickness, allowing us to classify the different retraction regimes in a morphological phase diagram.

3 Conclusions

We aim at establishing the effects of the capillary number and wall slip on the long-term dynamics of planar dewetting fronts, with emphasis on the conditions leading to secondary pinching events. Our results will eventually provide a phase diagram separating the parametric regions that distinguish between dampening oscillatory ridges and satellite hole generation induced by secondary pinch-offs.

References

[1] O. Bäumchen and K. Jacobs. Slip effects in polymer thin films. *Journal of Physics: Condensed Matter*, 22(3):033102, 2010.

[2] R. Fetzer, K. Jacobs, A. Münch, B. Wagner, and T. Witelski. New slip regimes and the shape of dewetting thin liquid films. *Physical Review Letters*, 95(12):127801, 2005.

[3] R. Fetzer, M. Rauscher, A. Münch, B. Wagner, and K. Jacobs. Slip-controlled thin-film dynamics. *Europhysics Letters*, 75(4):638, 2006.

[4] A. Ghatak, R. Khanna, and A. Sharma. Dynamics and morphology of holes in dewetting of thin films. *Journal of Colloid and Interface Science*, 212(2):483–494, 1999.

[5] S. Herminghaus, R. Seemann, and K. Jacobs. Generic morphologies of viscoelastic dewetting fronts. *Physical Review Letters*, 89(5):056101, 2002.

[6] A. Münch, B. Wagner, and T. P. Witelski. Lubrication models with small to large slip lengths. *Journal of Engineering Mathematics*, 53:359–383, 2005.

[7] C. Neto, K. Jacobs, R. Seemann, R. Blossey, J. Becker, and G. Grün. Correlated dewetting patterns in thin polystyrene films. *Journal of Physics: Condensed Matter*, 15(1):S421, 2002.

[8] C. Neto, K. Jacobs, R. Seemann, R. Blossey, J. Becker, and G. Grün. Satellite hole formation during dewetting: experiment and simulation. *Journal of Physics: Condensed Matter*, 15(19):3355, 2003.

[9] R. Seemann, S. Herminghaus, and K. Jacobs. Dewetting patterns and molecular forces: A reconciliation. *Physical Review Letters*, 86(24):5534, 2001.

2nd Spanish Fluid Mechanics Conference
Barcelona (2 - 5 July 2023)

Thin films coating a solid cylindrical fibre: wetting and nonwetting scenarios

Daniel Moreno-Boza[1] and Alejandro Sevilla[1]

damoreno@ing.uc3m.es

[1]Dpto. de Ingeniería Térmica y Fluidos, University Carlos III, Madrid, Spain

The linear dynamics of a very thin liquid film coating a solid cylindrical fibre are investigated in the limit of negligible inertia and gravity. The overall effects of long-range van der Waals (vdW) forces are incorporated through a disjoining pressure term proportional to the effective Hamaker constant A of the liquid-substrate pair. Two distinguishing regimes are identified, i.e., $A > 0$ or dewetting liquid, and $A < 0$ or wetting liquid. A leading-order lubrication model is provided herein in order to describe the long-term nonlinear dynamics of the film for both cases.

Introduction An initially static annular liquid layer of uniform radius $h_o + R$ coating the external surface of a cylindrical solid fibre of radius R is generically unstable due to the Plateau-Rayleigh mechanism, evolving into a sequence of axisymmetric collars along the fibre which are connected by thin annular lobes. The temporal linear stability of the uniform-radius state was solved by Goren [3] using the full axisymmetric Navier-Stokes equations, leading to an exact dispersion relation for the temporal modes involving modified Bessel functions. Since the linear cut-off wavelength is 2π times the radius of the coating, the typical axial length scales involved in the dynamics are much larger than the radial length scales, thus rendering lubrication theory as the natural framework in developing models able to tackle the linear and non-linear dynamics in a simple and accurate way. Indeed, it was shown in [2] that the linear stability properties of the film are correctly captured by a leading-order lubrication model, while its nonlinear long-time evolution was studied in a series of more recent papers [4, 5, 7].

When the thickness of the film is smaller than about 100 nm, the long-range van der Waals (vdW) forces become comparable to the surface tension forces, and their influence depends crucially on the wettability of the solid by the liquid. In cases where the liquid wets the solid, it was shown in [8] that vdW interactions are able to stabilise the annular film to a uniform thickness h^* that depends only on the fibre radius, the Hamaker constant associated with the disjoining pressure and the surface tension coefficient σ of the interface separating the liquid layer from the ambient air. In contrast, if the liquid does not wet the solid the coating is always unstable, since both the surface tension and the vdW forces contribute to destabilise the interface. The resulting unstable flow then combines the effects of both forces, and it is expected that the vdW interactions modify the dynamics when the film thickness is sufficiently small. In particular, the linear stability properties of these annular ultrathin non-wetting films are of interest to describe the resulting dewetting patterns. In contrast with the case of wetting films, where only axisymmetric modes are unstable, non-axisymmetric modes may also become unstable under non-wetting conditions, and that they may even become dominant depending on the thickness of the film and on the relative strength of the surface tension and vdW forces, as shown in [6]

Nondimensional formulation, Reynolds equation, and preliminary results By selecting h_o, σ/h_o, h_o^2/σ, and σ/μ, as relevant length, pressure, time, and velocity scales, the problem is governed by the dimensionless Stokes equations,

$$\nabla \cdot \boldsymbol{v} = 0, \quad 0 = -\nabla p + \nabla^2 \boldsymbol{v}, \tag{1}$$

to be integrated for $\eta < r < \eta + h(x, \theta, t)$ and $0 < x < L$, where h is the instantaneous thickness of the film, L is a characteristic lateral dimension, $\eta = R/h_o$ is the aspect ratio of the configuration, and $(p, \boldsymbol{v})$ are the liquid pressure and velocity fields. The boundary conditions include the no-slip condition at the fibre wall $\boldsymbol{v}(r = \eta) = 0$ and the stress balance condition at the liquid-gas interface

$$-p\boldsymbol{n} + \left(\nabla \boldsymbol{v} + \nabla \boldsymbol{v}^{\mathrm{T}}\right) \cdot \boldsymbol{n} = \left(\mathcal{A} h^{-3} - \nabla \cdot \boldsymbol{n}\right) \boldsymbol{n}, \tag{2}$$

where $\mathcal{A} = A/(6\pi\sigma h_o^2)$ is a dimensionless number that compares the relative effects of vdW to capillary forces. Wetting configurations correspond to $A < 0$ whereas dewetting occurs for $A > 0$.

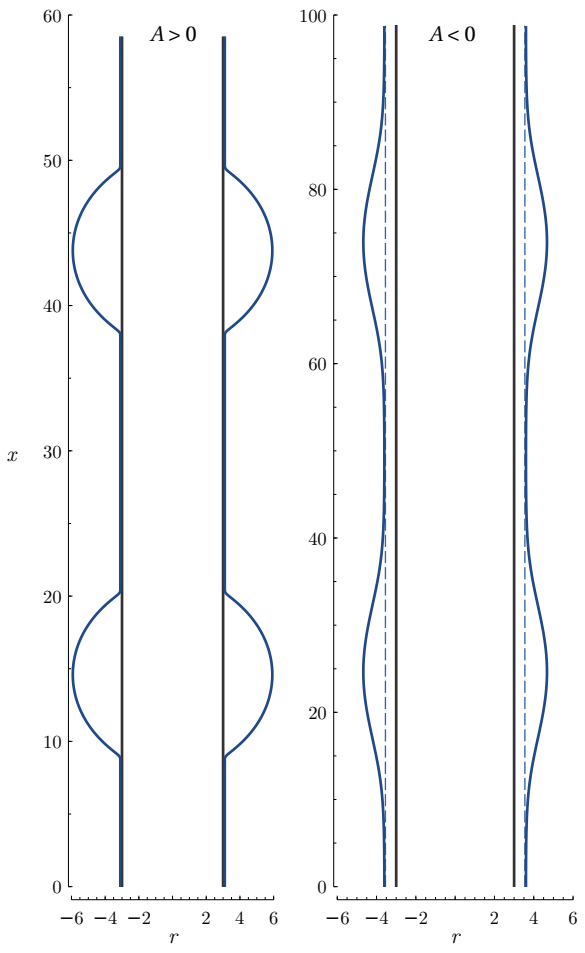

The Reynolds equation provides a leading-order lubrication model for the temporal evolution of the film thickness given by

$$(\eta + h)\frac{\partial h}{\partial t} + \frac{\partial}{\partial x}\left(G_x \frac{\partial p}{\partial x}\right) + \frac{\partial}{\partial \theta}\left(G_\theta \frac{\partial p}{\partial \theta}\right) = 0, \quad (3)$$

where the mobility functions G_x and G_θ are given by

$$G_x = \frac{h\,(h+2\eta)}{16}\left(3h^2 + 6h\eta + 2\eta^2\right) + \frac{(h+\eta)^4}{4}\log\frac{\eta}{h+\eta}, \quad (4)$$

$$G_\theta = \frac{(h+\eta)^2}{2}\log\frac{h+\eta}{\eta} - \frac{h(h+2\eta)(h^2+2h\eta+2\eta^2)}{8\eta^2}, \quad (5)$$

and the liquid pressure is $p = \mathcal{C} + \mathcal{A}h^{-3}$, where $\mathcal{C}$ is twice the mean curvature of the film.

The figure shows the saturated states, $t \to \infty$, of two separate configurations with $\mathcal{A} = 0.01 > 0$ (dewetting) and $\mathcal{A} = -0.01 < 0$ (wetting) obtained upon marching of the lubrication model presented above for $\eta = 3$. The initial condition is that of an initially corrugated film $h = 1 - 0.05\cos kx$, where k is the fastest growing wavenumber obtained from linear stability. The dewetting case includes a short-range potential of the form h_{prec}^6/h^9 [1] in order to circumvent the pinching singularity at finite times. The thickness of the precursor film is set to $h_{\text{prec}} = 0.1$. For the wetting evolution, the film is initially destabilized by means of the Plateau-Rayleigh mechanism and is seen to evolve towards the stable *Quéré thickness*, which reads in our variables $h^*/h_o = |A|^{1/4}\eta^{1/2}$, until stabilizing vdW forces balance surface tension. By way of contrast, for the dewetting case, the evolution of the film is markedly different. After the linear growth of the most unstable perturbation, for which surface tension is no longer able to counteract unstabilizing vdW forces, the annular film reaches a thickness h_{prec} that balances the disjoining pressure. Then, a receding front is created and the film evolves towards its coarsening, where a large bubble of radius comparable to that of the fibre is created as a result of the capillary drainage associated to the large curvature gradients.

Preliminary conclusions The lubrication model described herein facilitates a computationally inexpensive description of the dynamics of annular thin films. Non-axisymmetric simulations are yet to be explored, which will reveal the long-term dynamics of non-axisymmetric modes of instability for dewetting cases, which, to the best of our knowledge have not yet been reported.

References

[1] J. Becker, G. Grün, R. Seemann, H. Mantz, K. Jacobs, K. R. Mecke, and R. Blossey. Complex dewetting scenarios captured by thin-film models. *Nature materials*, 2(1):59, 2003.

[2] J. Dumbleton and J. Hermans. Capillary instability of a thin annular layer of liquid around a solid cylinder. *Industrial & Engineering Chemistry Fundamentals*, 9(3):466–469, 1970.

[3] S. L. Goren. The instability of an annular thread of fluid. *Journal of Fluid Mechanics*, 12(2):309–319, 1962.

[4] P. Hammond. Nonlinear adjustment of a thin annular film of viscous fluid surrounding a thread of another within a circular cylindrical pipe. *Journal of fluid Mechanics*, 137:363–384, 1983.

[5] M. Johnson, R. Kamm, L. Ho, A. Shapiro, and T. Pedley. The nonlinear growth of surface-tension-driven instabilities of a thin annular film. *J. Fluid Mech.*, 233:141–156, 1991.

[6] C.-K. Lin, C.-C. Hwang, and T.-C. Ke. Three-dimensional nonlinear rupture theory of thin liquid films on a cylinder. *Journal of colloid and interface science*, 256(2):480–482, 2002.

[7] J. Lister, J. Rallison, A. King, L. Cummings, and O. Jensen. Capillary drainage of an annular film: the dynamics of collars and lobes. *Journal of Fluid Mechanics*, 552:311–343, 2006.

[8] D. Quéré, J. Di Meglio, and F. Brochard-Wyart. Spreading of liquids on highly curved surfaces. *Science*, 249(4974):1256–1260, 1990.

2nd Spanish Fluid Mechanics Conference
Barcelona (2 - 5 July 2023)

A dual-grid approach for dispersed-flow simulations in turbulence

Maximilian Schenk[1], George Giamagas[1,2], Francesco Zonta[1], and Alfredo Soldati[1,2]

maximilian.schenk@tuwien.ac.at

[1]Institute of Fluid Mechanics and Heat Transfer, TU Vienna, Austria
[2]Polytechnic Department, University of Udine, Italy

Multiphase turbulence is a complex phenomenon characterised by a wide range of scales in space and time. On the one hand, there are the scales of the flow-field, $\mathbf{u}$, which range from the largest ones – of size comparable to the domain size – down to the smallest ones, of size of the order of the Kolmogorov scale (the scale at which energy is dissipated by viscosity). On the other hand, there are the scales of the interface separating the two phases, whose size is comparable to that of the molecular scale.

For this reason, performing an accurate simulation of a turbulent multiphase flow is at present extremely challenging. To tackle this problem, we propose here the adoption of a dual-grid approach, based on a combined pseudo-spectral DNS of turbulence, coupled with a Phase Field Method. We remark here that the Phase Field Method (PFM) is based on the introduction of an order parameter ϕ that is uniform in the bulk phases ($\phi = 1$ in one phase, and $\phi = -1$ in the other phase), while it varies continuously over the interface separating the two phases.

Since the solution of the Navier-Stokes equation to obtain the flow-field, $\mathbf{u}$, is extremely computationally demanding, we use two different computational grids: a reference grid for the flow field and pressure $\mathbf{u}$, p (i.e., fine enough to solve the flow down to the Kolmogorov scale), and a refined grid for the phase-field, ϕ. The finer the resolution of the phase-field, ϕ, the better the description of the interface deformation and of the morphology of the phase interaction. This is well represented in figure (1), where two simulations, with two different resolutions for the phase-field, ϕ, are compared (in panel b, the resolution is twice compared to panel a).

The performance of the current approach (in terms of reduction of computational time and required memory) has been evaluated for the well-known benchmark case of the deformation of a single drop in a two-dimensional flow. The applicability of the current method to a realistic 3D case has also been tested, by evaluating the dynamics of a thin sheet layer placed at the centre of a turbulent channel flow. The problem can be described in terms of the shear Reynolds number, Re_τ (which describes the ratio of inertia to viscous forces), and the Weber number, We (which quantifies the ratio between inertia and surface tension forces). The shear Reynolds number is set to $Re_\tau = 150$ while the Weber number is set to $We = 3$. All simulations are performed assuming two fluids with matched density ($\rho_1 = \rho_2 = \rho$) and viscosity ($\mu_1 = \mu_2 = \mu$).

The influence of the resolution of the phase-field, ϕ – while keeping constant the resolution of the flow field, $\mathbf{u}$ – on the dynamics of the flow and on the phase morphology (including also the droplet-size distribution) will be presented and discussed.

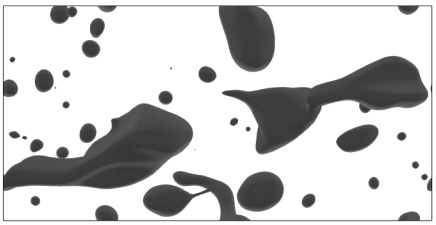

(a) `E1` - $t^+ = 2500$

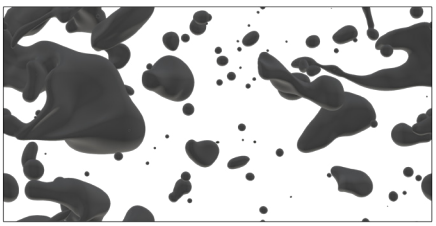

(b) `E2` - $t^+ = 2500$

Figure 1: Dynamics of drops in turbulence. For both panels, the resolution for the flow-field, $\mathbf{u}$, is the same (it is set in order to capture the Kolmogorov length scale). For the phase field, ϕ, simulation `E1` (panel a) is run using the same grid used for the velocity field, $\mathbf{u}$, while for the simulation `E2` (panel b) the grid for the phase-field, ϕ, is finer (twice the number of points in each direction). The improvement in the description of the phase morphology is apparent.

2nd Spanish Fluid Mechanics Conference
Barcelona (2 - 5 July 2023)

Cardiac-cycle inspired turbulent drag reduction

Jose M. López[1], Davide Scarselli[2], Atul Varshney[3], and Bjoern Hof[2]

jose.lopez@uma.es

[1]Departamento de Ingeniería Mecánica, Térmicas y de Fluidos, Universidad de Málaga, Spain
[2]Institute of Science and Technology, Austria
[3]School of Physical Sciences NISER Bhubaneswar, India

Flows through pipes and channels are in practice almost always turbulent and the eddying motion is responsible for the major part of the encountered friction losses and pumping costs. Conversely, for pulsatile flows, in particular for aortic blood flow, turbulence levels remain surprisingly low, despite relatively large peak velocities. Indeed, in this latter case high turbulence levels are intolerable as they would damage the shear sensitive endothelial cell layer. We here show that turbulence in ordinary pipe flow is diminished if the flow is driven in a pulsatile mode that incorporates all the key features of the cardiac waveform. At Reynolds numbers comparable to aortic blood flow, turbulence is largely inhibited, whereas at much higher speeds, the turbulent drag is reduced by more than 25%. This specific operation mode is considerably more efficient when compared to steady driving, which is the status quo for virtually all fluid transport processes ranging from heating circuits to water, gas and oil pipelines.

1 Introduction

Turbulent flows are associated with large friction levels and high pumping costs when compared to laminar conditions. Available estimates show that around 10% of global electric power is consumed for pumping fluids (Frenning , 2001). In addition to the excessive drag levels, fluctuations and alternating shear stresses can also have adverse effects in many enginnering applications. Hence, much effort has been dedicated to develop techniques for turbulence intensity reduction. However, despite many novel and innovative approaches (Brunton , 2015), so far a broadly applicable method remains elusive. Active control techniques require complex actuation devices and in experimental realizations the costs often far exceed the gains. Passive approaches equally suffer from high implementation costs and typically have a limited operation range. Available control techniques are hence problem specific and intrusive, requiring either manipulation of fluid properties or costly and often impractical implementations. Conversely, aortic flow provides an example where a specific propulsion scheme, consisting of impulsive bursts separated by quiescent intervals, appears to hold turbulence at bay despite relatively large peak velocities. Based on this observation, we propose an alternative approach to turbulence control, where drag reduction is achieved using unsteady, pulsatile driving, specifically mimicking the cardiac cycle, and show that the applicability of this method extends to Reynolds numbers well beyond those at which the human heart operates.

2 Methodology and results

We have conducted laboratory experiments and direct numerical simulations on turbulent pipe flow to investigate the drag reduction associated with a pulsatile operation mode under different conditions. In initial experiments and simulations, we tested a cycle consisting of a series of linear flow rate ramps smoothly joined together, corresponding to Re oscillating between $Re_{\min} = 3\,200$ and $Re_{\max} = 18\,800$ with a period $T = 4.5$ s, see Fig. 1 **a**. However, the drag measured in these experiments turned out to be 3% larger than for steady flow, showing that pulsation does not necessarily lead to drag reduction. Inspired by the diastolic phase found in the aortic flow and the low turbulence levels present in these flows, we designed a new cycle where a region of constant Re (rest phase) is inserted that effectively decouples the deceleration from the consecutive acceleration phase (Fig. 1 **b**). Remarkably, the flow responds with considerably lower values of wall shear stress during acceleration, as well as during part of the deceleration phase (Fig. 1 **e**). In this case we obtain a net drag reduction of 22%. However, the additional energy input required to accelerate the flow exceeds the energy savings due to drag reduction. There was however an important difference between this waveform and that of the aortic flow: the studied waveform is characterized by slower deceleration and faster acceleration rates, whereas the opposite holds for velocity waveforms in the aorta (Burk , 2012). Correcting for this,

we chose the waveform displayed in Fig. 1 **c**, with a higher acceleration rate, while the rest phase is left unchanged. With this adjustment, drag reduction reaches 27%, while producing a net energy saving of $\sim 8\%$ compared to steadily driven pipe flow.

We have also investigated how changing the acceleration and rest phase affects drag reduction and power savings. To this end, we have carried out a total of 540 experiments spanning different rest phase and acceleration durations, while keeping minimum and maximum Re and the period constant. It is found that shorter acceleration times consistently lead to higher power savings, hence suggesting the importance of a brief, intense acceleration followed up by a longer, more gentle deceleration. A non zero rest phase is always required to save power. However, there is an optimal rest phase and longer rest phases are counterproductive. The optimal value of rest phase depends weakly on the acceleration rate and it is approximately equal to half the period. Remarkably, the rest phase in aortic blood flow also matches this criterion.

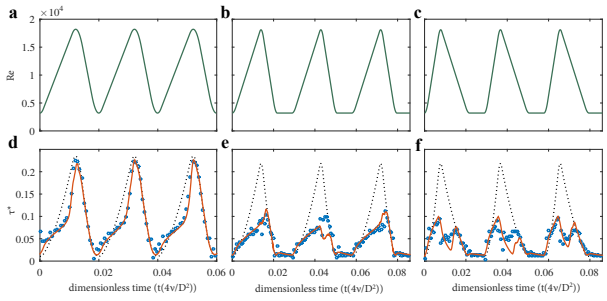

Figure 1: Friction reduction in pulsating flow. Effect of three different cycles on the wall shear stress. **a**, **b** and **c**, Reynolds number modulation imposed in experiments and DNS. **d**, **e** and **f**, corresponding friction dimensionless wall shear stress τ^* for experiments (blue circles) and DNS (red line). For comparison, the friction associated with the quasi–steady flow is shown in the black dotted line given by $\tau_{\mathrm{qs}}(t) = 0.079Re(t)^{-0.25}U_m(t)^2/U_{\mathrm{min}}^2$ (where the Blasius friction scaling is assumed).

3 Conclusions

We demonstrate that the existence of a rest phase (the diastolic phase) in the waveform of the cardiac cycle is crucial to diminish the wall shear stress and keep it at levels tolerable for the blood vessels' endothelial cell layer. This rest phase has to be optimally timed and combined with a subsquent rapid flow acceleration to not only reduce the flow drag, but to also optimize its efficiency and minimize power consumption. We also show that applying the same waveform to a turbulent pipe flow at significantly larger Reynolds numbers than those at which the cardiac cycle operates also produces significant drag reduction and net power saving. These findings unveil the potential of using a pulsatile operation mode as a drag reduction strategy in pipeline flows.

References

Frenning, L. (2001) "Pump Life Cycle Costs: A Guide to LCC Analysis for Pumping Systems" Hydraulic Institute.

Brunton, S. L. and Noack, B. R. (2015) "Closed-loop turbulence control: Progress and challenges". *Applied Mechanics Reviews* **67**.

Burk J. et al. (2012) "Evaluation of 3D blood flow patterns and wall shear stress in the normal and dilated thoracic aorta using flow–sensitive 4D CMR" *J. Cardiovasc. Magn. Reson.* **14**, 84.

2nd Spanish Fluid Mechanics Conference
Barcelona (2 - 5 July 2023)

Convergence of numerical simulations for pipe flow

Sergio Hoyas[1], Marcos Piedrabuena[1], Ezhilsabareesh Kannadasan[2], Hassan Nagib[3], and Ricardo Vinuesa[2]

serhocal@mot.upv.es

[1]Instituto Universitario de Matemática Pura y Aplicada, Universitat Politècnica de València, 46022 Valencia, Spain
[2]FLOW, Engineering Mechanics, KTH Royal Institute of Technology, SE-100 44 Stockholm, Sweden
[3]Armour College of Engineering, Illinois Tech (IIT), Chicago, IL , 60616, USA

In this talk, we will present an exhaustive study of the convergence of DNS of pipe flow for $Re_\tau = 180$ and $Re_\tau = 500$, preparing the field for larger simulations.

Numerical simulations have become, together with new experimental techniques, the key to understanding some of the most intriguing aspects of wall-bounded turbulence. The friction Reynolds number of the simulations has grown steadily in the last 35 years, recently reaching the boundary of $Re_\tau = 10,000$ [1]. Due to its immense technological importance, the flow in circular pipes is also receiving a large interest, as in the Ciclope initiative [2]. However, the numerical simulation of pipes is more difficult than that of channels due to the singularity in the pipe center when using cylindrical coordinates. Fourier methods in the azimuthal direction also impose very small cell sizes in the radial direction at the pipe center to avoid large skewness in the cells.

In this work, we propose a method to fully describe the statistical convergence of a pipe flow in a large pipe of streamwise length $L_z = 10\pi R$, where R is the pipe radius. Several simulations have been run for $Re_\tau = 180$ and 550 with different meshes in the radial direction r. Here we describe two, with 192 (LR) and 384 (HR) points in r. The employed code is OpenPipeFlow [3]. In physical space, the grid spacings are $\Delta z^+ = 3.67$ and $(\Delta\theta R)^+ = 2.94$ (where θ is the azimuthal direction), comparable to or better than many other Direct Numerical Simulations (DNSs). The mesh in r^+ has a resolution of $\Delta r^+ < 1.4$ for both meshes.

Figure 1 shows the evolution of the convergence parameter $\varepsilon_{\text{pipe}}$ defined as in Ref. [4]. In both cases, the sampling is in the safe zone of Ref. [4], with inner-scaled sampling times$\Delta t^+_{192} = 0.091$ and $\Delta t^+_{384} = 0.0337$. The horizontal axis represents the averaging time in eddy-turnover times (ETTs). Note that the ETT is defined as Tu_τ/R, where T is time, and u_τ is the friction velocity. We ran both simulations for 200 ETTs and divided the database into four groups. Convergence is obtained after 20 ETTs. A similar figure about a simulation at $Re_\tau = 550$ will be presented at the meeting, showing a similar threshold.

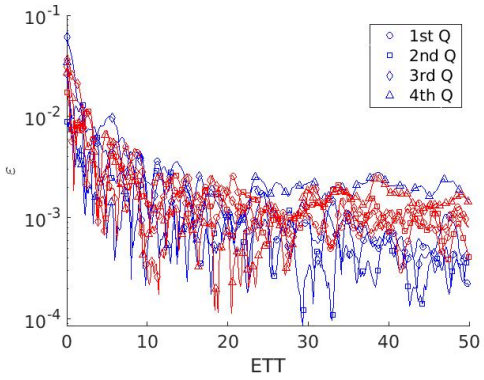

Figure 1: Evolution of the convergence indicator $\varepsilon_{\text{pipe}}$ with time in four segments of run. Red: High resolution in r. Blue: Lower resolution.

References

[1] Hoyas S., Oberlack M., Alcántara-Ávila F., Kraheberger S., and Laux J. (2021). "Wall turbulence at high friction Reynolds numbers". Physical Review Fluids 7, no 014602.

[2] Zanoun E.-S., Egbers C., Nagib H., Durst F., Bellani G, Talamelli A. (2021). "Wall friction in wall-bounded shear flows", European Journal of Mechanics - B/Fluids.

[3] Willis, A. (2017). "The Openpipeflow Navier–Stokes solver", SoftwareX,Volume 6, Pages 124-127, ISSN 2352-7110,

[4] Vinuesa R., Prus C., Schlatter P., Nagib H., (2016). "Convergence of numerical simulations of turbulent wall-bounded flows and mean cross-flow structure of rectangular ducts". Meccanica 51:3025–3042.

2nd Spanish Fluid Mechanics Conference
Barcelona (2 - 5 July 2023)

Fluidic Oscillators performance with shape modification and under incompressible and compressible flow.

Josep M Bergadà[1] and Masoud Baghaei[1]

josep.m.bergada@upc.edu

[1]Departamento de Mecánica de Fluidos, Universitat Politècnica de Catalunya, Barcelona, Spain

A given shape of a Fluidic Oscillator (FO) is studied via 3D-CFD simulations, the output flow pulsating frequency versus the inlet Reynolds number is initially obtained. The internal shape of the (FO) has then been modified to understand the effect of the different internal parts on the output frequency and amplitude. The modification of the feedback channel length has been performed under compressible flow conditions and clarified which is the origin of the self sustained oscillations. The same origin has been found regardless of the fluid being considered as compressible or incompressible and for all different internal shapes studied.

1 Introduction

Active Flow Control applications need to use Fluidic Actuators (FA) like Synthetic Jets (SJ), Fluidic Oscillators (FO) or Plasma Actuators (PA) to modify the boundary layer separation point and in turn interact with the forces acting on any bluff body. Among the different FA, the FO have the advantage of generating large momentum coefficients and having no moving parts, as a result they are seen as particularly effective and reliable. What so far appears to be unclear is which are the forces driving the self sustained oscillations. Some attempts to clarify this point are recently presented in Baghaei and Bergada (2019), Baghaei and Bergada (2020), and Bergada et al. (2021), where in the 3D-CFD simulations performed, the fluid was considered as incompressible or compressible depending of which FO internal dimension was considered. A parametrical analysis of the FO performance under incompressible flow conditions, when the Mixing Chamber (MC) inlet and outlet widths and angles were modified, see Figure 1, was initially undertaken. The effect of the feedback channel length under compressible flow conditions was as well investigated. Four different FC length were considered, L1, L2, L3 and L9. A direct correlation between the outlet flow frequency, the mixing chamber outlet inclined walls stagnation pressure and the net momentum acting on the incoming jet at the feedback channels outlet was observed for all cases studied.

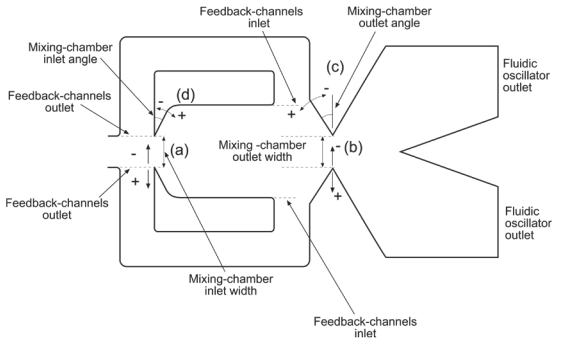

Figure 1: Fluidic oscillator mixing chamber internal shape and dimensions modification.

2 Computational model and Results

Incompressible fluid flow simulations were performed using the DDES turbulence model, DNS was employed for the compressible cases. The mesh was structured in all simulations and consisted of $2,242,000$ cells for the incompressible cases and between $21,736,832$ and $32,417,632$ cells for the compressible fluid cases, depending on the FC lenght evaluated. At the FO inlet, Dirichlet boundary condition (BC) for velocity and temperature as well as Neumann BC for pressure were considered. At the FO outlet, Neumann BC for temperature and velocity, and Dirichlet BC for pressure were used. At the walls, Neumann BC for pressure and temperature as well as Dirichlet BC for velocity were chosen. The time step used for all compressible fluid simulations was of $2.25 * 10^{-8} s$. Second-order discretization was used for all parameters except for time and convection where first-order discretization was employed. Temperature boundary conditions were just considered in compressible cases.

Figures 2, 3 and 4 introduce respectively the velocity field for different Mixing Chamber (MC) di-

mensional modifications, (incompressible fluid, $Re = 16034$), the Q criterion for the baseline feedback channel and inlet velocity of $97m/s$, and the instantaneous pressure and temperature fields for the longest feedback channel considered, inlet velocity $65m/s$. It is observed that, pressure waves originate at the MC outlet inclined surfaces and travel along the FC's towards the FC's outlet.

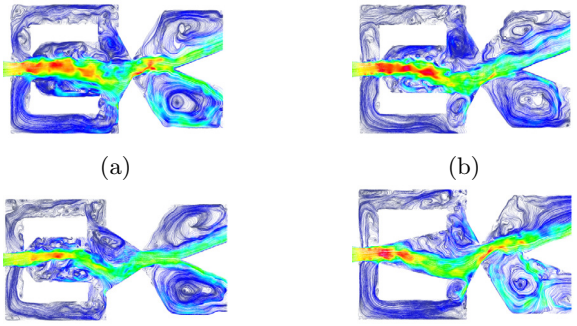

(a) (b) (c) (d)

Figure 2: Velocity fields for different Mixing Chamber (MC) dimensional configurations. a) Maximum inlet width. b) Maximum outlet width. c) Maximum MC outlet angle. d) Maximum MC inlet anle. Re=16034.

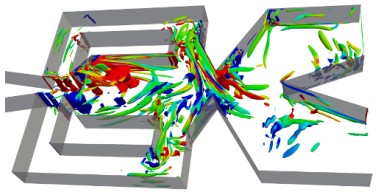

Figure 3: Q criterion vorticity fields. $Q = 11 * 10^8$, inlet velocity 97m/s.

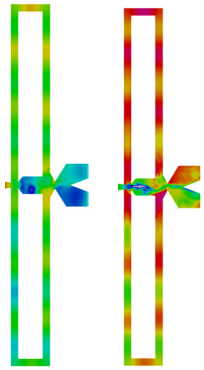

(a) (b)

Figure 4: Feedback channels a) pressure and b) temperature fields. Inlet velocity, 65 m/s, feedback channel length, L9.

In order to prove that the FO self-sustained oscillations are generated due to the alternative stagnation pressure oscillations occurring at the MC outlet inclined pressure walls, Figure 5 is introduced. Which shows a direct correlation between the FO outlet mass flow, the MC lower wall stagnation pressure, the FC mass flow and the net momentum acting on the jet at the the MC entrance. Such correlation was observed for all cases studied, although it became less clear at high FC lengths and high inlet velocities.

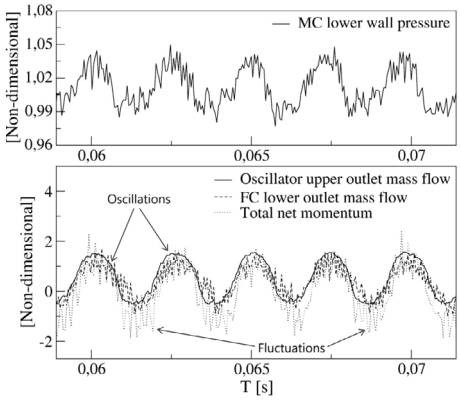

Figure 5: Non-dimensional pressure at the mixing chamber lower converging wall, oscillator mass flow, feedback channels mass flow and total net momentum applied to the incoming jet from both feedback channel outlets. Inlet velocity 97m/s.

3 Conclusions

The article clarifies how the FO output mass flow amplitude and frequency is being modified by the internal mixing chamber and feedback channel dimensions modifications and sheds lights towards the understanding of the origin of the self sustained oscillations.

References

Baghaei, M. and Bergada, J.M. (2019) "Analysis of the Forces Driving the Oscillations in 3D Fluidic Oscillators". *Energies*, **12**, 4720.

Baghaei, M. and Bergada, J.M. (2020) "Fluidic Oscillators, the Effect of Some Design Modifications". *Applied Sciences*, **10**, 2105.

Bergada, J.M. and Baghaei, M. and Prakash, B. and Mellibovsky, F. (2021) "Fluidic Oscillators, Feedback Channel Effect under Compressible Flow Conditions". *Sensors*, **21**, 5768.

2nd Spanish Fluid Mechanics Conference
Barcelona (2 - 5 July 2023)

Heat transfer control in a turbulent boundary layer with Large-Eddy Breakup devices

Qihong Li Hu[1], Firoozeh Foroozan[1], Stefano Discetti[1], and Andrea Ianiro[1]

qli@pa.uc3m.es

[1]Department of Aerospace Engineering, Universidad Carlos III de Madrid, Leganés, Spain

In this work the effect of LEBUs as passive method for the heat transfer control of turbulent boundary layers is investigated. Different LEBU configurations, with and without vortex generators, have been tested to analyse their effect on the convective heat transfer coefficient in a moderate friction-based Reynolds number turbulent boundary layer. Heat transfer measurements with infrared thermography are performed in order to estimate the wall convective heat transfer coefficient fluctuations.

Controlling the convective heat transfer of turbulent boundary layers (TBLs) is of utmost importance in a wide range of industrial applications, including turbomachinery, production processes and cooling of electronics. During the last decades, different investigations about turbulent transport have been targeted to identify strategies to increase heat transfer while at the same time reducing the skin friction drag, or at least increasing it at a lower rate than the heat transfer. Turbulent heat transfer enhancement and control strategies for turbulent skin friction drag reduction have been extensively studied separately obtaining satisfactory results in both aspects (1).

Large-Eddy BreakUp devices (LEBUs) are passive control devices that consist of thin plates installed inside the outer layer of the TBL. Their main task is to break up large coherent structures and change the structure of the boundary layer. Several numerical and experimental studies aimed to show their effect on reducing the skin friction coefficient. Nevertheless, it has not been demonstrated its effectiveness in the reduction of the net friction drag. This was due to the drag induced by the presence of the LEBU itself being of the same order of magnitude or even larger that any reduction achieved during simulations. Nonetheless, their effect on the organization of the TBL structures tickles the curiosity about their potential in other fields, e.g. heat transfer, and on whether proper geometrical modification can improve their capabilities. Vortex Generators (VGs) are also passive control methods that have been widely studied and, that were observed to improve the heat transfer (2). Indeed, in (3) it was observed that the heat transfer downstream of a LEBU plate was enhanced when attaching VGs onto a plate surface.

Although several studies targeting LEBUs as control methods have been done during last years, most of them focused on the skin friction and were based on simulations, so further experimental studies are needed to have a better understanding of the effects of LEBUs. Moreover, the demonstration of heat transfer enhancement/reduction due to the combination of VG and LEBUs has not been carried out experimentally to our knowledge, thus motivating the present work. An experimental setup has been developed to investigate the heat transfer improvement in a TBL at low friction-based Reynolds number Re_τ, manipulated using different configurations of LEBUs and VG. Infrared thermography and Particle Image Velocimetry (PIV) are used synchronously to acquire instantaneous wall heat transfer and flow fields in planes parallel to the wall.

The experiments are carried out in the water tunnel facility of the Department of Aerospace Engineering at Universidad Carlos III de Madrid, with a rectangular test section of 0.5×0.55 m^2 equipped with a vertically-mounted flat plate spanning the full length of the 2.5 m test section. For the present experiments, the tunnel is operated in an open channel configuration with the free-stream velocity of $U_\infty = 0.25$ m/s.

The LEBUs are located at $\Delta x_s \approx 4\delta_{99,s}$ upstream of the measurement region and a distance of $H \approx 0.65\delta_{99,s}$ away from the wall. The nominal LEBU is designed with the thickness of 2mm, the width of $W \approx 0.8\delta_{99,s}$, and the length of $L \approx 4\delta_{99,s}$. The VGs are attached to the bottom face of the LEBU facing the wall. Different configurations of VGs have been evaluated varying the main geometric parameters characterising the shape and position of the VGs. These parameters are: $\alpha = 0,\ 18°$; $d = 0,\ 10,\ 15$mm, and $s = 0,\ 50$mm, as shown in Figure 1. Note that the geometry of the VGs is fully defined given the height d and the angle $\gamma = 30°$.

Convective heat transfer measurements are done using a flush-mounted heated-thin-foil sensor (4) embedded on the flat plate where the boundary layer

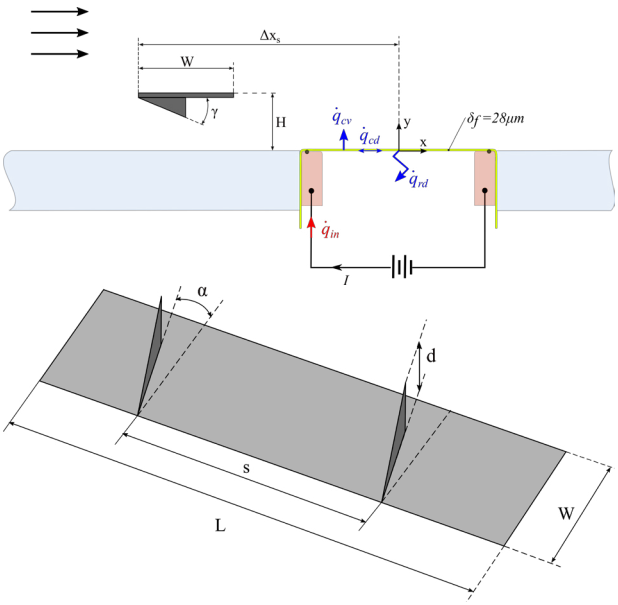

Figure 1: Schematic view of the LEBU system with main geometric and position parameters with respect to the sensor.

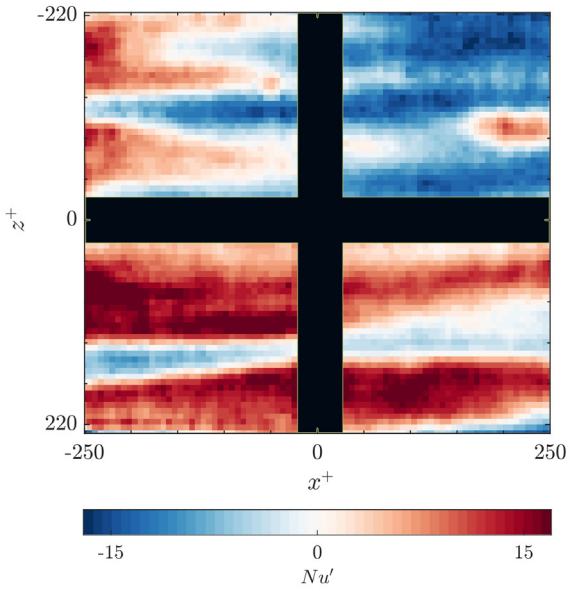

Figure 2: An instantaneous Nu fluctuations map for the case of $\alpha = 18°$, $d = 10$mm, and $s = 50$mm. It clearly shows the positive and negative regions of convective heat transfer.

thickness is $\delta_{99,s} = 34$mm. With this sensor, the instantaneous convective heat transfer coefficient (h) is estimated from the energy balance model through the thin foil, including heating by Joule effect, tangential conduction, radiation heat fluxes and an unsteady term accounting for wall thermal inertia. The temperature is considered practically uniform across the foil thickness. The convective heat transfer data are reported in terms of Nusselt number $Nu = hl/k$, where the characteristic length is the TBL thickness, and k is the thermal conductivity of water. The temporal evolution of the surface temperature of the foil is sampled at 60Hz using a FLIR SC4000 IR camera with a noise equivalent temperature difference of about 18mK and a spatial resolution of 1075pixels/m. Using this technique, the wall temperature fluctuations of the order of 3 to 5 degrees are obtained.

An example of an instantaneous map of the fluctuations of Nu is reported in Figure 2. For the final conference contribution, we will include an in-depth comparison of the performances of LEBUs with different VG configurations in terms of average Nusselt number and instantaneous flow features.

Acknowledgement

This work has been supported by the project ARTURO, funded by the Spanish State Research Agency. ref. PID2019-109717RB-I00/AEI/10.13039/501100011033

References

[1] Kasagi N. & Hasegawa Y. & Fukagata, K. & Iwamoto, K. (2012) "Control of Turbulent Transport: Less Friction and More Heat Transfer". *Journal of Heat Transfer*, **134**, 0022–1481.

[2] Gentry, M. C., & Jacobi, A. M. (2002). "Heat Transfer Enhancement by Delta-Wing-Generated Tip Vortices in Flat-Plate and Developing Channel Flows". *ASME. J. Heat Transfer*, **124**, 1158–1168.

[3] Inoaka, K. & Suzuki, K. (1995) "Structure of the Turbulent Boundary Layer and Heat Transfer Downstream of a Vortex Generator Attached to a LEBU Plate". *Turbulent Shear Flows 9*, **134**, 365–382.

[4] Nakamura, H. (2009) "Frequency response and spatial resolution of a thin foil for heat transfer measurements using infrared thermography". *Int. J. Heat Mass Transf.*, **52**, 5040–5045.

2nd Spanish Fluid Mechanics Conference
Barcelona (2 - 5 July 2023)

Hydrogen Injection and Turbulent Mixing Processes Using a Porous Plate Injector

David Rodríguez Gutiérrez,[1] Andrea Gruber,[2] Raquel Gómez Miguel,[1] Mario Sánchez Sanz,[3] and Eduardo Fernández Tarrazo[3]

[1] *Propulsion Dept., Instituto Nacional de Técnica Aeroespacial, SPAIN*
[2] *Energy and Process Engineering Dept., Norges Teknisk-Naturvitenskapelige Universitet, NORWAY*
[3] *Fluid Mechanics and Thermal Engineering Dept., Universidad Carlos III de Madrid, SPAIN*

This work studies the injection of hydrogen through a porous plate to a turbulent air flow and its latter mixing process. This novel technique aims to enhance the mixing process compared to the current injector configuration potentially achieving a better quality mixture, avoiding local peaks in the temperature field, and therefore reducing notably the NO_x emisions.

INTRODUCTION

Premixed combustion is receiving a raising attention in the last years, due to the fact that hot spots present in non-premixed combustion are suppressed. In addition to this, stoichiometry can be controlled, so that temperatures can be substantially reduced by increasing the air-to-fuel ratio, forcing combustion chambers to work in the lean or even ultra-lean regime ([1, 2]), minimizing in that way the NO_x formation.

In contrast, this combustion regime presents major challenges that must be tackled. Among the safety concerns, it can be highlighted that in this combustion set-up, fuel and oxidizer stay at the same place increasing the risk of undesired deflagrations or flashbacks provided the high reactivity level of hydrogen-air mixtures. Furthermore, premixed flames are strongly affected by their intrinsic instabilities as well as the acoustics, being strongly non-linear ([3–5]), what means that a poor understanding of the multiscale processes taking place can involve operating in an off-design point, having a poor combustion completion and increasing the NO_x emissions.

This work aims to study the H_2-air mixing processes in a porous wall injector, a concept proposed by Gruber et al. [6] in which H_2 flows through a selective permeable wall and is injected into the combustion chamber, where it mixes in cross-flow configuration with a turbulent flow of air.

PROBLEM FORMULATION

With this purpose, a turbulent channel air flow is solved where hydrogen is injected through the bottom wall. A sketch of the problem configuration can be visualized in Fig. 1.

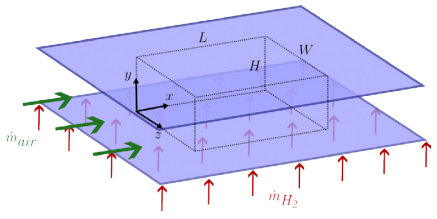

FIG. 1. Problem overview.

The problem proposed is tackled from a numerical approach. Full time-dependent, three-dimensional compressible Navier-Stokes equations are solved, extended with the species equations to evaluate the mass transport among N_2, O_2 and H_2. Large Eddy Simulation (LES) method is used to model the small scales of the turbulence using the turbulent kinetic energy transport equation.

$$\frac{\partial \rho}{\partial t} + \nabla \cdot (\rho \boldsymbol{v}) = 0 \tag{1}$$

$$\frac{\partial}{\partial t}(\rho \boldsymbol{v}) + \nabla \cdot (\rho \boldsymbol{v} \otimes \boldsymbol{v} + p\boldsymbol{I}) = \nabla \cdot \boldsymbol{\tau} + \boldsymbol{f_D} \tag{2}$$

$$\frac{\partial}{\partial t}(\rho E) + \nabla \cdot (\rho H \boldsymbol{v}) = \nabla \cdot (\boldsymbol{\tau} \cdot \boldsymbol{v} - \boldsymbol{q}) \tag{3}$$

$$\frac{\partial}{\partial t}(\rho Y_{H_2}) + \nabla \cdot (\rho Y_{H_2} \boldsymbol{v}) = \nabla \cdot (\rho D_{H_2} \nabla Y_{H_2}) \tag{4}$$

$$\frac{\partial}{\partial t}(\rho Y_{O_2}) + \nabla \cdot (\rho Y_{O_2} \boldsymbol{v}) = \nabla \cdot (\rho D_{O_2} \nabla Y_{O_2}) \tag{5}$$

$$\frac{\partial}{\partial t}(\rho k) + \nabla \cdot \left(\rho \left[k + \frac{p}{\rho}\right] \boldsymbol{v}\right) = \nabla \cdot (\,[\mu + \mu_{\text{sgs}}]\,\nabla k) - \epsilon - \boldsymbol{\tau_{\text{sgs}}} : \boldsymbol{S} \tag{6}$$

where ρ is the mixture density, $\boldsymbol{v} = \{u, v, w\}$ is the mixture velocity field, p, the pressure, I, the 3×3 identity matrix, $\boldsymbol{\tau}$, the viscous stress tensor, E, the mixture total energy, H, the mixture total enthalpy, $\boldsymbol{q}$, the heat conduction, Y_i, the mass fraction of species i, D_i, the mass diffusivity of the species i in the mixture, k the turbulent kinetic energy, μ, the mixture dynamic viscosity, and $\boldsymbol{S}$ the strain rate tensor. Note that the subscript sgs means sub-grid scale.

Special mention deserves the source term in momentum equation (eq. 2), hydrogen is injected in the air main stream through bottom wall due to a pressure difference Δp_{inj}, the wall is modeled as a porous material that provokes a pressure loss $\boldsymbol{f_P}$ in the H_2 stream, defined by Darcy's law:

$$\boldsymbol{f_P} = \begin{cases} \dfrac{\mu_{H_2}}{\varepsilon}(1,1,1) & \text{in the porous media} \\ \boldsymbol{0} & \text{elsewhere} \end{cases} \tag{7}$$

where μ_{H_2} is the dynamic viscosity of the hydrogen and ε is the permeability of the porous medium. It is important to remark that the material is orthotropic, so that the pressure loss is the same in all three directions.

Regarding the other boundaries of the problem, the top wall, impermeable and adiabatic, is located at a height $H = 2h$, being h the channel semiheight. The channel is assumed to be infinitely wide, so that the problem domain is truncated with a width $W = 3h$ setting periodic boundaries in this direction. A constant pressure outlet bounds the domain downstream located at $L = 6h$.

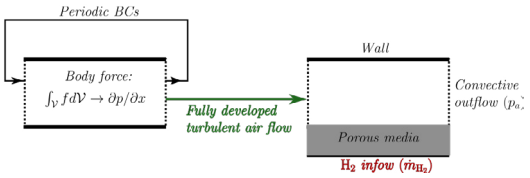

FIG. 2. Sketch of the computational domain and boundary conditions (constant z-plane slice).

The boundary conditions are closed with a fully developed turbulent flow of air at $Re = \rho u h/\mu = 11000$ entering in the problem domain. This flow is pre-computed using an infinitely long channel (i.e. forcing periodicity at inlet-outlet of a channel with the same dimensions). The flow is initialized with a perturbed Poiseuille profile and after a certain time this initial perturbation evolves to physical turbulence. It is important to highlight that due to the inlet-outlet periodicity, a body force which maintains a constant pressure gradient must be added to the momentum equation, otherwise the flow losses momentum with time and the developed turbulent flow has not the desired conditions. An outline of both precomputation of the turbulent air flow and the problem of hydrogen injection itself is presented in Fig. 2.

RESULTS AND CONCLUSIONS

Different qualitative features of the precomputed airflow can be observed. Fig. 3 presents isosurfaces of the

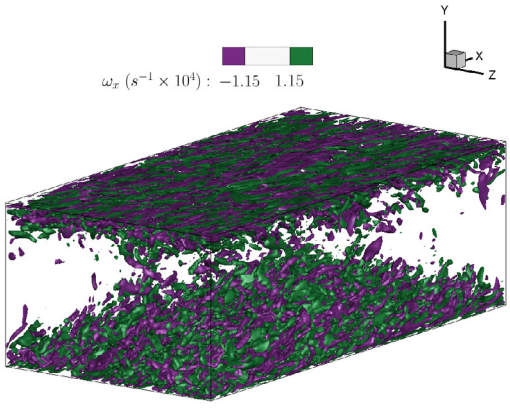

FIG. 3. x-Vorticity isosurfaces.

maximum (positive and negative) values of the streamwise component of the vorticity ($\boldsymbol{\omega}$) whereas Figs. 4 and 5 present false colormaps for the streamwise velocity (u) and the turbulent kinetic energy (k):

$$\boldsymbol{\omega} = \nabla \times \boldsymbol{v}, \quad k = \frac{1}{2}\mathrm{tr}\left(\boldsymbol{\tau}_{\mathbf{sgs}}\right) \tag{8}$$

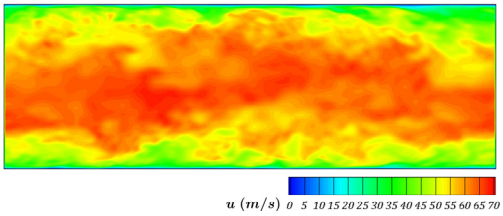

FIG. 4. x-Velocity false colormap at $z = 1.5h$ plane.

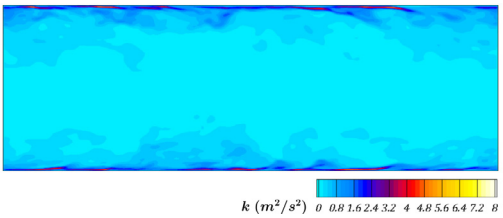

FIG. 5. Turbulent kinetic energy false colormap at $z = 1.5h$ plane.

Once the hydrogen is injected, detailed results of the mixing process are to be provided, including the final mixture quality, the overall mixture length needed to achieve premixed conditions as well as proposal of techniques to enhance the results obtained.

[1] Veiga-López F., Kuznetsov M., Martínez-Ruiz D., Fernández-Tarrazo E., Grune J. & Sánchez-Sanz M. (2020) "Unexpected propagation of ultra-lean hydrogen flames in narrow gaps". *Physical review letters*, **129 (17)**, 174501.

[2] Bosch J., Fernández-Galisteo D., Jiménez C. & Kurdyumov V. N. (2020) "Analytical study of superadiabatic small-scale combustors with a two-step chain-branching chemistry model: Lean burning below the flamability limit". *Combustion and Flame*, **235**, 111731.

[3] Fernández-Galisteo D., Kurdyumov V. N. & Ronney P. D. "Analysis of premixed flame propagation between two closely-spaced parallel plates". *Combustion and Flame*, **190**, 133–145.

[4] Veiga-López F., Martínez-Ruiz D., Fernández-Tarrazo E. & Sánchez-Sanz M. (2019) "Experimental Analysis of oscillatory premixed flames in a hele-shaw cell propagating towards a closed end". *Combustion and Flame*, **201**, 1–11.

[5] Rodríguez-Gutiérrez D., Gómez-Miguel R., Fernández-Tarrazo E. & Sánchez-Sanz M. (2022) "Characterization of symmetric to non-symmetric flamefront transtion in slender microchannels". *Proceedings of the Combustion Institute*.

[6] Gruber A., Salimath P. S. & Chen, J. H. (2014) "Direct numerical simulation of laminar flame–wall interaction for a novel H2-selective membrane/injector configuration". *International Journal of Hydrogen Energy*, **39 (11)**, 5906–5918.

2nd Spanish Fluid Mechanics Conference
Barcelona (2 - 5 July 2023)

Interventional Causality Analysis of Fully Developed Turbulent Channel Flow

Kosuke Osawa[1] and Javier Jiménez[1]

kosawa@torroja.upm.es

[1]School of Aeronautics, Universidad Politécnica de Madrid, 28040 Madrid, Spain.

The causal events in fully developed open channel flow at $Re_\tau = 609$ are studied using direct numerical simulations. Spatially localized perturbations are imposed on the flow, and the causal significance of perturbed flow structures is measured by the perturbation growth. The results show that for wall-attached perturbations, the causal event is local high shear, while for wall-detached perturbations, it is intense sweep.

1 Motivation

This study aims to identify causally important events in fully developed wall turbulence. We apply an interventional causality analysis method that was originally developed for 2D homogeneous isotropic turbulence (HIT) by Jiménez (2020), and recently extended to 3D HIT by Encinar and Jiménez (2023).

2 Methodology

Numerically simulated open channel flow at $Re_\tau = 609$ is perturbed by removing fluctuation velocity in a small cubic cell, and the causal significance of the flow structures in the cell is measured by the growth of energy of the perturbation velocity. We vary the size l^+_{cell} and bottom height y^+_{cell} of perturbation cells from 25 to 150 and 0 to 300, respectively. Here superscript $+$ denotes wall units. The experiment is repeated with changing perturbed location and snapshot. In total, 29520 experiments were conducted.

3 Results

Causal features depend on time and y_{cell}. At the moment when causal significance most diverges, causal features of wall attached perturbations turn out to be high mean shear, whereas detached perturbations are intense sweep. The amount of local shear experienced by the perturbations explains these characteristics. Conditioning reveal that the flow around causally significant/irrelevant wall detached cells are larger-scale sweep/ejections riding above smaller-scale ejection/sweeps (figure1), This is different from the typical conditional tall attached sweep-ejection pairs in Lozano-Durán et al (2012).

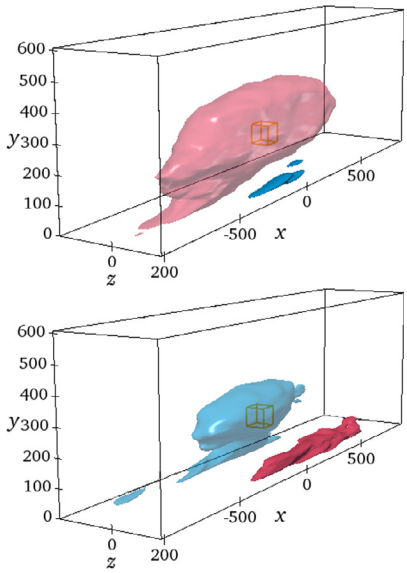

Figure 1: Iso-surfaces of conditional streamwise fluctuation velocity around significant (top) and irrelevant (bottom) perturbation cells, low-pass filtered at $\Delta = l_{cell}$. Red: u^+=0.6; blue: $u^+ = -0.03$. A small cube indicates the position and size of cell. $y^+_{cell} = 150$, $l^+_{cell} = 75$.

References

Jiménez J (2020) "Computers and turbulence". *European Journal of Mechanics - B/Fluids*, **79**, 1–11.

Encinar M & Jiménez J (2023) "Identifying causal significance in three-dimensional isotropic turbulence". *Under Review*, arXiv:2302.04630.

Lozano-Durán A, Flores O & Jiménez J (2012) "The three-dimensional structure of momentum transfer in turbulent channels". *Journal of Fluid Mechanics*, **694**, 100–130.

2nd Spanish Fluid Mechanics Conference
Barcelona (2 - 5 July 2023)

On the aerodynamic sound generated by a subsonic flow past a circular cylinder

Carlos Tur-Mongé[1], Benet Eiximeno[1,2], Oriol Lehmkuhl[2], and Ivette Rodriguez[1]

ivette.rodriguez@upc.edu

[1]Turbulence and Aerodynamics Research Group, Universitat Politècnica de Catalunya, Spain
[2]Large-scale Computational Fluid Dynamics Group, Barcelona Supercomputing Center, Spain

The aerodynamic sound generated by a three-dimensional cylinder on a turbulent flow with $Re = 10.000$ at $M_0 = 0.2$ and $M_0 = 0.5$ is studied. Compressible large-eddy simulations are performed using an explicit fourth-order spectral element method. The far-field noise generated by the interaction of the cylinder and the turbulent flow is then predicted using the Ffowcs Williams-Hawkings analogy.

1 Introduction

The subject of the noise generated by the turbulent flow is an area of research with increasing relevance due to its technological and societal implications. In this sense, to estimate the intensity of coherent fluctuations and noise produced by the flow is of importance in order to to find innovative solutions for noise reduction. The prediction of the acoustic field generated by the unsteady flow can be done using different approaches, e.g., direct computational aeroacoustics, boundary element integral method, or by using an acoustic analogy. Acoustic analogies allow performing aeroacoustic computations at a reduced computational cost since they detach the fluid dynamic problem from the acoustic one. The near-field fluid dynamics is first solved using a compressible CFD simulation. The obtained results are then interpolated into a permeable surface so that the acoustic pressure can be calculated at any point in the far field as a post-processing step. The focus of this paper is on the implementation of a Ffowcs Williams and Hawkings (FW-H) methodology to analyse the aeroacoustic noise generated by the turbulent flow past a circular cylinder at $Re = 10^4$ and $M_0 = 0.2$ and $M_0 = 0.5$. Here, the flow field is computed using compressible large-eddy simulation (LES), while far-field noise is calculated using the FW-H analogy. Validation of the methodology as well as the comparison of the compressibility effects on the noise radiated will be presented and discussed in detail.

2 Mathematical and numerical methodology

The near-field fluid dynamics is solved using SOD2D, an in-house GPU-capable CFD code that implements a numerical solution for the equations governing compressible fluid flow in three dimensions. The code is based on the high-order spectral element method (SEM) and is designed to be used for scale-resolving simulations (DNS/LES). Time integration is done explicitly using a 4th-order Runge-Kutta scheme.

Regarding the aeroacoustic post-processing, a Python code, based on the Ffowcs Williams-Hawkings analogy, has been developed. In particular, the algorithm follows the formulation proposed by Najafi-Yazdi et al. (2011) which considers that both the observer and the body are static, and takes into account the presence of a mean flow. Time derivatives are evaluated in the code by means of a first-order implicit scheme while a linear interpolation is performed in order to evaluate source terms at the emission time τ. The implemented code is validated using the Method of Manufactured Solutions (MMS), which yields a first-order accuracy in the computation of the acoustic pressure, as represented in Figure 1.

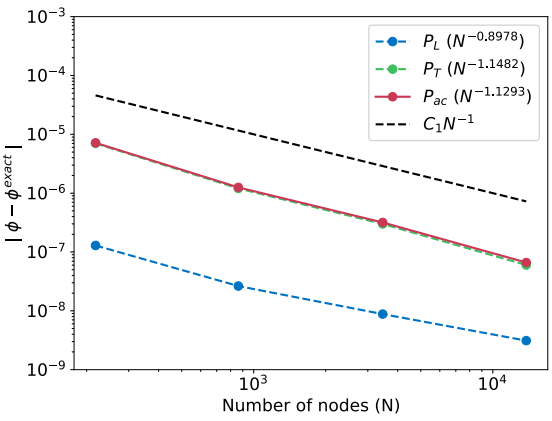

Figure 1: First-order accurate convergence of the acoustic pressure and its terms.

For the LES, a computational domain of $80D \times 60D \times \pi D$ in the streamwise, cross-stream and spanwise directions, respectively has been used. The mesh is generated by extruding a two-dimensional semi-structured grid in the spanwise direction. The final, three-dimensional mesh is formed by 3rd-order hexahedrons (64 nodes/element) for a total of 27.3 million nodes. Adequate refinement is applied in the wake region and the vicinities of the cylinder, specially at the boundary layer where a $y^+ < 1$ has been set. Finally, a FW-H permeable surface mesh is generated using 3rd-order quadrangular elements (16 nodes/element), with a total of 18.000 nodes. The surface extends down to $40D$ in the streamwise, and $[-6D, 6D]$ in the cross-stream directions, in order to capture the main sound generating turbulent features in the wake.

3 Results and further work

Comparison of the results at $M_0 = 0.2$ with those of the literature shows a quite good agreement, specially with the LES of Khaligi et al. (2010) which was performed at the same Mach number (see Table Table 1).

Case	St	$\overline{C_d}$	C_d^{rms}	C_L^{rms}	L_c/D
D&K05	0.203	1.143	—	—	0.820
GOP93	0.193	1.186	0.021	0.384	—
NOR03	0.202	—	—	—	—
KHA10	0.192	1.290	0.098	0.63	0.68
Present LES	0.196	1.269	0.120	0.64	0.67

Table 1: Physical quantities in the flow past a stationary cylinder at Re=10.000 and $M_0 = 0.2$. Data extracted from (D&K05) Dong *et al.* (2006) (DNS, incompressible), (GOP93) Gopalkrishnan (1993) (Exp., incompressible), (NOR03) Norberg (2003) (Exp., incompressible), and (KHA10) Khaligi et al. (2010) (LES, compressible, $M_0 = 0.2$).

Additionally, streamwise velocity fluctuations in the cross-stream direction at two stations in the cylinder's wake, see Figure 2, also yield an excellent agreement. Furthermore, results obtained at $M_0 = 0.5$ are also plotted in the figure. Notice the increase in the average velocity fluctuations. In general, the analysis of the flow for both studied Mach numbers indicates an increase not only in the drag coefficient, but also in the Reynolds stresses. This behaviour has been associated with an early transition to turbulence in the shear layers with an enhancement of the fluctuations in the vortex formation zone with the Mach number. The implications of this change in the behaviour of the flow and its effects on the aeroacoustic field will be studied in the final version of this work.

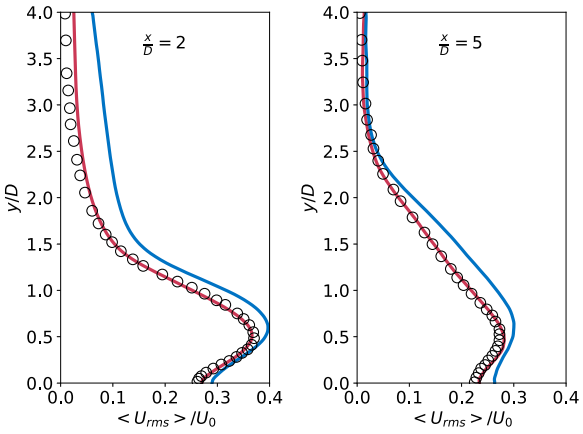

Figure 2: Average streamwise velocity fluctuations for two stations in the wake of the cylinder; red solid line, present LES ($M_0 = 0.2$); blue solid line, present LES ($M_0 = 0.5$); circle, reference solution by Khaligi et al. (2010) ($M_0 = 0.2$).

Acknowledgements

This work has been partially financially supported by the Ministerio de Economía y Competitividad, Secretaría de Estado de Investigación, Desarrollo e Innovación, Spain (ref. PID2020-116937RB-C21 and PID2020-116937RB-C22).

References

Najafi-Yazdi, A., Brès, G. A., & Mongeau, L. (2011). An acoustic analogy formulation for moving sources in uniformly moving media. Proceedings of the Royal Society A: Mathematical, Physical and Engineering Sciences, 467(2125), 144-165.

Khalighi, Y., Mani, A., Ham, F., & Moin, P. (2010). Prediction of sound generated by complex flows at low Mach numbers. AIAA journal, 48(2), 306-316.

Gopalkrishnan, R. (1993), Vortex-Induced Forces on Oscillating Bluff Cylinders. PhD Thesis.

Dong, S., Karniadakis, G. E., Ekmekci, A. & Rockwell, D. 2006 A combined direct numerical simulation-particle image velocimetry study of the turbulent near wake. *Journal of Fluid Mechanics* **569**, 185.

Norberg, C. 2003 Fluctuating lift on a circular cylinder: review and new measurements. *Journal of Fluids and Structures* **17** (1), 57–96.

2nd Spanish Fluid Mechanics Conference
Barcelona (2 - 5 July 2023)

On the stability of wall-bounded flows at high-pressure transcritical fluid conditions

Marc Bernades[1], Francesco Capuano[1], and Lluís Jofre[1]

marc.bernades@upc.edu

[1]Dept. Fluid Mechanics, Universitat Politècnica de Catalunya · BarcelonaTech (UPC), Barcelona 08019, Spain

1 Introduction

High-pressure transcritical fluids operate within thermodynamic spaces in which supercritical gas-like and liquid-like states can be differentiated across the pseudo-boiling line (Jofre & Urzay , 2020, 2021). As studied by Bernades & Jofre (2022), the thermophysical properties of these two regimes in the vicinity of the pseudoboiling region can be leveraged to significantly increase the Reynolds numbers with respect to atmospheric conditions. Among other fields, this result is notably important in microfluidics as it may enable the achievement of microconfined turbulence to obtain enhanced mixing and heat transfer rates.

In this regard, the recent direct numerical simulations (DNS) performed by Bernades et al. (2022, 2023) demonstrate the feasibility of achieving microconfined turbulence by means of utilizing high-pressure transcritical fluids. The resulting flow physics differ significantly from the typical behavior of turbulent wall-bounded flows, which is altered by the presence of localized baroclinic torques responsible for remarkably increasing flow rotation. As a result, the flow becomes unstable and rotation is transformed into a wide range of scales (i.e., turbulent flow motions) through vortex stretching mechanisms.

However, the phenomena responsible for destabilizing the flow are still not fully characterized. To that end, this work aims to conduct linear stability analysis of wall-bounded flows at high-pressure transcritical fluid conditions to carefully identify and quantify the underlying flow mechanisms. In this regard, Ren et al. (2019) have recently developed a linear stability analysis framework for highly non-ideal fluids from which this work will initially feed. In particular, focus will be placed on analyzing the principal modes for different values of the dimensionless numbers, and subsequently compare results to DNS data.

2 High-pressure transcritical fluids

The framework utilized for studying supercritical fluids in terms of (i) equations of fluid motion, and (ii) real-gas thermodynamics is briefly introduced below.

2.1 Equations of fluid motion

The turbulent flow motion of supercritical fluids is described by the following set of dimensionless equations of mass, momentum, and total energy

$$\frac{D^*\rho^*}{D^*t^*} = -\rho^*\left(\nabla^*\cdot\mathbf{v}^*\right), \tag{1}$$

$$\rho^*\frac{D^*\mathbf{v}^*}{D^*t^*} = -\nabla^*P^* + \frac{1}{Re}\nabla^*\cdot\boldsymbol{\tau}^*, \tag{2}$$

$$\rho^*\frac{D^*E^*}{D^*t^*} = -\frac{1}{RePrEc}\nabla^*\cdot\mathbf{q}^* - \nabla^*\cdot(P^*\mathbf{v}^*) + \frac{1}{Re}\nabla^*\cdot(\boldsymbol{\tau}^*\cdot\mathbf{v}^*), \tag{3}$$

where superscript * denotes dimensionless quantities, ρ is the density, $\mathbf{v}$ is the velocity vector, P is the pressure, $\boldsymbol{\tau}$ is the viscous stress tensor, E is the total energy, $\mathbf{q}$ is the Fourier heat flux, and Re, Pr and Ec are the Reynolds, Prandtl and Eckert numbers, respectively.

2.2 Real-gas thermodynamics

The Peng-Robinson equation of state is selected in this work to close the thermodynamics, together with the corresponding high-pressure thermodynamic potentials based on departure functions (Jofre & Urzay , 2021). When the compressibility factor is $Z \sim 1$, the dimensionless equation of state can be approximated as a function of the Mach number Ma and heat capacity ratio γ in the form

$$P^* = \frac{Z\rho^*T^*}{\gamma Ma^2}. \tag{4}$$

In addition, the high pressures involved in the analyzes conducted prevent the use of simple relations for the calculation of the dynamic viscosity μ and thermal conductivity κ. Instead, standard methods for computing these coefficients for Newtonian fluids at high pressures are utilized (Jofre & Urzay , 2021).

3 Linear stability analysis

The baroclinic torque responsible for destabilizing the flow is generated by the combination of the external force driving the flow and the density gradients

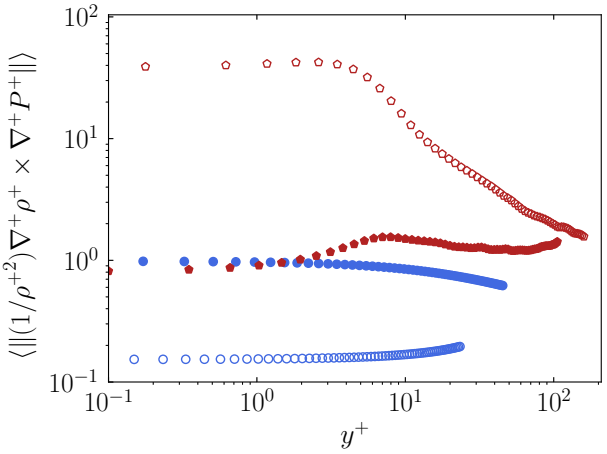

Figure 1: Ensemble-averaged values of normalized baroclinic torque along the wall-normal direction for low-pressure (blue) and high-pressure (red) cases: cold wall (solid circles), hot wall (hollow circles).

present in the system. As depicted in figure 1, the value of this torque is negligible in the case of systems at low pressure conditions. Instead, as a result of the large density gradients obtained across the pseudo-boiling region, it becomes extraordinarily important (approximately 500× larger) in the case of operating at high pressure transcritical fluid regimes.

Related to this problem, Ren et al. (2019) analyzed the stability of boundary layers at high pressures and identified the presence of a secondary mode when operating close to the pseudo-boiling line. They also found that the magnitude of the mode increased with the Ec number, and that the mode disappeared at supercritical conditions far from the pseudo-boiling region and at subcritical pressures. However, the effect of this mode on the value of the transition Reynolds number has not been characterized yet, and therefore this will be studied in detail in this work together with its sensitivity with respect to the dimensionless numbers of the problem.

4 Conclusions

The hydrodynamic and thermophysical properties that high-pressure transcritical fluids exhibit in the vicinity of the pseudo-boiling region result in the increase of flow mixing and heat transfer. This increment is consequence of the alteration of the flow behavior due to the presence of baroclinic instabilities, which leads to boundary layer characteristics different than in the case of low-pressure single-phase conditions. To this end, as initially explored by Ren et al. (2019), linear stability analysis can be potentially leveraged to discover the fundamental mechanisms responsible for flow destabilization at high-pressure transcritical fluid conditions by means of, for example, inferring the presence of unstable modes and their dependence to the operating conditions.

Acknowledgements

This work is funded by the European Union (ERC, SCRAMBLE, 101040379). Views and opinions expressed are however those of the authors only and do not necessarily reflect those of the European Union or the European Research Council. Neither the European Union nor the granting authority can be held responsible for them. Support from the *Formació de Professorat Universitari* scholarship (FPU-UPC R.D 103/2019) of the *Universitat Politècnica de Catalunya* · BarcelonaTech (UPC) (Spain), the *Serra Húnter* programme (Catalonia), and the *Beatriz Galindo* programme (Distinguished Researcher, BGP18/00026) of the *Ministerio de Ciencia, Innovación y Universidades* (Spain) is also acknowledged.

References

Bernades M. & Jofre L. (2022) "Thermophysical analysis of microconfined turbulent flow regimes at supercritical fluid conditions in heat transfer applications". *J. Heat Transfer*, **144**, 082501.

Bernades M., Capuano F., Maeda K. & Jofre L. (2022) "Flow physics characterization of microconfined high-pressure transcritical fluids turbulence". *Proceedings Summer Program, Center for Turbulence Research, Stanford University*, , 215–224.

Bernades M., Capuano F. & Jofre L. (2023) "Microconfined high-pressure transcritical fluid turbulence". *Phys. Fluids*, **35**, 015163.

Jofre L. & Urzay J. (2020) "Transcritical diffuse-interface hydrodynamics of propellants in high-pressure combustors of chemical propulsion systems". *Annual Research Briefs, Center for Turbulence Research, Stanford University*, , 277–282.

Jofre L. & Urzay J. (2021) "A characteristic length scale for density gradients in supercritical monocomponent flows near pseudoboiling". *Prog. Energy Combust. Sci.*, **82**, 100877.

Ren J., Marxen O. & Pecnik R. (2019) "Boundary-layer stability of supercritical fluids in the vicinity of the Widom line". *J. Fluid Mech.*, **871**, 831–864.

Ren J., Fu S. & Pecnik R. (2019) "Linear instability of Poiseuille flows with highly non-ideal fluids". *J. Fluid Mech.*, **859**, 89–125.

2nd Spanish Fluid Mechanics Conference
Barcelona (2 - 5 July 2023)

Smallest box sizes sustaining short-streak channels

Carlos Martinez-Lopez[1], Oscar Flores Arias[2], and Javier Jiménez[1]

cmarl@torroja.dmt.upm.es

[1]School of Aeronautics, Universidad Politécnica de Madrid, 28040 Madrid, Spain
[2]Department of Bioengineering and Aerospace Engineering, Universidad Carlos III de Madrid, 28911 Leganés, Spain

A comparison between the smallest computational box compatible with turbulence in streak-damped channels and minimal channels is done. The difference in dimensions suggest that in both cases the regenerating cycle needs to be sustained in wavelengths comparable to the latter to prevent from laminarization.

1 Introduction

The role of streaks in the turbulence regeneration cycle is for the moment an unclear topic. There is a line of thought considering that streak instabilities are drivers of the cycle (Jiménez, 1994; Hamilton et al., 1995). Another hypothesis, based on simulations where streamwise streaks are damped (as in (Jiménez and Pinelli, 1999)), suggests that streaks are by-products of the cycle and only have a passive role (Jiménez, 2022). The present work uses the previously mentioned methodology of damping streak modes (i.e wall normal vorticity ω_y modes) to seek for the smallest computational box size that sustains short-streak turbulence.

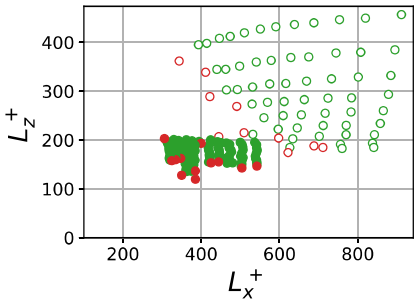

Figure 1: Computational box parametric map. Hollow circles correspond to symmetric damped channels and solid ones to conventional symmetric channels.

2 Methodology and results

Parametric maps, as the one in figure 1, can be used to determine the minimum box length (L_x^+) and width (L_z^+) required to sustain turbulence. This map is filled with dots, being each one a different simulation. Green dots correspond to simulations where box dimensions prevent laminarization during an arbitrary time interval $\Delta t u_\tau/h \approx 300$. Each red dot corresponds to a channel that laminarizes during that time. Results obtained for conventional symmetric (one-wall) channels are compared with those having their streamwise zero modes of ω_y set to zero. The latter are referred to as damped channels.

By observing the left frontier of the map for damped channels, a tradeoff between length and width is noticeable. If the channel is short, it can survive with a sufficiently large width. As the length increases, it accepts narrower boxes until reaching a saturation limit at the lower boundary of the map. A significant finding is that $L_z^+ \approx 180 - 200$ is a lower limit for the box width to sustain turbulence. This is remarkable, because the limit width of minimal channels is around $L_z^+ \approx 100$ (see Jiménez and Moin (1991)). However, any simulation in figure 1, L_z^+ could reach that lower limit for the undamped channels. The smallest widths were found around 130-150 wall units. This is possibly because these channels are symmetric in contrast with conventional minimal channels. Regarding L_x^+, it still needs to be substantially longer than for minimal channels.

To understand this phenomenon, 1-D spectra were depicted for different simulations. Table 1 contains more simulation details. Each simulation name contains the value for Re_τ. More information from simulation *Re180ND* can be seen in del Álamo and Jiménez (2003). Figure 2 shows that for different channels, velocity spectra peak at the same wavelengths. The other velocity components exhibit an even better collapse, as shown in figure 3.

	Damped?	Symmetric?	L_x^+	L_z^+
Re180ND	No	No	6800	2260
Re200D	Yes	Yes	630	230
Re210D	Yes	Yes	940	240
Re220Dxx	Yes	Yes	2040	250

Table 1: Simulations summary.

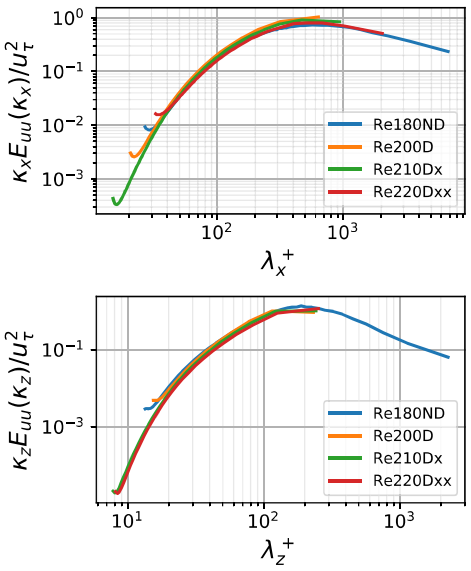

Figure 2: Streamwise velocity 1D spectra at $y^+ \approx 65$ as a function of wavelength in spanwise (above) and streamwise (below) directions.

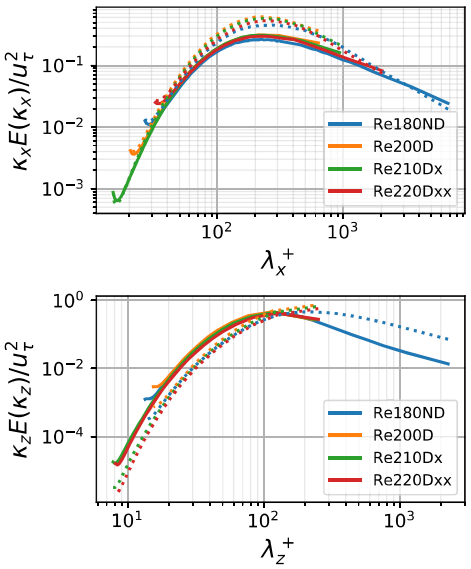

Figure 3: 1D spectra at $y^+ \approx 65$ for v (—) and w (···).

3 Conclusions

We show evidence that the dimensions of the smallest box that sustain turbulence in a streak-damped channel must be larger than on a minimal channel. It is also noteworthy that spectra are unaffected by streak damping, in agreement with the hypothesis that the streak is a passive by-product of the cycle.

These results seem to suggest that in order for damped channels to survive, they must sustain the turbulent cycle in wavelengths comparable to those of minimal channels. Meeting this condition seems to be more important than having long streaks.

References

del Álamo, J. C. and J. Jiménez (2003). Spectra of the very large anisotropic scales in turbulent channels. *Phys. Fluids A 15*, L41–L44.

Hamilton, J. M., J. Kim, and F. Waleffe (1995). Regeneration mechanisms of near-wall turbulence structures. *J. Fluid Mech. 287*, 317–348.

Jiménez, J. (1994). On the structure and control of near wall turbulence. *Phys Fluids 6*, 944–953.

Jiménez, J. and P. Moin (1991). The minimal flow unit in near-wall turbulence. *J. Fluid Mech. 225*, 221–240.

Jiménez, J. and A. Pinelli (1999). The autonomous cycle of near-wall turbulence. *J. Fluid Mech. 389*, 335–359.

Jiménez, J. (2022). The streaks of wall-bounded turbulence need not be long. *Journal of Fluid Mechanics 945*, R3.

2nd Spanish Fluid Mechanics Conference
Barcelona (2 - 5 July 2023)

Spectral analysis of the spatial evolution of energy-containing eddies

Ezhilsabareesh Kannadasan[1], Callum Atkinson[1], and Julio Soria[1]

ezhilsabareesh.kannadasanr@monash.edu

[1]Laboratory for Turbulence Research in Aerospace and Combustion (LTRAC), Department of Mechanical and Aerospace Engineering, Monash University, Melbourne, Victoria 3800, Australia.

The elementary structures of wall turbulence that carry most of the kinetic energy and momentum are typically referred to as energy-containing eddies (energy-eddies). Despite the general agreement that energy-eddies can sustain themselves at all relevant length scales, their exact genesis and spatial evolution are still not well-understood. In this study, energy-eddies at the inflow of a turbulent channel flow direct numerical simulation (DNS) are quenched and the spatial development of these eddies is studied at a friction Reynolds number of $Re_\tau = 550$. The results in the present study demonstrates that in a spatially evolving flow, the formation of near-wall streaks is the primary process necessary in the recovery of energy-eddies in a turbulent channel flow and energy-eddies are essential to maintain the eddies involved in the energy cascade.

1 Numerical experiment

In the present study two synchronised DNSs are used: one is a fully resolved streamwise periodic channel flow, which is subsequently denoted as PCH-DNS, while the other is a fully resolved channel flow DNS with inflow-outflow boundary conditions, which will be denoted as IOCH-DNS. In the IOCH-DNS the inlet boundary condition is an inflow velocity field, which is a filtered version of the inflow of the PCH-DNS, with a convective outflow boundary condition applied at the domain exit. The linear ridge $\lambda_z = 3y$ is considered as a reasonable boundary that separates the energy-eddies from the cascading eddies by analysing the spanwise spectra of turbulent transport (1). The inlet plane from the PCH-DNS is taken, and the energy-eddies are filtered out at each time step before it is fed to the IOCH-DNS.

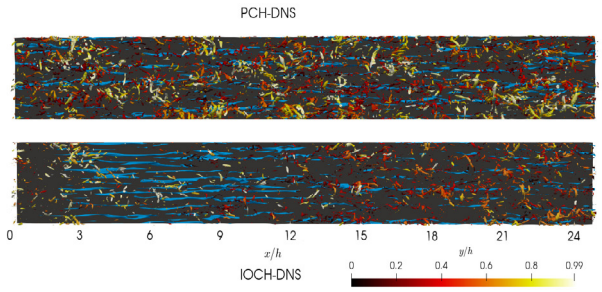

Figure 1: Vortices and low-speed structures visualised by the iso-surfaces of the second invariant of the velocity gradient tensor, $Q_A/\langle Q_W \rangle = 3$, the colour represents the distance from the wall, and the streamwise fluctuating velocity, $u^+ = -0.5$ in blue, respectively. The flow is from left to right.

2 Summary

The streamwise velocity spectra of the developing flow begin to recover at a spanwise wavelength of $\lambda_z^+ \simeq 100$, which is equal to the near-wall spacing of the streaks in the buffer layer at $y^+ \simeq 15$, whereas there are no active vortical motions in the streamwise vorticity spectra until the energy at the wall-normal streak location of $y^+ \simeq 15$ is re-established. This is consistent with the qualitative observation from the iso-surface of an instantaneous field shown in figure 1. It is evident from this visualisation that the energy-eddies, which are a combination of the streaks and streamwise vortices, are removed from the neighbourhood of the inflow of the IOCH-DNS, with the energy-cascade eddies at the inflow initially decaying in the streamwise direction. There is no evidence of the streaks or active vortical motions until $x > 3h$, where streaks start to reappear, while vortical motions only start to become active for $x > 12h$. Hence, the present study demonstrates that in a spatially evolving flow, the formation of near-wall streaks is the primary process necessary in the recovery of energy-eddies.

References

[1] Kannadasan, E., Atkinson, C., and Soria, J., (2023), Spectral analysis of the evolution of energy-containing eddies, *J. Fluid Mech., 955, R1.*

2nd Spanish Fluid Mechanics Conference
Barcelona (2 - 5 July 2023)

Spectral analysis of the spatial evolution of energy-containing eddies in turbulent boundary layers

Antonio Matas[1], Ezhilsabareesh Kannadasan[1], Callum Atkinson[1], and Julio Soria[1]

antonio.matassalva@monash.edu

[1]Laboratory for Turbulence Research in Aerospace and Combustion (LTRAC),
Department of Mechanical and Aerospace Engineering, Monash University

The streamwise evolution and multi-scale interaction of energy-eddies in incompressible zero pressure gradient (ZPG) turbulent boundary layers (TBLs) is investigated by removing these eddies at the inflow of a ZPG-TBL direct numerical simulation (DNS) and examining the turbulent kinetic energy (TKE) and Reynolds Shear stress transport using the spanwise spectral decomposition approach introduced by Kawata and Alfredson (2018).

1 Introduction

Turbulent wall-bounded flows can be interpreted as a cluster of recurrent patterns of energy-containing eddies (energy-eddies) Richardson (1922). These energy-eddies carry most of the momentum and kinetic energy and are considered to be the elementary structures capable of explaining how momentum and kinetic energy redistribute in wall-bounded turbulence. However, the specific issue of how energy-eddies generate and evolve is not well understood. In the present study, we remove the energy-eddies at the inflow of an incompressible ZPG-TBL DNS to study their spatial evolution and multi-scale interactions using spectral analisys based on the spanwise decomposition introduced by Kawata and Alfredson (2018).

2 Methodology

The DNS setup consists of two concatenated domains, the auxiliary domain and the main domain, which are run synchronously as described in Borrell et al. (2013). The auxiliary domain runs at a lower resolution and is used to provide a realistic turbulent inflow for the main domain. The inflow of the auxiliary domain is obtained from one of its own planes that is rescaled using the method proposed by Lund et al. (1998). The turbulent transport term in the TKE equation is used to identify the boundary that distinguishes the energy-eddies from the rest of eddies (cascading-eddies) at each spanwise Fourier mode. The separation between energy-eddies and cascading-eddies is found at $\lambda_z \approx 3y$, in agreement with previous studies in boundary layers Chan et al. (2021). The fluctuations and energy in the wall-normal profile with $y \lesssim \lambda_z/3$ are removed at the inflow of the main domain at each time step.

3 Conclusions

The preliminary statistics collected reveal that more DNS fields are required to conduct the spectral analysis of the inter-scale energy transport. In this paper, we will report results based on the extended DNS database.

References

Kawata T. & Alfredsson P.H., (2018), "Inverse interscale transport of the Reynolds shear stress in plane Couette turbulence" *Phys. Rev. Lett.*, **120** 244–501

Richardson L.F. (1922) "Weather Prediction by Numerical Process", Cambridge University Press.

Borrel G., Sillero J.A., Jiménez J. (2013) "A code for direct numerical simulation of turbulent boundary layers at high Reynolds numbers in BG/P supercomputers". *Comp. Fluids*, **80** 37–43.

Lund T.S., Wu X., Squires K.D. (1998) "Generation of Turbulent Inflow Data for Spatially-Developing Boundary Layer Simulations". *Journal of Computational Physics*, **140(2)** 233–258.

Chan C.I., Schlatter P., Chin R.C., (2021), "Inter-scale transport mechanisms in turbulent boundary layers". *J. Fluid Mech.*, **921**, A13

2nd Spanish Fluid Mechanics Conference
Barcelona (2 - 5 July 2023)

The effect of modulated driving on turbulent plane Couette flows

Rodolfo Ostilla-Mónico[1] and M. Wasy Akhtar[2]

rodolfo.ostilla@uca.es

[1]Escuela de Ingeniería, Universidad de Cádiz, Spain
[2]Department of Mechanical Engineering, University of Houston, Houston 77004, USA

Direct numerical simulations of turbulent non-rotating and rotating Plane Couette Flow with a periodically modulated plate velocity are conducted to study the effect of modulated forcing on turbulent shear flows. The time averaged shear Reynolds number is fixed to $Re_S = 3 \cdot 10^4$, which results in a frictional Reynolds number of approximately $Re_\tau \approx 400$. The modulating frequency is varied in the range $Wo \in (20, 200)$, while the modulating amplitude is kept fixed at 10% of the shear velocity except to demonstrate that varying this parameter changes little. The resulting shear at the plates are found to be independent of the forcing frequency, and equal to the non-modulated baseline. For the non-rotating simulations, two clear flow regions can be seen: a near wall region that follows Stokes' theoretical solution, and a bulk region that behaves similar to Stokes' solutions but with an increased effective viscosity. For high driving frequencies, the amplitude response follows the scaling laws for modulated turbulence of von der Heydt *et al.* (Physical Review E 67, 046308 (2003)). Cyclonic rotation is not found to modify the system's behaviour in a substantial way, but anti-cyclonic rotation significantly changes the system's response to periodic forcing. We find that the persistent axial inhomogeneities introduced by mild anti-cyclonic rotation make it impossible to measure the propagation of the modulation adequately, while stronger anti-cyclonic rotation creates regions where the modulation travels instantaneously.

2nd Spanish Fluid Mechanics Conference
Barcelona (2 - 5 July 2023)

Turbulent puffs and slugs in pulsatile pipe flow

Daniel Morón[1] and Marc Avila[1,2]

daniel.moron@zarm.uni-bremen.de

[1]Center of Applied Space Technology and Microgravity (ZARM),University of Bremen, Germany
[2]MAPEX Center for Materials and Processes,University of Bremen, Germany

Turbulence in steady driven pipe flow first appears in the form of localized puffs and slugs. A recently developed simple model by Barkley is able to reproduce their front speeds and lifetimes. Here we adapt this model to pulsatile pipe flow, driven by a periodic flow rate of arbitrary waveform. We perform DNS and causal analysis to identify the main dynamics that enable puffs to survive in pulsatile pipe flow. Using these analysis we modify Barkley's model to extend it to pulsatile pipe flow. The extended model captures the behaviour of localized turbulence in a wide range of pulsatile pipe flows.

1 Introduction

At $Re \approx 2000$, and when sufficiently disturbed, steady pipe flow transitions to turbulence in the form of turbulent patches known as turbulent puffs (Avila , 2023). Here $Re = \frac{UD}{\nu}$, being U the time-averaged bulk velocity, D the pipe diameter and ν the kinematic viscosity. Depending on Re, puffs can either decay, split or elongate (slugs). Recently Barkley developed a simple model known as the Barkley Model (BM) to reproduce the dynamics of localized turbulence in pipe and duct flow (Barkley , 2015). The main idea of the model is the non-linear interaction between turbulence intensity, q, and the mean shear, u. The turbulence intensity feeds on the mean shear to grow, but the mean shear decreases when the turbulence intensity increases. With two simple non-linearly coupled advection-diffusion-reaction partial differential equations the model reproduces the front speeds and lifetimes of turbulent puffs and slugs.

Transition in pulsatile pipe flow, with bulk velocity:

$$u_b(t) = U\left[1 + A \cdot \sin(2\pi f \cdot t)\right], \qquad (1)$$

first occurs in the form of turbulent patches too. Here A is the amplitude of the pulsation, and $f = 1/T$ its frequency. Instead of the frequency we will consider the non-dimensional Womersley number $Wo = \frac{D}{2}\sqrt{\frac{2\pi f}{\nu}}$. At $A \gtrsim 0.5$ and $5 \lesssim Wo \lesssim 17$ transition happens at lower Re than for steady pipe flow, due to the so-called helical instability (Xu and Avila, 2020; Morón , 2022). Once triggered, the behaviour of turbulent puffs greatly depends on the combination of Re, Wo and A. While at low frequencies and low amplitudes puffs behave quasi-steadily (Xu and Avila, 2018), recent studies suggest that at higher frequencies and amplitudes puffs make use of the helical instability to survive (Feldmann , 2021). In this project we study puffs in pulsatile pipe flow, the causes behind their survival, and we adapt the BM to the pulsatile case.

2 Methods

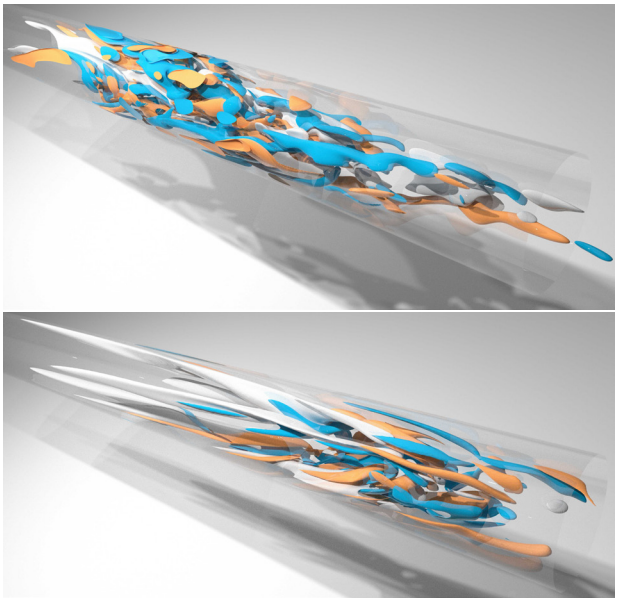

Figure 1: (Top) Turbulent puff in a steady driven pipe flow direct numerical simulation at $Re = 2000$. (Bottom) Turbulent puff in a pulsatile pipe flow at $Re = 2400$, $A = 1.4$ and $Wo = 8$, at a given phase of the period. In grey, low streak velocities, in red/blue excess of positive/negative axial vorticity ω_x.

We perform direct numerical simulations of pipe flow driven with a time dependant bulk velocity, eq. 1, at low Reynolds numbers $Re \approx 2000$ and high amplitudes $A \gtrsim 0.5$. We consider different combinations of Wo, A and Re, and we initialize the simula-

tions with a single turbulent puff. We observe that, similar to the behaviour at lower A, (Xu and Avila, 2018), at low frequencies $Wo \lesssim 5$ the puffs behave quasi-steadily while at high frequencies $Wo \gtrsim 20$ puffs are not sensibly affected by the pulsation. At $5 \lesssim Wo \lesssim 17$, we distinguish an intermediate regime, where the puffs remain localized and survive the pulsation by elongating and shrinking at a given phase lag with respect to the pulsation.

It has been suggested, (Feldmann , 2021), that at these intermediate frequencies, and sufficiently big amplitudes $A \gtrsim 0.5$, puffs take advantage of the aforementioned helical instability to survive. We test this hypothesis by performing DNS where we introduce a force that counteracts the helical instability. Our results show that, when the helical instability is sistematically damped, puff lifetimes are drastically reduced.

With the help of our causal analysis and simulation results, we modify the BM to adapt it to pulsatile pipe flow. With minimal changes, we show how the BM can be enhanced to also describe the behaviour of localized turbulence in a large parametric space of pulsatile pipe flow. We use the model to, in a fast way, characterize the lifetime of puffs depending on the flow parameters.

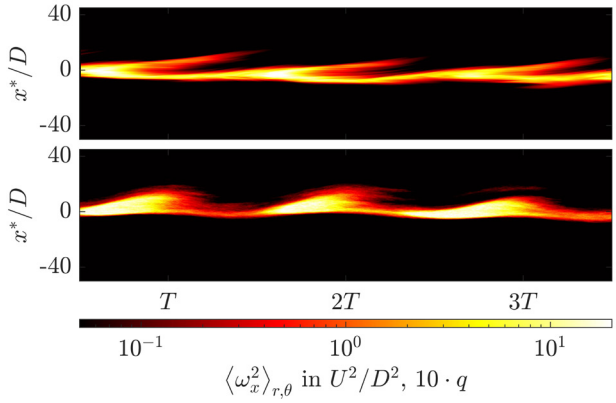

Figure 2: (Top) Space time diagram of the cross section integral of the axial vorticity ω_x squared, with respect to a reference frame moving at the bulk velocity. The results correspond to a direct numerical simulation at $Re = 2100$, $Wo = 11$ and $A = 1$. (Bottom) the variable q of our modified Barkley Model for the same flow parameters as in the top panel.

3 Conclusions

In this project we study the behaviour of turbulent puffs in pulsatile pipe flow at low Re. We perform direct numerical simulations and causal analyses to identify the dynamics that allow puffs to survive the pulsation. Using these dynamics, we extend a pre-existing model of puffs in steady pipe flow to the pulsatile case. With minimal changes our model is able to reproduce the behavior of turbulent puffs in pulsatile pipe flow reasonably well.

References

Avila M, Barkley D & Hof B "Transition to Turbulence in Pipe Flow", *Annual Review of Fluid Mechanics*, **55**, 575–602.

Barkley D. *et al* (2015) "The rise of fully turbulent flow". *Nature*, **526**, 550–553.

Feldmann D, Morón D & Avila M(2021) "Spatiotemporal Intermittency in Pulsatile Pipe Flow", *Entropy*, **23**, 46.

Morón D, Feldmann D & Avila M(2022) "Effect of waveform on turbulence transition in pulsatile pipe flow", *Journal of Fluid Mechanics*, **948**, A20.

Xu D & Avila M (2018) "The effect of pulsation frequency on transition in pulsatile pipe flow", *Journal of Fluid Mechanics*, **857**, 937–951.

Xu D *et al* (2020) "Nonlinear hydrodynamic instability and turbulence in pulsatile flow", *PNAS*, **117(21)**, 11233–11239.

2nd Spanish Fluid Mechanics Conference
Barcelona (2 - 5 July 2023)

Turbulent Statistics and Coherent Structures in an Asymmetrically Heated Channel Flow

Marina Garcia-Berenguer[1], Lucas Gasparino[2], Oriol Lehmkuhl[2], and Ivette Rodriguez[1]

marina.garcia.berenguer@upc.edu

[1]Turbulence and Aerodynamics Research Group, Universitat Politècnica de Catalunya, Spain
[2]Large-scale Computational Fluid Dynamics Group, Barcelona Supercomputing Center, Spain

A compressible direct numerical simulation (DNS) has been conducted to analyze the behavior of a fully developed turbulent channel flow. The problem has been set at mean friction Reynolds number $Re_{\tau m} = 400$ submitted to a high-temperature gradient between the two walls ($T_{hot}/T_{cold} = 2$).

1 Introduction

Wall bounded flows with large temperature gradients are present in many engineering applications. In recent years, fully-developed channels have been used to study the coupling effect of the temperature gradient and the turbulence. However, most of the studies of high-temperature gradient channels have been mainly limited to incompressible flows that transport the temperature as a passive scalar, or to low-speed flow limited to low mean friction Reynolds numbers (see for instance Nicoud (1998)).

Toutant and Bataille (2013) performed direct numerical simulations (DNS) with the same configuration as the present study, i.e., at mean friction Reynolds number $Re_{\tau m} = 400$ and temperature ratio $T_{hot}/T_{cold} = 2$. The mean Reynolds number is computed as the mean of the friction Reynolds number at each wall, $Re_\tau = \rho_w \delta u_\tau / \mu_w$, where $u_\tau = \sqrt{\tau_w/\rho_w}$ is the friction velocity, δ is the channel half-height, ρ_w and μ_w are the density and the dynamic viscosity, respectively. They studied the statistics of the flow with different scalings for the velocity and temperature profiles. However, the large-scale coherent structures were not discussed in detail.

The main goal of this work is to study the behavior of an asymmetrically heated channel flow and to analyze the large-scale coherence structures of the flow via two-point correlations and energy spectra of the channel. To do so, the mean friction Reynolds number has been imposed to $Re_{\tau m} = 400$ and the temperature ratio difference between the walls to $T_{hot}/T_{cold} = 2$.

2 Numerical methodology

A full compressible DNS of the channel has been performed considering thermo-dependent properties of the air (density, viscosity, and conductivity). The fluid has been defined as an ideal gas, with the ideal gas-specific constant set as $R_g = 286.86\ J\ kg^{-1}K^{-1}$ and the pressure heat capacity is considered constant $c_p = 1004\ J\ kg^{-1}K^{-1}$ for an initial thermodynamic pressure of $P_0 = 101325\ Pa$.

Sutherland's law has been used to solve the dynamic viscosity (μ) and the conductivity (λ) at Prandlt number $Pr = 0.71$:

$$\mu(T) = 1.458 \cdot 10^{-6} \frac{T^{2/3}}{T + 110.4} \tag{1}$$

$$\lambda(T) = \frac{\mu c_p}{Pr} \tag{2}$$

Simulations are carried out by means of a low-dissipation high-order spectral elements in-house code (*Sod*). The code combines a spectral-method version of Galerkin's finite-element continuous model with a modified version of Guermond's Entropy Viscosity stabilization tailored to work with this spectral elements approach. The scheme used, employs an operator split to the convective terms that counter the aliasing effects of the reduced order integration imposed by using a SEM model. For the time-advancing algorithm, a fourth-order Runge-Kutta method has been used. Simulations are performed on a computational domain of $2\pi\delta$x2δx$\pi\delta$ (where $\delta = 0.003\ m$). The domain is periodic in the streamwise (x) and the spanwise (z) directions and a 3rd-order numerical mesh with 74.6M grid points has been used. The grid spacings are $\Delta x^+ = 9.1$, $\Delta y^+_{center} = 6.6$, $y^+_w < 1$ and $\Delta z^+ = 4.0$, normalized by the hot wall properties as $y^+ = y\ u_\tau \rho_w / \mu_w$.

3 Results

In this study, the temperature at the cold wall is set at $T_{cold} = 293\ K$ and the hot one at $T_{hot} = 586\ K$. After averaging, the computed mean Reynolds number is

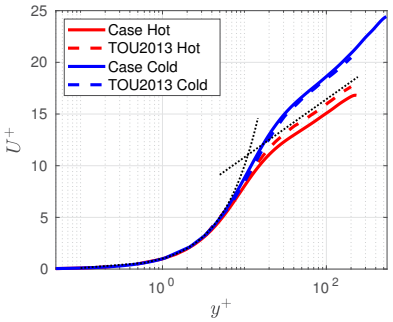

Figure 1: Mean velocity profiles at the cold wall (blue) and the hot wall (red) compared with Toutant and Bataille (2013) results (TOU2013).

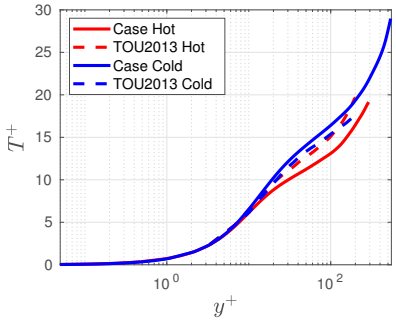

h]

Figure 2: Mean temperature profiles in wall units at the cold wall (blue) and the hot wall (red) compared with Toutant and Bataille (2013) results (TOU2013).

$Re_{\tau m} = 0.5(Re_{\tau cold} + Re_{\tau hot}) = 375.2$. At the walls, the friction Reynolds number is $Re_{\tau cold} = 514.6$ at the cold wall and $Re_{\tau hot} = 235.7$ at the hot one. The simulations are kept at subsonic Mach number ($M < 0.2$).

Figure 1 shows the mean velocity profile scaled by the local friction velocity u_τ along with the classical logarithmic law of the wall. Besides, in figure 2 the mean temperature profile can be seen scaled by the friction temperature T_τ computed with the wall heat flux $T_\tau = q_w/(c_p \rho_w u_\tau)$, where $q_w = \lambda_w(\partial T/\partial y)$. These results have been compared with the low-Mach computations of Toutant and Bataille (2013). In general good agreement with the results from the literature is observed, although some deviations in the mean temperature profile are observed.

The profiles expose the need of analysing new scaling methodologies for the cold and the hot wall to collapse. Compared with the isothermal channel (not shown here), the larger temperature gradient enhances the mixing, producing a decrease in the temperature inside the channel.

Figure 3 shows the instantaneous high and low-speed streaks, identified with contours at $u^+ = \pm 4$. They show significant differences between the walls. It can be seen that the fine-scale eddy structures in the cold wall are more than in the hot one. In fact, the flow regime at the hot wall exhibits a quasi-laminar flow regime.

In the final version of the manuscript, a detailed analysis of the effects of the temperature gradients on the turbulent structures will be performed via two-point correlations and energy spectra. In addition, the different coherent structures would be analyzed in detail.

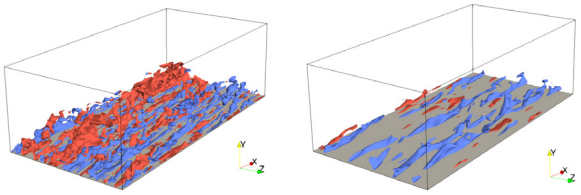

Figure 3: High and low-speed streaks ($u'^+ = 4$ in red and $u'^+ = -4$ in blue). Top for the cold wall and bottom for the hot one.

Acknowledgments

This work has been partially financially supported by the *Ministerio de Economía y Competitividad, Secretaría de Estado de Investigación, Desarrollo e Innovación*, Spain (ref. PID2020-116937RB-C21 and PID2020-116937RB-C22). We also acknowledge *Red Española de Supercomputación* (RES) for awarding access to the MareNostrum IV machine based in Barcelona, Spain (IM-2022-3-0010).

References

F. C. Nicoud, "Numerical study of a channel flow with variable properties", *Center for Turbulence Research Annual Research Briefs*, pp. 289–310, 1998.

A. Toutant and F. Bataille, "Turbulence statistics in a fully developed channel flow submitted to a high-temperature gradient", *International Journal of Thermal Sciences*, vol. 74, pp. 104–118, 2013, doi: 10.1016/j.ijthermalsci.2013.06.003.

2nd Spanish Fluid Mechanics Conference
Barcelona (2 - 5 July 2023)

Coherent structures in twin supersonic jets obtained from high-speed Schlieren measurements

Iván Padilla-Montero[1], Daniel Rodríguez[1], Vincent Jaunet[2], Stève Girard[2], Damien Eysseric[2], and Peter Jordan[2]

ivan.padilla@upm.es

[1]School of Aeronautics (ETSIAE/UPM), Universidad Politécnica de Madrid, 28040 Madrid, Spain
[2]Institut Pprime, CNRS-Université de Poitiers-ENSMA, 86036 Poitiers, France

Spectral proper orthogonal decomposition (SPOD) is applied to high-speed Schlieren measurements to identify coherent structures in twin supersonic jets and study the dominant modes of oscillation and jet coupling. The leading SPOD mode for overexpanded operating conditions is shown and its structure is briefly described, illustrating the feasibility of the methodology in extracting the desired coherent information and, especially, the associated acoustic radiation.

1 Introduction

Many propulsion systems found nowadays in rocket launchers and high-speed aircraft feature twin-jet engines. The mechanisms governing noise generation in such systems are still far from being fully understood. Closely-spaced twin jets are known to interact at the hydrodynamic and acoustic levels, giving rise to more complex flow structures than single jets.

Several different investigations on single round jets converge in the evidence that radiated sound is highly directional for both subsonic and perfectly-expanded supersonic jets [2, 7, 1], and that it is highly correlated with large-scale, low-frequency fluctuations in the mixing layer, which are known to be coherent over multiple nozzle diameters [6, 5].

This work presents the identification of coherent structures in supersonic twin-jet flow fields by means of spectral proper orthogonal decomposition (SPOD) [8] applied to a time series of high-speed Schlieren snapshots.

2 Twin-jet configuration and experimental setup

Two identical round convergent-divergent nozzles are considered for the twin-jet system. The spacing between the axisymmetry axis of each of them is denoted by the distance s. The the nozzle exit diameter is denoted by D. The nozzle geometry has been designed at the Institut Pprime (CNRS-Université de Poitiers-ENSMA), and features a TIC profile with an exit diameter of $D = 0.025$ m and an exit-to-throat area ratio of $A_e/A_t = 1.225$.

Experimental investigations on the twin-jet configuration studied in this work have been undertaken at the PROMÉTÉE platform of the Institut Pprime. Schlieren measurements have been performed for a wide range of twin-jet spacings and nozzle pressure ratios (defined by the isentropic Mach number M_j). The Schlieren setup consists of a classical Z-type configuration.

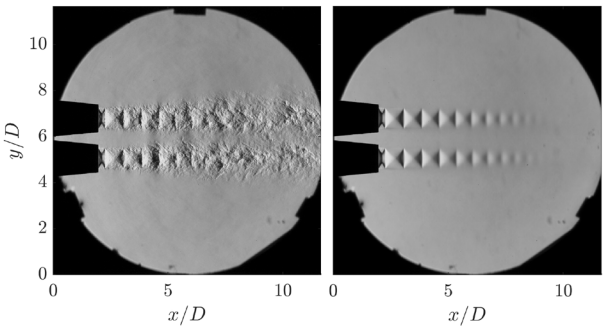

Figure 1: (left) instantaneous Schlieren visualization of the twin jet operating at $M_j = 1.26$ and $s/D = 1.76$; (right) mean flow field obtained by time-averaging 10,000 Schlieren images.

The left panel in figure 1 depicts an instantaneous Schlieren snapshot obtained for the twin-jet system operating at $M_j = 1.26$ (overexpanded condition) and $s/D = 1.76$, using a resolution of 768×768 pixels. The right panel shows the mean flow field obtained by averaging a time series of 10,000 snapshots recorded at a sampling frequency of $f_s = 35$ kHz. The mean flow illustrates that symmetric operating conditions were achieved in the experiment for both jets. The presence of shock cells in the jets allows the flow to support screech resonance [3, 4].

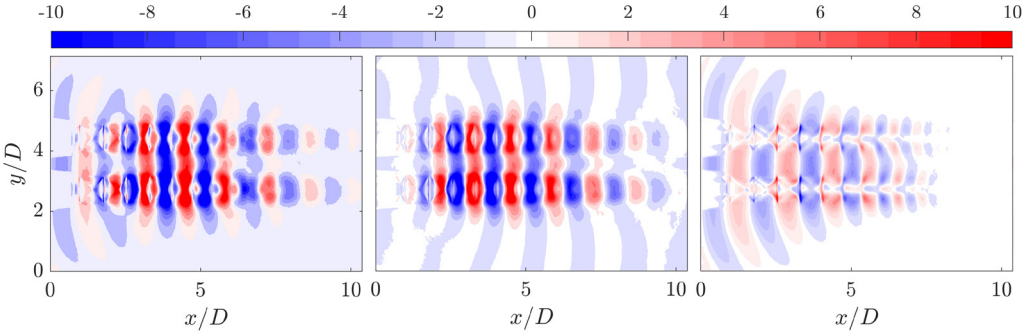

Figure 2: Real part of the leading SPOD mode at $M_j = 1.26$, $s/D = 1.76$ ($St = 0.56$). (left) original SPOD mode; (middle) downstream propagating (k^+) component; (right) upstream propagating (k^-) component.

3 SPOD results

For the SPOD analysis, a total of 30,000 Schlieren snapshots are employed, obtained at a resolution of 352×640 pixels at $f_s = 68$ kHz. To ensure a good trade-off between frequency resolution and variance of the estimates, the dataset is divided into 57 Hamming windows of 1024 snapshots each with a 50% overlap. For these conditions, the Strouhal number associated to the Nyquist frequency is $St = fD/u_j = 2.36$, which is considered to be well above the dominant frequencies of interest.

The left panel in figure 2 represents contours of the real part of the most energetic SPOD mode obtained for the flow configuration under analysis. This mode corresponds to the fundamental screech tone for the given operating conditions, which features a strong support in the potential core of the jets as well as in the region between them. In addition, a significant signature of downstream and upstream acoustic radiation can be observed, which is clearly visible in the middle and right panels of figure 2. These two pictures illustrate the downstream and upstream propagating components of the SPOD mode, which are obtained by respectively filtering out the negative (k^-) and positive (k^+) streamwise wavenumbers contained in the original mode [3].

4 Conclusions

SPOD has been successfully applied to high-speed Schlieren measurements of a supersonic twin-jet configuration. The methodology is capable of extracting the most energetic structures responsible for the hydrodynamic instability and the noise radiation of the jets. More interestingly, the structure of the obtained SPOD mode is coherent enough so as to allow to clearly extract the induced upstream and downstream acoustic radiation, which proves its potential for the study of novel noise-generation mechanisms that are not fully characterized yet, especially for twin-jet systems.

Acknowledgments

The work of D.R. and I.P.M is funded by the Government of the Community of Madrid through the Program of Excellence in Faculty (V-PRICIT line 3) and the Program of Impulse of Young Researchers (V-PRICIT lines 1 and 3, Grant No. APOYO-JOVENES-WYOWRI-135-DZBLJU). I.P.M also thanks financial support from the European Union's NextGenerationEU fund.

References

[1] A. Cavalieri, P. Jordan, T. Colonius, and Y. Gervais. *J. Fluid Mech.*, 704:388–420, 2012.

[2] D. G. Crighton and P. Huerre. *J. Fluid Mech.*, 220:355–368, 1990.

[3] D. Edgington-Mitchell, V. Jaunet, P. Jordan, A. Towne, J. Soria, and D. Honnery. *J. Fluid Mech.*, 855:1–12, 2018.

[4] D. Edgington-Mitchell, X. Li, N. Liu, F. He, T. Y. Wong, J. MacKenzie, and P. Nogueira. *J. Fluid Mech.*, 945:1–24, 2022.

[5] P. Jordan and T. Colonius. *Annu. Rev. Fluid Mech.*, 45(1):173–195, 2013.

[6] D. Juvé, M. Sunyach, and G. Compte-Bellot. *J. Sound Vib.*, 71:319–332, 1980.

[7] C. Tam. *Annu. Rev. Fluid Mech.*, 27(1):17–43, 1995.

[8] A. Towne, O. T. Schmidt, and T. Colonius. *J. Fluid Mech.*, 847:821–867, 2018.

2nd Spanish Fluid Mechanics Conference
Barcelona (2 - 5 July 2023)

Prediction and modelling coherent structures and noise radiation of supersonic twin jets

Daniel Rodríguez[1] and Iván Padilla-Montero[1]

daniel.rodriguez@upm.es

[1]School of Aeronautics (ETSIAE/UPM), Universidad Politécnica de Madrid, 28040 Madrid, Spain

The large-scale coherent structures present in high-speed turbulent jets are modelled for round nozzle twin-jet configurations at supersonic conditions based on industrial-type RANS simulations and plane-marching parabolised stability equations (PSE). These relatively inexpensive models predict jet-jet coupling, oscillation modes and mixing noise radiation directivity in agreement with experimental observations.

1 Introduction

Most of the tactical fighters developed since the 1960s feature fuselage-embedded twin jet engines. Additionally, multi-tube nozzles have been investigated as possible jet noise suppressors, and designs of future distributed-propulsion systems involve placing two or more parallel jet streams in close proximity. The closely spaced jets can interact both at the hydrodynamic and acoustic levels, giving rise to very complex flow structures compared with single round jets at the same operating conditions. Experiments on twin-jet configurations observed an overall reduction of the far-field noise with respect to an equivalent isolated jet [1], but remarkable enhancement on the plane perpendicular to jet centres [2].

Several different investigations on single round jets over the last decades converge in the evidence that mixing noise is highly directional, and that it is highly correlated with large-scale, low-frequency structures in the turbulent shear layer, which are known to be coherent over multiple nozzle diameters [3]. In turn, these coherent structures, often referred to as wavepackets, can be modelled faithfully using parabolised stability equations (PSE) [5]. However, the extension of the models from single round jets to twin jet systems is not straigth-forward, on account of the lack of axial symmetry and jet-jet interactions [4]. This work presents our recent developments in the modelling of the coherent structures on supersonic twin jets and their associated noise radiation.

2 Twin-jet mean flow

Two identical round convergent-divergent nozzles are considered for the twin-jet system. The spacing between their axes and their diameter are denoted by s and D respectively. The nozzle geometry has been designed at the Institut Pprime (CNRS-Université de Poitiers-ENSMA), and features a truncated ideally contoured (TIC) profile for design Mach number 1.54, with an exit diameter of $D = 0.025$ m and an exit-to-throat area ratio of $A_e/A_t = 1.225$. Turbulent mean flows are computed by solving the RANS equations with the DLR's finite solver TAU (figure 1) and Menter's SST eddy viscosity model with correction for compressible flow. Mean flows for different jet separations are computed. The results are compared with a tailored mean flow constructed as the linear superposition of two axisymmetric round jets to quantify jet-jet interactions at the mean flow level.

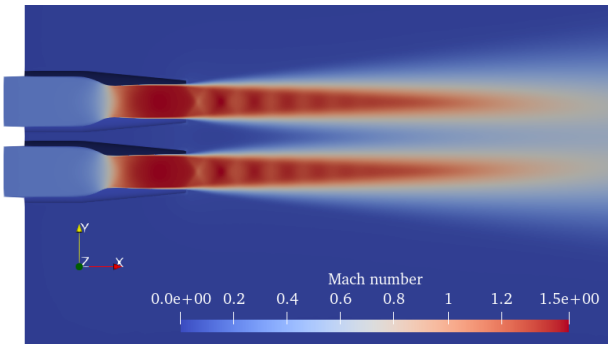

Figure 1: RANS simulation of a twin-jet system at nearly perfectly-expanded conditions; $M_j = 1.54$ and jet separation $s/D = 1.78$.

3 Wavepacket modelling

The turbulent coherent structures (i.e. wavepackets) are modelled as linear perturbations of the mean flow. Mixing noise is associated with structures originated by the convective Kelvin-Helmholtz instability of the mean shear layer, dominant in a range of Strouhal numbers $St = fD/U_j = 0.3 - 1$, where

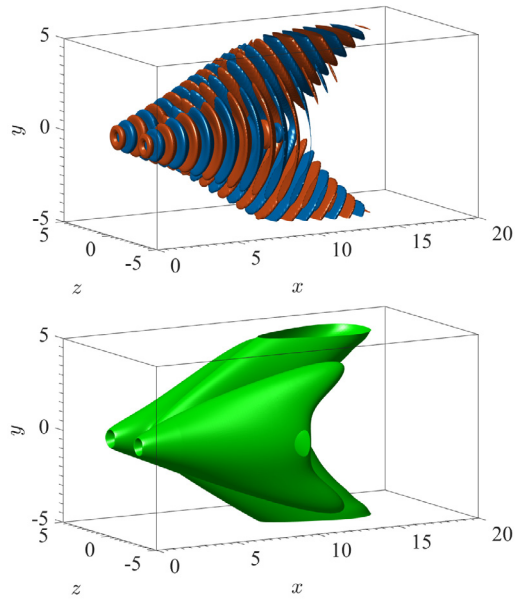

Figure 2: Real component (top) and absolute (bottom) fluctuation pressure fields computed as PSE solutions for a perfectly-expanded twin jet configuration with $s/D = 3.0$ and $St = 0.5$.

U_j is the jet exit velocity. At these frequencies, and in order to retain the relevant mean flow divergence, parabolised stability equations (PSE) are used to compute wavepacket models. As opposed to single round jets, the complex cross-section mean flow for twin jets prevents the use of classic 2D PSE integration that would follow from the introduction of azimuthal Fourier modes. Instead, the plane-marching PSE ansatz is used, based on a separation of scales on the streamwise flow direction (x and $x = \varepsilon X$, $\varepsilon \ll 1$) for perturbations that are arbitrary on the cross plane (y, z).

Figure 2 shows the pressure field of a wavepacket representative of the dominant mixing noise frequency range. For supersonic jets, linear wavepackets capture the Mach wave radiation directly. Fluctuations are classified according to their symmetric/antisymmetric behaviour about the plane containing the nozzles and the perpendicular one, and for each symmetry, according to their oscillating character. In agreement with experiments, PSE results show the dominance of symmetric toroidal oscillations of the jet plumes in the noise radiation, followed by lateral flapping oscillations in the nozzles plane. For these oscillations, noise radiation is reduced with respect to that of the linear superposition of two jets for most azimuthal angles; conversely, for the plane perpendicular to the nozzles plane, the noise predicted by PSE is increased by a factor of 50%.

4 Conclusions

Plane-marching PSE models can successfully model the turbulent wavepackets in supersonic twin-jet configurations and their noise radiation. As input, they require a mean flow that can be computed using relatively inexpensive RANS simulations of the twin-jet system, or a tailored flow employing the data from an axisymmetric simulation of a single jet. Plane-marching PSE introduces the coupling between the two jets fluctuation fields at the linear level, which seems to be sufficient for recovering important changes in the noise directivity. It also provides information on the competence between the different oscillation modes exhibited by twin jets. At the conference, PSE results will be compared to the Spectral Proper Orthogonal Decomposition of time-resolved Schlieren visualisation, that will be presented in a different talk by the same authors (Padilla-Montero *et al.* "Coherent structures in twin supersonic jets obtained from high-speed Schlieren measurements").

Acknowledgments

This work is funded by the Government of the Community of Madrid through the Program of Excellence in Faculty (V-PRICIT line 3) and the Program of Impulse of Young Researchers (V-PRICIT lines 1 and 3, Grant No. APOYO-JOVENES-WYOWRI-135-DZBLJU). I.P.M also thanks financial support from the European Union's NextGenerationEU fund.

References

[1] W. V. Bhat. Acoustic characteristics of two parallel flow jets. *AIAA Paper 77-1290*, 1977.

[2] R. Bozak and B. Henderson. Aeroacoustics experiments with twin jets. Number AIAA Paper 2011-2790.

[3] P. Jordan and T. Colonius. Wave Packets and Turbulent Jet Noise. *Annu. Rev. Fluid Mech.*, 45(1):173–195, 2013.

[4] D. Rodríguez, M. R. Jotkar, and E. M. Gennaro. Wavepacket models for subsonic twin jets using 3D parabolized stability equations. *Comptes Rendus Mécanique*, 346(10):890–902, oct 2018.

[5] A. Sinha, D. Rodríguez, G. Brès, and T. Colonius. Wavepacket models for supersonic jet noise. *J. Fluid Mech.*, 742:71–95, 2014.

Exact coherent structures in a fully developed round jet

Kengo Deguchi[1,*]

[1]*School of Mathematics, Monash University, VIC3800, Australia*

Self-similar three-dimensional nonlinear solutions are found in a fully developed round jet at high Reynolds numbers. These solutions satisfy the Navier-Stokes equations with the multiple scale far-field approximation and can be converted into travelling waves after a certain coordinate transformation. Analysis of these solutions may help in the theoretical understanding of the coherent structures in turbulent jets.

INTRODUCTION

In recent years, significant progress has been made in understanding the coherent structures present in turbulent jets through the analyses of data obtained from experiments and simulations [1,2]. However, when it comes to the theoretical explanation of the mechanisms behind these coherent structures based on the governing equations, there are still gaps that remain to be filled.

In the past two decades, Exact Coherent Structures (ECS), i.e. travelling wave or periodic solutions of the Navier-Stokes equations, have played a crucial role in understanding the coherent structures present in pipe and channel flows, among others [3,4]. Despite being unstable, these solutions remarkably well capture the essence of coherent structures in turbulent flows.

To calculate ECS, the Newton method, which is more expensive than the DNS, has to be used. For spatially developing flows such as jets such a computation is currently impossible. To overcome this challenge, in this study, we assume that the flow is sufficiently far away from the jet nozzle and that the Reynolds number is high. These assumptions allow us to eliminate certain terms from the Navier-Stokes equations and enable to compute self-similar solutions.

FORMULATION

We apply the method of multiple scales to the Navier-Stokes equations. The slow variable is taken in the principal direction of the jet and the phase variable Φ is used for the fast scale. The former originates from the non-parallel development of the jet, while the latter is related to the fluctuations of the coherent structures. We eliminate the asymptotically small terms when the Reynolds number is large and further apply the far-field approximation [5].

The equations averaged over the fast variable are the boundary region equations with a Reynolds stress term. Hence the base flow is the well-known Schlichting jet flow profile, which is the high-Re limit of the Slezkin-Landau-Squire jet.

By using the usual similarity variables, the governing equations become translationally invariant in the streamwise direction. For those who have a Newton code in cylindrical coordinates the computation of travelling wave solutions in the similarity coordinates should be easy, as they only need to add a few additional terms in the governing equations.

RESULTS

In the linear stability analysis of the base flow, instabilities appear only for |m|=1 modes, as Batchelor & Gill has shown for inviscid flows [6]. From the linear critical point, the spiral and ribbon solutions bifurcate subcritically. The former solution can be obtained from the unstable mode with m=1, whilst for the latter solution, both the m=1 and m=-1 modes need to be superimposed. Both flows are characterised by a strong vortex layer occurring at the critical layer. There must also be nonlinear solutions where |m| is not 1, which is responsible for self-sustained streaky structure seen in the turbulent jet experiments [2].

—

* kengo.deguchi@monash.edu

[1] Jung. D., Gamard, S. & George W. K. (2004) “Downstream evolution of the most energetic modes in a turbulent axisymmetric jet at high Reynolds number. Part 1. The near-field region”. *J. Fluid Mech,* **514**, 173-204.

[2] Nogueira P. A. S., Cavalieri, A. V. G., Jordan, P. & Jaunet V. (2019) “Large-scale streaky structures in turbulent jets”. *J. Fluid Mech,* **873**, 211-237.

[3] Kawahara G., Uhlmann, M. & van Veen, L. (2012) “The significance of simple invariant solutions in turbulent flows”. *Ann. Rev. Fluid Mech,* **44**, 203-225.

[4] Hof B., van Doorne, C. W., Westerweel, J., Nieuwstadt, F. T., Faisst, H., Eckhardt, B. Wedin, H., & Kerswell, R. R. (2004) “Experimental observation of nonlinear traveling waves in turbulent pipe flow”. *Science,* **305**, (5690) 1594-1598.

[5] Shtern V. & Hussain F. (2003) “Effect of deceleration on jet instability”. *J. Fluid Mech,* **480**, 283-309.

[6] Batchelor G. K. & Gill A. E. (1962) “Analysis of the stability of axisymmetric jets”. *J. Fluid Mech,* **14**, 529-551.

2nd Spanish Fluid Mechanics Conference
Barcelona (2 - 5 July 2023)

Experimental and numerical study of vortex induced vibrations on bluff bodies immersed in a water open-channel

Elena Martin[1], Francisco Sastre[2], and Angel Velazquez[2]

emortega@uvigo.es

[1]Universidade de Vigo. Fluid Mechanics Area. Department of Mechanical Engineering, Heat Engines and Fluids. School of Industrial Engineering, Campus Lagoas-Marcosende, 36310 Vigo, Spain
[2]Universidad Politécnica de Madrid. Fluid Mechanics and Aerospace Propulsion Department. Plaza del Cardenal Cisneros 3. 28040 Madrid, Spain

In this experimental and numerical study, the effect of the water flow in an open free-surface channel past different bluff bodies (prisms) is examined. Each prism was supported by a flexural plate and seven different shapes were experimentally tested: D-shape, inverse C-shape, circular, squared, triangular-120º, triangular-60º, and diamond-shape. All prisms had the same weight. The unsteady flow past the prism generated a prism span-wise motion whose amplitude and frequency was measured experimentally. The flow Reynolds numbers Re, based on the prism cross-wise width D, were varied between 400 and 1000. Hysteresis was also studied by decreasing the volumetric flow. Results show that the vibration amplitude strongly depends on the prism shape and the Re. In the range of this study, the D-shape, C-shape and triangular-120º-shape were the most efficient in terms of the prism motion amplitude. For $Re = 800 - 1000$ the minimum amplitude was obtained for the square section. Detailed analysis of the prisms wakes provided by the numerical simulations helped to understand the experimental results.

1 Introduction

In the context of mixing enhancement, the flow topology can be modified either by passive methods, which rely on geometry effects or self-sustained motions of moving parts, or by active methods. Passive methods do not require an external input of mechanical work (except for the pumping energy to sustain the continuous main flow) and are usually very robust Lee et al. (2016). In this context, Vortex-Induced-Vibrations (VIV) is an effective mean to create vorticity both for promotion of mixing (and heat transfer) Valeije et al. (2020) and for obtaining energy in flows at low and moderate Reynolds numbers. As the efficiency is closely related to the geometry and the unsteady wake generated past the bluff body, the study of these configurations is still an open field of work Hashemi-nejad and Fallahi (2022).

In this work, we analyse experimentally and numerically the VIV on prisms of different shapes subjected to an open-channel flow of Re 400 to 1000.

2 Experimental set-up

The open channel, of 50 mm of width and a total stream-wise length of 1800 mm, is filled with water up to a height of 45 mm. Prisms with different cross-sectional geometries (see figure 1), and same width $D = 20mm$, were tested: D-shape, inverse C-shape, circular, squared, triangular-120º, triangular-60º, and diamond-shape. For this study, the blockage number $\beta = D/H$ was equal to 0.4.

Figure 1: Sketch of the different prism sections tested.

The tested prisms, were submerged in the water channel up to a depth of 43 mm. The length of the flexural plate, which is not immersed in the water, was 300 mm. Figure 2 shows two pictures of the experimental set-up. The mass of the prism and the flexural plate ensemble, M, was equal to 0.021 kg. The suspended prisms are subjected to unsteady fluid forces due to the free-stream flow along the channel axis x, which induces a rigid body motion in the span-wise direction y over the prism. Accordingly, the prism can be considered as a simple mass-damper-spring oscillating system with mass M, spring stiffness $K = 2.31\ N/m$, and damping coefficient $C = 0.00093\ Ns/m$. Thus, the natural fre-

quency is 1.67 Hz.

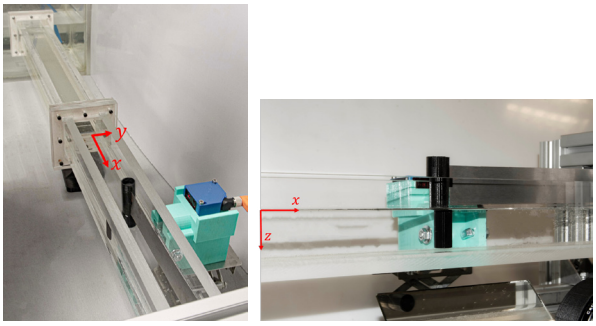

Figure 2: Pictures of the experimental setup; channel, prism and flexural plate

3 Numerical model and results

The following dimensionless equations of conservation of mass and linear momentum describe the flow motion for an incompressible and isothermal fluid :

$$\vec{\nabla} \cdot \vec{v} = 0 \quad (1)$$

$$\frac{d\vec{v}}{dt} + \vec{v} \cdot \vec{\nabla}\vec{v} = -\vec{\nabla}p + \frac{1}{Re}\vec{\nabla}^2\vec{v} \quad (2)$$

Vector position $\vec{x}$ (x stream-wise, y span-wise and z depth-wise coord.), time t, fluid velocity $\vec{v}$ and pressure p (due to fluid motion) in equations (1)-(2) were rendered dimensionless dividing by D, D/U_∞, U_∞ and $\rho_\infty U_\infty^2$ respectively, where D is the prims width, U_∞, the average velocity of the fluid in the open channel and ρ_∞ the fluid density. The Reynolds number is then $Re = \frac{\rho_\infty U_\infty D}{\mu_\infty}$, being μ_∞ the fluid viscosity. The equation for the dimensionless prism displacement y_p is the following:

$$r\frac{d^2y_p}{dt^2} + c\frac{dy_p}{dt} + ky_p = \frac{1}{2}C_L \quad (3)$$

where the prism span-wise displacement y_p is render dimensionless using D and C_L is the force coefficient in y-direction generated by the fluid. The rest of dimensionless numbers are the following:

$$r = \frac{M}{\rho_\infty D^3}, c = \frac{C}{\rho_\infty U_\infty D^2}, k = \frac{K}{\rho_\infty U_\infty^2 D} \quad (4)$$

Free surface was modeled as a horizontal plane with null tangential stress and zero pressure. Uniform stream-wise velocity condition was used at the inlet of the domain, as this profile was observed in the experiment using PIV. No slip conditions were imposed at the channel walls and zero gradient values for the velocity components at the outlet. Zero gradient pressure conditions were imposed at the inlet, channel walls and the outlet of the domain.

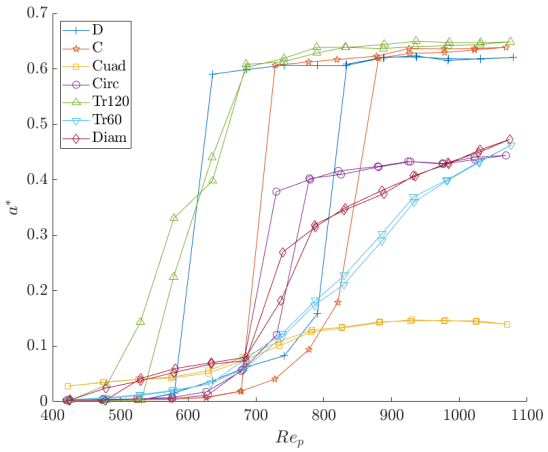

Figure 3: Dimensionless prism motion amplitude $a* = \frac{A}{D}$ vs. Re number obtained form the experiments for the different geometries.

4 Conclusions

Figure 3 shows the experimental dimensionless amplitudes $a* = \frac{A}{D}$ vs. Re number for the different geometries. D-shape, C-shape and triangular-120°-shape prism vibration reach the lateral walls of the channel when the Re exceeds a certain value (of the order of 600-700). D and C prism shapes also present a strong hysteresis. Detailed analysis of the prism wakes (in terms of its local topology) provided by the numerical simulations helped to understand the observed experimental trends.

References

Lee C, Wang W, Liu C, Fu L (2016) "Passive mixers in microfluidic systems: A review", *Chem. Eng. J.* **288**, 146–160.

Valeije A, Sastre F, Martín E, Velázquez A (2020) "Energy–efficient mixing generated by prescribed crosswise oscillations of a square prism in highly confined flows", *Chemical Engineering Science* **215**, 115456.

Hasheminejad S M & Fallahi R (2022) "Effects of cylinder cross-sectional geometry and blockage ratio on VIV-based mixing performance in two dimensional laminar channel flow". *Chemical Engineering and Processing - Process Intensification*, **177**, 108987.

2nd Spanish Fluid Mechanics Conference
Barcelona (2 - 5 July 2023)

Frequency response of Batchelor vortex

Carlos del Pino[1], Francisco J. Blanco–Rodríguez[2], Manuel Garrido–Martín[1], and Luis Parras[1]

cpino@uma.es

[1]Departamento de Ingeniería Mecánica, Térmica y de Fluidos, Universidad de Málaga, Spain
[2]Departamento de Ingeniería Aeroespacial y Mecánica de Fluidos, Universidad de Sevilla, Spain

We carried out a frequency response analysis of Batchelor vortex model in two different spatial configurations: punctual and annular jet. The theoretical base flow corresponds to the experimental setting of a wing model with airfoil NACA0012 for a chord-based Reynolds number Re_c=40000 and angle of attack of α=9°. We found that Batchelor model presents a gain in the annular jet configuration higher than the punctual jet for a pair of parameters k and ω_f. The results of this research work will be used to propose future candidates of active control.

1 Introduction

Aircraft generate wingtip vortices due to the finite length of their wingspans and the pressure difference between both sides of the wing model (Spalart, 2003). The generation of lift is associated with the presence of vortices. One of the best and widely extended theoretical descriptions of these trailing vortices corresponds to Batchelor's model (Batchelor, 1964) and its simplification called q-vortex. The stability of the q-vortex was studied by the pioneering work of Mayer and Powell (1992), among other studies that have been carried out up to the present day. These vortices are very stable in the range of Reynolds numbers (Re) and vortex intensity (q) corresponding to real aircraft and can, therefore, remain for a long time on airport runways (Jacquin and Pantano, 2002). This long-term presence on airport runways diminishes the number of take-off and landing operations.

2 Numerical methodology and results

The base flow has been obtained by adjusting Batchelor's model from 3D-2C PIV data. The experimental data has been divided into three areas: near (NF), intermediate (IF) and far-field (FF) since it provides a better understanding in terms of vorticity decay (Gutierrez-Castillo *et al.*, 2022).

We carried out the frequency response or the three-dimensional stability of the q-vortex, $[\boldsymbol{U}(r,\theta), P(r,\theta)]^T$, using two-dimensional simulations of the linear equations forced by a given out-of-plane (axial) wavenumber (Blanco-Rodríguez *et al.*, 2016). We will solve the equations in a rectangular periodic domain of size L_x and L_y and periodic boundary conditions. The cartesian base flow $[\boldsymbol{U}(x,y), P(x,y)]^T$ has infinitesimal three-dimensional perturbations for the velocity $\boldsymbol{u}(x,y,z) = (u_x, u_y, w)$ and pressure $p(x,y,z)$ governed by the forced incompressible linearised Navier-Stokes (LNS), which can be written as

$$\nabla \cdot \boldsymbol{u} = 0, \tag{1}$$

$$\frac{\partial \boldsymbol{u}}{\partial t} + (\boldsymbol{u}\cdot\nabla\boldsymbol{U} + \boldsymbol{U}\cdot\nabla\boldsymbol{u}) = -\nabla p + \frac{1}{Re}\Delta\boldsymbol{u} + \mathbf{f}, \tag{2}$$

where $\mathbf{f}$ denotes a volumetric forcing function. We used forcing jets that act only in the streamwise direction ($\mathbf{f} = F_z(x,y,t)\,\mathbf{e}_z$) varying harmonically in time with a frequency ω_f as

$$\mathbf{f}(x,y,t) = W_f(x,y)\left(\mathrm{e}^{i\omega_f t} + c.c.\right)\mathbf{e}_z. \tag{3}$$

The spatial structure of the forcing has a general mathematical expression given by

$$W_f(x,y) = \eta\,\mathrm{e}^{-\beta\, d^2(x,y)}, \tag{4}$$

where η is the maximum value of the forcing and β is a parameter that controls the jet spreading. Two different spatial configurations are proposed in this work: an annular structure centered in the vortex axis which is applied at $r = a_f$, and an off-axis (θ_f) single-point injection which is located at a distance a_f of the vortex center. The exact expressions of the forcing in both configurations are
Annular jet (AJ)

$$d^2(x,y) = (r - a_f)^2, \quad a_f = 2, \tag{5}$$

and Single-point injection (SPI)

$$d^2(x,y) = (x - x_c)^2 + (y - y_c)^2, \quad \theta_f = \pi/3, a_f = 2, \tag{6}$$

where $(x_c,\, y_c)$ is the vortex center.

Finally, we analyse the variation of the gain at large times, G_∞, for a constant k and ω_f. We define G_∞ as the value where $G(t)$ defined as

$$G(t;k,\omega) = \frac{\int_{\mathcal{D}} (u\,u^* + v\,v^* + w\,w^*)\,dx\,dy}{\int_{\mathcal{D}} W_f^2\,dx\,dy}. \qquad (7)$$

reaches a steady value at $t \to 120$.

In the Lamb-Oseen vortex, if we excite with a function at low frequencies and low wavenumbers, resonance modes are expected (Blanco-Rodríguez *et al.*, 2016) for both configurations (AJ and SPI). However, this is not the case when we consider the presence of the axial component in the q-vortex. In other words, for this type of vortices, we must excite the perturbations at a higher frequency ($\omega_f = 1$) and, consequently, we do obtain significant gains for small axial wavenumber values as shown in figure 1 where $G_\infty \approx 300$. Furthermore, the system selects the mode $m = 0$, as one should expect from an axisymmetric excitation of the annular jet.

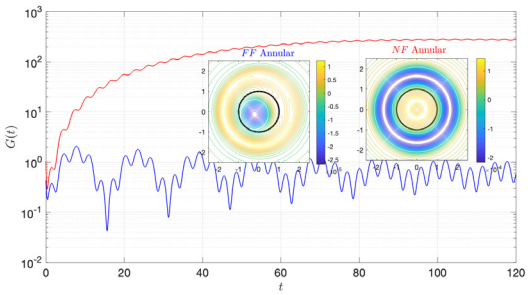

Figure 1: AJ configuration. Time evolution of the energy gain of Batchelor's experimental vortex in two areas ($q = 4$, $Re = 300$, NF) and ($q = 2.25$, $Re = 600$, FF) for the same wavenumber $\log_{10} k = -1$ and $\log_{10} \omega_f = 0$.

As in the annular case, we observe significant gains for the point excitation case for high frequencies and small axial wavenumber. Figure 2 also shows the combined effect of the Reynolds number and the vortex strength on the most unstable mode ($m = 0$ for the near field and m= 1 for the far field). Logically, smaller q values produce smaller energy gains.

3 Conclusions

In this work, we develop a stability analysis based on the frequency response of Batchelor vortex. We obtained the numerical base flow from experimental data. The Reynolds number based on the vortex core increases from 300 to 600, and the parameter q decreases from 4 to 2.25 as the vortex evolves spatially

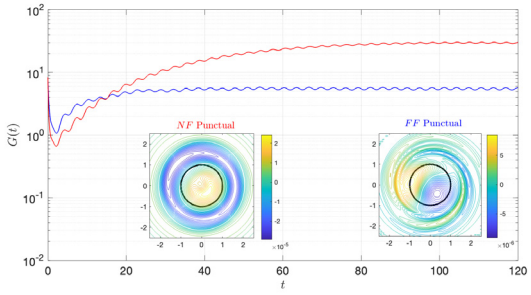

Figure 2: SPI configuration. Time evolution of the energy gain of Batchelor's experimental vortex in two areas ($q = 4$, $Re = 300$, NF) and ($q = 2.25$, $Re = 600$, FF) for the same wavenumber $\log_{10} k = -1$ and $\log_{10} \omega_f = 0$.

downstream. We observe two main changes concerning Lamb-Oseen vortex, i.e. by including the effect of axial velocity in the theoretical model. Firstly, the gains of Batchelor vortex are small for the same values of k and ω_f compared to the existing Lamb-Oseen vortex results. Secondly, and for a pair of values of k and ω_f, the annular configuration produces higher gains in the q-vortex compared to those obtained in Lamb Oseen vortex case.

References

Spalart, P (2003) "Airplane trailing vortices". *Annual Review of Fluid Mechanics*, **30**, 107–138.

Batchelor, G K (1964) "Axial flow in trailing line vortices". *Journal of Fluid Mechanics*, **20**, 645–658.

Mayer, E W & Powell, K G (1992) "Viscous and inviscid instabilities of a trailing vortex". *Journal of Fluid Mechanics*, **245**, 91–114.

Jacquin, L & Pantano, C (2002) "On the persistence of trailing vortices". *Journal of Fluid Mechanics*, **471**, 159–168.

Blanco-Rodríguez, F J & Parras, L & del Pino, C (2016) "Frequency response of Lamb-Oseen vortex". *Fluid Dynamics Research*, **48**, 061417.

Gutiérrez-Castillo, P & Garrido-Martín, M & Bölle, T & García-Ortiz, J H & Aguilar-Cabello, J & del Pino, C (2022) "Higher order dynamic mode decomposition of an experimental trailing vortex". *Physics of Fluids*, **34**, 107116.

Numerical Investigation of Cavitation Effects on the Vortex Shedding Behind a Wedge

Jian Chen and Xavier Escaler

Barcelona Fluids & Energy Lab (IFLUIDS), UPC, SPAIN

To determine the influence of cavitation on the dynamic behavior of alternating vortices shed behind a bluff body with a sharp edge, the realizable k-ε turbulence model coupled with the default Zwart cavitation model from ANSYS Fluent v18.2 have been used to simulate the cavitating and non-cavitating wake flow. The predicted vortex shedding frequencies show a good agreement with experimental measurements. In addition, the numerical results have permitted to assess plausible explanations elucidating the impact of cavitation on the vortex shedding frequency. In summary, a strong correlation between the vorticity dilatation and the change of vortex shedding frequency has been confirmed.

INTRODUCTION

The complex wake flow behind a bluff body with sharp edges is the result of the intricate interplay between the shear layers. Therefore, the formation of cavitation will certainly modify the dynamics and morphology of the alternating vortices shed downstream the trailing edge. In the present work the attention has been centered on the change of the shedding frequency which is parametrized by the dimensionless Strouhal number, St, as a function of the cavitation level which is quantified using the Cavitation number, σ. As illustrated in FIG. 1, previous experimental observations have confirmed that the existence of cavitation has a significant effect on St. Although there is no a widely accepted explanation of the effect of cavitation on the vortex shedding frequency, two potential mechanisms have been put forward in previous investigations. The first one argues that the alteration of the vortex shedding frequency arises from changes in vorticity dilatation due to the presence of cavitation, as suggested by Gnanaskandan et al. [1]. The second explanation, suggests that variations in the different characteristic lengths resulting from cavitation are responsible for changes in the shedding frequency as proposed by Kumar et al. [2].

In the present numerical study, a URANS turbulence model and a homogenous mixture cavitation model have been employed to simulate the cavitating wake flow behind a sharp-edged wedge. The obtained results have been used to assess the validity of the two aforementioned explanations elucidating the impact of cavitation on the vortex shedding frequency.

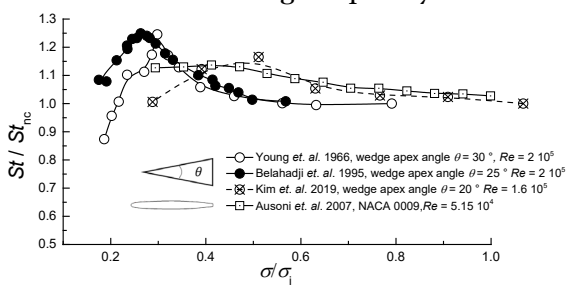

FIG 1. Experimental results of St evolution as a function of σ found in literature [3-6], where σ_i represents the cavitation inception and subscript nc denotes the non-cavitating regime.

NUMERICAL MODEL

In particular, the realizable k-ε turbulence model coupled with the default Zwart cavitation model from ANSYS Fluent v18.2 have been used. A uniform inflow with a velocity of 7.2 m/s has been set at the inlet. Depending on σ, the corresponding average static pressure has been fixed at the outlet following the experimental conditions from Kim et al. [5]. The computational domain and the discretized mesh are shown in FIG 2, where $b = 0.22$ m is the height of the wedge.

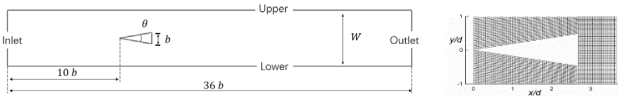

FIG 2. Computational domain and corresponding mesh around the wedge.

RESULTS AND DISCUSSION

FIG 3 presents the calculated St against σ and compares it with the experimental results showing a good agreement.

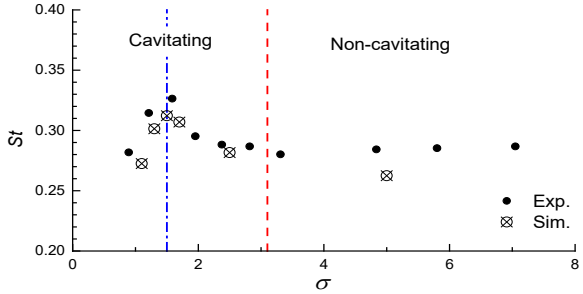

FIG 3. Comparison of experimental and numerical St as a function of σ.

Three distinct characteristic lengths have been defined: (i) the vortex formation length, L_V, from the location of the maximum cross-stream velocity fluctuations at the centerline to the base of the wedge; (ii) the cavity length, L_C, from the wedge base to the cavity edge where the mean vapor volume fraction, α_{mean}, equals 0.05; and (iii) the cavity formation length, L_{CF}, from the

location of the maximum vapor fraction fluctuations to the wedge base.

The evolutions of these lengths as a function of σ are shown in FIG 4. It can be observed that all of them increase monotonically as σ decreases, which implies that they cannot be used to explain the shedding frequency variation.

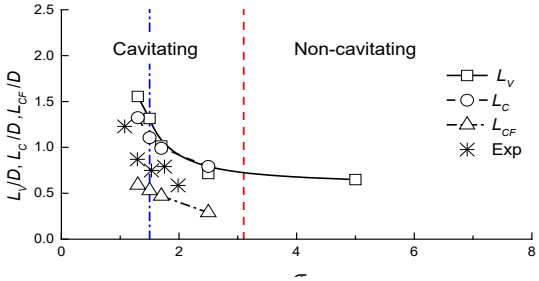

FIG 4. Evolution of the different length scales against σ.

If the vortex center is defined at the location of the local maximum vorticity around the near wake, FIG 5 displays the trajectory of the lower vortex center during one shedding period at various σ. Additionally, the evolution of the vorticity levels at the vortex center during one shedding period are plotted in FIG 6 as well as the corresponding linear curve fittings which permit to estimate the average rates of change.

FIG 7 illustrates the relationship between the average rate of change of vorticity at the vortex center and the corresponding St at different σ. These results demonstrate a strong linear relation between these two variables. Following the idea of Budich et al. [7], the variation of vorticity at the vortex center can be attributed to both vorticity dilatation and baroclinic torque, with the former being the dominant factor. Therefore, our finding supports the hypothesis that the presence of cavitation leads to vorticity dilatation, which in turn contributes to the variation in vortex shedding frequency.

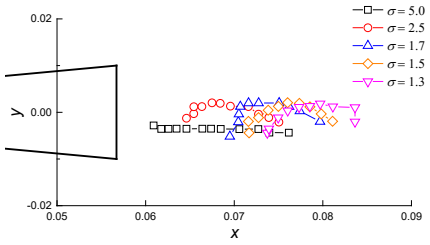

FIG 5. Evolution of lower vortex centers during one shedding period at different σ.

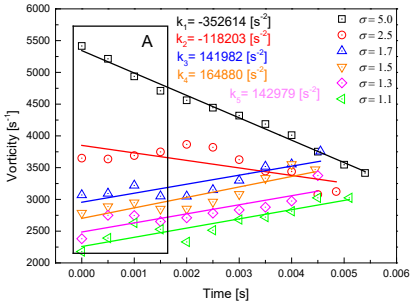

FIG 6. Evolutions of the vorticity levels at the vortex center during one shedding period at different σ.

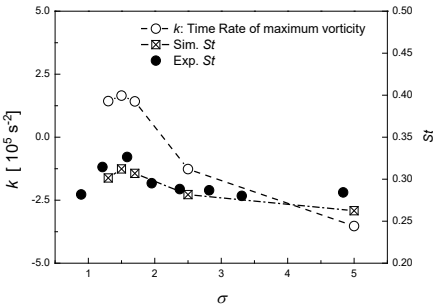

FIG 6. Average rate of change of the vortex center vorticity and the corresponding St at different σ.

CONCLUSIONS

The cavitating wake flow behind a wedge was numerically investigated uing a URANS model coupled with the Zwart cavitation model in Fluent. The changes of vortex shedding frequency induced by cavitation were in good agreement with experimental measurements. The numerical results showed a strong correlation between the vorticity dilatation and the change of vortex shedding frequency as proposed by Gnanaskandan et al [1]. Conversely, there seemed not to be a good correlation between the variations of characteristic lengths and the changes of vortex shedding frequency.

—

[1] Gnanaskandan A. & Mahesh K. (2016) “Numerical investigation of near-wake characteristics of cavitating flow over a circular cylinder”. Journal of Fluid Mechanics, 790, 453-491.
[2] Kumar P., Chatterjee D. & Bakshi S. (2017) “Experimental investigation of cavitating structures in the near wake of a cylinder”. International Journal of Multiphase Flow, 89, 207-217.
[3] Young J O. & Holl J W. (1966) “Effects of cavitation on periodic wakes behind symmetric wedges”. Journal of Basic Engineering, 03, 163-176.
[4] Belahadji B., Franc J P., & Michel J M. (1995) “Cavitation in the rotational structures of a turbulent wake”. Journal of Fluid Mechanics, 287, 383-403.
[5] Kim J H., Jeong S W., & Ahn B K. (2019) “Numerical and experimental study on unsteady behavior of cavitating flow around a two-dimensional wedge-shaped body”. Journal of Marine Science and Technology, 24, 1256-1264.
[6] Ausoni P., Farhat M., Escale X., Egusquiza E., & Avellan F. (2007) “Cavitation influence on von Kármán vortex shedding and induced hydrofoil vibrations”. Journal of Fluids Engineering, 8, 966–973.
[7] Budich B., Schmidt S J., & Adams N A. (2018)” Numerical simulation and analysis of condensation shocks in cavitating flow”. Journal of Fluid Mechanics, 838, 759-813.

2nd Spanish Fluid Mechanics Conference
Barcelona (2 - 5 July 2023)

Numerical Investigation on the Effect of Active Injection Location on the Frequency Response of a Batchelor Vortex

Manuel Garrido–Martín[1], Francisco J. Blanco–Rodríguez[2], Paloma Gutierrez–Castillo[1], and Carlos del Pino[1]

manolouma@uma.es

[1]Departamento de Ingeniería Mecánica, Térmica y de Fluidos, Universidad de Málaga, Spain
[2]Departamento de Ingeniería Aeroespacial y Mecánica de Fluidos, Universidad de Sevilla, Spain

This study investigates the effect of the variation of the active control application distance on the frequency response of a Batchelor vortex. The theoretical base flow pertains to the experimental configuration of a wing model with a NACA0012 airfoil at an angle of attack of α=9° and a chord-based Reynolds number of Re_c=40000. The injection was implemented using punctual and annular jet configurations. The findings of this research will serve as a basis for the optimization of the experimental parameters that characterize potential candidates for active control.

1 Introduction

Wingtip or trailing vortices are generated by aircraft due to the presence of lift forces in wings, remaining for a long time over airport runways. These persistent and highly rotating axial flows (Jacquin and Pantano, 2002) are, in fact, the main reason for the restrictive rules in air traffic management and close UAVs flight configuration (Z. Yu *et al.*, 2018). Therefore, the decay of trailing vortices is a fundamental problem in fluid mechanics and constitutes the basis of control applications that intend to alleviate the wake hazard.

A possible strategy to alleviate vortices would be an efficient vorticity reduction using an active control device based on pulsating spanwise blowing of a jet (J. H. García-Ortiz *et al.*, 2020). The importance of accurately tuning the experimental parameters that characterize the active control, namely the distance of application of the jet to the vortex core, has been previously noted (Tobias Bölle *et al.*, 2023), observing qualitative differences in the vortex response.

2 Numerical methodology and results

The numerical base flow used has been obtained by adjusting the theoretical parameters of Batchelor's model from 3D-2C PIV data. The experimental data has been divided into three areas: near (NF), intermediate (IF) and far-field (FF), since it provides a better understanding in terms of vorticity decay (Gutierrez-Castillo *et al.*, 2022).

We carried out the frequency response of the q-vortex, $[\boldsymbol{U}(r,\theta), P(r,\theta)]^T$, using 2-D simulations of the linear equations forced by a given out-of-plane (axial) wavenumber (Blanco-Rodríguez *et al.*, 2016). The equations are solved in a rectangular periodic domain of size L_x and L_y and periodic boundary conditions.

We used forcing jets that act only in the axial direction ($\mathbf{f} = F_z(x,y,t)\,\mathbf{e}_z$) varying harmonically in time with a frequency ω_f as

$$\mathbf{f}(x,y,t) = W_f(x,y)\left(\mathrm{e}^{i\omega_f t} + c.c.\right)\mathbf{e}_z. \tag{1}$$

The spatial structure of the axial forcing jet is given by

$$W_f(x,y) = \eta\,\mathrm{e}^{-\beta\, d^2(x,y)}, \tag{2}$$

where η is the maximum value of the forcing and β is a parameter that governs the jet spreading. Two different spatial configurations are proposed in this work: an annular jet (AJ) centered in the vortex axis which is applied at $r = a_f$,

$$d^2(x,y) = (r - a_f)^2, \quad a_f = 2, \tag{3}$$

and an off-axis (θ_f) single-point injection (SPI) which is located at a distance a_f of the vortex center

$$d^2(x,y) = (x - x_c)^2 + (y - y_c)^2, \quad \theta_f = \pi/3, a_f = 2, \tag{4}$$

where $(x_c,\, y_c)$ is the vortex center.

The variation of the gain at large times, G_∞, is studied for a constant k and ω_f. We define $G(t)$ as

$$G(t;k,\omega) = \frac{\int_{\mathcal{D}} (u\,u^* + v\,v^* + w\,w^*)\,dx\,dy}{\int_{\mathcal{D}} W_f^2\,dx\,dy}. \tag{5}$$

A parameter analysis has been conducted on the axial wavenumber k and the forcing frequency ω_f, revealing that the highest gains correspond to low values of k and values around $\omega_f = 0.1$. Once we select a particular set of these parameters, we study the effect of the distance of the forcing jet to the vortex core. Not only does the steady gain value change significantly, but the flow structures also exhibit two distinct patterns, as it can be observed in the axial vorticity plots shown in Figure 1.

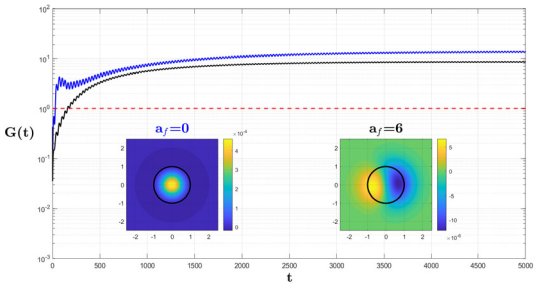

Figure 1: Time evolution of the energy gain of Batchelor's experimental vortex in two different SPI jet configurations, ($q = 4$, $Re = 300$, $a_f = 0$, in blue) and ($q = 4$, $Re = 300$, $a_f = 6$, in black) for the same axial wavenumber $k = 0.001$ and forcing frequency $\omega_f = 0.1$.

3 Conclusions

A parametric study of the active control of a trailing vortex has been achieved through the frequency response analysis of a Batchelor vortex varying the jet type and its distance to the vortex center. Different numerical base flows obtained from experimental data were also analyzed, ranging from the near to the far field of the vortex domain. The influence of the active control is clear not only in terms of the gain but also in the main vortex structure. Further investigation is necessary to complete the flow characterization to optimize the active control.

Acknowledgements

This research has been supported by the project PID2021-124692OA-I00 from the Ministerio de Ciencia e Innovación and from "Ayuda UMA Plan Propio".

References

Jacquin, L & Pantano, C (2002) "On the persistence of trailing vortices". *Journal of Fluid Mechanics*, **471**, 159–168.

Yu, Z & Qu, Y & Zhang, Y (2018) "Safe control of trailing UAV in close formation flight against actuator fault and wake vortex effect". *Aerospace Science and Technology*, **77**, 189–205.

García-Ortiz, J H & Blanco-Rodríguez, F J & Parras, L & del Pino, C (2020) "Experimental observations of the effects of spanwise blowing on the wingtip vortex evolution at low Reynolds numbers". *European Journal of Mechanics*, **80**, 133–145.

Bölle, T & Brion, V & Couliou, M & Molton, P (2023) "Experiment on jet–vortex interaction for variable mutual spacing". *Physics of Fluids*, **35**, 015117.

Gutiérrez-Castillo, P & Garrido-Martín, M & Bölle, T & García-Ortiz, J H & Aguilar-Cabello, J & del Pino, C (2022) "Higher order dynamic mode decomposition of an experimental trailing vortex". *Physics of Fluids*, **34**, 107116.

Blanco-Rodríguez, F J & Parras, L & del Pino, C (2016) "Frequency response of Lamb-Oseen vortex". *Fluid Dynamics Research*, **48**, 061417.

2nd Spanish Fluid Mechanics Conference
Barcelona (2 - 5 July 2023)

Parametric instability analysis of the flow past a square cylinder in the interface of two different-velocity streams

Reda ElMansy[1], Josep M Bergadà[1], and Fernando Mellibovsky[2]

reda.mohamed.yousif@upc.edu

[1]Departamento de Mecánica de Fluidos, Universitat Politècnica de Catalunya, Barcelona, Spain
[2]Departamento de Física, Universitat Politècnica de Catalunya, Barcelona, Spain

In the present manuscript, we place a square cylinder downstream of a splitter plate precisely located at cylinder mid-height and separating the top U_T and bottom U_B homogeneous streamwise velocities. Linear stability analysis is employed to analyze, as a function of the velocity ratio $R = U_T/U_B$, the different instability modes appearing for several splitter plate lengths and different gaps between the splitter plate and the square cylinder. The symmetries associated with each mode and their corresponding equations are also determined. Mode C instability is predominant in the vast majority of the cases studied.

1 Introduction

The flow past a square cylinder immersed in the wake of an upstream splitter plate separating two different-velocity streams is presented in the present manuscript. The top-to-bottom Reynolds numbers ratio $R \equiv Re_T/Re_B$ is evaluated in the range $R \in [2.4, 6.5]$, corresponding to a variation of the bulk Reynolds number $Re \equiv (Re_T + Re_B)/2 \in [95.5, 210]$. Based on linear stability analysis theory, the paper analyses which three-dimensional modes destabilise the two-dimensional vortex-shedding solution at different velocity ratios R, splitter plate lengths $L_p \in [6.5, 9, 13, 20]$ and splitter plate-square cylinder gaps $G \in [2.5, 4, 6]$, see Figure 1. The same configuration was initially studied two-dimensionally by Mushyam and Bergada (2017); An et al. (2020) and three-dimensionally by ElMansy et al. (2022a,b). In fact, the present research is the continuation of authors' previous work ElMansy et al. (2022a,b), where employing the same domain configuration and fixing the splitter plate length as well as the distance between the splitter plate trailing edge and the cylinder center $L_p = 6.5$ and $G = 2.5$, respectively, extensive three-dimensional Direct Numerical Simulations (3D-DNS) were undertaken. The incompressible viscous flow is evolved in time with the (Incompressible Navier-Stokes solver) of NEKTAR++, based on spectral/hp element method. The baseline configuration $L_x^u = 9D$, is discretized using $120x107$ quadrilateral elements with polynomial expansions of second order in the streamwise-cross-stream plane following ElMansy et al. (2022a,b). A particularly refined mesh has been set-up in the vicinity of sharp edges and the wake to adequately resolve complex flow field features. Time is discretized via second order accurate velocity correction splitting scheme with a time step of $\Delta t = 0.0045$. Extensive checks for domain size, mesh resolution and numerical schemes are to be found in (ElMansy et al., 2022a,b). While the cross-stream resolution is kept constant at $N_y = 107$, the streamwise resolution has been varied in the range $N_x \in [120, 200]$ in order to keep a similar mesh density when considering the different splitter plate lengths L_p and gaps G employed in the present study.

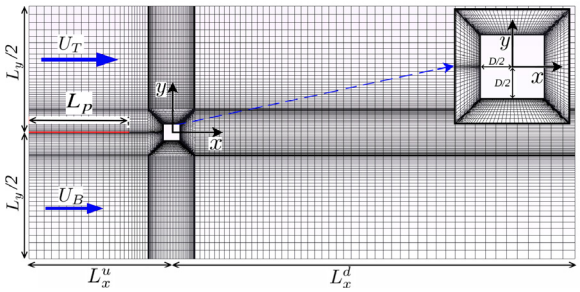

Figure 1: Sketch of the computational domain and mesh. The square cylinder, of side D, is centred at the origin. The splitter plate (Red), of length L_p and negligible thickness, starts at the upstream boundary, located at $x = -L_x^u$, and extends horizontally at mid-height. The downstream boundary is located at $x = L_x^d$ and the top and bottom boundaries at $y = \pm L_y/2$.

2 Results

The study summarizes the topology and symmetries of all instability modes appearing, discussing and comparing them with those typical of similar flow problems. The underlying two-dimensional vortex-

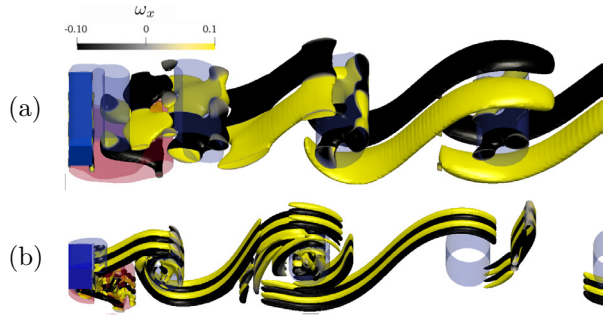

Figure 2: Instantaneous snapshot of dominant eigenmodes for modes A* and B*. (a) mode-A* for (R, λ_z) = $(2.8, 6.28)$, ($L_p = 9D, G = 2.5D$) and using Iso-surfaces of $Q = 0.09$, (b) mode-B* for (R, λ_z) = $(6.5, 1.05)$, ($L_p = 6.5D$, $G = 4D$) and using Iso-surfaces of $Q = 0.01$. Spanwise vortices are shown with transparent iso-surface for $\tilde{\omega}_z = \pm 0.1$.

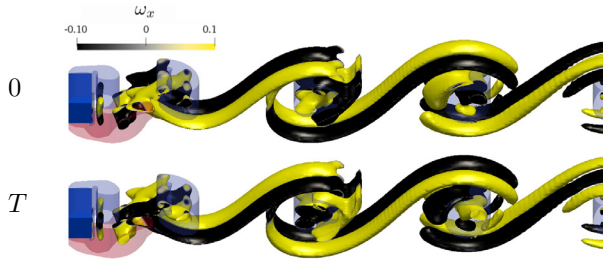

Figure 3: Instantaneous snapshots of dominant eigenmode mode-C for (R, λ_z) = $(3.4, 2.5)$, ($L_p = 9D, G = 2.5D$). Normalised streamwise vorticity ($\tilde{\omega}_x \in [-0.1, 0.1]$) colourmaps and Iso-surfaces of $Q = 0.09$ are used to display nonlinear three-dimensional vortical structures. Spanwise vortices are shown with transparent iso-surface for $\tilde{\omega}_z = \pm 0.1$.

shedding flow resembles an asymmetric Kármán vortex street with vortices only showing on the high-velocity side of the wake. Modes akin to the A and B types that characterise the three-diensionalisation of the flow past a circular cylinder are observed within some parameters range. Mode C instability appears under almost all operational conditions studied.

Figure 2a, introduces the long wavelength mode A*, $\lambda_z = 6.28$, which is observed when the gap distance is fixed to $G/D = 2.5$ and for splitter plate lengths in the range $L_p/D \in [9, 13, 20]$. Mode B*, shown in figure 2b, is defined as the shortest wavelength mode $\lambda_z \in [1.05, 1.5]$ and it is observed for gaps ranging from $G/D \in [2.5, 4]$ while keeping the splitter plate length to $L_p/D = 6.5$. Using the streamwise vorticity to characterise these two unstable modes, brings up the following common equation:

$$\tilde{\omega}_x(x, y, z, t) = \tilde{\omega}_x(x, y, z, t + T) \text{ (modes A*, B*)} \quad (1)$$

Mode C instability arises under all conditions studied, except when the splitter plate is attached to the square cylinder front face and the velocity ratio $R = 1$, see Figure 3. It has associated a spanwise wavelength of $\lambda_z \approx 2.5$ and it is characterized by a spanwise shifting of half spanwise wavelength every vortex shedding cycle. Its corresponding streamwise vorticity equation is:

$$\tilde{\omega}_x(x, y, z, t) = -\tilde{\omega}_x(x, y, z, t + T) \quad \text{(mode C)} \quad (2)$$

To further understand what triggers the different modes and in order to remove some of the parameters which affect the flow performance, we decided to keep the bulk Reynolds $Re = (U_T + U_B)D/2\nu$ constant and place the splitter plate attached to the square cylinder front face. When the Reynolds numbers below and above the splitter plate were identical, the inception of the longest wavelength mode, mode A, appeared whenever the Reynolds number was slightly higher than $Re = 270$. With the Reynolds number increase, mode A, keept growing and for a $Re \approx 460$ mode B appeared, until $Re = 540$, both modes A and B, coexisted, mode C never appeared.

3 Conclusions

Via linear stability analysis, the different modes, A*, B*, A, B and C, are obtained as a function of L_p, G and R. Mode C instability is observed in all cases where the input flow is asymmetric $R \neq 1$.

References

Mushyam, A., Bergada, J.M.(2017) "A numerical investigation of wake and mixing layer interactions of flow past a square cylinder". *Meccanica*, **52(1)**, 107-123.

An, B., Bergadà, J.M., Mellibovsky, F.(2020) "Numerical investigation on the flow around a square cylinder with an upstream splitter plate at low Reynolds numbers". *Meccanica*, **55(5)**, 1037-1059.

El Mansy, R., Bergadà, J.M. and Sarwar, W. and Mellibovsky, F.(2022) "Aerodynamic performances and wake topology past a square cylinder in the interface of two different-velocity stream". *Physics of Fluids*, **34(6)**, 064106.

El Mansy, R., Sarwar, W., Bergadà, J.M., Mellibovsky, F.(2022) "Square cylinder in the interface of two different velocity streams". *Journal of Fluid Mechanics*, **950**, A30.

2nd Spanish Fluid Mechanics Conference
Barcelona (2 - 5 July 2023)

Unraveling the Generation and Destruction Mechanisms of Arch Vortices in Urban Fluid Flows: A Comprehensive Analysis

Eneko Lazpita[1], Álvaro Martínez-Sánchez[2], Sergio Hoyas[3]
Ricardo Vinuesa[4] , and Soledad Le Clainche[1]

e.lazpita@upm.es

[1]School of Aerospace Engineering, Universidad Politécnica de Madrid, Spain
[2]École nationale supérieure de l'aéronautique et de l'espace, ISAE-SUPAERO, France
[3]Instituto de Matematica Pura y Aplicada, Universitat Politécnica de València, Spain
[4]FLOW, Engineering Mechanics, KTH Royal Institute of Technology, Sweden

Our study employs higher-order dynamic mode decomposition to analyze a high-fidelity database of turbulent flow in an urban environment featuring two buildings separated by a certain distance. Through our analysis, we were able to identify and document the generation and destruction mechanisms of the well-known arch vortex forming on the leeward side of the first building, which may play a significant role in the dispersion of pollutants. Our findings demonstrate that the arch vortex's formation leads to an increase in pollutant concentration, highlighting the crucial importance of the reported mechanisms in promoting urban sustainability.

1 Introduction

The study of fluid dynamics in urban environments has gained significant attention in recent years due to the numerous practical applications and challenges that arise from the interaction between the built environment and the natural flow of air. One of the most fascinating phenomena observed in these fluid flows is the formation of arch vortices, which are swirling patterns of air that form over urban canyons and between buildings. Arch vortices have been found to have significant impacts on the dispersion of pollutants, wind comfort, and urban climate(1).

The objective of this study is to offer a fresh perspective on the current understanding of the generation and destruction mechanisms of arch vortices in urban fluid flows. To achieve this goal, sophisticated modal decomposition tools will be employed. By utilizing these advanced techniques, the study seeks to uncover new insights into the physical principles that govern the formation of arch vortices, as well as the factors that contribute to their persistence and dissipation in urban environments. Ultimately, the findings of this study may have important implications for the design and planning of urban areas, as well as for the mitigation of the negative impacts of arch vortices on urban air quality and climate.

2 Methodology

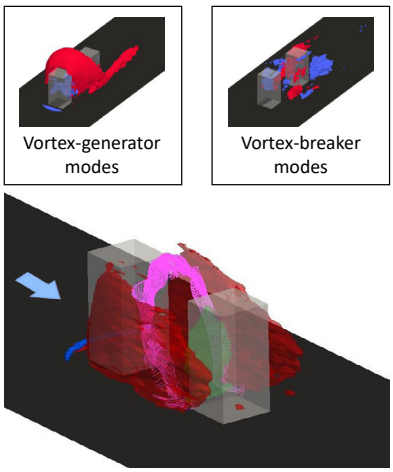

Figure 1: The figure illustrates the classification of various modes obtained using HODMD. The bottom panel shows the main velocity and vortical structures of the flow. The top panels depict the streamwise velocity of the generator and breaker modes.

In this work, we have employed various modal-decomposition techniques, including proper-orthogonal decomposition (POD)(2), higher-order dynamic-mode decomposition (HODMD)(3) and spatio-temporal Koopman decomposition

(STKD)(4). The POD decomposes a snapshot matrix into a set of orthonormal basis vectors (modes) that capture the dominant spatial and temporal features of the system represented by the snapshots. The HODMD decomposes spatio-temporal data $\boldsymbol{v}(x, y, z, t_k)$, collected at time instant t_k (for convenience expressed as $\boldsymbol{v}_k$), as an expansion of M modes $\boldsymbol{u}_m$, which are weighted by an amplitude a_m as:

$$\boldsymbol{v}(x, y, z, t_k) \simeq \sum_{m=1}^{M} a_m \boldsymbol{u}_m(x, y, z) e^{(\delta_m + i\omega_m)t_k}, \quad (1)$$

for $k = 1, \ldots, K$. These modes oscillate in time with frequency ω_m and may grow, decay or remain neutral in time according to their growth rate δ_m.

3 Results

We conducted a LES simulation of turbulent flow within a simplified urban setting containing two obstacles (5). The spacing between the buildings was varied, resulting in three distinct regimes: the skimming-flow (SF), the wake-interference (WI) and the isolated-roughness (IR), which go from the smallest spacing to the largest one respectively.

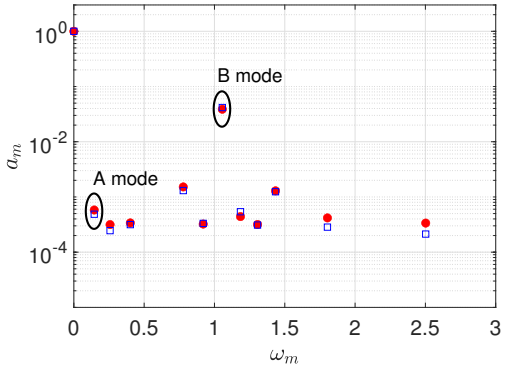

Figure 2: The temporal modes obtained with HODMD for the WI case are displayed on a spectrum that shows their amplitudes plotted against their frequencies.

In this study, we analyzed the coherent structures in the fluid flow of the databases obtained with these simulations using various modal decomposition tools. The analysis allowed us to identify the primary mechanisms present in the flow for both spatial and temporal analysis. For instance, the HODMD technique allowed us to differentiate between two distinct mode groups: generator or A modes and breaker or B modes. The generator modes could be associated with the generation of the arch vortex, while the breaker modes suggest to be related to the destruction and shedding of these primary structures. Figure 2 presents the frequencies associated with these modes.

4 Conclusions

According to existing literature, coherent structures can impede the dispersion of pollutants. Therefore, it may be worthwhile to reduce the presence and intensity of A modes while promoting B modes. To delve deeper into this idea, further investigations are needed, specifically ones that involve multi-phase flows. These studies would aim to establish a connection between the aforementioned flow structures and the mechanisms that drive particle dispersion.

More details can be found at Lazpita el al.(6) and will be presented by the time of the conference.

References

[1] B. Monnier, S. A. Goudarzi, R. Vinuesa, and C. Wark, "Turbulent structure of a simplified urban fluid flow studied through stereoscopic particle image velocimetry," *Boundary-layer meteorology*, vol. 166, pp. 239–268, 2018.

[2] J. L. Lumley, "The structure of inhomogeneous turbulent flows," *Atmospheric turbulence and radio wave propagation*, pp. 166–178, 1967.

[3] J. M. Vega and S. Le Clainche, *Higher order dynamic mode decomposition and its applications*. Academic Press, 2020.

[4] S. L. Clainche and J. M. Vega, "Spatio-temporal koopman decomposition," *Journal of Nonlinear Science*, vol. 28, pp. 1793–1842, 2018.

[5] M. Atzori, P. Torres, A. Vidal, S. L. Clainche, S. Hoyas, and R. Vinuesa, "High-resolution large-eddy simulations of simplified urban flows," *arXiv preprint arXiv:2207.07210*, 2022.

[6] E. Lazpita, Á. Martínez-Sánchez, A. Corrochano, S. Hoyas, S. Le Clainche, and R. Vinuesa, "On the generation and destruction mechanisms of arch vortices in urban fluid flows," *Physics of Fluids*, vol. 34, no. 5, p. 051702, 2022.

[7] Á. Martínez-Sánchez, E. Lazpita, A. Corrochano, S. Le Clainche, S. Hoyas, and R. Vinuesa, "Data-driven assessment of arch vortices in simplified urban flows," *International Journal of Heat and Fluid Flow*, vol. 100, p. 109101, 2023.

2nd Spanish Fluid Mechanics Conference
Barcelona (2 - 5 July 2023)

Vortex-induced vibrations of a rigidly linked pair of circular cylinders

Francisco Huera-Huarte[1]

francisco.huera@urv.cat

[1]Departament of Mechanical Engineering, Universitat Rovira i Virgili, Spain

Vortex-induced vibration (VIV) experiments with an elastically mounted low mass-damping system have been conducted. The system consists of a pair rigidly linked circular cylinders with the same mass m, length L and diameter D, and it is submerged in a uniform flow with velocity U_∞, generated by the free surface channel at the Laboratory for Fluid-Structure Interaction (LIFE - labfsi.com) of the Universitat Rovira i Virgili. The cylinders are separated a distance S_x in the flow direction and S_y in the perpendicular to the flow or transverse direction (see lower part of fig. 1). The set-up hangs from an air bearing system to minimise friction when oscillating. A similar set-up was used by the author with a system showing the dynamic response of side-by-side (Huera-Huarte, 2018) and tandem cylinders (Huera-Huarte, 2018).

In one of the configurations studied, different S_x and S_y are used, ranging from the tandem or in-line positioning to the side-by side configuration. Restoring forces are provided by a set of springs with stiffness constant k.

In a second configuration, the system is not allowed to move transversely but rotationally around point O (see fig. 1), with inertia (I_O). Restoring forces are provided by a torsional spring with constant k_O. Finally, combinations of both motions, i.e. a system with two degrees-of-freedom, are considered.

Given all these scenarios, the dynamic response, including transverse and rotational amplitude, frequency of oscillation and rotation, together with the fluid excitation, were measured, covering a large parametric space, consisting of variations in the separation and the free stream velocity, leading to a wide range of reduced velocities and Reynolds numbers.

The flow dynamics in the near wake was also measured using planar particle image velocimetry (DPIV). The upper part of fig. 1 shows dimensionless vorticity maps at approximately half the length of the system, in a case in which the cylinders were in tandem configuration ($S_x = 1.25D$ and $S_y = 0$). At the same Reynolds number and reduced velocity, a single cylinder would respond to vortex shedding with its maximum amplitude, but in this case the wake is heavily altered by the trailing one, leading to practically no vibrations.

The rich fluid-structure interaction phenomena observed in the experiments will be discussed and analysed in detail.

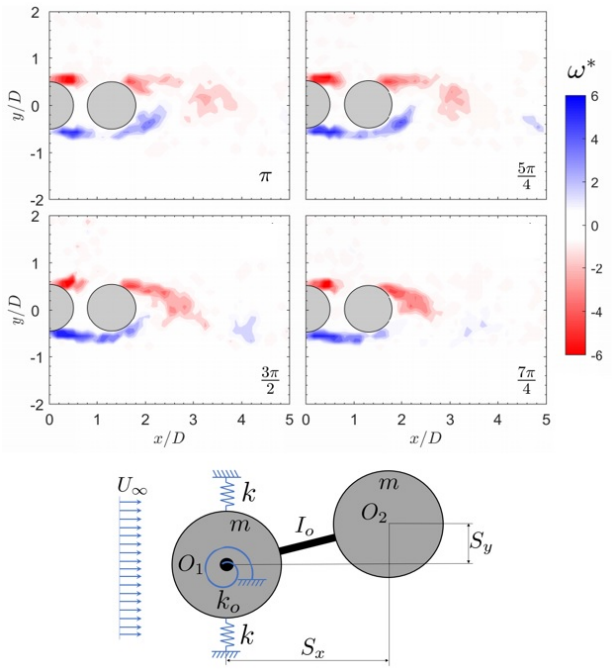

Figure 1: Dimensionless vorticity maps for a case with both rigidly linked cylinders in a pure in-line configuration, free to move with a single degree-of-freedom, transversely to the incoming flow. In the lower part of the figure a cross-sectional schematic view of the experiments is shown.

References

Huera-Huarte F. (2018). Dynamics and excitation in a low mass-damping cylinder in cross-flow with side-by-side interference. *J. Fluid Mech.*, **850**, 370–400.

Huera-Huarte F & Jiménez-González J. I. (2019). Effect of diameter ratio on the flow-induced vibrations of two rigidly coupled circular cylinders in tandem. *J. Fluids Struct.*, **89**, 96–107.

AUTHORS INDEX


CIMNE
EXCELENCIA
SEVERO
OCHOA